Physics of the Solid State, Vol. 43, No. 5, 2001, pp. 801–807. Translated from Fizika Tverdogo Tela, Vol. 43, No. 5, 2001, pp. 769–775.

METALS AND SUPERCONDUCTORS

Temperature Behavior of Electron Transport in Normal-Metal–HTSC Heterojunctions

F. V. Komissinskiĭ[1, 2], G. A. Ovsyannikov[1], and Z. G. Ivanov[2]

[1]*Institute of Radio Engineering and Electronics, Russian Academy of Sciences, Mokhovaya ul. 11, Moscow, 103907 Russia*
e-mail: gena@hitech.cplire.ru

[2]*Chalmers Institute of Technology, S-41296 Göteborg, Sweden*

Received July 25, 2000; in final form, October 6, 2000

Abstract—Current transport in micron-sized normal-metal–high-temperature superconductor heterojunctions ($Au/YBa_2Cu_3O_{6+x}$) was studied for two crystallographic orientations of YBCO films. It is shown that depending on the transport-current flow direction relative to the crystallographic axes of the YBCO film, the electronic transport properties of Au/YBCO heterojunctions with highly transparent boundaries change from quasi-tunneling (along the YBCO *c* axis) to close-to-Ohmic (in the directions lying in the YBCO basal plane). © *2001 MAIK "Nauka/Interperiodica".*

INTRODUCTION

The electronic parameters of high-temperature superconducting (HTSC) metal–oxide materials are very sensitive to oxygen content. $YBa_2Cu_3O_{6+x}$ (YBCO), a typical representative of the HTSCs, is an insulator for oxygen contents of $0 < x < 0.4$ and a superconductor exhibiting metallic conduction along the basal planes at oxygen doping levels of $0.4 < x < 1$ (see, e.g., [1]). An HTSC layer close to an interface with a vacuum or other material can change its parameters from those of a metal to those of an insulator, depending on the extent of external influence on the oxygen content (heating, precipitation of carbon dioxide from the atmosphere, etc.). Another essential feature of the HTSCs is the high anisotropy of their electron transport characteristics [2]. The conductivities for currents flowing along the *c* axis of YBCO and the directions lying in the (*a*–*b*) YBCO basal plane differ greatly. As a result, when the transport current changes its orientation with respect to the crystallographic axes of a superconductor, the ratios of the characteristic resistances of the normal-metal–HTSC (N–S_d) interface, $r = R_N S$ (R_N is the resistance of a junction of area S), which characterize the boundary transparency, can change a hundredfold [3, 4]. Depending on the actual YBCO film orientation and the technology of preparation, N–S_d heterojunctions experimentally exhibit a large variety of properties, from quasi-tunneling [5, 6] to Ohmic characteristics [7]. Heterojunctions with a low boundary transparency ($r > 10^{-4}\ \Omega\ \text{cm}^2$) usually have quasi-tunneling characteristics, namely, tunneling at low voltages and an increase in resistance with decreasing temperature [6]. This experimental observation suggests that the surface HTSC layer was depleted in oxygen to the extent that it became an insulator. The quasi-tunneling characteristics of the heterojunctions were not questioned in these conditions. However, in order for the surface layer to be an insulator while the remaining part of the HTSC film is doped by oxygen to the extent corresponding to the superconducting state, one has to admit substantial oxygen content gradients across the film thickness. This condition can hardly be realized in an experiment even when oxygen diffusion along the *c* axis is weak. The *I*–*V* characteristics of N–S_d junctions with a low-transparency boundary in both *c* and *a*–*b* oriented HTSC films frequently exhibited conductivity anomalies even at low voltages, namely, a conductivity peak at zero bias. The reasons for this anomaly were attributed either to the presence of ferromagnetic impurities in the HTSC surface layer [8, 9] or to the formation of bound states as a result of the Andreev reflection at the interface between a *d*-type superconductor and an insulator [10–12].[1]

In this work, the experimental data obtained on the temperature dependence of the resistance of N–S_d heterostructures and the shape of the *I*–*V* curves suggest a conclusion on the mechanism of conduction in normal-metal–HTSC heterojunctions for current flow both along the *c* axis and along the directions lying in the basal plane of a YBCO.

1. YBCO FILMS AND EXPERIMENTAL SAMPLES

The sequence of the technological operations used to fabricate Au/YBCO heterojunctions is presented in Fig. 1 [13, 14]. Epitaxial YBCO films 150 nm thick were grown by laser ablation at temperatures of 780–800°C and at an oxygen pressure of 0.8 mbar. Epitaxial *c*-oriented YBCO films were grown on (001)$LaAlO_3$

[1] The anomalies in the *I*–*V* curves appearing at low bias across our junctions will be discussed in a forthcoming paper.

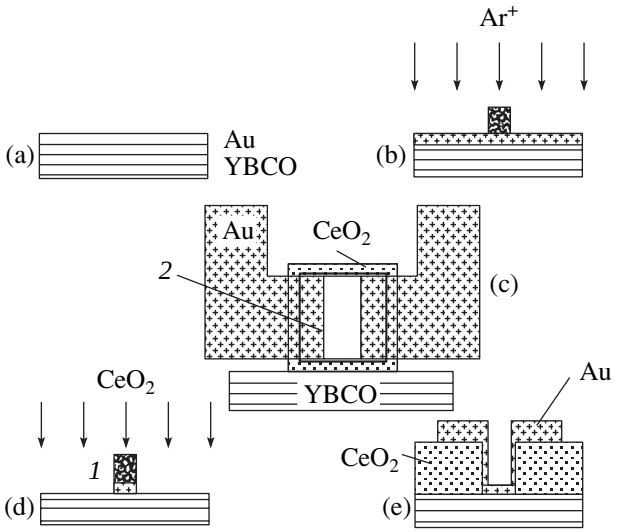

Fig. 1. Sequence of Au/YBCO junction fabrication steps: (a) Deposition of the Au(20 nm)/YBCO(150 nm) double-layer structure; (b) formation of the junction region by photolithography and ion milling; (c) junction geometry (top view); (d) deposition of the 150-nm thick CeO_2 insulating layer; and (e) formation of Au contact pads. (*1*) Photoresistor and (*2*) contact region.

and (110)$NdGaO_3$ (NGO) substrates. Heterostructures fabricated on these substrates provide information on the transport current flowing along the [001]YBCO direction; we shall subsequently call such structures direct heterojunctions (DH). In the work, we also used tilted heterojunctions (TH) in which the [001]YBCO crystallographic axis deviates from the normal to the substrate plane. These films were grown epitaxially on (120)NGO substrates. After YBCO film deposition, a thin layer of normal metal (Au) 20 nm thick was deposited on it without impairing the vacuum (Fig. 1a). The Au layer thickness was increased to 100 nm by additional *ex situ* electron beam deposition (entailing vacuum deterioration). A heterojunction of area $S = 10 \times 10$ μm was produced by photolithography and ion beam milling in an Ar atmosphere (Fig. 1b). To avoid undesirable contact with the YBCO face end, the heterojunction regions were isolated by an amorphous CeO_2 film deposited by laser ablation at 60°C in an oxygen environment at a pressure of 0.2 mbar (Fig. 1d). The isolating layer in the region of the heterojunctions and of the contact pads was removed by explosive photolithography (Fig. 1e). The spatially separated supply of the current and voltage provided in the Au/YBCO heterojunction geometry (Fig. 1c) permits one to measure the heterojunction characteristics by the four-probe technique for $T < T_c$ of the YBCO.

We measured curves *I–V* and the dependences of the resistance *R* on temperature *T* (4.2–300 K) with bias currents in the range 1–5 μA for Au/YBCO heterojunctions and test bridges 4 μm wide located on the same substrate. The critical temperature and width of the superconducting transition in the YBCO films (T_c and ΔT_c, respectively) were found from the temperature dependence of the magnetic susceptibility for the Au/YBCO heterostructure before junction topology formation. For the *c*-oriented YBCO films, we have $T_c > 88$ K and $\Delta T_c = 0.5$ K. The YBCO films grown on (120)NGO had slightly worse superconducting parameters ($T_c > 85$ K and $\Delta T_c \leq 2$ K) because of a lower oxygen content. A decrease in T_c and ΔT_c is typical of films with the *c* axis off the surface normal [14, 15].

X-ray diffraction measurements (θ–2θ scanning) showed that the epitaxial relation (001)YBCO//{110}NGO is retained for both the (110)NGO and (120)NGO substrates; in other words, the [001] direction of the YBCO film is always parallel to the ⟨110⟩NGO directions (if there are more than one of them). The (120)NGO substrates have two directions, [110] and $[1\bar{1}0]$NGO; therefore, two domains, (101) and (109)YBCO, form in the growth, whose *c* axes make angles $\psi = 71.6°$ and 18.4° with the surface normal, respectively. Our estimates showed that both domains are present in the YBCO films on the [120]NGO substrates in equal amounts. For both domains, the condition (001)YBCO//{110}NGO holds and one of the basal plane axes (either [100]YBCO or [010]YBCO) lies in the substrate plane. The current in a TH flows primarily along the basal YBCO planes. The contribution of the *c*-axis current in this case is small because of the high YBCO resistivity in this direction. By contrast, in a DH, the transport current flows along the YBCO *c* axis because of the small area of the junction along the *a–b* planes. The parameters of the experimental samples studied are given in the table. Note that at the values $r = 10^{-5}$–10^{-7} Ω cm^2 observed in the experiment, the characteristic current spreadout length $L_\perp = \sqrt{d_{Au} r/\rho_{Au}}$ ($d_{Au} = 100$ nm and $\rho_{Au} = 10^{-6}$ Ω cm are the thickness and electrical resistivity of the gold film, respectively) [16] significantly exceeds the heterojunction dimensions. Hence, the current spreadout process should not affect the electrophysical parameters of the heterojunctions.

2. EXPERIMENTAL RESULTS

Figure 2 displays *R*(*T*) plots measured by the three-point technique (with the current and voltage applied to one point on the YBCO electrode) for two types of Au/YBCO heterojunctions. For $T > T_c$, the *R*(*T*) relations of DHs exhibit metallic conduction, i.e., a decrease in the resistance with temperature, which is characteristic of a transport current flowing in the basal plane of an YBCO film. This is due to the predominant contribution to the measured *R*(*T*) relation of the conducting HTSC electrode films, which carry current in the YBCO *a–b* planes. At the same time, when the master transport current propagates along the $[\bar{2}10]$NGO direction in a TH, one observes an increase of *R* typical

Low–temperature heterojunction parameters

Sample	T_c, K	R_N ($T = T_c$, $V = 0$), Ω	$R_d(0)$, Ω	$R_d(0)/R_N$	R_NS, μΩ cm^2
			DH		
P32J2	89.3	33.2	103.0	3.1	33.2
P32J3	89.5	19.5	52.0	2.7	19.5
P32J4	89.9	22.9	55.3	2.4	22.9
P34J3	89.2	56.1	102.0	2.1	56.1
			TH		
H2J2	18.7	1.6	0.7	0.4	1.6
H2J3	48.2	1.6	1.0	0.6	1.6
H2J4	40.1	1.8	1.3	0.7	1.8
H5J2	42.3	0.4	0.2	0.5	0.4
H5J3	60.3	0.3	0.2	0.7	0.3
H5J4	61.1	0.5	0.3	0.6	0.5

of transport along the *c* axis of the YBCO. The temperatures T_c of the microbridges in the THs studied turn out to be lower than those of the YBCO films immediately after Au/YBCO heterostructure deposition, which is apparently due to oxygen escaping from the surface layer of the YBCO films in the course of ion milling. In the THs, oxygen diffuses out of the basal planes of the YBCO films on the surface much more intensively than in the DHs. As a result, the T_c of the bridges on the (120)NGO substrates is lower than that of the original Au/YBCO heterostructures by 5–10 K.

The $R(T)$ relations change dramatically for $T < T_c$; more specifically, in the DHs, one observes a growth characteristic of the superconductor–insulator–normal-metal tunneling junctions (SIN, with I standing for the insulator), while in the THs, the resistance falls off monotonically with decreasing temperature.

Figure 3 presents the dependences of the differential resistance of the Au/YBCO heterojunctions on the bias $R_d(V)$. One likewise observes substantial differences both in the characteristic interface resistance *r* and in the field dependence. For the THs, $r_{ab} = 10^{-7}$–10^{-6} Ω cm^2, whereas r_c for the DHs is larger by one to two orders of magnitude (see the table).

To estimate the interface surface, we studied the YBCO film surface morphology with atomic force microscopy. As shown by YBCO film profile measurements, the maximum surface roughness of the (001)YBCO films over an area of 1×1 μm is $\delta_c \approx 4$ nm (in Fig. 4a, rms = 2 nm). The roughness of tilted YBCO films on (120)NGO is substantially larger: $\delta_{ab} \approx 45$ nm (Fig. 4b), with rms = 50 nm.

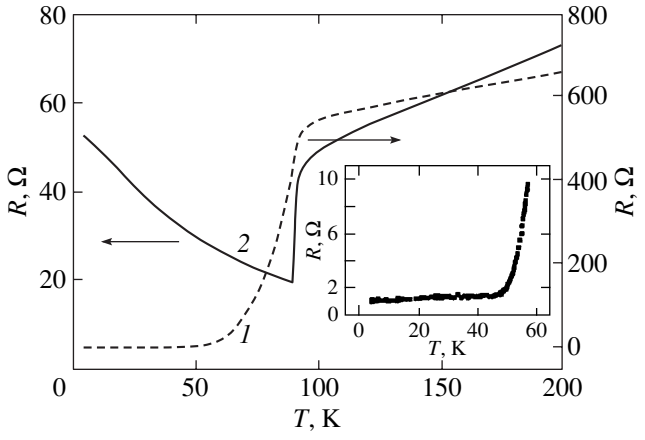

Fig. 2. $R(T)$ dependences for (*1*) TH H2J3 and (*2*) DH P32J3. Inset shows the low-temperature part of the $R(T)$ plot for the TH H2J3.

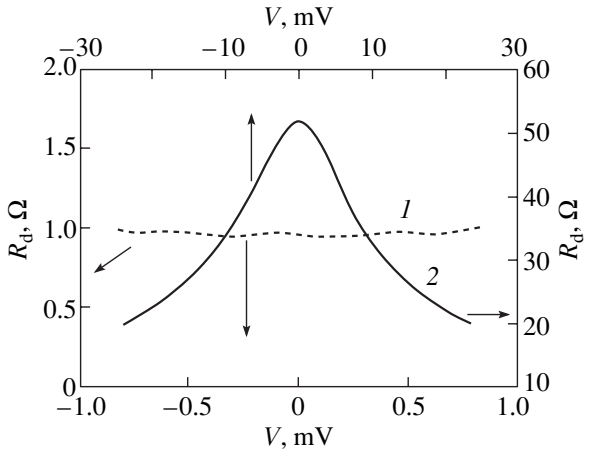

Fig. 3. $R_d(V)$ relations for (*1*) TH H2J3 and (*2*) DH P32J3 measured at $T = 4.2$ K.

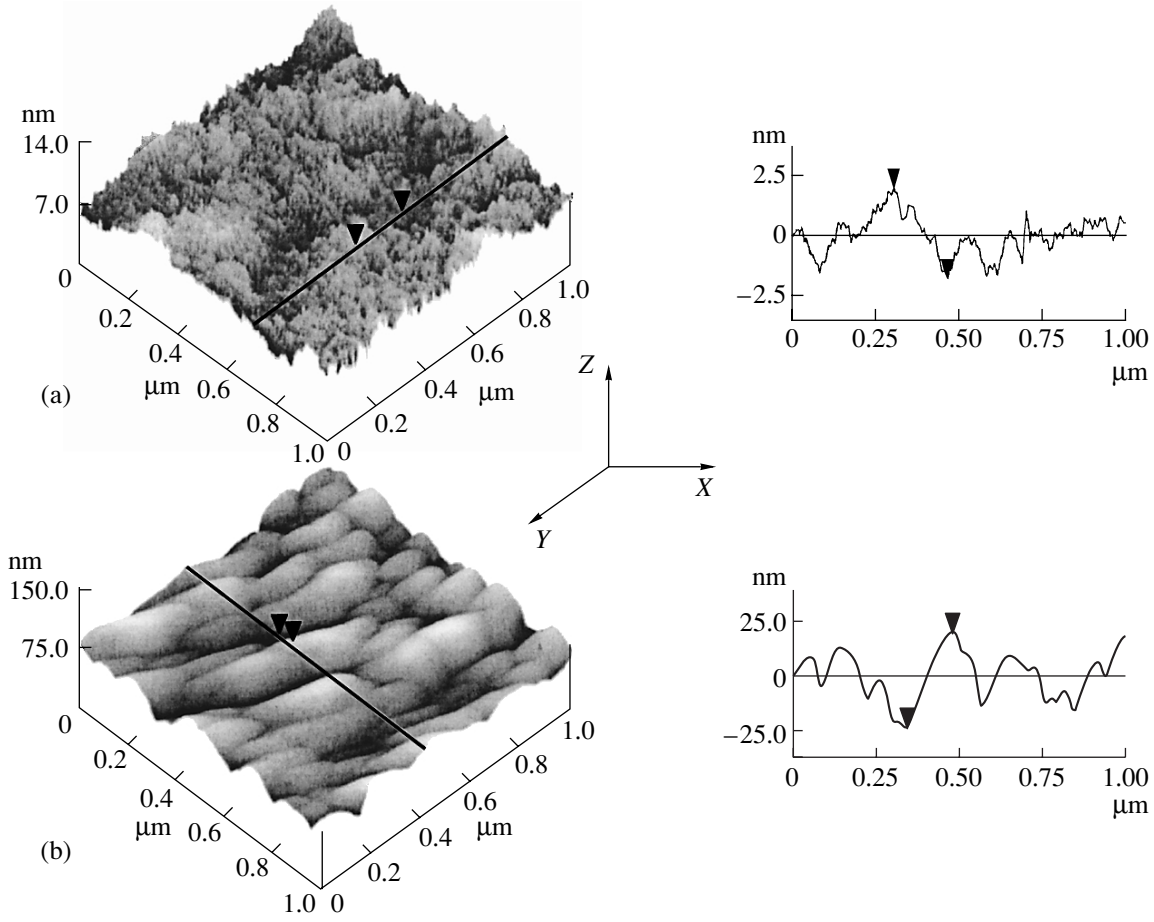

Fig. 4. YBCO film surface profile measurements with an atomic force microscope. (a) DH, the vertical and horizontal mark separations are 3.7 and 160 nm, respectively; (b) TH, the vertical and horizontal mark separations are 44 and 132 nm, respectively.

3. DISCUSSION OF EXPERIMENTAL RESULTS

It is well known that the resistance of metals connected in series, even if they are in direct contact, is not the sum of their resistances if the Fermi momenta of the contacting materials are different [4, 17, 18]. As a result of the mismatch between the electronic parameters of two contacting materials, in particular, of the Fermi momenta p_{fi} ($i = 1, 2$), the characteristic contact resistance becomes [17]

$$r_c^{-1} = (e^2 p_f^2/2\pi^2\hbar^3)2\langle xD(x)\rangle, \quad (1)$$

where $p_f = \min\{p_{f1}, p_{f2}\}$, $D(x)$ is the boundary transparency, and the angular brackets denote averaging over the directions of the quasiparticle momenta. In the case of a sharp and plane interface between two metals with $p_{f1} \ll p_{f2}$ and of spherical Fermi surfaces, the transparency is given by [17]

$$D(x) = 4x p_{f1}/p_{f2}, \quad 2\langle xD(x)\rangle = 8v_{f1}/3v_{f2}, \quad (2)$$

where v_{fi} ($i = 1, 2$) are the Fermi velocities in the contacting materials. One readily sees that in the case of a large enough Fermi velocity mismatch between the contacting metals, the transparency $D \ll 1$ even in the absence of an insulating spacer. If, however, the interface is smooth on a scale of $\hbar/p_f$, then $D \approx 1$, irrespective of the Fermi momentum difference between the materials in contact [17].

Using for the estimation of p_f the relation [19]

$$p_f^2 = 3\pi^2\hbar^3/(e^2\rho l) \quad (3)$$

and the resistivities of the YBCO film of sample H5 ($\rho_c = 2 \times 10^{-1}$ Ω cm along the c axis and $\rho_{ab} = 4 \times 10^{-3}$ Ω cm in the basal plane, as determined from bridge measurements), as well as the mean free path lengths $l_c = 1$ nm [20] and $l_{ab} = 10$ nm [21] ($\rho_c l_c = 2 \times 10^{-8}$ and $\rho_{ab} l_{ab} = 4 \times 10^{-9}$ Ω cm^2), we obtain $p_{fab}/p_{fc} \approx 2.2$ for the Fermi momentum anisotropy. As shown by our estimates, this value of the ratio p_{fab}/p_{fc} still permits one to use relations (1)–(3) to calculate the transport along the c axis. Using the experimental values for r and ρl from Eqs. (1) and (3), we obtain $2\langle xD(x)\rangle \approx 7 \times 10^{-4}$ for the interface transparency of sample P32J3, which is close to the value $2\langle xD(x)\rangle \approx 8 \times 10^{-4}$ calcu-

lated from Eq. (2) under the assumption of the carrier effective mass along the c axis being $m = 100\ m_e$ [22]. The difference between the transparencies obtained by different techniques is most likely associated with the fact that the ρ_c of YBCO films derived from bridge resistance measurements is smaller by an order of magnitude than those for the thin layer at the N–S_d interface, which were determined from four-point measurements of the junction resistance at $T = T_c$.

When determining the experimental value of the transparency along the a–b plane in THs, one should take into account the layered HTSC structure. As a result, in averaging over the momentum directions, the main contribution should be due to electrons within the angular range $\alpha < \arctan(d/\lambda_N) \approx 84°$ ($\lambda_N \approx 0.12$ nm is the de Broglie wavelength for electrons in Au, and $d \approx 1.2$ nm is the distance between the CuO planes in YBCO). One should also take into account the sharpness of the interface, which radically changes its transparency. A comparison of δ_{ab} and δ_c (Fig. 4) with λ_{ab} and λ_c (the de Broglie wavelength for electrons in YBCO), respectively, shows that in the THs ($\delta_{ab} \gg \lambda_{ab} \approx 2$ nm), the interface is smooth, whereas in the DHs with $\delta_c \sim \lambda_c \approx 4$ nm, we most likely have a sharp interface. As a result, relation (2) is applicable to the DHs, while the interface transparency in the THs is substantially larger ($D_{ab} \approx 1$); however, when averaged over the momentum directions, we obtain for the THs

$$2\langle xD(x)\rangle = (\lambda_N/d)^2 = 10^{-2}. \qquad (4)$$

Note that the value $2\langle xD(x)\rangle = 9 \times 10^{-3}$, found from Eqs. (1) and (3), is close to the estimate in Eq. (4) made for the H5J3 sample. Hence, while the transparency of a smooth interface for electrons with momenta oriented close to the normal is of order unity, the transparency averaged over the momentum directions is small because of the layered structure of the YBCO and does not contribute noticeably to the characteristic resistance of the interface. Relation (4) also shows that for abrupt N–S_d interfaces, r_{ab} is nearly equal to r_c, despite the large anisotropy of the Fermi momenta.

As shown by calculations [4, 17], for $v_{f1}/v_{f2} \ll 1$, the N–S_d and NIS junctions have similar electrophysical properties. Figure 3 shows that the I–V curves obtained in our experiment for $T \ll T_c$ are, on the whole, close to those measured on NIS junctions; namely, one observes an increase of R_d at low bias. However, in our experiment, in contrast to the theory of [17], R_d does not exhibit any features associated with the YBCO superconducting gap. One could conceive of two reasons for the diffuse character of the gap feature in the I–V curves. The first of them is the existence of a direct contact between the superconductor and the normal metal. By [17], for $T = 0$, we have $R_\mathrm{d}(\Delta/e)/R_N = \langle xD(x)\rangle$; i.e., the I–V characteristics of NcS junctions ("c" stands for constriction) do not have a divergence of the $((eV)^2 - \Delta^2)^{-1/2}$ type characteristic of NIS junctions for $T \ll T_c$. Second, the absence of a gap feature in the I–V curves agrees with the model of a superconductor with gapless superconductivity, including a d-type superconducting order parameter [11, 12]. By calculations [11], the feature in the I–V characteristics at $eV \approx \Delta$ caused by growth of the density of states of a d superconductor at energies $\varepsilon \approx \Delta$ yields a logarithmic dependence $R_\mathrm{d} \sim \ln(T)$ and $\ln(|eV| - \Delta|)$, which is subject to a temperature-induced spread, as in the case of gapless superconductivity. Note that the Nb–Au–YBCO heterojunctions, as well as the Pb–Au–YBCO structures produced on c-oriented YBCO films, exhibit a gap feature of a low-temperature superconductor, but the YBCO I–V curves do not have a gap feature at $V \approx \Delta/e$ [23, 24]. This is an additional indication of the YBCO order parameter exerting a fairly strong effect on gap feature formation in the I–V curves at $V \approx \Delta/e$. While both these effects cause a smoothing of the gap feature at $V \approx \Delta/e$, the tunnel feature at $V \ll \Delta/e$ observed experimentally persists up to fairly high interface transparencies ($D \sim 10^{-1}$).

The number of quasiparticles excited at low temperatures ($kT \ll \Delta$) in a superconductor with s-type order parameter symmetry decreases exponentially with temperature; hence, the magnitude of $R_\mathrm{d}(0) \sim \exp(-\Delta/T)$ in SIN junctions increases proportionally. The presence of zero order parameter sites in a superconductor with d-type pairing makes it possible to excite quasiparticles even at a very low temperature, $T \ll \Delta$. As a result, $R_\mathrm{d}(0)$ should grow more slowly with decreasing T than occurs in s superconductor junctions [11]. The existence of direct conduction in a junction acts in the same sense. In addition to the scattering mechanism originating from a p_{fi} mismatch, one observes Andreev reflection for electrons with energies $\varepsilon < p_f^2/2m$. The electrons carrying the current in the normal metal are reflected from the interface with a superconductor in the form of a hole with about the same $|p_f|$, and the current in the superconductor is transported by superconducting pairs [17]. As a result of the combined action of the two above mechanisms, the temperature dependence of $R_\mathrm{d}(0)$ differs from the exponential $\exp(-\Delta/kT)$. As seen from Fig. 5, the conductivity $\sigma = 1/R_\mathrm{d}(0)$ for a DH does decrease in our experiment by a power law with temperature.

An additional experiment indicating the Fermi momentum mismatch as a factor governing the electrophysical parameters of the heterostructures studied is annealing in an oxygen atmosphere. It was experimentally established earlier that the main process taking place in heterostructures made of HTSCs with noble metals (silver, gold, platinum, etc.) and subjected to annealing is an increase in the oxygen content in the surface layer of the (001)YBCO film [25, 26]. When heated in an oxygen environment, an increase in oxygen content in the YBCO surface layer is accompanied

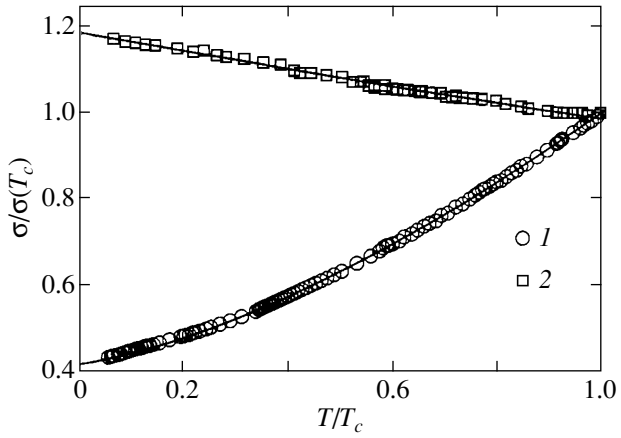

Fig. 5. Normalized temperature dependences of the conductivity: (*1*) for the DH and (*2*) for the TH measured for $T < T_c$. The corresponding fitting curves are shown by solid lines: $\sigma/\sigma(T_c) \approx 0.4 + 0.3(T/T_c) + 0.3(T/T_c)^2$ for a DH, and $\sigma/\sigma(T_c) \approx 1.2 - 0.2(T/T_c)$ for a TH.

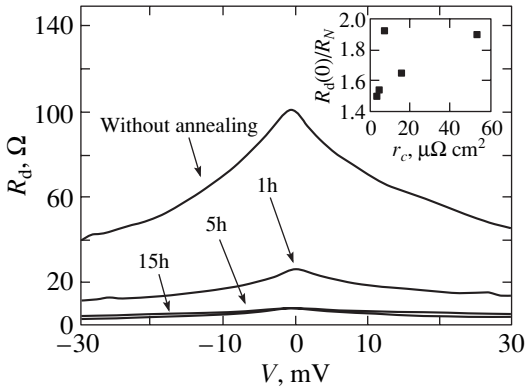

Fig. 6. Variation of the $R_d(V)$ dependence for the P34J3 DH with annealing in an atomic-oxygen environment at T = 600°C. Inset shows the $R_d(0)/R_N$ dependence on r_c, which characterizes the variation of DH conductivity in the course of the anneal.

by a change in its $\rho_c l_c$ and, as a consequence, the Fermi momentum of YBCO increases and r_c decreases. Unlike other noble metals, gold is not observed to diffuse in YBCO. Figure 6 displays $R_d(V)$ relations for a DH obtained after the anneal of a sample for 0, 1, 5, and 15 h in an oxygen environment at T = 600°C. The value of r_c decreases rapidly with increasing anneal time to reach $r_c = 4 \times 10^{-6}\ \Omega\ \text{cm}^2$ after 5-h of annealing in place of the original $r = 5.6 \times 10^{-5}\ \Omega\ \text{cm}^2$. Further annealing for 15 h did not noticeably affect the value of r. Because the *I–V* curve in our experiment does not undergo a qualitative change in shape, the surface layer S_d is located, most probably, on the metallic (superconducting) side of the transition and saturation with oxygen changes its conduction parameters, in particular, the Fermi momentum. As a result, as the oxygen content increases, the resistance of the interface r, which is determined by its transparency D and the value of p_f, should change; this is exactly what was observed in the experiment. The quasi-tunneling component, which can be characterized by the ratio $R_d(0)/R_N$, decreases with annealing, which causes a decrease in r_c (see inset to Fig. 6). One readily sees that by the end of the anneal, the $R_d(0)/R_N$ ratio decreased from 2 to 1.5, while r_c changed by an order of magnitude. This behavior of the *I–V* curves of heterojunctions is in qualitative agreement with the calculations of [17]; namely, as the Fermi momentum mismatch decreases, the quasi-tunneling *I–V* characteristic transfers to the *I–V* curve of junctions with an ScN-type direct conduction. For $D \approx 1$, the properties of the junctions are described by the model of the ScN junction, for which $R_d(0)/R_N = 0.5$ [17].

In a TH, as seen from Figs. 2–4, $R_d(V) \approx$ const within the bias range considered and $R(T)$ falls off linearly with temperature. All this is typical of an N–S_d junction with direct (not tunneling) conduction. Note that r is changed in a TH by an order of magnitude compared with that of a DH and that the transparencies differ by three orders of magnitude because of the additional effect of the roughness of the interface separating the two materials.

Thus, we have observed in *c*-oriented and tilted Au/YBCO heterostructures a strong anisotropy in the temperature dependence of the resistance and the *I–V* curves, which are caused by a change in the direction of the transport current flowing through the normal-metal–YBCO interface. It has been shown that the experimental results obtained can be described within the model of direct contact between the normal metal and the HTSC, if the substantial mismatch in the Fermi momenta p_{fi} between the materials in contact is taken into account. For a large p_{fi} mismatch, a situation met usually in heterostructures grown on *c*-oriented YBCO films, one observes quasi-tunneling characteristics and the heterostructures on YBCO films with a tilted *c* axis are close in properties to Ohmic contacts because of the smaller p_{fi} mismatch and the interface roughness, which reduces electron reflection from the interface. The oxygen-depleted layer existing on the (001)YBCO surface increases the characteristic heterostructure resistance; however, in our experiments, the doping level of this layer is such that it is always on the metallic side of the metal–insulator transition.

ACKNOWLEDGMENTS

The authors are indebted to A.V. Zaĭtsev and A. Kadigrobov for fruitful discussions of the conduction mechanisms in heterostructures, to I.K. Bdikin, P.B. Mozhaev, and I.M. Kotelyanskiĭ for assistance in x-ray diffraction characterization of the HTSCs and

discussion of the experimental data, and to T. Claeson for his interest in the work.

The partial support of the Russian Foundation for Basic Research, Russian Program "Current Problems in Condensed Matter Physics" (subprogram "Superconductivity"), and the INTAS, project no. 97-11459, is gratefully acknowledged.

REFERENCES

1. *The Gap Symmetry and Fluctuations in High-T_c Superconductors*, Ed. by J. Bok, G. Deutscher, D. Pavuna, and S. A. Wolf (Plenum, New York, 1998), NATO ASI Ser., Ser. B **371**, 560 (1998).
2. S. W. Tozer, A. W. Kleinsasser, T. Penney, *et al.*, Phys. Rev. Lett. **59** (15), 1768 (1987).
3. R. Krupke and G. Deutscher, Phys. Rev. Lett. **83**, 4634 (1999).
4. M. Yu. Kupriyanov and K. K. Likharev, IEEE Trans. Magn. **27** (2), 2460 (1991).
5. S. C. Sanders, S. E. Russek, C. C. Clickner, and J. W. Ekin, Appl. Phys. Lett. **65** (17), 2232 (1994).
6. S. G. Lee, Y. Huh, Y. S. Hwang, *et al.*, Physica C (Amsterdam) **282–287**, 1491 (1997).
7. Yuzi Xu, J. W. Ekin, S. E. Russek, *et al.*, IEEE Trans. Appl. Supercond. **7** (2), 2836 (1997).
8. M. Gurvitch, J. M. Valles, Jr., A. M. Cucolo, *et al.*, Phys. Rev. Lett. **63** (9), 1008 (1989).
9. J. Lesueur, L. H. Greene, W. L. Feldmann, and A. Inam, Physica C (Amsterdam) **191**, 325 (1992).
10. Chia-Ren Hu, Phys. Rev. Lett. **72** (10), 1526 (1994).
11. Yu. S. Barash, A. V. Galaktionov, and A. D. Zaikin, Phys. Rev. B **52** (1), 665 (1995).
12. Y. Tanaka and S. Kashiwaya, Phys. Rev. Lett. **74** (17), 3451 (1995).
13. F. V. Komissinskiĭ, G. A. Ovsyannikov, N. A. Tulina, and V. V. Ryazanov, Zh. Éksp. Teor. Fiz. **116** (6), 2140 (1999) [JETP **89**, 1160 (1999)].
14. F. V. Komissinskiĭ, G. A. Ovsyannikov, N. A. Tulina, and V. V. Ryazanov, in *Proceedings of the XXXI Conference on Physics of Low Temperatures, Moscow, 1998*, p. 236.
15. Y. Y. Divin, U. Poppe, P. M. Shadrin, *et al.*, in *Proceedings of the 2nd European Conference on Applied Superconductivity, EUCAS, Edinburgh, 1995*, Inst. Phys. Conf. Ser. 148, **2**, 1359 (1995).
16. A. M. Klushin, A. Golubov, W. Prusseit, and H. Kolstedt, J. Low Temp. Phys. **106**, 265 (1997).
17. A. V. Zaĭtsev, Zh. Éksp. Teor. Fiz. **86** (5), 1742 (1984) [Sov. Phys. JETP **59**, 1015 (1984)].
18. G. E. Blonder, M. Tinkham, and T. M. Klapwijk, Phys. Rev. B **25** (7), 4515 (1982).
19. P. G. de Gennes, *Superconductivity of Metals and Alloys* (Benjamin, New York, 1966; Mir, Moscow, 1968).
20. J. Yoshida, T. Hashimoto, S. Inoue, *et al.*, Jpn. J. Appl. Phys., Part 1 **31** (6A), 1771 (1992).
21. K. Krishana, J. M. Harris, and N. P. Ong, Phys. Rev. Lett. **75** (19), 3529 (1995).
22. L. N. Bulaevskiĭ, V. L. Ginzburg, and A. A. Sobyanin, Zh. Éksp. Teor. Fiz. **94** (7), 355 (1988) [Sov. Phys. JETP **67**, 1499 (1988)].
23. A. S. Katz, A. G. Sun, R. C. Dynes, and K. Char, Appl. Phys. Lett. **66** (1), 105 (1995).
24. P. V. Komissinski, E. Il'ichev, G. A. Ovsyannikov, *et al.*, cond-mat/0008077.
25. J. W. Ekin, T. M. Larson, N. F. Bergen, *et al.*, Appl. Phys. Lett. **52** (21), 1819 (1988).
26. Siu-Wai Chan, L. Zhao, C. Chen, *et al.*, J. Mater. Res. **10** (10), 2428 (1995).

Translated by G. Skrebtsov

Physics of the Solid State, Vol. 43, No. 5, 2001, pp. 808–810. Translated from Fizika Tverdogo Tela, Vol. 43, No. 5, 2001, pp. 776–778.

SEMICONDUCTORS AND DIELECTRICS

Bound-Exciton Emission Bands in ZnSe Single Crystals and Mixed Plasmon–Phonon Modes

V. S. Vavilov, A. A. Klyukanov*, K. D. Sushkevich*, M. V. Chukichev**, A. Z. Awawdeh*, and R. R. Rezvanov****

**Moldova State University, ul. Mateevich 60, Chishinau, 2009 Moldova*
e-mail: klukanov@cinf.usm.md
***Moscow State University, Vorob'evy gory, Moscow, 119899 Russia*
Received September 18, 2000

Abstract—The paper reports a cathodoluminescence study of ZnSe single crystals annealed in a Bi melt at 1200 K for 120 h. It is found that the distance between the phonon structure satellites in the bound-exciton series I_1^s–nLO and I_1^d–nLO and the relative satellite intensity are different in samples with different conduction electron concentrations. It is shown that this difference is due to the mixing of the plasmon and phonon modes. The shape of the bound-exciton emission spectrum in ZnSe crystals in the 450–470 nm region is calculated, and a satisfactory agreement with the experiment calculations is obtained. © *2001 MAIK "Nauka/Interperiodica".*

It was conjectured [1] that the region of the I_1^d–2LO emission line (λ = 456 nm) of ZnSe crystals annealed in a Bi melt contains a new bound-exciton line I_1^s with a rich LO-phonon and plasmon structure. A distinctive feature of the I_1^s line (compared to I_1^d) is the large magnitude of its coupling constants with LO phonons and plasmons, which determine the emission line intensity. This paper reports on further study of the spectral shape, relative intensities, and distances between the satellites in the bound-exciton line series $I_1^{s,d}$–nLO.

The luminescence was excited by a 40-keV electron beam with the sample maintained at 4.2 K. The pulse duration was 0.4 μs, and the repetition frequency was 200 Hz. The radiation was analyzed by a DFS-12 monochromator in the visible region of the spectrum. Figure 1 presents experimental data on the cathodoluminescence of two ZnSe samples annealed in a Bi melt and having different conduction electron concentrations. Curve *1* exhibits the lines I_1^d–LO (λ = 451.0 nm) and I_1^d–2LO (λ = 456.2 nm). The latter is superposed on a broad I_1^s line peaking near λ = 456 nm. The two long-wavelength satellites of the I_1^s line are its LO-phonon replicas, I_1^s–LO (λ = 461 nm) and I_1^s–2LO (λ = 467 nm). The multiplasmon structure of the I_1^s–nLO lines is not resolved, because the plasmon lifetime τ in crystals with a low electron concentration ($\omega_p \ll \omega_{LO}$) is not sufficiently long and plasmons are not elementary excitations of crystals. Nevertheless, interaction of the recombining electron and hole with the plasma brings about a broadening of the I_1^s–nLO series lines. Curve *1* in Fig. 1 convincingly suggests that in the wavelength interval $\lambda \approx$ 456 nm, there is a superposition of the I_1^s and I_1^d–2LO lines. This can be considered as direct evidence of the conjecture on the existence of a new line I_1^s and its satellites. Similar spectra were also obtained on other ZnSe samples with a low conduction-electron plasma concentration. Depending on the relative concentrations of the centers accounting for the I_1^s and I_1^d lines, superposition of the spectra can be observed to occur in regions of both the I_1^s and I_1^d–2LO lines (λ = 456 nm) and the I_1^s–LO and I_1^d–3LO lines (λ = 461 nm). Despite the weak coupling of the bound exciton responsible for the I_1^d line with the free-electron plasma, the interaction also manifests itself in a broadening of the I_1^d line at plasma concentrations $n_e \le 10^{16}$ cm^{-3}. For comparison, consider the cathodoluminescence spectra taken from [1] (Fig. 1); they exhibit a narrowing of the plasmon-free I_1^d–2LO lines for $n_e \le 10^{17}$ cm^{-3}, where the plasmon satellite splits off from the plasmon-free line.

In crystals with a relatively high plasma concentration ($n_e \approx 10^{17}$ cm^{-3}, $\hbar\omega_p \approx 10$ meV), the multiplasmon structure in the I_1^s–nLO series is resolved (curve *2* in Fig. 1) and the plasmon-free lines I_1^s–LO (λ = 461.3 nm) and I_1^s–2LO (λ = 466.8 nm) are more narrow and intense than the plasmon satellites as a result of strong plasmon dispersion and decay.

Thus, if one considers a broad conduction-electron plasma concentration range, $n_e \approx 10^{14}$–10^{18} cm^{-3}, one can say that in the initial stage, at low concentrations [in

the sense that the inequality $\omega_p \ll \omega_{LO}$) still holds], as one crosses over from $n_e \approx 10^{14}$ to 10^{16} cm^{-3}, the Coulomb interaction of bound excitons with the plasma manifests itself in a broadening of the $I_1^{s,d}$–nLO lines. For the I_1^s–nLO series, this effect is more significant than that for I_1^d–nLO (curve *1* in Fig. 1). However, as the concentration grows to $n_e \approx 10^{17}$–10^{18} cm^{-3}, the broadening is replaced by a narrowing of the $I_1^{s,d}$–nLO lines. This takes place when the plasmon energy becomes high enough for the plasmon satellite to split off from the plasmon-free line.

As seen from an analysis of the $I_1^{s,d}$–nLO series, the relative intensity and spacing between the satellites are different in different samples. The spacing varies from 31 to 32 meV, and the relative intensity of the I_1^s–LO and I_1^s–2LO lines is 1.2 : 1 (curve *2* in Fig. 1), 1 : 1 (curve *1* in Fig. 1 from [1]), and 0.9 : 1 (curve *2* in Fig. 1 [1]). We believe all these results to be due to the mixing of the plasmons with the LO phonons, which gives rise to frequency renormalization of the elementary crystal excitations and, depending on the actual plasma concentration, to variation of the average number (per photon) of emitted longitudinal mixed plasmon–phonon excitations with frequencies ω_+ and ω_- [2–4]. The critical quantity is the conduction electron concentration $n_e \approx 10^{16}$–10^{17} cm^{-3}. The frequencies of the mixed plasmon–phonon elementary excitations are given by the relation [2]

$$\omega_\pm = \frac{1}{2}\left\{\omega_{LO}^2 + \omega_{p\infty}^2 \pm \left[(\omega_{LO}^2 + \omega_{p\infty}^2)^2 - 4\omega_{p\infty}^2\omega_{TO}^2\right]^{\frac{1}{2}}\right\}^{\frac{1}{2}}. \quad (1)$$

In the limit of low plasma concentrations satisfying the inequality $\omega_p \ll \omega_{LO}$ ($n_e \le 10^{16}$ cm^{-3}), the frequency $\omega_+ \longrightarrow \Omega_{LO}$ and $\omega_- \longrightarrow \omega_p$, whereas in the case of the inequality $\omega_p \gg \omega_{LO}$, i.e., for high concentrations $n_e \ge 10^{18}$ cm^{-3}, the frequency $\omega_- \longrightarrow \omega_{TO} = \omega_{LO}(\varepsilon_\infty/\varepsilon_0)^{1/2}$ and $\omega_+ \longrightarrow \omega_{p\infty}$. Here, $\omega_p = (4\pi n_e e^2/\varepsilon_0 m_e^*)^{1/2} = \omega_{p\infty}(\varepsilon_\infty/\varepsilon_0)^{1/2}$.

For $n_e \approx 10^{16}$ cm^{-3}, the plasmon energy is $\hbar\omega_p$ = 2.9 meV, so that, by Eq. (1), the mixing of the plasmon and LO-phonon modes can be neglected. However, for $n_e \approx 10^{17}$ cm^{-3}, the mixing should be taken into account. Indeed, using Eq. (1) and the values of the parameters of the ZnSe crystal, we find, for the concentration $n_e \approx 1.7 \times 10^{17}$ cm^{-3} and $\hbar\omega_{LO}$ = 31 meV, the following plasmon–phonon mode energies: $\hbar\omega_+$ = 32 meV and $\hbar\omega_-$ = 11.6 meV ($\hbar\omega_p$ = 12 meV). Both frequencies ω_+ and ω_- grow with increasing plasma concentration. Thus, we may conclude that the observed change in the $\hbar\omega_+$ energy from $\hbar\omega_{LO}$ = 31 meV at low concentrations to

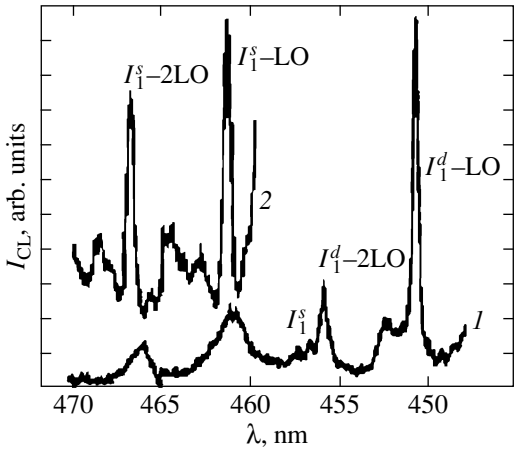

Fig. 1. Cathodoluminescence spectra of ZnSe crystals obtained at T = 4.2 K: (*1*) high-resistivity sample, (*2*) low-resistivity sample.

$\hbar\omega_+$ = 32 meV at high concentrations is due to the mixing of the plasmons with the phonons. Note that an energy spread of the longitudinal optical phonons of the same order of magnitude is also quoted in other studies (see, e.g., [5]). The increase in the concentration from $n_e \approx 10^{16}$ to 10^{17} cm^{-3} more strongly affects the relative satellite intensity, which is determined by the average numbers N_+ and N_- (per photon) of emitted mixed plasmon–phonon excitations with frequencies ω_+ and ω_-. It was pointed out [1] that a strong coupling with plasmons and phonons is characteristic of centers of the acceptor or donor type, where the radii of the electron and hole states differ considerably. Here, $N_+ \sim 1/a_+$, where a_+ is the smallest radius (of the electron or the hole). In accordance with relation (2) from [1], we find

$$\frac{N_+}{N_{LO}} = \frac{a_{LO}}{a_+}\frac{\omega_{LO}}{\omega_+}\frac{\omega_+^2 - \omega_{TO}^2}{\omega_+^2 - \omega_-^2}\frac{\omega_{LO}^2 - \omega_p^2}{\omega_{LO}^2 - \omega_{TO}^2}. \quad (2)$$

For $n_e \le 10^{16}$ cm^{-3}, no mixing occurs, $N_+ = N_{LO}$, and the ratio $a_{LO}/a_+ = 1$, whereas for $n_e = 1.7 \times 10^{17}$ cm^{-3}, we obtain $N_+ = 1.3N_{LO}a_{LO}/a_+$. Because the concentrations considered here are far from the threshold of the Mott transition, we have $a_{LO}/a_+ \approx 1$ and $N_+ = 1.3N_{LO}$. This effect accounts for both the position and the relative intensity of the I_1^s–nLO lines in spectrum *1* of Fig. 1. Taking into account the superposition of the two series, I_1^s–nLO and I_1^d–nLO, in the wavelength region λ = 450–470 nm, the spontaneous emission spectrum of ZnSe crystals can be presented in the form

$$I(x) = A\sum_{n=0}^{\infty}\frac{\gamma(N_{LO}^d)^n/n!}{(x+n)^2+\gamma^2} + B\sum_{n=0}^{\infty}\sum_{m=-\infty}^{\infty} e^{\frac{\beta}{2}m} I_m(z)\frac{\gamma_1(N_{LO}^s)^n/n!}{(x+1+n+\delta+bm)^2+\gamma_1^2}. \quad (3)$$

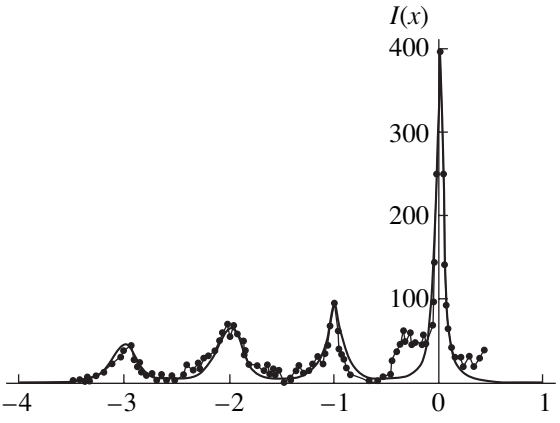

Fig. 2. Bound-exciton emission spectrum in ZnSe. The solid line is the spectrum calculated from Eq. (3). Circles are experimental points.

Here, $x = (\omega - \omega_0)/\omega_{LO}$ and $\hbar\omega_0$ is the energy position of the I_1^d–LO line (450.9 nm). All the frequencies are in units of ω_{LO}: $b = \omega_p/\omega_{LO}$, $\beta = \hbar\omega_p/k_0T$, $z = N_p/\sinh(\beta/2)$, N_{LO} is the average number of phonons (N_p plasmons) emitted per photon, and $I_m(z)$ is the Bessel function of an imaginary argument. Relation (3) includes both Stokes and anti-Stokes satellites. For $N_p \gg 1$, the envelope of the multiplasmon satellites is a Gaussian whose half-width is dominated by the Coulomb interaction with the free-electron plasma.

In accordance with Eq. (3), in order to construct a theoretical emission spectrum, one should know the widths γ and γ_1 of the LO phonon and plasmon satellites, as well as the position of the I_1^s line, which is determined by the δ parameter. As follows from our results, the I_1^s line is shifted by 0.3 nm toward shorter wavelengths relative to the I_1^d–2LO line and N_{LO}^s for the I_1^s–nLO series is about two for plasma concentrations $n_e \geq 10^{17}$ cm^{-3}. Using these data, we find that the theoretical calculations are at odds with experimental calculations for low plasma concentrations. The theoretical series I_1^s–nLO for $N_{LO}^s = 2$ and $\delta = 0.06$ is found to be shifted toward longer wavelengths relative to the experimental one, and the intensity of the I_1^s–2LO line is overestimated with respect to that of the I_1^s–LO line. The problem consists in that the δ parameter cannot be directly determined experimentally. However, when one takes into account the plasmon and phonon mixing, it becomes clear how this parameter and the N_{LO}^s constant should be changed when going over to lower concentrations. Indeed, with the mixing properly included, the contribution of the interaction with longitudinal plasmon–phonon modes to the exciton binding energy is given by

$$\Delta E_B = N_+\hbar\omega_+ + N_-\hbar\omega_-. \quad (4)$$

By our estimates, as the concentration increases, the ΔE_B energy in Eq. (4) increases and the I_1^s line shifts toward longer wavelengths. Thus, at low concentrations, the δ parameter is larger than that at high ones. The δ parameter was varied to obtain the best fit of the theoretical to the experimental spectrum (curve *1* in Fig. 1). For plasma concentrations $n_e \leq 10^{16}$ cm^{-3}, the I_1^s line was found to be shifted relative to the I_1^s–2LO line toward shorter wavelengths by $\delta = 0.15$ ($\delta\hbar\omega = 4.6$ meV). Note that taking into account the optical phonon dispersion and plasma heating is not sufficient for explaining the purpose of this shift. The half-widths of the I_1^d–nLO lines can be derived directly from experimental data. For the multiplasmon satellites, the half-width $2\gamma_1$ is constrained by the condition that, as shown by the experiment, the multiplasmon structure is not resolved ($a/\gamma_1 < 1$). The relative intensity of the I_1^d–nLO and I_1^s–nLO series is determined by the constants A and B in Eq. (3). Thus, as seen from Fig. 2, for the parameters $A = 16$, $B = 0.25$, $b = 0.05$ ($\hbar\omega_p = 1.55$ meV), $N_{LO}^d = 0.25$, $N_{LO}^s = 1.4$, $N_p = 3$, $\gamma_1 = 0.07$ (for a lower value of γ_1, the multiplasmon structure is not smoothed), $\gamma = 0.04$, and $T = 4.2$ K, the agreement with the experiment turns out to be satisfactory. The sensitivity of the emission and absorption spectra of bound excitons to plasma concentration (the nonlinearity of the spectral functions depending on excitation intensity) can be used to advantage in optical information processing devices.

REFERENCES

1. V. S. Vavilov, A. A. Klyukanov, K. D. Sushkevich, *et al.*, Fiz. Tverd. Tela (St. Petersburg) **41** (7), 1176 (1999) [Phys. Solid State **41**, 1070 (1999)].
2. P. M. Platzman and P. A. Wolff, *Solid State Physics*, Suppl. 13 (Academic, New York, 1973); *Waves and Interactions in Solid Plasma* (Mir, Moscow, 1975).
3. V. S. Vavilov, A. A. Klyukanov, É. A. Senokosov, *et al.*, Fiz. Tverd. Tela (Leningrad) **33** (1), 63 (1991) [Sov. Phys. Solid State **33**, 35 (1991)].
4. V. S. Vavilov, A. A. Klyukanov, M. V. Chukichev, *et al.*, Fiz. Tekh. Poluprovodn. (St. Petersburg) **28** (12), 2113 (1994) [Semiconductors **28**, 1178 (1994)].
5. D. D. Nedeoglo and A. V. Simashkevich, *Electrical and Luminescent Properties of Zinc Selenide* (Shtiintsa, Chishinau, 1994).

Translated by G. Skrebtsov

Physics of the Solid State, Vol. 43, No. 5, 2001, pp. 811–817. Translated from Fizika Tverdogo Tela, Vol. 43, No. 5, 2001, pp. 779–785.

SEMICONDUCTORS AND DIELECTRICS

Calculation of the Thermal Effect of an Electron Probe on a Sample of GaN

L. A. Bakaleĭnikov, E. V. Galaktionov, V. V. Tret'yakov, and É. A. Tropp

Ioffe Physicotechnical Institute, Russian Academy of Sciences, Politekhnicheskaya ul. 26, St. Petersburg, 194021 Russia

e-mail: bakal@ammp.ioffe.rssi.ru

Received August 3, 2000; in final form, October 6, 2000

Abstract—Stationary temperature fields due to the interaction of an electron probe with a GaN sample are examined. In order to calculate the density of generated heat, the process of electron energy loss is modeled by the Monte Carlo method. The heat generation region is assumed to have the shape of a half-ellipsoid. In the case of uniform heat generation in the ellipsoid, an analytical solution to the heat conduction problem is found and expressed in terms of elementary functions. It is shown that the maximum heating temperature and the temperature field distribution depend only slightly on the shape of the heat generation region. An approximation of the density of heat sources by a uniform distribution over a hemisphere of radius equal to the ultimate range of electrons leads to a considerably underestimated maximum heating temperature. An expression is derived for determining the characteristic size of the heat generation region in GaN; this expression allows one to calculate the maximum heat temperature with an accuracy of 3% in a wide range of electron beam energies. © *2001 MAIK "Nauka/Interperiodica".*

INTRODUCTION

An analysis of the temperature fields caused by the interaction of an electron probe with a sample is of importance in interpreting experimental data on cathodoluminescence and Auger-electron and x-ray spectrum microanalysis [1–3]. Taking the temperature effect into account can also be essential in the electron-beam processing of samples. Problems of this kind arise, in particular, when *p*-type conductivity is activated in samples of GaN [4, 5], which is one of the most promising materials for optoelectronic devices in the visible spectral region.

The thermal effect of an electron probe on a sample was treated in a number of investigations both experimentally [6, 7] and theoretically [1–3, 8, 9]. It should be noted that an experimental measurement of the heating temperature [6, 7] is complicated by the fact that the heat generation region is small; therefore, the results have a considerable margin of error and should be considered qualitative. For this reason, theoretical estimations of the spatial distribution of heat sources and the sample heating temperature caused by the electron probe are of particular value. In [1], the stationary heat conduction problem was solved and a much used formula for the maximum heating temperature was obtained. It should be noted that in deriving this formula, the heat generation region was assumed to be a hemisphere of radius equal to that of the probe. In [2], the heat conduction problem was considered for the case of a sample covered with a film of a material having a high heat conductivity and the same approximation to the heat generation region was used. An expression derived for the temperature at the sample surface includes an improper integral of a combination of the Bessel function of order zero and an exponential. The heat problem for the case of a cylindrical region of heat sources was treated in [8]; the height of the cylinder was taken to be equal to the penetration depth of the probing electrons, and the base diameter equaled the sum of the electron-beam diameter and was twice the penetration depth. The final expression involved an integral of special functions. In [9], the heat generation region was approximated by a hemisphere of radius equal to the sum of the radius of the electron beam and the electron penetration depth; simple analytical expressions were obtained for the maximum heating temperature, the size of the heat source, and the transient time of the temperature field.

It should be noted that the actual shape of the heat generation region differs from the approximations indicated above. The main reason for their use in the papers cited above is that these approximations make it possible to derive analytical expressions for estimating the basic parameters of the temperature field. In order to determine the actual shape of the region of heat generation, one should analyze the process of electron-beam energy loss in detail.

The objective of this paper is to investigate the temperature distribution in a sample with allowance for the actual density of heat sources. The problem is approached in two steps. We first determine the density of heat sources by solving the kinetic equation for probing electrons and then solve the heat problem on the basis of the generated-heat distribution found before.

1063-7834/01/4305-0811$21.00

1. CALCULATION OF THE DISTRIBUTION OF THE HEAT SOURCE DENSITY

Heat generation is a result of relaxation of probing electrons, the energy of which is transferred to the target. If one assumes that the entire energy of electrons is converted into heat, then the distribution of heat sources will be identical to that of electron energy losses. The one-dimensional depth distribution of electron energy losses dE/dz has been calculated in many papers. In particular, a much used universal empirical expression for dE/dz is presented in [10]. However, the information on the depth distribution does not suffice for the spatial distribution of the energy loss density to be determined. One of the methods for calculating the spatial distribution is to solve the kinetic equation that describes probing-electron transport in the target. For this purpose, we performed computer simulation by the Monte Carlo method. In the calculation procedure for the computer program, we used the single-collision approximation. Elastic scattering of electrons by atoms was described by the Mott differential cross section, which we calculated using the Hartree–Fock–Slater atomic potential [11]. Inelastic electron scattering in the material was described by a model differential cross section. The distinctive features of this cross section are as follows. At high energy losses, it approaches the cross section for free electrons, whereas moderate energy losses per unit length are described by the Bethe or Rao-Sahib–Wittry formula [12].

In order to verify the adequacy of the computer simulation, we compared the calculated depth dependences of the energy loss density with the universal dependences for low [13] and high [10] electron-beam energies. The two-dimensional energy loss distribution was compared with the corresponding distribution proposed in [14] for GaAs. The comparison showed that our results are in reasonable agreement with the data from the papers cited above.

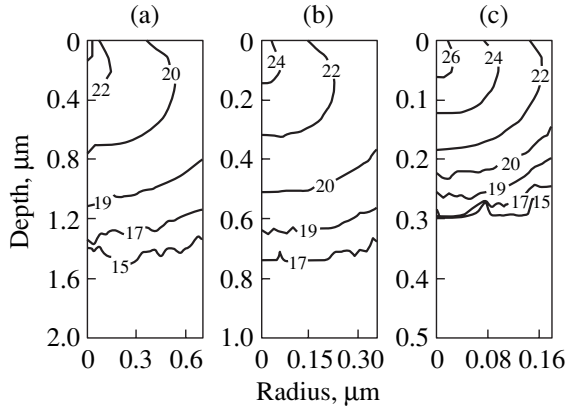

Fig. 1. Isolines of the heat source density distribution $q_f(\rho, z)$ (ρ is the radius, z is the depth) in a semi-infinite GaN sample irradiated by an electron beam focused at a point for electron energies E_0 equal to (a) 15, (b) 10, and (c) 5 keV. The depth and radius are reckoned from the point of incidence of the probing electrons. The values of $\ln q_f(\rho, z)$ are indicated on the isolines.

By using the simulation program, we calculated the distribution of the energy loss density and, therefore, the distribution of heat sources $q_f(\rho, z)$ in GaN for energies E_0 = 5, 10, and 15 keV, where the depth z and radius ρ were reckoned from the point at which the electron beam was focused on the sample. The electron beam current was taken to be 100 nA. Isolines of the calculated distribution are shown in Fig. 1. The distribution of the heat source density produced in the sample by an electron beam of finite diameter d is related to the distribution q_f produced by a beam focused at a point by the equation

$$q(x, y, z) = \iint q_f(x - x_0, y - y_0, z) I_d(x_0, y_0) dx_0 dy_0, \quad (1)$$

where $I_d(x_0, y_0)$ is the intensity distribution over the cross section of the beam.

2. CALCULATION OF THE TEMPERATURE FIELD

Now, we are coming to the second part of the problem, namely, to the calculation of the temperature field in the sample for a given density of generated heat.

From the calculated distribution q_f produced by the electron beam focused at a point (Fig. 1) it is seen that the distribution of the generated heat density in the bulk of the sample differs noticeably from a spherically symmetric one. A similar situation takes place in the more general case of beams of finite diameter. This raises the question of whether the heat generation region can be approximated by a hemisphere [9]. The solution to the heat conduction problem found in [8] for a source uniformly distributed over a cylinder allows one, in principle, to estimate the effect of the shape of the heat generation region on the temperature distribution. However, this solution is represented in the form of an integral of special functions, which makes its use difficult. Furthermore, the boundary of the heat generation region is not smooth in this case, which is in contradiction with the results presented in Fig. 1.

In this paper, we take into account the difference in the characteristic dimensions of the heat generation region in the transverse and longitudinal directions by considering the region in the form of a half-ellipsoid with semiaxes a and b. The distribution of generated heat over this region is assumed to be uniform. The temperature field is described by the equation

$$\Delta T = -q/k,$$

where k is the heat conductivity coefficient and the heat source density q as a function of the cylindrical coordinates ρ and z has the form

$$q = \begin{cases} q_0, & \dfrac{\rho^2}{b^2} + \dfrac{z^2}{a^2} < 1 \\ 0, & \dfrac{\rho^2}{b^2} + \dfrac{z^2}{a^2} > 1. \end{cases}$$

Since there is no heat flux through the boundary, and the temperature field decays far away from the heat source, the boundary conditions have the form

$$\left.\frac{\partial T}{\partial z}\right|_{z=0} = 0, \quad T|_{z\to\infty} \longrightarrow 0, \quad T|_{\rho\to\infty} \longrightarrow 0.$$

The axial symmetry of the problem allows one to use the degenerate ellipsoidal coordinates α and β [15], in terms of which the problem can be solved analytically. In the case of a prolate ellipsoid of revolution ($a \geq b$), the relation between the cylindrical and ellipsoidal coordinates has the form

$$\rho = c\sinh\alpha\sin\beta, \quad z = c\cosh\alpha\cos\beta,$$

where c is a scale factor. In the case of an oblate ellipsoid of revolution ($a < b$), these relations are replaced by

$$\rho = c\cosh\alpha\sin\beta, \quad z = c\sinh\alpha\cos\beta.$$

In the former case, one of the families of coordinate surfaces is the family of prolate ellipsoids of revolution α = const with foci at points $(0, 0, \pm c)$.

If the scale factor c and the coordinate $\alpha = \alpha_0$ are taken such that

$$c^2\sinh^2\alpha_0 = b^2, \quad c^2\cosh^2\alpha_0 = a^2,$$

then the ellipsoid within which heat is generated coincides with the coordinate surface $\alpha = \alpha_0$. The families of coordinate lines of the degenerate ellipsoidal coordinate system are shown in Fig. 2.

In the (α, β) coordinates, the Laplacian has the form

$$\Delta T = \frac{1}{c^2(\sinh^2\alpha + \sin^2\beta)} \times\left[\frac{1}{\sinh\alpha}\frac{\partial}{\partial\alpha}\sinh\alpha\frac{\partial T}{\partial\alpha} + \frac{1}{\sin\beta}\frac{\partial}{\partial\beta}\sin\beta\frac{\partial T}{\partial\beta}\right].$$

By solving the problem by the method of separation of variables, we arrive at the formulas

$$T_{\text{int}}(\alpha, \beta) = -\frac{q_0}{k}c^2\left\{\frac{1}{4}\sinh^2\alpha\sin^2\beta - \frac{1}{6}\sinh^2\alpha_0 \times\left[1 + 2\cosh\alpha_0\ln\coth(\alpha_0/2) + 2(1 - \cosh\alpha_0\ln\coth(\alpha_0/2)) \times\frac{(3\cosh^2\alpha - 1)}{2}\frac{(3\cos^2\beta - 1)}{2}\right]\right\},$$

$$T_{\text{ext}}(\alpha, \beta) = \frac{q_0}{4k}ab\sinh(\alpha_0)\{(3\cos^2\beta - 1)\cosh\alpha + [2(\sin^2\beta - \sinh^2\alpha) + 3\sinh^2\alpha\sin^2\beta]\ln\coth(\alpha/2)\}.$$

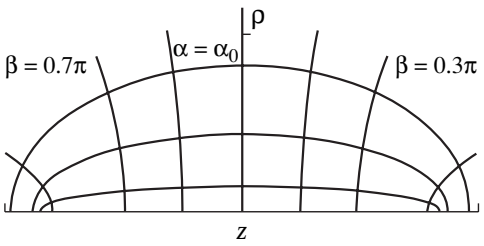

Fig. 2. Families of coordinate lines α = const and β = const for the degenerate coordinate system in the case of a prolate ellipsoid of revolution for $a = 10$ and $b = 5$. The scale factor c and coordinate α_0 are 8.66 and 0.55, respectively. The curves correspond to the following values of the coordinates: $\alpha = 0.1$, 0.3, and α_0; $\beta = 0.1\pi$, 0.3π, 0.4π, 0.6π, 0.7π, and 0.9π.

(2)

Here, T_{int} and T_{ext} are the temperatures inside and outside the ellipsoid, respectively. In the limit case $b \longrightarrow a$, these formulas are reduced to the solution for a source distributed uniformly over a hemisphere of radius a:

$$T_{\text{int}}(\rho, z) = \frac{q_0}{6k}(3a^2 - \rho^2 - z^2),$$
$$T_{\text{ext}}(\rho, z) = \frac{q_0}{3k}\frac{3a^2}{\sqrt{\rho^2 + z^2}}. \quad (3)$$

Putting $\rho = z = 0$ in Eqs. (2) and (3), we obtain the maximum heating temperatures for the cases of a half-ellipsoid,

$$T_{\max}^{\text{ell}} = \frac{q_0}{4k}\frac{ab^2}{\sqrt{a^2 - b^2}}\ln\frac{a + \sqrt{a^2 - b^2}}{a - \sqrt{a^2 - b^2}},$$

and a hemisphere,

$$T_{\max}^{\text{sph}} = \frac{q_0}{2k}a^2. \quad (4)$$

For an oblate ellipsoid of revolution ($a < b$), the scale factor c and the coordinate $\alpha = \alpha_0$ are taken such that

$$c^2\cosh^2\alpha_0 = b^2, \quad c^2\sinh^2\alpha_0 = a^2.$$

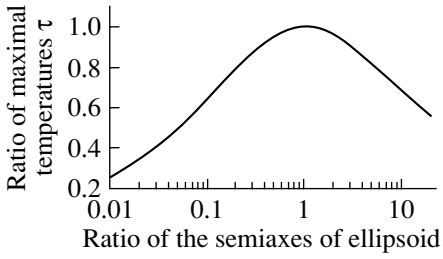

Fig. 3. Ratio $\tau = T_{max}^{ell}/T_{max}^{sph}$ of the maximum heating temperatures calculated for heat sources having the shape of a half-ellipsoid and a hemisphere of the same volume and power as a function of the ratio of the semiaxes of the ellipsoid.

In this case, the solution can be written as

$$T_{int}(\alpha, \beta) = -\frac{q_0}{k}c^2\left\{\frac{1}{4}\cosh^2\alpha\sin^2\beta - \frac{1}{6}\cosh^2\alpha_0 \times\left[1 + 2\sinh\alpha_0\,\mathrm{arccot}(\sinh\alpha_0) - 2(1 - \sinh\alpha_0\,\mathrm{arccot}(\sinh\alpha_0)) \times\frac{(3\sinh^2\alpha + 1)}{2}\frac{(3\cos^2\beta - 1)}{2}\right]\right\},$$

$$T_{ext}(\alpha, \beta) = \frac{q_0}{4k}ab\cosh\alpha_0\{-(3\cos^2\beta - 1)\sinh\alpha + [2(\sin^2\beta + \cosh^2\alpha) - 3\cosh^2\alpha\sin^2\beta]\,\mathrm{arccot}(\sinh\alpha)\}.$$

From these formulas, the maximum heating temperature is found to be

$$T_{max}^{ell} = \frac{q_0}{2k}\frac{ab^2}{\sqrt{b^2 - a^2}}\,\mathrm{arccot}\frac{a}{\sqrt{b^2 - a^2}}.$$

Figure 3 shows the ratio $\tau = T_{max}^{ell}/T_{max}^{sph}$ as a function of the ratio of the semiaxes of the ellipsoid η for a fixed volume of the heat generation region. It is seen that the difference between T_{max}^{ell} and T_{max}^{sph} becomes significant at $\eta < 0.15$ and $\eta > 5$.

We note that the method applied in this paper, in contrast to that used in [8], leads to simple expressions for the maximum heating temperature T_{max} and allows one to calculate (using only elementary functions) the temperature field produced by heat sources whose characteristic dimensions in the longitudinal and transverse directions are different.

Let us estimate the effect of the shape of the heat generation region on the T_{max} for the case of an electron beam focused at a point. We approximate the heat source distribution $q_f(\rho, z)$ by the Gaussian $A\exp(-z^2/\sigma_z^2 - \rho^2/\sigma_\rho^2)$ and find the half-widths σ_z and σ_ρ. We note that the isolines of the Gaussian distribution are ellipses with the ratio of their semiaxes $\eta = \sigma_z/\sigma_\rho$. Estimations show that $0.2 < \eta < 0.24$ for energies E_0 equal to 5, 10, and 15 keV. As can be seen from Fig. 3, the ratio τ varies within the interval $0.8 < \tau < 0.85$ in this case; therefore, for heat generation regions differing from a hemisphere, the difference in T_{max} calculated from Eq. (4) does not exceed 20%.

The influence of the shape of the heat source on the temperature field is illustrated in Fig. 4, where isother-

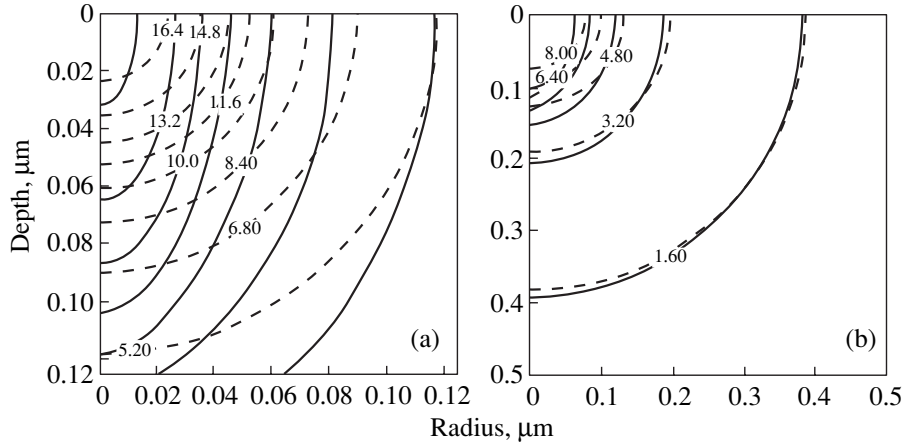

Fig. 4. Comparison of the isothermal lines of the temperature field for heat sources having the shape of a hemisphere (dashed lines) and a half-ellipsoid (solid lines). The heating temperatures indicated on the isothermal lines correspond to both the hemisphere and the half-ellipsoid. The isolines show the temperature field structure (a) near the source and (b) far from the source. In the latter case, it is evident that the temperature field distribution for the half-ellipsoid-shaped source approaches that for the hemispherical source.

mal lines are shown for the cases where the source has the shape of a semicircle and a semiellipse. The semiaxes of the ellipsoid a and b are taken to be twice the half-widths σ_z and σ_ρ, respectively, of the Gaussian distribution that approximates $q_f(\rho, z)$ for $E_0 = 5$ keV; the radius r_s of the sphere is calculated from the condition that the heat generation regions have the same volume. Thus, we have

$$a = 2\sigma_z = 0.072\ \mu\text{m}, \quad b = 2\sigma_\rho = 0.018\ \mu\text{m},$$

$$r_s = a\eta^{2/3} = 0.026\ \mu\text{m}.$$

The temperature field is calculated for the electron beam current $I = 100$ nA, which corresponds to the total generated heat power in the sample $P = IE_0 = 0.5$ mW. From Fig. 4, it is seen that the difference in the temperature distribution is noticeable only at distances of the order of a and becomes negligibly small at distances larger than $3a$.

Thus, the departure of the shape of the heat generation region from that of a hemisphere leads to relatively small changes in the maximum heating temperature and in the temperature field.

In order to estimate the error that results from the assumption of the heat generation being uniform over the hemisphere (which allows one to find an analytical solution to the problem), we also solved the problem numerically, with the heat source distribution found in the first stage for the case of an electron beam focused at a point.

The heat problem was solved by the finite-element method. The numerically calculated values of the maximum heating temperature $T_{\max}^{\text{cal}}$ are listed in the table. Usually, for the case of a beam focused at a point, the temperature $T_{\max}$ is estimated from Eq. (4) for a hemispherical heat source whose radius R is equal to the ultimate range of electrons R_0. The density of generated heat q_0 is calculated as the ratio of the total heat power P generated in the sample to the volume of the hemisphere. As a result, one obtains

$$T_{\max}^1 = \frac{R^2 q_0}{2k} = \frac{3}{2\pi}\frac{P}{2Rk}, \quad R = R_0. \tag{5}$$

According to [16], the ultimate range R_0 of an electron with energy E_0 in a substance of density $\tilde{\rho}$ is

$$R_0 = 0.0276 A E_0^{1.67}/Z^{0.889}\tilde{\rho}. \tag{6}$$

Here, E_0 is measured in keV, A in g/mol, $\tilde{\rho}$ in g/cm^3, and R_0 in μm; Z is the atomic number of the target. As indicated in [17], the range of electrons thus calculated agrees well with the data obtained from the experimental dependence of the transmission coefficient on the thickness of the film.

We calculated the range of electrons in GaN by putting $\tilde{\rho} = 6.0$ g/cm^3, $A = 41.864$ g/mol, and $Z = 27$. From Eq. (6), the values of a are found to be 0.15, 0.48, and 0.95 μm for $E_0 = 5$, 10, and 15 keV, respectively. The estimated temperature $T_{\max}^1$ for these energies is presented in the table. A comparison of $T_{\max}^1$ and $T_{\max}^{\text{cal}}$ shows that this estimation method gives a maximum heating temperature which is about twice as small. This discrepancy is due to the peaked heat source distribution, for which the ultimate range of electrons cannot be taken as the characteristic dimension of the heat generation region. We will assume that heat generation occurs predominantly in a hemisphere of a smaller radius and find this radius by equating the estimated temperature from Eq. (5) to $T_{\max}^{\text{cal}}$. Since the ratio $T_{\max}^{\text{cal}}/T_{\max}^1$ depends on the energy only slightly, we take the radius of the hemisphere to be

$$R = 0.571 R_0. \tag{7}$$

The value of $T_{\max}^1$ calculated using Eq. (7) is designated as $T_{\max}^2$ and also presented in the table. It is seen that this choice of the size of the heat generation region allows one to estimate the maximum heating temperature with an accuracy of about 3%.

Maximum heating temperatures calculated for GaN by solving the heat problem numerically ($T_{\max}^{\text{cal}}$), or from Eqs. (5) and (6) ($T_{\max}^1$), or from Eqs. (5) and (7) ($T_{\max}^2$)

$T_{\max}$	E_0		
	5 keV	10 keV	15 keV
$T_{\max}^{\text{cal}}$	10.95	6.52	5.09
$T_{\max}^1$	6.08	3.82	2.90
$T_{\max}^2$	10.67	6.68	5.07

It is of interest to compare the calculated temperature field and the distribution in Eq. (3) produced by a hemispherical source. Isothermal lines for this case are depicted in Fig. 5a. A comparison of the temperature fields for $E_0 = 5$ keV shows that the maximum deviations of the distribution in Eq. (3) from the calculated values do not exceed 60%. The values of the temperature at large distances from the origin for the distribution in Eq. (3) exceed the calculated values by about 15%. This is because the total heat power generated in the sample is taken to be $P = IE_0 = 0.5$ mW and the decrease in this quantity due to backward scattering of the electrons is not taken into account. The isothermal lines in Fig. 5b are calculated equating the power of the hemispherical source to the generated heat power found by integrating the calculated distribution of the energy loss density. It is seen that in this case, the temperature fields coincide at large distances from the

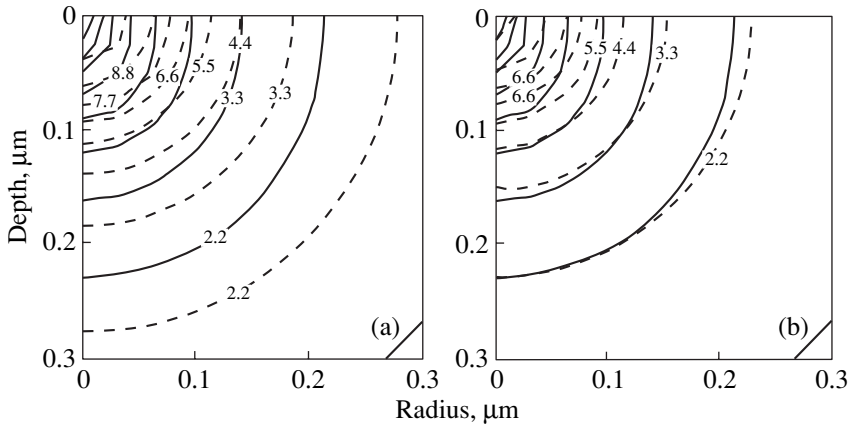

Fig. 5. Comparison of the numerically calculated temperature field and the temperature field for a hemispherical source for E_0 = 5 keV. (a) The power of the hemispherical source is $P = IE_0$ = 0.5 mW (energy losses due to backward scattering of electrons are ignored). (b) The power of the hemispherical source is taken equal to the heat power found by integrating the calculated energy loss density distribution.

source. From Fig. 5 it follows that the departure of the distribution of the generated heat density from a uniform distribution over a hemisphere is manifested only at distances of the order of the heat source dimensions and, at the same time, allows one to estimate the maximum temperature and size of the heated region.

The results obtained for the case of an electron beam focused at a point are also of interest and can be used to estimate the temperature distribution produced by a beam of finite diameter. Indeed, since the problem is linear, the temperature can be found from a formula similar to Eq. (1):

$$T(x, y, z) = \iint T_f(x - x_0, y - y_0, z) I_d(x_0, y_0) dx_0 dy_0,$$

where T_f is the temperature distribution produced in the sample by the beam focused at a point. We also note that the maximum value of T_f can be considered an upper estimate for the heating temperature in the case of a sample irradiated by a beam of finite diameter.

For beams of finite diameter, the heat generation region can be approximated by a half-ellipsoid whose characteristic cross-sectional dimension $2b_d$ is

$$2b_d = \sqrt{d^2 + (2b)^2},$$

where $2b$ is the characteristic dimension of the heat source produced by the beam focused at a point. In this case, the ratio of the semiaxes of the ellipsoid η_d is given by

$$\eta_d = \sqrt{(d/2a)^2 + \eta^2}.$$

The maximum heating temperature can be estimated from Eq. (4) for a hemispherical source with radius $R = R_d = a\eta_d^{2/3}$ and the $\tau(\eta_d) = T_{\max}^{\text{ell}}/T_{\max}^{\text{sph}}$ dependence presented in Fig. 3. When the beam diameter far exceeds the dimensions of the heat generation region, one can assume that $b \approx a \approx R$ and, therefore, $\eta_d = \sqrt{(d/2R)^2 + 1}$ and $R_d = R^{1/3}(d/2)^{2/3}$. This, in turn, leads to the following expression for the maximum heating temperature:

$$T_{\max} = \tau(\eta_d)\frac{3P}{4\pi R^{1/3}(d/2)^{2/3}k}.$$

3. CONCLUSIONS

Thus, we investigated the temperature distribution in a GaN sample irradiated with an electron probe. Account was taken of the actual heat source density, whose distribution was determined by performing numerical simulation of the probing-electron kinetics by the Monte Carlo method. The heat problem was solved numerically by using the distribution of generated heat found before. To examine the influence of the shape of the heat generation region on the temperature field, we analytically solved the problem in the case of uniform heat distribution generated in a half-ellipsoid. The results allow the following conclusions to be drawn.

The shape of the heat generation region arising in GaN samples under the action of an electron beam focused at a point is different from a hemisphere, but this fact affects the maximum heating temperatures and the temperature field only slightly. The influence can be significant only if the characteristic dimensions of the heat source in the transverse and longitudinal directions differ markedly, which is the case, for example, when the sample is irradiated with a broad beam of low-energy electrons.

The spatial distribution of the stationary temperature field produced in a GaN sample by an electron beam focused at a point and the maximum heating temperature can be estimated by approximating the heat

source density by a uniform distribution over a hemisphere. Taking the ultimate range of electrons as the characteristic dimension of the heat generation region leads to a considerably underestimated maximum heating temperature. By decreasing the characteristic dimension of the heat generation region in accordance with Eq. (7), one can determine the maximum heating temperature with an accuracy of 3% over a wide range of probing-electron energies. The temperature field distribution calculated for a hemispherical source differs by no more than 60% from the more exact calculated distribution for $E_0 = 5$ keV. The temperatures calculated in the hemispherical source approximation are about 15% higher than their more exact calculated values at large distances from the origin, because backward scattering of electrons is ignored. This discrepancy is decreased to 3% if the actual power of the source is taken into account.

ACKNOWLEDGMENTS

This work was supported in part by the Russian Foundation for Basic Research, grant no. 98-02-18109.

REFERENCES

1. R. Castaing, Adv. Electron. Electron Phys. **13**, 317 (1960).
2. G. S. Almasi, J. Blair, R. E. Ogilvie, and R. J. Schwartz, J. Appl. Phys. **36** (6), 1848 (1965).
3. C. F. Friskney and C. W. Haworth, J. Appl. Phys. **38** (9), 3796 (1967).
4. H. Amano, M. Kito, K. Hiromatsu, and I. Akasaki, Jpn. J. Appl. Phys. **28** (12), L2112 (1989).
5. S. K. Obyden, G. A. Perlovskiĭ, G. V. Saparin, and S. I. Popov, Izv. Akad. Nauk SSSR, Ser. Fiz. **48** (12), 2374 (1984).
6. I. G. Stoyanova and E. M. Belavtseva, Izv. Akad. Nauk SSSR, Ser. Fiz. **23** (6), 754 (1959).
7. I. G. Stoyanova and I. V. Anaskin, *Physical Foundations of Transmission Electron Microscopy Methods* (Nauka, Moscow, 1972).
8. V. N. Korolyuk and Yu. G. Lavrent'ev, in *X-ray Microanalysis with Electron Probe in Mineralogy* (Nauka, Leningrad, 1980), p. 7.
9. M. N. Filippov, Izv. Akad. Nauk, Ser. Fiz. **57** (8), 165 (1993).
10. T. E. Everhart and P. H. Hoff, J. Appl. Phys. **42** (13), 5837 (1971).
11. Electron Database, http://www.ioffe.rssi.ru/ES.
12. T. Rao-Sahib and D. B. Wittry, J. Appl. Phys. **45** (11), 5060 (1974).
13. H.-J. Fitting, H. Glaefeke, and W. Wild, Phys. Status Solidi A **43** (1), 185 (1977).
14. S. G. Konnikov, V. A. Solov'ev, V. E. Umanskiĭ, and V. M. Chistyakov, Fiz. Tekh. Poluprovodn. (Leningrad) **21** (11), 2028 (1987) [Sov. Phys. Semicond. **21**, 1229 (1987)].
15. N. N. Lebedev, I. P. Skal'skaya, and Ya. S. Uflyand, *Collection of Problems of Mathematical Physics* (Moscow, 1955).
16. K. Kanaya and S. Okayama, J. Phys. D **5** (1), 43 (1972).
17. J. I. Goldstein *et al.*, *Scanning Electron Microscopy and X-ray Microanalysis* (Plenum, New York, 1981; Mir, Moscow, 1984).

Translated by Yu. Epifanov

Physics of the Solid State, Vol. 43, No. 5, 2001, pp. 818–822. Translated from Fizika Tverdogo Tela, Vol. 43, No. 5, 2001, pp. 786–790.

SEMICONDUCTORS AND DIELECTRICS

Features of the Optical Response of Dielectric Crystals with Incommensurate Phases

O. S. Kushnir and L. O. Lokot

Lviv National University, Lviv, P.O. Box 3154, 790054 Ukraine

e-mail: kolinko@franko.lviv.ua

Received July 24, 2000

Abstract—The constitutive relation describing the optical response of dielectric crystals in incommensurately modulated phases is derived for the plane-wave range of modulation. The symmetry properties of modulation corrections to the permittivity tensor of such crystals are analyzed with allowance for spatial dispersion. These properties are dictated by the Onsager principle for a nonabsorbing medium and by the mesoscopic periodicity of the medium. It is shown that the basic results are consistent with the general conventional approach in crystal optics of spatially inhomogeneous media. *© 2001 MAIK "Nauka/Interperiodica".*

The optical properties of crystal dielectrics having intermediate phases with an incommensurately modulated superstructure, in particular, crystals of the A_2BX_4 family, attract the considerable interest of researchers (see review [1]). A striking example is the problem of optical activity in incommensurate (IC) phases of the crystals mentioned above. This problem is still far from being completely understood and has been widely discussed in recent literature [2–5]. The existence of this phenomenon is inconsistent with the inversion point symmetry of the IC phase structure, which is obtained by "averaging" the influence of modulation; therefore, further theoretical and experimental research is required.

In terms of macroscopic electrodynamics, the optical response of an IC crystal depends on the permittivity tensor at optical frequencies. A number of authors discussed some of its properties determined by the symmetry of the IC phase, as well as the specific features of the transition from a microscopic to a macroscopic description [2, 6–10]. An analysis of electromagnetic-wave propagation in IC crystals with allowance for spatial-dispersion effects was carried out in [9, 11]. The purpose of the present work is to consider the features of the optical response of an incommensurately modulated medium with spatial dispersion and, in particular, to analyze the symmetry of the part of the dielectric tensor that depends on the wave vector of light and to refine the constitutive relation for the dielectrics with IC phases.

For the frequency range far from resonance, it is possible to neglect the frequency dispersion effects and to write the initial constitutive relation for a linear anisotropic nonmagnetic medium (taking into account its nonlocal spatial response) in the form [12]

$$D_i(\mathbf{r}) = \int \hat{\varepsilon}_{ij}(\mathbf{r}, \mathbf{r}')E_j(\mathbf{r}')d\mathbf{r}', \qquad (1)$$

where **D** and **E** are the electric displacement and the electric field strength of a light wave, respectively, and the response function $\hat{\varepsilon}_{ij}(\mathbf{r}, \mathbf{r}')$ defines the permittivity tensor. The subscripts in Eq. (1) denote Cartesian coordinates, and repeated indices are understood to be summed over.

Basically, Eq. (1) can be used for analysis of the crystal optics of IC phases. However, the wave vector of IC modulation $\mathbf{q}_{IC}$ is incommensurate with the basic vectors of the base lattice. Strictly speaking, this leads to a loss of translational periodicity in the crystal medium in the direction of the modulation axis (we are further interested in the case of one-dimensional modulation) and to the corresponding difficulties of analysis of the properties of IC crystals by using well-developed methods of the solid state theory. The translational invariance can be restored within the framework of the approach based on superspatial symmetry in four-dimensional space $(\mathbf{r}, \varphi)$, where φ is the phase of the modulation wave (see, e.g., [13]). This technique was concretized for crystal optics of IC phases in [9], where the initial integral coupling equation (1) was written in a modified form:

$$D_i(\mathbf{r}, \varphi) = \int \hat{\varepsilon}_{ij}(\mathbf{r}, \mathbf{r}', \varphi)E_j(\mathbf{r}', \varphi)d\mathbf{r}'. \qquad (2)$$

Using Eq. (2), we introduce the Fourier transform of the microscopic permittivity tensor and analyze some of its properties (see also [9]). The kernel $\hat{\varepsilon}_{ij}(\mathbf{r}, \mathbf{r}', \varphi)$ must be invariant with respect to the transformations of the superspatial group describing the symmetry of the IC phase. In particular, for the subgroup of translations, we have

$$\hat{\varepsilon}_{ij}(\mathbf{r}, \mathbf{r}', \varphi) = \hat{\varepsilon}_{ij}(\mathbf{r} + \mathbf{a}, \mathbf{r}' + \mathbf{a}, \varphi + \mathbf{q}_{IC}\mathbf{a}), \qquad (3)$$

where $\mathbf{a} = l_i\mathbf{a}_i$ are translation vectors of the base lattice of the initial higher-temperature phase ($\mathbf{a}_i$ are the basic

vectors of the lattice and l_i are integers). It is possible to write the dielectric function satisfying Eq. (3) as (cf. [12])

$$\hat{\varepsilon}_{ij}(\mathbf{r}, \mathbf{r}', \varphi) = \sum_{n_i, m} f_{ij}^{n_i, m}(\mathbf{R}) \exp(im\varphi) \exp(-i\mathbf{hr}'), \quad (4)$$

where $\mathbf{R} = \mathbf{r} - \mathbf{r}'$ and summation is actually carried out over all reciprocal-lattice vectors $\mathbf{h}$ that are involved in the crystal structure with IC modulation ($\mathbf{h} = n_i\mathbf{a}_i^* + m\mathbf{q}_{\mathrm{IC}}$, where $\mathbf{a}_i^*$ are the basic vectors of the reciprocal lattice, n_i and m are integers (see, e.g., [2])). In the notation of [2], modulation in crystals A_2BX_4 takes place along the $\mathbf{a}_3$ direction, i.e., $\mathbf{q}_{\mathrm{IC}} = \gamma\mathbf{a}_3^*$, where $\gamma = r/s + \delta$; the integers r and s characterize the crystal structure of the commensurate lock-in phase [with wave vector $\mathbf{q}_C = (r/s)\mathbf{a}_3^*$]; and $\delta \ll 1$ is a small incommensurateness parameter dependent on temperature [1].

After standard Fourier transformation of Eq. (2), we obtain

$$D_i(\mathbf{k}, \varphi) = \int \hat{\varepsilon}_{ij}(\mathbf{k}, \mathbf{k}', \varphi) E_j(\mathbf{k}', \varphi) d\mathbf{k}', \quad (5)$$

where

$$\hat{\varepsilon}_{ij}(\mathbf{k}, \mathbf{k}', \varphi) = (2\pi)^{-6} \iint \hat{\varepsilon}_{ij}(\mathbf{r}, \mathbf{r}', \varphi) \times \exp[i(\mathbf{k}'\mathbf{r}' - \mathbf{kr})] d\mathbf{r} d\mathbf{r}'. \quad (6)$$

Substituting Eq. (4) into Eq. (6) yields

$$\hat{\varepsilon}_{ij}(\mathbf{k}, \mathbf{k}', \varphi) = \sum_{n_i, m} \varepsilon_{ij}^{n_i, m}(\mathbf{k}) \exp(im\varphi) \delta(\mathbf{k}' - \mathbf{k} - \mathbf{h}), \quad (7)$$

where $\delta(\mathbf{k})$ is the Dirac delta function and

$$\varepsilon_{ij}^{n_i, m}(\mathbf{k}) = (2\pi)^{-3} \int f_{ij}^{n_i, m}(\mathbf{R}) \exp(-i\mathbf{kR}) d\mathbf{R} \quad (8)$$

is the microscopic Fourier transform of the dielectric tensor corresponding to the spatial period $\lambda_h = 2\pi/|\mathbf{h}|$. In the limiting case $\mathbf{q}_{IC} = \mathbf{q}_C$ ($\delta = 0$), Eq. (7) describes the well-known structure of the tensor for usual (commensurate) crystals [12].

Generally speaking, only the symmetry of macroscopic quantities describing a crystal has a physical sense. Nevertheless, we consider, as in [9], the symmetry properties of the Fourier transform $\varepsilon_{ij}^{n_i, m}(\mathbf{k})$ for the purpose of making further comparison with the symmetry of the macroscopic dielectric tensor. Using the Onsager principle of symmetry of kinetic coefficients [12, 14] and Eqs. (4) and (8), one can arrive at the relation

$$\varepsilon_{ij}^{n_i, m}(\mathbf{k}) = \varepsilon_{ji}^{n_i, m}(-\mathbf{k} - \mathbf{h}). \quad (9)$$

The trivial requirement of reality of the kernel of the integral operator in Eq. (2) for an optical medium without dissipation leads to the condition

$$\varepsilon_{ij}^{n_i, m}(\mathbf{k}) = [\varepsilon_{ij}^{-n_i, -m}(-\mathbf{k})]^*. \quad (10)$$

From Eqs. (9) and (10), we obtain

$$\varepsilon_{ij}^{n_i, m}(\mathbf{k}) = [\varepsilon_{ji}^{-n_i, -m}(\mathbf{k} + \mathbf{h})]^*. \quad (11)$$

From Eq. (11), it is seen that the microscopic components $\varepsilon_{ij}^{n_i, m}(\mathbf{k})$ are non-Hermitian in contrast to the well-known result for the macroscopic dielectric tensor [14]. We note that Eq. (11) has escaped the attention of the authors of [9]. It is obvious that this result is valid for both nonmodulated and incommensurately modulated crystals; therefore, the source of this relation has to do with the inhomogeneity of the crystal structure at the microscopic level. It is known [12] that the procedure of macroscopic averaging for crystals with lattice periodicity alone enables one to express the microscopic Fourier components of the field $\mathbf{E}(\mathbf{k} + \mathbf{h})$ in terms of the macroscopic field $\mathbf{E}(\mathbf{k})$ and, as a consequence, to reduce the dielectric tensor to a single component $\varepsilon_{ij}^0(\mathbf{k})$ corresponding to $\mathbf{h} = 0$. According to Eq. (11), this leads to a Hermitian macroscopic permittivity tensor for a transparent optical medium.

Let us now discuss the basic points of the macroscopic averaging for IC crystals (see [12]). It follows from Eqs. (5) and (7) that

$$D_i(\mathbf{k}, \varphi) = \sum_{n_i, m} \varepsilon_{ij}^{n_i, m}(\mathbf{k}) E_j(\mathbf{k} + \mathbf{h}, \varphi) \exp(im\varphi). \quad (12)$$

Keeping only one term of this sum with $\varepsilon_{ij}^{0,0}(\mathbf{k})$, which describes a homogeneous medium, would correspond to a rough approximation frequently called the averaged IC structure approximation [6]. The approximation that takes into account the additional longest wavelength Fourier components $\varepsilon_{ij}^{n_i, m}(\mathbf{k})$ with nonzero vectors $\mathbf{h}$ [2, 9–11, 15] is more adequate. In the plane-wave IC modulation range, which is of further interest, the most important is the "difference" vector $\mathbf{q} = s(\mathbf{q}_{IC} - \mathbf{q}_C) = s\delta\mathbf{a}_3^*$, which makes an essential contribution to various properties of IC phases (see [15–18]). The indices of this vector are $n_1 = n_2 = 0$, $n_3 = \mp r$, and $m = \pm s$; therefore, the corresponding wavelength of the modulation wave ($\lambda_q = a_3/s\delta$) is much larger than the typical values of the lattice parameters, but is less than the wavelength of light λ in the visible range ($\lambda_q/\lambda \sim 0.1$, see also estimations in [2, 10, 11]). Taking the above analysis into account, we present Eq. (12) in the form

$$D_i(\mathbf{k}, \varphi) = \varepsilon_{ij}^{0,0}(\mathbf{k}) E_j(\mathbf{k}) + \varepsilon_{ij}^{\pm s}(\mathbf{k}, \varphi) E_j(\mathbf{k} \pm \mathbf{q}, \varphi) + \sum_{\substack{n_1, n_2; \\ n_3 \neq \mp r, m \neq \pm s; \\ n_i, m \neq 0}} \varepsilon_{ij}^{n_i, m}(\mathbf{k}) E_j(\mathbf{k} + \mathbf{h}, \varphi) \exp(im\varphi), \quad (13)$$

where

$$\varepsilon_{ij}^{\pm s}(\mathbf{k}, \varphi) = \varepsilon_{ij}^{\pm s}(\mathbf{k})\exp(\pm is\varphi). \quad (14)$$

We notice that the components $\varepsilon_{ij}^{\pm s}(\mathbf{k}, \varphi)$ corresponding to the reciprocal lattice vector $\mathbf{q}$ virtually do not depend on the microscopic indices n_i that are associated with the periodicity of the base lattice (see definition of $\mathbf{q}$).

Following a procedure similar to that described in [12], one will arrive at the macroscopic constitutive relation. Namely, neglecting the transverse components $\mathbf{E}_\perp(\mathbf{k} + \mathbf{h}, \varphi)$ of the short-wavelength microscopic Fourier transform $\mathbf{E}(\mathbf{k} + \mathbf{h}, \varphi)$ of the field (the corresponding accuracy is of the order $(a_i/\lambda)^2$, since $\mathbf{k} + \mathbf{h} \approx \mathbf{h}$ for the vectors of the reciprocal lattice with indices $n_i \neq 0$; $n_3 \neq \mp r$; $m \neq 0, \pm s$) and expressing the longitudinal components $\mathbf{E}_\parallel(\mathbf{k} + \mathbf{h}, \varphi)$ in terms of $\mathbf{E}(\mathbf{k})$ and $\mathbf{E}(\mathbf{k} \pm \mathbf{q}, \varphi)$, we obtain

$$\begin{aligned} D_i(\mathbf{k}, \varphi) &= \varepsilon_{ij}^0(\mathbf{k})E_j(\mathbf{k}) \\ &+ \varepsilon_{ij}^{\pm q}(\mathbf{k}, \mathbf{k} \pm \mathbf{q}, \varphi)E_j(\mathbf{k} \pm \mathbf{q}, \varphi), \end{aligned} \quad (15)$$

where the quantities $\varepsilon_{ij}^0(\mathbf{k})$ and $\varepsilon_{ij}^{\pm q}(\mathbf{k}, \mathbf{k} \pm \mathbf{q}, \varphi)$ contain contributions from the last sum in Eq. (13) in addition to the initial contributions $\varepsilon_{ij}^{0,0}(\mathbf{k})$ and $\varepsilon^{\pm s}(\mathbf{k}, \varphi)$.

Equation (15) corresponds to a "semimacroscopic" (or "mesoscopic" in terms of [10]) approximation describing the optical properties of IC phases. As mentioned above, this approximation is more accurate than the usual macroscopic approximation, which corresponds to keeping only the first term in Eq. (15). This term is characterized by the symmetry of the IC phase structure in which the modulation effect is spatially averaged [10] (see also [6, 7]). It is clear that the components $\varepsilon_{ij}^{\pm q}(\mathbf{k}, \mathbf{k} \pm \mathbf{q}, \varphi)$ are defined by the amplitude of the IC modulation wave and, consequently, are small in comparison with $\varepsilon_{ij}^0(\mathbf{k})$. We also note that the use of the permittivity in the classical sense is limited for inhomogeneous media (among which are the IC phases, as follows from the discussion above; for more details, see [19]). This is seen even from the fact that the constitutive tensor ε, which connects the field vectors $\mathbf{D}$ and $\mathbf{E}$, cannot be written in an explicit form. This is especially important for the soliton modulation range, for which it is necessary to take into account an infinite spectrum of the Fourier components of the dielectric tensor.

The symmetry properties of the modulated components of the constitutive tensor in Eq. (15) can be easily obtained from Eqs. (9), (11), and (14):

$$\varepsilon_{ij}^{\pm q}(\mathbf{k}, \mathbf{k} \pm \mathbf{q}, \varphi) = \varepsilon_{ji}^{\pm q}(-\mathbf{k} \mp \mathbf{q}, -\mathbf{k}, \varphi), \quad (16)$$

$$\varepsilon_{ij}^{\pm q}(\mathbf{k}, \mathbf{k} \pm \mathbf{q}, \varphi) = [\varepsilon_{ji}^{\mp q}(\mathbf{k} \pm \mathbf{q}, \mathbf{k}, \varphi)]^*. \quad (17)$$

Expression (17) shows that the modulated contributions $\varepsilon_{ij}^{\pm q}(\mathbf{k}, \mathbf{k} \pm \mathbf{q}, \varphi)$ associated with spatial dispersion are non-Hermitian. It is obvious that the reason for this behavior is the inhomogeneity of the crystal on a mesoscopic scale, which, in turn, is due to the IC structural modulation. In connection with the questions discussed, it is also pertinent to note that, as is well known, one of the consequences of the Hermitian property of the dielectric tensor, namely, the orthogonality of normal electromagnetic waves in a crystal, is not valid if one takes into account spatial dispersion [12]. However, the reason for this phenomenon is different; it is explained by the actual dependence of $\varepsilon_{ij}^0(\mathbf{k})$ on the refraction indices for these waves.

Let us now expand the tensor $\varepsilon_{ij}^{\pm q}(\mathbf{k}, \mathbf{k} \pm \mathbf{q}, \varphi)$ in Eq. (15), as is usually done, in a power series in $\mathbf{k}$ and retain only the linear term. Taking into account the inversion symmetry of the averaged structure of IC phases in crystals of compounds A_2BX_4 [$\varepsilon_{ij}^0(\mathbf{k} \neq 0) = 0$], we arrive at the relation

$$\begin{aligned} D_i(\mathbf{k}, \varphi) &= \varepsilon_{ij}^0 E_j(\mathbf{k}) \\ &+ [\varepsilon_{ij}^{\pm q}(\varphi) + i\gamma_{ijl}^{\pm q}(\varphi)k_l]E_j(\mathbf{k} \pm \mathbf{q}, \varphi), \end{aligned} \quad (18)$$

where ε_{ij}^0 corresponds to $\mathbf{k} = 0$. It follows from Eq. (16) that the gyrotropy tensor $\gamma_{ijl}^{\pm q}(\varphi)$ defined by Eq. (18) is antisymmetric with respect to the indices i and j. According to Eq. (17), this tensor is not necessarily real and can have an imaginary part, which contradicts the classical understanding of transparent media [14]. The reason for this discrepancy is actually connected with the fact that the definition of the tensor $\gamma_{ijl}^{\pm q}(\varphi)$, according to Eq. (18), does not take into account the terms that are proportional to the mesoscopic modulation vector $\mathbf{q}$; the results obtained in the present work for incommensurately modulated crystals are reduced to results that are already known in the literature for spatially inhomogeneous media.

In order to refine the features of the optical response of the IC phases, we perform the inverse Fourier transformation of Eq. (18) and take into account that the originals of the Fourier transforms $\varepsilon_{ij}^{\pm q}(\varphi)$ and $\gamma_{ijl}^{\pm q}(\varphi)$ are spatially dependent. Therefore, the structure of Eq. (18) corresponds to the product of two transforms. For any originals $f(t)$ and $g(t)$ and their Fourier transforms $F(x)$ and $G(y)$, one can write

$$\begin{aligned} \iint F(x)G(y-x)\exp(iyt)dxdy &= f(t)g(t), \\ \iint F(x)iyG(y-x)\exp(iyt)dxdy &= \frac{d}{dt}[f(t)g(t)]. \end{aligned} \quad (19)$$

Using Eqs. (18) and (19) and the formal correspondence $t \longrightarrow \mathbf{r}$, $x \longrightarrow \mp\mathbf{q}$, and $y \longrightarrow \mathbf{k}$, as well as $F \longrightarrow$

ε, γ, and $G \longrightarrow \mathbf{E}, \mathbf{D}$, we arrive at the constitutive relation in the coordinate space:

$$D_i(\mathbf{r}, \varphi) = [\varepsilon_{ij}^0 + \varepsilon_{ij}(\varphi + \mathbf{qr})]E_j(\mathbf{r}, \varphi) + \nabla_l[\gamma_{ijl}(\varphi + \mathbf{qr})E_j(\mathbf{r}, \varphi)], \quad (20)$$

where

$$E_i(\mathbf{r}, \varphi) = \int E_i(\mathbf{k} \pm \mathbf{q}, \varphi)\exp[i(\mathbf{k} \pm \mathbf{q})\mathbf{r}]d(\mathbf{k} \pm \mathbf{q}),$$
$$\varepsilon_{ij}(\varphi + \mathbf{qr}) = \int \varepsilon_{ij}^{\pm q}(\varphi)\exp(\mp i\mathbf{qr})d(\pm\mathbf{q}), \quad (21)$$

and the originals of the other quantities are defined in a similar way. Equation (20) can be concretized by specifying the spatial dependence $\varepsilon_{ij}(\varphi + \mathbf{qr})$ and $\gamma_{ijl}(\varphi + \mathbf{qr})$. For example, when solving the problem of light propagation in the plane-wave modulation range in crystals of compounds A_2BX_4 in actual practice, the parameter $\gamma_{ijl}(\varphi + \mathbf{qr})$ can be taken equal to $\gamma_{0,ijl}\sin(\varphi_0 + \mathbf{qr})$, where $\gamma_{0,ijl}$ and φ_0 are constants [2, 9–11]. Then, the last term in Eq. (20) includes a term which is proportional to the modulation vector $\mathbf{q}$.

Thus, analysis of the symmetry of the permittivity tensor of crystals in the IC phase reveals that it is necessary to take into account the spatial variation of the constitutive parameters of the medium by including the gradient term $\nabla_j\gamma_{ijl}(\varphi + \mathbf{qr})$ in Eq. (20). This result was missed in the analysis of optical properties of crystals with IC phases in all previous investigations (see [2, 3, 9–11]). At the same time, coupling equation (20) is a particular case of the equation that was earlier offered for the description of crystal optics of inhomogeneous anisotropic media [20, 21]. Using the Onsager principle leads to a modified equation in the final form

$$D_i(\mathbf{r}, \varphi) = [\varepsilon_{ij}^0 + \varepsilon_{ij}(\varphi + \mathbf{qr})]E_j(\mathbf{r}, \varphi) + \gamma_{ijl}(\varphi + \mathbf{qr})\nabla_l E_j(\mathbf{r}, \varphi) + \frac{1}{2}E_j(\mathbf{r}, \varphi)\nabla_l\gamma_{ijl}(\varphi + \mathbf{qr}), \quad (22)$$

and the tensors ε_{ij}^0 and $\varepsilon_{ij}(\varphi + \mathbf{qr})$ defined according to Eq. (22) are symmetric; the tensor $\gamma_{ijl}(\varphi + \mathbf{qr})$ is antisymmetric with respect to the first two indices; all tensors are real in the absence of absorption (see [20, 21] and also [22, 23]).

Despite the already mentioned difficulties associated with the introduction of the dielectric tensor which connects the electric displacement and the electric field strength in spatially dispersive inhomogeneous media, it is interesting to compare the symmetry properties of the contributions to the permittivity of IC crystals from various terms in Eq. (22). For electromagnetic waves of the form $\mathbf{E}(\mathbf{r}, \varphi) = \mathbf{E}(\varphi)\exp[i(\mathbf{k} \pm \mathbf{q})\mathbf{r}]$ in the plane-wave modulation range (see, for example, [11, 15]), the contribution from the third term in Eq. (22) behaves according to $\Delta\varepsilon_{ij}^{III} = i(k_l \pm q_l)\gamma_{ijl} = (\Delta\varepsilon_{ji}^{III})^*$, which can be qualified as the Hermitian property. This is also the case with the first and the second terms ε_{ij}^0 and ε_{ij}. However, the last term in Eq. (22) represents a real and antisymmetric, i.e., non-Hermitian, contribution to the permittivity [$\Delta\varepsilon_{ij}^{IV} = \nabla_l\gamma_{ijl} = -(\Delta\varepsilon_{ji}^{IV})^*$]. This additionally makes clear the sense of Eq. (17) following from symmetry analysis. Finally, it follows from the discussion above that the statement in [9] about the possible appearance of a symmetric (in indices i and j) part of the gyration tensor γ_{ijl} in a transparent medium with IC modulation is groundless.

It is necessary to note that in [20–23] the introduction of a coupling equation which includes spatial derivatives of material parameters was substantiated first of all by the requirement of the consistent description of gyrotropic media with due regard for the boundary conditions (see also discussions in [12, 24]). The key moment here was the sharply inhomogeneous boundary between a medium and vacuum. In our case, spatial inhomogeneities are of essentially the consequence volume effects and are due to the long-wavelength mesoscopic periodic structure of an incommensurately modulated crystal.

The dielectric crystal in the IC phase is probably the first example of a material for which the coupling equation in the form offered in [20, 21] is necessary for correct analysis of its optical properties. Indeed, for the plane-wave modulation range, the last term in the right-hand part of Eq. (22) includes the factor $q_l\gamma_{ijl}$, the modulus of which is at least an order of magnitude greater than the term $ik_l\gamma_{ijl}$ which is usually taken into account in the theory of optical activity and is connected with spatial derivatives of the field of a light wave. Thus, the neglect of the contribution $\nabla_l\gamma_{ijl}$ for the IC phases is inadmissible even as a rough approximation. This contribution causes, as a matter of fact, an additional physical mechanism of spatial dispersion in a periodic modulated medium, which is characterized not by the parameter a_i/λ (see, for example, [12, 14]), but by the parameter a_i/λ_q. It was assumed in one of the first papers on the crystal optics of IC phases [7] that spatial dispersion can be very strong and described by the parameter λ_q/λ. However, it is doubtful that the size of the spatial region in which the kernel $\hat{\varepsilon}_{ij}(\mathbf{r}, \mathbf{r}')$ in Eq. (1) is significant is increased from the lattice-parameter a_i scale to the period of an IC superstructure λ_q, because the potential of IC modulation is extremely weak.

Summarizing, we emphasize once again that the features of the nonlocal optical response of dielectric crystals with IC phases and the specific symmetry properties of their permittivity that we discussed in this paper are manifestations of the general behavior inherent to spatially inhomogeneous optical media. The results obtained indicate that it is necessary to reconsider a number of groundless, from our point of view, conclusions [25] concerning the crystal optics of IC phases. In particular, the coupling equation of a mesos-

copically inhomogeneous medium should be properly taken into account when interpreting experimental data on the optical activity of crystals of compounds A_2BX_4.

REFERENCES

1. H. Z. Cummins, Phys. Rep. **185**, 211 (1990).
2. H. Meekes and A. Janner, Phys. Rev. B **38** (12), 8075 (1988).
3. J. Kobayashi, Phys. Rev. B **42** (13), 8332 (1990).
4. C. L. Folcia, J. Ortega, J. Etxebarria, and T. Breczewski, Phys. Rev. B **48** (2), 695 (1993).
5. M. Kremers and H. Meekes, J. Phys.: Condens. Matter **7**, 8119 (1995).
6. R. M. Pick, in *Geometry and Thermodynamics: Common Problems in Quasi-Crystals, Liquid Crystals and Incommensurate Systems*, Ed. by J.-C. Toledano (Plenum, New York, 1990), p. 439.
7. V. A. Golovko and A. P. Levanyuk, Zh. Éksp. Teor. Fiz. **77** (4), 1556 (1979) [Sov. Phys. JETP **50**, 780 (1979)].
8. J. Fousek and J. Kroupa, Czech. J. Phys., Sect. B **36**, 1192 (1986).
9. I. V. Stasyuk and A. M. Shvaika, Preprint No. 91-53P (Inst. of Physics of Condensed Systems, Academy of Sciences of Ukraine, Kiev, 1991).
10. E. Dijkstra, A. Janner, and H. Meekes, J. Phys.: Condens. Matter **4**, 693 (1992).
11. O. S. Kushnir and L. O. Lokot', Fiz. Tverd. Tela (St. Petersburg) **39** (8), 1360 (1997) [Phys. Solid State **39**, 1207 (1997)].
12. V. M. Agranovich and V. L. Ginzburg, *Crystal Optics with Spatial Dispersion, and Excitons* (Nauka, Moscow, 1979; Springer-Verlag, New York, 1984).
13. A. Janner and T. Jannsen, Acta Crystallogr., Sect. A: Cryst. Phys., Diffr., Theor. Gen. Crystallogr. **A36**, 399 (1980).
14. L. D. Landau and E. M. Lifshitz, *Course of Theoretical Physics*, Vol. 8: *Electrodynamics of Continuous Media* (Gostekhizdat, Moscow, 1957; Pergamon, New York, 1984).
15. O. S. Kushnir, J. Phys.: Condens. Matter **9**, 9259 (1997).
16. K. Hamano, Y. Ikeda, T. Fujimoto, *et al.*, J. Phys. Soc. Jpn. **49**, 2278 (1980).
17. B. A. Strukov and A. P. Levanyuk, *Physical Principles of Ferroelectric Phenomena in Crystals* (Nauka, Moscow, 1983).
18. O. S. Kushnir, L. O. Lokot, L. P. Lutsiv-Shumski, *et al.*, Phys. Status Solidi B **214**, 487 (1999).
19. V. L. Ginzburg, *The Propagation of Electromagnetic Waves in Plasmas* (Nauka, Moscow, 1967; Pergamon, Oxford, 1970).
20. V. M. Agranovich and V. I. Yudson, Opt. Commun. **9** (1), 58 (1973).
21. B. V. Bokut' and A. N. Serdyukov, Zh. Prikl. Spektrosk. **20** (4), 677 (1974).
22. B. V. Bokut' and A. N. Serdyukov, Zh. Éksp. Teor. Fiz. **61** (5), 1808 (1971) [Sov. Phys. JETP **34**, 962 (1972)].
23. V. M. Agranovich and V. L. Ginzburg, Zh. Éksp. Teor. Fiz. **63** (3), 838 (1972) [Sov. Phys. JETP **36**, 440 (1973)].
24. F. I. Fedorov, *The Theory of Gyrotropy* (Nauka i Tekhnika, Minsk, 1976).
25. M. Kremers, *Optical and Morphological Aspects of Incommensurate Crystals, PhD Thesis* (Nijmegen Univ., Nijmegen, 1995).

Translated by O. Ivanov

Physics of the Solid State, Vol. 43, No. 5, 2001, pp. 823–829. Translated from Fizika Tverdogo Tela, Vol. 43, No. 5, 2001, pp. 791–797.

SEMICONDUCTORS AND DIELECTRICS

The Influence of the Matrix Element on Angle-Resolved Photoemission Spectra of Insulating Cuprates

A. S. Moskvin, E. N. Kondrashov, and V. I. Cherepanov

Ural State University, pr. Lenina 51, Yekaterinburg, 620083 Russia

e-mail: Alexandr.Moskvin@usu.ru

e-mail: Evgeniy.Kondrshov@usu.ru

Received August 31, 2000

Abstract—Microscopic model calculations of the matrix element of a dipole moment are carried out in terms of the cluster model. This matrix element determines the transition probability of electron photoemission from a one-electron orbital with symmetry $\gamma\mu$ to a free state. The effect of the matrix element on the angular and polarization dependences in the angle-resolved photoemission spectra of insulating cuprates, such as $Sr_2CuO_2Cl_2$ and $Ca_2CuO_2Cl_2$, is analyzed under the assumption of a well-isolated ground state of the two-hole CuO_4^{5-} cluster, namely, the Zhang–Rice singlet. The angular **k** dependence of the matrix element gives rise to effects, such as the residual Fermi surface, which are typical of metallic systems. An analysis of the experimental data reveals the presence of another electronic state (with different symmetry) in the vicinity of the Zhang–Rice singlet. © *2001 MAIK "Nauka/Interperiodica".*

INTRODUCTION

In recent years, angle-resolved photoemission spectroscopy (ARPES) has been used extensively to investigate the electronic structure of both undoped and doped copper oxides. Of special interest is investigation of the lower states of an additional isolated hole in an undoped CuO_2 plane of cuprates. The copper oxychlorides $Sr_2CuO_2Cl_2$ and $Ca_2CuO_2Cl_2$ are ideally suited, in a certain sense, to such an investigation. They are isostructural to the famous La_2CuO_4, the base compound of the family of high-temperature superconductors. The $Sr_2CuO_2Cl_2$ compound is a tetragonal antiferromagnet with nearly perfect CuO_2 planes, in which the apical oxygen anions are replaced by chlorine, with the $Cu–Cl_{apex}$ spacing (2.86 Å) being significantly larger than the $Cu–O_{apex}$ distance in La_2CuO_4 (2.42 Å). Therefore, in $Sr_2CuO_2Cl_2$, one has a good opportunity to investigate the states of both copper and oxygen atoms in the CuO_2 planes without any influence of apical oxygen on them. Numerous ARPES measurements have recently been made on these compounds with the aim of investigating the dispersion of the states near the Fermi level. ARPES spectra of $Sr_2CuO_2Cl_2$ were first measured by Wells *et al.* [1] at room temperature (and later at T = 150 K [2]). The dispersion of the lowest electronic state was investigated in [1] in three symmetry directions of the two-dimensional Brillouin zone, and the experimentally determined dispersion law was compared with that predicted from the t–J model [3]. The comparison showed reasonable agreement for the Γ–(π, π) direction, but there was no agreement for the $(0, \pi)$–$(\pi, 0)$ and $(0, 0)$–$(\pi, 0)$ directions. Subsequently, many attempts have been made to interpret the experiments in [1]. A satisfactory explanation was given in terms of the extended t–t'–t''–J model, which takes into account transitions of the hole to both the nearest and more distant neighbors [4]. However, more comprehensive measurements of the photoemission spectra of insulating cuprates [5–9] show that there are specific features in the spectral, angular, polarization, and energy dependences of the photocurrent intensity that cannot be explained in the framework of the conventional interpretation of ARPES spectra on the basis of the photocurrent being determined only by the spectral function of quasiparticles.

In this paper, we show that the angular and polarization dependences of the matrix element of a dipole moment that describes electron transitions from a one-electron orbital of symmetry $\gamma\mu$ to a free state in the process of photoemission are also of importance.

Our consideration is based on the conventional approximation in which the ARPES spectra of insulating cuprates, such as $Sr_2CuO_2Cl_2$ and $Ca_2CuO_2Cl_2$, are associated in the low-energy range (up to the energy that is 1.0 eV lower than the Fermi level) only with the isolated Zhang–Rice singlet $(b_{1g}^2)\,{}^1A_{1g}$. In other words, in this approximation, a hole is created in the one-particle state b_{1g} of the same symmetry $d_{x^2-y^2}$ as the original hole in the CuO_4 cluster.

1063-7834/01/4305-0823$21.00 © 2001 MAIK "Nauka/Interperiodica"

1. GENERAL EXPRESSION FOR THE PHOTOEMISSION INTENSITY

We consider the general expression for the intensity of photoemission which is accompanied by the creation of a photohole in a state of symmetry $\gamma\mu$; that is, we assume that the electron is removed from a one-electron molecular orbital $\gamma\mu$ of the CuO_4^{6-} cluster. The effective interaction Hamiltonian of an electromagnetic wave of frequency ω and polarization e with the crystal can be written in the form

$$\hat{H}_{\text{int}} = \sum_{\gamma\mu}\sum_{k} M_{\gamma\mu}(\mathbf{k}, \mathbf{e})\hat{c}^{\dagger}_{-\mathbf{k}\sigma}\hat{h}^{\dagger}_{\gamma\mu\mathbf{k}\sigma} + \text{H.c.}, \quad (1)$$

where $(-\mathbf{k})$ is the wave vector of the final state in which the photoelectron is detected and $\hat{c}^{\dagger}_{-\mathbf{k}\sigma}$ and $\hat{h}^{\dagger}_{\gamma\mu\mathbf{k}\sigma}$ are the creation operators of a photoelectron and a photohole, respectively. The matrix element is given by

$$M_{\gamma\mu}(\mathbf{k}, e) = \left\langle \psi_{\mathbf{k}}(\mathbf{r})\Psi^{(N-1)}_{\gamma\mu\mathbf{k}}\middle|\hat{H}_{eR}\middle|\Psi^{(N)}_{g}\right\rangle, \quad (2)$$

where

$$\hat{H}_{eR} = \frac{e\hbar}{2mc}(\mathbf{p}\cdot\mathbf{A} + \mathbf{A}\cdot\mathbf{p})$$

is the interaction Hamiltonian of electrons having a total momentum $\mathbf{p}$ in the crystal with the photon field characterized by the vector potential $\mathbf{A}$, $\Psi^{(N)}_{g}$ is the wave function of the ground state, $\Psi^{(N-1)}_{\gamma\mu\mathbf{k}}$ is the wave function of the crystal state $\gamma\mu\mathbf{k}$ with one electron removed (one extra hole), and $\psi_{\mathbf{k}}(\mathbf{r})$ is the wave function of a photoelectron. It should be noted that Eq. (2) is derived under some essential simplifying assumptions (see, e.g., [10]).

Approximating the wave function of the photoelectron by a plane wave, the matrix element in Eq. (2) can be written in the dipole approximation as

$$M_{\gamma\mu}(\mathbf{k}, \mathbf{e}) = \langle\psi_{\gamma\mu}(\mathbf{r})|\mathbf{e}\cdot\mathbf{r}|e^{i\mathbf{kr}}\rangle. \quad (3)$$

The final expression for the intensity of photoemission has the form

$$I(\mathbf{k}, \omega, e) \propto \sum_{\gamma_1\mu_1;\,\gamma_2\mu_2} M^{*}_{\gamma_1\mu_2}(\mathbf{k}, \mathbf{e})M_{\gamma_2\mu_2}(\mathbf{k}, \mathbf{e})A_{\gamma_1\mu_1;\,\gamma_2\mu_2}(\mathbf{k}, \omega). \quad (4)$$

The emission spectral function is written in the standard form

$$A_{\gamma_1\mu_1;\,\gamma_2\mu_2}(\mathbf{k}, \omega) = \frac{1}{2}\sum_{\sigma, e, g} e^{-\beta E_g}\left\langle e\middle|\hat{h}^{\dagger}_{\gamma_1\mu_1\sigma}\middle|g\right\rangle\left\langle g\middle|\hat{h}_{\gamma_2\mu_2\sigma}\middle|e\right\rangle \quad (5)$$

$$\times\,\delta(\omega + E_e - E_g) = \frac{1}{2}\sum_{\sigma}\int dt e^{i\omega t}\langle\hat{h}^{\dagger}_{\gamma_1\mu_1\sigma}(t)\hat{h}_{\gamma_2\mu_2\sigma}(0)\rangle,$$

where $|g\rangle$ and $|e\rangle$ are the ground and excited states of the cluster, respectively. The spectral functions carry complete information on the complex structure of the photohole and describe both the partial γ contributions and interference contributions (from repeated irreducible representations $\gamma_1 = \gamma_2$). They fulfill the sum rule

$$\int\frac{d\omega}{2\pi}A_{\gamma_1\mu_1;\,\gamma_2\mu_2}(\mathbf{k}, \omega) = n_{\gamma_1\mu_1}\delta_{\gamma_1\mu_1;\,\gamma_2\mu_2}. \quad (6)$$

In spite of the very rough approximations, the intensity of photoemission in Eq. (4) exhibits an extremely complicated multilevel structure with nontrivial polarization and $\mathbf{k}$, ω dependences.

The calculation of the spectral function $A(\mathbf{k}, \omega)$ for the photohole is a very complicated problem even in the simplest models [4]. In this paper, we will not discuss this problem, but consider the matrix element $M_{\gamma\mu}(\mathbf{k}, \mathbf{e})$ in the formula for the photoemission intensity. The necessity of calculating the matrix elements and taking the dispersion of the intensity into account when analyzing the experimental data for various cuprates was also indicated in [8, 11–13]. The effect of the interaction between different photohole states on the ARPES spectra of $Sr_2CuO_2Cl_2$ was partly demonstrated in [14].

2. ONE-ELECTRON MATRIX ELEMENTS

2.1. Copper Contribution

The copper atomic orbital with symmetry $\gamma\mu$ can be written as

$$d_{\gamma\mu}(\mathbf{r}) = R_{3d}(r)\sum_{m}\alpha_{2m}(\gamma\mu)Y_{2m}(\mathbf{r}),$$

where $\alpha_{2m}(\gamma\mu)$ are coefficients which are determined by symmetry and $R_{3d}(r)$ is the radial wave function, which will be taken in the simplest Slater form:

$$R_{3d}(r) = \frac{2}{81}\sqrt{\frac{2}{15}}\frac{r^2}{a_d^3\sqrt{a_d}}\exp\left\{-\frac{r}{3a_d}\right\}.$$

By substituting these expressions into Eq. (3) and using the standard expansion of the plane wave [15], we represent Eq. (3) in the form

$$e^{i\mathbf{kr}} = 4\pi\sum_{L=0}^{\infty}\sum_{M=-L}^{L} i^L j_L(kr)Y^{*}_{LM}(\mathbf{k})Y_{LM}(\mathbf{r}), \quad (7)$$

where we have introduced the notation

$$M^{(\text{Cu})}_{\gamma\mu}(\mathbf{k}, \mathbf{e}) = \langle d_{\gamma\mu}(\mathbf{r})|(\mathbf{e}\cdot\mathbf{r})|e^{i\mathbf{kr}}\rangle$$

$$= \frac{4\pi}{\sqrt{5}}\{\sqrt{2}D_1(k)K_1^{(\gamma\mu)}(\mathbf{e}, \mathbf{k}) + \sqrt{3}D_3(k)K_3^{(\gamma\mu)}(\mathbf{e}, \mathbf{k})\}, \quad (8)$$

$$D_1(k) = \langle R_{3d}(r)|r|j_1(kr)\rangle = 864\sqrt{\frac{6}{5}}\frac{a_d^3\sqrt{a_d}k(5-27a_d^2k^2)}{(1+9a_d^2k^2)^5},$$

$$D_3(k) = \langle R_{3d}(r)|r|j_3(kr)\rangle = 62\,208\sqrt{\frac{6}{5}}\frac{a_d^5\sqrt{a_d}k^3}{(1+9a_d^2k^2)^5},$$

$$K_L^{(\gamma\mu)}(\mathbf{e},\mathbf{k}) = \sum_{M,q,m}(-1)^q e_{-q}C_{LM1q}^{2m}Y_{LM}^*(\mathbf{k})\alpha_{2m}^*(\gamma\mu).$$

Here, C_{LM1-q}^{2m} are the Clebsch–Gordan coefficients. The dependence of $D_1(k)$ and $D_3(k)$ on the energy of the photoelectron is shown in Fig. 1 for the Cu 3*d* radial parameter $a_d = 0.35$ Å.

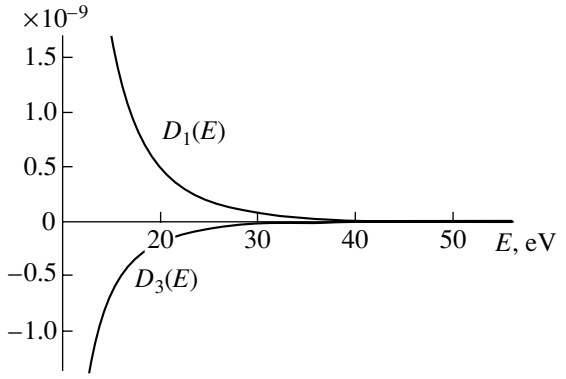

Fig. 1. Dependence of the Cu 3*d* atomic radial parameters $D_1(E)$ and $D_3(E)$ on the photoelectron energy ($a_d = 0.35$ Å).

2.2. Oxygen Contribution

The oxygen molecular orbital can be written as a linear combination of atomic O 2*p* functions centered at the corresponding oxygen sites:

$$p(\mathbf{r}) = \sum_{tm}C_m(\mathbf{t})R_{2p}(|\mathbf{r}-\mathbf{t}|)Y_{1m}(\mathbf{r}-\mathbf{t}), \quad (9)$$

where $C_m(\mathbf{t})$ are the coefficients determined by symmetry and $R_{2p}(r)$ is the radial wave function. By substituting Eq. (9) into Eq. (3) and introducing the variable $\mathbf{r}' = \mathbf{r}-\mathbf{t}$, we represent Eq. (3) in the form

$$M(\mathbf{k},\mathbf{e}) = \sum_{\mathbf{t}m}C_m^*(\mathbf{t})(\mathbf{e}\cdot\mathbf{t})e^{i\mathbf{kt}}\langle R_{2p}(\mathbf{r}')Y_{1m}(\mathbf{r}')|e^{i\mathbf{kr}'}\rangle + \sum_{\mathbf{t}m}C_m^*(\mathbf{t})e^{i\mathbf{kt}}\langle R_{2p}(r')Y_{1m}(\mathbf{r}')|(\mathbf{e}\cdot\mathbf{r}')|e^{i\mathbf{kr}'}\rangle. \quad (10)$$

It is convenient to introduce the following two vectors which meet the periodicity condition:

$$G_m(\mathbf{k},\mathbf{e}) = \sum_{\mathbf{t}}C_m^*(\mathbf{t})(\mathbf{e}\cdot\mathbf{t})e^{i\mathbf{kt}},$$
$$Z_m(\mathbf{k}) = \sum_{\mathbf{t}}C_m^*(\mathbf{t})e^{i\mathbf{kt}}. \quad (11)$$

Then Eq. (10) can be written in a more compact form:

$$M(\mathbf{k},\mathbf{e}) = \sum_m G_m(\mathbf{k},\mathbf{e})\langle R_{2p}(r)Y_{1m}(\mathbf{r})|e^{i\mathbf{kr}}\rangle + \sum_m Z_m(\mathbf{k})\langle R_{2p}(r)Y_{1m}(\mathbf{r})|(\mathbf{e}\cdot\mathbf{r})|e^{i\mathbf{kr}}\rangle. \quad (12)$$

Using the expansion of the plane wave in Eq. (7), we represent Eq. (12) in the form

$$M_{\gamma\mu}^{(\mathrm{O})}(\mathbf{k},\mathbf{e}) = 2\sqrt{3\pi}iB(k)(\mathbf{G}_{\gamma\mu}\cdot\mathbf{k})/k + \sqrt{\frac{4\pi}{3}}\left\{A_0(k)(\mathbf{Z}_{\gamma\mu}\cdot\mathbf{e}) - A_2(k)\frac{3(\mathbf{e}\cdot\mathbf{k})(\mathbf{Z}_{\gamma\mu}\cdot\mathbf{k})-k^2(\mathbf{Z}_{\gamma\mu}\cdot\mathbf{e})}{k^2}\right\}, \quad (13)$$

where we restored the indices γμ of the molecular orbitals. The simplest analytical expressions for the integrals over the radius in Eq. (13) are obtained if one uses the simplest Slater O 2*p* radial wave function:

$$R_{2p}(r) = \frac{1}{2\sqrt{6}}\frac{1}{\sqrt{a_p^3}}\frac{r}{a_p}\exp\left\{-\frac{r}{2a_p}\right\}. \quad (14)$$

In this case, we have

$$B(k) = \langle R_{2p}(r)|j_1(kr)\rangle = \frac{64\sqrt{6}a_p^2\sqrt{a_p}k}{3(1+4a_p^2k^2)^3},$$

$$A_0(k) = \langle R_{2p}(r)|r|j_0(kr)\rangle = \frac{64\sqrt{6}a_p^2\sqrt{a_p}(1-4a_p^2k^2)}{(1+4a_p^2k^2)^4},$$

$$A_2(k) = \langle R_{2p}(r)|r|j_2(kp)\rangle = \frac{512\sqrt{6}a_p^4\sqrt{a_p}k^2}{(1+4a_p^2k^2)^4}.$$

The dependence of the parameters $B(k)$, $A_0(k)$, and $A_2(k)$ on the photoelectron kinetic energy is shown in Fig. 2 for the O 2*p* radial parameter $a_p = 0.52$ Å.

2.3. Expression for $M_{b_{1g}}(\mathbf{k},\mathbf{e})$

Now, we analyze the matrix element that determines the process in which an electron is removed from the

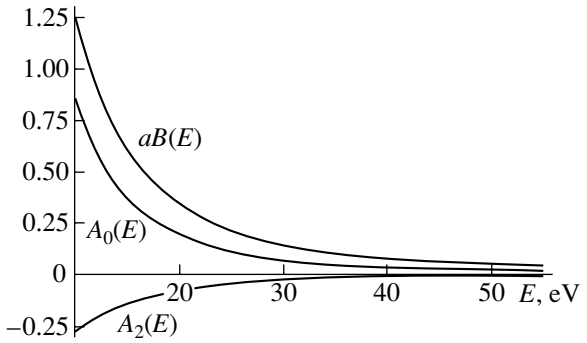

Fig. 2. Dependence of the O 2*p* atomic radial parameters $aB(E)$, $A_0(E)$, and $A_2(E)$ on the photoelectron energy (a_p = 0.52 Å); a = 4.0 Å is the lattice parameter.

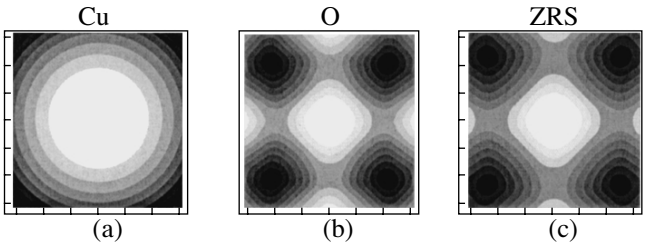

Fig. 3. Contour lines for the **k** dependence of the polarization-averaged quantity $|M_{b_{1g}}|^2$: (a) the copper contribution, (b) oxygen contribution, and (c) the contribution from the Zhang–Rice singlet ($\theta_{b_{1g}} = 0.4\pi$).

b_{1g} orbital and the hole remaining in the crystal forms the Zhang–Rice singlet.

For $\gamma\mu = b_{1g}$ (when the photon energy is $E_{ph} > 20$ eV and the binding energy is $E < 1$–2 eV), Eq. (8) gives

$$M_{b_{1g}}^{(\mathrm{Cu})}(\mathbf{k}, \mathbf{e}) = 2i\sqrt{\frac{3\pi}{5}}\left\{D_1(k) + \frac{7}{2}D_3(k)\right\}\frac{e_x k_x - e_y k_y}{k}. \quad (15)$$

With the numerical values of the coefficients $C_m^{(b_{1g})}(\mathbf{t})$ listed in the table, we obtain

$$M_{b_{1g}}^{(\mathrm{O})}(\mathbf{k}, \mathbf{e}) = i\sqrt{\frac{\pi}{3}}\left\{-3aB(k)\left[k_x e_x \cos\left(\frac{ak_x}{2}\right) - k_y e_y \cos\left(\frac{ak_y}{2}\right)\right] - 2[A_0(k) + A_2(k)]\right.$$
$$\left.\times\left[e_x \sin\left(\frac{ak_x}{2}\right) - e_y \sin\left(\frac{ak_y}{2}\right)\right] + 6A_2(k)\right.$$
$$\left.\times\,[e_x k_x + e_y k_y]\left[k_x \sin\left(\frac{ak_x}{2}\right) - k_y \sin\left(\frac{ak_y}{2}\right)\right]\right\}, \quad (16)$$

where $\hat{k}_\alpha = k_\alpha/k$, with $\alpha = x, y, z$.

The one-electron bonding molecular b_{1g} orbital can be written as

$$\Psi_{b_{1g}}(\mathbf{r}) = d_{b_{1g}}(\mathbf{r})\sin\theta_{b_{1g}} + \psi_{b_{1g}}(\mathbf{r})\cos\theta_{b_{1g}},$$

where $\theta_{b_{1g}}$ is the covalent mixing parameter of the copper and oxygen orbitals. Therefore, the photocurrent intensity is proportional to the quantity

$$\left|\langle\Psi_{b_{1g}}(\mathbf{k})|(\mathbf{e}\cdot\mathbf{r})|e^{i\mathbf{kr}}\rangle\right|^2 = \left|M_{b_{1g}}^{(\mathrm{Cu})}\right|^2\sin^2\theta_{b_{1g}} + \left|M_{b_{1g}}^{(\mathrm{O})}\right|^2\cos^2\theta_{b_{1g}} + \sin\theta_{b_{1g}}\cos\theta_{b_{1g}} \times\{(M_{b_{1g}}^{(\mathrm{Cu})})^* M_{b_{1g}}^{(\mathrm{O})} + M_{b_{1g}}^{(\mathrm{Cu})}(M_{b_{1g}}^{(\mathrm{O})})^*\}. \quad (17)$$

Figure 3 shows the **k** dependence of the photocurrent intensity $\overline{\left|\langle\Psi_{b_{1g}}(\mathbf{r})|(\mathbf{e}\cdot\mathbf{r})|e^{i\mathbf{kr}}\rangle\right|^2}$ averaged over the photon polarization $\mathbf{e} = (e_x, e_y, 0)$ for $\theta_{b_{1g}} = -0.3\pi$. The contour lines are also shown separately for the copper and oxygen contributions. The photoemission cross section for copper is assumed to be smaller than that for oxygen [16]. It is to be noted that the **k** dependence of the matrix element for the Zhang–Rice singlet is strongly anisotropic. (This dependence is determined fundamentally by the distribution of the oxygen hole density in the CuO_4 cluster.)

Figure 4 shows the polarization dependences of the photoemission intensity calculated from Eqs. (15) and (16) for the parallel ($\mathbf{e} \parallel \mathbf{k}$) and perpendicular ($\mathbf{e} \perp \mathbf{k}$) polarizations. Figure 4a corresponds to the partial Cu 3*d* contribution to the photoemission intensity (with the photohole created in the Zhang–Rice singlet state) for the parallel ($\propto\cos^2 2\phi$) and perpendicular ($\propto\sin^2 2\phi$) polarizations, respectively. Figure 4b shows the partial O 2*p* contribution. It should be noted that although the oxygen contribution has a more complicated **k** dependence than the copper contribution does, their polarization dependences are qualitatively similar.

3. DISCUSSION OF RESULTS

*3.1. Angular **k** Dependence of the Matrix Element and the "Residual Fermi Surface" Effect*

Model calculations of the transition matrix element show that the photocurrent intensity has a strong **k** dependence not associated with photohole dispersion. This result calls into question many conclusions based on the simplest single-band interpretation of the ARPES spectra [17], in which the **k** dependence of the

matrix element is ignored and the photocurrent intensity is assumed to be

$$I(\mathbf{k}\omega, e) \propto A(\mathbf{k}, \omega).$$

Therefore, the positions of the spectral peaks are assumed to correspond to the peak positions in the spectral function. This simple model is used to determine the two-dimensional profile of the Fermi surface from the experimental ARPES spectra of metals and to detect the "residual Fermi surface" effects in insulators [6]. In both these "experimental methods for determining the Fermi surface," one proceeds as follows. From the experimental data, one calculates the quantity

$$n_{\text{exp}}(\mathbf{k}, \mathbf{e}) = \int_{E_F - E_c}^{E_F} I(\mathbf{k}, E, \mathbf{e})dE,$$

where E_F is the Fermi energy and E_c is the energy (usually, about 1.0 eV) that is the presumable limit of the interval covering all low-energy excitations. Then, one finds the set of points corresponding to $\max\{\nabla_{\mathbf{k}} n_{\text{exp}}(\mathbf{k}, \mathbf{e})\}$, which determines the contour of the "Fermi surface." Theoretically, the contour of the Fermi surface is found in the same way, but, instead of $n_{\text{exp}}(\mathbf{k}, \mathbf{e})$, one makes use of the expression

$$n_{\text{th}}(\mathbf{k}) = \int_{E_F - E_c}^{E_F} A(\mathbf{k}, E)dE,$$

which, in general, differs essentially from n_{exp}.

Naturally, the topology of the "Fermi surface" must not depend on the polarization and energy of photons and the geometry of the experiment.

Since the matrix element in Eq. (2) depends heavily on **k**, a comparison between n_{exp} and n_{th}, as well as this method of determining the Fermi surface, becomes controversial or even makes no sense at all.

The "residual Fermi surface" effects in $Ca_2CuO_2Cl_2$, reported in [6], can be explained even in terms of the completely localized photohole state approximation, where the spectral function in the expression for the photocurrent is independent of the wave vector. In this limiting case, the supposed "Fermi surface" is determined only by the matrix element effects and does not characterize any real band structure or, for example, strong antiferromagnetic correlations [18]. By the way, the contour lines, such as those presented in Fig. 3, graphically illustrate the topology of this supposed "Fermi surface."

3.2. The Polarization Dependence of the Matrix Element

The strong and nontrivial polarization dependence of the matrix element is one of the most important properties of angle-resolved photoemission. An experimental study of the ARPES polarization characteristics can provide important information not only on the effects of the matrix element but also on the symmetry and electronic structure of the photohole. On the whole, the polarization dependences of the matrix element calculated in this paper for the b_{1g} state of a photohole (Fig. 3) agree with the experimental data [9] for the main directions in the Brillouin zone, such as (π, π) and $(0, \pi)$, in $Sr_2CuO_2Cl_2$; however, this fact should not be taken as an argument in favor of the model of the isolated Zhang–Rice singlet. The point is that a similar polarization dependence can also take place in the case of complex hole states, such as a large nonadiabatic polaron [19]. In this regard, it is instructive to investigate the polarization dependence of the photocurrent in a larger region of the Brillouin zone.

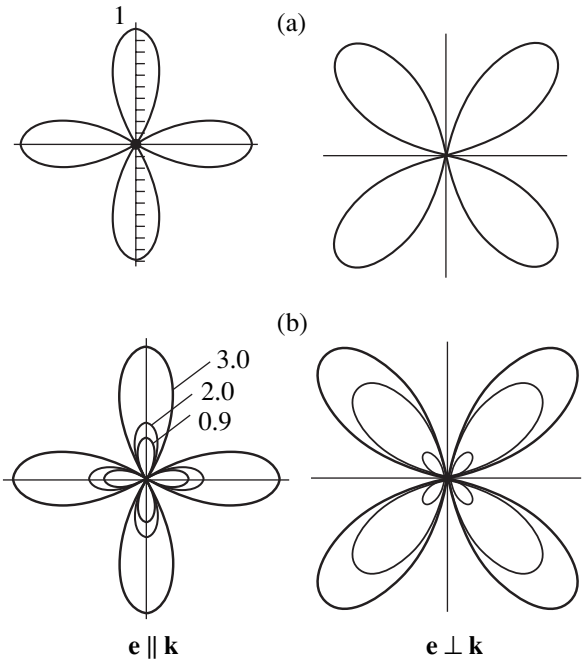

Fig. 4. Effects of the photon polarization (the angular dependence of the contribution from the Zhang–Rice singlet to the photoemission intensity for the parallel **e** ∥ **k** and perpendicular **e** ⊥ **k** polarizations): (a) the Cu 3*d* and (b) O 2*p* partial contributions. The figures near the curves indicate the value of the wave vector.

Coefficients $C_m^{(b_{1g})}(\mathbf{t})$

$C^{(\gamma\mu)}(\mathbf{t})$	$\frac{x}{2}$	$-\frac{x}{2}$	$\frac{y}{2}$	$-\frac{y}{2}$
$C_{+1}^{(b_{1g})}(\mathbf{t})$	$\frac{1}{2\sqrt{2}}$	$-\frac{1}{2\sqrt{2}}$	$\frac{i}{2\sqrt{2}}$	$-\frac{i}{2\sqrt{2}}$
$C_{-1}^{(b_{1g})}(\mathbf{t})$	$-\frac{1}{2\sqrt{2}}$	$\frac{1}{2\sqrt{2}}$	$\frac{i}{2\sqrt{2}}$	$-\frac{i}{2\sqrt{2}}$

3.3. Nonzero Photocurrent Intensity at the Center of the Brillouin Zone and Other Evidence of the Complicated, Non-Zhang–Rice Structure of the Valence State of a Photohole

As follows from our model calculations, the photocurrent intensity vanishes at the center of the Brillouin zone if the photohole is localized on the even b_{1g} orbital or on any other even in-plane γ orbital. This result is a fairly general consequence of symmetry and is not associated with the model description of the $\gamma\mu$ states. At the center of the Brillouin zone, the photocurrent intensity is nonzero only if the photohole is in an odd e_u or a_{1u} symmetry state. When light is polarized in the CuO_2 plane, such photohole states can be only the e_u orbitals of the CuO_4^{6-} center, which belong predominantly to copper (Cu 4*p*) or to oxygen alone (O 2*p*).

Thus, the contribution from the isolated Zhang–Rice singlet to the photoemission intensity vanishes at the center of the Brillouin zone. However, the experiments with both nonpolarized and polarized photons provide strong evidence that the photoemission intensity does not possess this property. The ARPES signal intensity at the Γ point of the Brillouin zone is finite in both $Sr_2CuO_2Cl_2$ [20] and $Ca_2CuO_2Cl_2$ [6], which suggests that, in addition to the Zhang–Rice singlet, there is a photohole valence state of the e_u symmetry type which presumably belongs to oxygen. Furthermore, it is this state that can give rise to an extra maximum in the ARPES spectrum of $Sr_2CuO_2Cl_2$; this maximum is separated by about 0.4–0.5 eV from the maximum attributed to the Zhang–Rice singlet. Many authors believe that the finite intensity in the spectral range between the low-energy peak and the strong emission band situated 2.7 eV below the Fermi level is associated with the noncoherent contributions [11] from the interaction of the photohole with phonons. However, a detailed analysis of the experimental data for $Sr_2CuO_2Cl_2$ carried out in [9] revealed that the additional spectral weight in the ARPES spectra is associated with the low-energy photohole state (located near the Zhang–Rice singlet) rather than with the noncoherent contributions.

The assumption of two states, b_{1g} and e_u, closely spaced in energy, for a photohole or a "doping" hole in the CuO_4 cluster agrees with many experimentally observed independent properties of undoped and lightly doped insulating cuprates. Among these properties, in the first place, is the appearance of midinfrared bands in the optical absorption spectra, which are associated with the allowed electric dipole (charge-transfer) transitions $b_{1g} \longrightarrow e_u$ in the CuO_4 clusters [21]. The energy of these bands in insulating cuprates $Sr_2CuO_2Cl_2$ and La_2CuO_4 ($\approx$0.4 eV) [22] correlates well with the relative positions of the corresponding peaks (determined from the ARPES spectra).

The e_u hole belonging to oxygen alone can be coupled to the b_{1g} hole both antiferromagnetically and ferromagnetically. Therefore, the valence multiplet should contain both the spin singlet $(b_{1g}e_u)^1E_u$ and the spin triplet $(b_{1g}e_u)^3E_u$; the energy of the latter can be even lower, because the b_{1g}–e_u exchange is ferromagnetic in character. Actually, the lower (Δ_{ST} = 0.13 eV) spin-triplet state of the two-hole CuO_4^{5-} center in $La_2Cu_{0.5}Li_{0.5}O_4$ was detected by NQR measurements for ^{63,65}Cu nuclei [23]. An analysis of the data on the Knight shift in NSR spectra of the 123-YBaCuO system provided indirect evidence of the O 2*p* π and e_u valence states [24]. As for the model of the $^1A_{1g}$–$^{1,3}E_u$ valence multiplet for copper oxides, it should be noted that Tjeng *et al.* [25] reported that they succeeded in separating different spin states in the one-particle spectrum of antiferromagnetic CuO and in showing that the top of the valence band is a pure spin singlet, which, in their opinion, is strong evidence of the existence of the stable (isolated) Zhang–Rice singlet in cuprates. However, their conclusions are based on experimental photoemission spectra measured in the vicinity of the Cu $2p_{3/2}$ (L_3) resonance, which permit one to unambiguously detect only the copper photohole states; in other words, this technique is insensitive to the presence of the pure oxygen e_u states.

The assumption of the activation mechanism for the hole conductivity of insulating cuprates with carriers being in the e_u states allowed one to explain the unusual anisotropy of the magnetoresistance discovered recently in systems such as $YBa_2Cu_3O_{6+x}$ ($x \sim 0.3$) [26].

In spite of this and some other evidence of the existence of at least two competing valence states of an extra localized hole in the CuO_4 center, most current theoretical models of the electronic structure of cuprates are based on the assumption that the ground state of an extra hole in the CuO_2 plane is a well-isolated Zhang–Rice singlet. It is suggested that the first excited state of the extra hole in the CuO_4^{6-} cluster (i.e., of the CuO_4^{5-} cluster) is 2 to 3 eV higher than the Zhang–Rice singlet and has little or no effect on the low-energy dynamics of charge carriers.

Some authors follow another point of view. Quantum-chemical calculations of multicenter copper–oxygen clusters [27] strongly suggest that the formation of valence states of a doping hole involves two competing orbitals, one of which is the basically copper b_{1g} and the other is the pure oxygen O 2*p* orbital. Analogous calculations [21, 28] taking into account all states (of both copper and oxygen) in the CuO_4^{5-} cluster show the presence of the two-hole ^1E_u state in the vicinity ($\simeq$0.5 eV) of the Zhang–Rice singlet. Calculations based on the exactly diagonalized Hamiltonian of the

p–d model for the CuO_6 cluster with a single hole or two holes [14] suggest that the triplet state $^3B_{1g}$ is fairly close (<1 eV) to the Zhang–Rice singlet for reasonable values of the model parameters.

4. CONCLUSIONS

In this paper, we performed microscopic model cluster calculations of the matrix element that determines the intensity of the photoemission current with creating a hole in the Zhang–Rice singlet state. A direct model calculation showed that the angular and polarization dependence of the matrix element is strong and leads in many cases to such effects as a residual or supposed Fermi surface, which are observed in the ARPES spectra of insulating cuprates. The photocurrent intensity vanishes at the center of the two-dimensional Brillouin zone for any photon polarization. This behavior does not agree with the finite spectral weight at the Γ point in the ARPES spectra observed in $Sr_2CuO_2Cl_2$ and $Ca_2CuO_2Cl_2$ and is indicative of the existence of an additional E_u electronic state in the two-hole CuO_4^{5-} center in the vicinity of the Zhang–Rice singlet. This conclusion is also supported by the experimentally observed dependence of the low-energy spectral weight of photoemission on the photon energy. A number of independent experimental measurements of the optical, resonance, and kinetic properties of insulating cuprates also suggest that the model of the isolated Zhang–Rice singlet in cuprates should be generalized.

On the whole, analysis and theoretical interpretation of the ARPES spectra of the insulating cuprates $Sr_2CuO_2Cl_2$ and $Ca_2CuO_2Cl_2$ remain a very complicated problem at the present time. It should be noted that the recently discovered oscillatory dependence of the photocurrent on the energy of incident photons and, hence, on k_z [9] remains to be explained. In our opinion, such photocurrent behavior is due to the photohole having a three-dimensional, rather than two-dimensional, structure with a partial delocalization on the nearest CuO_2 planes [19].

ACKNOWLEDGMENTS

This work was supported in part by the REC-005 CRDF grant and by the Ministry of Higher Education of the RF, grant no. 97-0-7.3-130.

REFERENCES

1. B. O. Wells, Z.-X. Shen, A. Matsuura, *et al.*, Phys. Rev. Lett. **74**, 964 (1995).
2. C. Kim, P. J. White, Z.-X. Shen, *et al.*, Phys. Rev. Lett. **80** (19), 4245 (1998).
3. A. Nazarenko, K. J. E. Vos, S. Haas, *et al.*, J. Supercond. **8**, 671 (1995).
4. O. P. Suchkov, G. A. Sawatzky, R. Eder, and H. Eskes, Phys. Rev. B **56** (18), 11769 (1997).
5. S. La Rosa, I. Vobornik, F. Zwick, *et al.*, Phys. Rev. B **56**, R525 (1997).
6. F. Ronning, C. Kim, D. L. Feng, *et al.*, Science **282**, 2067 (1998).
7. R. Hayn, H. Rosner, V. Yu. Yushankhai, *et al.*, Phys. Rev. B **60** (1), 645 (1999).
8. S. Haffner, D. M. Brammeier, C. G. Olson, *et al.*, cond-mat/0006366; S. Haffner, D. M. Brammeier, C. G. Olson, *et al.*, Phys. Rev. B **61** (21), 14378 (2000).
9. C. Duerr, S. Legner, R. Hayn, *et al.*, cond-mat/0007283.
10. Peter J. Feibelman and D. E. Eastman, Phys. Rev. B **10** (12), 4932 (1974).
11. A. S. Alexandrov and C. J. Dent, cond-mat/9905185.
12. J. M. Eroles, C. D. Batista, and A. A. Aligia, cond-mat/9812325.
13. A. Bansil and M. Lindroos, cond-mat/9910496.
14. V. A. Gavrichkov and S. G. Ovchinnikov, Fiz. Tverd. Tela (St. Petersburg) **40** (2), 184 (1998) [Phys. Solid State **40**, 163 (1998)].
15. D. A. Varshalovich, A. N. Moskalev, and V. K. Khersonskiĭ, *Quantum Theory of Angular Momentum* (Nauka, Leningrad, 1975; World Scientific, Singapore, 1988).
16. J. J. Yeh and I. Lindau, At. Data Nucl. Data Tables **32** (1), 1 (1985).
17. M. Randeria, G. Jennings, Hong Ding, *et al.*, Phys. Rev. Lett. **74**, 4951 (1995).
18. V. Oganesyan, cond-mat/0003270.
19. A. S. Moskvin, E. N. Kondrashov, and V. I. Cherepanov, cond-mat/0007470.
20. P. W. Leung, B. O. Wells, and R. J. Gooding, cond-mat/9702016.
21. A. S. Moskvin, N. N. Loshkareva, Yu. P. Sukhorukov, *et al.*, Zh. Éksp. Teor. Fiz. **105**, 967 (1994) [JETP **78**, 518 (1994)].
22. A. Zibold, H. L. Liu, S. W. Moore, *et al.*, Phys. Rev. B **53**, 11734 (1996).
23. Y. Yoshinari, P. C. Hammel, J. A. Martindale, *et al.*, Phys. Rev. Lett. **77**, 2069 (1996).
24. Y. Yoshinari, Physica C (Amsterdam) **276**, 147 (1997).
25. L. H. Tjeng, B. Sincovic, N. B. Brookes, *et al.*, Phys. Rev. Lett. **80** (19), 4245 (1998).
26. A. S. Moskvin and Yu. D. Panov, cond-mat/0008035.
27. Jiro Tanaka and Chizuko Tanaka, J. Phys. Chem. Solids **59** (10–12), 1861 (1998).
28. A. S. Moskvin and Yu. D. Panov, Phys. Status Solidi B **212**, 141 (1999).

Translated by Yu. Epifanov

Physics of the Solid State, Vol. 43, No. 5, 2001, pp. 830–835. Translated from Fizika Tverdogo Tela, Vol. 43, No. 5, 2001, pp. 798–803.

SEMICONDUCTORS AND DIELECTRICS

Color Center Formation by Synchrotron Radiation in the $Na_6Al_6Si_6O_{24}(NaI)_{1.6}$ Optical Ceramic

I. Kudryavtseva, P. Liblik, A. Lushchik, Ch. Lushchik, V. Nagirnyĭ, and E. Vasil'chenko

Institute of Physics, Tartu University, Riia 142, Tartu, 51014 Estonia

Received October 19, 2000

Abstract—The spectrum of F-center excitation by 5- to 27-eV photons in the $Na_6Al_6Si_6O_{24}(NaI)_{2x}$ sodalite optical ceramic ($x = 0.8$) was measured at 80 K by high-sensitivity photoexcited luminescence techniques. The F centers are created by photons with an energy of 5.6- to 8.5 eV through the excitation and ionization of iodine centers of two types; in the 8.2- to 27-eV region, through the generation of electronic excitations in the aluminosilicate framework of alternating Al^{3+} and Si^{4+} ions, each coordinated tetrahedrally by oxygen ions. At the low irradiation doses used, the F centers are created primarily through photoelectron capture by the iodine vacancies which exist before irradiation. In the 23- to 25-eV region, the efficiency of F-center formation doubles as a result of the multiplication of electron–hole pairs. © *2001 MAIK "Nauka/Interperiodica".*

INTRODUCTION

The investigation of the spectra of F-center and anion vacancy formation by VUV radiation carried out in recent years has permitted one to detect and study the exciton and electron–hole mechanisms of creation of elementary radiation-induced defects in alkali halide crystals [1, 2]. The use of synchrotron radiation extended the region of measurement of F-center creation spectra to 30 eV, where radiation-induced defects form in KBr, KCl, and RbCl crystals under the conditions for multiplication of electronic excitations; these conditions were found to favor F-center stabilization at 300–450 K [3, 4]. The high-sensitivity luminescence technique was applied earlier to measure the spectra of F-center creation by 5- to 10-eV photons in the halide-containing aluminosilicates $Na_6Al_6Si_6O_{24}(NaBr)_{2x}$ [5] and $Na_6Al_6Si_6O_{24}(NaI)_{2x}$ [6, 7].

We present here, for the first time, the spectra of color-center formation by synchrotron radiation (SR) for $Na_6Al_6Si_6O_{24}(NaI)_{2x}$ sodalite ($x = 0.8$) obtained in the 5- to 27-eV region. The processes involved in the excitation of various kinds of luminescence in this ceramic in the spectral region indicated above were studied by us earlier [8].

It is known that the halide-containing aluminosilicates (sodalites) were developed for use as high-efficiency cathodochromic materials for black-line recording and long-term information storage in skiatrons (see, e.g., [9, 10]). The mechanisms involved in the creation in sodalites of high F-center concentrations (of more than 10^{20} centers in 1 cm^3), which are practically not destroyed in the visible region at 300 K, were studied optically and by EPR [11] (see reviews [10, 12]). We studied the initial stages in the formation of small amounts of color centers by photons with energies from 5 to 27 eV at 80–300 K. The color centers formed at 80 K were rapidly destroyed under irradiation by 2.05-eV photons (at the maximum of the F absorption band); this made it possible to measure the spectrum of F-center creation by synchrotron radiation within a broad spectral region by a technique which did not require heating of the sodalite to 500 K after measuring each point in the spectrum. An investigation of small amounts of photoerasable color centers by high-sensitivity luminescence techniques provided a means of studying one of the mechanisms of F-center formation under optical generation of electronic excitations on iodine centers and the aluminosilicate framework. Particular attention was focused on the spectral interval from 19 to 27 eV, where one photon absorbed in sodalite creates two electron–hole pairs.

1. SUBJECTS AND TECHNIQUES OF INVESTIGATION

The structure of the halide-containing aluminosilicates (sodalites) is described in [13, 14]. The aluminosilicate sodalite framework made up of alternating AlO_4 and SiO_4 tetrahedra forms a three-dimensional system of cubooctahedral voids (β cells). In $Na_6Al_6Si_6O_{24}(NaI)_{2x}$ (the so-called I-sodalite) at $x = 1$, an iodine ion I^-, coordinated tetrahedrally by four Na^+ ions, rests at the center of each cell. At $x = 0.8$, parts of the β cells contain only three Na^+ ions each. One might conventionally consider this to be equivalent to the existence in such a void of a divacancy (an anion vacancy V_a and a cation vacancy V_c). About 10^{17} cells in 1 cm^3 contain one vacancy each (V_a or V_c). Following the creation in sodalite of a conduction electron and a hole in the valence band, the electron becomes local-

ized in a cell with a single V_a to form an F center with a characteristic absorption band. The EPR spectrum of such a center contains 13 lines characterizing the interaction of a localized electron with four Na^+ ions, the nuclear angular momentum of each being 3/2 [11]. We also detected color centers whose EPR signal contains 10 lines, which are due to the interaction of a localized electron with three Na^+ ions [15]. The holes generated by the irradiation are trapped by iodine ions I^- coordinated by four or only three Na^+ ions [5].

Sodalites were studied for a long time in the form of powders or thin layers used as coatings on screens in skiatrons. Optical ceramics of halide-containing aluminosilicates, transparent within a broad spectral range, were first described in [16], and their color centers produced by x-rays were studied in [12, 17]. The optical ceramics were obtained by high-temperature recrystallization of sodalite powder at a high pressure in vacuum. $Na_6Al_6Si_6O_{24}(NaI)_{1.6}$ plates $10 \times 10 \times 0.8$ mm in size were cut from a ceramic block and polished. Such plates were studied earlier in our laboratory by high-sensitivity luminescence techniques [7, 8, 18].

The main SR experiments dealing with the luminescence and color centers were performed on the BL52 beam of the MAX-I storage ring in Lund (Sweden). The SR with the desired photon energy $h\nu_e$, which was cut out by a primary vacuum monochromator, impinged on the ceramic under study in a vacuum cryostat (8–300 K, 10^{-8}–10^{-9} mbar). The luminescence was detected in the photon counting mode through a secondary monochromator. After termination of the irradiation, visible radiation with the desired photon energy $h\nu_s$, which stimulated a luminescence flash, was directed from an incandescent lamp through another optical window and one more monochromator on the sodalite. This flash is produced by photoionization of the F centers and subsequent recombination of the conduction electrons with the holes localized at the iodine centers and other sodalite defects. After irradiation to a constant SR quantum dose at each $h\nu_e$, we detected (at 80 K for 15 s) a light sum of the 3.5-eV luminescence (S_F) photoexcited by photons with $h\nu_s = 2.1$ eV, and it was this light sum that characterized the number of F centers created by the irradiation. Having measured S_F, we performed additional illumination with $h\nu_s$, which completely destroyed the radiation-induced F centers. A similar technique of investigating F center spectra in alkali halide crystals is described in more detail in [3, 19]. Figure 1 presents dose dependences of S_F measured at 80 K for $h\nu_e = 16$ and 24 eV. In our subsequent measurements of the total F-center creation spectrum, we employed the same dose of 5×10^5 arbitrary units within the region of the linear dependence of the light sum S_F on the quantum irradiation dose.

In addition to the SR measurements, we studied the same $Na_6Al_6Si_6O_{24}(NaI)_{1.6}$ ceramics using the equipment in the Institute of Physics laboratory at the Tartu University. Following irradiation of a ceramic by an electron beam (6 keV) or x-rays (50 keV), the absorption spectra of the ceramic were measured with a SPECORD 40M spectrophotometer. The cathodoluminescence spectra were obtained in the photon counting mode through a double-grating vacuum monochromator (4–10 eV) or a DMR-4 (2–6 eV) double-grating monochromator at temperatures from 8 to 300 K. The optical burst excitation spectra, as well as the thermal activation characteristics, were measured on a ceramic sodalite irradiated at 80–300 K by 5- to 10-eV monochromatic radiation through a VMR-2 monochromator. The equipment permitted one to excite a luminescence pulse through the DMR-4 double-grating monochromator and to measure the thermally and photostimulated luminescence under heating from 80 to 550 K through a large-aperture MZD-2 monochromator or an UFS-6 color filter. A similar technique used to study alkali halide crystals is described in [19].

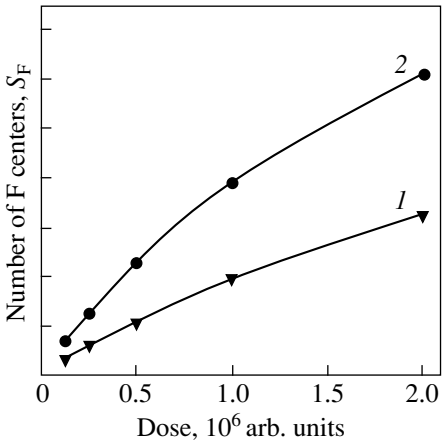

Fig. 1. Number of F centers, S_F, vs. irradiation dose of photons with $h\nu_e$ equal to (*1*) 16 and (*2*) 24 eV, measured at 80 K in the $Na_6Al_6Si_6O_{24}(NaI)_{1.6}$ ceramic.

2. LUMINESCENCE AND OPTICAL-BURST EXCITATION SPECTRA

Figure 2 presents cathodoluminescence spectra of I-sodalite measured at 9 K through a DMR-4 monochromator (curve *1*) and through a double-grating vacuum monochromator (curve *2*). Three main luminescence bands peaking at 4.2, 3.6, and ~2.9 eV were detected in the long-wavelength region (as under x-ray irradiation [18]). In the short-wavelength region, we were the first to succeed in detecting a weaker luminescence band in the 5- to 6-eV interval. The 3.6-eV band was shown earlier to be due to the luminescence of the I^- centers in the cubooctahedral β cells containing three Na^+ ions. In this case, the presence of the cation vacancy favors efficient hole trapping by such I^- centers [5]. The 4.2-eV peak originates from the excimer luminescence of the iodine centers created under the excita-

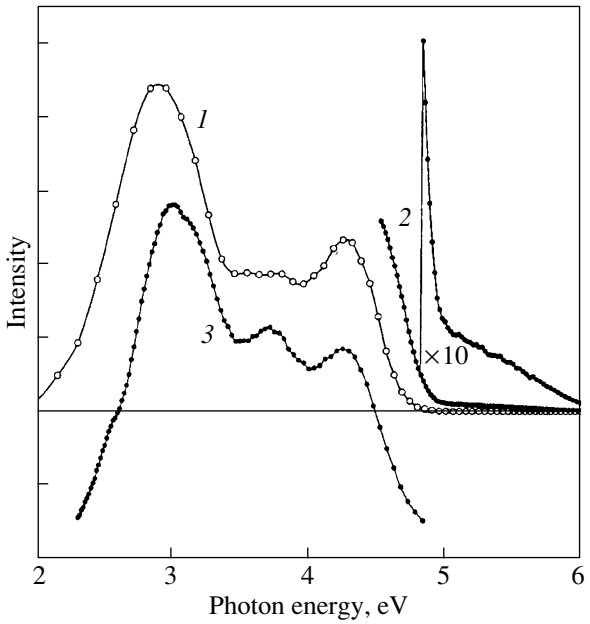

Fig. 2. Cathodoluminescence spectra at 9 K (*1*, *2*) and a luminescence spectrum obtained at 80 K under excitation with $h\nu_e$ = 24 eV (*3*) of the $Na_6Al_6Si_6O_{24}(NaI)_{1.6}$ ceramic. Spectrum *2* measured with a solar-blind PM tube through a double-grating vacuum monochromator.

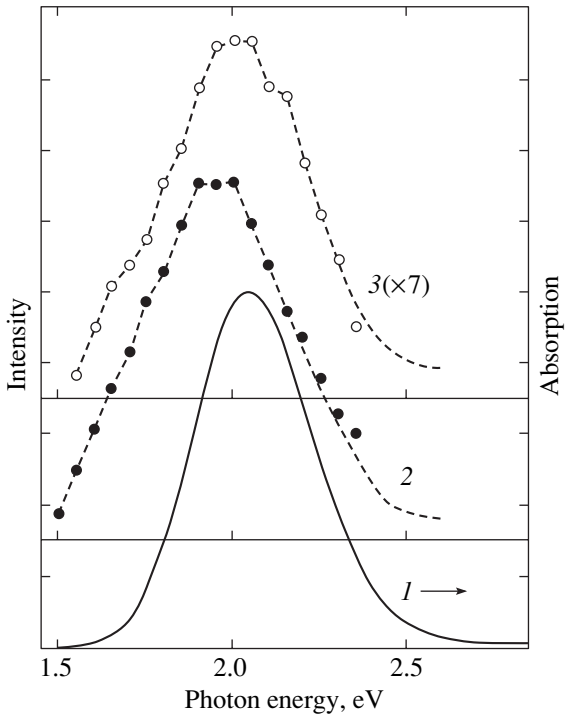

Fig. 3. Absorption spectrum of the $Na_6Al_6Si_6O_{24}(NaI)_{1.6}$ ceramic measured after irradiation by 6-keV electrons at 80 K and subsequent heating to 300 K (*1*) and spectra obtained by excitation by equal numbers of 3.5-eV luminescence photons directly after irradiation by 7.7-eV photons at 80 K (*2*) and after heating of the irradiated sample to 195 K and cooling to 80 K (*3*).

tion of the I^- centers in a regular β cell, which is located close to the β cell containing V_c [18]. We made numerous attempts to detect, in halide-containing aluminosilicates, the luminescence of single I^- ions in β voids surrounded by the same regular voids, which had to preclude the excimer luminescence of the iodine centers. We believe to have succeeded in detecting the luminescence of such centers in the 5- to 6-eV interval under irradiation by a 6-keV electron beam. A similar weak luminescence of metastable one-halide excitons at low temperatures was also observed in some alkali halide crystals [20, 21]. As follows from studies of halide-free aluminosilicates (e.g., the G zeolite), the luminescence seen at 2–3 eV may be due to radiative decay of electronic excitations of the aluminosilicate framework [10]. As can be seen from Fig. 2 (curve *3*), excitation by 24-eV photons in the region of absorption of the aluminosilicate framework at 80 K creates, in the emission spectrum of sodalite, the same luminescence bands peaking at 2.9 (for the most well-developed structure), 3.6, and 4.2 eV, as in the case of electron beam excitation.

Curve *1* in Fig. 3 is the absorption spectrum of the $Na_6Al_6Si_6O_{24}(NaI)_{1.6}$ ceramic obtained after irradiation by a 6-keV electron beam at 80 K and subsequent heating to 300 K. Similar to other authors who studied the absorption spectra of the x- or electron-irradiated I-sodalite ceramics [12], we obtained, at 300 K, a slightly asymmetric F band with a maximum at 2.05 eV and a half-width of 0.39 eV, which tails out toward shorter wavelengths. When cooled down to 80 K, this band becomes more narrow (to ~0.3 eV) and shifts slightly toward higher energies (with the maximum now at 2.08 eV). This band can be identified, on the whole, with an F center, i.e., an electron which is trapped by a halide vacancy coordinated by four Na^+ ions.

Figure 3 also presents excitation spectra (generated by equal numbers of photons of different frequencies) of 3.5-eV luminescence isolated by a MZD-2 monochromator (equipped with an additional UFS-6 filter). Curve *2* was obtained directly after irradiation by photons of 7.7 ± 0.1 eV at 80 K; curve *3*, after additional heating of the irradiated sample to 195 K and cooling to 80 K. This heating results in a weakening of the flash intensity at the maximum by nearly seven times. The weakening occurs nonuniformly over the profile; namely, the long-wavelength part of the excitation spectrum weakens substantially more than does the short-wavelength one. This and other experiments showed that 7.7-eV photons produce, in the ceramic at 80 K, not only main F centers but also color centers characterized by longer-wavelength absorption. The excitation spectra of the I-sodalite ceramics irradiated at 80 K are evidence of the existence of at least two types of color centers. Photoionization of the I^- centers by 7.7-eV photons produces, in addition to main F centers, centers with an absorption maximum at ~1.7 eV,

which, as follows from EPR studies, are due to an electron which is captured in a β cell and surrounded by three rather than four Na^+ ions [15]. We measured burst excitation spectra (in the 1.8- to 2.4-eV region) of 2.8- to 3.6-eV luminescence, isolated by a UFS-6 filter, from a ceramic irradiated by equal quantum doses of 5.7-, 6.7-, 7.6-, and 10.2-eV photons. Immediately after irradiation at 80 K, the excitation spectrum profiles were found to be nearly identical. Additional selective illumination of this sample at 80 K by photons of 1.7 eV brought about a stronger weakening of the long-wavelength part of the excitation spectrum obtained after this procedure. When performed with different $h\nu_e$, irradiation creates not only main F centers but also color centers with longer-wavelength absorption.

3. SPECTRA OF F-CENTER CREATION BY SYNCHROTRON RADIATION

Our subsequent work was focused on obtaining the spectra of creation of the main F centers in $Na_6Al_6Si_6O_{24}(NaI)_{1.6}$ by measuring the light sum of the 3.5-eV luminescence burst stimulated by photons with $h\nu_s = 2.1 \pm 0.03$ eV in a ceramic irradiated at 80 K. Figure 4 presents a ceramic reflectance spectrum obtained at 8 K and a spectrum of F center creation by photons with 5.0–10.5 eV. In the long-wavelength part of the F-center creation spectrum, one can see two narrow maxima at 5.75 and 6.7 eV, which are shifted relative to the reflectance maxima (6.1 and 6.97 eV) by approximately 0.3 eV toward longer wavelengths. The data presented in [8] permitted us to identify the reflectance maxima with a spin–orbit doublet in the electronic transitions in the I^- ions located in regular β cells. The F-center creation spectrum also exhibits a spin–orbit doublet (displaced by 0.3 eV), which can be interpreted as a manifestation of electronic transitions in I^- centers surrounded by three Na^+ ions only. Such centers carry an effective negative charge, which substantially increases the effective cross section with which they capture the holes created by the aluminosilicate framework absorbing the radiation ($h\nu_e \geq 8.5$ eV). Because of the superposition of second-order SR, we have not been able, thus far, to measure the F-center creation spectrum in the 10.5- to 12.5-eV region.

Figure 5 presents an 8-K reflectance spectrum and an 80-K F-center creation spectrum, which were measured on I-sodalite in the 13- to 27-eV region. The parts of the F-center creation spectrum displayed in Figs. 4 and 5 were measured at equal irradiation doses, and the light sums S_F are plotted along the ordinate axes in the same scale. The 8.5- to 27-eV region of the F-center creation spectrum corresponds to a practically unstudied region of fundamental absorption of the aluminosilicate framework [6, 8] and requires special analysis. We can presently discuss this problem only in a first approximation based on the quantitative data available on the optical characteristics of α-Al_2O_3 single crystals

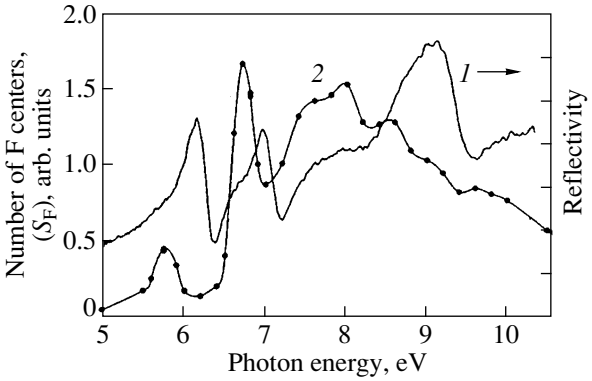

Fig. 4. (*1*) Reflectance spectrum at 8 K and (*2*) spectrum of F-center creation by 5- to 10.5-eV photons at 80 K obtained on the $Na_6Al_6Si_6O_{24}(NaI)_{1.6}$ ceramic.

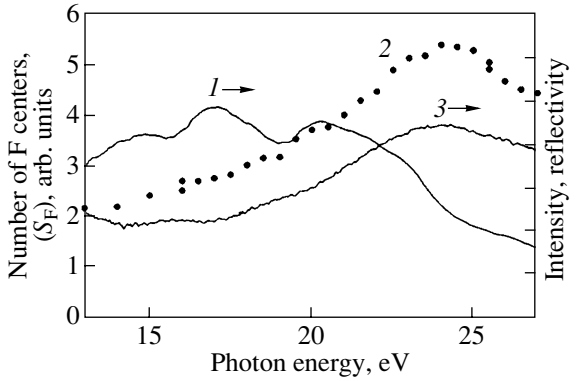

Fig. 5. (*1*) Reflectance spectrum at 8 K, (*2*) spectrum of F-center creation by 13- to 27-eV photons at 80 K, and (*3*) 3.5-eV luminescence excitation spectrum at 80 K obtained on the $Na_6Al_6Si_6O_{24}(NaI)_{1.6}$ ceramic.

(see [22, 23] and references therein), the theoretical band-structure calculations made for the α-Al_2O_3 and $MgAl_2O_4$ crystals (see, e.g., [24, 25]), and on a general analysis of the electronic excitation spectra in crystalline quartz (see, e.g., [26]).

The long-wavelength exciton absorption band in single-crystal α-Al_2O_3 peaks near 8.97 eV at 8 K. The self-trapped exciton luminescence (7.6 eV) is excited by 8.9- to 9.3-eV photons in the direct optical generation of excitons [22]. $Na_6Al_6Si_6O_{24}(NaI)_{2x}$ exhibits a distinct reflectance peak at 8 K in the 8.5- to 9.3-eV region (Fig. 4). As follows from calculations made for the AlO_6 octahedron in α-Al_2O_3, the transitions involving charge transfer from the oxygen to the Al^{3+} ions lie at shorter wavelengths than those for the AlO_4 tetrahedron in crystalline $MgAl_2O_4$ [24]. In quartz single crystals built of SiO_4 tetrahedra, the excitons generated in direct optical transitions are created by 10.6-eV photons and indirect band-to-band transitions occur for $h\nu > 8$ eV [26].

Photo-induced exciton creation in the sodalite aluminosilicate framework at 8 K can be expected to occur at 8.5–11 eV. In the same energy region, part of the absorbed photons can apparently also produce separated electrons and holes. In the 12- to 30-eV region, the spectrum should be dominated by electronic transitions producing holes in the broad, structurally complex oxygen valence band and electrons in the complex conduction band.

4. MULTIPLICATION OF ELECTRONIC EXCITATIONS

As can be seen from Fig. 5, the efficiency of creation of F centers, whose ionization gives rise to 3.5-eV recombination luminescence, increases strongly as one goes over from 18 to ~25 eV. As follows from Fig. 1, the efficiency of the F center creation doubles as one transfers from 16 to 24 eV throughout the SR quantum dose region studied by us. We associate this effect with the multiplication of electronic excitations (EEM), a process studied in considerable detail on many alkali metal halides [2–4], as well as on metal oxides (see, e.g., [22]), in which absorption of one photon produces a hole and a hot conduction electron whose energy is high enough to create a secondary electron–hole pair.

The electron–hole mechanism of EEM manifests itself in $Na_6Al_6Si_6O_{24}(NaI)_{1.6}$ both in the 3.5-eV luminescence excitation spectrum at 80 K (Fig. 5) and in the excitation of this luminescence at 8 K, in which case the spectrum is dominated by the 4.2-eV luminescence [8]. We were the first to detect a similar EEM effect for sodalites in the F-center creation spectrum (Fig. 5). Note that within the spectral region extending from 18 to 23 eV, the coefficients of reflection (and absorption) are of approximately the same magnitude and, therefore, in this region, there should not be any sharp variation of the luminescence efficiency caused by the different penetration depths of the exciting radiation into the ceramic. Our measurements showed that surface nonradiative electron–hole recombination manifests itself considerably more weakly in sodalites than in single crystals of metal oxides with a simple structure (e.g., in MgO), where the conduction electron and hot-hole ranges are markedly larger.

The electron–hole EEM mechanisms in wide-bandgap dielectrics are usually characterized by the lowest threshold energy, which is twice the bandgap (E_g). However, in real practice, a reliably discriminated EEM effect is observed, as a rule, only at energies noticeably in excess of $2E_g$. The point is that the absorbed photon imparts its energy in excess of E_g not only to the electron but also to the hole. However, because of the valence bands being narrow (compared to E_g), the energy received by the hole is not high enough to create a secondary electron–hole pair.

In α-Al_2O_3 crystals, E_g = 9.4 eV and the EEM processes are clearly pronounced only for $h\nu_e > 23$ eV > $2E_g$ [22]. In α-SiO_2 crystals, strong enhancement of the intrinsic luminescence at 2.26 eV starts at 8 K for $h\nu_e$ = 21.5 eV > $2E_g$ [8]. We reliably detected the EEM processes in $Na_6Al_6Si_6O_{24}(NaI)_{1.6}$ for $h\nu_e > 19$ eV. In sodalite, the luminescence efficiency starts to grow in the EEM region less sharply than it does in Al_2O_3 or SiO_2 and S_F doubles only at 25 eV. We believe that the doubled E_g in sodalite is larger than 19 eV, which is in accord with the suggestion of a predominantly excitonic nature of the electronic excitation corresponding to the 9-eV peak in the reflectance spectrum (Fig. 4). The onset of the growth in the efficiency of the electron–hole mechanism of F-center creation is distant from the region of efficiency doubling by more than 6 eV, which indicates a large width (>6 eV) of the complex aluminosilicate valence band derived primarily from the oxygen 2*p* states.

The falloff in the efficiency of F-center creation for $h\nu_e > 26$ eV (Fig. 5) can be due to a change of the SR absorption mechanism in this region. In α-Al_2O_3 crystals, photons with $h\nu_e > 25$ eV ionize the $2s^2$ rather than $2p^6$ oxygen shells, which markedly complicates the EEM processes [22, 24]. Similar transitions apparently also occur for $h\nu_e > 25$ eV in the sodalite aluminosilicate framework.

Thus, our experiments showed that the F centers created at 80 K, whose photoionization gives rise to the excitation of the iodine center recombination luminescence, are completely annealed when heated up to 320 K. This anneal, accompanied by thermally stimulated luminescence, acts particularly strongly in the 200–260 K region. Irradiation of $Na_6Al_6Si_6O_{24}(NaI)_{1.6}$ by high doses of x-rays or electrons produces, in the ceramic at 295 K, photostable F centers whose annealing requires heating of the sodalite to 450–550 K. The mechanism of this phenomenon differs naturally from the electron–hole process involving I^- centers and preirradiation anion vacancies, which was considered here. The creation of thermally and photostable F centers in sodalites by synchrotron radiation in the region of direct excitation and ionization of I^- centers and, particularly, in the formation of excitons and electron–hole pairs at the fundamental absorption edge of the aluminosilicate framework is a problem that is still awaiting solution.

ACKNOWLEDGMENTS

The authors are indebted to M. Kirm and I. Martinson for assistance in this work and fruitful discussions.

The support of the Estonian Science Foundation, grant nos. 3867 and 3868, and of the Crawford Science Foundation (Sweden) is gratefully acknowledged.

REFERENCES

1. Ch. B. Lushchik, G. G. Liĭdja, and M. A. Élango, Fiz. Tverd. Tela (Leningrad) **6** (8), 2256 (1964) [Sov. Phys. Solid State **6**, 1789 (1965)].
2. Ch. B. Lushchik and A. Ch. Lushchik, *Electron Excitation Decay with Formation of Defects in Solids* (Nauka, Moscow, 1989).
3. A. Lushchik, I. Kudryavtseva, Ch. Lushchik, *et al.*, Phys. Rev. B **52** (14), 10069 (1995).
4. A. Lushchik, E. Feldbach, R. Kink, *et al.*, Phys. Rev. B **53** (9), 5379 (1996).
5. V. P. Denks, A. É. Dudel'zak, Ch. B. Lushchik, *et al.*, Zh. Prikl. Spektrosk. **24** (1), 37 (1976).
6. V. P. Denks, Fiz. Tverd. Tela (St. Petersburg) **36** (6), 1679 (1994) [Phys. Solid State **36**, 918 (1994)].
7. R. A. Denisov, V. P. Denks, A. É. Dudel'zak, *et al.*, Zh. Prikl. Spektrosk. **27** (1), 149 (1977).
8. M. Kirm, V. Demidenko, V. Denks, *et al.*, J. Electron Spectrosc. Relat. Phenom. **101**–**103**, 593 (1999).
9. B. W. Faughnan, I. Gorog, P. M. Heyman, and I. Shidlovsky, Proc. IEEE **61** (7), 927 (1973); Adv. Image Pickup Disp. **4**, 87 (1981).
10. V. P. Denks, Tr. Inst. Fiz. Akad. NaukÉst. SSR **55**, 14 (1984).
11. S. D. McLaughlan and D. J. Marshall, Phys. Lett. A **32A** (5), 343 (1970).
12. L. S. Bolyasnikova, A. N. Vostrov, V. A. Demidenko, *et al.*, Tr. Inst. Fiz. Akad. NaukÉst. SSR **58**, 142 (1986).
13. J. Löns and H. Schulz, Acta Crystallogr. **23** (5), 434 (1967).
14. *Zeolite Molecular Sieves: Structure, Chemistry and Use*, Ed. by D. W. Breck (Wiley, New York, 1974; Mir, Moscow, 1976).
15. V. P. Denks, E. A. Vasil'chenko, V. S. Korsakov, *et al.*, Fiz. Tverd. Tela (Leningrad) **36** (6), 1679 (1994) [Phys. Solid State **36**, 918 (1994)].
16. F. K. Volynets, V. A. Demidenko, R. A. Denisov, and V. P. Denks, Pis'ma Zh. Tekh. Fiz. **8** (4), 232 (1982) [Sov. Tech. Phys. Lett. **8**, 102 (1982)].
17. V. P. Denks, Fiz. Tverd. Tela (St. Petersburg) **35** (6), 1499 (1993) [Phys. Solid State **35**, 756 (1993)].
18. V. P. Denks, V. V. Mürk, and E. A. Vasil'chenko, Fiz. Tverd. Tela (St. Petersburg) **38** (4), 1004 (1996) [Phys. Solid State **38**, 558 (1996)].
19. Ch. B. Lushchik, E. A. Vasil'chenko, I. A. Kudryavtseva, *et al.*, Izv. Vyssh. Uchebn. Zaved., Fiz., No. 11, 30 (1996) [Russ. Phys. J. **39** (11), 1029 (1996)].
20. Ch. B. Lushchik, A. Ch. Lushchik, E. A. Vasil'chenko, and F. A. Savikhin, Fiz. Tverd. Tela (St. Petersburg) **37** (2), 528 (1995) [Phys. Solid State **37**, 284 (1995)].
21. K. Kan'no, N. Itoh, and Y. Nakai, J. Phys. Soc. Jpn. **47** (3), 915 (1979).
22. M. Kirm, G. Zimmerer, E. Feldbach, *et al.*, Phys. Rev. B **60** (1), 502 (1999).
23. V. N. Abramov, M. G. Karin, A. I. Kuznetsov, and K. K. Sidorin, Fiz. Tverd. Tela (Leningrad) **21** (1), 80 (1979) [Sov. Phys. Solid State **21**, 47 (1979)].
24. W. Y. Ching and Y.-N. Xu, J. Am. Ceram. Soc. **77**, 404 (1994).
25. Shang-Di Mo and W. Y. Ching, Phys. Rev. B **54** (23), 16555 (1996).
26. I. Godmanis, A. Trukhin, and K. Hübner, Phys. Status Solidi B **176**, 279 (1983).

Translated by G. Skrebtsov

Physics of the Solid State, Vol. 43, No. 5, 2001, pp. 836–840. Translated from Fizika Tverdogo Tela, Vol. 43, No. 5, 2001, pp. 804–808.

SEMICONDUCTORS AND DIELECTRICS

Fracton Vibrations in Vitreous SiO_2 as Revealed from Raman Spectroscopy Study

A. E. Chmel*, A. N. Smirnov, and V. S. Shashkin****

**Ioffe Physicotechnical Institute, Russian Academy of Sciences, Politekhnicheskaya ul. 26, St. Petersburg, 194021 Russia*
e-mail: chmel@ae.ioffe.rssi.ru

***Vavilov State Optical Institute, All-Russia Research Center, Birzhevaya liniya 12, St. Petersburg, 193171 Russia*

Received October 23, 2000

Abstract—Low-frequency Raman spectroscopy is used to study the sensitivity of the dynamic (vibrational) properties of the fractal structure of nanocracks in vitreous SiO_2 to the mechanical and thermal previous history of the sample. The material is obtained by vacuum-compression fritting of the sol–gel synthesis products. After fritting, continuity defects having a nanostructural scale and possessing fractal geometry are left at the site of microcracks in the course of preliminary mechanical processing of the sample. The features of such defects are an absence of the boson peak in the Raman spectrum and a monotonic decrease of the intensity according to the law of light scattering from acoustic vibrations of fractals. The conditions for the emergence of the fractal structure and its dependence on the rigidity of the walls of nanocracks are determined from the scattering mode.

INTRODUCTION

In our earlier publication [1], we reported the discovery of acoustic vibrations of fractals localized on submicrocracks in vitreous SiO_2 in the Raman scattering spectrum. It was proved later [2] that the data on the intensity of light scattering from this type of vibrations can be used to compare the density (compactness) of materials and to estimate the size of continuity defects. While interpreting the experimental data, we proceeded from the fracton model [3–8] developed for coupled percolation clusters and used for describing high-porosity objects such as aerogels and some products of the chemical deposition of silicon chloride [8–13]. These materials consist of coagulated globules having a size of the order of a nanometer and forming fractal clusters. The vibrational properties of such systems were described for the first time by Alexander and Orbach [3], who introduced the concept of a fracton, i.e., localized vibrational excitation of a fractal unit, and defined the density-of-states function $g(\omega)$ as

$$g(\omega) \propto \omega^{\tilde{d}-1}, \quad (1)$$

where ω is the frequency and $\tilde{d}$ is the so-called fracton dimension [1]. Being a parameter of the vibrational system, $\tilde{d}$ depends not only on the fractal geometry, but also on the rigidity of fractal structural bonds [14].

In high-density amorphous SiO_2 saturated with tiny fractal cracks, the Raman scattering of light takes place not at the vibrations of the self-similar skeleton in the "empty" space as in the case of aerogels, but at vibrations of hollow inclusions of the nanostructural scale. Here, the fractal dimesion is dictated by the geometry of the crack walls, while the vibrational properties of the fractal are determined by the rigidity of the surrounding matrix, which corresponds to the principles of the fracton model [3–8]. Indeed, we verified the applicability of definition (1) to describing the vibrations of fractal cracks on the basis of our earlier experiments [1, 2]. The fracton dimension for SiO_2 of the gel origin calculated from the spectra was found to be in reasonable agreement with the available experimental data on aerogels (related materials). As expected, the most significant discrepancy with the theory of vibrations of rarefied percolation clusters was observed in [1] for cracks in the material with the highest density (fused quartz).

In the present paper, the conditions for the emergence of fractal cracks and the dependence of their vibrational properties on the connectivity of a vitreous medium are determined by varying the conditions of sample preparation.

1. RAMAN SCATTERING FROM FRACTAL VIBRATIONS

The polarizability tensor determining the Raman scattering from a fractal is defined by the local elastic strains emerging during its vibrations. On the basis of the definition of the density-of-states function (1) and under the assumption of the scalar elasticity of a fractal cluster, the following relation has been derived for the Raman scattering intensity $I(\omega)$ [5, 8]:

$$I(\omega)\omega \propto [n(\omega) + 1]\omega^{3-\tilde{d}}, \quad (2)$$

or, in terms of the reduced intensity $I_{red}(\omega) = I(\omega)\omega/[n(\omega) + 1]$,

$$I_{red}(\omega) \propto \omega^{3-\tilde{d}}, \quad (3)$$

where $n(\omega)$ is the Bose factor.

On the log–log scale, dependence (3) is depicted by a segment of a straight line whose slope is given by

$$\nu = 3 - \tilde{d}. \quad (4)$$

The real size of fractal units is bounded from above either by the structural correlation length beyond which the material is actually homogeneous or by the physical size of the region of the existence of a fractal cell (crack size in our case). For a crack of length L, the minimal frequency of fracton vibrations $\omega_{out-off}$ amounts approximately to

$$\omega_{out-off} \approx 2\pi v/cL, \quad (5)$$

where v is the transverse velocity of sound and c is the velocity of light (if the Raman shift is measured in cm^{-1}).

2. EXPERIMENT

The measurements were made on amorphous SiO_2 samples obtained by vacuum-compression fritting of pairs of flat plates synthesized according to the sol–gel technique.

The fractal structure may be formed in a dense material only at continuity defects whose role under definite conditions can be played by residual cracks [1]. In order to create a layer of microcracks, the surfaces of the plates being fritted were subjected either to mechanical polishing or to dry grinding by an abrasive with a grain size of ≈10 μm; this allowed us to obtain samples with, presumably, various microscopic profiles of the surface. The thickness of the layer damaged by the grinding/polishing is, as a rule, considerably larger than the abrasive grain size; in our case, it was of the order of ten micrometers. It was proved by us earlier [1, 2] that microscopic mechanical defects are healed during fritting, but continuity defects having a length of a few nanometers are left in place of the cracked layer. In view of such a small size of the residual defects, the fritting layer in the bulk is not manifested visually and can be observed in the samples only in the regions where it emerges on the lateral surface. Quartz glass obtained by fritting the products of the sol–gel synthesis is a highly transparent optical material.

The samples were fritted in a vacuum of 5×10^{-3} Torr; the temperature and pressure are given below for specific experiments.

The Raman spectra were recorded in the 90° geometry during the passage of a beam, emitted by a pumping argon-ion laser (488 nm), along the fritting interface (in the case of fritting along planes) or through the bulk of the block (in the case of fritting of powders). The light beam at the caustic had a diameter of ≈100 μm. The source of scattering was confined to the caustic region with the help of an aperture. The spectra were recorded on the Spex 1401 spectrometer.

3. RESULTS

Figure 1 shows the low-frequency Raman spectra excited from the bulk of the plates fritted from the gel-synthesized SiO_2, as well as from the interface (contact layer) between the plates. Polished plates were fritted at the temperature $T = 1150$°C under a pressure of 7 MPa, while for fritting ground planes, the pressure was doubled (at the same temperature) in order to compensate for the looseness of the surface layer.

The bulk spectrum (Fig. 1a) has a boson peak typical of the vitreous state of amorphous materials, while the interface spectra (Fig. 1b) display a monotonic decrease in the intensity of scattering with frequency. The $\log I_{red}$ vs. $\log\omega$ dependences in the reduced coordinates (Fig. 2) have linear segments typical of the scattering from fractals. The linear region on the graph for the interface of a polished sample begins from 26 cm^{-1}, while the linearity region for fritted ground samples is small and begins only from ≈70 cm^{-1}. Since the lowest frequency of vibrations of fractals corre-

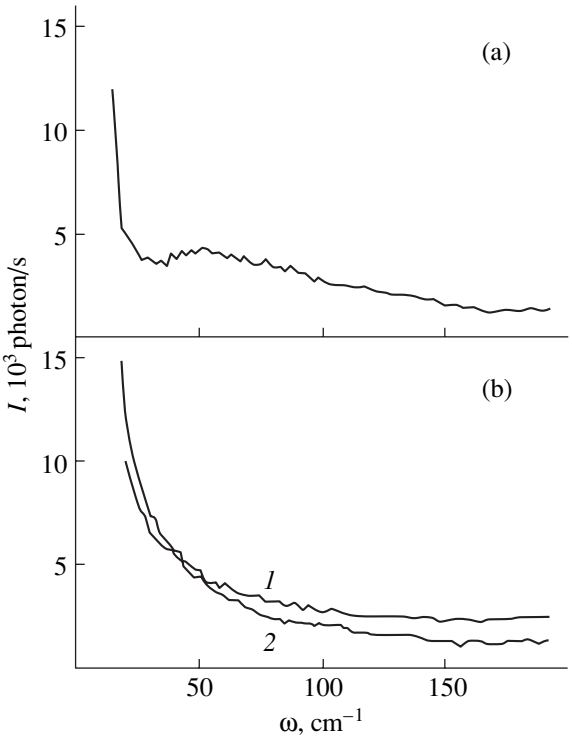

Fig. 1. Low-frequency Raman spectra (a) for the bulk of a sample and (b) for the fritting region of polished (curve *1*) and ground (curve *2*) planes. Pairs of plates were fritted into a monolith at 1150°C under a pressure of 7 (curve *1*) and 14 MPa (curve *2*).

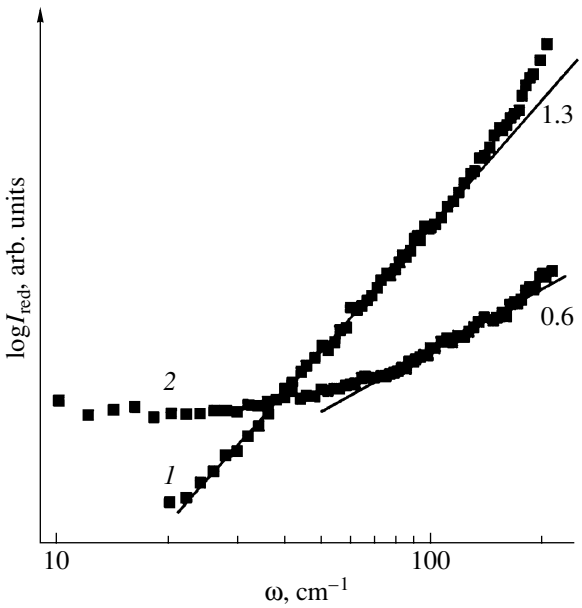

Fig. 2. Spectra presented in Fig. 1b, but plotted in reduced coordinates. Fractional numbers on the curves indicate the slopes of the linear segments shown by straight lines.

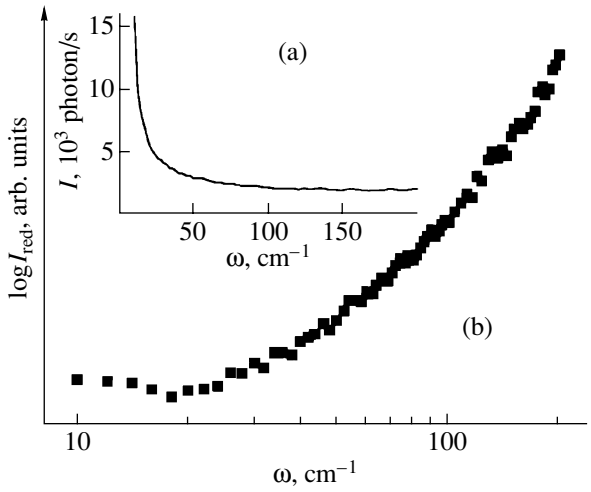

Fig. 3. Low-frequency Raman spectra excited in the zone of fritting of polished surfaces in (a) linear and (b) reduced coordinates. The plates were fritted into a monolith at 1200°C under a pressure of 14 MPa.

sponds to the largest cracks, such a significant increase in the value of $\omega_{out-off}$ for samples with a rougher finish can hardly be explained by a decrease in the size of the continuity defects. We should rather assume that the fritting of a rough relief under the conditions of water deficiency leads to the emergence of microscopic inhomogeneities and, consequently, to an increase in Rayleigh scattering. As a result, the low-frequency regions on the $\log I_{red}$ vs. $\log\omega$ curve in the spectrum of the ground sample are distorted by the superposition of elastically scattered light and the data on the fracton dimension can be obtained only from the slopes of short segments of straight lines on the high-frequency side (in our case, above $\approx$70 cm^{-1}). Such a possibility was indicated by Hassan *et al.* [15], who considered the methods of measurement of light scattering from vibrations of fractals in aerogels.

The fracton dimension calculated using relation (4) amounted to 2.4 for the ground sample and 1.7 for the polished one. The latter value is close to the experimental data reported for aerogels ($\tilde{d}$ = 1.5 [8, 15]) but is higher than the theoretically predicted value of $\tilde{d}$ = 4/3 [3]. The discrepancy between the experimental value and the result of an analytic description was indicated for the first time by Freltoft *et al.* [13], who obtained the value $\tilde{d}$ = 2.1 for the fractal structure of aggregates of amorphous SiO_2 deposited chemically from $SiCl_4$. Later, the experiments [11, 12] on neutron scattering from aerogels confirmed that the value $\tilde{d}$ = 4/3 is not universal. The dependence of $\tilde{d}$ on the density of the material was established, and it was found that the fracton dimension increases with the short-range order, i.e., with the connectivity of the silicon–oxygen skeleton of SiO_2.

In order to verify that the absence of a boson peak in the Raman spectra of amorphous SiO_2 is indeed associated with the presence of hollow inclusions with the fractal geometry in the material, we have selected the fritting mode ensuring complete "healing" of residual defects in the sample. The fritting temperature T for the polished plates was increased to 1200°C, which is higher than the glass-formation temperature for SiO_2 (T_g = 1160°C). It could be expected that continuity defects will disappear under the conditions of intensified viscous flow and that the continuous network of glass will be restored.

The spectrum for the interface formed at $T > T_g$ under a pressure of 14 MPa is shown in Fig. 3 together with the $\log I_{red}$ vs. $\log\omega$ dependence. It can be seen that the boson peak in the original spectrum (Fig. 3a) does not appear as before, but the law $\omega^{3-\tilde{d}}$ in Eq. (4), typical of fractal structures, is not observed either: a linear segment in the double logarithmic coordinates is absent (Fig. 3b). The connected structure of glasslike SiO_2 in the interface was restored only after the fritting pressure was increased to 180 MPa at T = 1200°C, which is indicated by the emergence of the boson peak in the Raman spectrum (Fig. 4).

4. DISCUSSION

It is well known [16, 17] that the height of the boson peak in the Raman spectrum for quartz glass saturated with water is very small or the peak is absent altogether in view of the percolation effect of the OH end groups, i.e., in view of the dynamic isolation of the structural units of glass. Heating such samples to above 900°C removes water from SiO_2, and the low- frequency peak is manifested clearly in the region of 60 cm^{-1} [17, 18].

In our case, dehydration during dry grinding, when cracks are formed under abrasive grains at a high temperature, and subsequent fritting at $T = 1150$°C did not lead to the emergence of the boson peak but only caused a decrease in the slope of the linear segment on the frequency dependence of the intensity I_{red}, indicating an increase in the fracton dimension.

The maximum possible value of $\tilde{d}$ corresponds to a continuous, homogeneous, three-dimensional medium for which the fracton dimension coincides with the fractal and euclidean dimensions; i.e., it is equal to three. In the presence of a free surface, the value of $\tilde{d} = 3$ is attainable only at absolute zero. Above absolute zero, stable states of a nanocrack (or of the end of a macrocrack) are formed under the action of thermal fluctuations, which necessarily leads to the variability of the crack surface even in a perfectly homogeneous material [19]. Ultimately, the fractal nature of a crack is the result of the thermal motion of nanostructural elements. The values of the fractal and fracton dimensions reflect the lack of smoothness in the crack profile.

In this work, we obtained $\tilde{d} = 2.4$ for the interface between the surfaces subjected to dry grinding. Such a high value of the dimension reflects the high connectivity of the glass-forming network and its low molecular mobility for a low water content, i.e., the OH end groups. Since the variations of the surface relief in a more rigid material are poorer, the fractal geometry of cracks is found to be less pronounced; cracks are "smoothed" in real space.

The role of bound water is manifested due to the nanoscopic size of the continuity defects. Indeed, linear segments of the graph of function $\log[I_{red}(\omega)]$ in a polished sample of gel origin appear starting from 26 cm^{-1}, which gives, in accordance with Eq. (5), a maximum size of fractals of approximately 5 nm. This value is two orders of magnitude smaller than the size of the original (microscopic) cracks existing on a mechanically polished surface before fritting but is comparable with the structural parameter for glasses (1 to 2 nm [19]), which determines the elementary step in the motion/collapse of a crack.

The frequency range for vibrations of fractal units has an obvious structural limitation. The linear increase observed in the graph describing the dependence of $\log I_{red}$ on $\log\omega$ for the samples under investigation extends to frequencies below 170 cm^{-1}, which determines the minimum size of fractals (and, accordingly, the minimum size of discontinuities, which is equal to 0.8 nm). This value is close to the diameter of the six-membered ring of the SiO_4 tetrahedra, which is the basic unit cell of the silicon–oxygen skeleton of vitreous SiO_2. The breakage of the single Si–O bond is equivalent to the dissociation of such a ring and to the formation of an elementary continuity defect having a size of 0.8 nm. Its geometry depends only on the connectivity of the matrix.

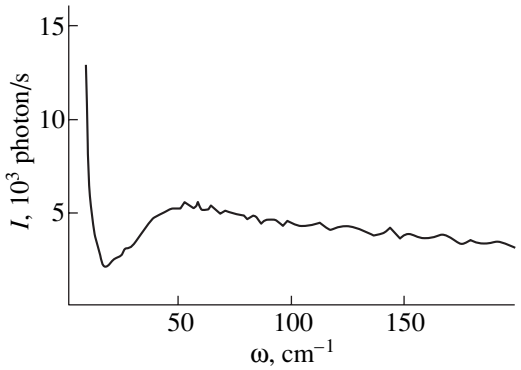

Fig. 4. Low-frequency Raman spectra excited in the fritting zone of polished surfaces. The plates were fritted into a monolith at 1200°C under a pressure of 180 MPa.

The experiments on the fritting of polished surfaces at $T > T_g$ revealed that the collapse of a crack and the corresponding disappearance of the fractal surface do not necessarily lead to the reconstruction of the material continuity on the molecular level. An intermediate state is possible, in which there is no free surface, but the connectivity of the glass-forming network in the region of closed cracks is insufficient for dynamic interaction between the structural units of glass. In this case, the vibrational spectrum displays neither scattering from fractals nor the boson peak. The complete reconstruction of the vitreous state (which is characterized by the emergence of the boson peak) can also be accomplished when the conditions of highly viscous flow are combined with a large compressive force.

It was reported by us earlier [2] that the dynamic properties of fractal cracks in a continuous medium depend on the density of the material, as in the case of the vibrations of a fractal cluster in "empty" space. Here, we have demonstrated the increase in the fracton dimension (i.e., the improvement of the material homogeneity) as a result of the reconstruction of the structural bonds of amorphous SiO_2 after the removal of chemically bound water from it. In real space, this corresponds to the smoothing of the profile of nanocracks upon an increase in the matrix connectivity.

REFERENCES

1. A. E. Chmel, A. D. Semenov, A. N. Smirnov, and V. S. Shashkin, Fiz. Tverd. Tela (St. Petersburg) **41** (6), 1030 (1999) [Phys. Solid State **41**, 938 (1999)].
2. A. Chmel, G. T. Petrovsky, V. S. Shashkin, and A. N. Smirnov, Int. J. Fract. **101** (4), L41 (2000).
3. S. Alexander and R. Orbach, J. Phys. Lett. **43** (17), L625 (1982).
4. S. Alexander, C. Laermans, R. Orbach, and H. M. Rosenberg, Phys. Rev. B **28** (8), 4615 (1983).
5. R. Rammal and G. Toulouse, J. Phys. Lett. **44** (1), L13 (1983).
6. A. Boukenter, B. Champagnon, E. Duval, *et al.*, Phys. Rev. Lett. **57** (19), 2391 (1986).
7. A. Aharony, S. Alexander, O. Entin-Wohlman, and R. Orbach, Phys. Rev. Lett. **58** (2), 132 (1987).
8. A. Boukenter, B. Champagnon, E. Duval, and J. L. Rousset, Philos. Mag. B **59** (1), 125 (1989).
9. R. Vacher, T. Woigner, J. Pelous, and E. Courtens, Phys. Rev. B **37** (11), 6500 (1988).
10. R. Vacher, E. Courtens, G. Goddens, *et al.*, Phys. Rev. Lett. **65** (8), 1008 (1990).
11. R. Vacher, E. Courtens, G. Coddens, *et al.*, Phys. Rev. B **39** (10), 7384 (1989).
12. E. Stoll and E. Courtens, J. Phys. B **81** (1), 1 (1990).
13. T. Freltoft, J. Kjems, and D. Richter, Phys. Rev. Lett. **59** (11), 1212 (1987).
14. S. Alexander, Phys. Rev. B **40** (11), 7953 (1989).
15. H. A. Hassan, S. R. P. Smith, and J. H. Page, Solid State Commun. **68** (8), 733 (1988).
16. K. Dahmouche, A. Boukenter, C. Bovier, *et al.*, J. Non-Cryst. Solids **147**–**148** (2), 251 (1992).
17. J. L. Rousset, E. Duval, A. Boukenter, *et al.*, J. Non-Cryst. Solids **107** (1), 27 (1988).
18. A. Chmel, T. Pesina, and V. S. Shashkin, J. Non-Cryst. Solids **210** (2), 254 (1997).
19. J. K. West, J. J. Mecholsky, and L. L. Hench, J. Non-Cryst. Solids **260** (1), 99 (1999).

Translated by N. Wadhwa

Physics of the Solid State, Vol. 43, No. 5, 2001, pp. 841–844. Translated from Fizika Tverdogo Tela, Vol. 43, No. 5, 2001, pp. 809–812.

DEFECTS, DISLOCATIONS, AND PHYSICS OF STRENGTH

ESR Study of Impurities in Strontium Titanate Films

M. D. Glinchuk*, I. P. Bykov*, A. M. Slipenyuk*, V. V. Laguta*, and L. Jastrabik**

**Institute of Materials Sciences Problems, National Academy of Sciences of Ukraine, Kiev, 03142 Ukraine*
e-mail: dep4@materials.kiev.ua
***Institute of Physics, Academy of Sciences of the Czech Republic, Prague 8, 18040 Czech Republic*
Received July 27, 2000; in final form, October 10, 2000

Abstract—The paper reports on an ESR study of Cr- and Ca-codoped $SrTiO_3$ films, 1700 and 350 nm thick, before and after UV irradiation (λ = 365 nm). The spectrum of the thick film (1700 nm) exhibits two ESR lines with *g* factors of 1.977 and 1.974, which belong to the Cr^{3+} centers. In the spectrum of the thin film (350 nm), one observes only one line, which is due to the chromium center with a *g* factor of 1.974. Calculations showed that the line with the smaller *g* factor belongs to the Cr^{3+} center located close to the film surface. The weak line observed in the spectrum after UV irradiation (*g* factor = 2.012) is most likely due to the O^- center. The regions of thermal stability of the observed centers were studied. A comparative analysis of the characteristics of impurities in bulk samples and films was carried out. © *2001 MAIK "Nauka/Interperiodica"*.

INTRODUCTION

The intense investigation of ferroelectric films witnessed in the past few years was stimulated by their device potential for nondestructive readout of information from main memory units [1, 2]. There was proposed, in particular, a new mechanism of information readout from ferroelectric memory devices, which is free of problems associated with the aging of thin films [3]. This mechanism is based on the dependence of the photoemf or photocurrent on electric polarization [4, 5]. The electric and photoelectric phenomena observed in thin ferroelectric films, or heterostructures of the ferroelectric–semiconductor type, are known to depend strongly on traps, i.e., defects and impurities, which can play a substantial role in charge transport processes [6]. Only a few papers, however, deal with the investigation of the effect of traps on the electric and photoelectric properties of ferroelectric films [7, 8].

There are also no publications on the investigation of ferroelectric films by the ESR method, which was employed successfully for detecting impurities [9, 10], as well as other lattice imperfections, in films of a number of semiconductor materials and diamonds [11, 12].

We report here on an ESR investigation of a thick (1700 nm) and a thin (350 nm) $SrTiO_3$ film grown on a single-crystal Al_2O_3 substrate and codoped by Cr (0.1 at. %) and Ca (0.2 at.%). We identified ESR spectra belonging to Cr^{3+} centers in the bulk and near the film surface. An O^- center in UV irradiated films was detected.

1. EXPERIMENTAL TECHNIQUES

$SrTiO_3$ films codoped by 0.1 at. % Cr and 0.2 at. % Ca, 1700 and 350 nm thick, were prepared by laser ablation. The substrates were (1102)-oriented, optically polished sapphire plates. Films of optimum quality and properties were obtained by 30-min deposition on a substrate heated to 680°C in a nitrogen atmosphere at a pressure of 200 mTorr. The ESR spectra were measured in the X range with the use of an ESR-9 Oxford temperature-control attachment within the 18–300 K range. The dc magnetic field coincided in direction with the film surface. The samples were illuminated directly in the spectrometer resonator for 2 min by a 200-W mercury lamp equipped with an optical filter with λ = 365 nm. The region of thermal stability of the paramagnetic centers was determined by heating the samples to a fixed temperature, with their subsequent cooling down to T = 18 K to record the ESR spectra.

2. ESR SPECTRA

2.1. Thick Film (h = 1700 nm)

The ESR spectra of the thick film (h = 1700 nm) observed before and after irradiation by UV light (λ = 365 nm) are shown by solid lines in Figs. 1a and 1b, respectively.

The strongest line with g = 1.977 is known [11] to belong to the Cr^{3+} ion substituting for the Ti^{4+} ion. The weak line appearing in the spectrum after UV irradiation (*g* factor = 2.012) is most probably due to the O^- center. A similar O^- spectrum associated with an aluminum impurity was observed earlier in bulk $SrTiO_3$ after UV irradiation [12].

One readily sees that the spectra of the thick film are slightly asymmetrical, with a weak anomaly, identified by an arrow in Fig. 1, presented on the right-hand wing of the spectral line. To understand the nature of the observed anomaly, the spectral lines were deconvolved

by means of the Peak Fit computer code. The results of this deconvolution are presented in Fig. 1 by dashed lines.

As can be seen from the results, the observed spectrum actually represents a superposition of two lines with $g = 1.977$ and 1.974, which belong to the Cr^{3+} centers. The line with the g factor of 1.974 is observed for the first time, and its nature will be discussed later.

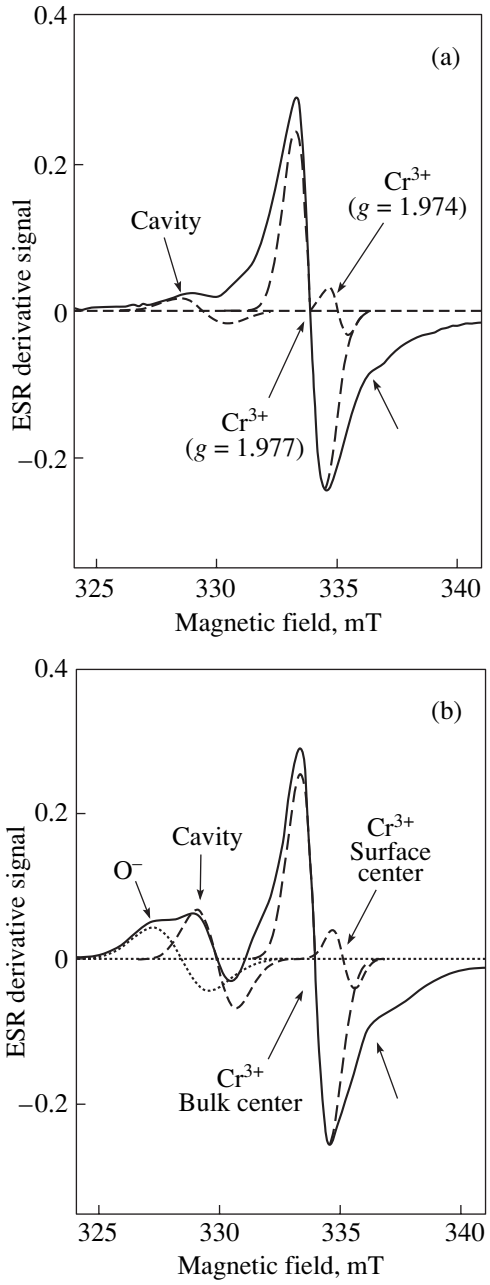

Fig. 1. ESR spectra of a $SrTiO_3$: Ca, Cr film h = 1700 nm thick measured (a) before and (b) after UV irradiation. Dashed lines are resolved spectral lines.

2.2. Effect of Heating Temperature on ESR Spectra of the Thick Film

To determine the region of thermal stability of the centers, the UV-irradiated sample was heated to a fixed temperature, held for 2 min, and cooled down to 18 K to record the ESR spectrum. The results of the measurements are displayed in Fig. 2. The intensity of the Cr^{3+} line is seen to depend only weakly on temperature. An increase in temperature to 300 K brings about a decrease in the ESR line intensity of this center by only two times. One may thus conclude that the chromium center is the most stable and long-lived, and that the line intensity depends on the measurement temperature.

The intensity of the second center (g factor = 2.012) also decreased with increasing temperature, to vanish altogether above 130 K. It should be pointed out that increasing the heating time at T = 90 K even to 5 min resulted in a complete disappearance of this line. It thus

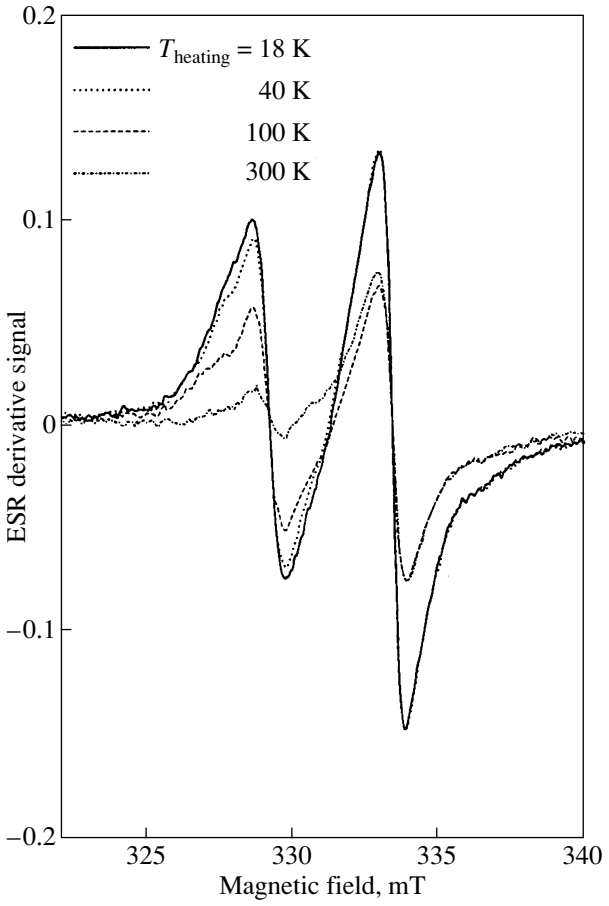

Fig. 2. Temperature dependence of the intensity of an ESR spectrum of a thick $SrTiO_3$: Ca, Cr film measured after UV irradiation at T = 18 K.

becomes clear that the O^- center creates a shallow impurity level in the band gap of the $SrTiO_3$ film.

2.3. Thin Film (h = 350 nm)

Figure 3 displays the ESR spectrum of the thin film. For comparison, the spectrum of the thick film is also shown. The Cr^{3+} line in the thin film is seen to be shifted toward higher magnetic fields. The *g* factor of this line is 1.974. This observation suggests that this line belongs to the Cr^{3+} center located near the film surface. The O^- center spectrum was not observed in the thin film.

The temperature dependence of the thin-film ESR spectra was not studied because of their low intensity even at low temperatures (T = 18 K).

3. THEORY OF THE ESR OF ELECTRONIC CENTERS NEAR THE SURFACE

The theory of electronic centers near the surface in bulk samples and in films was developed in [13] and [14], respectively. The solution of the Schrödinger equation taking into account the interaction of a center with its image shows that the energy of the center grows as it approaches the surface. Therefore, centers at the surface become shallower and can be ionized much more easily than those in bulk samples. The local electronic levels of centers more than 100–150 nm distant from the surface were shown to be the same as in the bulk. This suggests the conclusion that in thin films (h < 500 nm) most of the centers "feel" the surface, as it were, whereas in a thick film (h > 1000 nm), the major part of the electronic centers should behave as they do in bulk samples. The ESR spectrum of such centers should coincide with that of bulk samples, while surface centers should produce a different spectrum. First of all, the number of lines should increase, because the symmetry in this case is lower. One could also expect a specific dependence of the resonant-line position on magnetic-field orientation with respect to the surface normal. A change in the line position is associated, as usual, with the crystal-field parameters and a change in the *g* factor. It was shown, in particular, that the shift of the *g* factor of an electronic center at the surface relative to its value in the bulk material can be written as

$$\Delta g = -\frac{e\hbar}{2m^2c^2}\frac{1}{\Delta E}M\sin^2\theta \equiv -A\sin^2\theta, \qquad (1)$$

$$M = \int \psi^* L_x [\nabla U \times \mathbf{p}]_x \psi d^3 r, \qquad (2)$$

where ΔE is the difference between the ground- and excited-state energies; **L**, U, and **p** are the angular momentum, potential, and momentum of a paramagnetic electron, respectively; and θ is the angle between the direction of the dc magnetic field and the surface normal.

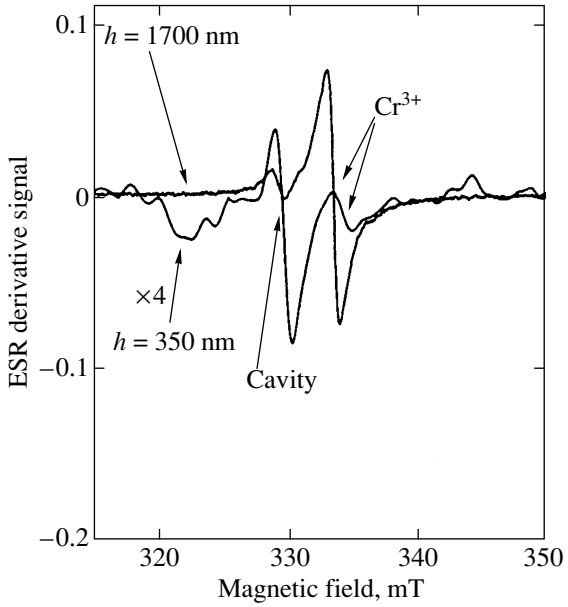

Fig. 3. ESR spectra of a thin (h = 350 nm) and a thick (h = 1700 nm) $SrTiO_3$: Ca, Cr film measured after UV irradiation at T = 18 K. The thin-film spectrum is fourfold expanded.

The coefficient A is estimated to be of the order of $(2–5) \times 10^{-3}$. Hence, the ESR line of a surface center could be shifted toward higher magnetic fields. The *g* factor shift will be zero for the magnetic fields H aligned with the surface normal and maximum for the in-plane H direction.

4. DISCUSSION OF RESULTS

4.1. ESR Line with g = 1.974: The Cr^{3+} Center at the Surface

The shift of the ESR line of the Cr^{3+} surface center relative to the line corresponding to the bulk center toward higher magnetic fields and the change in the *g* factor $\Delta g = 3 \times 10^{-3}$ (the angle $\theta = 90°$ for an in-plane magnetic field) agree well with theoretical calculations. Hence, the ESR line with g = 1.974, observed in the films, belongs to the Cr^{3+} surface center. Because the spectrum of the thin film did not exhibit the line with g = 1.977 produced by the Cr^{3+} bulk center, this means that the Cr^{3+} centers in thin films (h = 350 nm) feel the presence of the surface. Thus, the ratio of the number of Cr^{3+} centers in the bulk to the number of those feeling the surface can be estimated from the thickness ratio of the films studied; it was found to be 4.8. As follows from experimental data, the intensity of the ESR line with g = 1.977 (Cr^{3+} bulk center) is five times that of the surface center with g = 1.974, which is in good agreement with the value derived from the film thickness ratio.

4.2. ESR Line with g = 2.012: The O^- Center

As was already mentioned, the ESR spectrum of the O^- center could be observed only at low temperatures ($T \leq 130$ K) and only under UV irradiation. The O^- hole center in bulk $SrTiO_3$ is known to retain its charge state after UV irradiation [12]. This observation confirms the short lifetime of a hole trapped at the oxygen level in the film. It may be conjectured that ultraviolet light creates shallower levels in the film, which do not produce an ESR signal. After irradiation, the whole system of local-levels relaxes rapidly to the equilibrium state which existed in the film before irradiation. The fast local-center relaxation could also be initiated by the growth of conductivity associated with the large number of defects and the high density of local surface centers in the film.

Obviously, the available experimental data are not enough to allow exact identification of the local structure of the observed hole centers. The polycrystallinity of the films complicates analysis of the ESR spectra and determination of the principal axes and of the magnitude of the *g* tensor, which are needed to identify the model of the center. We are planning to perform the corresponding calculations and measurements on films with different thicknesses in the immediate future. We note in conclusion that the dielectric permittivity and photoluminescence of the films studied in detail in [15] reveal certain features that can be associated with the electronic centers detected in this work.

REFERENCES

1. S. K. Dey, Ferroelectrics **135**, 117 (1992).
2. D. Dimos, W. L. Warren, M. B. Sinclair, *et al.*, J. Appl. Phys. **76** (7), 4305 (1994).
3. H. M. Duiker, P. D. Beale, J. F. Scott, *et al.*, J. Appl. Phys. **68** (11), 5783 (1990).
4. J. Lee, S. Esayan, J. Prohaska, and A. Safari, Appl. Phys. Lett. **64** (3), 294 (1994).
5. A. Matsumura, Y. Kamaike, T. Horiuchi, *et al.*, Jpn. J. Appl. Phys. **34**, 5258 (1995).
6. W. L. Warren, D. Dimos, B. A. Tuttle, *et al.*, Appl. Phys. Lett. **65** (8), 1018 (1994).
7. J. Handerek, Z. Ujma, C. Carabatos-Nedelec, *et al.*, J. Appl. Phys. **73** (1), 367 (1993).
8. M. Jelinek, L. Jastrabik, F. Smutny, *et al.*, Ferroelectrics **152**, 73 (1994).
9. A. B. Roĭtsin and V. M. Maevskiĭ, *Radioscopy of Solid Surfaces* (Naukova Dumka, Kiev, 1992), p. 256.
10. D. F. Talbot-Ponsonby, M. E. Newton, J. M. Baker, *et al.*, J. Phys.: Condens. Matter **8**, 837 (1996).
11. K. A. Muller, Arch. Sci. (Ganeva) **11**, 150 (1985).
12. T. C. Encign and S. E. Stokowski, Phys. Rev. B **1** (6), 2799 (1970).
13. M. G. Deigen and M. D. Glinchuk, Surf. Sci. **3** (3), 243 (1965).
14. M. D. Glinchuk, Ukr. Fiz. Zh. **8** (7), 805 (1963).
15. V. Trepakov, V. Vikhnin, T. Shaplygina, *et al.*, Ferroelectrics **184**, 41 (1996).

Translated by G. Skrebtsov

Physics of the Solid State, Vol. 43, No. 5, 2001, pp. 845–849. Translated from Fizika Tverdogo Tela, Vol. 43, No. 5, 2001, pp. 813–817.

DEFECTS, DISLOCATIONS, AND PHYSICS OF STRENGTH

The Statistical Theory of Dislocation Motion in Spontaneous Locking–Unlocking Processes

B. V. Petukhov

Shubnikov Institute of Crystallography, Russian Academy of Sciences, Leninskiĭ pr. 59, Moscow, 117333 Russia

Received September 8, 2000

Abstract—Explanation of the stick–slip dislocation motion, which is experimentally observed *in situ*, goes beyond the scope of the simplest models. The inclusion of extra degrees of freedom which govern the change-over between the glide and sessile dislocation states makes possible a general description of the dislocation dynamics. The solution to the appropriate statistical model is obtained in the present work. This solution describes the mechanisms of the stick–slip dislocation motion and the associated features of plasticity of the materials. *© 2001 MAIK "Nauka/Interperiodica".*

1. INTRODUCTION

Electron-microscopic observations of the behavior of dislocations under load revealed a discontinuous character of their motion in a number of materials. An interesting example of this sort is provided by the stick–slip motion of dislocations in prismatic planes in Be and Ti [1]. In this case, a dislocation moves through a few lattice spacings and is spontaneously stopped (locked) for a while; this process further recurs many times. In the case of macroplastic deformation, this manifests itself in a plateau on the temperature dependence of the strain stress and in an anomalous peak of the activation volume. The qualitative interpretation of this phenomenon is based on the assumption that the dislocation core can be in different (mobile or immobile) states and can undergo transitions between them (locking–unlocking transitions) [1]. The mechanism of the transition to the immobile sessile state can be treated as a transformation into an energy-favorable configuration of the core split in the cross-sectional plane; the transition to the mobile glide state supposedly occurs through cross sliding. Anomalies in the plasticity characteristics were explained in terms of a transition from the dislocation motion controlled by the cross sliding to the motion within the Peierls–Nabarro mechanism [1] (for the description of these elementary dislocation mechanisms, see, for example, [2]).

In the present work, we investigated a more general situation, because the specific mechanisms of dislocation motion were not included in the model and, in general, could be of a different nature. Moreover, and this is principal, the change in the mechanism by itself was studied within a generalized unified description using the distribution functions, rather than within a qualitative approach which postulates a different behavior on opposite sides of the transition. This allowed us to propose a more correct pattern of the transient behavior. In addition to the calculation of the modified mobility of individual dislocations, we described a number of specific features of the macroplastic deformation of materials, which are associated with the spontaneous transitions of dislocations into locked states and the liberation from them.

2. KINETICS OF THE GLIDE AND SESSILE DISLOCATION STATES

First, we will analyze the influence of extra degrees of freedom. The contribution of the usual glide states of the dislocation core will be described in the simplest fashion. Let us consider the dislocation displacement between different stable states in the slip plane, which are numbered with the index i: $i = 1, 2, 3, \ldots$. The probability of the transition between the neighboring glide states in a unit time is J_0. The direction of the transitions (toward the increase in i) is specified by the external load; the reverse transitions will be ignored. The extra degrees of freedom are taken into account by assuming that an additional sessile state exists in each dislocation position i, so that mutual transitions become possible: from the glide to the sessile state, with a frequency J_-; and from the sessile to the glide state, with a frequency J_+. It is assumed that, unlike the glide states, transitions between different sessile states do not occur (Fig. 1).

We introduce the filling numbers f_i and φ_i for the glide and sessile states, respectively. The kinetics of changes in the filling numbers of the states can be described by the following equations:

$$\frac{df_i}{dt} = J_0(f_{i-1} - f_i) - J_- f_1 + J_+ \varphi_i, \quad (1)$$

$$\frac{d\varphi_i}{dt} = J_- f_i - J_+ \varphi_i. \quad (2)$$

For a continual description, we use the continuous coordinate $x = ia$ (a is the lattice constant) and the dis-

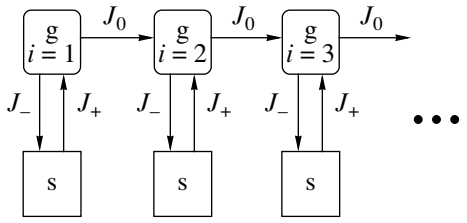

Fig. 1. Schematic drawing of transitions between glide (g) and sessile (s) dislocation states.

tribution functions $f(x, t)$ and $\varphi(x, t)$ which describe the density of the probability of finding the dislocation in the interval between x and $x + dx$. By substituting the derivative adf/dx for the finite difference $f_{i+1} - f_i$ in Eq. (1), we obtain the following equations instead of Eqs. (1) and (2):

$$\frac{\partial f}{\partial t} = -v\frac{\partial f}{\partial x} - J_- f + J_+ \varphi, \tag{3}$$

$$\frac{\partial \varphi}{\partial t} = J_- f - J_+ \varphi. \tag{4}$$

Here, $v = aJ_0$. Note that, in the absence of extra states, Eq. (3) has the form $\frac{\partial f}{\partial t} = -v\frac{\partial f}{\partial x}$ with the solution $f(x, t) = \delta(x - vt)$ at the initial condition $f(x, 0) = \delta(x)$. Thus, a simple translation of the system takes place in this case and v is the sliding velocity. Obviously, there always exist reasons for the broadening of the δ function in real situations. However, this aspect of the problem is of no importance here and will further be taken into account only in illustrations without specifying the corresponding mechanism. The inclusion of the extra states opens the way to a "walk" of the system over different states and detention in them, as a result of which the character of the evolution considerably changes. We will analyze this by using Eqs. (3) and (4), because the system remains simple enough for analytical investigation.

In order to find the solution of the set of Eqs. (3) and (4), we apply the Laplace transform with respect to time:

$$F(x, s) = \int_0^\infty \exp(-st) f(x, t) dt,$$

$$\Phi(x, s) = \int_0^\infty \exp(-st) \varphi(x, t) dt.$$

Then, Eq. (4) is reduced to the relationship

$$\Phi(x, s) = (J_-/(s + J_+))F(x, s), \tag{5}$$

which allows exclusion of φ from the set of equations and obtainment of a closed equation from Eq. (3), that is,

$$v\frac{dF}{dx} + s\left(1 + \frac{J_-}{s + J_+}\right)F = 0. \tag{6}$$

The solution of Eq. (6), which satisfies the normalization condition $\int[f(x, t) + \varphi(x, t)]dx = 1$, has the form

$$F(x, s) = (1/v)\exp[-(sx/v)(1 + J_-/(s + J_+))]. \tag{7}$$

The inverse Laplace transform of $F(x, s)$ yields

$$f(x, s) = \frac{1}{2\pi i}\int_{c-i\infty}^{c+i\infty} \frac{1}{v}\exp\left(-\frac{sx}{v}\left(1 + \frac{J_-}{s + J_+}\right) + st\right)ds.$$

By shifting the integration variable $s = s' - J_+$ and regrouping the integrand, we obtain

$$f(x, t) = \frac{\exp\left(-\frac{x}{v}(J_- - J_+) - J_+ t\right)}{2\pi i} \times \int_{c'-i\infty}^{c'+i\infty} e^{s't'}\left\{\left[e^{\frac{x(J_- - J_+)}{vs'}} - 1\right] + 1\right\}ds'. \tag{8}$$

Here, $t' = t - x/v$ and $c' = c + J_+$.

The inverse Laplace transform of unity leads to $\delta(t')$. The transform of the first term under the integration sign can be calculated by formula 5.5.31 taken from [3], that is,

$$\exp(\alpha/s) - 1 \propto (\alpha/t)^{1/2} I_1(2(\alpha t)^{1/2}),$$

where $I_1(z)$ is the modified first-order Bessel function [4]. Therefore, we obtain the distribution function consisting of two contributions: $f(x, t) = f_1(x, t) + f_2(x, t)$, where

$$f_1(x, t) = \exp(-x(J_- - J_+)/v - J_+ t)\delta(x - vt), \tag{9}$$

$$f_2(x, t) = \exp(-x(J_- - J_+)/v - J_+ t) \times (xJ_-J_+/[v^3(t - x/v)])^{1/2} \times I_1(2[xJ_-J_+(t - x/v)/v]^{1/2}). \tag{10}$$

The δ-function peak describes the displacement with an undisturbed velocity, as is the case in the absence of extra states. However, in their presence, this peak decreases as the path increases. Its content is "transferred" to the second peak, whose shape corresponds to the redistribution between the glide and sessile states. According to the relationship $x = vt$, which is dictated by the δ function, the exponential factor in Eq. (9) is equal to $\exp(-xJ_-/v)$; i.e., it represents the probability of the dislocation not transforming into the sessile state at a distance x or, in other words, the probability of the jump length of the dislocation being no less than x. The

density of the probability that the jump length lies within the interval from x to $x + dx$ is the derivative $-d/dx(\exp(-xJ_-/v)) = (J_-/v)\exp(-xJ_-/v)$. Hence, the mean jump length x_1 is given by

$$x_1 = \frac{J_-}{v}\int_0^\infty x\exp\left(-\frac{xJ_-}{v}\right)dx = \frac{v}{J_-}. \quad (11)$$

The distribution function with respect to the sessile states $\varphi(x, t)$ can be expressed through $f(x, t)$ with the use of Eq. (4). As a result, we obtain

$$\varphi(x, t) = (J_-/v)\exp(-x(J_- - J_+)/v - J_+t) \times I_0(2[xJ_-J_+(t - x/v)/v]^{1/2}). \quad (12)$$

Here, $I_0(z)$ is the modified zero-order Bessel function [14].

At relatively short times, small compared to the time of dislocation activation from the sessile state, $1/J_+$, the combined distribution $f_2(x, t) + \varphi(x, t)$ has a maximum near $x = 0$ and decreases as x increases (Fig. 2). However, at $t \gg 1/J_+$, when many locking–unlocking acts take place and a mean velocity is established, the distribution becomes displaced from $x = 0$ and its maximum shifts with time toward increasing x.

Let us find how the mean path length changes with time:

$$\langle x(t)\rangle = \int_0^\infty [f(x, t) + \varphi(x, t)]x dx.$$

According to the known distribution functions (9), (10), and (12), we obtain

$$\langle x(t)\rangle = (v/(J_+J_-)^{1/2})\chi(t(J_+J_-)^{1/2}), \quad (13)$$

where

$$\chi(z) = \frac{J_+/J_-}{1 + J_+/J_-}z + \frac{(J_+/J_-)^{1/2}}{(1 + J_+/J_-)^2} \times \left[1 - \exp\left\{-\frac{(1 + J_+/J_-)}{(J_+/J_-)^{1/2}}z\right\}\right].$$

Thus, the dislocation motion is nonuniform in time in the case under consideration. As follows from Eq. (13), the time dependence of the mean path length has an undisturbed form $\langle x(t)\rangle \approx vt$ at small t. After a lapse of time, long enough in comparison with the duration of an individual jump $t \gg 1/(J_- + J_+)$, the mean path length is mainly determined by the renormalized averaged velocity of motion:

$$\langle x(t)\rangle \approx vtJ_+/(J_- + J_+). \quad (14)$$

In the case when the difference between the probability of the transition into sessile states and the probability of the liberation from them is rather large ($J_+ \ll J_-$), the decrease in the velocity of dislocation motion can be significant. Equation (13) also permits one to describe the transient behavior when, with a change in parameters, for example, the temperature, the controlling mechanism changes over from the simple glide to the stick–slip motion. This also leads to a change in the mechanism of the macroplastic flow of the material.

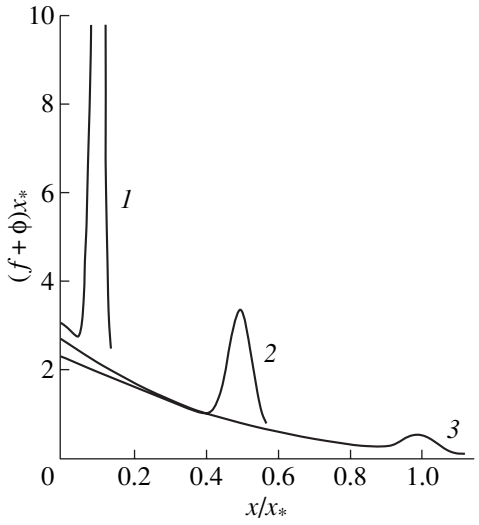

Fig. 2. Evolution of the spatial distribution $f(x, t) + \varphi(x, t)$ of dislocations starting from the point $x = 0$, $x_* = v/(J_+J_-)^{1/2}$ at $t = 0$. The instants of time $t =$ (*1*) $0.1/(J_+J_-)^{1/2}$, (*2*) $0.5/(J_+J_-)^{1/2}$, and (*3*) $1/(J_+J_-)^{1/2}$.

3. TEMPERATURE DEPENDENCE OF THE STRAIN STRESS AND ACTIVATION VOLUME

Let us apply the results obtained to the description of the macroplastic deformation. The plastic strain rate $\dot\varepsilon$ for the motion of dislocations with the mean velocity v and the density ρ is given by the Orowan relationship $\dot\varepsilon = \rho bv(\sigma, T)$, where b is the Burgers vector. This relationship can be used for determining the temperature dependence of the strain stress $\sigma(T)$ at a constant strain rate, provided that the dependences of the velocity of dislocation motion on the stress σ and temperature T are known.

For thermally activated motion, the dependence of v on σ and T is determined by the Arrhenius factor $v = v_0\exp(-E(\sigma, T))$, where $E(\sigma, T)$ is the corresponding activation energy and v_0 is an insignificant preexponential factor. In order to illustrate the dislocation motion, we will use a model dependence of the activation energy on the stress [5]:

$$E(\sigma) = E_0[1 - (\sigma/\sigma_*)^q]^p. \quad (15)$$

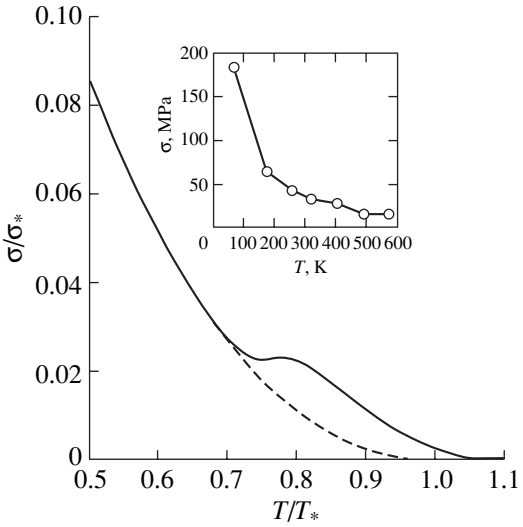

Fig. 3. Calculated temperature dependence of the strain stress [$T_* = E_0/(k\ln(\dot{\varepsilon}_0/\dot{\varepsilon}))$, σ_*, and E_0 are determined by formula (15)]. The inset shows the experimental data for a prismatic slip in Ti [1].

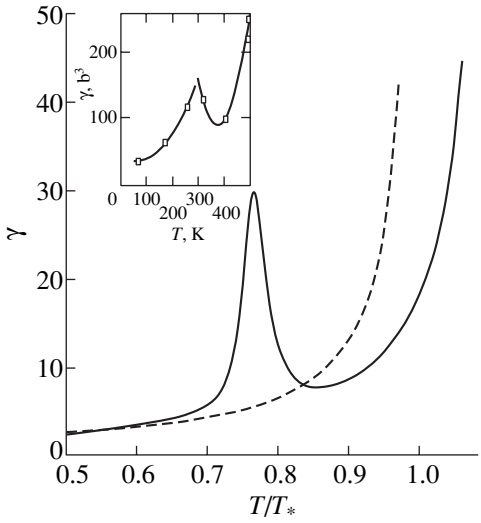

Fig. 4. Calculated temperature dependence of the activation volume normalized to E_0/σ_*. The inset shows the experimental data for a prismatic slip in Ti [1].

The resulting temperature dependence of the strain stress in the absence of locking is shown by the dashed line in Fig. 3 ($\ln(\dot{\varepsilon}_0/\dot{\varepsilon}) = 25$, $\dot{\varepsilon}_0 = \rho b v_0$, $p = 2$, and $q = 0.5$).

In the case of motion accompanied by spontaneous transitions to and from sessile states, we take into account the temporal inhomogeneity of the process and replace the velocity of dislocation motion v by its effective value $v_{ef} = l_{fp}/t_{fp}$. Here, l_{fp} is the mean free path of the dislocation before it leaves "the action field" (crops out at the surface, annihilates with other dislocations, etc.) and t_{fp} is the time of dislocation travel. For a specified mean free path l_{fp}, the travel time can be obtained using the equation $\langle(t_{fp})\rangle = l_{fp}$ and the kinetic law (13). This makes it possible to determine the modified temperature dependence of the strain stress. For an illustrative calculation, we assume that the transitions between the glide and sessile states have a thermally activated character, $J_{+,-} = J_0\exp(-E_{+,-}/kT)$, with constant activation energies E_+ and E_-. By employing the Orowan formula for expressing the travel time, $t_{fp} = \rho b l_{fp}/\dot{\varepsilon}$, and substituting it into Eq. (13), we obtain the modified equation for determining the temperature and rate dependences of the strain stress:

$$E(\sigma) = kT\ln(\dot{\varepsilon}_0/\dot{\varepsilon}) + kT\ln[\chi(z)/z]. \qquad (16)$$

Here,

$$z = t_{fp}(J_-J_+)^{1/2} = (l_{fp}J_0/v_0)$$
$$\times(\dot{\varepsilon}_0/\dot{\varepsilon})\exp(-(E_+ + E_-)/(2kT)).$$

When the barrier E_- for transition to the sessile state is high, the value of z is small, $\chi(z)/z \approx 1$; the second term on the right-hand side of Eq. (16) vanishes; and this equation is reduced to the conventional relationship for determining $\sigma(T)$ in a simple glide. Otherwise, if the barrier is not too high and the thermal activation of locking proceeds with a noticeable frequency, the strain stress changes. Figure 3 displays the modified temperature dependence $\sigma(T)$, which was obtained from the above relationships for the following parameters: $E_- = 1.1E_0$, $E_+ = E_0$, and $l_{fp}J_0/v_0 = 10^4$.

In general, the effect of dislocation locking in sessile states naturally leads to an increase in the strain stress. Since the temperature dependences have a pronounced exponential character in the case of thermally activated kinetics, the transition to a modified value of the strain stress occurs in the immediate vicinity of a certain transition temperature T_{tr}, above which the decrease in stress with an increase in temperature becomes slower and the slope of the $\sigma(T)$ curve diminishes (a plateau is observed). For comparison, the inset in Fig. 3 shows the temperature dependence of the strain stress upon prismatic slip in Ti according to the data taken from [1].

Figure 4 depicts the temperature dependence of the activation volume γ calculated by the formula $\gamma = kT/(d\sigma/d\ln\dot{\varepsilon})$. The dashed line represents the activation volume for a simple glide in the absence of dislocation locking. As is seen from this figure, the locking processes result in a peak in the activation volume as T_{tr} is approached. The inset shows the temperature dependence of the activation volume measured experimentally for the prismatic slip in Ti [1]. The dependence shows an anomalous peak. This indicates a qualitative

agreement between the behavior calculated in terms of the model proposed and that observed experimentally.

The theory developed allows a satisfactory description of the transient behavior upon changing from an ordinary glide to motion with spontaneous locking and unlocking of dislocations. The above illustrations demonstrate that this transition can be considered a possible mechanism of the anomalies observed in the temperature dependences of the characteristics of plastic deformation of materials subjected to mechanical tests.

Note that similar anomalies of plasticity were also observed in α-Fe [6, 7], Mo [8], Nb [9], Sn [10, 11], and other materials. However, the stick–slip motion of dislocations was not revealed, because *in situ* investigations were not carried out. In these cases, the observed anomalies were explained in the framework of the conventional glide mechanism, i.e., by assuming a complex double-humped relief of the Peierls–Nabarro barrier [12, 13] or other hypotheses. Microscopic investigations into the dislocation motion in these materials would be useful for a more reliable identification of the mechanism responsible for the plastic anomalies.

REFERENCES

1. S. Farenc, D. Caillard, and A. Couret, Solid State Phenom. **35–36**, 429 (1994).
2. J. P. Hirth and J. Lothe, *Theory of Dislocations* (McGraw-Hill, New York, 1967; Atomizdat, Moscow, 1972).
3. *Tables of Integral Transforms (Bateman Manuscript Project)*, Ed. by A. Erdelyi (McGraw-Hill, New York, 1954; Nauka, Moscow, 1969), Vol. 1.
4. *Handbook of Mathematical Functions*, Ed. by M. Abramowitz and I. A. Stegun (Dover, New York, 1971; Nauka, Moscow, 1979).
5. U. F. Kocks, A. S. Argon, and M. F. Ashby, in *Thermodynamics and Kinetics of Slip*, Ed. by B. Chalmers, J. W. Christian, and T. B. Massalski (Pergamon, Oxford, 1975), Prog. Mater. Sci. **19** (1975).
6. D. I. Quesnel, A. Sato, and M. Meshii, Mater. Sci. Eng. **18** (2), 199 (1975).
7. Y. Aono, K. Kitajima, and E. Kuramoto, Scr. Metall. **15** (3), 275 (1981).
8. H.-J. Kaufman, A. Luft, and D. Schulze, *Dislocations in Solids*, Ed. by H. Suzuki, T. Ninomiya, K. Sumino, and S. Takeuchi (Univ. of Tokyo Press, Tokyo, 1985), p. 455.
9. F. Ackerman, H. Mughrabi, and A. Seeger, Acta Metall. **31** (9), 1353 (1983).
10. G. I. Kirichenko, V. D. Natsik, and V. P. Soldatov, Fiz. Met. Metalloved. **65** (2), 386 (1987).
11. A. N. Diulin, G. I. Kirichenko, V. D. Natsik, and V. P. Soldatov, Fiz. Nizk. Temp. **24** (6), 595 (1998) [Low Temp. Phys. **24**, 452 (1998)].
12. S. Takeuchi and E. Kuramoto, J. Phys. Soc. Jpn. **38** (2), 480 (1975).
13. T. Suzuki, H. Koizumi, and H. O. K. Kircher, Acta Metall. Mater. **43** (6), 2177 (1995).

Translated by M. Lebedkin

Physics of the Solid State, Vol. 43, No. 5, 2001, pp. 850–853. Translated from Fizika Tverdogo Tela, Vol. 43, No. 5, 2001, pp. 818–821.

DEFECTS, DISLOCATIONS, AND PHYSICS OF STRENGTH

Contribution of Dislocation Cores to X-ray Scattering by Crystals with Dislocations

A. I. Dekhtyar

Institute of Metal Physics, National Academy of Sciences of Ukraine, pr. Vernadskogo 36, Kiev, 03680 Ukraine
e-mail: dekhtyar@imp.kiev.ua

Received October 10, 2000

Abstract—The contribution of dislocation cores to the broadening of the reciprocal lattice point due to dislocations in a crystal is estimated using the lattice Green functions for the description of the static displacements of the atoms. It is shown that this contribution is proportional to the angle of the integral misorientation of the dislocation substructure, which is experimentally determined by the x-ray method, and depends on some fundamental characteristics of the subatomic structure and the condensed state. © *2001 MAIK "Nauka/Interperiodica".*

It was established earlier in [1] that the shape of the intensity distribution of x-ray scattering in the azimuthal direction varies with an increase in the angle of the integral misorientation δ and successively takes the form of Gaussian, Lorentz, and uniform distributions. This angle is proportional to the distribution width $\delta q_\perp$, which corresponds to the size of the reciprocal lattice point in the azimuthal direction. The simplest relationship for δ for uniform distribution is obtained in the case of a bent crystal which contains an excess of dislocations of the same sign. In the theory of x-ray diffraction by imperfect crystals for the case under consideration [2], this relationship has the form

$$\delta \sim \delta q_\perp \sim a_L b Q L |\Delta n_\alpha|, \quad (1)$$

where a_L is the geometric factor, b is the Burgers vector of dislocation, Q is the magnitude of the diffraction vector, L is the dimension of the crystal (or the dimension of the irradiated region), and Δn_α is the excess density of dislocations of the same sign.

The main contribution to the experimentally determined intensity of x-ray scattering is made by the crystal regions being far away from the dislocations [2]. Expression (1) justifies this law. However, in deformation processes during hardening, an essential role is played by the distorted crystal regions immediately adjacent to the dislocation lines. These regions make the main contribution to the forces of the contact interaction between dislocations and between the dislocations and point defects. This particularly holds true for the high-temperature creep in which these interactions determine the strain rate. This is all the more interesting because a fundamental relationship has recently been established between the creep rate $\dot{\varepsilon}$ and the experimentally determined angle δ of the integral misorientation of the substructure in the form $\dot{\varepsilon} \sim \delta^{-2}$ [3].

In this connection, it is necessary to determine the contribution of the crystal regions near the dislocations to the x-ray scattering, even though this contribution will undoubtedly be several orders of magnitude smaller than the contribution of the regions far away from the dislocations. The term "near the dislocations" means that the law of the decrease in the static displacements u with the distance r from the center of the defect in this region should differ from the law $u \sim 1/r$, which is typical of large distances from dislocations [2]. At the same time, it should also differ from the law $u \sim 1/r^2$, which is characteristic of point defects and which probably holds for dislocations at distances of the order of 0–1b from the dislocation line [2]. Note that the law of decrease in the displacements with distance, $u \sim 1/r^{3/2}$, is determined in [2] as a limiting law for defects of the second kind, to which dislocations belong. Therefore, it can be assumed that this law holds near the dislocation lines (at distances of the order of the radius of the dislocation core r_0, which varies from b to several b).

The static displacements in this region can be described by the following expression with the use of the lattice Green functions [2]:

$$u_{si} = \sum_s \tilde{G}_{ss'ij} W_{s'tj}, \quad (2)$$

where $\tilde{G}_{ss'ij}$ is the Green function for an ideal crystal with one atom per cell which is equal to the ith component of the displacement of the sth atom under the action of a unit external force applied to atom s' and directed along the j axis. Although the dislocations lead to variations in the force constants of the crystal, one can restrict oneself to the zeroth approximation, because these variations are sufficiently small.

In this case, the defect with the center at point t acts on the s' atoms of the crystal with forces $W_{s'tj}$. Consid-

ering these forces external and taking into account the definition of $\tilde{G}_{ss'ij}$, we deduce that the displacement of the sth atom due to the defect is reduced to the sum of displacements caused by the field of forces acting on the s' atoms around the defect and is described by expression (2).

For monatomic crystals, the Green function can be represented as the sum over the normal coordinates [2]:

$$\tilde{G}_{ss'ij} = \frac{1}{N}\sum_{\mathbf{k}}\sum_{p=1}^{3}\frac{\mathbf{e}_{\mathbf{k}pi}\mathbf{e}_{\mathbf{k}pj}}{M\omega_{\mathbf{k}p}^2}\exp(i\mathbf{k}\mathbf{R}_{ss'}), \quad (3)$$

where N is the number of the elementary cells, $\mathbf{e}_{\mathbf{k}p}$ are polarization vectors, $\omega_{\mathbf{k}p}$ is the frequency of the normal modes, M is the atomic mass, and $\mathbf{R}_{ss'} = \mathbf{R}_{s'} - \mathbf{R}_s$.

When we solve the problem of scattering by crystal regions located near dislocations, it is necessary to assume that atoms s and s' are arranged in the region limited by a distance r_0 from the dislocation line. In this case, the expression for the intensity of scattering in these regions takes the form [2]

$$I_1 = f^2\sum_{ss'(r_0)}\exp(i\mathbf{q}\boldsymbol{\rho})\exp[-T_1(\mathbf{R}_s^0, \boldsymbol{\rho})],$$
$$T_1 = \sum_{\alpha}c_{\alpha}\sum_{t}[1-\exp(i\mathbf{Q}\mathbf{u}_{ss't\alpha})], \quad (4)$$

where f^2 is the structure amplitude of the crystal free from defects, $c_\alpha = S_0 n_\alpha$, S_0 is the area per possible location of the dislocation in the plane perpendicular to it, n_α is the density of dislocations of the system α, $\boldsymbol{\rho} = \mathbf{R}_{ss'}^0 = \mathbf{R}_s^0 - \mathbf{R}_{s'}^0$ ($\mathbf{R}_s^0$ corresponds to a crystal free from defects), and $\mathbf{u}_{ss't\alpha}$ is the difference between the displacements: $\mathbf{u}_{ss't\alpha} = \mathbf{u}_{st\alpha} - \mathbf{u}_{s't\alpha}$.

In the case of a bent crystal, we have $S_0 = \pi r_0^2$ and $c_\alpha = \pi r_0^2 \Delta n_\alpha$, where Δn_α is the excess density of dislocations of the same sign. The quantity T_1 is a complex one,

$$T_1 = T_1' + iT_1''. \quad (5)$$

Here, the imaginary component (T_1'') describes the intensity distribution in the azimuthal direction. Then, according to expression (4), we have

$$T_1'' = -\sum_{\alpha}\pi r_0^2\Delta n_\alpha\sum_{t}\sin(\mathbf{Q}\mathbf{u}_{ss't\alpha}). \quad (6)$$

In the limits of dislocation cores (the radius of which does not exceed a tenth of b), it can be assumed that the differences between the displacements $\mathbf{u}_{ss't\alpha}$ are sufficiently small. Then, $\sin(\mathbf{Q}\mathbf{u}_{ss't\alpha}) \approx \mathbf{Q}\mathbf{u}_{ss't\alpha}$. The latter can be expanded in a power series of $\mathbf{Q}\mathbf{u}_{st\alpha}$, and we can restrict ourselves to the first term of the expansion: $\mathbf{Q}\mathbf{u}_{ss't\alpha} \approx \mathbf{R}_{ss'}^0\mathbf{q}_1\frac{\partial}{\partial R_s^0}(\mathbf{Q}\mathbf{u}_{st\alpha})$, where $\mathbf{q}_1$ is a unit diffraction vector. When we choose the reflections for which $\mathbf{Q}$ is approximately parallel to $\mathbf{u}_{st\alpha}$, we obtain

$$\mathbf{Q}\mathbf{u}_{ss't\alpha} \approx Q\mathbf{R}_{ss'}^0 q_1\frac{\partial}{\partial R_s^0}u_{st\alpha}. \quad (7)$$

For simplicity, we carry out the calculations for a single system of dislocations. In this case, we obtain

$$T_1'' = -\pi r_0^2\Delta n Q\mathbf{R}_{ss'}^0\mathbf{q}_1\frac{\partial}{\partial R_s^0}\sum_t u_{st}, \quad (8)$$

and for the edge dislocations [2], this quantity is determined by the expression

$$T_1'' = R_s^0\mathbf{A}\mathbf{R}_{ss'}^0, \quad (9)$$

where $\mathbf{A}$ is the vector of the scattering amplitude.

It follows from the theoretical results that the intensity has a detectable value when the vector $\mathbf{q}$ satisfies

$$\mathbf{q} - \mathbf{A}R_s^0 = 0. \quad (10)$$

The contribution to the azimuthal width of the scattering intensity distribution due to the dislocation cores is a variation in the quantity $\mathbf{q}$ in the cores. Since the displacements u_{st} depend on the distance R_s^0 from the dislocation center, from formulas (8)–(10), we deduce

$$\delta q_\perp' = \frac{dq_\perp}{du_{st}}\delta u_{st} = -\pi r_0^2\Delta n Q\frac{\partial}{\partial R_s^0}\sum_t\frac{du_{st}}{dR_s^0}\delta R_s^0. \quad (11)$$

From formulas (2) and (3), we derive the expression for u_{st} and then can write the contribution of the dislocation cores $\delta q_\perp'$ to the total broadening in the form

$$dq_\perp' = -\frac{\pi}{N}\Delta n Q r_0^2\frac{\partial^2}{\partial(R_s^0)^2}$$
$$\times\sum_t\sum_{s'}\sum_{\mathbf{k}}\sum_{p=1}^{3}\frac{\mathbf{e}_{\mathbf{k}pi}\mathbf{e}_{\mathbf{k}pj}}{M\omega_{kp}^2}\exp(i\mathbf{k}\mathbf{R}_{ss'}^0)W_{s'tj}\delta R_s^0, \quad (12)$$

where the maximum distance is $R_s^0 = r_0/b$.

First, let us note that taking into account the conservation of dimensionality, the polarization vectors should appear as dimensionless quantities e/b.

Second, only the factor $\exp(i\mathbf{k}\mathbf{R}_{ss'}^0)W_{s'tj}$ in expression (12) depends on R_s^0. As was shown above, this dependence can be represented in the form

$$\exp(i\mathbf{k}\mathbf{R}_{ss'}^0)W_{s'tj} \cong C_1 R_s^{-3/2}, \quad (13)$$

where C_1 is a constant independent of R_s^0.

Third, $\delta R_s^0 = r_0/b$.

We can carry out a simple summation in expression (12). This is favored by the small size of the dislocation cores and the discrete nature of the terms of the sum. It is assumed in the summation that the variable u_{st} is substituted by an average value, after which the law of the variation in u_{st} with distance is introduced. We can expect an error of no more than 100% in comparison with exact integration.

In order to have the possibility of summing over t, let us consider the edge dislocation as a set of point defects, each of which has its center at point t. The distance between each point t and the adjacent one is of the order of b (more precisely, it is the distance between the atoms in the direction of the dislocation line). However, the displacements of atoms from their sites predominantly occur in the plane perpendicular to the dislocation line. Therefore, the difference between a single bulk point defect and a "point" defect from the dislocation set is that a "defect" in the edge dislocation induces atomic displacements only in the perpendicular plane. The combined effect for a dislocation depends on the number of point defects which fall within the length of the dislocation. In the framework of the given approximation, this number is equal to L/b.

It follows from the above that the summation over s' determines the number of displaced atoms for each point defect. In this case, the summation over s' results in the factor $\pi N(r_0/b)^2$.

The summation over $\mathbf{k}$ should be performed over singular points of the reciprocal lattice with inclusion of the weight contributions. With the results obtained in [4], we deduce that, for bcc and fcc structures, the factor associated with the summation over $\mathbf{k}$ is equal to 4.59 and 4.41, respectively. This result differs only slightly from the value of the spherical approximation: $4\pi/3 \cong 4.19$.

The summation over p for the isotropic crystal gives a factor of 3.

The polarization vectors can be estimated from the dielectric properties of the atom. According to [5], the formula for the polarization vector has the form

$$\mathbf{e} = \frac{4\pi\varepsilon_\nu R_a^3 \mathbf{E}}{Z|e|}, \tag{14}$$

where ε_ν is the permittivity of free space, R_a is the atomic radius, $\mathbf{E}$ is the vector of the external electric field, Z is the total number of electrons in the atom, and $|e|$ is the electron charge.

In the case of a dislocation, the quantity $\mathbf{E} = \mathbf{F}/Z|e|$ describes the electric field created as a result of the atomic displacement. This expression can be rewritten in the form $\mathbf{E} = \mathbf{F}/Z|e| = W_c/Z|e|\mathbf{e}$. Here, W_c is the energy of the dislocation core per atom. For simplicity, it can be assumed that the ith component of the polarization vector coincides with the magnitude of the polarization vector in the j direction; that is, $e_i = e_j = e$.

The frequency of normal modes can be determined as follows. The displacements near the dislocation line are probably so large that interatomic distances become close to those characteristic of the liquid or amorphous states. This is evident from the following facts. First, the linear theory of elasticity is inapplicable to the dislocation core, and the core region is best represented in the form of a singularity [6]. Second, the rate of diffusion along the dislocation core is 4–5 orders of magnitude larger that in the bulk of the crystal lattice [7], which approximates the rates of diffusion in liquids. Therefore, it is reasonable to assume that the maximum possible frequencies $\omega_{\mathbf{k}p}$ of normal modes in the dislocation core correspond not to the Debye temperature, as is the case in an ideal lattice, but to the melting point T_m, i.e., $\hbar\omega_{\mathbf{k}p} = kT_m$.

The energy of the dislocation core per atom is equal to [6]

$$W_c = \frac{Gb^2}{4\pi(1-\nu)}, \tag{15}$$

where G is the shear modulus at the temperature of the measurement of the misorientation angle and ν is the Poisson ratio.

The value of C_1 can be found from condition (13) when $R_s^0 = r_0/b = 1$. Let us set $\exp(i\mathbf{k}\mathbf{R}_{ss'}^0) \cong 1$. This assumption is justified, because the most prominent displacements which lead to the reflection diffusion in the case of edge dislocations can be measured when the wave vector $\mathbf{k}$ is perpendicular to the $R_{ss'}^0$ vector. Then, C_1 is determined only by the interatomic interaction forces $W_{s'tj}$. Since $R_s^0 = r_0/b = 1$, these forces can be calculated from the principle of the pair interaction. In this case, the expression for the pair interaction energy $V_{s't}$ can most conveniently be represented via the pseudopotentials of ions $w_0(q)$ at $q = 2k_F'$ [8]:

$$G_1 = W_{s't} = \frac{V_{s't}}{b} = \frac{18\pi z_e^2 [w_0(2k_F')]^2}{bk_F'^2} \frac{\cos(2k_F'b)}{(2k_F'b)^3}. \tag{16}$$

Here, z_e is the number of effectively coupling electrons per atom [9], m is the electron mass, and k_F' is the radius of the Fermi pseudosphere occupied by the almost free, effectively coupling electrons z_e [9]:

$$k_F' = \sqrt[3]{\frac{3\pi^2 z_e}{\Omega_0}} \cong \frac{1}{b}\sqrt[3]{18\pi z_e}, \tag{17}$$

where Ω_0 is the atomic volume. The quantity $w_0(2k'_F)$ is determined in the following manner [8]:

$$w_0(2k'_F) = -\frac{C_2\pi z_e}{\Omega_0 k'^2_F}, \quad (18)$$

where C_2 is the quantity equal to the ratio n^3/Z and n is the principal quantum number of the almost free, effectively coupling electrons. The latter will be demonstrated in a separate work dedicated to the problems of the electronic structure and interatomic interaction in transition metals.

The value of $\cos(2k'_F b)$ is negative and, in most cases, approaches –1. Taking into account that calculation of expression (16) was carried out in atomic units and substituting the values of k'_F and $w_0(2k'_F)$, expression (16) can be rewritten in the form

$$C_1 = -2.43\times10^{-19}\frac{n^6 z_e}{\pi^2 Z^2 b}. \quad (19)$$

Substituting relationship (13) into expression (12), using the results of the summation, carrying out differentiation with respect to R_s^0, replacing R_s^0 by r_0/b in expression (13), and carrying out the substitution of all the quantities determined above, we obtain the expression for $\delta q'_\perp$ in the form

$$\delta q'_\perp = 4.56\times10^{-19}\frac{\pi\varepsilon_\nu\hbar^2}{e^2k^2}\Delta nLQ\left(\frac{r_0}{b}\right)^{3/2} \times\frac{z_e n^6 Gb^3}{(1-\nu)Z^4 M T_m^2}. \quad (20)$$

Substituting relationship (1) into expression (20) and taking into account the numerical values of the fundamental constants, we can derive a relationship between $\delta q'_\perp$ and $\delta q_\perp$ measured experimentally:

$$\delta q'_\perp = 2.88\times10^{-14}\frac{z_e n^6}{Z^4 M a_L(1-\nu)T_m^2}\frac{Gb^2}{}\left(\frac{r_0}{b}\right)^{3/2}\delta q_\perp. \quad (21)$$

Let us now substitute the numerical values of all the quantities for particular crystals (for example, for metals from [10], for r_0/b from [9], and for z_e from [11]) into relationship (21) and deduce that the values of $\delta q'_\perp$ truly represent a small part of the experimentally determined smearing of the reciprocal lattice site $\delta q_\perp$ (see table).

Summing up the results obtained, we can conclude that, first, the contribution of the dislocation cores to the angle of the integral misorientation of the substructure depends on the dimension of the dislocation core or, what is the same, on the width of the splitting of the dislocations, because they are proportional to each other [6]. Second, this contribution depends on the fundamental properties of metals in the condensed state (melting temperature, elastic constants, lattice parameter, and the concentration of effectively coupling electrons), and also on the individual features of the atom (atomic mass, the principal quantum number of outer shell electrons that determine the interatomic interaction, and the number of electrons of the ion core).

Calculated ratio of the smearing of the reciprocal lattice site due to the contribution of dislocation cores to the experimentally observed smearing due to the dislocations in the crystal according to formula (21) for a number of metals

Metal	$\delta q'_\perp/\delta q_\perp$
Cu	1.1×10^{-4}
Ni	3.0×10^{-5}
Ag	1.4×10^{-4}
Mo	2.6×10^{-5}
W	3.4×10^{-6}
Nb	3.1×10^{-5}
Ta	5.0×10^{-6}

ACKNOWLEDGMENTS

This work was supported by the Ukrainian Scientific and Technological Center, project no. 050.

REFERENCES

1. L. V. Demchenko, A. I. Dekhtyar, V. A. Kononenko, and K. P. Ryaboshapka, Metallofizika **11** (4), 84 (1989).
2. M. A. Krivoglaz, *Diffraction of X-rays and Neutrons in Imperfect Crystals* (Naukova Dumka, Kiev, 1983).
3. A. I. Dekhtyar and L. V. Demchenko, in *Proceedings of the Fourth International Conference "Tungsten, Refractory Metals, and Alloys,"* Ed. by A. Bose and R. J. Dowding (Metal Powder Industry Federation, Princeton, 1998), p. 309.
4. R. A. Evarestov and V. P. Smirnov, Phys. Status Solidi B **119** (1), 9 (1983).
5. C. A. Wert and R. M. Thomson, *Physics of Solids* (McGraw-Hill, New York, 1964; Mir, Moscow, 1969).
6. J. P. Hirth and J. Lothe, *Theory of Dislocations* (McGraw-Hill, New York, 1967; Atomizdat, Moscow, 1972).
7. R. F. Balluffi, in *News of Physics of Solid State*, Vol. 2: *Thermally Activated Processes in Crystals* (Mir, Moscow, 1973), p. 42.
8. W. A. Harrison, *Pseudopotentials in the Theory of Metals* (Benjamin, New York, 1966; Mir, Moscow, 1968).
9. A. I. Dekhtyar, G. Ya. Kozyrskiĭ, and V. A. Kononenko, Fiz. Tverd. Tela (Leningrad) **20** (4), 964 (1978) [Sov. Phys. Solid State **20**, 557 (1978)].
10. *Structure and Properties of Metals and Alloys: A Handbook* (Naukova Dumka, Kiev, 1987).
11. B. Rosenfeld, Acta Phys. Pol. **31** (1), 197 (1967).

Translated by O. Moskalev

Physics of the Solid State, Vol. 43, No. 5, 2001, pp. 854–858. Translated from Fizika Tverdogo Tela, Vol. 43, No. 5, 2001, pp. 822–826.

DEFECTS, DISLOCATIONS, AND PHYSICS OF STRENGTH

Dislocations as Linear Topological Defects

G. A. Malygin

Ioffe Physicotechnical Institute, Russian Academy of Sciences, Politekhnicheskaya ul. 26, St. Petersburg, 194021 Russia
e-mail: malygin.ga@pop.ioffe.rssi.ru

Received September 18, 2000; in final form, October 11, 2000

Abstract—Dislocations and dislocation plasticity are considered and compared with such dissimilar physical phenomena as superfluidity of liquid helium and type II superconductivity. These phenomena share the common property that the dislocations, as well as quantum vortices in superconductors and superfluid helium, are topological defects. They arise during a phase transformation which is accompanied by spontaneous symmetry breaking caused by Bose condensation of acoustic phonons. The general problems of the evolution of ensembles of linear topological defects and the character of the spatial structures formed by them are discussed.

INTRODUCTION

The notion of a dislocation as a defect which reduces the resistance of the crystal to a crystallographic shear and whose gliding is an elementary act of plastic deformation of the crystal was introduced purely phenomenologically in [1, 2]. In spite of this circumstance, the essential features of plastic deformation of crystals were interpreted in terms of dislocations in succeeding decades. At the present time, the notion of crystal plasticity primarily implies dislocation plasticity, that is, translation of dislocations along the most closely packed planes, which gives rise to plastic deformation of the crystal. In the general case, dislocation–disclination plasticity takes place in circumstances where dislocation gliding is hampered and rotations occur in the crystal; at high temperatures, vacancy fluxes make a dominant contribution to the deformation of crystals and, therefore, vacancy plasticity takes place.

The microscopic mechanism of the formation of dislocations in an originally dislocation-free crystal was unclear for a long time. However, this was not a serious handicap to investigations into plastic deformation, because an actual crystal has a sufficient amount of dislocation sources, such as Frank–Read sources, which generate dislocations at the very beginning of deformation. As the deformation proceeds further, the mechanism of double cross slip of screw dislocations starts to operate and the dislocation density increases rapidly with deformation.

If there are no dislocations and no Frank–Read sources in a crystal, the formation of dislocations is presumed to be due to geometric stress concentrators in the form of steps of atomic sizes, which are present on the surface of the crystal. Near the stress concentrators, the local stress can be as high as the theoretical shear strength (about $\approx G/2\pi$, where G is the shear modulus) and the dislocations are nucleated at these sites.

Once dislocations have been formed, they can move through the crystal, far from stress concentrators, under the action of negligibly low stresses, $10^{-5}G$ to $10^{-4}G$. Resistance to the dislocation movement along slip planes can be offered by various crystal defects (impurity atoms, phase precipitates, forest dislocations, etc.) and, in crystals with directed atomic bonding, by the Peierls potential. These obstacles increase the dislocation friction stress up to $(10^{-3}–10^{-2})G$ and make dislocation loops stable (when the external stress is removed), because the dislocation lines are pinned by obstacles.

What is the reason for the low resistance of the lattice to dislocation movement when the lattice has no special obstacles which limit motion? According to [3, 4], the formation of dislocations near stress concentrators in an originally dislocation-free crystal is due to a spontaneous breaking of the symmetry (regularity in atomic positions) and Bose condensation of acoustic phonons. Obviously, the coherent phonon state produced by the Bose condensation is the reason for the low lattice resistance to the motion of dislocations. Therefore, one can think of the crystal plasticity as a manifestation of the superfluidity of the crystal, which is associated with the formation of dislocations and their motion through the crystal; that is, the plasticity is similar to the superconductivity of metals and the superfluidity of ^{4}He and ^{3}He.

In this paper, we discuss (keeping in mind the aforesaid) the general problems of the formation (and the properties) of topological defects such as dislocations and quantum vortices in condensed media (Section 1), the problems of the evolution of ensembles of such defects (Section 2), and the spatial inhomogeneous structures formed by them (Section 3).

1063-7834/01/4305-0854$21.00

1. DISLOCATIONS AS TOPOLOGICAL DEFECTS

We consider dislocations in parallel with other diversified physical phenomena which are outside the framework of the physics of strength and plasticity of crystals. These phenomena are associated with a large class of topological defects which arise in various condensed media (crystals, liquid crystals, superfluids) as a result of phase transformations accompanied by a spontaneous breaking of the symmetry [5–9]. These defects can also be thought of as nonlinear topological excitations of a medium under a specified external field.

For example, in the case of type II superconductors, topological defects in the form of quantum vortices (fluxoids) arise when a magnetic field of strength $H > H_{c1}$ is applied to a superconductor. In the case of superfluid ^{4}He and ^{3}He, quantum vortices appear when a mechanical impulse is applied to a superfluid and causes it to move at a velocity $V > V_c$. In crystals, quantum vortices in the form of dislocations are produced, as mentioned above, by applying a local mechanical stress of the order of the theoretical shear strength of the crystal lattice.

In recent publications, the subject of wide speculation was one more type of topological defects, hypothetical cosmic strings, which carry an enormous gravitational charge. According to [10, 11], they arise in the initial stage of the expansion of the Universe and, in time, become the centers at which matter is condensed and stars and galaxies are formed. Cosmic strings, as well as other topological defects, are a result of the phase transformation that occurs in the process of rapid expansion and cooling of hot and extremely dense primary cosmic matter.

What do all these topological defects have in common which would allow one to consider them as belonging to the same class of phenomena in spite of the sharp distinction between the physical media in which they are formed? There are several properties of this kind.

First, as indicated above, the defects under study are formed during phase transformations with a spontaneous breaking of the symmetry.

Second, although the defects arise in quantum systems, they, once formed, can be treated as classical macroscopic objects [4]. The relation to the quantum system is manifested only in the type and magnitude of the quantized (topological) charge carried by a defect. This is a magnetic flux quantum in the case of vortices in a superconductor, a quantum of the liquid particle velocity circulation in superfluid helium, the Burgers vector (a quantum of displacement circulation) in the case of dislocations, and the gravitational charge per unit string length in the case of cosmic strings.

Third, a property common to the defects is that Bose condensation takes place in the quantum systems of particles in which these defects are formed. The Bose condensate can be separated from the normal state by an energy gap (as is the case with Cooper electrons and ^{4}He atoms) or can have no gap (in the case of dislocations [3, 4], quantum vortices in the A phase of ^{3}He [8], and cosmic strings [12, 13]) if so-called Goldstone bosons with zero minimum energy exist. In the latter case, the order parameter is determined by the magnitude and direction of the wave vector [3, 8] rather than by the energy gap.

Fourth, the topological defects at hand are characterized by a self-energy per unit length (line tension) and have a singular field, the strength of which diminishes with distance from the defect line in proportion to r^{-1}. In this respect, the defects under discussion can be classified as "charged" strings.

Fifth, all the topological excitations in question can be described using standard techniques of the gauge field theory [3, 4, 11]. In this respect, the theory of their formation is similar to the current theory of elementary particles, which treats these particles as various excitations of a vacuum [14].

Finally, sixth, a common property, which has not yet been studied theoretically in detail, is the evolution of an ensemble of linear topological defects after they arise in the specific actual physical medium. The equations of the gauge field theory describe the formation of individual defects rather than of their ensemble, because the average distance between defects in an ensemble can be much larger than the distance at which the quantum effects are substantial. The problem of evolution of an ensemble of linear topological defects is considered in the next section.

2. EQUATIONS OF EVOLUTION OF AN ENSEMBLE OF LINEAR DEFECTS

As already noted, once the topological defects have arisen, they can be treated as classical macroscopical objects at distances exceeding the mean spacing between the particles of the microcanonical ensemble in which they are formed. Experiments show [15–21] that the number of defects increases and the interaction between defects become important with an increase in the external field that causes these defects to arise.

At the present time, ensembles of dislocations [18–21] and of quantum vortices in superfluid helium [15–17] are the best investigated both experimentally and theoretically. Attempts have also been made to derive equations for the evolution of vortices in superconductors [22, 23] and for cosmic strings [11, 24, 25]. The equations describing the time t dependence of the average density $n(t)$ of vortices in helium and of dislocations were first derived in a model developed to explain the corresponding experimental dependences [15, 20, 21]. They have the form

$$\frac{dn}{dt} = w + \left(\delta' - \frac{\gamma}{d}\right)n + \alpha n^{3/2} - \beta n^2. \qquad (1)$$

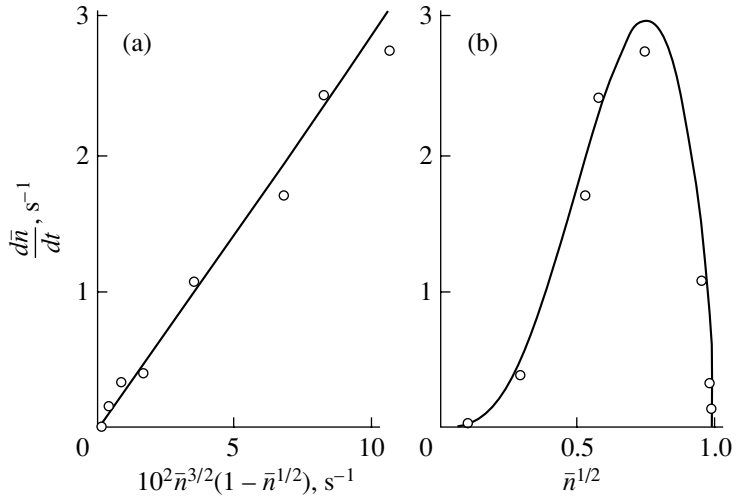

Fig. 1. Dependence of the generation rate of quantum vortices in ^{4}He (a) on the vortex density $\bar{n}$ [15] in accordance with Eq. (3) and (b) on the quantity $\bar{n}^{1/2}$.

Here, $n(t) = L(t)/V$, where $L(t)$ is the overall length of dislocations in a crystal or of vortices in a vessel at a given instant of time and V is the volume of the crystal or the vessel; w is the density of vortex sources (or of stress concentrators and Frank–Read sources in the case of dislocations); δ' is the dislocation (or vortex) multiplication factor on various inhomogeneities in the corresponding media; the coefficient γ/d characterizes the decrease in the density of topological defects caused by their leaving the thin crystal (or a channel in the case of vortices in helium) of thickness d; α is the dislocation (vortex) multiplication factor due to their crossing each other; and β is the annihilation factor of defects opposite in sign.

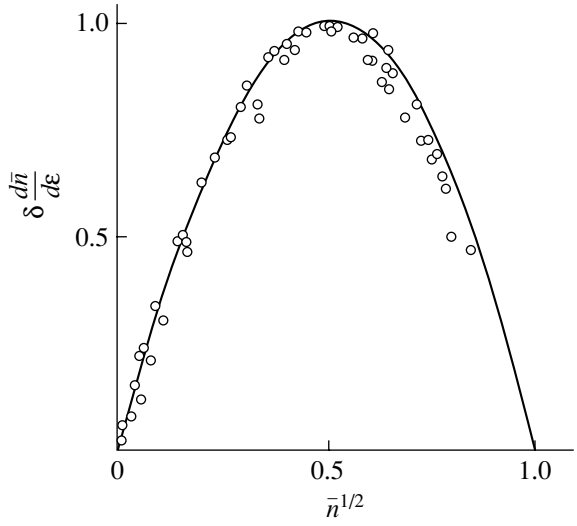

Fig. 2. Dependence of the dislocation multiplication rate in an Al–Mg alloy on the quantity $\bar{n}^{1/2}$ at different temperatures in the range from 77 to 473 K [21].

Equation (1) was formulated for the vortex density in helium and for the dislocation density independently and at different times. A theoretical substantiation of this equation for vortices can be found in [16, 17] and, for dislocations, in [21, 26]. Figures 1 and 2 compare the experimental data for the evolution of the density of vortices in ^{4}He [15] and of dislocations in an aluminum–magnesium alloy [21], respectively, with the specific case of Eq. (1):

$$\frac{dn}{dt} = \alpha n^{3/2} - \beta n^2. \tag{2}$$

In Fig. 1a, the solid line is the dependence in Eq. (2) expressed in terms of the dimensionless vortex density $\bar{n} = n/n_0$:

$$\frac{d\bar{n}}{dt} = \frac{\alpha^2}{\beta}\bar{n}^{3/2}(1-\bar{n}^{1/2}), \tag{3}$$

where $n_0 = (\alpha/\beta)^2$. The curve in Fig. 1b describes the dependence of the same quantity on $\bar{n}^{1/2}$.

The solid line in Fig. 2 describes the dependence of the dislocation multiplication rate (with increasing strain) on the dimensionless dislocation density:

$$\delta\frac{d\bar{n}}{d\varepsilon} = 4\bar{n}^{1/2}(1-\bar{n}^{1/2}). \tag{4}$$

Equation (4) is derived from Eq. (1) in the case of dislocations by putting $dn/dt = (dn/d\varepsilon)\dot{\varepsilon}$, where ε is the strain, $\dot{\varepsilon} = bnu$ is the plastic strain rate, b is the Burgers vector, u is the dislocation velocity, $\alpha = k_1 bu$, $\beta = k_2 bu$, $n_0 = (\alpha/\beta)^2 = (k_1/k_2)^2$, and $\delta = 4/k_2$. The rising branches of the parabolas in Figs. 1b and 2 describe the process

of multiplication of linear defects due to their crossing each other, and the descending branches correspond to the process of annihilation of defects opposite in sign.

It is seen that Eqs. (2)–(4) agree well with the experiment. Clearly, Eq. (1) describes the evolution of an ensemble of topological defects, regardless of the microscopic quantum system in which the defects arise. This equation accounts for the kinetic properties of the defects as classical objects and for the processes of generation, multiplication, and annihilation, which are characteristic of linear defects. Earlier, no attention was drawn to this important circumstance.

3. SPATIAL STRUCTURES

Another characteristic feature of the defects under discussion is that they can form spatial structures. These can be separated into homogeneous (chaotic [16], ordered [27], net [28]) and inhomogeneous (band [19, 21], cell [18, 21]) structures. The homogeneous and inhomogeneous dislocation structures have been best studied experimentally [18, 19, 21, 28–30]. As an example, we will consider the formation of a cell dislocation structure.

For this purpose, we represent Eq. (1) in the form

$$\frac{\partial n}{\partial t} + \nabla \cdot \mathbf{j} = -\nu n + \alpha n^{3/2} - \beta n^2, \qquad (5)$$

where $\nu = (\gamma/d - \delta') > 0$ is a coefficient characterizing the dislocation immobilization rate at obstacles and d is the dislocation mean free path to these obstacles (in thin crystal plates, d is the thickness of the crystal in the direction of motion of dislocations).

There are at least two reasons for the occurrence of a spatially inhomogeneous dislocation flux. One of them is associated with the long-range interaction of dislocations and the occurrence of a correlation diffusion flux due to screening of the dislocations of one sign by dislocations of the opposite sign [21, 29, 30]:

$$\mathbf{j}^{cr} = \hat{D}_1^{cr} \cdot \nabla n + \hat{D}_2^{cr} \cdot (\nabla^2)\nabla n + \ldots, \qquad (6)$$

where $\hat{D}_{1,2}^{cr}$ are the diffusion coefficients of the first and second order, respectively.

The other reason is the short-range (contact) interaction of dislocations, which decreases the dislocation velocity and leads to a reversed diffusion flux in the regions where the dislocation density is higher because of dislocation (strain) hardening of the dislocation ensemble [21]:

$$\begin{aligned}\mathbf{j}^{df} &= -(1-M)\hat{D}_1^{df} \cdot \nabla n \\ &- (1-M)\hat{D}_2^{df} \cdot (\nabla^2)\nabla n + \ldots,\end{aligned} \qquad (7)$$

where $M = -\partial \ln u/\partial \ln n > 0$ is the coefficient of hardening (and reversing, when $M > 1$) of the dislocation flux.

By substituting Eq. (6) or (7) for the flux in Eq. (5), one can find that the dislocation density becomes unstable with respect to spatial fluctuations $\delta n \sim \exp(\omega t + i\mathbf{q} \cdot \mathbf{r})$ with critical wave vector $q_c = (D_1/2D_2)^{1/2}$ and critical increment

$$\omega(q_c) = \left(\frac{\partial \Phi}{\partial n}\right)_0 + (M-1)\frac{D_1^2}{4D_2} > 0, \qquad (8)$$

where $\Phi(n)$ stands for the right-hand side of Eq. (5). The derivative $(\partial\Phi/\partial n)_0$ corresponds to the values of n at which $\Phi(n) = 0$.

If the kinetic coefficients in Eq. (5) are such that $\nu\beta/\alpha^2 < 1$, the equation $\Phi(n) = 0$ has three roots [21]:

$$n_1 = 0, \quad n_2 \approx \left(\frac{\nu}{\alpha}\right)^2, \quad n_3 \approx \left(\frac{\alpha}{\beta}\right)^2. \qquad (9)$$

An analysis shows that the singular point n_2 is an unstable focus and n_3 is a saddle point. Neglecting the diffusion fluxes of the second order in Eqs. (5) and (7), we find that nonlinear equation (5) has a stationary solution,

$$n(x, y, z) = \frac{n_3}{\left[1 + (f-1)\sin^2\left(\pi\frac{\pm x \pm y \pm z}{\Lambda}\right)\right]^2}, \qquad (10a)$$

if $f = (n_3/n_2)^{1/2} = \alpha^2/\nu\beta > 1$. This solution describes a periodic (cell) dislocation structure with spatial period

$$\Lambda = 4\pi\sqrt{3}\left[\frac{(M-1)D_1}{\nu}\right]^{1/2} \qquad (10b)$$

and a dislocation density equal to n_3 at the walls of the cells and to $n_2 < n_3$ in the interior of the cells. From Eq. (9), it is seen that the value of n_2 is determined by the competing processes of immobilization and multiplication of dislocations; n_3, by the competing processes of multiplication and annihilation of dislocations. As an illustration of Eq. (10a), Fig. 3 shows the

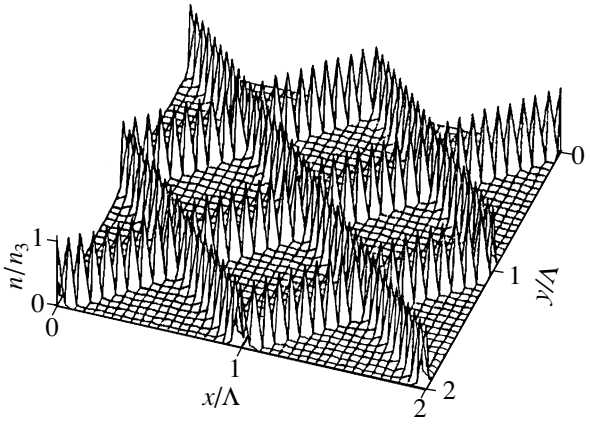

Fig. 3. Distribution of dislocations in a cell structure in the $z = 0$ plane according to Eq. (10a) for $f = 10^2$.

distribution of the dislocation density n/n_3 over the cell structure in the $z = 0$ plane for the case where the ratio of the dislocation densities at the walls and in the interior of the cells is $n_3/n_2 = 10^4$.

As for inhomogeneous structures in other ensembles of linear topological defects, they have not been observed, as far as we know, in ensembles of quantum vortices in superconductors and superfluid helium. From the calculations presented above, it is seen that certain, fairly stringent requirements have to be met in order for such structures to arise. In this connection, it is of interest to discuss the large-scale cell structure of the matter distribution (galaxies and stars) in the present-day Universe [31]. In accordance with the heterogeneous mechanism of galaxy nucleation through the accretion of primary matter on cosmic strings [10, 11], one can suppose that, by analogy with cell dislocation structures, the inhomogeneous matter distribution in the Universe is due to the cell structure of the cosmic-string distribution in it. This hypothetical mechanism of formation of large-scale inhomogeneities can be considered an alternative to the traditional mechanism of their formation due to quantum fluctuations of the density of the primary matter.

Thus, comparison of the properties of dislocations and topological defects of other types showed that, on the whole, dislocations possess properties that are typical of many other defects and, therefore, the phenomenon of plastic deformation of crystals is universal in character. Furthermore, the evolution of an ensemble of dislocations and that of an ensemble of vortices in superfluid helium are described by the same equation; this equation takes into account the kinetic specific features of these linear objects which differentiate them from point objects. These findings suggest that the equations of evolution of other linear topological defects, as well as the structures formed by them, are similar in character.

REFERENCES

1. E. Orowan, Z. Phys. **89** (9), 605 (1934).
2. G. I. Taylor, Proc. R. Soc. London, Ser. A **145** (855), 362 (1934).
3. M. Wadati, H. Matsumoto, and H. Umezawa, Phys. Rev. B **18** (8), 4077 (1978).
4. H. Umezawa, H. Matsumoto, and M. Tachiki, *Thermofield Dynamics and Condensed States* (North-Holland, Amsterdam, 1982; Mir, Moscow, 1985).
5. G. Toulouse and M. Kleman, J. Phys. Lett. **37** (1), 149 (1976).
6. V. P. Mineev and G. E. Volovik, Phys. Rev. B **18** (7), 3197 (1978).
7. N. D. Mermin, Rev. Mod. Phys. **51** (3), 591 (1979).
8. G. E. Volovik, Usp. Fiz. Nauk **143** (1), 73 (1984) [Sov. Phys. Usp. **27**, 363 (1984)].
9. I. A. Ovid'ko and A. E. Romanov, in *Theoretical and Experimental Research of Disclination* (Fiz.-Tekh. Inst. im. A. F. Ioffe Akad. Nauk SSSR, Leningrad, 1986), p. 6.
10. M. Hindmarsh and T. W. Kibbel, Rep. Prog. Phys. **58** (5), 47 (1995).
11. A. Vilenkin and E. P. Shellard, *Cosmic Strings and Other Topological Defects* (Cambridge Univ. Press, Cambridge, 1994).
12. A. Vilenkin and A. E. Everette, Phys. Rev. Lett. **48** (26), 1867 (1982).
13. N. Turok, Phys. Rev. Lett. **76** (7), 1015 (1996).
14. J. Polchinsky, *String Theory* (Cambridge Univ. Press, Cambridge, 1998).
15. W. F. Vinen, Proc. R. Soc. London, Ser. A **242** (1231), 493 (1957); **243** (1234), 400 (1957).
16. K. W. Schwarz, Phys. Rev. B **38** (4), 2398 (1988).
17. S. K. Nemirovskii and W. Fiszdon, Rev. Mod. Phys. **67** (1), 37 (1995).
18. F. R. N. Nabarro, Z. S. Basinski, and D. B. Holt, Adv. Phys. **13**, 193 (1964); *Plasticity of Pure Single Crystals* (Metallurgiya, Moscow, 1967).
19. B. I. Smirnov, *Dislocation Structure and Hardening of Crystals* (Nauka, Leningrad, 1981).
20. U. F. Kocks, A. S. Argon, and M. F. Ashby, *Thermodynamics and Kinetics of Slip* (Pergamon, New York, 1975).
21. G. A. Malygin, Usp. Fiz. Nauk **169** (9), 979 (1999).
22. J. R. Clem, Phys. Rev. B **26** (5), 2463 (1982).
23. S. E. Savel'ev, L. I. Fisher, and V. A. Yampol'skiĭ, Zh. Éksp. Teor. Fiz. **112** (3), 936 (1997) [JETP **85**, 507 (1997)].
24. P. P. Avellino, R. R. Caldwall, and C. J. Martins, Phys. Rev. B **56** (8), 4568 (1997).
25. C. J. Martins and E. P. Shellard, Phys. Rev. D **54** (4), 2535 (1996).
26. G. A. Malygin, Fiz. Tverd. Tela (St. Petersburg) **38** (8), 2418 (1996) [Phys. Solid State **38**, 1329 (1996)].
27. U. Essmann and H. Trauble, Phys. Lett. A **24A** (9), 526 (1967).
28. S. Amelinckx, in *Solid State Physics*, Suppl. 6 (Academic, New York, 1964); *Direct Observation Methods of Dislocations* (Mir, Moscow, 1968).
29. Sh. Kh. Khannanov, Fiz. Met. Metalloved., No. 10, 34 (1992).
30. G. F. Sarafanov, Fiz. Tverd. Tela (St. Petersburg) **39** (9), 155 (1997) [Phys. Solid State **39**, 1403 (1997)].
31. M. S. Turner and J. A. Tyson, Rev. Mod. Phys. **71** (2), S145 (1999).

Translated by Yu. Epifanov

Physics of the Solid State, Vol. 43, No. 5, 2001, pp. 859–864. Translated from Fizika Tverdogo Tela, Vol. 43, No. 5, 2001, pp. 827–832.

DEFECTS, DISLOCATIONS, AND PHYSICS OF STRENGTH

A New Type of Magnetoplastic Effects in Linear Amorphous Polymers

Yu. I. Golovin and R. B. Morgunov

Tambov State University, Internatsional'naya ul. 33, Tambov, 392622 Russia

e-mail: golovin@tsu.tmb.ru

Received October 4, 2000

Abstract—A new type of magnetoplastic effects in polymers is revealed. This effect cannot be explained by the reorientation of macromolecular units that possess a magnetic susceptibility anisotropy. It is shown that the joint action of magnetic and electric fields and the rotational mobility of side groups in macromolecules are factors of crucial importance in changing the plasticity of polymers in pulsed magnetic fields. © *2001 MAIK "Nauka/Interperiodica".*

1. INTRODUCTION

It is generally believed that magnetoplastic and other effects associated with the influence of magnetic fields on the macroproperties of polymers are reduced to the activation of reorientation of the macromolecular segments possessing anisotropy of the magnetic susceptibility [1–5]. However, a number of experimental results obtained in recent works [6, 7] showed that there are factors other than the orientational effects (this concept, even if reliably confirmed, is far from universal) which can also account for changes in the plasticity of polymers under the action of magnetic fields. It is reasonable to suppose that other unknown channels for changes in the molecular or supramolecular structure of polymers are realized in magnetic fields. Evidence for their existence is provided, for example, by the magnetoplastic effects observed in ionic and ionic–covalent crystals [8]. In these crystals, the magnetic field affects spin-dependent chemical reactions between structural defects [9, 10] and, thus, induces a considerable change in the plastic properties even in weak constant magnetic fields in the case when the energy transferred to a paramagnetic particle, $U_M \sim \mu_B B$, is substantially less than the mean energy of thermal fluctuations $U_T \sim kT$ (where μ_B is the Bohr magneton, B is the magnetic field induction, k is the Boltzmann constant, and T is the temperature). Another reason for the existence of different magnetoplastic effects in these materials is the fact that the effect of alternating magnetic fields on the plasticity of polymers is stronger than that of constant magnetic fields [11, 12]. The same feature is observed in many other solids with molecular [13], covalent [14], and metallic [15] interatomic bonds. In this respect, the aim of the present work was to investigate experimentally the regularities in the influence of pulsed magnetic and electric fields on the plasticity of polymers and to reveal the objects susceptible to magnetic field effects.

2. EXPERIMENTAL TECHNIQUE

The samples to be studied were linear amorphous polymers that differ from one another in their polarity, the magnetic susceptibility, and the sizes and mobility of their side groups [16]: a CO-95 commercial poly(methyl methacrylate) (PMMA) plasticized by dibutyl phthalate, H1-475K-KG2-HYOSUNG-BASF poly(styrene) (PS) obtained by milling of granules followed by pressing, and a C7058M sheet suspended poly(vinyl chloride) (PVC) prepared by powder pressing. This allowed us to provide the appropriate conditions for examination of the role played by each of the aforementioned factors in magnetoplastic effects.

Separate investigation into different channels of magnetic-field effects on plasticity is complicated by the simultaneous manifestation of reorientational effects in magnetically anisotropic segments of macromolecules. It should be noted that the reorientation of macromolecules in a magnetic field of ~0.4 T at room temperature in the polymers under consideration proceeds over a long period of time (~30 days) [4, 5]. For this reason, in order to separate and examine other processes sensitive to the magnetic field and capable of affecting the plasticity, we used short magnetic-field pulses with an amplitude of 2–30 T and a duration of 25–1300 μs, which, according to the estimates made in [6], was insufficient to achieve reorientation of the macromolecules. The pulsed magnetic field was induced using a capacitor bank. The capacitor bank discharged into a solenoid with a small number of turns, which made it possible to generate magnetic-field pulses having a shape close to a half-cycle of a sinusoid.

The macroproperties of polymers (including plasticity) substantially depend on the characteristic frequencies of intermolecular and intramolecular vibrations [17]. These frequencies vary over a wide range (from ~10^{15} to 10^5 Hz), which makes elucidation of the

role of the thermofluctuation motions of macromolecules in the magnetoplastic effect with the use of only one experimental technique difficult. Hence, the influence of high-frequency (10^{15}–10^{13} Hz) vibrations of macromolecules on the magnetoplastic effect was studied not only by testing the crystal plasticity but also with the use of a SPECORD spectrometer. This made it possible to compare the absorption spectra of film samples prior to and after their exposure to the magnetic field. The role of the intramolecular torsional and intermolecular vibrations with frequencies of 10^{13}–10^5 Hz was investigated by comparing the magnitudes of the magnetoplastic effect in samples exposed to a magnetic field at different temperatures in the range 77–490 K, which covered the critical temperatures of defreezing the corresponding degrees of freedom [17].

The polymer plasticity and its change after the magnetic-field pulse action were judged from the Vickers microhardness H. The microhardness was measured on a PMT-3 microhardness tester at an indenter load of 0.2 N prior to and after exposure of the samples to a magnetic field. Each experimental value was obtained by averaging over the results of 20–30 individual microhardness measurements. The magnitude of the magnetic-field effect on the plastic properties of polymers could be judged from the difference $\Delta H = H_B - H_0$, where H_B and H_0 are the microhardnesses after and before exposure to the magnetic field, respectively. Since the exposure of samples to the magnetic field and the indentation were separated in time in all experiments, the magnetic field could not affect movable parts of the PMT instrument and did not lead to artefacts. In all experiments, the indentation was performed at the same controlled temperature $T = 295 \pm 3$ K, which was below the glass transition temperatures T_g of all the polymers under investigation.

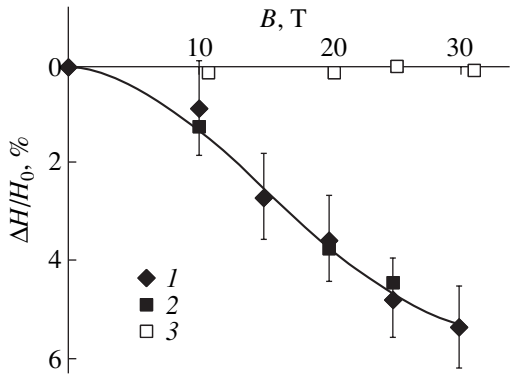

Fig. 1. Dependences of the microhardness difference $\Delta H = H_B - H_0$ (H_B and H_0 are the microhardnesses after and before exposure to the magnetic field, respectively) normalized to the initial microhardness H_0 for (*1*) PMMA, (*2*) PS, and (*3*) PVC samples. The pulse amplitude is 24 T, and the pulse duration is 80 μs.

3. RESULTS

It was found that exposure of PMMA and PS samples to a single magnetic-field pulse with an induction $B = 30$ T and a duration of 140 μs leads to a decreases in the microhardness by 5%. The microhardness monotonically decreases with the amplitude of the magnetic-field pulse at constant duration (Fig. 1). The microhardness of PVC samples after their exposure to a single magnetic pulse under the same conditions remains virtually unchanged.

With the time passed after exposure of PMMA and PS samples to the magnetic field, the microhardnesses regained their initial values (Fig. 2). By repeatedly switching on the magnetic pulse generator (after the recovery of the initial microhardnesses of PMMA and PS samples), the microhardness H could be reproducibly decreased to virtually the same value as in the first exposure of the samples to the magnetic field (Fig. 2). This implies that changes induced by the magnetic-field pulses in the samples are reversible; i.e., they are caused by the energy transfer from the magnetic field and the excitation of particular structural elements of polymers from an equilibrium state.

Thermoactivation analysis of the height of a potential barrier to relaxation of the polymeric structure excited in the magnetic field revealed that the time constant τ of the microhardness recovery decreased with an increase in the temperature T at which the samples were held after exposure to the magnetic field. The exponential temperature dependence of τ (see the inset in Fig. 3b) allowed us to evaluate the activation energy for the microhardness recovery after the action of the magnetic field for both polymers in which the magnetoplastic effect was observed: $U_{PMMA} \sim 0.25 \pm 0.06$ eV and $U_{PS} \sim 0.32 \pm 0.06$ eV.

In order to elucidate the mechanisms of the energy transfer to structural units of polymers and the role of magnetic-field pulse edges, we examined how the total time of exposure to the magnetic field affects the microhardness of the samples in the case when the exposure was accomplished by the repetition of identical pulses. It was found that an increase in the number N of pulses with the amplitude $B = 2$ T and the duration $t_p = 80$ μs up to $N = 50$ (so that the total time of exposure Σt_p to the magnetic field is equal to 4 ms) can result in a loss of strength of PMMA that noticeably exceeds the experimental error (Fig. 4). However, exposure of the sample to a constant magnetic field with $B = 2$ T for a time in the range $1 < t_p < 10^3$ s (which is considerably longer than the total duration of exposure to the pulsed magnetic field) does not lead to a change in H. Consequently, unlike the results obtained for PMMA in [1–5], in our experiments, the presence of the magnetic field alone did not ensure a change in the microhardness H. The necessary condition is a variation in the magnetic field with time. The most evident consequence of this variation is the generation of a vortex electric field. Its maximum strength E for a single magnetic-field pulse

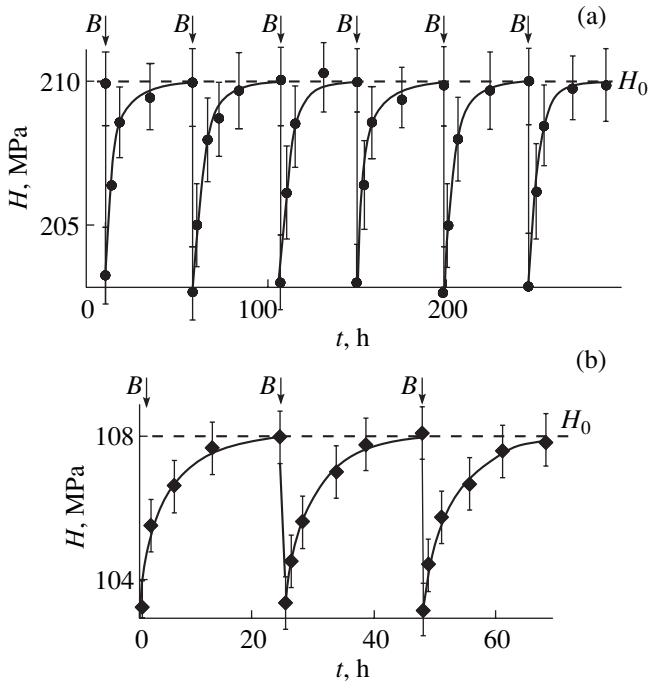

Fig. 2. Dependences of the microhardness on the current time t for (a) PMMA and (b) PS under periodic exposure of the samples to single pulses of a magnetic field (B = 24 T, t_p = 80 μs) at T = 293 K. Arrows indicate the instants of switching on the magnetic pulse generator. Dashed lines correspond to the microhardness H_0 of the samples not exposed to the magnetic field.

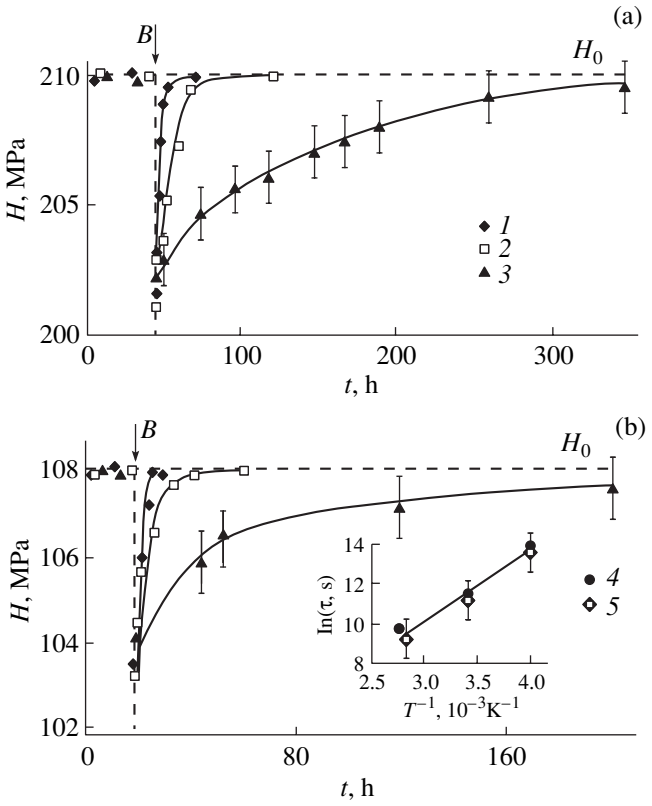

Fig. 3. Dependences of the microhardness H of (a) PMMA and (b) PS samples on the time t (indicated by the arrow) passed after their exposure to a single magnetic-field pulse (B = 24 T, t_p = 80 μs, T = 293 K). After the action of the magnetic-field pulse, the samples were held at temperatures of (*1*) 363, (*2*) 293, and (*3*) 253 K. The microhardness was measured at T = 293 K. The inset shows the dependences of the time constant τ of the microhardness recovery after exposure of the samples to a single magnetic-field pulse on the reciprocal of the temperature for (*4*) PMMA and (*5*) PS.

with $B \sim 10$ T and a duration of ~100 μs for a sample 10^{-2} m in size is estimated at ~10^3 V/m.

The role of the vortex electric field in the magnetoplastic effect was determined by comparing the results of two series of experiments. In the first series, the PMMA samples were exposed to a pulsed magnetic field with different frequencies of the fundamental harmonic $\nu_B = 1/t_p$ and the same pulse amplitude. In this case, we determined the threshold frequency $\nu_B^* \sim 3 \times 10^3$ Hz. At $\nu_B < \nu_B^*$; the magnetoplastic effect was not observed (Fig. 5, curve *1*). In the second series of experiments, the pulsed magnetic field was replaced by the joint action of a constant magnetic field ($B \sim 2$ T) and an alternating electric field with the frequency $\nu_E = 10^2$–4×10^4 Hz and the amplitude $E = 2 \times 10^4$ V/m. This treatment of the samples for 30 min also results in the loss of their strength, and, at $\nu_E < 3 \times 10^3$ Hz, the loss of strength of PMMA is not observed (Fig. 5, curve *2*). Note that the alternating electric field alone, i.e., when applied in the absence of a constant magnetic field for 30 min, does not lead to a change in the microhardness at any value of ν_E in the studied range (Fig. 5, curve *3*). It is worth noting that ν_E^* and ν_B^* virtually coincide and the mutual orientation of the vectors **B** and **E** in the

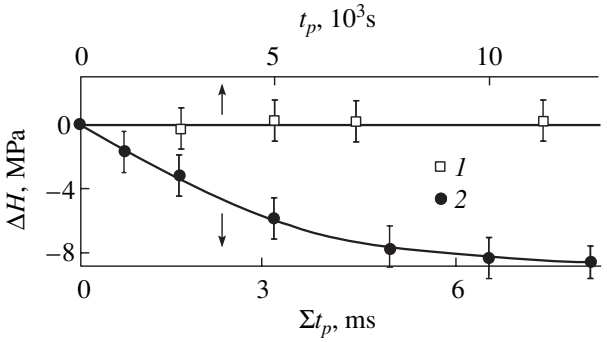

Fig. 4. Dependences of the microhardness change ΔH in a PMMA sample on (*1*) the duration of the exposure t_p to a constant magnetic field with B = 2 T and (*2*) the total time Σt_p of the sample exposure to magnetic-field pulses with pulse amplitude B = 2 T, t_p = 80 μs, and a 15-s interval between pulses.

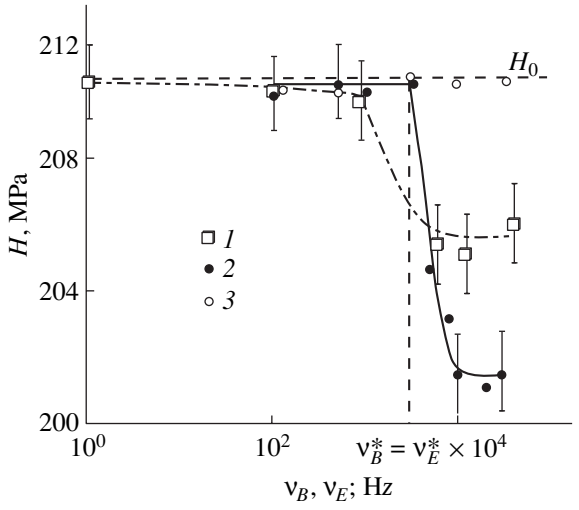

Fig. 5. Dependences of the microhardness of PMMA samples on (*1*) the frequency ν_B of the fundamental harmonic in the Fourier spectrum of a single magnetic-field pulse (B = 20 T), (*2*) the frequency ν_E of an alternating electric field (E = 20 kV/m) in the presence of a constant magnetic field ($B \sim 2$ T), and (*3*) the frequency of the electric field applied in the absence of a magnetic field.

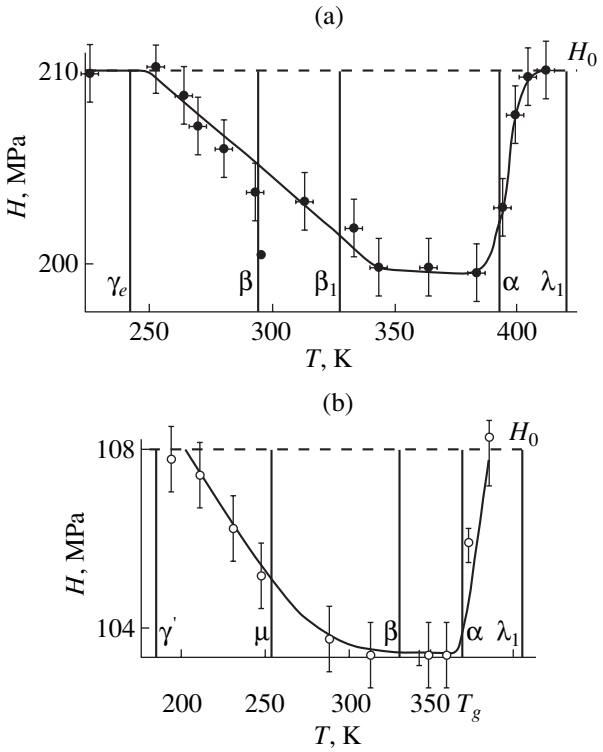

Fig. 6. Dependences of the microhardness of (a) PMMA and (b) PS samples on the temperature T of their exposure to magnetic-field pulses (B = 20 T, t_p = 80 μs) whose number is sufficient to reach saturation of the magnetoplastic effect. Dashed lines correspond to the microhardnesses H_0 of the samples not exposed to the magnetic field. Vertical lines indicate the temperatures of relaxation transitions (α, β, β_1, γ_e, and λ_1) in PMMA [17]. Indentation temperature was performed at T = 293 K.

joint action of magnetic and electric fields does not affect the loss of strength in polymers.

Analysis of the temperature dependences of the magnetoplastic effect demonstrates that a decrease in the microhardness ΔH of the samples upon exposure to a pulsed magnetic field is observed only in the specific range of temperatures at which the samples are treated in the magnetic field: $250 < T < 390$ K for PMMA and $230 < T < 370$ K for PS (Fig. 6). Outside these ranges, the magnetic-field pulse does not affect the microhardness of the polymers under investigation. No changes in the IR absorption spectra of the polymers in the vibrational frequency range 400–4000 cm^{-1} were found at any temperature of exposing the samples to the magnetic field.

The change in the microhardness of PMMA upon exposure to a single magnetic-field pulse depends not only on the temperature at which the samples are exposed to the magnetic field, but also on the uniaxial tensile strain ε of the sample before its treatment in the magnetic field (Fig. 7a). The sensitivity of the plastic properties to the magnetic-field pulse (the magnitude of ΔH) increases with an increase in ε. Since the samples were strained at a higher temperature close to the glass transition point, in a special series of experiments, we demonstrated that a short-duration heating of samples by itself does not affect the sensitivity of polymer plasticity to the magnetic-field pulse. Therefore, it is this plastic strain that brings about changes in the sensitivity of polymers to the magnetic field. An increase in the time interval between the strain and the magnetic-field pulse is accompanied by a gradual decrease in the strain-induced sensitivity of the plastic properties of polymers to the magnetic field (Fig. 7b).

4. DISCUSSION

The absence of changes in the IR spectra of polymers after exposure to a pulsed magnetic field suggests that the magnetoplastic effect under consideration is unrelated to stretching and bending intramolecular vibrations of the kinetic units of macromolecules. At the same time, the activation energies U_{PMMA} and U_{PS}, which were determined for the microhardness recovery after the action of the magnetic field pulse (Fig. 3), are in reasonable agreement with the activation energies available in the literature [17] for the γ relaxation transitions in PMMA and PS (Fig. 8a). The activation energies for other transitions (Fig. 8b), which were obtained from independent measurements [17], substantially differ from those found in our experiments. Furthermore, it is these critical temperatures of "defreezing" the γ transitions that bound from below the temperature range in which the magnetoplastic effect is observed (Fig. 6). Thus, the results obtained indicate that the high mobility of side groups [CH_3 methyl groups in PMMA and C_6H_5 phenyl groups in PS (Fig. 8b)] is the necessary condition for the sensitivity of the plastic proper-

ties of polymers to the magnetic field. This inference is also confirmed by the absence of the magnetoplastic effect in PVC (Fig. 1), in which the mobility of side groups is substantially less than that in PMMA and PS.

The plastic deformation of polymers also considerably affects the free volume and the mobility of the side groups in macromolecules. Therefore, the sensitivity of the magnetoplastic effect to the preliminary uniaxial tension of the samples can be explained by the increase in the free volume under deformation of the polymers and its decrease upon subsequent annealing (Fig. 7).

In our experiments, we established that the critical frequency of an alternating electric field applied simultaneously with a constant magnetic field is in good agreement with the frequency of the fundamental harmonic of the magnetic-field pulse (Fig. 5). This suggests that the vortex electric field plays an essential role in the magnetoplastic effect. Since the side groups of macromolecules in the studied polymers have dipole moments, it can be assumed that the role of the electric field consists in initiating their rotation. However, the alternating electric field alone in the absence of a constant magnetic field does not affect the plasticity of polymers. Therefore, the effect under investigation can be termed electromagnetoplastic. Note that the threshold duration ($\sim 3 \times 10^{-3}$ s) of the magnetic-field pulse affecting the sensitivity of polymers to the magnetic field coincides in the order of magnitude with the waiting time τ_0 for attempting to overcome the barrier, which is derived from the Arrhenius equation

$$\tau = \tau_0 \exp(U_1/kT).$$

Here, U is the activation energy which we obtained for PMMA from the thermoactivation analysis of the plasticity recovery after exposure to the magnetic field (Fig. 3) and τ is the recovery duration equal to $\sim 10^5$ s at $T = 293$ K. To put it differently, if the duration of the joint action of magnetic and vortex electric fields is shorter than the characteristic time of waiting for thermoactivated attempts of relaxation, the magnetic-field pulse efficiently affects the plasticity of polymers. Otherwise, when the exposure time is large compared to τ_0, the magnetoplastic effect is absent.

It should be noted that the energies transferred by the magnetic and electric (vortex electric field) components of a pulsed magnetic field ($B \approx 2$–30 T, $t_p \approx 10^{-4}$ s) to the units and side groups of macromolecules are equal to $U_M \cong \mu_B B \approx 10^{-4}$–$10^{-3}$ eV and $U_E \cong p_E B \approx 10^{-7}$ eV, respectively. These energies are considerably less than the activation energy for rotation of the side groups, $U \approx 0.3$ eV. However, with allowance made for the experimentally determined number N of magnetic-field pulses required to reach saturation of the magnetoplastic effect ($N \approx 3$ at $B = 20$ T, $N \approx 15$ at $B = 5$ T, and $N \approx 50$ at $B = 2$ T), the total transferred energy per side group becomes comparable to U. In the case when a constant magnetic field is used instead of a pulsed magnetic field and the vortex electric field is replaced by an external alternating electric field with the same strength, the saturation is reached after $\sim 10^7$ pulses of the electric field, which, in the presence of the mechanism for energy accumulation, is comparable to or even exceeds the activation energy U.

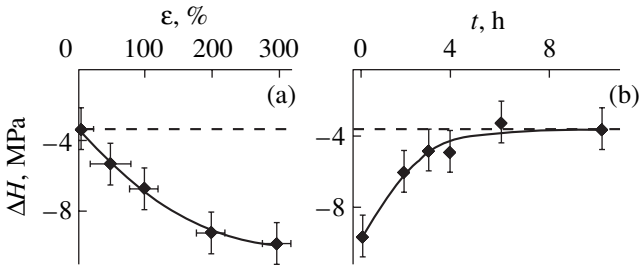

Fig. 7. Dependences of the loss of strength ΔH in PMMA samples after exposure to a pulsed magnetic field ($B = 24$ T, $t_p = 80$ μs) on (a) the preliminary strain ε and (b) the time passed after the extension of the sample at ε = 300% ($T = 413$ K). The strained sample was held at $T = 353$ K, and the microhardness was measured at $T = 293$ K.

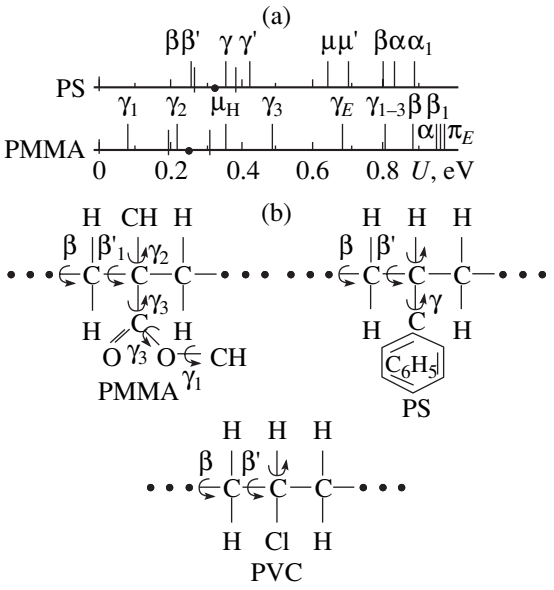

Fig. 8. (a) Activation energies for the recovery of polymer microhardness after exposure to a magnetic field (hatched regions) on the scale of activation energies for the known relaxation transitions [17]. Kinetic units responsible for the transitions: segments of macromolecules for α, polymer chain units for β, side groups for γ, absorbed water (hydrogen bonds) for μ_H, physical unit $-C_6H_5\cdots C_6H_5-$ for μ and μ', and physical sites of a molecular network for λ and π. (b) Structure of macromolecular chains and intramolecular motions in PMMA, PS, and PVC.

We made an attempt to measure the electron paramagnetic resonance from the change in the microhardness of PMMA. The experimental technique of these measurements was described in detail in [9, 10]. In these works, we revealed that the plasticity of ionic

crystals changes in microwave and constant magnetic (with a certain induction) crossed fields. In the present work, we found that the joint effect of microwave (with a frequency of 9.5 GHz) and constant magnetic fields on the plasticity of polymers is virtually identical to that of the microwave field in the absence of a constant magnetic field; i.e., unlike the results obtained in [9, 10], the excitation of electron paramagnetic resonance in paramagnetic particles of a polymer does not lead to a change in its plasticity. This fact, together with the above findings, which indicate the significant role of the side groups in the magnetoplastic effect, have demonstrated that the magnetoplastic effect should be treated on the atomic level rather than within the electron–spin approach, and, furthermore, it does not reduce to the magnetoplastic effects observed earlier.

ACKNOWLEDGMENTS

This work was supported by the Russian Foundation for Basic Research, project no. 00-02-16094.

REFERENCES

1. Yu. P. Rodin, Mekh. Kompoz. Mater., No. 3, 490 (1991).
2. V. E. Gul', S. M. Sadykh-zade, B. Yu. Trifel', *et al.*, Mekh. Polim., No. 4, 611 (1971).
3. V. A. Zhorin, L. L. Mukhina, and I. V. Razumovskaya, Vysokomol. Soedin., Ser. B **40** (7), 1213 (1998) [Polym. Science, Ser. B **40**, 233 (1998)].
4. N. N. Peschanskaya, V. Yu. Surovova, and P. N. Yakushev, Fiz. Tverd. Tela (St. Petersburg) **34** (7), 2111 (1992) [Sov. Phys. Solid State **34**, 1127 (1992)].
5. N. N. Peschanskaya and P. N. Yakushev, Fiz. Tverd. Tela (St. Petersburg) **39** (9), 1690 (1997) [Phys. Solid State **39**, 1509 (1997)].
6. Yu. I. Golovin, R. B. Morgunov, and S. Yu. Liksutin, Vysokomol. Soedin., Ser. B **40** (2), 373 (1998) [Polym. Science, Ser. B **40**, 63 (1998)].
7. Yu. I. Golovin, R. B. Morgunov, and S. Yu. Liksutin, Vysokomol. Soedin., Ser. A **42** (2), 277 (2000) [Polym. Science, Ser. A **42**, 189 (2000)].
8. V. I. Al'shits, E. V. Darinskaya, T. M. Perekalina, and A. A. Urusovskaya, Fiz. Tverd. Tela (Leningrad) **29** (2), 467 (1987) [Sov. Phys. Solid State **29**, 265 (1987)].
9. Yu. I. Golovin, R. B. Morgunov, V. E. Ivanov, and A. A. Dmitrievskiĭ, Zh. Éksp. Teor. Fiz. **117** (6), 1080 (2000) [JETP **90**, 939 (2000)].
10. Yu. I. Golovin and R. B. Morgunov, Zh. Éksp. Teor. Fiz. **115** (2), 605 (1999) [JETP **88**, 332 (1999)].
11. S. N. Lasarov, A. A. Homic, T. V. Ljashko, and V. V. Lapinsky, Bolg. Fiz. Zh. **15** (6), 600 (1988).
12. S. N. Lazarov, V. L. Velev, and N. P. Nikolov, Nauch. Tr. Plovdiv. Univ. Fiz. **24** (1), 75 (1986).
13. Yu. A. Osip'yan, Yu. I. Golovin, D. V. Lopatin, *et al.*, Pis'ma Zh. Éksp. Teor. Fiz. **69** (2), 110 (1999) [JETP Lett. **69**, 123 (1999)].
14. M. N. Levin and B. A. Zon, Zh. Éksp. Teor. Fiz. **111** (4), 1373 (1997) [JETP **84**, 760 (1997)].
15. O. I. Datsko and V. I. Alekseenko, Fiz. Tverd. Tela (St. Petersburg) **39** (7), 1234 (1997) [Phys. Solid State **39**, 1094 (1997)].
16. A. A. Tager, *Physical Chemistry of Polymers* (Khimiya, Moscow, 1978).
17. G. M. Bartenev and A. G. Barteneva, *Relaxation Properties of Polymers* (Khimiya, Moscow, 1992).

Translated by O. Borovik-Romanova

Physics of the Solid State, Vol. 43, No. 5, 2001, pp. 865–870. Translated from Fizika Tverdogo Tela, Vol. 43, No. 5, 2001, pp. 833–838.

DEFECTS, DISLOCATIONS, AND PHYSICS OF STRENGTH

Mechanical Behavior of Microcrystalline Aluminum–Lithium Alloy under Superplasticity Conditions

M. M. Myshlyaev*, M. A. Prokunin*, and V. V. Shpeizman**

** Baĭkov Institute of Metallurgy and Materials Science, Russian Academy of Sciences, Leninskiĭ pr. 49, Moscow, 117334 Russia*

*** Ioffe Physicotechnical Institute, Russian Academy of Sciences, Politekhnicheskaya ul. 26, St. Petersburg, 194021 Russia*

e-mail: shpeizm.v@pop.ioffe.rssi.ru

Received September 18, 2000; in final form, October 6, 2000

Abstract—Aluminum–lithium alloy 1420, which, after equal-channel angular pressing, has a grain size of about 3 μm, is shown to possess superplasticity in a temperature range of $T = 320$–395°C upon tension at a constant relative strain rate of 10^{-2}–10^{-3} s^{-1}. The axial deformation at fracture can exceed 1800%. The data processing at such large deformations should be carried out using true strains ε_t and stresses σ_t. In the flow curve, a short stage of hardening is followed by a long softening stage. They can be described by the relation $\dot{\varepsilon}_t \sim \sigma_t^n \exp(-U/kT)$ with a constant exponent $n \approx 2$ and activation energies $U \approx 1$ eV for the softening stage and $U \approx 1.4$ eV for the hardening stage. The deformation is supposed to be controlled by grain-boundary sliding at the stage of softening and by self-diffusion in the bulk of grains at the hardening stage. © *2001 MAIK "Nauka/Interperiodica".*

INTRODUCTION

In recent years, materials scientists, designers, and metals physicists paid much attention to aluminum–lithium alloys, since these alloys possess a unique combination of physicomechanical properties, such as enhanced elasticity modulus, small density, and relatively high strength and plasticity. The application of these alloys makes it possible to substantially reduce the weight of aerospace vehicles with all related advantages. Of the alloys of this class, one of the most promising and widely applied is the lightest (a density of 2.47 g/cm^3), corrosion-resistant, weldable alloy, 1420, which was designed in Russia [1–6]. This alloy finds application in various welded structures, reducing their weight by 20–25% and increasing their rigidity by up to 6%. The alloy is superplastic and is widely used in the production of articles of complex profile. The typical characteristics of superplasticity (SP) in its conventional state (with a grain size of about 50 μm) are as follows: deformation at fracture $\varepsilon = 350\%$ and strain-rate sensitivity coefficient (σ) $m = d\ln\sigma/d\ln\varepsilon = 0.45$ when being deformed at a rate $\dot{\varepsilon} = 5 \times 10^{-3}$ s^{-1} at 480°C [7, 8]. For the alloys with grain size $d = 6$–8 μm deformed under the same conditions, the SP characteristics were $\varepsilon = 800\%$ and $m = 0.55$ [9].

At present, intense works are being carried out that are directed at improving the properties of these alloys, e.g., at the expense of the formation of a nanocrystalline or a microcrystalline structure in them by virtue of severe plastic deformation. It is commonly accepted that one of the most promising methods of severe plastic deformation is equal-channel angular (ECA) pressing [10, 11]. By using this method, a grain structure with $d = 4.5$ μm was obtained in the 1420 alloy [12] and deformation exceeding 700% was attained at a temperature of 320°C and deformation rate close to 10^{-3} s^{-1}; later [13, 14], a structure with grain size $d = 1.2$ μm and deformation to 1180% at a temperature of 350°C and deformation rate close to 10^{-2} s^{-1} was obtained; in [15], superplasticity was obtained on samples with a grain size of ~3 μm at a strain rate of 1.7×10^{-2} s^{-1} in a temperature range of 340–395°C and deformation of 1878% was attained at 370°C.

With the above in mind, it seemed expedient to investigate the mechanical behavior under superplasticity conditions on samples of the same type (of the same series) as those used in [15]. Main attention will be given to establishing the dependence that describes the relation between the strain rate, stress, and temperature, and to determining the numerical values of the parameters that enter into this dependence.

1. EXPERIMENTAL

The experiments were performed on aluminum–lithium alloy 1420 (Al–5.5% Mg–2.2% Li–0.12% Zr). The samples for ECA pressing were cut from a hot-rolled plate with a recrystallized structure with a grain size of about 20 μm. These samples were quenched in water from 470°C and then subjected to tenfold ECA pressing in air at 370°C to obtain rods 20 mm in diam-

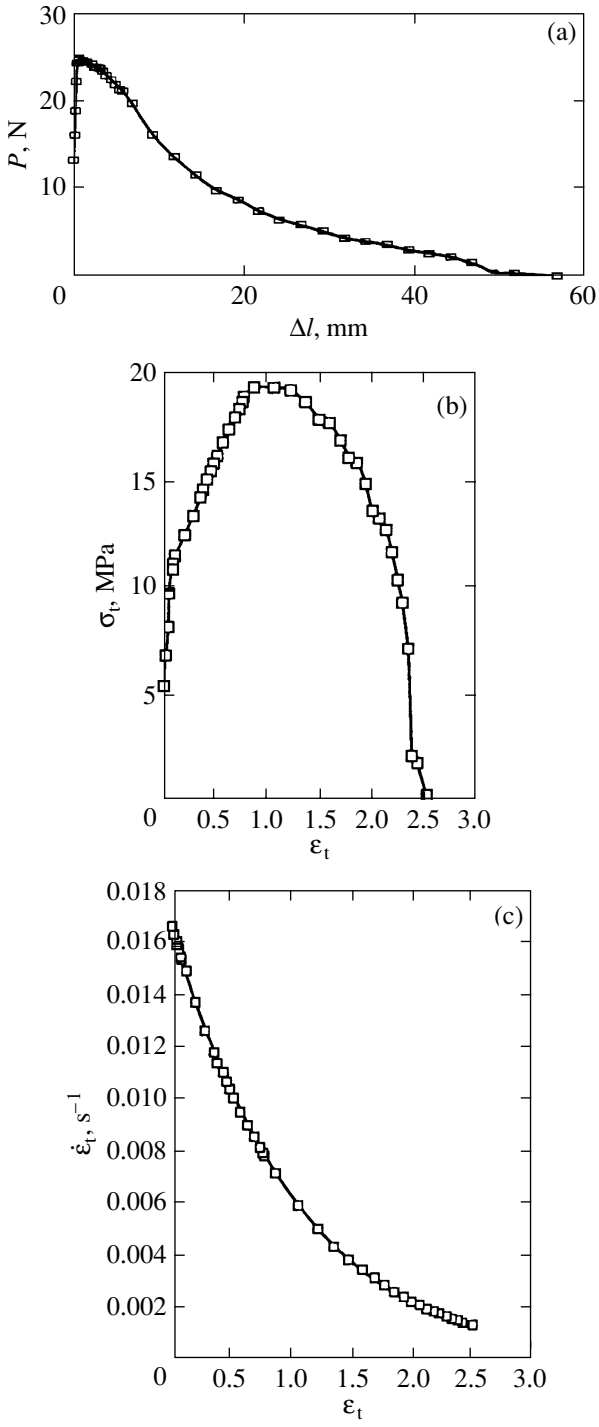

Fig. 1. Tensile diagram of the aluminum–lithium alloy 1420 plotted using various coordinates: (a) load–elongation; (b) true stress–true strain; and (c) true strain rate–true strain. The initial strain rate $\dot{\varepsilon} = 1.7 \times 10^{-2}$ s^{-1}, $T = 395$°C.

eter and 70–80 mm in length. The quenching and ECA pressing were carried out in the Ufa State Technical University of Aviation. The structural condition of the rods proved to be qualitatively analogous to that observed in the rods of the first batch in [15]. The structure consisted of grains with an average size of about 3 μm (with isolated coarser grains of 10–15 μm) with a pronounced substructure (subgrains, dislocation cells and tangles, isolated dislocations, precipitates of the Al_2LiMg phase, and particles of the δ' (Al_3Li) phase).

The ECA-pressed rods were used to prepare plane dumbbell samples for mechanical tests 0.85 mm thick with a gage portion 5 mm long. The surface layers with damages that were introduced during the sample preparation were removed. The front and side surfaces of the samples were carefully polished. The differences in both the thickness and the width along the gage portion of the samples did not exceed 0.01 mm. The symmetry axis of the sample directed along its long side was chosen so that it was parallel to the axis of the initial rod.

The samples were deformed on an Instron testing machine by uniaxial tension along their axes at a constant rate and temperature. The errors of measuring the load applied to the sample and the sample elongation were no more than 0.25 and 1%, respectively. The temperature was maintained during the tests to an accuracy of ±2.5 K.

The main characteristics that were used in the analysis of deformation were the true stress σ_t, the true strain ε_t, and the rate of true strain $\dot{\varepsilon}_t$. They were determined by the formulas

$$\sigma_t = P(l_0 + \Delta l)/S_0 l_0, \quad (1)$$

$$\varepsilon_t = \ln(l + \Delta l/l_0), \quad (2)$$

$$\dot{\varepsilon}_t = V/(l_0 + \Delta l). \quad (3)$$

Here, P is the load; S_0 and l_0 are the initial cross-sectional area and the length of the sample, respectively; Δl is the elongation; and V is the rate of the sample extension. The passage to true stresses, strains, and their rates from the conventional characteristics (σ, ε, and $\dot{\varepsilon}$) is primarily required because of the large deformation of the samples (their length increased by a factor of almost 20).[1]

2. RESULTS AND DISCUSSION

The primary diagram that is obtained upon tensile tests reflects the dependence of the load on the sample elongation at a given velocity of extension V (or strain rate $\dot{\varepsilon} = V/l_0$) at a temperature T. Such a diagram, obtained under superplasticity conditions, is shown in Fig. 1a. It is seen that the stage of elastic deformation is followed by a short stage of hardening, after which a stationary stage of a constant load follows, which often degenerates into a point, and then a long stage of softening is observed. The total elongation under optimum conditions was up to 90.4 mm, which corresponded to a relative deformation of 1808%. This diagram is a primary document, but it does not reflect the true depen-

[1] The true strain was also used in the analysis of superplasticity of metals in [16].

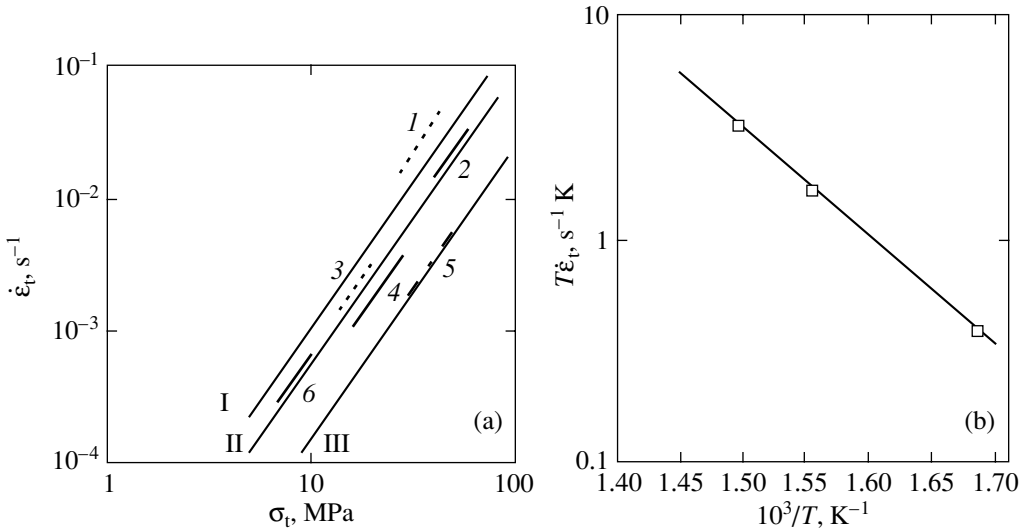

Fig. 2. Variation of the true strain rate of the 1420 alloy in the region of softening as functions of (a) true stress and (b) reciprocal temperature (the coordinates used correspond to Eq. (4)): (a) (*1*), (*2*) $\dot{\varepsilon} = 1.7 \times 10^{-1}$; (*3*)–(*5*) 1.7×10^{-2}; and (*6*) 1.7×10^{-3} s^{-1}. (*1*), (*3*) $T = 395$; (*2*), (*4*), (*6*) 370; and (*5*) 320°C. Roman numerals correspond to averaged straight lines for various temperatures: (I) 395, (II) 370, and (III) 320°C; $n = 2.23$. (b) $\sigma_t = 20$ MPa, $U = 0.98$ eV.

dence of deformation on the stresses. Therefore, we also plotted a diagram that reflected the relation between the true stress and true strain in the approximation of a uniform deformation along the sample (Fig. 1b). This diagram also exhibits three stages of plastic deformation. The first stage, which follows the region of elasticity, is a very long (in contrast to the diagram constructed in conventional coordinates) stage of strain hardening. The second (stationary) stage is very short but nevertheless much more clearly pronounced than that in Fig. 1a. This stage is characterized by a constant σ_t. The third stage is the stage of a monotonic decrease in σ_t with increasing ε_t, which extends through about half the diagram.

In order to determine what the true strain rates are at which deformation occurs at these stages, we plotted the dependence of $\dot{\varepsilon}_t$ on ε_t under the same test conditions (Fig. 1c). This diagram exhibits a monotonic decrease in the strain rate with increasing deformation. It follows from the comparison of data shown in Figs. 1b and 1c that the first and second stages correspond to strain rates of about 10^{-2} and 10^{-3} s^{-1}, respectively. The first value is characteristic of a superplastic deformation (SPD) due to intragranular slip [17–20]. The second value is typical of the SPD related to grain-boundary sliding [9, 21–23].

An analysis of the whole body of experimental data with allowance for literature data shows that the relation between $\dot{\varepsilon}_t$, σ_t, and T can most adequately be described by the well-known equation

$$\dot{\varepsilon}_t = \dot{\varepsilon}_{t0}\exp(-U/kT) = A(\sigma/\sigma_0)^n T^{-1}\exp(-U/kT), \quad (4)$$

where $n \approx 2$ for the case of SPD, U is the activation energy for SPD, k is the Boltzmann constant, A is a constant, and σ_0 is a parameter that is introduced from the dimensionality considerations ($\sigma_0 = 1$ MPa).

The estimates of n and U from our experiments were performed using standard techniques. Thus, in order to estimate n, we plotted dependences of $\dot{\varepsilon}_t$ on σ_t at various temperatures in the superplasticity region. The dependences obtained for the third stage are depicted in Fig. 2a. The thick solid and dashed lines correspond to experimental data. It is seen that, to a sufficiently good accuracy, averaged straight lines whose slope is $n = 2.23 \pm 0.10$ can be drawn for all temperatures. This value of n is in very good agreement with the magnitude of $n = 2$ in Eq. (4). The experimental value of the activation energy for plastic deformation at the third stage was determined in accordance with Eq. (4) from the slope of the dependence shown in Fig. 2b. The value obtained was $U = 0.98$ eV. Here, we took into account that the temperature enters into Eq. (4) not only in the exponent, but also in the denominator of the preexponential factor. Without allowance for this circumstance, we obtained $U = 0.94$ eV. The difference is not very significant. With the known parameters n and U, we can determine that $A = 1.6 \times 10^6$ K/s. This value of the activation energy for SPD is in agreement with the energy of self-diffusion along grain boundaries $Q_{sb} = W + R_{sb} = 0.99$ eV, where $W = 0.8$ eV [24] is the energy of vacancy formation and $R_{sb} = 0.19$ eV [25] is the energy of vacancy migration along grain boundaries or along dislocations (pipe diffusion).

The above discussion refers to the third stage. Now, we turn to the first stage. In order to use Eq. (4) for such an analysis, we should take samplings from the data

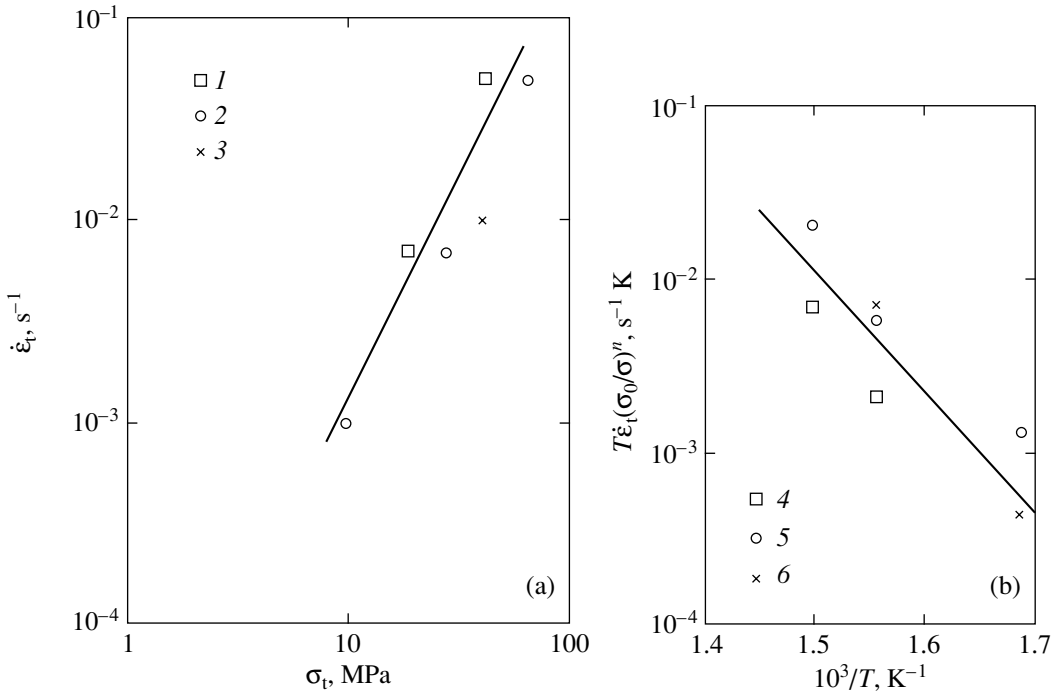

Fig. 3. Same as in Fig. 2 but for the region of hardening: (a) $\varepsilon_t = 1$: (*1*) $T = 395$, (*2*) 370, and (*3*) 320°C, $n = 2.23$; (b) $\varepsilon_t = 0.5$: (*4*) $\dot{\varepsilon} = 1.7 \times 10^{-1}$, (*5*) 1.7×10^{-2}, and (*6*) 1.7×10^{-3} s^{-1}, $U = 1.4$ eV.

array $\{\dot{\varepsilon}_t, \sigma_t, T\}$ that can be considered to have the same structure. In the first approximation, we may take points in the diagram with the same magnitude of deformation ε_t.

Using this procedure, we chose several sets $\{\dot{\varepsilon}_t, \sigma_t, T\}$ for $\varepsilon_t = 0.5$ and 1. As an example, Fig. 3a displays the $\dot{\varepsilon}_t(\sigma_t)$ dependence for $\varepsilon_t = 1$, which demonstrates the validity of the relation $\dot{\varepsilon}_t \sim \sigma_t^n$, where $n = 2.23$. The data for $\varepsilon_t = 0.5$ are analogous. Figure 3b displays the $\ln\dot{\varepsilon}_t - T^{-1}$ dependence at $\sigma_t = \text{const}$ and various extension rates in the modified coordinates for $\varepsilon_t = 0.5$. The activation energy obtained is $U = 1.4$ eV. It agrees with the energy of self-diffusion in the grain bulk (1.4–1.5 eV [24, 26–29]). The data for $\varepsilon_t = 1$ are analogous. An analysis of the data shown in Fig. 3 shows that the preexponential term is $\dot{\varepsilon}_{t0} = 5 \times 10^{10}$ s^{-1}.

It seems natural to relate the deformation at the first stage, at the stage of hardening, and the hardening itself with the motion and interaction of dislocations. Then, the parameter $\dot{\varepsilon}_{t0}$ should be written in the form

$$\dot{\varepsilon}_{t0} = \rho b \lambda \nu, \tag{5}$$

where ρ is the density of mobile dislocations, b is the Burgers vector, λ is the dislocation free path after it overcomes a barrier, and ν is the frequency of attacking a barrier. Let us estimate the lower boundary for λ. To this end, we find the maximum density of dislocation from the formula

$$\sigma = Gb\sqrt{\rho}, \tag{6}$$

where G is the shear modulus, by taking the maximum value of $\sigma = 20$ MPa corresponding to the end of the stage under consideration (Fig. 1b). We take into account that the frequency of the attacks cannot exceed the Debye frequency; then, using the experimentally found value of $\dot{\varepsilon}_{t0}$ and assuming that $b = 3 \times 10^{-8}$ cm [23] and $G = 28.5$ GPa [30], we obtain that the dislocation free path should satisfy the condition $\lambda \geq 3 \times 10^{-4}$ cm, which corresponds to the average grain size. Note that $\lambda \leq b$ for all known mechanisms of dislocation motion.

On the whole, it follows from the above that the SPD at the first stage is due to the cooperative action of all structural elements, including grain-boundary sliding, with the intragranular deformation by dislocation slip being dominant. It seems reasonable that the SPD is realized by processes that are similar to those responsible for creep of metals at moderate temperatures [20, 31–33] and superplasticity of aluminum upon torsion [17–20] under conditions of dynamic *in situ* recrystallization (or dynamic recrystallization on the subgrain level).

The obtained different values of the activation energies corresponding to the first and third stages indicate the occurrence of plastic deformation at these stages by

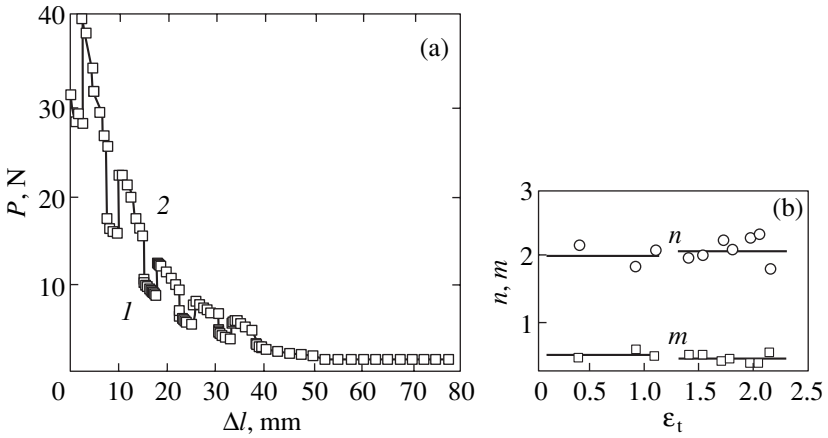

Fig. 4. (a) Load–elongation diagram of the 1420 alloy at $T = 370°C$ and changes in the strain rate from 0.5 (point *1*) to 1.0 cm/min (point *2*) and vice versa. (b) Magnitudes of the parameters n and m calculated from the data presented in Fig. 4a.

different mechanisms. Then, naturally, the second stage is a transition stage from one to another mechanism and it makes no sense to determine the parameters of Eq. (4) for this stage.

In order to increase the reliability of the results obtained, we performed experiments in which the magnitude of n was determined by changing the extension rate from V_1 to V_2 or from V_2 to V_1 and measuring the load P_1 at V_1 and P_2 at V_2. Note that these experiments also make it possible to check the validity of the above analysis of extension diagrams and of the parameters of Eq. (4).

The value of n was found from the known formula

$$n = m^{-1} = [\ln(P_2/P_1)/\ln(V_2/V_1)]^{-1}, \qquad (7)$$

where m is the strain-rate sensitivity of the flow stress.

Figure 4a demonstrates a primary diagram $P(\Delta l)$ for the extension velocities $V_1 = 0.5$ and $V_2 = 1.0$ cm/min under the conditions that are optimum for SPD. The results of determining the parameters n and m are shown in Fig. 4b. It is seen that their values for the first and third stages are virtually coincident and are 2.05 ± 0.05 and 0.49 ± 0.01, respectively. They also agree well with the values of n obtained for these stages in the above analysis.

The obtained values of the strain at fracture and the parameters m and n in Eq. (4) are commonly accepted as corresponding to SPD.

CONCLUSIONS

Thus, in this work, we established the multistage nature of superplastic deformation (SPD) and determined dependences of the true strain rate on the temperature and stress for various stages of strain hardening and softening. The conventional deformations of the alloy were shown to reach 1800%; for both stages (hardening and softening), the values of the strain-rate sensitivities are $n \approx 2$ and $m \approx 0.5$, which actually corresponds to SPD.

The deformation at the stage of hardening occurs at a rate $\dot{\varepsilon}_t \approx 10^{-2}$ s^{-1} and is controlled by self-diffusion in the bulk of grains, which is characteristic of SPD by the mechanism of intragranular dislocation slip. This mechanism corresponds to so-called *in situ* dynamic recrystallization (or dynamic recrystallization at the level of subgrains).

At the stage of softening, the deformation occurs at a rate $\dot{\varepsilon}_t \approx 10^{-3}$ s^{-1} and is controlled by self-diffusion along grain boundaries, which is typical of the SPD in fine-grain materials and is due to grain-boundary sliding.

ACKNOWLEDGMENTS

This work was supported in part by the Russian Foundation for Basic Research, project no. 00-01-00482; by the Scientific Council of MNTP on the Physics of Solid-State Nanostructures, project no. 97-3006; and by INTAS, project no. 1997-1243.

REFERENCES

1. I. N. Fridlyander, *Aluminum Wrought Structural Alloys* (Metallurgiya, Moscow, 1979).
2. I. N. Fridlyander and V. S. Sandler, in *Metal Science of Aluminum Alloys* (Nauka, Moscow, 1985), p. 40.
3. I. N. Fridlyander, Metalloved. Term. Obrab. Met. **4,** 2 (1990).
4. I. N. Fridlyander, Alum.-Lithium Alloys **3**, 1359 (1989).
5. I. N. Fridlyander, V. S. Sandler, and Z. N. Archakova, in *Aluminum Alloys. Industrial Aluminum Alloys* (Metallurgiya, Moscow, 1984), p. 207.
6. *Registration Record of International Alloy Designation and Chemical Composition Limits for Wrought Aluminium and Wrought Aluminium Alloys* (The Aluminium Association, 1985).

7. I. N. Fridlyander, N. I. Kolobnev, L. V. Khokhlatova, and E. Yu. Semyonova, Aluminium **5** (11), 21 (1990).
8. I. Ya. Novikov, V. K. Portnoĭ, I. L. Konstantinov, and N. I. Kolobnev, in *Metal Science of Aluminum Alloys* (Nauka, Moscow, 1985), p. 84.
9. M. Kh. Rabinovich, O. A. Kaĭbyshev, and V. G. Trifonov, Metalloved. Term. Obrab. Met., No. 9, 58 (1981).
10. V. M. Segal, V. I. Reznikov, A. E. Drobyshevskiy, and V. I. Kopylov, Russ. Metall. **1**, 99 (1981).
11. V. M. Segal, Mater. Sci. Eng., A **197**, 157 (1995).
12. M. V. Markushev, C. C. Bampton, M. Yu. Murashkin, and D. A. Hardwick, Mater. Sci. Eng., A **234**–**236**, 927 (1997).
13. P. B. Berbon, N. K. Tsenev, R. Z. Valiev, *et al.*, in *Proceedings of a TMS Meeting on Superplasticity and Superplastic Forming, San Antonio, 1998*, Ed. by A. K. Ghosh and T. R. Bieler (The Metallurgical Society, Warrendale, Pa., 1998), p. 127.
14. P. B. Berbon, M. Furukawa, Z. Horita, *et al.*, in *Proceedings of the 2nd Symposium on Hot Deformation of Aluminum Alloys II, Rosemont, 1998*, Ed. by T. R. Bieler, L. A. Lalli, and S. R. MacEwen (The Minerals, Metals, and Materials Society, Warrendale, Pa., 1998), p. 111.
15. M. M. Myshlyaev, L. D. Grigor'eva, and M. A. Prokunin, in *Proceedings of the XVIII Russia Conference on Electron Microscopy* (IPTM, Ross. Akad. Nauk, Chernogolovka, 2000), p. 178.
16. I. E. Kurov, V. A. Stepanov, and V. V. Shpeĭzman, *Physics of Metals and Metal Science* (LPI, Leningrad, 1969), No. 305, p. 71.
17. V. A. Likhachev, M. M. Myshlyaev, and O. N. Sen'kov, *Superplastic Behavior of Aluminum in Torsion* (Inst. Fiziki Tverdogo Tela, Akad. Nauk SSSR, Chernogolovka, 1981), p. 1.
18. V. A. Likhachev, M. M. Myshlyaev, and O. N. Sen'kov, *Problems of Mechanics of Deformable Solids* (Lening. Gos. Univ., Leningrad, 1982), No. 14, p. 179.
19. V. A. Likhachev, M. M. Myshlyaev, and O. N. Sen'kov, *Laws of the Superplastic Behavior of Aluminum in Torsion* (Lawrence Livermore National Laboratory, Livermore, 1987), p. 1.
20. M. M. Myshlyaev, Author's Abstracts of Doctoral Dissertation (Chernogolovka, 1981).
21. M. W. Grabski, *Structural Superplasticity of Metals* (Slask, Katowice, 1973; Metallurgiya, Moscow, 1975).
22. O. A. Kaĭbyshev, *Plasticity and Superplasticity of Metals* (Metallurgiya, Moscow, 1975).
23. O. A. Kaĭbyshev, *Superplasticity of Industrial Alloys* (Metallurgiya, Moscow, 1984).
24. J. Friedel, *Dislocations* (Pergamon, Oxford, 1964; Mir, Moscow, 1967).
25. J. P. Stark, *Solid State Diffusion* (Wiley, New York, 1976; Énergiya, Moscow, 1980).
26. P. M. Brick and A. Phillips, Trans. Metall. Soc. AIME **124**, 331 (1937).
27. A. H. Beerwald, Z. Elektrochem. Angew. Phys. Chem. **45**, 789 (1939).
28. J. E. Dorn, *Creep and Recovery* (American Society for Metals, Cleveland, 1957; Metallurgizdat, Moscow, 1961), p. 255.
29. G. B. Gibbs, Mem. Sci. Rev. Metall. **62**, 841 (1965).
30. I. N. Fridlyander, K. V. Chuistov, A. L. Berezina, and N. I. Kolobnev, *Aluminum–Lithium Alloys. Structure and Properties* (Naukova Dumka, Kiev, 1992).
31. M. M. Myshlyaev, *Creep and Dislocation Structure of Crystals at Moderate Temperatures* (Inst. Khim. Fiz., Akad. Nauk SSSR, Chernogolovka, 1977).
32. M. M. Myshlyaev, Annu. Rev. Mater. Sci. **11**, 31 (1981).
33. M. M. Myshlyaev, Cryst. Res. Technol. **14** (10), 1185 (1979).

Translated by S. Gorin

Physics of the Solid State, Vol. 43, No. 5, 2001, pp. 871–877. Translated from Fizika Tverdogo Tela, Vol. 43, No. 5, 2001, pp. 839–845.

DEFECTS, DISLOCATIONS, AND PHYSICS OF STRENGTH

Anomalies in the Temperature Dependences of the Bulk and Shear Strength of Aluminum Single Crystals in the Submicrosecond Range

G. I. Kanel* and S. V. Razorenov**

**Institute of Thermal Physics of Extremal States, Russian Academy of Sciences, Moscow, 127412 Russia*
***Institute of Chemical Physics in Chernogolovka, Russian Academy of Sciences, Chernogolovka, Moscow oblast, 142432 Russia*

Received July 18, 2000; in final form, October 24, 2000

Abstract—The results of measurements of the dynamic yield stress and the ultimate strength of aluminum single crystals in the temperature range from 15 to 650°C, which is only 10°C lower than the melting point, are presented. The measurements are made on samples under the action of plane shock waves with a pressure up to 5 GPa behind the front and of a duration of $\sim 2 \times 10^{-7}$ s. It is found that the dynamic yield stress anomalously increases, attaining, in the vicinity of the melting point, a value four times as high as that measured at room temperature. The dynamic strength of the single crystals in this temperature range decreases approximately by 40%, a high strength being preserved in the state in which melting during extension is expected. *© 2001 MAIK "Nauka/Interperiodica".*

INTRODUCTION

The elastoplastic properties and strength of materials in the submicrosecond range of the duration of an action at strain rates exceeding 10^4 s^{-1} are investigated by studying the compression and dilatation waves generated in a sample by a high-velocity impact, explosion, or by a pulse from a high-intensity laser or corpuscular radiation [1, 2]. The measurements are based on the fact that the wave structure and the dynamics of wave interactions are determined, apart from the thermodynamic equation of state for the substance, by the processes of elastoplastic deformation and fracture in the material.

Information on the effect of temperature on the strength properties of metals under shock-wave loading is scarce. In experiments with iron [3], it was found that the dynamic yield stress is independent of temperature in the range from 76 to 573 K, while the quasi-static yield stress in this temperature range decreases by a factor of 2.5. A similar result was obtained for bismuth [4] and zinc single crystals [5] in the range from room temperature to 0.96 of the absolute melting point (T_m). Experiments with polycrystalline aluminum and magnesium [6] even demonstrated a slight increase in the dynamic yield stress near the melting point.

Shock-wave measurements also indicate the athermal nature of the strength of metals. It was found [6] that the rupture strength of polycrystalline aluminum and magnesium varies insignificantly upon change from room temperature to a value amounting to 85–90% of T_m and rapidly decreases to zero upon further heating. In the case of zinc single crystals [5], the athermal nature of the dynamic strength is preserved up to $\sim 0.95T_m$, after which a decrease in strength is also observed.

The athermal nature of the dynamic yield stress and ultimate strength can be explained by the mechanism of dislocation movement under high-rate deformation [7]. It is well known that under low-rate deformation conditions, dislocations overcome obstacles because of the combined action of the applied stress and thermal fluctuations. For a high-rate deformation, higher stresses are required. For a strain rate exceeding $\sim 10^4$ s^{-1}, the acting stresses are high enough for the obstacles to be overcome by dislocations in the absence of an additional contribution to the stresses from thermal fluctuations.

The experiments discussed by us here were aimed at studying the main patterns of high-rate athermal deformations over a wide temperature range and at determining the strength parameters of solids in states close to melting. In this respect, the experiments with single crystals, which provide data on the elementary mechanisms and dynamics of deformation and fracture (they are not complicated by the effect of grain boundaries, impurities, and other structural inhomogeneities), are most informative.

1. MATERIAL AND EXPERIMENTAL TECHNIQUES

The experiments were made on aluminum single crystals of 99.999% purity, which were grown by directional crystallization from a melt in molds made of pure graphite [8]. Plane 10×15-mm single crystals about 3 mm thick were oriented during their growth so that

the normal to their surface coincided with the [100] direction. The sample surface was subjected to polishing followed by electrochemical etching to remove surface defects.

Plane shock waves were created in the samples by the impact of an aluminum plate 0.4 mm thick at a velocity of 600 to 700 m/s, which corresponds to an impact compression pressure in the range from 4 to 5 GPa. The explosion devices used for throwing percussion plates are described in detail in [2]. For measurements at high temperatures of the samples, resistive heaters were used, which were fixed at the back surface of the sample in the same way as described in [5, 6]. The time of sample heating by a 1-kW resistive heater to a preset temperature did not exceed 10 min. The temperature was permanently monitored to within ±5°C by a Chromel–Alumel thermocouple fixed at the back surface of the sample in the vicinity of the point at which the shock wave process was recorded. The measurements were made in the temperature range from 15 to 650°C, which is only 10°C lower than the melting point for aluminum.

In our experiments, we measured the time variation of the velocity of the free back surface of the samples during its loading by the arriving shock-wave pulse. The measurements were made using the VISAR laser-based Doppler interferometric velocity meter [9]. Interference beats were recorded by a digital oscillograph with a recorded signal numbering frequency of 0.5 GHz, which corresponds to 2-ns time intervals between points on the oscillogram. The frequency characteristics of the apparatus also ensured the recording of signals with a buildup time at the 2-ns level.

2. RESULTS OF MEASUREMENTS

Figure 1 shows typical velocity profile $W(t)$ for the free surface at normal and elevated temperatures. A shock wave loses its stability due to a change in the material compressibility with the onset of plastic deformation and splits into an elastic precursor and a plastic compression wave. The elastic precursor propagates at a velocity slightly higher than the longitudinal velocity c_l of sound, while the velocity of the plastic compression wave $D \le c_b$ corresponds to the bulk compressibility of the material and is determined by the wave intensity [1]. Here, c_b is the "bulk" velocity of sound calculated from the bulk elastic modulus K. The amplitude of the precursor corresponds to the dynamic limit of elasticity for uniaxial deformation. The width of the steady-state compression wave is determined by the ductility or the stress relaxation time. For the ratio of the thicknesses of the sample and the striker used in our experiments, the dilatation wave front overtook the shock wave by the instant of its emergence at the surface; as a result, the measured wave profiles do not exhibit regions of parameter constancy behind the compression wave front.

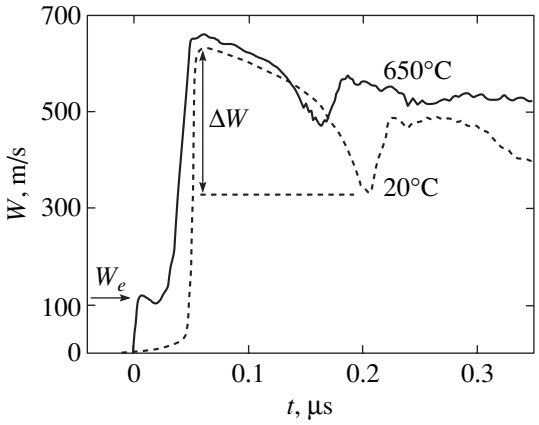

Fig. 1. Free-surface velocity profiles for monocrystalline aluminum samples under shock-wave loading. The experimental temperature is indicated on the curves. The sample thickness measured at the standard temperature was 2.87 nm.

After a compression wave emerges at the free sample surface, a reflected dilatation wave is generated in the sample, creating in it a tensile stress as a result of the interaction with the relief wave of the initial compression pulse. The maximum value of the tensile stress increases as the reflected wave penetrates into the bulk of the sample and attains a value sufficient for rapid cleavage fracture at a certain distance from the surface. The fracture generates in the stretched material a compression wave which emerges at the surface in the form of a so-called cleavage pulse and increases its velocity again. Subsequent velocity oscillations are caused by the reverberation of the wave in the split-off plate. The decrease ΔW in the velocity of the surface from the maximum value to its value in front of the cleavage pulse is proportional to the breaking stress (the so-called cleavage strength of the material), while the period of the oscillations of the surface velocity is proportional to the thickness of the split-off layer. The rate of damping of the reverberation of the waves in the cleavage plate is determined, among other things, by the dispersion of waves on the fracture surface and is an indicator of the degree of localization of the fracture.

The profiles shown in Fig. 1 readily show that the amplitude of the elastic precursor strongly increases with temperature; i.e., the dynamic yield stress of the material becomes higher. The build-up time for the parameters at the front of the elastic precursor does not exceed 2 ns. The decrease in the time interval between the elastic and plastic waves is a consequence of the decrease in the shear modulus upon heating. The decrease in the parameters behind the elastic precursor front is usually associated with stress relaxation [10]. The parameter build-up time in the plastic shock wave (from 0.1 to 0.9 of its amplitude) increases from 4–6 ns at room temperature to 12–16 ns in the vicinity of the melting point, which corresponds to strain rates of $\sim(3\text{–}7) \times 10^6\ s^{-1}$.

The resistance to cleavage fracture decreases slightly upon heating, remaining high up to 650°C. The large steepness of the cleavage pulse front indicates a high rate of fracture evolution in the entire temperature range. The average velocity of the surface remains virtually unchanged after the passage of the first cleavage pulse. It can therefore be concluded that the mechanical coupling between the split-off plate and the remaining part of the sample almost vanishes ~100 ns or less after the beginning of fracture. A comparison of the first and next periods of the surface velocity oscillation indicates a possible delay of fracture by 5–10 ns in the entire temperature range. The free surface velocity profiles obtained in experiments at elevated temperatures display more rapid damping of oscillations after cleavage. In all probability, the discontinuities formed at low temperatures are localized in a narrower layer and the roughness of the fracture surface is smaller than at high temperatures.

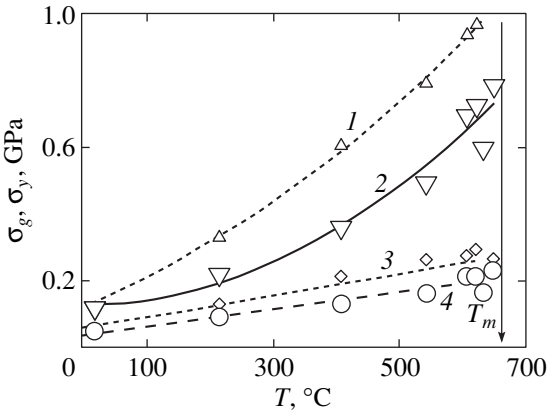

Fig. 2. The results of measurements of the dynamic limit of elasticity under the conditions of uniaxial deformation (σ_g) and uniaxially stressed states (σ_y) as functions of temperature (T_m is the melting point). Points on curves *1* and *3* correspond to the values of σ_g and σ_y, respectively, corresponding to the peak at the elastic precursor front, and points on curves *2* and *4* mark the values of σ_g and σ_y, respectively, corresponding to the minimum behind the front.

3. PROCESSING OF EXPERIMENTAL RESULTS

The calculations were made taking into account the temperature dependences of the elastic coefficients of monocrystalline aluminum reported in [11]. The nonlinear compressibility of the material was calculated using the impact adiabat in the form $D = c_0 + bu$ [1], where D is the velocity of the shock wave, c_0 is a constant equal to the bulk velocity of sound under zero pressure, u is the mass velocity jump in the shock wave, and b is a constant characterizing the nonlinearity of the material compressibility. We used the values of c_0 calculated from isentropic bulk elastic moduli as the functions of temperatures given in [11]; the value of constant b was assumed to be equal to 1.34 irrespective of temperature.

The longitudinal stress σ_g at the elastic precursor front, which is equal to the dynamic limit of elasticity under uniaxial deformation, is calculated from the measured jump in the surface velocity W_e at the corresponding instant on the basis of the relation [1]

$$\sigma_g = \rho_0 D_l W_e/2, \quad (1)$$

where ρ_0 is the density of the material and D_l is the velocity of the elastic shock wave in it. The quantity σ_g is connected with the yield stress σ_y for the standard conditions of the uniaxial stressed state through the relation [1]

$$\sigma_g = (1-\nu)\sigma_y/(1-2\nu), \quad (2)$$

where ν is the Poisson ratio. For small-amplitude elastic waves, the calculation in the acoustic approximation with $D_l = c_l$ gives a sufficiently high degree of accuracy. However, in actual practice, the velocity of a finite-amplitude elastic shock wave front is higher than the longitudinal velocity of sound. Since the experimentally determined amplitudes of precursors are quite large, their velocity was calculated as follows. For moderate pressures of impact compression, the velocity of the shock wave front is equal, to a high degree of accuracy, to the average velocity of perturbations ahead of (c_i) and behind (c_s) the shock front [2]:

$$D = (c_i + c_s\rho/\rho_0)/2.$$

In this approximation, the values of c_b (for a given compression ratio and taking into account the constancy of the Poisson ratio c_l behind the precursor front) were calculated from the measured surface velocity W_e at the front and then the velocity D_l of the elastic precursor was determined. The precursor velocity determined in this way exceeds the longitudinal velocity of sound under zero pressure by 1.5%.

The results of the measurements of the dynamic limit of elasticity are summarized in Fig. 2, which shows the values of the stresses corresponding to the peak at the front of the elastic precursor and to the minimum behind the front. All data were obtained for a sample thickness of 2.86 to 2.97 mm at room temperature. The values of the parameters at the top of the peak may be slightly underestimated since the duration of the stress peak at the elastic precursor front is close to the time resolution limit of the measurements. Since the Poisson ratio increases with temperature, the amplitude of the elastic precursor increases upon heating much more strongly than does the dynamic yield stress.

An analysis of the measured wave profiles shows that at temperatures above 500°C, elastic precursors are noticeably suppressed by the instant of their emergence at the sample surface. This is manifested in that the time intervals between an elastic and a plastic wave were 2 to 8 ns longer than the values calculated for steady-state elastic and plastic shock waves with the measured

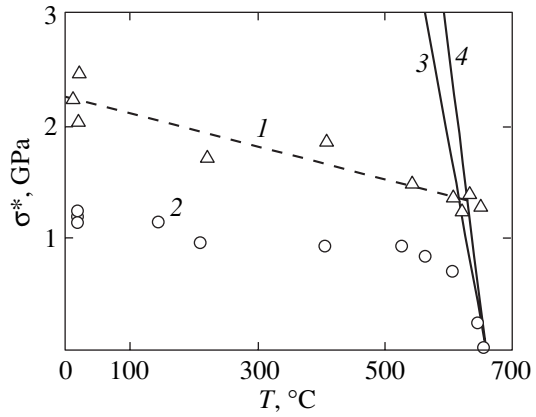

Fig. 3. Cleavage strength for aluminum single crystals (symbols *1*) and for polycrystalline aluminum AD1 [6] (symbols *2*) as functions of temperature. Lines *3* and *4* describe the estimates of the tensile stresses corresponding to the beginning of melting under the adiabatic expansion of aluminum as functions of temperature: calculated with (*3*) dT_m/dp = 64.1 (according to the results from [24]) and (*4*) 54.6 K/GPa.

amplitudes. In all probability, the velocity of the elastic precursor front at the impact surface was slightly higher and the velocity of the plastic shock wave was slightly lower than at the instant of emergence at the sample surface. To a certain extent, the difference between the calculated and measured time intervals separating the elastic and plastic waves is due to the fact that the calculations are based on underestimated values of the parameters at the precursor front, which leads to lower values of the precursor velocity.

The breaking stresses appearing during splitting off were calculated by the method of characteristics [1, 2] from the decrease ΔW in the surface velocity from the maximum value to its value at the front of the cleavage pulse. In fact, this method of determining the dynamic strength of the material is based only on the fundamental conservation laws and is not connected with any assumptions concerning the mechanism and extent of fracture. In the acoustic approximation [12], the tensile stress at the onset of cleavage breaking (cleavage strength σ^*) is defined as

$$\sigma^* = \frac{1}{2}\rho_0 c \Delta W, \qquad (3)$$

where c is the velocity of sound. In this expression, we must take into account the nonlinearity in the material compressibility; for this purpose, the extrapolation of impact adiabats to the region of negative pressures was carried out in the pressure vs. mass velocity coordinates. The choice of the velocity of sound in Eq. (3) is not quite clear. Stepanov [13] paid attention to the fact that from the onset of fracture, the plastic extension in the split-off layer changes to elastic compression. For this reason, the velocity of the cleavage pulse front must be equal to the velocity c_l of the longitudinal elastic waves, while the relief part of the incident compressive pulse ahead of this front propagates at the velocity of sound $c_b < c_l$ determined by the bulk compressibility of the material. As a result, the velocity profile for the free surface becomes distorted and the surface velocity decrement ΔW in Eq. (3) turns out to be smaller than the value that should be expected when disregarding the yield stress. According to Stepanov [13], the breaking stress is defined as

$$\sigma^* = \rho_0 c_b \Delta W \frac{1}{1 + c_b/c_l}. \qquad (4)$$

It should be noted that the difference between the values of the cleavage strength calculated from the experimental data by using expressions (3) and (4) decreases from 8% at room temperature to 5% near the melting point. A more detailed analysis [14] confirms the validity of formula (4) in the case when the impact compression pulse has a triangular shape of its profile at the instant of its emergence at the surface. Since the shape of the wave profiles for the used ratio of the thicknesses of the striker and the sample is close to triangular, the possible error obtained when relation (3) is used does not exceed 3 to 5% according to our estimates, which is within the spread in the experimental data.

The obtained values of breaking stresses during cleavage in aluminum single crystals are presented in Fig. 3. In view of the irreversible heating in the shock wave, the temperature of the material at the beginning of extension exceeds its value indicated in the figure by 3° to 5°. In our experiments, the strain rate in the relief part of the initial compression pulse was ~$(3–6) \times 10^5$ s^{-1} and the thickness of the split-off layer was from 0.3 to 0.4 mm. Figure 3 also presents, for comparison, the results obtained for polycrystalline aluminum AD1 [6].

The results obtained have a spread which is generally typical of such measurements with a high spatial resolution. The resistance to cleavage fracture of the single crystals is twice as high as the strength of polycrystalline aluminum. It should be noted, for comparison, that the dynamic strength of molybdenum and copper single crystals is also higher than the dynamic strength of these materials in the polycrystalline state by a factor of 2 or 3 [15, 16]. The higher values of strength of single crystals under uniaxial deformation can obviously be attributed to their high homogeneity. Polycrystalline materials always contain relatively coarse potential seats of destruction, such as inclusions of impurities, micropores, and grain boundaries, which are absent in high-purity single crystals.

4. DISCUSSION OF RESULTS

The obtained experimental data show that the dynamic yield stress near the melting point is at least four times as large as its value at room temperature. Since the shear modulus in this temperature interval

decreases approximately by half, the ratio of the yield stress to the shear modulus increases accordingly by almost an order of magnitude. It should be noted, for comparison, that the ratio of the stress corresponding to the onset of plastic deformation in aluminum single crystals to the shear modulus remains virtually unchanged under quasi-static conditions in the temperature range from 300 to 600 K and then decreases by a factor of 1.5–2 upon further heating to 900 K [17].

The plastic deformation of crystalline solids occurs through the displacement of dislocations. The equation connecting the velocity of dislocations with frictional forces has the form [18]

$$Bv = b\tau, \tag{5}$$

where the left-hand side contains the friction force and the right-hand side contains the projection of the external load (per unit length of a dislocation) on the Burgers slip vector, B is the friction coefficient, v is the velocity of dislocations, b is the Burgers vector, and τ is the shear stress acting on the sample. The larger the friction coefficient, the higher the stress required to ensure the given velocity of dislocations and, hence, the given strain rate.

Without analyzing the possible mechanisms of high-rate deformation in detail, we will compare the observed effect of temperature on the dynamic yield stress with the contributions of various factors to dislocation drag. The motion of dislocations is decelerated by various obstacles, as well as by frictional forces associated with electrons and phonons [17, 18]. The interaction between a moving dislocation and electrons is weak and plays a noticeable role only at low temperatures. The phonon drag coefficient B_p in the high-temperature range increases linearly with temperature [18]:

$$B_p = \frac{k_B T \omega_D^2}{\pi^2 c^3}, \tag{6}$$

where k_B is the Boltzmann constant, ω_D is the Debye frequency, and c is the velocity of sound. The resistance offered by obstacles is obviously proportional to the concentration of these obstacles in the crystal structure. In particular, the thermodynamically equilibrium concentration of point defects in a crystal exponentially increases with temperature [19]:

$$c_d = A\exp(-H_F/k_B T), \tag{7}$$

where H_F is the enthalpy of the defect formation.

According to the results of measurements, the dynamic yield stress varies almost linearly with temperature, increasing approximately fourfold upon an increase in absolute temperature by a factor of 3.2. These results are in reasonable agreement with the temperature dependence of the phonon drag coefficient. Consequently, the dislocation drag under high-rate deforming conditions in shock waves is probably associated mainly with thermal vibrations of atoms.

The resistance to plastic deformation can be quantitatively characterized using the available experimental data only in the vicinity of the yield stress. However, the decrease in the steepness of a plastic shock wave profile with heating indicates an increase in the ductility of the material as a result of a decrease in the velocity of dislocations at the level of shear stresses observed in a steady-state shock wave. The similarity of wave profiles behind the shock front indicates that there is no significant decrease in the resistance to plastic deformation upon heating at this stage of the process.

The cleavage fracture of plastic materials includes generation, growth, and coalescence of numerous pores [20]. The resistance to the pore growth is determined by the yield stress and ductility of the surrounding material [21]. In this connection, it is not quite clear why an increase in the yield stress upon heating is accompanied by a decrease in the strength of the material with increasing temperature. We should probably assume that the coalescence of high-temperature vacancies involving the formation of micropores generates additional potential seats of destruction, ensuring an increase in the size of the existing seats and thereby reducing the resistance to high-rate destruction during cleavage.

Theoretical analyses of the behavior of perfect metallic crystals under extension [22] proved that at temperatures above 0.5 of the melting point, ruptures are preceded by the disordering of the crystal structure, which was interpreted as the onset of melting. The large-scale molecular-dynamic simulation of the onset of destruction in copper crystals [23] also shows that discontinuities are formed as a result of the loss of stability and the disordering of the crystalline structure in small regions which can be identified as melting sites. Naturally, we are speaking of metastable melting, since all states in the range of negative pressures are metastable relative to the body split into several parts.

If we disregard the ductility and the yield stress of a solid, its extension following impact compression can be regarded as isentropic. If the melting curve in the pressure vs. specific-volume coordinates has a larger slope than that of the isentrope, the adiabatic expansion in the range of negative pressures brings the state of the material to the boundary of the melting region. At temperatures close to T_m, the expansion isentrope intersects the boundary of the melting region at tensile stresses lower than the dynamic rupture strength of the material.

Let us consider the thermodynamic meaning of melting under extension in greater detail. In contrast to gases, negative pressures can be created in solids and liquids. However, in the extension region, all states of a substance lie below the triple point and are lower on the pressure scale than the entire curve describing the equilibrium between the solid and its vapor (sublimation curve), which lies completely in the region of positive pressures. For this reason, all states with a negative pressure, including those at the boundary of the melting

region, are metastable. On the other hand, the region of the existence of the solid and liquid phases and the position of the boundaries of this region for negative pressures are determined by the equality of the chemical potentials of the phases, as in the case of compression. In this sense, the boundary of the melting region (including its part lying in the range of negative pressures) is in equilibrium. Melting during extension (if any is observed) is the transformation of a metastable solid phase into a metastable liquid.

The isentropic expansion of a substance is accompanied by its cooling. Let us estimate, in the linear approximation, the pressure for which the isentrope of the solid phase intersects the melting curve in the p vs. V coordinates. In order to determine the slope of the curve in these coordinates, we can use the reference data on the pressure dependence of the melting point $T_m(p)$:

$$\frac{dV}{dp} = \left(\frac{\partial V}{\partial T}\right)_p \frac{dT_m}{dp} + \left(\frac{\partial V}{\partial p}\right)_T. \quad (8)$$

The linearized equation of state for the isentrope of a solid with initial temperature T_0 (for $p = 0$) can be presented in the form

$$V = V(T_{m0}) + (T_0 - T_{m0})\left(\frac{\partial V}{\partial T}\right)_{p=0} + \left(\frac{\partial V}{\partial p}\right)_S p, \quad (9)$$

where T_{m0} is the melting point under zero pressure. Equations (8) and (9) lead to the condition for the intersection of the isentrope, which describes the expansion of the solid, with the melting curve (or, to be more precise, the solidus line)

$$p\alpha\frac{dT_m}{dp} - \frac{p}{K_T} = \alpha(T_0 - T_{m0}) - \frac{p}{K_S}, \quad (10)$$

where the derivative dT_m/dp reflects the dependence of the melting temperature T_m on pressure p; $\alpha = 1/V(dV/dT) = 1.12 \times 10^{-4}$ K^{-1} is the volumetric thermal expansion coefficient; $T_{m0} = 933.2$ K; T_0 is the initial temperature of the test; and $K_T = -V(dp/dV)_T = 56.7$ GPa and $K_S = -V(dp/dV)_S = 71.1$ GPa [11] are the isothermal and isentropic bulk elastic moduli of the material, respectively.

Figure 3 shows the estimates of tensile stresses at which the melting of the material begins. The estimates were obtained on the basis of Eq. (10) by using the experimental value of $dT_m/dp = 64.1$ K/GPa (according to the results obtained in [24]) and the value of this quantity calculated on the basis of the Clapeyron equation:

$$dT_m/dp = \Delta V_m/\Delta S_m = 54.6 \text{ K/GPa},$$

where $\Delta V_m = 2.34 \times 10^{-5}$ m^3/kg is the change in the specific volume during melting and $\Delta S_m = 428$ J/kg K is the increase in entropy. Generally speaking, a decrease in pressure to below the triple point leads to a transition from melting to sublimation of the solid directly into the gaseous phase, so that $dT_s/dp > dT_m/dp$ along the sublimation curve. Accordingly, this must decrease the slope of the boundary of the solid-phase states in Fig. 3. It is meaningless, however, to estimate the position of the boundary of solid-phase states by extrapolating the sublimation curve from the triple point to the region of extension, since the line of equilibrium between the solid and the vapor completely lies in the region of positive pressures.

After the pressure intersects the boundary of the melting region in the course of extension, the solid-phase states become thermodynamically nonequilibrium states. It is natural to expect that the strength of a solid should decrease abruptly after the beginning of melting; i.e., the theoretical curves in Fig. 3 must set a limit on the strength of the material at high temperatures. However, while the experimental data for polycrystalline aluminum lie below the theoretical estimates, the high- temperature data for aluminum single crystals lie above this limit. It should be noted that an impact compression of polycrystalline materials can lead to energy localization in the vicinity of impurities, grain boundaries, and micropores, with the formation of "hot spots" in analogy with the pattern observed in explosive materials [2]. At high experimental temperatures, the material in hot stops might melt before the main mass of the sample attains the boundary of the melting region. This probably explains the spread in the experimental temperature dependences of the dynamic strength relative to the melting threshold.

Thus, the intersection of the theoretical boundary of the melting region during extension, which is observed in experiments with shock waves, is not accompanied by an abrupt decrease in the breaking strength of the material. Since the onset of melting is accompanied by an increase in compressibility and a decrease in the flow stress, structural anomalies must be formed in the expansion wave as we enter the two-phase region. However, the measured wave profiles in the vicinity of the melting point are completely similar to those recorded at lower temperatures. It can be stated that, in our experiments, the material did not melt and the measured strength in all cases corresponds to the strength of the solid body. Consequently, the states of the superheated solid were realized for a short time in high-temperature experiments. The superheating was as high as 20°C relative to the threshold line *4* in Fig. 3 and 30°C relative to curve *3*.

Thus, our experiments with aluminum single crystals revealed an increase in the dynamic yield stress with temperature, which is probably due to an increase in the phonon drag. The states of superheated solids are detected in the case of dynamic expansion to the melting region.

ACKNOWLEDGMENTS

The authors are grateful to L.G. Ermolov and P.V. Skachkov (Institute of Chemical Physics, Russian Academy of Sciences, Chernogolovka) for their help in setting up the experiments and to V.G. Sursaeva and S.G. Protasova (Institute of Solid-State Physics, Russian Academy of Sciences, Chernogolovka), who provided the monocrystalline aluminum samples for the experiments.

This work was supported by the Russian Foundation for Basic Research, program no. 00-02-17604.

REFERENCES

1. Ya. B. Zel'dovich and Yu. P. Raĭzer, *Physics of Shock Waves and High-Temperature Hydrodynamic Phenomena* (Nauka, Moscow, 1966, 2nd ed.; Academic, New York, 1966).
2. G. I. Kanel, S. V. Razorenov, A. V. Utkin, and V. E. Fortov, *Impact–Wave Phenomena in Condensed Media* (Yanus-K, Moscow, 1996).
3. R. W. Rohde, Acta Metall. **17**, 353 (1969).
4. J. R. Asay, J. Appl. Phys. **45**, 4441 (1974).
5. A. A. Bogach, G. I. Kanel', S. V. Razorenov, *et al.*, Fiz. Tverd. Tela (St. Petersburg) **40** (10), 1849 (1998) [Phys. Solid State **40**, 1676 (1998)].
6. G. I. Kanel, S. V. Razorenov, A. A. Bogatch, *et al.*, J. Appl. Phys. **79** (11), 8310 (1996).
7. A. Kumar and R. G. Kumble, J. Appl. Phys. **40** (9), 3475 (1969).
8. A. V. Antonov, S. V. Kopetskiĭ, L. S. Shvindlerman, and V. G. Sursaeva, Dokl. Akad. Nauk SSSR **213**, 318 (1973) [Sov. Phys. Dokl. **18**, 736 (1974)].
9. J. R. Asay and L. M. Barker, J. Appl. Phys. **45** (6), 2540 (1974).
10. R. A. Graham, *Solids under High-Pressure Shock Compression* (Springer-Verlag, New York, 1993).
11. J. L. Tallon and A. Wolfeden, J. Phys. Chem. Solids **40**, 831 (1979).
12. S. A. Novikov, I. I. Divnov, and A. G. Ivanov, Fiz. Met. Metalloved. **25** (4), 608 (1964).
13. G. V. Stepanov, Probl. Prochn., No. 8, 66 (1976).
14. G. I. Kanel, Fatigue Fract. Eng. Mater. Struct. **22** (11), 1011 (1999).
15. S. V. Razorenov and G. I. Kanel, Fiz. Met. Metalloved. **78** (11), 141 (1992).
16. G. I. Kanel, S. V. Razorenov, A. V. Utkin, *et al.*, J. Appl. Phys. **74** (12), 7162 (1993).
17. R. Berner and H. Kronmüller, *Plastische Verformung von Einkristallen*, in *Moderne Probleme der Metallphysik*, Ed. by A. Seeger (Springer-Verlag, Berlin, 1965; Mir, Moscow, 1969).
18. T. Suzuki, H. Yosinaga, and S. Takeucti, *Dislocation Dynamics and Plasticity* (Syokabo, Tokyo, 1986; Mir, Moscow, 1989).
19. P. G. Cheremskoĭ, V. V. Slezov, and V. I. Betekhtin, *Pores in Solids* (Énergoatomizdat, Moscow, 1990).
20. D. R. Curran, L. Seaman, and D. A. Shockey, Phys. Rep., Phys. Lett. **147** (5–6), 254 (1987).
21. J. N. Johnson, J. Appl. Phys. **52** (4), 2812 (1981).
22. R. M. Lynden-Bell, J. Phys.: Condens. Matter **7**, 4603 (1995).
23. J. Belak, in *Shock Compression of Condensed Matter-1997*, Ed. by S. C. Schmidt, D. D. Dandekar, and J. W. Forbes, AIP Conf. Proc. **429**, 211 (1998).
24. T. Gorecki, High Temp. High Press. **11**, 683 (1979).

Translated by N. Wadhwa

Physics of the Solid State, Vol. 43, No. 5, 2001, pp. 878–883. Translated from Fizika Tverdogo Tela, Vol. 43, No. 5, 2001, pp. 846–850.

MAGNETISM AND FERROELECTRICITY

The Role of Surface States in Magnetic Properties of Nanocrystalline CuO

T. I. Arbuzova, S. V. Naumov, A. A. Samokhvalov, B. A. Gizhevskiĭ, V. L. Arbuzov, and K. V. Shal'nov

Institute of Metal Physics, Ural Division, Russian Academy of Sciences, ul. S. Kovalevskoĭ 18, Yekaterinburg, 620219 Russia
e-mail: viglin@imp.uran.ru

Received August 17, 2000

Abstract—The temperature behavior of the magnetic susceptibility of a CuO low-dimensional antiferromagnet subjected to spherically converging isentropic shock wave loading is investigated. The grain sizes in CuO polycrystalline samples range from 5 to 110 nm. It is demonstrated that a decrease in the grain size leads to an increase in the role of the surface states in the magnetic properties. Unlike polycrystals prepared by standard methods, the susceptibility of nanocrystalline samples in the range 78 K < T < 150 K decreases with an increase in temperature, which is explained by the formation of Cu^{2+} paramagnetic ions on the surface of nanocrystalline particles. © *2001 MAIK "Nauka/Interperiodica".*

1. INTRODUCTION

It is known that the electrical and magnetic properties and the electronic structure of bulk samples can differ from those of surface layers due to the disturbance of their three-dimensional periodicity. Considerable progress achieved in microelectronics has required knowledge of the role played by the surface in the formation of physical properties of bulk materials. In this work, we investigated the influence of the surface on the magnetic properties of copper monoxide. The choice of CuO as the object of our investigation was motivated by its specific position among the transition metal oxides. As a rule, the 3*d* metal oxides are three-dimensional Heisenberg antiferromagnets. The exchange interaction between magnetic ions occurs by way of superexchange through oxygen ions. Copper monoxide CuO possesses the properties of a low-dimensional antiferromagnet with the high Néel temperature T_N = 230 K. Neutron diffraction measurements revealed that Cu^{2+} ions in CuO undergo a three-dimensional antiferromagnetic ordering at temperatures below T_N [1]. However, above T_N, the magnetic susceptibility χ does not decrease according to the Curie–Weiss law but increases and passes through a broad maximum near T = 550 K [2]. The temperature behavior of the magnetic susceptibility, a large deviation of the magnetic moment of Cu^{2+} ions $n_s = 0.68\mu_B$ from a pure spin value of 1 μ_B, and the available data on the heat capacity [3] indicate the presence of strong spin correlations and quasi-one-dimensional antiferromagnetism in the temperature range 230 K < T < 550 K. Among all the known low-dimensional antiferromagnets, the highest temperatures T_N and, hence, large exchange parameters are observed for CuO, La_2CuO_4, and $YBa_2Cu_3O_6$. Relatively simple crystallographic and magnetic sublattices, a low spin value of bivalent copper ions, and a strong exchange interaction along the preferential direction $[10\bar{1}]$ allow us to consider copper monoxide a model material for an infinite or broken antiferromagnetic chain [4]. Moreover, CuO is a basic component in cuprate high-temperature superconductors. In our previous work [5], we studied copper-containing high-T_c compounds and Cu–O-based heterophase systems and revealed the local superconductivity which, most likely, is realized in interfacial and surface layers.

The majority of works dealing with CuO were devoted to the study of its bulk properties. Recently, Sohma and Kawaguchi [6] reported the data on the magnetic properties of CuO multilayer films. The aim of the present work was to investigate the effect of grain size on the magnetic susceptibility of copper monoxide polycrystals.

2. SAMPLE PREPARATION AND EXPERIMENTAL TECHNIQUE

Copper monoxide has a monoclinic structure ($C2/c$ symmetry) with the unit cell parameters a = 4.685 Å, b = 3.422 Å, c = 5.130 Å, and β = 99.42°. A small deviation of the angle between the a and c axes from 90° can be associated with the Jahn–Teller effect due to the presence of bivalent copper ions.

Copper monoxide samples with different grain sizes were produced under the action of spherically converging isentropic shock waves. The procedure for preparing these sample was described in detail in [7]. After shock action, ceramic copper monoxide had the form of

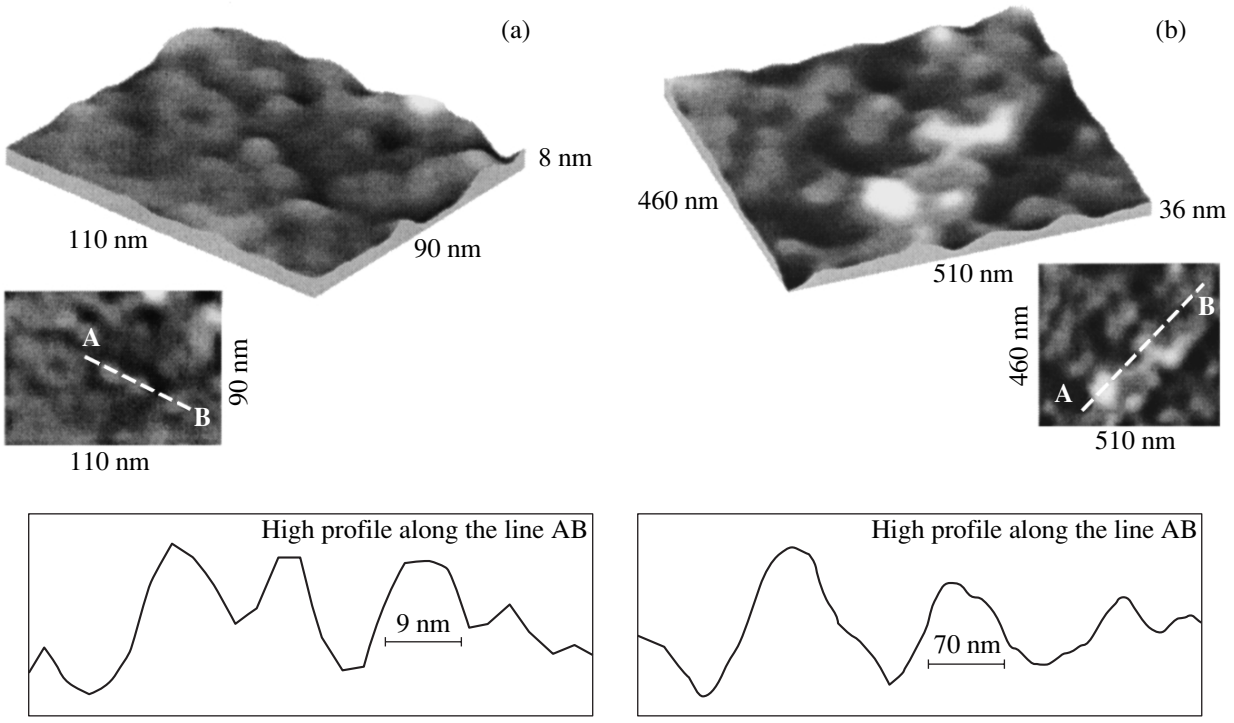

Fig. 1. Microstructure observed with a scanning tunneling microscope in different layers of a shocked spherical sample of CuO: r = (a) $0.7R$ and (b) $0.9R$.

a spherical sample with radius $R = 22$ mm, from which plates were cut out normally to the radius. The density of initial polycrystals of CuO was equal to 70% of the theoretical value. The density of shocked CuO reached a maximum value of 99% for layers at a depth $r > 0.5R$, which was close to the density of single crystals (98%). However, the central region ($r < 0.4R$) of the compressed spherical sample contained weakly pressed CuO with a low density. The phase and structure analyses of the samples were performed on a DRON-2.0 x-ray diffractometer. The grain size in the samples was estimated by scanning tunneling microscopy (STM) using an STM-U1 microscope (ZAO KPD, Zelenograd, Russia). Ten and more images at different points were obtained for each sample. The crystalline grain sizes in the samples were determined by averaging over all the images obtained. The magnetic susceptibility was measured on a magnetic balance over a wide temperature range (80–600 K).

According to x-ray diffraction investigations, the samples cut out from the dense region of the shocked ball are single-phase. For shocked CuO samples, the unit cell parameters a, b, and c increased only slightly, the β angle decreased, and the diffraction lines broadened considerably. The broadening of the diffraction lines for shocked CuO samples can be associated with both elastic stresses arising in the crystal lattice after shock action and small sizes of coherent scattering regions. Analysis of the x-ray diffraction data revealed that the small grain size in the CuO samples made the main contribution to the diffraction line broadening. This agrees well with the STM data. The grain size d in the initial polycrystal was equal to 5–15 μm. After shock loading, grains with a maximum size $d = 110$ nm were observed in the outer ($r = 0.95R$) and inner ($r = 0.5R$) layers of the dense region of the spherical sample. Intermediate layers with a relative radius $r = 0.7R$ contained grains with a minimum size $d = 10$ nm. Figure 1 shows the microstructure observed with a scanning tunneling microscope in different layers of a shocked CuO ball. It is seen that the grain sizes in layers with $r = 0.7R$ and $0.9R$ differ by the order of magnitude. Grains with the smallest size $d = 5$ nm were observed in friable CuO samples cut out from the central region ($r < 0.4R$) of the ball. It should be noted that small amounts of the Cu_2O nonmagnetic phase were found in these samples. The CuO ceramics produced by the blast method can be considered nanocrystalline materials.

3. MAGNETIC PROPERTIES OF CuO NANOCRYSTALLINE SAMPLES

The magnetic order in CuO is governed by the Cu^{2+} superexchange interaction through oxygen ions, because direct exchange is impossible. The Cu–O–Cu angle has the closest value to 180° and lies in the plane

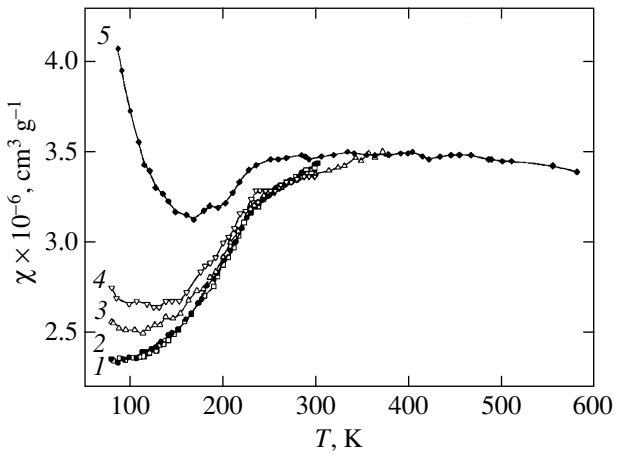

Fig. 2. Temperature dependences of the magnetic susceptibility of polycrystalline CuO samples subjected to spherical shock wave action. Magnetic field H = 9 kOe. Crystallite size d, nm: (*1*) 110, (*2*) 70, (*3*) 30, (*4*) 15, and (*5*) 5.

parallel to the $[10\bar{1}]$ direction. Therefore, magnetic ions are antiferromagnetically ordered in this direction. In all other directions, the Cu–O–Cu angle is close to 90°, which provides ferromagnetic coupling. The magnetic structure of CuO can be represented in the form of zigzag antiferromagnetic chains extended along the $[10\bar{1}]$ direction with a strong intrachain interaction and a weak ferromagnetic coupling between the chains. Competition between the antiferromagnetic and ferromagnetic interactions leads to a three-dimensional collinear antiferromagnetism at low temperatures (T < 212 K). A three-dimensional noncolinear (spiral) magnetic structure is realized in the range 212 < T < 230 K. Above T_N = 230 K, as follows from the neutron diffraction, magnetic, and heat capacity data, strong spin correlations are observed in CuO. Since the interchain exchange parameter is substantially less than the intrachain exchange parameter, an increase in kT results in cessation of the interaction between the chains and the system transforms into a low-dimensional state. The temperature dependence of the magnetic susceptibility has a shape characteristic of low-dimensional antiferromagnets which undergo a phase transition to a three-dimensional state with a long-range magnetic order as the temperature decreases. A distinguishing feature of low-dimensional antiferromagnets is that the susceptibility χ exhibits a flattened maximum in the temperature range comparable to the exchange parameter in a chain or a plane.

In [2, 8], it was demonstrated that the susceptibility of CuO polycrystals with a stoichiometric composition at low temperatures (T < 140 K) remains virtually constant. As the temperature increases (T > 140 K), the susceptibility also increases and reaches a maximum near T = 550 K. In the high-temperature range (T > 550 K), an increase in T brings about a decrease in the susceptibility, which indicates a paramagnetic state of CuO. In the vicinity of T_N, a peak typical of the susceptibility of three-dimensional antiferromagnets is absent and only the slope of the $\chi(T)$ curve changes. The absence of the peak in the $\chi(T)$ dependence near T_N indicates a smeared transition from the three-dimensional state with a long-range magnetic order to the low-dimensional state with strong spin correlations.

Earlier [9], we investigated the influence of intrinsic defects and specially introduced impurity magnetic and nonmagnetic ions on the magnetic properties of CuO. It was shown that intrinsic defects lead to a change in magnitude of the susceptibility χ and a shift in the temperature of its maximum toward the low-temperature range. The presence of impurity ions can result in a change in the temperature ranges of the long- and short-range orders. The temperature range of the long-range order is estimated from the T_N temperature. The temperature of the short-range order is evaluated from the location of the susceptibility maximum above T_N and the deviation of the effective magnetic moment from the theoretical value. At high temperatures, spin correlations disappear, all Cu^{2+} ions become paramagnetic, and their effective magnetic moment should correspond to μ_{eff} for isolated ions.

As was already mentioned, many works dealing with CuO have focused on the study of its bulk properties. However, the properties of bulk samples and their surface layers can differ because of the breaking of bonds on the surface. In order to elucidate the role of the surface magnetism in the formation of magnetic properties of CuO, we measured the magnetic susceptibility of ceramic samples with different crystallite sizes. A decrease in the crystallite size should bring about an increase in the number of intercrystalline interfaces and, correspondingly, an increase in the contribution of surface states to the measured susceptibility. Figure 2 depicts the temperature dependences of the magnetic susceptibility in an external magnetic field H = 9 kOe for CuO polycrystalline samples with different mean crystallite sizes d which were subjected to spherical shock wave action. The temperature dependences of the susceptibility for samples with large crystallite sizes ($d \geq 70$ nm), which were cut out from different regions of the shocked ball, are identical to those for CuO polycrystals prepared by the standard method. In this d range, the crystallite size does not affect the behavior of $\chi(T)$ (curves *1*, *2* in Fig. 2). A decrease in the crystallite sizes (d < 70 nm) is accompanied by an increase in the susceptibility χ in the low-temperature range ($T < T_N$) and a decrease in the difference between the minimum and maximum susceptibilities. For a sample with d = 5 nm (curve *5*), the susceptibility χ depends inversely on the temperature in the range T < 140 K; i.e., the susceptibility increases with a decrease in temperature ($\chi \sim 1/T$). In the high-temperature range (T > 300 K), the susceptibilities of all the samples coincide.

As was noted above, sample no. 5 contains a small amount of the Cu_2O phase. Copper in this phase is in the univalent state ($3d^{10}$), and, hence, the cuprous oxide should be diamagnetic. The presence of a foreign nonmagnetic phase in CuO should not strongly affect the behavior of $\chi(T)$. In order to verify this assumption, we measured the temperature dependences of the magnetic susceptibility for single-crystal and polycrystalline samples of Cu_2O (Fig. 3). As the temperature increases, the susceptibility of Cu_2O polycrystals linearly decreases from $\chi = 0.81 \times 10^{-6}$ cm^3/g at $T = 78$ K to $\chi = 0.23 \times 10^{-6}$ cm^3/g at $T = 290$ K. For a single crystal, the dependence $\chi(T)$ is stronger and the susceptibility is higher ($\chi = 1.27 \times 10^{-6}$ cm^3/g at $T = 78$ K), which can be associated with the presence of uncontrollable impurities. Note that the magnetic susceptibility of Cu_2O in the temperature range covered is substantially less than the susceptibility of CuO. We calculated the temperature dependences of the susceptibility for the CuO–Cu_2O two-phase samples. The magnetic susceptibility of the two-phase sample is determined by the sum of the contributions of these two phases: $\chi_\Sigma = (1 - x)\chi(\mathrm{CuO}) + x\chi(\mathrm{Cu_2O})$, where x is the concentration of the Cu_2O phase. The values of χ were taken from the experimental dependences $\chi(T)$ for CuO and Cu_2O stoichiometric polycrystals. The calculated dependences $\chi(T)$ for compositions containing 10 and 50% Cu_2O are displayed in Fig. 3. It is seen that the behavior of $\chi(T)$ is similar to the temperature dependence of the susceptibility for CuO. Even for a composition containing 50% CuO and 50% Cu_2O, the susceptibility in the low-temperature range should not exhibit as strong a dependence $\chi \sim 1/T$ as in curve *5* in Fig. 2. Since our sample contains no more than 3–5% Cu_2O, the observed behavior of $\chi(T)$ cannot be explained by the presence of the Cu_2O phase. As follows from the results obtained, a decrease in the size of crystallites in shocked CuO polycrystals does not affect the short-range magnetic order at $T > 300$ K. The role of the surface states at the intercrystalline interfaces manifests itself in the region of the long-range magnetic order; however, the Néel temperature remains unchanged.

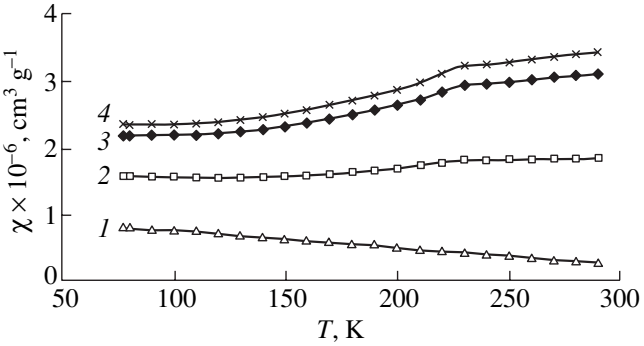

Fig. 3. Experimental and calculated temperature dependences of the magnetic susceptibility for single-phase and two-phase polycrystalline samples: (*1*) Cu_2O, (*2*) 50% CuO + 50% Cu_2O, (*3*) 90% CuO + 10% Cu_2O, and (*4*) CuO.

4. DISCUSSION

An increase in the susceptibility of CuO polycrystals with a decrease in temperature ($T < 65$ K) was observed in a number of works [10–12]. The reason for this increase in χ remains unclear. According to Seehra *et al.* [12], the low-temperature increase in χ is explained by the presence of vacancies in the cationic sublattice and the formation of trivalent copper ions. The magnetic moment of copper ions Cu^{3+} ($3d^8$) is larger than that of Cu^{2+} ions. Trivalent copper ions can behave as a paramagnetic impurity. However, the experimental data obtained in our earlier work [9] for stoichiometric CuO and $Cu_{1-x}Li_xO$ solid solutions demonstrated that the anomalous behavior of the susceptibility at low temperatures cannot be explained by the presence of Cu^{3+} ions. Experimental evidence of the presence of Cu^{3+} ions in copper-containing oxides is unavailable.

Above the Néel temperature, CuO is a quasi-one-dimensional antiferromagnet. Bonner and Fisher [13] calculated the temperature dependences of the antiferromagnetic susceptibility in a zero magnetic field for Heisenberg broken chains consisting of a limited number ($N = 3, 4, 5, \ldots, 11$) of spins $S = 1/2$. For chains with an even number of spins, the susceptibility below the temperature of the maximum $kT_{\max}/|J| = 1.282$ decreases monotonically with a decrease in temperature. For chains with an odd number of spins, the susceptibility below the temperature of the maximum also first decreases but then increases with a further decrease in the temperature ($kT_{\max}/|J| < 0.6$). Note that the susceptibility of chains with a smaller number of spins is higher. The $\chi(T)$ dependences for chains with $N = 7$, 9, and 11 are similar to our experimental curves shown in Fig. 3. The broken chains in CuO nanocrystalline samples can arise from the breaking of the Cu–O–Cu exchange bonds in the surface layers of crystallites upon disturbance of their three-dimensionality. The smaller the crystallite size, the greater the contribution of the surface states and the larger the number of dangling bonds. However, it is unlikely that the low-temperature increase in the susceptibility χ of CuO nanocrystalline samples is associated with one-dimensional antiferromagnetism. In this case, the long-range magnetic order should either be absent or be retained at low temperatures ($T < 78$ K). For our samples, $T_N = 230$ K. One of the reasons for the low-temperature increase in the susceptibility can be the frustration of antiferromagnetic interactions between the Cu^{2+} ions on the crystallite surface. It is known that both perpendicular ($\chi_\perp$) and parallel ($\chi_\parallel$) susceptibilities of strongly

Experimental and calculated magnetic susceptibilities of CuO with inclusion of Cu^{2+} paramagnetic ions

T, K	$\chi_{exp} \times 10^{-6}$, cm^3/g						
	Cu^{2+} ion content *x*, %						$\chi_{exp} \times 10^{-6}$, cm^3/g for sample no. 5
	1%	2%	3%	4%	5%	100%	
77	2.94	3.53	4.12	4.70	5.29	61.20	4.11
100	2.81	3.26	3.70	4.15	4.60	47.12	3.63
150	2.80	3.10	3.39	3.67	3.96	31.42	3.15
200	3.11	3.31	3.52	3.73	3.93	23.56	3.22
250	3.43	3.58	3.74	3.89	4.05	18.85	3.46
300	3.56	3.69	3.84	3.93	4.05	15.70	3.50

frustrated antiferromagnets can increase at low temperatures (for polycrystals, $\chi = 2/3\chi_\perp + 1/3\chi_\parallel$).

The most probable reason for the complex temperature behavior of the susceptibility is the formation of Cu^{2+} paramagnetic ions on the crystallite surface due to the frustration of three-dimensional exchange interactions. Sohma and Kawaguchi [6] investigated the magnetic properties of multilayers in polycrystalline and epitaxial CuO films (with different thicknesses) on Al_2O_3 and MgO nonmagnetic substrates. The Néel temperature of polycrystalline films 1000 Å thick was T_N = 160 K, which is considerably less than the value T_N = 230 K found for polycrystals. It was shown that the susceptibility of all film samples in the temperature range 4.2 K < *T* < 300 K is inversely proportional to the temperature: $\chi \sim 1/T$. At the same thickness of multilayers, the susceptibility is higher for thinner films. It was revealed that the susceptibility at 4.2 K increases linearly with an increase in the number of interfaces. These authors made the conclusion that the observed character of the $\chi(T)$ dependence is determined by the paramagnetic component [6]. Paramagnetic ions Cu^{2+} are located in the planes with an effective thickness of 2–4 Å, which are adjacent to the interfacial layers. In the CuO (20 Å)/Al_2O_3 (30 Å) thin films composed of 100 layers, the concentration of Cu^{2+} paramagnetic ions was estimated at 6.7% of the total number of copper ions.

The dependences $\chi(T)$ obtained in the present work for the CuO nanocrystalline samples are slightly different: the susceptibility exhibits a minimum in the temperature range *T* = 120–160 K. We attempted to describe the experimental dependences $\chi(T)$ under the assumption that the measured values of χ are the sum of the contributions from bulk CuO and paramagnetic ions Cu^{2+} on the crystallite surface. The total susceptibility can be represented in the form

$$\chi = (1 - x)\chi(\mathrm{CuO}) + x\frac{Ng^2S(S+1)\mu_B^2}{3kT}, \qquad (1)$$

where *x* is the concentration of Cu^{2+} paramagnetic ions. The first term in relationship (1) can be determined from curve *1* in Fig. 2 for samples with large-sized crystallites ($d > 1000$ Å). The Curie law can be used for the second term in the sum, because magnetic copper ions do not interact on the crystallite surface. The total susceptibilities calculated for small concentrations *x* of Cu^{2+} paramagnetic ions at different temperatures are listed in the table. The experimental values of $\chi(T)$ for sample no. 5 with d = 5 nm are also given in the table for comparison. If the Cu^{2+} ions were predominantly in the paramagnetic state, the first term in relationship (1) could be ignored, because the contribution of CuO to the total susceptibility is relatively small. However, at small concentrations *x*, both contributions are comparable, which determines the nonmonotonic behavior of $\chi(T)$. As can be seen from the table, at $x \le 0.05$, the susceptibility χ should exhibit a minimum in the vicinity of *T* = 150 K, which agrees with the experimental data. We failed to achieve complete qualitative agreement between the calculated and experimental dependences $\chi(T)$. However, the proposed model adequately describes the behavior of $\chi(T)$. For a sample with the smallest crystallite size (Fig. 2, curve *5*), the Cu^{2+} ion concentration *x* was estimated at 0.03. An increase in the crystallite size should lead to a decrease in the concentration *x* due to the decrease in the fraction of surface layers in the bulk sample. The Cu^{2+} paramagnetic ions can have a higher concentration in CuO multilayer films. At concentrations $x > 0.07$, the susceptibility should gradually decrease with an increase in temperature, which is in reasonable agreement with the data obtained in [6].

5. CONCLUSION

Thus, the complex temperature behavior of susceptibility in nanocrystalline samples of the CuO low-dimensional antiferromagnets can be explained by the presence of Cu^{2+} paramagnetic ions. The Cu^{2+} ions located in the surface layers of nanocrystals are not involved in the interactions and behave as a paramagnetic impurity due to the lack of three-dimensional periodicity and the breaking of exchange bonds. The role of the surface states of copper ions in the magnetic

properties increases with a decrease in the crystallite size.

ACKNOWLEDGMENTS

We are grateful to E.A. Kozlov for performing the experiments on shock wave compression.

This work was supported by the Ministry of Science and Technology of the Russian Federation, project no. 2.4.99.

REFERENCES

1. J. B. Forsyth, P. J. Brown, and B. M. Wanklyn, J. Phys. C **21**, 2917 (1988).
2. T. I. Arbuzova, A. A. Samokhvalov, I. B. Smolyak, *et al.*, J. Magn. Magn. Mater. **95**, 168 (1991).
3. J. W. Loran, K. A. Mirza, C. P. Joyce, and A. J. Osborne, Europhys. Lett. **8**, 263 (1989).
4. R. Carlin, *Magnetochemistry* (Springer-Verlag, Heidelberg, 1986; Mir, Moscow, 1989).
5. A. A. Samokhvalov, T. I. Arbuzova, N. A. Viglin, *et al.*, Fiz. Tverd. Tela (St. Petersburg) **41** (2), 293 (1999) [Phys. Solid State **41**, 262 (1999)].
6. M. Sohma and K. Kawaguchi, J. Appl. Phys. **77**, 1189 (1995).
7. B. A. Gizhevskiĭ, E. A. Kozlov, M. V. Degtyarev, *et al.*, Fiz. Khim. Obrab. Mater. **3**, 52 (1999).
8. M. O'Keefe and F. S. Stone, J. Phys. Chem. Solids **23**, 261 (1962).
9. T. I. Arbuzova, I. B. Smolyak, S. V. Naumov, and A. A. Samokhvalov, Fiz. Tverd. Tela (St. Petersburg) **40** (10), 1876 (1998) [Phys. Solid State **40**, 1702 (1998)].
10. A. Junod, D. Eckert, and G. Triscone, J. Phys.: Condens. Matter **1**, 8021 (1989).
11. H. Bizette and B. Tsai, C. R. Hebd. Seances Acad. Sci. **241**, 183 (1955).
12. M. Seehra, Z. Feng, and G. R. Gopalakrishnan, J. Phys. C **21**, 1051 (1988).
13. J. C. Bonner and M. E. Fisher, Phys. Rev. **135**, A640 (1964).

Translated by O. Borovik-Romanova

Physics of the Solid State, Vol. 43, No. 5, 2001, pp. 884–887. Translated from Fizika Tverdogo Tela, Vol. 43, No. 5, 2001, pp. 851–854.

MAGNETISM AND FERROELECTRICITY

The Influence of Continuous-Wave Pumping on the Propagation of Envelope Solitons of Magnetostatic Spin Waves

A. V. Kokin and S. A. Nikitov

Institute of Radio Engineering and Electronics, Russian Academy of Sciences, ul. Mokhovaya 18, Moscow, 103907 Russia
e-mail: nikitov@mail.cplire.ru

Received September 21, 2000

Abstract—The influence of continuous-wave pumping on the propagation of solitons of magnetostatic spin waves is studied. It is shown that, at certain conditions when the frequency of the continuously excited wave falls into the spectrum of a soliton-like pulse, the nonlinear interaction results in soliton decay. Numerical calculations of this effect are presented. © *2001 MAIK "Nauka/Interperiodica".*

The properties of envelope solitons of traveling magnetostatic spin waves (MSWs) in ferromagnetic films are investigated in detail for the cases of direct and inverse bulk MSWs [1, 2]. An important property of solitons, namely, the conservation of their shape in colliding with and penetrating through each other, was observed for solitons propagating in opposite directions [3]. In a typical experimental study of MSW solitons, ferromagnetic films are used; the exciting and receiving antennas are placed on the surface of the film at a distance of 1 cm from each other. The initial length of MSW solitons is about 20 to 40 ns. This means that the distance at which solitons interact at a collision is approximately 0.02 to 0.2 cm (for an MSW group velocity of 10^6 to 5×10^6 cm/s). The interaction effects are not able to accumulate and, therefore, do not affect the character of the soliton propagation. On the other hand, it has been shown recently that the mutual influence of MSWs could alter the character of the wave propagation. It has been demonstrated [4, 5] that a modulation instability occurs as a result of the cross-modulation of nonlinear surface MSWs, which are usually modulation-stable, and the waves become unstable with respect to the modulation. At the interaction with each other, the direct bulk MSWs also reveal the induced modulation instability due to the cross-modulation that is additional to the self-modulation (since, contrary to the surface MSWs, these waves are modulation unstable). Moreover, propagating along the same direction in ferromagnetic films, the surface MSW pulses can form envelope solitons at the interaction [6]. The character of their propagation corresponds to the behavior at the collision of solitons considered in [7]. Thus, when two waves interact, the MSW propagation significantly depends on the character of the interaction between them. In [8], it was proposed to control the propagation of optical solitons in a fiber with the aid of continuously excited light, thereby solving the problem of developing optical devices using only light. In the present paper, the influence of the continuous-wave MSW pumping on the properties of propagating envelope solitons of direct bulk MSWs is considered. Thus, we demonstrate the possibility of controlling the formation and propagation of MSW solitons by a propagating microwave signal.

The propagation of weakly nonlinear MSWs in a ferromagnetic film is considered in the nonlinear Shrödinger equation (NSE) approximation for the magnetostatic potential of the wave obtained in solving the coupled Landau–Lifshitz and Maxwell equations. The interaction between an MSW pulse and a continuous wave is described by the coupled NSEs supplemented by the corresponding boundary conditions and initial conditions. The system of coupled NSEs for direct bulk MSWs has the form

$$\begin{aligned} i\frac{\partial A}{\partial t} + iv_{g1}\frac{\partial A}{\partial y} + \frac{1}{2}\beta_1\frac{\partial^2 A}{\partial y^2} &= f_1(a^2|A|^2 + b^2|B|^2)A, \\ i\frac{\partial B}{\partial t} + iv_{g2}\frac{\partial B}{\partial y} + \frac{1}{2}\beta_2\frac{\partial^2 B}{\partial y^2} &= f_2(a^2|A|^2 + b^2|B|^2)B, \end{aligned} \tag{1}$$

where

$$a^2 = k_1^2(\sin k_1 d + |\alpha|^2 \cos k_1 d),$$

$$b^2 = k_1^2(\sin k_1 d + |\beta|^2 \cos k_1 d),$$

$$f_1 = \frac{\omega_H}{M_0^2\omega_1}[\omega_H \cos k_1 d + \omega_M \sin k_1 d](\chi_1^2 + \chi_2^2),$$

$$\chi_1 = \frac{\omega_M\omega_H}{\omega_H^2 - \omega^2}, \quad \chi_1 = \frac{\omega_M\omega}{\omega_H^2 - \omega^2}.$$

Here, $\omega_H = \gamma H$, $\omega_0^2 = \omega_H^2 + \omega_H\omega_M$, $\omega_M = \gamma 4\pi M$, H is the external magnetic field, M is the saturation magnetiza-

tion of the ferromagnet, $v_{gi} = \frac{\partial \omega_i}{\partial k_i}$ are the group velocities of the waves, and $\beta_i = \frac{\partial^2 \omega_i}{\partial k_i^2}$, where $\omega_i(k_i)$ is the dispersion relation of MSWs (index i indicates the first or second wave), which is found from the transcendental equation

$$\tan(\xi k_i d) = \frac{2\xi}{\xi^2 - 1}, \quad \xi = \sqrt{-(1 + 4\pi\chi_{1i})},$$

where d is the thickness of the ferromagnetic film, χ_1 and χ_2 are the components of the magnetic susceptibility tensor, k_1 and k_2 are the wave numbers of the MSWs, and A and B are the amplitudes of the MSW potentials.

To describe a propagating MSW pulse, the following initial conditions are chosen:

$$A(x, 0) = \begin{cases} A_0\zeta(0), & x = 0 \\ 0, & 0 < a \le L_x, \end{cases} \qquad (2)$$
$$A(0, t) = A_0\zeta(t), \quad t \ge 0,$$

where A_0 is the pulse amplitude. The function $\zeta(t)$ is taken in the form

$$\zeta(t) = \operatorname{sech}\left(\frac{T}{2} - t\right), \quad 0 \le t \le T, \qquad (3)$$
$$0, \quad t > T.$$

At $T = t_{max}$, where t_{max} is the time of the propagation of the MSWs, this mathematical model corresponds to the case of a continuous excitation of a wave, and at $T < t_{max}$, to the pulse excitation. Thus, the initial conditions for the wave propagating in the continuous regime can also be taken into account by Eqs. (2) and (3).

The system of equations (1) describes the evolution of the wave propagation, including the effects of self-modulation, cross-modulation, and mismatch between the group velocities. In the case of MSWs, the last effect becomes crucial in determining the spectrum and shape of the propagating pulses. The dispersion and nonlinear lengths are the main parameters determining the propagation of the pulse in a nonlinear dispersion medium. The dispersion length is the distance at which the pulse in the linear medium becomes twice as broad due to dispersion spreading, and the nonlinear length is the distance at which the phase of the peak of the pulse amplitude changes by π in the absence of dispersion:

$$L_{D,i} = \frac{T_0^2 v_{gi}^3}{|\beta_i|}, \qquad (4a)$$

$$L_{NL,i} = \frac{v_g}{f_i P_i}, \qquad (4b)$$

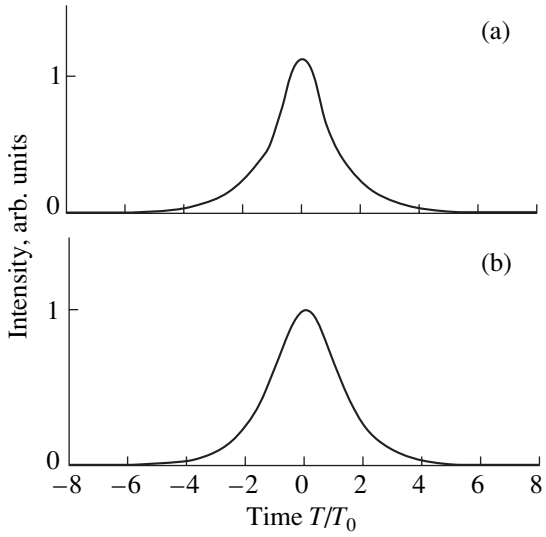

Fig. 1. (a) Formation of a soliton of a direct bulk magnetostatic wave from an initial 100-ns Gaussian pulse presented in (b). The vertical axis corresponds to the amplitude of the pulse measured in arbitrary units, and the horizontal axis, to the propagation time normalized to the initial duration of pulse.

where T_0 is the initial duration of the pulse, f_1 is defined in Eq. (1), and P_1 is the dimensionless wave power. When these lengths become equal and the necessary condition for the soliton existence (Lighthill criterion) is fulfilled, this length is approximately equal to the distance at which the envelope soliton is formed from the initial square pulse. In the case of direct bulk MSWs, the distances L_D and L_{NL} can be made equal to several millimeters by varying the operating frequency, the initial duration of the pulse, and its power. The formation and observation of direct bulk MSW solitons are possible in this situation. Figure 1 shows the results of numerical simulation of the propagation of a pulse of the direct bulk MSW with an initial duration of 100 ns and a wave frequency of 3.7 GHz for a ferromagnetic 7.5-μm thick film in an external magnetic field of 2.35 kOe. In particular, Fig. 1a shows the initial pulse (at the entry into the film) and Fig. 1b shows the formed soliton (after propagating over a distance of 1.5 cm along the film).

In the case of the simultaneous propagation of the pulse and a continuous signal, the latter significantly affects the process of the soliton formation. In this case, according to Eq. (1), this process, as was already mentioned, essentially depends on the mismatch between the group velocities of the pulse and the continuous wave. This is due to the fact that the magnetic permeability and susceptibility of the ferromagnet are changed in the process of propagation of the nonlinear wave in the ferromagnetic film because of a nonlinear frequency shift of the propagating wave. If a second wave has a frequency which falls into the frequency

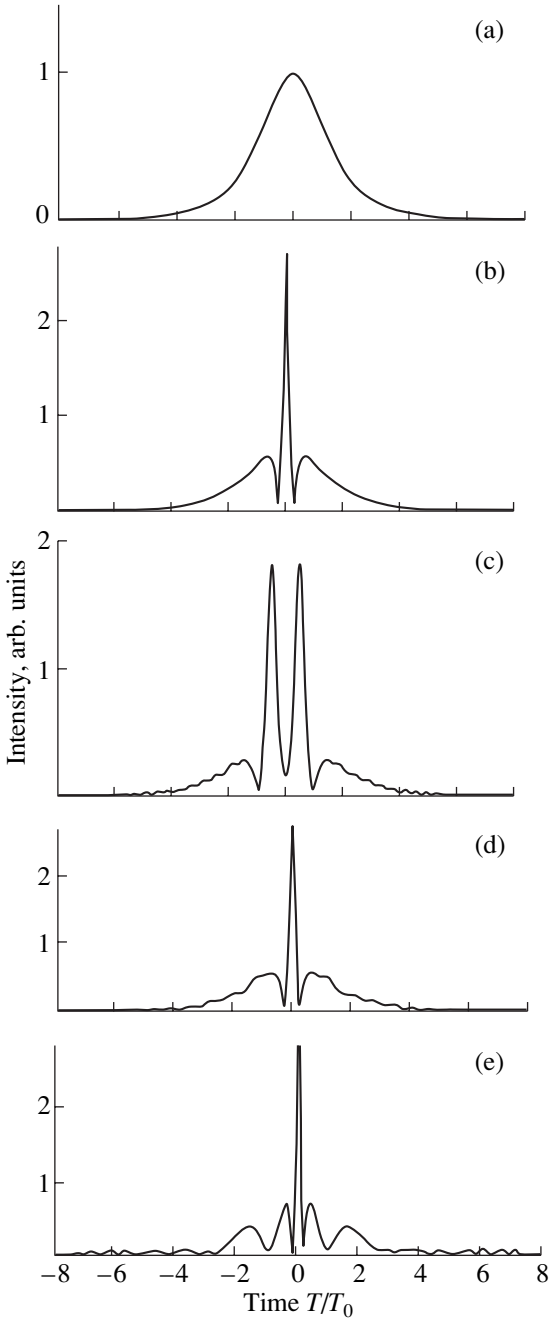

Fig. 2. The decay of the soliton of a direct bulk magnetostatic spin wave in the process of its interaction with the continuous pumping wave of a close frequency which differs from the central frequency of the pulse by 10 MHz (the intensity of the continuous wave is 0.2 times the power of the pulse peak). (a) The shape of the pulse fed to the receiving antenna; (b, c, d, e) the pulse shape at a distance of 1, 2, 3, and 4 mm away from the receiving antenna, respectively.

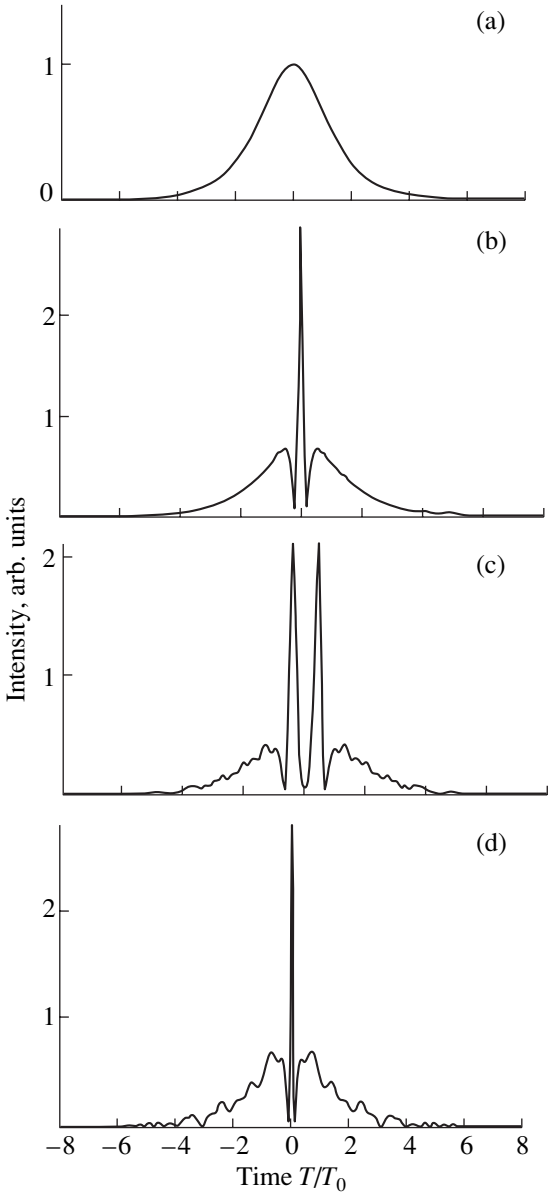

Fig. 3. The decay of the soliton of a direct bulk magnetostatic spin wave in the process of its interaction with the continuous pumping wave of a close frequency which differs from the central frequency of the pulse by 10 MHz (the intensity of the continuous wave is 0.8 times the power of the pulse peak). (a) The shape of the pulse fed to the receiving antenna; (b, c, d) the pulse shape at a distance of 1, 2, and 3 mm away from the receiving antenna, respectively.

region of the susceptibility change, then its characteristics can also be strongly changed. Phase cross-modulation, as well as self-modulation, induces frequency–phase modulation between two wave fronts. If the frequency mismatch between the pulse and the continuous wave is so large that the frequency of the continuous wave is out of the pulse spectrum, the interaction between two wave fronts will also be weak. In turn, the change in the shape and spectrum of the propagating pulse will also be weak. Due to the large mismatch between the group velocities of the interacting pulse and the continuous wave, the changes in the shape and spectrum of the pulse caused by cross-modulation have no time to accumulate and the change in the pulse shape

is entirely due to the self-modulation. A numerical simulation of this process shows that there are no changes in the shape of the output pulse, and the evolution of the interaction is similar to that shown in Fig. 1. In the case where the frequency of the continuous wave falls into the spectral range of the propagating pulse, the phase modulation due to the cross-modulation can lead to significant changes in the shape and spectrum of the pulse. If the intensity of the continuous wave is not small, the pulse can decay altogether, as demonstrated in Fig. 2. Figure 2a corresponds to the pulse entering the receiving antenna, Figs. 2b–2e show the shape of the pulse at a distance of 1, 2, 3, and 4 mm away from the receiving antenna, respectively.

The pulse carrier frequency is 3.7 GHz, and the continuous-wave frequency is 3.69 GHz. In this case, the interaction between the pulse and continuous wave becomes strong and this results in the soliton splitting into a number of pulses. This is possible even at small intensities of the propagating continuous wave (for Fig. 2, the intensity of the wave is 1 mW and the complete decay of the soliton takes place at distances of about 2 cm). The soliton decay becomes faster and occurs at shorter distances for increased continuous-wave intensity. Figure 3 shows the soliton decay in the process of its interaction with a continuous wave of intensity 10 mW. In this case, the soliton decays at distances of less than 1 cm.

Similar to Fig. 2, Fig. 3a corresponds to a pulse fed into the receiving antenna; Figs. 3b–3d demonstrate the pulse shape at distances of 1, 2, and 3 mm away from the entrance antenna, respectively. In the numerical calculations, we did not take into account the MSW damping in the process of propagation through the ferromagnetic films; it can be taken into account by introducing the corresponding terms into Eq. (1). However, damping should not change the general picture of the interaction between the solitons and the continuous pumping wave; it is possible that the effects leading to the soliton decay due to its interaction with the continuous wave will be revealed earlier and at smaller distances. Recently [9], it was demonstrated experimentally that a sufficiently intense MSW could completely suppress another MSW with a different, close frequency propagating in the same direction in the case of excitation of both waves in the continuous regime.

Thus, the interaction between MSW solitons and a continuous pump wave propagating in ferromagnetic films is studied in the present paper. It is shown that if the frequency of the continuous wave falls into the soliton spectral range, their interaction is strong and the soliton is split into separate pulses. This effect enables one to investigate the formation and propagation of solitons with the aid of continuously excited propagating waves of similar natures.

ACKNOWLEDGMENTS

This work was supported by the Russian Foundation for Basic Research, project no. 99-02-17600.

REFERENCES

1. M. Chen, M. A. Tsankov, J. M. Nash, and C. E. Patton, Phys. Rev. B **49**, 12773 (1994).
2. J. M. Nash, C. E. Patton, and P. Kabos, Phys. Rev. B **51**, 15079 (1995).
3. N. G. Kovshikov, B. A. Kalinikos, C. E. Patton, *et al.*, Phys. Rev. B **54**, 15210 (1996).
4. J. W. Boyle, S. A. Nikitov, A. D. Boardman, and K. Xie, J. Magn. Magn. Mater. **173**, 241 (1997).
5. A. O. Korotkevich and S. A. Nikitov, Zh. Éksp. Teor. Fiz. **116** (12), 2058 (1999).
6. R. Marcelli and S. A. Nikitov, Europhys. Lett. (in press).
7. N. J. Zabusky and M. D. Kruskal, Phys. Rev. Lett. **15**, 240 (1965).
8. Q. Park and H. J. Shin, Phys. Rev. Lett. **82**, 4432 (1999).
9. Yu. K. Fetisov, Pis'ma Zh. Tekh. Fiz. **26** (4), 8 (2000) [Tech. Phys. Lett. **26**, 315 (2000)].

Translated by A. Poushnov

Physics of the Solid State, Vol. 43, No. 5, 2001, pp. 888–889. Translated from Fizika Tverdogo Tela, Vol. 43, No. 5, 2001, pp. 855–856.

MAGNETISM AND FERROELECTRICITY

Effect of Frustration on the Magnetization in Nickel Ferrite–Chromites

L. G. Antoshina and A. N. Goryaga

Moscow State University, Vorob'evy gory, Moscow, 119899 Russia

Received October 3, 2000

Abstract—A study is reported on the behavior of the isotherms of the magnetization $\sigma(H)$ and of the longitudinal $\lambda_{\parallel}(H)$, transverse $\lambda_{\perp}(H)$, volume $\omega(H)$, and anisotropic $\lambda_t(H)$ magnetostrictions measured at $T = 80$ K in the $Cu_{0.4}Fe_{0.6}[Ni_{0.6}Cr_{1.4}]O_4$ and $Zn_{0.4}Fe_{0.6}[Ni_{0.6}Cr_{1.4}]O_4$ ferrite–chromites having a frustrated magnetic structure. It has been established that these ferrite–chromites do not undergo technical magnetization and that the growth of the magnetization with the field is accounted for by two paraprocesses of different natures. © *2001 MAIK "Nauka/Interperiodica".*

The frustrated magnetic structure in ferrites can be considered as consisting of spatially separated, spontaneously magnetized, ferrimagnetically ordered regions.

We earlier established [1, 2] that the ferrite–chromites of copper and cobalt with a high Cr^{3+} concentration in the octahedral sites have a frustrated magnetic structure. A Mössbauer study showed the $Fe[NiCr]O_4$ ferrite–chromite to be magnetically frustrated [3]. Therefore, we believe that the $Ni_{0.4}Fe_{0.6}[Ni_{0.6}Cr_{1.4}]O_4$ ferrite–chromite having a still higher content of Cr^{3+} ions should also possess a frustrated magnetic structure. The frustrated magnetic structure in the ferrite–chromites under study is possibly due to the fact that these samples contain more than three different species of magnetic cations, which are coupled through exchange interactions, opposite in sign and different in magnitude. Furthermore, the presence of strong direct exchange coupling between the Cr^{3+} ions on the octahedral sublattice can bring about noncollinear magnetic ordering in spatially separated, spontaneously magnetized regions.

This paper reports on a study of the magnetization processes in the $Cu_{0.4}Fe_{0.6}[Ni_{0.6}Cr_{1.4}]O_4$ and $Zn_{0.4}Fe_{0.6}[Ni_{0.6}Cr_{1.4}]O_4$ ferrites, because the $Ni_{0.4}Fe_{0.6}[Ni_{0.6}Cr_{1.4}]O_4$ ferrite–chromite possesses a strong magnetic anisotropy due to the presence of Ni^{2+} ions in the triplet state on the *A* sublattice with an incompletely quenched orbital angular momentum, which requires investigation of its properties in strong magnetic fields.

Samples of these ferrites were prepared using ceramic technology. Both anneals were performed in air at a temperature of 1270 K for 20 h, with subsequent slow cooling. X-ray diffraction measurements showed the samples to be single-phase spinels. The magnetization and coercive force were determined by the ballistic technique, and the magnetostriction, by strain measurements. The studies were carried out in magnetic fields of up to 10 kOe, the magnetization was measured at temperatures from 80 K to the Curie point, and the magnetostriction, at temperatures from 80 to 400 K.

The magnetization process in ferro- and ferrimagnets is known to consist of technical magnetization and the paraprocess (the true magnetization), whereas in the case of frustrated magnets, one would expect the magnetization to proceed in a different manner, because they do not have domains.

While the field dependence of magnetization cannot provide an answer to the question of the nature of magnetization, studying the $\lambda(H)$ isotherms can shed light on this problem, because the $\lambda(H)$ relation behaves differently in different processes. For instance, in conventional ferrimagnets, the longitudinal ($\lambda_{\parallel}$) and transverse ($\lambda_{\perp}$) magnetostrictions have opposite signs in the region of technical magnetization, and when saturation is reached, Akulov's rule $\lambda_{\parallel} = -2\lambda_{\perp}$ holds. Therefore, in the technical magnetization region, the volume magnetostriction $\omega = 0$ and the anisotropic magnetostriction $\lambda_t = \text{const}$. By contrast, in the region of the paraprocess, $\Delta\lambda_{\parallel}$ and $\Delta\lambda_{\perp}$ have the same sign and are equal in magnitude, which results in the volume magnetostriction ω becoming field-dependent, but the anisotropic magnetostriction remains constant, $\lambda_t = \text{const}$. It should be pointed out that in nonfrustrated ferrimagnets, the susceptibilities of the paraprocess, $\Delta\lambda_{\parallel}$ and $\Delta\lambda_{\perp}$, which are associated with the paraprocess, are, as a rule, negative.

Figures 1 and 2 present the isotherms of the magnetization σ and of the longitudinal ($\lambda_{\parallel}$) transverse ($\lambda_{\perp}$) volume (ω) and anisotropic (λ_t) magnetostrictions obtained at the temperature $T = 80$ K on the $Cu_{0.4}Fe_{0.6}[Ni_{0.6}Cr_{1.4}]O_4$ and $Zn_{0.4}Fe_{0.6}[Ni_{0.6}Cr_{1.4}]O_4$ samples, respectively. (The volume ω and anisotropic λ_t magnetostrictions were calculated from the expressions $\omega = \lambda_{\parallel} + 2\lambda_{\perp}$ and $\lambda_t = \lambda_{\parallel} - \lambda_{\perp}$.) The coercive force H_c of

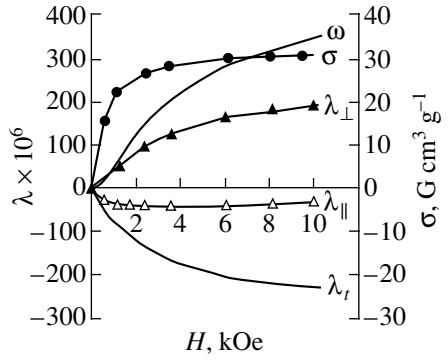

Fig. 1. Isotherms of the magnetization $\sigma(H)$ and of the longitudinal $\lambda_\parallel(H)$, transverse $\lambda_\perp(H)$, volume $\omega(H)$, and anisotropic $\lambda_t(H)$ magnetostrictions for the $Cu_{0.4}Fe_{0.6}[Ni_{0.6}Cr_{1.4}]O_4$ ferrite–chromite obtained at T = 80 K.

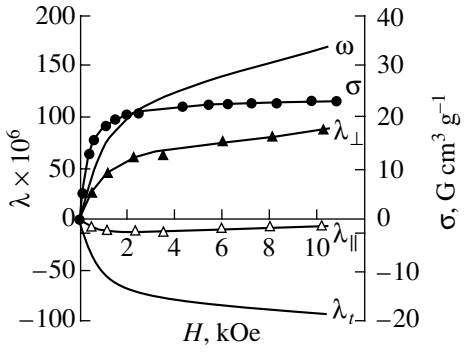

Fig. 2. Isotherms of the magnetization $\sigma(H)$ and of the longitudinal $\lambda_\parallel(H)$, transverse $\lambda_\perp(H)$, volume $\omega(H)$, and anisotropic $\lambda_t(H)$ magnetostrictions for the $Zn_{0.4}Fe_{0.6}[Ni_{0.6}Cr_{1.4}]O_4$ ferrite–chromite obtained at T = 80 K.

the $Cu_{0.4}Fe_{0.6}[Ni_{0.6}Cr_{1.4}]O_4$ and $Zn_{0.4}Fe_{0.6}[Ni_{0.6}Cr_{1.4}]O_4$ samples at the liquid nitrogen temperature was found to be 390 and 76 Oe, respectively, which means that the applied magnetic fields were certainly high enough. The isotherms $\sigma(H)$ of both samples are seen not to saturate; i.e., we have here a paraprocess, and a fairly weak one: in fields above 5 kOe, we have $\Delta\sigma \approx 2.6 \times 10^{-4}$ G cm^3 g^{-1} Oe^{-1} for the $Cu_{0.4}Fe_{0.6}[Ni_{0.6}Cr_{1.4}]O_4$ ferrite and $\Delta\sigma \approx 1.1 \times 10^{-4}$ G cm^3 g^{-1} Oe^{-1} for the $Zn_{0.4}Fe_{0.6}[Ni_{0.6}Cr_{1.4}]O_4$ ferrite. Note that the magnetostriction follows an anomalous behavior; namely, in all fields, the transverse magnetostriction $\lambda_\perp$ is substantially larger than the longitudinal one, $\lambda_\parallel$; i.e., Akulov's rule does not hold. It should be pointed out that the susceptibilities of the magnetostriction paraprocess $\Delta\lambda_\parallel$ and $\Delta\lambda_\perp$ are positive, but, in contrast to conventional ferrimagnets with a nonfrustrated magnetic structure, they are different in magnitude, $\Delta\lambda_\parallel < \Delta\lambda_\perp$.

As can be seen from Figs. 1 and 2, the volume magnetostriction ω is positive starting from low fields and it reaches a large magnitude $\omega \approx 3.5 \times 10^{-4}$ at H = 10 kOe for the $Cu_{0.4}Fe_{0.6}[Ni_{0.6}Cr_{1.4}]O_4$ ferrite and 1.7×10^{-4} for the $Zn_{0.4}Fe_{0.6}[Ni_{0.6}Cr_{1.4}]O_4$ ferrite. At the same time, the anisotropic magnetostriction λ_t does not saturate in all fields, while it is also quite large: $\lambda_t \approx -2.3 \times 10^{-4}$ for the $Cu_{0.4}Fe_{0.6}[Ni_{0.6}Cr_{1.4}]O_4$ ferrite and -0.9×10^{-4} for the $Zn_{0.4}Fe_{0.6}[Ni_{0.6}Cr_{1.4}]O_4$ ferrite.

Hence, our observation of the field dependence of the anisotropic magnetostriction λ_t indicates no technical magnetization in the $Cu_{0.4}Fe_{0.6}[Ni_{0.6}Cr_{1.4}]O_4$ and $Zn_{0.4}Fe_{0.6}[Ni_{0.6}Cr_{1.4}]O_4$ ferrites having a frustrated magnetic structure. The data on the volume magnetostriction ω also suggest that the magnetization is initiated primarily by the paraprocess.

Thus, we have established that the technical magnetization, which consists of displacement and canting processes, does not take place in the frustrated $Cu_{0.4}Fe_{0.6}[Ni_{0.6}Cr_{1.4}]O_4$ and $Zn_{0.4}Fe_{0.6}[Ni_{0.6}Cr_{1.4}]O_4$ ferrites and that the growth of the magnetization with the field occurs in two paraprocesses differing in nature. The first paraprocess involves rotation of the magnetic moments of spontaneously magnetized regions toward the external magnetic field, whereas the second of them, operating in higher fields, is caused by a decrease in the ion magnetic-moment noncollinearity in these spontaneously magnetized regions.

REFERENCES

1. L. G. Antoshina, A. N. Goryaga, E. N. Kukudzhanova, and I. A. Fil'gus, Zh. Éksp. Teor. Fiz. **111** (5), 1732 (1997) [JETP **84**, 948 (1997)].
2. K. P. Belov, A. N. Goryaga, R. R. Annaev, *et al.*, Fiz. Tverd. Tela (Leningrad) **31** (5), 117 (1989) [Sov. Phys. Solid State **31**, 785 (1989)].
3. J. K. Srivastava, K. Muraleedharan, and R. Vijayaraghavan, Phys. Status Solidi B **140**, K47 (1987).

Translated by G. Skrebtsov

Physics of the Solid State, Vol. 43, No. 5, 2001, pp. 890–897. Translated from Fizika Tverdogo Tela, Vol. 43, No. 5, 2001, pp. 857–864.

MAGNETISM AND FERROELECTRICITY

Magnon Spectrum Features Associated with the Linear Magnetoelectric Effect in a Finite Magnet

S. V. Tarasenko

Donetsk Physicotechnical Institute, National Academy of Sciences of Ukraine, Donetsk, 83114 Ukraine

Received October 9, 2000

Abstract—Using a mechanically free plate of a centrally antisymmetric tetragonal antiferromagnet of the easy-plane type as an example, it is shown that the linear magnetoelectric effect causes earlier unknown anomalies to occur in the bulk magnon spectrum. The character of these anomalies depends critically on the relationship between the Néel and Debye temperatures of the antiferromagnetic crystal. © *2001 MAIK "Nauka/Interperiodica".*

INTRODUCTION

The linear magnetoelectric effect in a magnetic crystal is of special interest when a spin wave propagating in the magnet is accompanied by an electrostatic rather than magnetostatic field, i.e., when the spin wave is of the electric-dipole type in this sense because of the magnetoelectric effect. Such a situation can be realized in centrally antisymmetric antiferromagnetic crystals, in which the linear magnetoelectric interaction can be generally represented in the form [1–5]

$$F_{pe} = \hat{\gamma}\mathbf{ImP}, \quad (1)$$

where γ is the tensor of the magnetoelectric coupling constants. In the two-sublattice antiferromagnet (AFM) model, $\mathbf{m} = (\mathbf{M}_1 + \mathbf{M}_2)/2M_0$ is the ferromagnetism vector, $\mathbf{l} = (\mathbf{M}_1 - \mathbf{M}_2)/2M_0$ is the antiferromagnetism vector, $\mathbf{M}_1$ and $\mathbf{M}_2$ are the sublattice magnetizations ($|\mathbf{M}_1| = |\mathbf{M}_2| = M_0$), and $\mathbf{P}$ is the electric polarization vector.

Calculations showed that both optical [6] and acoustic modes of the magnon spectrum [7] can be of the electric-dipole type in antiferromagnetic crystals exhibiting certain symmetry properties and possessing the magnetoelectric interaction (1). This makes possible the formation of surface and bulk magnetic polaritons of the TM and EM types in such AFMs [8]. There are many papers in which the conditions for the formation and propagation of magnetic polaritons in centrally antisymmetric antiferromagnetic crystals were analyzed, but the dependence of these conditions on the relationship between the Néel (T_N) and Debye (T_D) temperatures in a real AFM was not taken into account in them. At the same time, it is well known that in the case of low-temperature AFMs ($T_N < T_D$), the crystal lattice can dramatically affect the bulk magnon spectrum of the finite magnetic crystal [9, 10]. Furthermore, the influence of the lattice on the spin-wave spectrum is exchange-enhanced in AFMs [11].

In this paper, we consider a specific example to determine the conditions under which the presence of the linear magnetoelectric interaction in a centrally antisymmetric finite AFM leads to anomalies, hitherto unstudied, in the bulk magnon spectrum of the electric-dipole type, which are the result of combined electric-dipole, magnetic-dipole, magnetostatic, and inhomogeneous exchange interactions.

1. BASIC EQUATIONS

We assume that $|\mathbf{m}| \ll |\mathbf{l}| \approx 1$, i.e., that the relativistic interactions are weak in comparison with the exchange interaction between the sublattices. In this case, the energy density of a magnetoelectric two-sublattice AFM (including the magnetoelastic interaction) can be written in terms of the vectors $\mathbf{m}$ and $\mathbf{l}$ in the form [7]

$$F = F_m + F_{pe} + F_{me} + F_e + F_p, \quad (2)$$

where

$$F_m = M_0^2\left(\frac{\delta}{2}\mathbf{m}^2 + \frac{\alpha}{2}(\nabla\mathbf{l})^2 + \frac{b}{2}l_z^2 + \frac{\beta}{2}l_x^2l_y^2\right),$$

$$F_{me} = B_{iklm}l_il_ku_{lm}, \quad F_e = c_{iklm}u_{ik}u_{lm},$$

$$F_p = \frac{1}{2\kappa}P_z^2 + \frac{1}{2\kappa_\perp}(P_x^2 + P_y^2) - \mathbf{PE};$$

δ and α are the exchange constant and the exchange stiffness between the sublattices, respectively; b and β are the anisotropy constants ($b \gg \beta$); $\mathbf{E}$ is the electric field; $\kappa_\perp$ and κ are the dielectric susceptibilities; u_{ik} is the magnetoelastic strain tensor; and $\hat{B}$ and $\hat{c}$ are the magnetoelastic and elastic constants, respectively.

In the particular case of a tetragonal AFM with $4_z^{\pm}2_x^{+}I^{-}$ or $4_z^{\pm}2_x^{-}I^{-}$ structure, the magnetoelectric interaction energy F_{pe} has the form [3–5]

$$F_{pe} = -\gamma_1 P_z(m_x l_y \pm m_y l_x) - \gamma_2 m_z(P_x l_y \pm P_y l_x) - \gamma_3 l_z(m_x P_y \pm m_y P_x),$$
$$F_{pe} = -\gamma_1 m_z(l_x P_x \pm l_y P_y) - \gamma_2 P_z(m_x l_x \pm m_y l_y) - \gamma_3 l_z(m_x P_x \pm m_y P_y) - \gamma_4 l_z m_z P_z, \quad (3)$$

where $\hat{\gamma}$ are the magnetoelectric coupling constants. The dynamic properties of the system at hand are described phenomenologically by a set of coupled vector equations:

$$2/(gM_0)\mathbf{m}_t = [\mathbf{m}H_\mathbf{m}] + [\mathbf{l}H_\mathbf{l}],$$
$$2/(gM_0)\mathbf{l}_t = [\mathbf{l}H_\mathbf{m}] + [\mathbf{m}H_\mathbf{l}],$$
$$\mathbf{P}_{tt} = fH_\mathbf{P}, \quad \mathrm{curl}\,\mathbf{H} = \frac{\partial \mathbf{D}}{c\partial t}, \quad \mathrm{curl}\,\mathbf{E} = -\frac{\partial \mathbf{B}}{c\partial t}, \quad (4)$$
$$\mathrm{div}\,\mathbf{D} = 0, \quad \mathrm{div}\,\mathbf{B} = 0, \quad \rho\frac{\partial^2 u_i}{\partial t^2} = \frac{\partial^2 F}{\partial x_i \partial u_{ik}},$$

where $H_\mathbf{j} \equiv \delta H/\delta \mathbf{j}$ ($\mathbf{j} = \mathbf{m}, \mathbf{l}, \mathbf{P}$) and g is the gyromagnetic ratio. Calculations show that either of the two equilibrium magnetic configurations [of the easy-axis ($\mathbf{l} \parallel z$) and easy-plane ($\mathbf{l} \perp z$) types] is possible [7].

From Eq. (4), one can calculate the spectrum of normal vibrations of the model AFM; their dispersion relation is generally a seventh-degree algebraic equation in k^2. In order to simplify analytical calculations, we make the following assumptions.

(1) We restrict our consideration of the polariton spectrum to the short-wavelength limit case $\omega/c \longrightarrow 0$.

(2) In the magnon spectrum of the easy-plane-type configuration $\mathbf{l} \parallel x$, $|\mathbf{M}| = |\mathbf{P}| = 0$, symmetry $4_z^{\pm}2_x^-I^-$, we consider only normal spin-wave vibrations with $\tilde{m}_z$, $\tilde{l}_y \neq 0$,[1] because this branch of the magnon spectrum of the centrally antisymmetric AFM has fairly low activation energy and, therefore, is most strongly affected by the magnetoelectric and magnetoelastic interactions.

In the case where the frequency of vibrations of the system at hand satisfies the condition

$$\omega^2 \ll \min(g^2\delta^2 M_0^2, f/\kappa_\perp, f/\kappa), \quad (5)$$

one can eliminate **P** between Eqs. (4) and reduce them to a set of equations which describes the magnetoelastic dynamics of the magnetoelectric tetragonal easy-plane AFM in the electrostatic and magnetostatic approximation ($\omega/c \longrightarrow 0$) and involves only the variables $\tilde{m}_z$, $\tilde{l}_y$, ϕ, ψ, and $\mathbf{u}$ (with $\mathbf{H} = \nabla\phi$; $\mathbf{E} = \nabla\psi$). These coupled equations must be supplemented by boundary conditions, because we consider the spin dynamics of a finite magnetoelectric crystal. The magnetic medium is assumed to be an infinite plate with thickness $2d$, and at either of its surfaces, the boundary conditions for the exchange variables are taken to be of the form [12]

$$\frac{\partial \tilde{\mathbf{m}}}{\partial \zeta} + \delta_1 \tilde{\mathbf{m}} = 0, \quad \frac{\partial \tilde{\mathbf{l}}}{\partial \zeta} + \delta_1 \tilde{\mathbf{l}} = 0, \quad \zeta = \pm d, \quad (6)$$

where ζ is the coordinate along the normal **n** to the plate surface and δ_1 is the surface anisotropy constant. As for the elastic and electrodynamic boundary conditions, we assume that the corresponding expressions for the magnetostatic (ϕ) and electrostatic (ψ) potentials depend on the relative orientation of the normal **n**, the equilibrium direction of the antiferromagnetism vector **l**, and the direction of the spin-wave propagation $\mathbf{k}_\perp$. Thus, these boundary conditions are

$$\sigma_{ik} n_k = 0, \quad \zeta = \pm d, \quad (7)$$

$$\psi + \alpha^* \frac{\partial \psi}{\partial \zeta} = 0, \quad \zeta = \pm d,$$
$$\phi + \beta^* \frac{\partial \phi}{\partial \zeta} = 0, \quad \zeta = \pm d, \quad (8)$$

where $\hat{\sigma}$ is the elastic stress tensor, $\alpha^* = \alpha^*(\mathbf{l}/|\mathbf{l}|, \mathbf{k}_\perp/|\mathbf{k}_\perp|)$, and $\beta^* = \beta^*(\mathbf{l}/|\mathbf{l}|, \mathbf{k}_\perp/|\mathbf{k}_\perp|)$. For an extended discussion of the physical reasons for these boundary conditions, see, e.g., [13, 14].

Calculations in the rigid-lattice approximation ($\omega/c_{ph}|\mathbf{k}| \longrightarrow \infty$, with c_{ph} being the minimum phase velocity of elastic waves) show that the dispersion relation of the low-frequency magnon mode of an infinite high-temperature magnetoelectric AFM ($T_D < T_N$) for any direction of the wave vector **k** has the form

$$\omega^2 = [\omega_0^2 + \omega_{me}^2 + s^2\mathbf{k}^2] \times [1 + A_p k_x^2(\epsilon_\perp(k_x^2 + k_y^2) + \epsilon k_z^2)^{-1} + A_d k_z^2 \mathbf{k}^{-2}], \quad (9)$$

where $\omega_0^2 \equiv d^2 M_0^2 \delta\alpha$, $\epsilon_\perp = 1 + 4\pi\kappa_\perp$, $\epsilon = 1 + 4\pi\kappa$, $A_p \equiv 4\pi\alpha_1^2/\delta$, $A_d \equiv 4\pi/\delta$, $\alpha_1 \equiv \kappa_\perp\gamma$, $k^2 = k_x^2 + k_y^2 + k_z^2$, $s^2 = g^2 M_0^2 \alpha\delta$, and $\omega/c \longrightarrow 0$.

For an infinite low-temperature centrally antisymmetric AFM ($T_D > T_N$) described by Eq. (2), the dispersion relation of analogous normal low-frequency spin waves in the elastostatic approximation $\omega/c_{ph}|\mathbf{k}| \longrightarrow 0$ ($\omega/c \longrightarrow 0$) can be written in the form [13]

$$\omega^2 = [\omega_0^2 + \omega_{me}^2(1 - c_{66}(k_x^2 D_{11} + k_y^2 D_{22} - 2D_{12}k_x k_z)\rho^{-1}D^{-1}) + s^2\mathbf{k}^2] \times [1 + A_p k_x^2(\epsilon_\perp(k_x^2 + k_y^2) + \epsilon k_z^2)^{-1} + A_d k_z^2 \mathbf{k}^{-2}], \quad (10)$$

where $D \equiv \det|\Lambda_{ik}|$, with $i, k = 1, 2, 3$; D_{ik} is the algebraic adjunct of the element (i, k) of the determinant D; $\hat{\Lambda}$ is the Christoffel tensor; and δ_{ik} is the Kronecker delta.

[1] The tilde indicates that the oscillations of the corresponding quantity about its equilibrium value are small.

An analysis of Eqs. (2), (9), and (10) shows that spin waves of the type under consideration ($\tilde{m}_z, \tilde{l}_y \neq 0$) are accompanied by an electrostatic field (i.e., they are of the electric dipole type) at $k_x \neq 0$ and by a magnetostatic field (i.e., they are of the magnetic dipole type) at $k_z \neq 0$. For this reason, we restrict our consideration to the case of spin waves with $\mathbf{k} \in xz$ ($k_y = 0$). Thus, in this geometry, even if electromagnetic retardation is not taken into account, this type of normal vibrations of the magnetoelectric crystal corresponds to a propagating bulk polariton wave of the *EH* type. In what follows, we assume that one of the two coordinate axes in the *xz* plane coincides with the normal to the plate surface **n**.

To calculate the spectrum of bulk spin waves in a finite magnetoelectric crystal, one can employ the method developed in [15–17] for treating the effect of the magnetic dipole interaction on the spectrum of bulk exchange-type magnons propagating in a thin ferromagnetic film. For this purpose, by using Green's functions and the electrostatics and magnetostatics equations (for $\omega/c \longrightarrow 0$) subject to the boundary conditions in (8), one can express the amplitudes of the electrostatic (ψ) and magnetostatic (ϕ) potentials in terms of the amplitude of oscillations of the *z* component of the ferromagnetism vector **m** under the assumption that this vector is a given function of space coordinates. Therefore, the variables that are associated with the electrostatic and magnetostatic interaction can be excluded from consideration and the boundary-value problem at hand is reduced to a set of two integro-differential equations for $\tilde{m}_z, \tilde{l}_y \neq 0$ with exchange [Eq. (6)] and elastic [Eq. (7)] boundary conditions. Following the technique developed in [15–17], we solve the boundary-value problem by expanding $\tilde{m}_z$ in terms of the eigenfunctions of the exchange boundary-value problem (6). Introducing the notation $\boldsymbol{\tau} \perp \mathbf{n}$, $\kappa_\nu \equiv \pi\nu/2d$, where $\nu = 1, 2, \ldots$, we write

$$m_z(r, t) = \sum_\nu A_\nu \cos(\kappa_\nu \zeta) \exp(i\omega t - i\mathbf{k}_\perp \boldsymbol{\tau}),$$
$$\mathbf{n} \parallel x \quad (\delta_1 = 0),$$
$$m_z(r, t) = \sum_\nu A_\nu \sin(\kappa_\nu \zeta) \exp(i\omega t - i\mathbf{k}_\perp \boldsymbol{\tau}), \tag{11}$$
$$\mathbf{n} \parallel z \quad (1/\delta_1 = 0).$$

With this expansion, an infinite set of linear algebraic equations for the unknown amplitudes A_ν is arrived at, from which one can find the corresponding dispersion relation, which describes (in the short-wavelength limit) the spectrum of normal low-frequency spin waves ($\tilde{m}_z, \tilde{l}_y \neq 0$) with allowance for the magnetic-dipole, electric-dipole, and magnetoelastic interactions in a film of the centrally antisymmetric AFM.

Since the structure of this set of equations is qualitatively the same for different directions of the spin-wave propagation and the film normal **n**, we present here the corresponding expressions for the case of $\mathbf{k} \in xz$ and $\mathbf{n} \parallel z$ (see Appendix):

$$(W_{\nu\nu}(k_\perp) - \omega^2) A_\nu = W_{\nu\rho}(k_\perp) A_\rho, \quad \nu \neq \rho, \quad \nu, \rho = 1, 2, \ldots, \tag{12}$$

$$W_{\nu\nu}(k_\perp) = \left[\omega_0^2 + \omega_{me}^2 \frac{c_{44}\kappa_\nu^2}{c_{66}k_\perp^2 + c_{44}\kappa_\nu^2} + s^2(k_\perp^2 + \kappa_\nu^2) \right] \times [1 + A_p P_{\nu\nu}(k_\perp)/\epsilon_\perp + A_d R_{\nu\nu}(k_\perp)],$$
$$W_{\nu\rho}(k_\perp) = \left[\omega_0^2 + \omega_{me}^2 \frac{c_{44}\kappa_\nu^2}{c_{66}k_\perp^2 + c_{44}\kappa_\nu^2} + s^2(k_\perp^2 + \kappa_\nu^2) \right] \times [A_p P_{\nu\rho}(k_\perp)/\epsilon_\perp + A_d R_{\nu\rho}(k_\perp)]. \tag{13}$$

Thus, using Green's functions, we derived the spectrum of bulk magnons in a thin magnetoelectric film; this spectrum is represented in a form typical of the spectra obtained by the coupled-mode method [18]. In Eqs. (12) and (13), a diagonal element of the matrix $W_{\nu\rho}(k_\perp)$ determines the dispersion curve of the νth mode of the spectrum of bulk spin waves in the magnetoelectric film at hand. Each of the off-diagonal elements of the matrix $W_{\nu\rho}$ in Eqs. (12) and (13) can be considered a matrix element characterizing the coupling between the νth and ρth modes, the dispersion law of which is determined from Eqs. (12) and (13) to be $\omega^2 = W_{\nu\nu}(k_\perp)$ and $\omega^2 = W_{\rho\rho}(k_\perp)$, respectively. From Eqs. (12) and (13), it follows that for the spin-wave geometry under consideration, we have $W_{\nu\rho}(k_\perp) = 0$ if $\partial\phi/\partial\zeta = \psi = 0$ at $\mathbf{n} \parallel z$ ($1/\delta_1 = 0$) or at $\mathbf{n} \parallel x$ ($\delta_1 = 0$). In this case, the infinite matrix of the coefficients $W_{\nu\rho}(k_\perp)$ in Eqs. (12) and (13) becomes diagonal and the dispersion law of the bulk spin waves under study is given by

$$\Omega_\nu^2(k_\perp) = W_{\nu\nu}(k_\perp). \tag{14}$$

In order to analyze the contributions from different mechanisms to the magnon spectrum, we will apply the general expression (14) to some specific cases. One of them, as was mentioned in the Introduction, is the elastostatic approximation [13] for $T_N < T_D$, in which one ignores the fact that the velocity of elastic waves is finite ($\omega/c_{ph} \longrightarrow 0$); another case is the rigid-lattice approximation ($\omega/c_{ph} \longrightarrow \infty$) for $T_N > T_D$; and another corresponds to $\alpha \longrightarrow 0$, i.e., to a negligibly weak inhomogeneous exchange interaction (exchangeless approximation [12]).

2. SPIN DYNAMICS OF A MAGNETOELECTRIC FILM IN THE EXCHANGELESS APPROXIMATION

From Eq. (14), it follows that, in the approximations indicated above, the spectrum of bulk exchangeless magnons with $\mathbf{k} \in xz$ in a thin magnetoelectric film can be represented in the form (depending on the relationship between the Néel T_N and the Debye temperature T_D)

$$T_N > T_D, \quad \Omega_\nu^2(k_\perp) = R(k_\perp)(\omega_0^2 + \omega_{me}^2), \tag{15}$$

$$T_N < T_D, \quad \Omega_\nu^2(k_\perp) = R(k_\perp)(\omega_0^2 + \omega_{me}^2 c_{44} k_z^2 \times (c_{66}k_x^2 + c_{44}k_z^2)^{-1}), \tag{16}$$

where $R(k_\perp) \equiv 1 + A_d k_z^2 k^{-2} + A_p k_x^2 (\epsilon_\perp k_x^2 + \epsilon k_z^2)^{-1}$. In Eqs. (15) and (16), $k_z = \kappa_\nu$ and $k_x = k_\perp$ for $\mathbf{n} \parallel z$ and $k_z = k_\perp$ and $k_x = \kappa_\nu$ for $\mathbf{n} \parallel x$. Equations (15) and (16) show that the spectra of exchangeless spin waves have a condensation point at both $k_\perp \longrightarrow 0$ and $k_\perp \longrightarrow \infty$; that is, for two modes with fixed indices ν and ρ, we have $|\Omega_\nu(k_\perp) - \Omega_\rho(k_\perp)| \longrightarrow 0$. For a high-temperature centrally antisymmetric AFM, even without magnetostatic interaction ($A_d \longrightarrow 0$), the dispersion relation of bulk magnons of the electric-dipole type [Eq. (15)] corresponds to a direct wave ($\partial\Omega_\nu/\partial k_\perp > 0$) at $\mathbf{n} \parallel z$ and to a back wave ($\partial\Omega_\nu/\partial k_\perp < 0$) at $\mathbf{n} \parallel x$ (electrostatic spin waves), irrespective of the mode index ν. For a given wave number $k_\perp$ and a fixed mode index $\nu < \rho$, from Eq. (15) it follows that $\Omega_\nu(k_\perp) > \Omega_\rho(k_\perp)$ for $\mathbf{n} \parallel z$ and $\Omega_\nu(k_\perp) < \Omega_\rho(k_\perp)$ for $\mathbf{n} \parallel x$. For both types of spin waves, regardless of the mode index ν, the dispersion curves in Eq. (15) have an inflection point ($\partial^2\Omega_\nu/\partial k_\perp^2 = 0$) at $k_\perp \neq 0$. If the electric-dipole interaction is weak in comparison with the magnetic-dipole interaction ($\gamma \longrightarrow 0$), then for the geometry at hand, the character of the dispersion relation is changed, as follows from Eq. (15); for a given mode index ν, we have a back wave at $\mathbf{n} \parallel z$ and a direct wave at $\mathbf{n} \parallel x$. As for the effect of the magnetoelastic interaction on Eq. (15) for a high-temperature AFM, this interaction determines only the magnitude of the magnetoelastic gap ω_{me} and renormalizes the magnetic anisotropy constant, both these quantities being independent of the magnitude and direction of the wave vector $\mathbf{k}_\perp$.

When the magnetic-dipole and electric-dipole interactions are both represented in Eq. (15), the dispersion relation of exchangeless magnons for a given mode index ν at $\mathbf{n} \parallel x$, as well as at $\mathbf{n} \parallel z$, is a combination of both specific cases considered above and exhibits the following features:

(1) At $k_\perp = k_\nu$, an extremum can occur, which is a maximum or a minimum, depending on the parameters of the magnetoelectric AFM and the relative orientation of the film normal $\mathbf{n}$ in the xz plane.

(2) The dispersion curves of modes with indices ν and ρ ($\nu < \rho$) described by Eq. (15) can cross [$\Omega_\nu(k_\perp) = \Omega_\rho(k_\perp)$] at a certain point $k_\perp = k_{\nu\rho}$ ($k_\nu < k_{\nu\rho} < k_\rho$). In this case, if in the vicinity of the long-wavelength condensation point ($k_\perp \longrightarrow 0$) we have $\Omega_\nu(k_\perp) < \Omega_\rho(k_\perp)$ [or, alternatively, $\Omega_\nu(k_\perp) > \Omega_\rho(k_\perp)$] for $\nu < \rho$, then for the same curves in the vicinity of the short-wavelength condensation point ($k_\perp \longrightarrow 0$), we will have the opposite inequality $\Omega_\nu(k_\perp) > \Omega_\rho(k_\perp)$ [or $\Omega_\nu(k_\perp) < \Omega_\rho(k_\perp)$, respectively].

The physical reason for these anomalies in the spectrum of bulk exchangeless magnons in a finite high-temperature magnetoelectric crystal is the magnetoelectric effect, which gives rise to hybridization of the magnetic-dipole and electric-dipole indirect spin–spin interactions.

In a thin film of a low-temperature magnetoelectric AFM, the spectrum of exchangeless spin waves exhibits further anomalies in addition to those described by Eq. (15). A comparison of Eqs. (15) and (16) shows that, at $T_N < T_D$, in addition to the electric-dipole and magnetic-dipole mechanisms of dispersion of exchangeless magnons, there is also an indirect spin–spin interaction through the long-range field of quasi-static magnetoelastic deformations. For this reason, the dispersion of exchangeless spin waves in a thin AFM film takes place even if $A_{p,d} \longrightarrow 0$. In this case, the exchangeless magnons are called elastostatic spin waves [9, 10]. Because of this indirect spin–spin interaction in the geometry $\mathbf{k} \in xz$ and $\mathbf{n} \parallel x$ or $\mathbf{n} \parallel z$, even in the absence of magnetic-dipole and electric-dipole waves, the dispersion relation of an exchangeless magnon mode with index ν corresponds to a back wave at $\mathbf{n} \parallel z$ and to a direct wave at $\mathbf{n} \parallel x$ and has a condensation point at $k_\perp \longrightarrow 0$ and ∞.

Now, we will take into account that, in a film of a low-temperature magnetoelectric AFM, the indirect spin–spin exchange occurs not only through the long-range field of quasi-static magnetoelastic deformations but also through the electric-dipole and magnetic-dipole fields (i.e., $A_{p,d} \neq 0$ and $\hat{B} \neq 0$). An analysis of Eq. (16) reveals that hybridization of the magnetoelastic and dipolar mechanisms of dispersion of bulk exchangeless magnons gives rise to further anomalies in addition to those described by Eqs. (15) and (16) with $A_{p,d} \longrightarrow 0$. In particular, for $\mathbf{k} \in xz$, two extrema can occur at $k_\perp = k_{\pm\nu}$ on the dispersion curve of a magnon mode with a given index ν. One of these extrema is a maximum, and the other, a minimum. The extreme points $k_{\pm\nu}$ are determined from Eq. (16) by putting $\partial\Omega_\nu/\partial k_\perp = 0$. Furthermore, in contrast to Eqs. (15) and (16) with $A_{p,d} \longrightarrow 0$, the dispersion curves of modes with indices ν and ρ ($\nu < \rho$) have, in addition to the condensation points at $k_\perp \longrightarrow 0$ and ∞, not one but two cross points (crossovers) at $k_\perp = k_{\pm\nu\rho}$ (with $k_{-\nu} < k_{-\nu\rho} < k_{+\nu} < k_{+\nu\rho}$); that is, $\Omega_\nu(k_{\pm\nu\rho}) = \Omega_\rho(k_{\pm\nu\rho})$.

It should be noted that if, for the spectrum of bulk exchangeless spin waves which is considered in this section and described by Eq. (16), the equation $\partial\Omega_\nu/\partial k_\perp = 0$ has two positive roots ($k_{\pm\nu} \neq 0$), then the following rule is always fulfilled for modes with indices ν and ρ ($\nu < \rho$): if the inequality $\Omega_\nu < \Omega_\rho$ (or $\Omega_\nu > \Omega_\rho$) takes place in the vicinity of the long-wavelength degeneracy point of the spectrum (at $k_\perp \longrightarrow 0$), then it is also true in the vicinity of the short-wavelength condensation point (at $k_\perp \longrightarrow \infty$).

Up to this point, we have analyzed the spectrum of bulk spin waves of a finite centrally antisymmetric magnetoelectric AFM without considering the inhomogeneous exchange interaction ($\alpha \longrightarrow 0$). However, as we already mentioned in the Introduction, consistent theory must take into account not only the direct Heisenberg exchange interaction between the sublattices, but also the indirect (magnetic-dipole, electric-dipole, and elastostatic) spin–spin interaction in the magnetic subsystem of the crystal at hand. An analysis of the bulk magnon spectrum of a finite centrally antisymmetric AFM with regard to the inhomogeneous exchange interaction in addition to the magnetic-dipole, electric-dipole, and magnetoelastic interactions is presented in the following section.

3. EFFECTS OF THE INHOMOGENEOUS EXCHANGE INTERACTION

Now, we consider the case of $\alpha \neq 0$. From Eq. (14), it follows that if $\omega/c \longrightarrow 0$ and $\omega/c_{ph} \longrightarrow 0$ for $T_N < T_D$ (or $\omega/c \longrightarrow 0$ and $\omega/c_{ph} \longrightarrow \infty$ for $T_N > T_D$), then Eqs. (15) and (16) can be represented in the form

$$T_N > T_D, \quad \Omega_\nu^2(k_\perp) \equiv R(k_\perp)(\omega_0^2 + s^2k^2 + \omega_{me}^2), \quad (17)$$

$$T_N < T_D, \quad \Omega_\nu^2(k_\perp) \equiv R(k_\perp)(\omega_0^2 + s^2k^2 + \omega_{me}^2 c_{44}k_z^2 \times (c_{66}k_x^2 + c_{44}k_z^2)^{-1}). \quad (18)$$

Here, $k_z = \kappa_\nu$ and $k_x = k_\perp$ for $\mathbf{n} \parallel z$ ($1/\delta_1 = 0$) and $k_z = k_\perp$ and $k_x = \kappa_\nu$ for $\mathbf{n} \parallel x$ ($\delta_1 = 0$).

A comparison of Eqs. (15) and (16) with Eqs. (17) and (18) shows that if in the exchangeless limit [Eqs. (15) and (16)] the inequality $\Omega_\nu(k_\perp) < \Omega_\rho(k_\perp)$ takes place for modes with given indices ν and ρ ($\nu < \rho$) in the vicinity of a condensation point ($k_\perp \longrightarrow 0$ or ∞), then even in the case of an infinitely small exchange stiffness α, the condensation point can disappear and an additional crossover of the $\Omega_\nu(k_\perp)$ and $\Omega_\rho(k_\perp)$ dispersion curves described by Eqs. (17) and (18) can arise at $k_\perp \neq 0$. If this inequality does not take place in the vicinity of a condensation point of the dispersion curves of Eqs. (15) and (16), then at $\alpha \neq 0$ this point simply disappears in Eqs. (17) and (18). If in the vicinity of the short-wavelength condensation point of the spectrum in Eqs. (15) and (16) we have $\partial\Omega_\nu(k_\perp)/\partial k_\perp < 0$, then, in the presence of the inhomogeneous exchange ($\alpha \neq 0$), this condensation point will disappear and an additional minimum will occur on the $\Omega_\nu(k_\perp)$ dispersion curve at some point $k_\perp \neq 0$. A comparison of Eqs. (17) and (15) shows that the spectrum of propagating bulk spin waves in the high-temperature centrally antisymmetric AFM with $\alpha \neq 0$ differs dramatically from the spectrum in Eq. (15). In particular, if Eq. (15) is such that the equation $\partial\Omega_\nu/\partial k_\perp = 0$ has a positive root at $k_\perp \neq 0$ and this root corresponds to a maximum on the dispersion curve, then, in the presence of inhomogeneous exchange ($\alpha \neq 0$), an additional cross point will appear at $k_\perp \neq 0$ for the dispersion curves of modes with given indices ν and ρ, $\Omega_\nu(k_{\nu\rho}) = \Omega_\rho(k_{\nu\rho})$. It also follows from Eq. (17) that these two crossover points in the spectrum of bulk spin waves will occur only if the electric-dipole, magnetic-dipole, and inhomogeneous spin–spin exchange interactions are all present in the high-temperature AFM (i.e., $\hat{\gamma} \neq 0$, $\alpha \neq 0$). If in the vicinity of the short-wavelength condensation point in Eq. (15) we have $\Omega_\nu(k_\perp) < \Omega_\rho(k_\perp)$ for modes with indices $\nu < \rho$, then, as can be seen from Eq. (17), the indirect (electric-dipole and magnetic-dipole) spin–spin exchange in combination with the direct (Heisenberg) exchange will cause the appearance of a minimum at some $k_\perp \neq 0$ on the dispersion curve of a mode with index ν of the spectrum of dipole–exchange spin waves in a thin film of the magnetoelectric AFM with $T_N > T_D$. In the case of a film of the low-temperature centrally antisymmetric AFM, an analysis of Eq. (18) shows that even in the absence of the dipole interaction (which formally corresponds to the limit $4\pi \longrightarrow 0$, $\hat{\gamma} \longrightarrow 0$), the hybridization of the elastostatic and Heisenberg spin–spin interactions leads to the following specific features in the bulk magnon spectrum in comparison with the exchangeless ($\alpha \longrightarrow 0$) extreme case [Eq. (16)]: (i) the presence of two crossover points ($k_{\nu\rho}$) on the dispersion curves of elastic–exchange spin-wave modes with indices ν and ρ for $\mathbf{n} \parallel z$ or $\mathbf{n} \parallel x$ and (ii) a minimum on the $\Omega_\nu(k_\perp)$ dispersion curve of Eq. (18). In the exchangeless limit $\alpha \longrightarrow 0$, we have the following limit transition to the characteristic points of the spectrum in Eq. (16): $k_{\nu\rho} \longrightarrow 0$ and $k_{\nu\rho} \longrightarrow \infty$. When the electrostatic and magnetostatic indirect spin–spin interaction are taken into account in addition to the elastostatic and Heisenberg interactions, further anomalies occur in the bulk spin-wave spectrum in comparison with the pure elastic–exchange magnon spectrum (in the limit $4\pi \longrightarrow 0$, $\hat{\gamma} \longrightarrow 0$) considered above. First, in the cases where, in the vicinity of the short-wave length condensation point, the dispersion relation of exchangeless bulk spin waves in Eq. (16) is of the backwave type ($\partial\Omega_\nu/\partial k_\perp < 0$), the inclusion of the inhomogeneous exchange interaction leads to the appearance of a minimum on the corresponding dispersion curve. Second, from Eq. (18) it follows that at $\mathbf{n} \parallel x$ or $\mathbf{n} \parallel z$, the dispersion curves of modes with indices ν and ρ can cross each other [$\Omega_\nu/(k_\perp) = \Omega_\rho(k_\perp)$] as many as four

times, if at $\alpha \longrightarrow 0$ each of these curves has two extremum points at some $k_\perp \neq 0$. There is always an even number ($N_{\nu\rho}$) of crossings of dispersion curves of modes with indices ν and ρ at $\alpha \neq 0$, as can be seen from Eq. (18); with an increase in $(\kappa_\nu^2 - \kappa_\rho^2)$, the quantity $N_{\nu\rho}$ can change (increase or decrease), but always by an even number. For large enough indices ν and ρ, or for a sufficiently small thickness of the $2d$ magnetic film, the dispersion relation $\Omega_\nu(k_\perp)$ in Eqs. (17) and (18) is of the direct-wave type ($\partial\Omega_\nu/\partial k_\perp > 0$) for any value of the wave number $k_\perp$ and has no inflection point ($\partial^2\Omega_\nu/\partial k_\perp^2 = 0$) and no crossover [$\Omega_\nu(k_\perp) = \Omega_\rho(k_\perp)$].

As is known from crystallography [19], when analyzing the reflection and refraction of a bulk normal wave at the boundary of a crystal, the shape of the refraction (slowness) surface of the normal wave is of prime importance. Therefore, the local geometry of the wave-vector surface of normal bulk waves of an infinite crystal significantly affects the structure of the spectrum of normal bulk vibrations of a finite crystal, because the spatial distribution of the amplitude of bulk vibrations is determined by the interference of bulk waves incident on and reflected from the boundaries of the crystal. In the next section, we analyze the effect of the electric-dipole, magnetic-dipole, elastostatic, and inhomogeneous exchange interactions on the shape of the refraction surface of normal spin waves in an infinite magnet and the relationship between the local geometry of this surface and the anomalies of the bulk magnon spectrum investigated above in thin films of magnetoelectric high-temperature and low-temperature AFMs.

4. THE SHAPE OF THE REFRACTION SURFACE

In Eqs. (17) and (18), the wave vector of the spin waves under study lies in the xz plane. Therefore, we should examine the shape of the intersection of the k_xk_z plane and the constant-frequency surface ($\omega = \text{const}$) of magnons under study in $\mathbf{k}$ space by using Eqs. (9) and (10), derived under the assumption that $\omega/c \longrightarrow 0$ and $\omega/c_{ph} \longrightarrow 0$ for $T_N < T_D$ and $\omega/c \longrightarrow 0$ and $\omega/c_{ph} \longrightarrow \infty$ for $T_N > T_D$. These equations can be rewritten in the form

$$T_N > T_D, \quad s^2\mathbf{k}^2 = \omega^2[1 + A_p\sin^2\theta(\epsilon_\perp\cos^2\theta + \epsilon\sin^2\theta)^{-1} + A_d\cos^2\theta]^{-1} - \omega_0^2 - \omega_{me}^2, \tag{19}$$

$$T_N < T_D, \quad s^2\mathbf{k}^2 = \omega^2[1 + A_p\sin^2\theta(\epsilon_\perp\cos^2\theta + \epsilon\sin^2\theta)^{-1} + A_d\cos^2\theta]^{-1} - \omega_0^2 - \omega_{me}^2c_{44}\cos^2\theta \times (c_{66}\sin^2\theta + c_{44}\cos^2\theta)^{-1}, \tag{20}$$

where $k_x^2/k^2 \equiv \sin^2\theta$ and $\mathbf{k}^2 \equiv k_x^2 + k_z^2$. An analysis of the extremum points of the curves described by Eqs. (19) and (20) and a comparison with the results of the analysis of the dispersion relations (17) and (18) presented above shows that a local maximum on the dispersion curve of the waveguide magnon under study is associated with the region of maximum negative curvature in the corresponding cross section of the refraction surface of the normal spin wave of the same polarization in the infinite crystal described by Eqs. (19) and (20). The position of a maximum on the curve in $\mathbf{k}$ space described by Eqs. (19) and (20) is determined by the condition $\partial k/\partial\theta = 0$ and is a single-valued function of frequency ω, mode index ν, film thickness $2d$, and wave number $k_\perp$ of the waveguide magnon described by Eqs. (17) and (18). If the refraction surface of Eqs. (19) and (20) has a portion in which its curvature reaches a local maximum ($\partial k/\partial\theta = 0$), then, as analysis shows, the dispersion curve of a bulk spin wave of the electric-dipole type of Eqs. (17) and (18) has a local minimum at the corresponding values of ω, ν, d, and $k_\perp$.

Now, we consider the intersection points of a curve described by Eq. (19) or Eq. (20) and a straight line $k_x = \text{const}$ or $k_z = \text{const}$. An analysis of common points of such a straight line and the refraction surface of Eqs. (19) and (20) allows one to obtain further information on the spectrum of the corresponding waveguide magnon with a given wave number $k_\perp$, frequency ω, and mode index ν [i.e., on the curves described by Eqs. (17) and (18)]. In particular, if the normal $\mathbf{n}$ to the film surface, lying in the k_xk_z plane, coincides with the z axis ($\mathbf{n} \parallel z$), then the number of common points of the straight line $k_x = k_\perp$ and the curve described by Eq. (19) or Eq. (20) determines the mode indices ν of bulk spin waves of the electric-dipole type that can propagate along the x axis in the $2d$-thick film and have the same wave number $k_\perp$ and frequency ω; that is, the number of crossovers is determined. In this geometry, the common points of a curve in Eq. (19) or (20) and the straight line $k_x = \kappa_\nu$ determine the values of the wave number $k_\perp$ with which a waveguide magnon of the given type (with the fixed mode index ν and frequency ω) can propagate in the thin film $2d$ thick. An analysis of Eqs. (17)–(20) shows that the local geometry of a cross section of the constant-frequency surface described by Eqs. (19) and (20) dictates the type of wave (direct or back) associated with that portion of the dispersion curve in Eqs. (17) and (18) which corresponds to a waveguide magnon with a given ω, κ_ν, and $k_\perp$, because the outward normal to the refraction surface determines the direction of the group velocity of waves [19]. In the particular case of $\mathbf{k} \in xz$ considered here, a bulk spin wave corresponding to Eq. (17) or Eq. (18) and propagating along the film with $\mathbf{n} \parallel z$ will be of the back-wave type if the x component of the outward normal to the refraction surface at the intersection point of this surface and the straight line $k_z = \kappa_\nu$ is negative; if the x component of the outward normal is negative, the corresponding wave will be of the direct-wave type for the given values of $k_\perp$, ω, and κ_ν. This component can

be equal to zero at some point $k_\perp \neq 0$; this will be the case if there is an extremum at this value of $k_\perp$ on the dispersion curve of a bulk wave propagating with mode index ν and frequency ω along the $2d$-thick film. The character of this extremum (maximum or minimum) is determined by the sign of the local curvature of the dispersion curve of Eq. (19) or Eq. (20) at this point.

Up to this point, we have analyzed the magnon spectrum of a thin film of a magnetoelectric AFM by treating the interaction of the spin and elastic subsystems only in the elastostatic approximation ($\omega/c_{ph} \longrightarrow 0$) for $T_N < T_D$ or in the rigid-lattice approximation ($\omega/c_{ph} \longrightarrow \infty$) for $T_N > T_D$. At the same time, the dispersion relations (12) and (13), which take into account the electric-dipole, magnetic-dipole, and inhomogeneous exchange interactions, have been derived for an arbitrary value of $\omega/c_{ph}|\mathbf{k}|$. This allows one to make a more comprehensive analysis of the spectrum of normal bulk magnetoelastic vibrations of a thin film of a centrally antisymmetric AFM. This will be done in another paper.

5. CONCLUSIONS

In this paper, by using a film of a centrally antisymmetric antiferromagnet as an example, we have found the necessary conditions under which the linear magnetoelectric effect gives rise to earlier unknown anomalies in the bulk magnon spectrum. For these anomalies to occur, both the finite size of the crystal and the relationship between the Néel and Debye temperatures are of fundamental importance. Among the specific features of the bulk magnon spectrum affected by the magnetoelectric interaction are the following:

(1) Exchangeless bulk spin waves can propagate in a thin film of the centrally antisymmetric AFM; their spectrum $\Omega_\nu(k_\perp)$ depends critically on the relationship between the Néel and Debye temperatures, shows a nonmonotonic dependence on the wave number $k_\perp$, and has condensation points at $k_\perp \longrightarrow 0$ and ∞.

(2) In the presence of the inhomogeneous exchange interaction, as well as in the exchangeless approximation, the $\Omega_\nu(k_\perp)$ dispersion curve can have portions in which $\partial\Omega_\nu/\partial k_\perp = 0$ at some points $k_\perp \neq 0$. These points can correspond to both a local maximum and a local minimum of this dispersion curve.

(3) Crossover of $\Omega_\nu(k_\perp)$ dispersion curves (caused by elastostatic, magnetostatic, electrostatic, and Heisenberg exchange spin–spin interactions) can occur at some points $k_\perp \neq 0$ for normal bulk spin waves with mode indices ν and ρ propagating in the thin magnetoelectric film.

(4) The interrelation takes place between the local geometry of the refraction surface of normal spin waves in an infinite crystal and the spectrum of waveguide vibrations in a thin film of the same material. The correlation between the shape of the refraction surface and the spectrum and type (direct or back waves) of waveguide vibrations also takes place for other types of normal excitations of an infinite crystal (phonons, excitons, etc.).

In this paper, all calculations were carried out for the easy-plane AFM with $4_z^{\pm}2_x^- I^-$ in the case where the equilibrium state is characterized by $\mathbf{l} \parallel x$ and $|\mathbf{m}| = 0$ and the wave vector is $\mathbf{k} \in xz$ ($k_y = 0$). It is easy to verify that similar features of the bulk magnon spectrum will also be observed in a centrally antisymmetric easy-plane AFM with a $4_z^{\pm}2_x^+ I^-$ magnetic structure. All the results obtained above are valid in this case for the same configuration of the equilibrium state ($\mathbf{l} \parallel x$, $|\mathbf{m}| = 0$), but $\mathbf{k} \in yz$ ($k_x = 0$) if the substitution $k_z \longrightarrow k_y$ is made. It can be shown that in both these cases the magnon spectrum in question is the short-wavelength limit of the low-frequency branch of the spectrum of bulk magnetic *EH* polaritons in the magnetoelectric crystal under study.

ACKNOWLEDGMENTS

The author is grateful to E.P. Stefanovskiĭ, V.E. Tarasenko, and I.E. Dragunov for their encouragement and helpful discussions.

APPENDIX

$$W_{\nu\nu}(k_\perp) = [\omega_0^2 + s^2(k_\perp^2 + \kappa_\nu^2)] \times [1 + A_p P_{\nu\nu}(k_\perp)/(\epsilon + A_d R_{\nu\nu}(k_\perp))],$$

$$W_{\nu\rho}(k_\perp) = [\omega_0^2 + s^2(k_\perp^2 + \kappa_\nu^2)] \times [A_p P_{\nu\rho}(k_\perp)/\epsilon + A_d R_{\nu\rho}(k_\perp)],$$

$$P_{ik}(k_\perp) = \kappa_i\kappa_k \int_{-d}^{d} dy \cos(\kappa_i y) \frac{\partial}{\partial y} \int_{-d}^{d} dt G(y, t) \sin(\kappa_k t),$$

$$R_{ik}(k_\perp) = k_\perp^2 \int_{-d}^{d} dz \cos(\kappa_i z) \int_{-d}^{d} dt F(z, t) \cos(\kappa_k t),$$

$$G(\zeta, t) \equiv \begin{cases} \sinh(ak_\perp(t - d + \zeta_\alpha)) \\ \times \sinh(ak_\perp(\zeta + d + \zeta_\alpha))/\Delta_G, & -d \le \zeta \le t \\ \sinh(ak_\perp(t + d + \zeta_\alpha)) \\ \times \sinh(ak_\perp(\zeta - d + \zeta_\alpha))/\Delta_G, & t \le \zeta \le d, \end{cases}$$

$$\coth(\zeta_\alpha ak_\perp) = \alpha^*/a, \quad \Delta_G \equiv ak_\perp \sinh(2ak_\perp d),$$

$$a^2 \equiv \epsilon/\epsilon_\perp, \quad \alpha^* \equiv \epsilon_2/\epsilon_\perp,$$

$$F(\zeta, t) \equiv \begin{cases} \cosh(ak_\perp(t - d + \zeta_\beta)) \\ \times \cosh(ak_\perp(\zeta + d + \zeta_\beta))/\Delta_F, \quad -d \le \zeta \le t \\ \cosh(ak_\perp(t + d + \zeta_\beta)) \\ \times \cosh(ak_\perp(\zeta - d + \zeta_\beta))/\Delta_F, \quad t \le \zeta \le d, \end{cases}$$

$$\tanh(\zeta_\beta k_\perp) = \beta^*, \quad \Delta_F \equiv k_\perp \sinh(2k_\perp d), \quad \beta^* \equiv \mu_2.$$

REFERENCES

1. R. V. Pisarev, Ferroelectrics **162** (1–4), 191 (1994).
2. S. Bluck and H. G. Kahle, J. Phys. C **21** (29), 5193 (1988).
3. E. A. Turov, V. V. Men'shenin, and V. V. Nikolaev, Zh. Éksp. Teor. Fiz. **104** (6), 4157 (1993) [JETP **77**, 1014 (1993)].
4. E. A. Turov, Zh. Éksp. Teor. Fiz. **104** (5), 3886 (1993) [JETP **77**, 868 (1993)].
5. E. A. Turov, Ferroelectrics **162** (1–4), 253 (1994).
6. V. N. Krivoruchko and D. A. Yablonskiĭ, Zh. Éksp. Teor. Fiz. **94** (9), 268 (1988) [Sov. Phys. JETP **67**, 1886 (1988)].
7. V. D. Buchel'nikov and V. G. Shavrov, Zh. Éksp. Teor. Fiz. **109** (2), 706 (1996) [JETP **82**, 380 (1996)].
8. S. V. Tarasenko, Opt. Spektrosk. **87** (6), 1024 (1999) [Opt. Spectrosc. **87**, 936 (1999)].
9. A. L. Sukstanskiĭ and S. V. Tarasenko, Zh. Éksp. Teor. Fiz. **105** (4), 928 (1994) [JETP **78**, 498 (1994)].
10. S. V. Tarasenko, Zh. Éksp. Teor. Fiz. **110** (4), 1411 (1996) [JETP **83**, 778 (1996)].
11. E. A. Turov and V. G. Shavrov, Usp. Fiz. Nauk **140** (3), 429 (1983) [Sov. Phys. Usp. **26**, 593 (1983)].
12. A. G. Gurevich and G. A. Melkov, *Magnetic Oscillations and Waves* (Nauka, Moscow, 1994).
13. V. A. Krasil'nikov and V. V. Krylov, *Introduction to Physical Acoustics* (Nauka, Moscow, 1984).
14. V. I. Alshits, A. N. Darinskii, and J. Lothe, Wave Motion **16** (3), 265 (1992).
15. O. G. Vendik and D. N. Chartorizhskiĭ, Fiz. Tverd. Tela (Leningrad) **12** (5), 1538 (1970) [Sov. Phys. Solid State **12**, 1209 (1970)].
16. B. A. Kalinikos, Izv. Vyssh. Uchebn. Zaved., Fiz. **24** (8), 42 (1981).
17. B. A. Kalinikos and A. N. Slavin, J. Phys. C **19** (35), 7013 (1986).
18. A. Yariv and P. Yeh, *Optical Waves in Crystals: Propagation and Control of Laser Radiation* (Wiley, New York, 1984; Mir, Moscow, 1987).
19. Yu. I. Sirotin and M. P. Shaskol'skaya, *Fundamentals of Crystal Physics* (Nauka, Moscow, 1979; Mir, Moscow, 1982).
20. Yu. V. Gulyaev and P. E. Zil'berman, Izv. Vyssh. Uchebn. Zaved., Fiz. **31** (11), 6 (1988).

Translated by Yu. Epifanov

Physics of the Solid State, Vol. 43, No. 5, 2001, pp. 898–901. Translated from Fizika Tverdogo Tela, Vol. 43, No. 5, 2001, pp. 865–868.

MAGNETISM AND FERROELECTRICITY

Effect of Cu^{2+}–O^{2-} Covalency on the Magnetostriction of Ferrite Spinels

L. G. Antoshina and A. N. Goryaga

Moscow State University, Vorob'evy gory, Moscow, 119899

Received October 17, 2000

Abstract—The magnetostriction of a number of copper-containing ferrite spinels was measured. In all the ferrites studied, below room temperature, $|\lambda_{||}|$ was found to decrease with temperature. It is conjectured that this decrease in $|\lambda_{||}|$ originates from an increase in the degree of covalency among the Cu^{2+}–O^{2-} ions, which, in turn, reduces their spin–orbit coupling. © *2001 MAIK "Nauka/Interperiodica".*

The large magnetostriction of the ferrite spinels is due to the spin–orbit coupling of the 3*d* cations in the ferrite, whose ground state in a crystal field of cubic symmetry is the orbital triplet. Note that the magnetostriction can grow only at temperatures comparable with the spin–orbit coupling energy.

At the same time, ferrites having 3*d* ions whose ground state is the orbital doublet can also possess considerable magnetostriction, provided the upper triplet state can be admixed to the lower doublet orbital state [1]. This admixture was found by EPR to exist for Cu^{2+} ions residing at the octahedral sites of the spinel lattice [1].

The formation of covalent bonding, due to which the electron spin is no longer localized at the central ion, does not affect the spin angular momentum [2], but this is not the case with the orbital angular momentum. It was shown [2] that covalent bonding results in a decrease in the matrix elements of the orbital angular momentum, which changes the shape of the spin–orbit coupling spectrum if the covalency is taken into account. One cannot, therefore, exclude the possibility that a change in the degree of covalent bonding between the O^{2-} ligand and the 3*d* cation, which gives rise to a change in the cation orbital state, can affect the contribution of these 3*d* cations to the magnetostriction.

X-ray diffraction studies [3] showed that the degree of covalent bonding in the copper ferrite $CuFe_2O_4$ is the greatest among the simple ferrites $CuFe_2O_4$, $CoFe_2O_4$, $ZnFe_2O_4$, and $MnFe_2O_4$.

Our earlier study of the polycrystalline, tetragonally distorted ferrite $CuFe_2O_4$ revealed an anomalous behavior of the magnetostriction; namely, as the temperature was lowered below 350 K, the $\lambda_\perp$ and $|\lambda_{||}|$ magnetostrictions exhibited a rapid growth followed by a pronounced decrease for $T \le 250$ K [4]. Based on these observations, we suggested that the copper ferrite undergoes a phase transition at $T_{t2} = 240 \pm 5$ K caused by the increased degree of covalency between the Cu^{2+} and O^{2-} ions, which, in turn, brings about a stronger lattice compression [5].

To check this conjecture, in this work, we studied the behavior of the magnetostriction of a number of copper-containing ferrites possessing a spinel structure. The table shows the compositions of the ferrites

Sample parameters

Sample	*c*, Å	*b*, Å	*a*, Å	*c*/*a*	*b*/*a*	$\lambda_{||} \times 10^6$
$CuFe_2O_4$	8.536	–	8.260	1.034	–	–27.6
$Cu_{1.2}Ge_{0.2}Fe_{1.6}O_4$	8.570	8.328	8.085	1.060	1.030	–4.67
$CuFe_{1.8}Al_{0.2}O_4$	8.504	8.332	8.124	1.047	1.027	–4.15
$CuFe_{1.7}Al_{0.3}O_4$	8.488	8.312	8.180	1.038	1.016	–10.2
$CuFe_{1.8}Cr_{0.2}O_4$	8.579	–	8.259	1.038	–	–16.0
$CuFe_{1.7}Cr_{0.3}O_4$	8.568	–	8.259	1.037	–	–6.6
$CuGa_{0.2}Al_{0.2}Fe_{1.6}O_4$	8.599	8.221	8.211	1.047	1.001	–5.2
$CuGa_{0.3}Al_{0.3}Fe_{1.4}O_4$	–	–	8.299	–	–	–11.25

1063-7834/01/4305-0898$21.00 © 2001 MAIK "Nauka/Interperiodica"

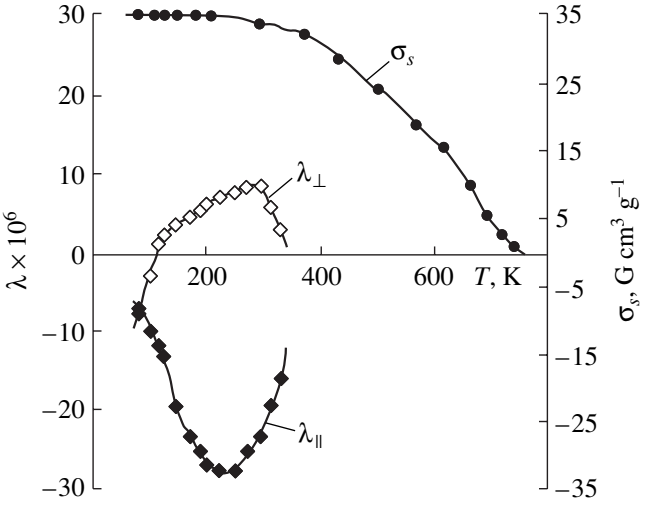

Fig. 1. Temperature dependences of the spontaneous magnetization σ_s and longitudinal $\lambda_{\parallel}$ and transverse $\lambda_{\perp}$ magnetostrictions of the $CuFe_2O_4$ ferrite obtained at H = 10.25 kOe.

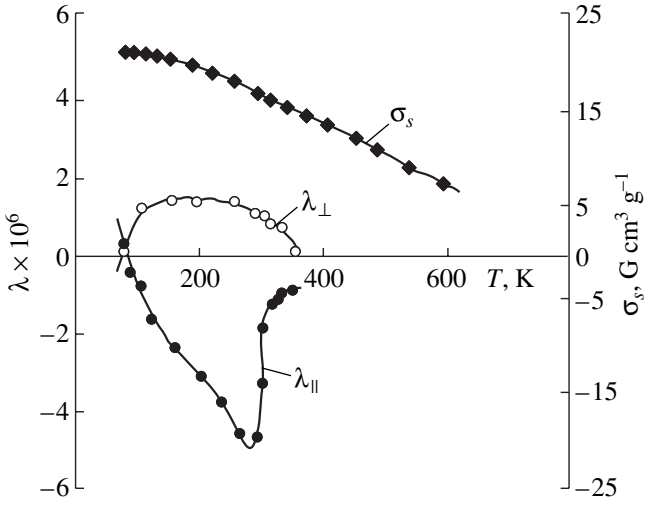

Fig. 2. Temperature dependences of the spontaneous magnetization σ_s and longitudinal $\lambda_{\parallel}$ and transverse $\lambda_{\perp}$ magnetostrictions of the $Cu_{1.2}Ge_{0.2}Fe_{1.6}O_4$ ferrite obtained at H = 12 kOe.

studied. All the samples were prepared using ceramic technology. The first anneal was performed at 750°C; the second, at 900°C, followed by a slow cooling. Both anneals were carried out in air. The x-ray diffraction analysis, made at room temperature, showed all the samples to be single-phase; the lattice parameters and the tetragonal axis ratio are specified in the table. The magnetization was determined by the ballistic method within the temperature interval from 80 to 650 K, and the magnetostriction was determined by strain gauge measurements in magnetic fields of up to 12 kOe at temperatures ranging from 80 to 100 K. The maximum longitudinal magnetostriction $\lambda_{\parallel}$ of each sample is also specified in the table.

Figure 1 presents temperature dependences of the spontaneous magnetization σ_s and of the longitudinal ($\lambda_{\parallel}$) and transverse ($\lambda_{\perp}$) magnetostrictions of $CuFe_2O_4$ (the data were taken from [5]). One readily sees that below room temperature, the longitudinal magnetostriction $|\lambda_{\parallel}|$ grows rapidly in magnitude, but it falls off as the temperature is lowered further.

Because the tetragonal sites are energetically preferable for the Ge^{4+} ion, the cations in the germanium-substituted copper ferrite should be distributed as $Ge_{0.2}Fe_{0.8}[Cu_{1.2}Fe_{0.8}]O_4$. Thus, substitution of the quadrivalent Ge^{4+} ion for the trivalent Fe^{3+} ions in $CuFe_2O_4$ increases the number of the Cu_B^{2+} divalent ions occupying the octahedral sites of the $Cu_{1.2}Ge_{0.2}Fe_{1.6}O_4$ ferrite. Figure 2 displays the temperature dependences of σ_s, $\lambda_{\parallel}$, and $\lambda_{\perp}$ for this ferrite. One readily sees that the $|\lambda_{\parallel}|$ and $\lambda_{\perp}$ magnetostrictions grow rapidly in magnitude near 300 K; however, the former decreases as the temperature is lowered further. Interestingly, no anomalies were observed in the temperature dependence $\sigma_s(T)$. A comparison of Figs. 1 and 2 reveals that the $\sigma_s(T)$, $\lambda_{\parallel}(T)$, and $\lambda_{\perp}(T)$ characteristics (H = 12 kOe) of the $Cu_{1.2}Ge_{0.2}Fe_{1.6}O_4$ sample behave similarly to those of the $CuFe_2O_4$ copper ferrite.

Note that the lattice parameter a for the sample with germanium is substantially smaller than that of the unsubstituted copper ferrite $CuFe_2O_4$. Therefore, the tetragonal axis ratio c/a of $Cu_{1.2}Ge_{0.2}Fe_{1.6}O_4$ is larger than that of $CuFe_2O_4$ (see table). By contrast, the magnetostriction magnitude $|\Delta\lambda_{\parallel}|$ of the sample with a higher Cu^{2+} concentration at the B sites of the spinel lattice became six times lower. Also, the maximum derivative of the magnetostriction with respect to temperature, $|\Delta\lambda_{\parallel}|/\Delta T$, for the $Cu_{1.2}Ge_{0.2}Fe_{1.6}O_4$ ferrite in the region of 300 K is $\approx 1.4 \times 10^{-6}$ K^{-1}, and that for $CuFe_2O_4$ is $|\Delta\lambda_{\parallel}|/\Delta T \approx 0.21 \times 10^{-6}$ K^{-1}, which is nearly seven times smaller. This gives us grounds to assume that the strong decrease in the absolute value of the magnetostriction $|\Delta\lambda_{\parallel}|$ of the $Cu_{1.2}Ge_{0.2}Fe_{1.6}O_4$ ferrite can only be associated with the increasing degree of covalency with decreasing temperature.

Similar results were obtained by us when measuring the magnetostriction of the $CuFe_{1.7}Al_{0.3}O_4$ ferrite, whose lattice parameters were earlier determined within the temperature range from 10 to 290 K [6]. An x-ray diffraction study of $CuFe_{1.7}Al_{0.3}O_4$ and $Cu_{1.2}Ge_{0.2}Fe_{1.6}O_4$ samples [6] showed them to have an orthorhombically distorted spinel structure (see table). It was established that the lattice parameters of the $CuFe_{1.7}Al_{0.3}O_4$ ferrite behave anisotropically with temperature; more specifically, the variation of the dimensions is strongest along the a axis, while along the c

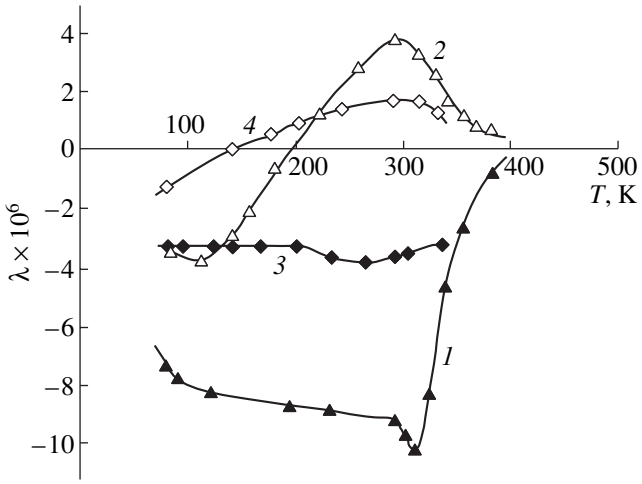

Fig. 3. Temperature dependences of (*1*, *3*) longitudinal $\lambda_{\parallel}$ and (*2*, *4*) transverse $\lambda_{\perp}$ magnetostrictions for (*1*, *2*) the $CuFe_{1.7}Al_{0.3}O_4$ and (*3*, *4*) $CuFe_{1.8}Al_{0.2}O_4$ ferrites obtained in a field $H = 12$ kOe.

axis no changes were observed to occur within the temperature interval studied. As a result of the anisotropy in thermal expansion, the deviation from the cubic structure (c/a, b/a) is likewise a function of temperature, and while the c/a ratio decreases smoothly with increasing temperature, the b/a ratio starts to decrease noticeably only above 150 K. This also suggests concluding that the enhancement of the cation–anion covalent bonding in the $CuFe_{1.7}Al_{0.3}O_4$ ferrite results in a stronger lattice compression.

Figure 3 presents the temperature dependences of the longitudinal ($\lambda_{\parallel}$) and transverse ($\lambda_{\perp}$) magnetostrictions for the $CuFe_{1.7}Al_{0.3}O_4$ ferrite obtained in a field $H = 12$ kOe. The steep growth of $|\lambda_{\parallel}|$ is seen to stop when the sample is cooled below room temperature, as is the case in the unsubstituted copper ferrite $CuFe_2O_4$. A similar behavior of the temperature dependences of the longitudinal $|\lambda_{\parallel}|$ and transverse $\lambda_{\perp}$ magnetostrictions was also observed by us to hold in the $CuFe_{1.8}Al_{0.2}O_4$ ferrite (Fig. 3). However, the $|\lambda_{\parallel}|$ for this composition became one-half that for the $CuFe_{1.7}Al_{0.3}O_4$ ferrite. As can be seen from the table, as the Fe^{3+} ions continue to be replaced by the Al^{3+} ions, the c and b parameters, as well as the c/a and b/a ratios, decrease.

It should also be pointed out that the maximum of the magnitude of the longitudinal magnetostriction $|\lambda_{\parallel}|$ depends directly on the degree of tetragonal distortion of the sample lattice. For instance, the room-temperature c/a ratios for the $CuFe_2O_4$, $CuFe_{1.7}Al_{0.3}O_4$, and $CuFe_{1.8}Al_{0.2}O_4$ compositions are 1.034, 1.038, and 1.047, respectively, while the $|\lambda_{\parallel}|_{max}$ are 27.6×10^{-6}, 10.2×10^{-6}, and 4.15×10^{-6}.

These results support our assumption on the effect of the degree of covalency on the magnetostriction of copper-containing ferrites. As the lattice distortion increases, the overlap of the Cu^{2+} e_g orbitals (more specifically, of the $d_{x^2-y^2}$ orbitals) obviously also increases, and this gives rise to an enhancement of the covalent bonding, which, in turn, decreases the spin–orbit coupling in these ions.

Similar dependences of the longitudinal and transverse magnetostrictions on temperature were also obtained in a study of the copper ferrite–chromites $CuFe_{1.8}Cr_{0.2}O_4$ and $CuFe_{1.7}Cr_{0.3}O_4$. The copper gallate–aluminates $CuGa_{0.2}Al_{0.2}Fe_{1.6}O_4$ and $CuGa_{0.3}Al_{0.3}Fe_{1.4}O_4$ also exhibit a decrease in $|\lambda_{\parallel}|_{max}$ with increasing distortion of the lattice (see table) [7].

All the copper-containing ferrites studied include octahedral Cu_B^{2+} ions, whose orbital doublet splits into two singlets below the Jahn–Teller transition temperature in the copper ferrite ($T_c \approx 630$ K). Therefore, the orbital angular momenta of the Cu_B^{2+} ions should be, in a first approximation, quenched completely by the crystal field, thus resulting in a practically zero spin–orbit coupling. However, as follows from EPR data [1], spin–orbit coupling in the Cu_B^{2+} ions admixes some of the triplet states to the ground doublet state. This gives rise not only to deviation of the g factor from its pure spin value but also to its anisotropy; indeed, we have $g_{\perp} \sim 2.1$, while $g_{\parallel} \sim 2.4$. Thus, EPR data suggest that the orbital angular momentum of the Cu_B^{2+} ion is not completely quenched; i.e., its spin–orbit coupling is not zero.

It is known that ferrites with a spinel structure are ionic compounds with a noticeable admixture of cation–anion covalent bonding. The formation of covalent bonding in ionic compounds does not affect the magnitude of the spin magnetic moment, whereas the orbital angular momentum decreases [2]. Hence, a change in the degree of covalency should affect the magnitude of the spin–orbit coupling. Based on the above results on magnetostriction, we believe that, for $T \leq T_{t2}$, the degree of covalent bonding between the Cu_B^{2+} and O^{2-} ions in a copper ferrite increases, which, in turn, reduces the spin–orbit coupling in these ions.

Our experimental study of the magnetostriction of copper-containing ferrites permits one to conclude that, in order to prepare materials with a high magnetostriction, one should choose compositions with a very small degree of covalent bonding between the 3d ions and oxygen.

REFERENCES

1. A. Abragam and B. Bleaney, *Electron Paramagnetic Resonance of Transition Ions* (Clarendon Press, Oxford, 1970; Mir, Moscow, 1972), Vol. 1.
2. A. Abragam and B. Bleaney, *Electron Paramagnetic Resonance of Transition Ions* (Clarendon Press, Oxford, 1970; Mir, Moscow, 1972), Vol. 2.
3. V. Sahastabudhe and A. S. Vaingahar, Solid State Commun. **43** (4), 299 (1982).
4. K. P. Belov, A. N. Goryaga, and L. G. Antoshina, Fiz. Tverd. Tela (Leningrad) **15** (10), 2895 (1973) [Sov. Phys. Solid State **15**, 1935 (1973)].
5. L. G. Antoshina, A. N. Goryaga, E. A. Kamzolov, and E. N. Kukudzhanova, Zh. Éksp. Teor. Fiz. **110** (6), 2087 (1996) [JETP **83**, 1149 (1996)].
6. K. P. Belov, L. G. Antoshina, and A. S. Markosyan, Fiz. Tverd. Tela (Leningrad) **25** (9), 2791 (1983) [Sov. Phys. Solid State **25**, 1609 (1983)].
7. L. G. Antoshina and E. N. Kukudzhanova, Fiz. Tverd. Tela (St. Petersburg) **40** (8), 1505 (1998) [Phys. Solid State **40**, 1366 (1998)].

Translated by G. Skrebtsov

Physics of the Solid State, Vol. 43, No. 5, 2001, pp. 902–907. Translated from Fizika Tverdogo Tela, Vol. 43, No. 5, 2001, pp. 869–873.

MAGNETISM AND FERROELECTRICITY

Phase Transformation Kinetics Induced in Thin Sol–Gel PZT Films under Thermal Annealing

V. Ya. Shur, E. B. Blankova, A. L. Subbotin, E. A. Borisova, and A. V. Barannikov

Institute of Physics and Applied Mathematics, Ural State University, Yekaterinburg, 620083 Russia

e-mail: Vladimir.Shur@usu.ru

Received August 24, 2000

Abstract—The surface morphology evolution and phase transformation kinetics in thin lead zirconate–titanate (PZT) sol–gel films during rapid thermal annealing were studied by *in situ* measurement of scattered light intensity and by recording successive instantaneous optical microscope images. We also studied the variation of the texture perfection, the fraction of the growing phase, and the angular dependence of the scattered intensity in partially annealed samples. The parameters characterizing the kinetics of the pyrochlore–perovskite phase transformation were derived by a mathematical treatment of the experimental data. The phase transformation kinetics and the film crystalline texture are shown to depend substantially on the pyrolysis temperature. The texture formation mechanism is considered. © *2001 MAIK "Nauka/Interperiodica".*

INTRODUCTION

Thin ferroelectric films are presently prepared mostly by chemical techniques. The most widely used approaches capable of producing high-quality films are the sol–gel technique and decomposition of metal-organic compounds. In all these methods, crystallization and formation of the corresponding phase are achieved by thermal treatment of amorphous films. Annealing sol–gel films of lead zirconate–titanate $Pb(Zr,Ti)O_3$ (PZT) produces a perovskite phase (which possesses ferroelectric properties) through an intermediate phase of a pyrochlore-type structure.

The thermal treatment conditions strongly affect the film microstructure [1–3] and ferroelectric characteristics [4]. Obviously, the kinetics of formation of the intermediate phase in the course of crystallization and the pyrochlore–perovskite phase transformation depends substantially on the heating rate. The best ferroelectric characteristics were shown to be obtained under thermal annealing performed at high heating rates (rapid thermal anneal) [5]. However, there are practically no reports of *in situ* studies on the crystallization/phase transformation kinetics under rapid thermal anneal conditions because traditional methods are not capable of providing a high enough time resolution. *In situ* studies making use of x-ray diffraction measurements [6] and spectroscopic ellipsometry [7] were done only for slow crystallization/phase transformation processes. We have developed a method based on *in situ* measurement of the elastically scattered light intensity, which is sensitive to instantaneous changes in the surface morphology and has a high enough time resolution [8–11]. The method proposed for the mathematical treatment of experimental data provides a possibility of extracting information on the phase transformation kinetics [10].

In this work, the light-scattering method was used for a comprehensive study of the evolution of the surface morphology of PZT sol–gel films under isothermal anneal with rapid heating. It is shown that by analyzing experimental data one can derive the main parameters characterizing the kinetics of formation of texturized perovskite in PZT. To check the validity of the interpretation of the results obtained, the optical data were compared with traditional x-ray diffraction measurements on partially annealed films.

1. EXPERIMENTAL TECHNIQUES

We studied phase transformation kinetics occurring under an isothermal anneal performed at a fast heating rate in $Pb_{1.1}(Zr_{0.47}Ti_{0.53})O_3$ (110/47/53) films with a 10% excess of Pb in order to compensate for its annealing-induced losses. 400–600 nm thick films, found to be amorphous by x-ray diffraction, were deposited on $Pt/Ti/SiO_2/Si$ substrates coated by an epitaxial platinum layer (about 200 nm thick). Two lots of films prepared in identical conditions and differing in the pyrolysis temperature T_{pyr}, 380 and 490°C, were studied.

The annealing employed was isothermal (within the range of 600 to 750°C) with a heating rate of about 100°C/s. We measured the integrated scattered light intensity within an angular interval of 2°–30° directly in the course of the anneal and obtained a sequence of instantaneous videorecorded images of the heterophase structure viewed through an optical microscope. To compare the results of optical measurements with other experimental data and to measure the angular dependences of scattered light, the studies were performed on

partially annealed samples representing fragments of the same plate, which were annealed in different conditions.

To study x-ray diffraction characteristics of the partially annealed films, we obtained θ–2θ diffraction profiles with Co K_α radiation at room temperature within an angular interval of 20° to 65°. We measured the anneal time dependences of the textured-perovskite (111) reflection intensity, integrated pyrochlore (222) reflection intensity, and integrated intensities of the untextured-perovskite (011), (001), and (002) reflections.

The difference in the refractive indices between the perovskite and pyrochlore phases permitted visualization of the spatial phase distribution with an optical microscope [12]. A comparison of the scattered light-intensity measurements with the film surface images obtained by optical and electron microscopy showed that (i) the light scattering at the bottom electrode–film interface and in the bulk of the film is negligible and (ii) the measured angular dependences are sensitive only to changes in the surface morphology [13, 14].

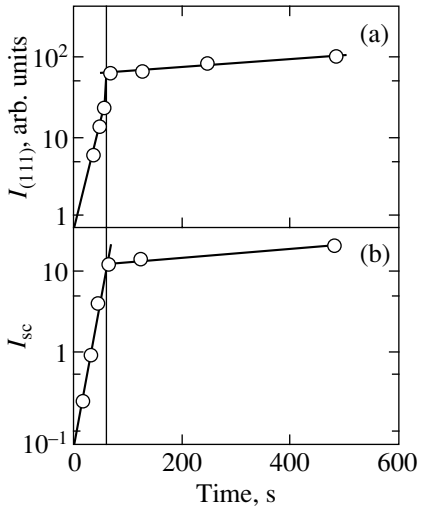

Fig. 1. Anneal time dependences of (a) x-ray diffraction intensity of the textured perovskite phase (111) reflection and (b) integrated scattered light intensity. The experimental data are fitted by exponential relations. T_{an} = 600°C, T_{pyr} = 380°C.

2. EXPERIMENTAL RESULTS

The phase transformation kinetics was studied in considerable detail by making partial anneals lasting from 15 s to 16 min. The low annealing temperature, T_{an} = 600°C, permitted one to ensure reproducibility of the anneal conditions even in the fast initial stage of the process.

As can be seen from a comparison of the optical and x-ray diffraction studies, the dependences of the texture reflection intensity and of the integrated scattered-light intensity on the anneal time follow a similar course (Fig. 1). These dependences can be divided into two stages of exponential growth with substantially different time constants (Fig. 1). For samples with T_{pyr} = 380°C, the fast growth stage lasts 60 s with a time constant $\tau_f \sim 12$ s. The time constant of the slow growth stage τ_s is 880 s.

Direct observation of the evolution of film morphology under annealing revealed that the different growth stages are specified by different geometries of the growing regions filled by perovskite grains. In the rapid anneal stage, isolated regions were observed to grow and coalesce, while the transition to the slow growth stage was marked by the formation of a maze structure.

The obtained anneal time dependences of the integrated scattered intensity I_{sc} and of the intensity of the textured perovskite phase reflection $I_{(111)}$ were fitted by a modified Kolmogorov–Avrami formula [15–17], describing the kinetics of two-dimensional growth in the α model (for constant nucleation intensity and growth rate) with due account of the geometric catastrophe (decrease in the growth dimensionality):

$$I(t) = \begin{cases} I_0 + \Delta I_f\{1 - \exp[-(t - t_d)^3/\tau_{f\alpha}^3]\}, & t < t_{cat} \\ I_0 + \Delta I_s\{1 - \exp[-(t - t_d)^2/\tau_{s\alpha}^2]\}, & t > t_{cat}, \end{cases} \quad (1)$$

where t_d is the delay time; t_{cat} is the catastrophe time; and $\tau_{f\alpha}$ and $\tau_{s\alpha}$ are the time constants for the fast and slow growth stages, respectively.

2.1. Studies of Samples with a Low Pyrolysis Temperature

X-ray diffraction measurements showed that, in the initial state (T_{pyr} = 380°C), a PZT film represents a mixture of an amorphous phase and a pyrochlore phase (Fig. 2d).

The phase transformation process occurring under thermal annealing can be divided into three stages, namely, delay, fast growth, and slow growth.

In the delay stage, the textured perovskite phase does not form (Fig. 2b) and the scattered light intensity associated with the variation of the film surface morphology I_{sc} practically does not change (Fig. 2c). X-ray diffraction studies revealed a noticeable growth of the amount of pyrochlore (Fig. 2a). A small number of crystallites of untextured perovskite were observed by optical microscopy and x-ray diffraction to form and grow slowly. This growth is apparently associated with crystallization on defects.

The fast stage reflects a fast growth of the amount of textured perovskite and a decrease in the amount of

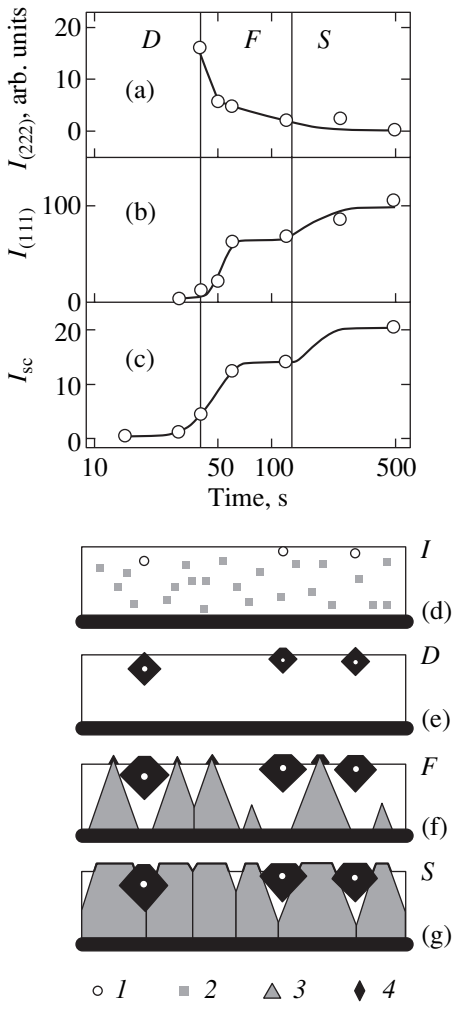

Fig. 2. Anneal time dependences of (a) x-ray diffraction intensity $I_{(222)}$ of the pyrochlore phase reflection, (b) x-ray diffraction intensity $I_{(111)}$ of the textured perovskite phase reflection, and (c) integrated scattered light intensity I_{sc}. Schematic illustration of the main stages in film morphology evolution in the course of annealing: (d) initial film stage after the pyrolysis (*I*), (e) growth delay stage (*D*), (f) fast growth (*F*), and (g) slow growth (*S*). T_{an} = 600°C, T_{pyr} = 380°C. (*1*) Defects, (*2*) pyrochlore, (*3*) textured perovskite, and (*4*) untextured perovskite.

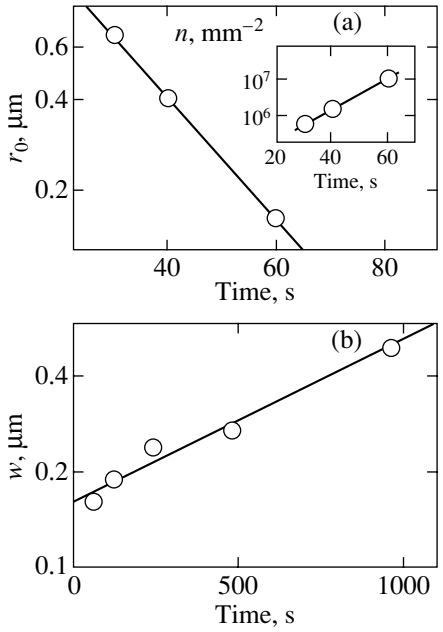

Fig. 3. Anneal time dependences of (a) average separation between scattering centers r_0 in the fast growth stage and (b) average perovskite-phase strip width in the maze structure w in the slow growth stage. The experimental data are fitted by exponentials. Inset: increase in the perovskite crystallite concentration in the fast growth stage. T_{an} = 600°C, T_{pyr} = 380°C.

pyrochlore. The perovskite phase grows epitaxially on textured platinum. Perovskite crystallites form at the film–substrate interface and thread rapidly through the bulk of the film as a result of the growth anisotropy (Fig. 2f) [1, 3]. This is paralleled by a slow increase in the amount of untextured perovskite. The fast rise of $I_{(111)}$ is accompanied by clearly pronounced optical effects. The rise of I_{sc} (Fig. 2c) indicates a change in the surface morphology. This change was observed through an optical microscope, and it brought about changes in the angular dependence of the scattered light intensity I_{sc}. The increase in the angle ϕ_{max} corresponding to the scattered light maximum can be related to the decreasing average distance between individual scattering centers r_0 because of the increasing number of the crystallites. The position of the maximum was used to determine the average distance between the scattering centers $r_0(t)$:

$$r_0(\phi_{max}) = \lambda/(4\pi\sin\phi_{max}), \quad (2)$$

where λ is the incident light wavelength.

The $r_0(t)$ relation (Fig. 3a) was fitted by an exponential (τ_f = 22 s). We determined the variation of the perovskite crystallite concentration in the fast growth stage (see inset in Fig. 3a):

$$n(t) \approx 0.25 r_0^{-2}. \quad (3)$$

The slow growth stage is accompanied by a qualitative change in the surface morphology observed by means of an optical microscope. The slowing down of the lateral growth rate gives rise to the formation of a maze structure, which corresponds to a percolation-type geometric transition and a decrease in the growth dimensionality, $2D \longrightarrow 1D$. The growth of $I_{(111)}$ slows down (τ_s = 850 s).

The change in the film surface morphology results in an increase in I_{sc} and a decrease in ϕ_{max} because of the increasing average maze period of the heterophase structure w:

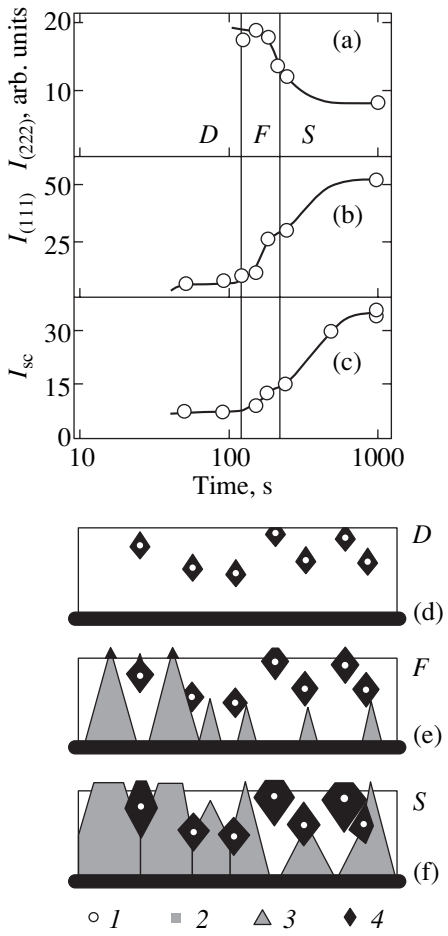

Fig. 4. Anneal time dependences of (a) x-ray diffraction intensity $I_{(222)}$ of the pyrochlore phase reflection, (b) x-ray diffraction intensity $I_{(111)}$ of the textured-perovskite-phase reflection, and (c) integrated scattered light intensity I_{sc}. Schematic illustration of the main stages in film morphology evolution in the course of annealing: (d) growth delay (*D*), (e) fast growth (*F*), and (f) slow growth (*S*). (*1*) Defects, (*2*) pyrochlore, (*3*) textured perovskite, and (*4*) untextured perovskite. T_{an} = 600°C, T_{pyr} = 490°C.

$$w(\phi_{max}) = \lambda/(4\pi\sin\phi_{max}). \quad (4)$$

The experimental data on $w(t)$ (Fig. 3b) were fitted by an exponential dependence (τ_s = 870 s). The features obtained were assigned to the perovskite recrystallization accompanied by a slow decrease in the pyrochlore fraction.

2.2. Studies of Samples with a High Pyrolysis Temperature

Samples with T_{pyr} = 490°C were also subjected to annealing at T_{an} = 600°C (Fig. 4). The observed variation of the main characteristics is similar to that obtained for samples with a low-temperature pyrolysis, but with substantially longer time constants (see Table 1).

In the initial stage, the amorphous phase was practically absent, with the films consisting of pyrochlore and untextured perovskite only. The increase in the delay stage time (Fig. 4d) may be caused by substantial lead losses in the course of the pyrolysis. The associated pyrochlore stabilization [18] impedes the formation of textured perovskite. In addition, we observed a slow growth of the amount of untextured perovskite.

The fast growth of textured perovskite from the substrate is hampered (Fig. 4b), because the untextured perovskite forming during the anneal suppresses the growth of perovskite grains in the direction perpendicular to the film surface (Fig. 4e).

In the slow growth stage (Fig. 4f), the pyrochlore transforms gradually to textured perovskite. We also observed a slow growth in the amount of untextured perovskite.

2.3. In Situ Measurements of the Fast Phase Transformation Kinetics

The methods of analysis of optical measurements developed here made it possible to study the kinetics of the fast phase transformation at T_{an} = 650°C, which cannot be investigated by conventional x-ray diffraction (Fig. 5). The variation of the integrated scattered intensity was measured directly in the course of annealing of a sample. Obviously, the measurement accuracy is, in this case, substantially higher than that for a series of partially crystallized samples. The value t_{cat} thus obtained corresponds to completion of the fast perovskite growth stage and to a decrease in the growth dimensionality, $\alpha(2D) \longrightarrow \alpha(1D)$.

The variation of the film surface morphology in the course of isothermal annealing at T_{an} = 650°C was studied by optical microscopy in a modified thermostat. We

Table 1. Parameters derived from an experimental data treatment for partially annealed films (T_{an} = 600°C)

	τ_f, s	τ_s, s	t_{d1}, s	$\tau_{f\alpha}$, s	$\tau_{s\alpha}$, s	t_{cat}, s		τ_f, s	τ_s, s	t_{d1}, s	$\tau_{f\alpha}$, s	$\tau_{s\alpha}$, s	t_{cat}, s
	T_{pyr} = 380°C							T_{pyr} = 490°C					
$I_{(222)}$	–17	–125	32	14	178	65	$I_{(222)}$	–180	–1550	132	83	225	220
$I_{(111)}$	13	850	36	18	162	115	$I_{(111)}$	113	1230	83	90	278	245
I_{sc}	12	890	18	33	119	140	I_{sc}	250	3160	85	101	362	240
r_0	22	870											

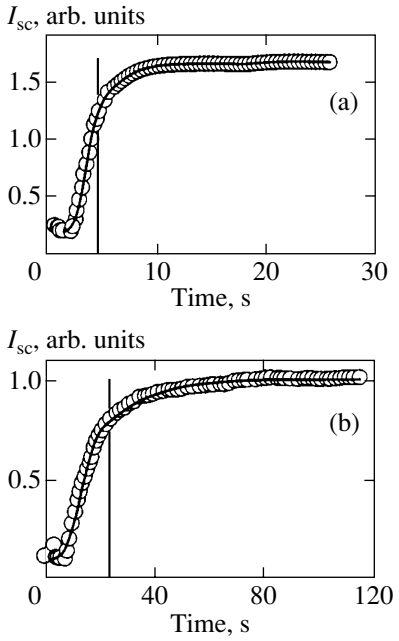

Fig. 5. Integrated scattered light intensities measured directly in the course of annealing. The experimental data are approximated by Eq. (1). T_{an} = 650°C; T_{pyr}: (a) 380, and (b) 490°C.

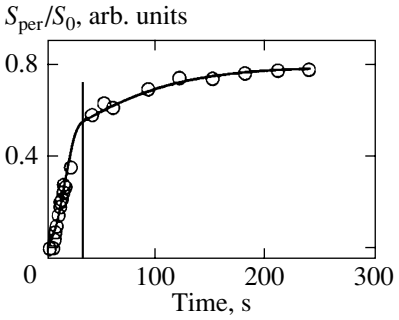

Fig. 6. Evolution of the film surface area fraction occupied by perovskite grains in the course of annealing. The experimental data are approximated by Eq. (1). T_{an} = 650°C; T_{pyr} = 490°C.

succeeded in experimentally discriminating regions corresponding to different phases [12]. The phase transition was accompanied by a growth in the number and size of the regions formed by grains of the textured perovskite.

By an appropriate treatment of video images we could determine the time evolution of the fraction of the area occupied by the perovskite phase (Fig. 6) and calculate the parameters of the phase transformation kinetics (see Table 2). Note that they are close to the parameters derived from an analysis of the integrated scattered light intensity. The slight difference observed can be attributed to the incomplete reproducibility of the anneal conditions caused by the thermostat modification.

Thus, it has been shown that an *in situ* analysis of the integrated scattered light intensity and of the evolution of the film surface morphology in the course of a rapid thermal anneal permits one to study the kinetics of the pyrochlore–perovskite phase transformation without recourse to x-ray diffraction measurements. The parameters characterizing the nucleation and growth of perovskite crystallites in different stages of the phase transformation were obtained. The validity of the method was confirmed by comparing the light scattering data with x-ray diffraction measurements made on partially annealed films. It should be pointed out that the *in situ* method proposed here permits one to study the phase transformation process in different films deposited on any substrate and with any bottom electrode. This method makes it possible to optimize the anneal conditions for commercial-scale production of integrated circuits containing ferroelectrics.

Table 2. Parameters of phase transformation kinetics derived from *in situ* optical measurements (T_{an} = 650°C)

	T_{pyr}, °C	t_{d1}, s	$\tau_{f\alpha}$, s	$\tau_{s\alpha}$, s	t_{cat}, s
I_{sc}	380	1.3	2.5	5.6	4.9
I_{sc}	490	1.4	13	42	21
S_{per}/S_0	490	−6.2	24	175	33

ACKNOWLEDGMENTS

The authors are grateful to D. Bolten, R. Gerhardt, and R. Waser for providing the films for this study.

The partial support of the Program “Universities of Russia: Fundamental Studies” (grant no. 5563), Ministry of Education of the RF (grant no. 97-0-7.1-236), and of the US Civilian Research & Development Foundation for the Independent States of the Former Soviet Union (CRDF) (grant no. REC-005) is gratefully acknowledged.

REFERENCES

1. K. G. Brooks, I. M. Reaney, R. Klissurka, *et al.*, J. Mater. Res. **9**, 2540 (1994).
2. J. Chen, K. R. Udayakumar, K. G. Brooks, and L. E. Cross, J. Appl. Phys. **71**, 4465 (1992).
3. E. Griswold, L. Weaver, M. Sayer, *et al.*, Micron **26**, 559 (1995).
4. M. Huffman, F. D. Gealy, L. Kammerdiner, *et al.*, Ferroelectrics **134**, 303 (1992).
5. M. Klee and P. K. Larsen, Ferroelectrics **133**, 91 (1992).
6. A. P. Wilkinson, J. S. Speck, A. K. Cheetham, *et al.*, Chem. Mater. **6**, 750 (1994).
7. S. Trolier-McKinstry, J. Chen, K. Vedam, and R. Newnham, J. Am. Ceram. Soc. **78**, 1907 (1995).
8. M. Libera and M. Chen, J. Appl. Phys. **73**, 2272 (1993).

9. V. Ya. Shur, S. A. Negashev, E. L. Rumyantsev, *et al.*, Ferroelectrics **169**, 63 (1995).

10. V. Ya. Shur, S. A. Negashev, A. L. Subbotin, *et al.*, Mater. Res. Soc. Symp. Proc. **433**, 351 (1996).

11. V. Ya. Shur, S. A. Negashev, A. L. Subbotin, and E. A. Borisova, Ferroelectrics **196**, 183 (1997).

12. I. P. Pronin, N. V. Zaĭtseva, E. Yu. Kaptelov, and V. P. Afanas'ev, Izv. Ross. Akad. Nauk, Ser. Fiz. **61** (2), 379 (1997).

13. V. Ya. Shur, E. B. Blankova, A. L. Subbotin, *et al.*, J. Eur. Ceram. Soc. **19**, 1391 (1999).

14. V. Ya. Shur, S. A. Negashev, A. L. Subbotin, *et al.*, Fiz. Tverd. Tela (St. Petersburg) **41** (2), 306 (1999) [Phys. Solid State **41**, 274 (1999)].

15. A. N. Kolmogorov, Izv. Akad. Nauk SSSR, Ser. Mat. **3**, 355 (1937).

16. M. Avrami, J. Chem. Phys. **7**, 1103 (1939).

17. V. Ya. Shur, E. L. Rumyantsev, and S. D. Makarov, J. Appl. Phys. **84** (1), 445 (1998).

18. C. V. R. Kumar, R. Pascual, and M. Sayer, J. Appl. Phys. **71** (2), 864 (1992).

Translated by G. Skrebtsov

Physics of the Solid State, Vol. 43, No. 5, 2001, pp. 908–913. Translated from Fizika Tverdogo Tela, Vol. 43, No. 5, 2001, pp. 874–879.

MAGNETISM AND FERROELECTRICITY

Effect of Low-Angle Boundaries on the Dielectric Properties of Epitaxial $Ba_{0.8}Sr_{0.2}TiO_3$ Films

B. M. Gol'tsman, Yu. A. Boĭkov, and V. A. Danilov

Ioffe Physicotechnical Institute, Russian Academy of Sciences, Politekhnicheskaya ul. 26, St. Petersburg, 194021 Russia

Received October 3, 2000

Abstract—The effect of low-angle boundaries on the dielectric properties of epitaxial $Ba_{0.8}Sr_{0.2}TiO_3$ films is studied by comparing films differing in crystalline-block size. It is found that the permittivity diminishes considerably when the block sizes are reduced. The maximum of the temperature-dependent permittivity is shifted towards lower temperatures, and the sensitivity of the permittivity to an electric field is reduced. Moreover, it is found that the maximum in the permittivity temperature dependence is displaced towards lower temperatures when the applied measured voltage is increased and becomes higher than the coercive voltage. The width of a hysteresis loop decreases significantly when the frequency of the controlling field is reduced. The reasons for the observed behavior are analyzed. © *2001 MAIK "Nauka/Interperiodica".*

INTRODUCTION

Epitaxial films of solid (Ba, Sr)TiO_3 solutions are promising for use in memory cells, controllable delay lines, pyroelectric detectors, etc. Monocrystalline blocks that form an epitaxial film have a well-defined orientation in the azimuth plane and with respect to the normal to the substrate plane and are separated by low-angle boundaries. The azimuthal misorientation of blocks is determined, to a great extent, by the misfit of the lattice parameters of the film and the substrate. As is known [1], in perovskite-structure dielectrics ($SrTiO_3$, in particular), nonstoichiometry with respect to oxygen takes place in the vicinity of high-angle boundaries. This should considerably influence the dielectric parameters. In contrast to thin polycrystalline layers, epitaxial films do not contain high-angle grain boundaries and the effect of low-angle boundaries on the dielectric properties of epitaxial films has practically not been studied. At the same time, in spite of the relatively low density of dislocations at low-angle boundaries (which is due to insignificant disorientation of the blocks), this effect can be considerable, since some defects and impurities can be concentrated in the vicinity of boundaries. They are displaced in the course of film formation due to the growth of crystalline nuclei and to impurity aggregation in the pits dividing the blocks at the film surface (see below). The influence of low-angle boundaries in epitaxial films of $Ba_{0.8}Sr_{0.2}TiO_3$ (BSTO) on their dielectric properties is studied in this work by comparing the properties of films differing in block size. The compound studied is promising for use in sensitive elements of noncooled pyroelectric detectors of IR radiation, since the temperature of the ferroelectric phase transition at which the pyroeffect is maximal is close to room temperature in this case.

1. EXPERIMENT

Heterostructures containing a (100)$LaAlO_3$ (LAO) substrate, upper and lower film electrodes made of conducting $SrRuO_3$ (SRO) oxide, and a BSTO film were prepared. These heterostructures were prepared by the laser evaporation method, using an excimer laser (KrF working mixture) with a radiation wavelength of 248 nm and a pulse duration of 30 ns. The sputtering of the initial ceramic SRO and BSTO targets was carried out in an oxygen atmosphere under pressure P_0 = 0.4 mbar. The SRO electrodes were formed at a substrate temperature T_s equal to 750°C. The BSTO films were grown at two different temperatures T_s: 750 and 800°C. The obtained SRO/BSTO/SRO heterostructures were cooled at a rate of 5°C per minute under an oxygen pressure P_0 = 1 atm. To diminish the influence of the electrodes on the measured parameters of the plane-parallel SRO/BSTO/SRO capacitor structures, relatively thick (700 nm) ferroelectric films were chosen.

The structure of the obtained three-layered systems was investigated by x-ray diffraction methods (CuK_α radiation, $\omega/2\theta$ and ϕ scans, rocking curves). An atomic-force microscope was utilized to obtain images of the free surface of BSTO films.

Electrodes with area of 200×200 μm in the upper SRO layer were formed using photolithography and ion etching.

The capacity C and $\tan\delta$ (δ is the dielectric loss angle) of the plane-parallel SRO/BSTO/SRO capacitor structures prepared were measured with an HP 4263A meter and an E7–8 bridge.

2. EXPERIMENTAL RESULTS

For the obtained SRO/BSTO/SRO/LAO heterostructures, only the (*n*00) reflections from the ferroelectric layers, electrodes, and substrate were visible in the x-ray ω/2θ diffractograms obtained under the conditions when the incident and reflected x-ray beams were perpendicular to the substrate plane (Fig. 1a). When the incident and reflected x-ray beams were tilted at an angle of 45° to the substrate plane, only the (*n*0*n*) peaks from the ferroelectric layers, film, and substrate were visible on the diffractogram (Fig. 1b). Four peaks (placed at 90° intervals) were observed at the ϕ scan for the (111)BSTO reflection (see the inset in Fig. 1a). Thus, grains with the 45° azimuthal disorientation were absent in the film. Hence, the BSTO and SRO films grown epitaxially and independently of the temperature T_s had the following orientational relations for the layers that formed the obtained heterostructures: (100)[101]SRO ‖ (100)[101]BSTO ‖ (100)[101]SRO ‖ (100)[101]LAO.

The half-width (FWHM) of the peak in the x-ray ϕ scan for the (111) reflection from the BSTO films was found to be 0.6° to 0.8° independent of the T_s value. The peak FWHM in the x-ray ϕ scan for the (111) reflection from the LAO substrate was equal to 0.23°. One of the main reasons for the 2 to 3 time broadening of the peak in the x-ray ϕ scan for the epitaxial BSTO film compared to the data for the monocrystalline substrate was the azimuthal disorientation of the monocrystalline blocks forming the substrate. Thus, the relative azimuthal disorientation of the monocrystalline blocks in the (100)BSTO films grown on (100)SRO ‖ (100)LAO was able to be as large as 0.4°–0.6°, with allowance for instrument error.

The half-width of the rocking curve for the x-ray (200) reflection of the BSTO films grown at T_s equal to 800 and 750°C was 0.29° and 0.35°, respectively. The FWHM of the rocking curve for the (200) substrate peak was 0.11°. Thus, taking into account the instrument error, the FWHMs of rocking curves for the films prepared at 800 and 750°C were 0.18° and 0.24°, respectively. These values prove the perfection of the film structure (for comparison, the corresponding value for the epitaxial BSTO films used in [2] equals 1.1°).

The crystalline lattice parameters for the grown BSTO films were determined from the x-ray data obtained. The crystalline lattice parameters for the BSTO film in the (100)SRO ‖ (100)BSTO ‖ (100)SRO heterostructure (T_s = 800°C) measured in the substrate plane and along a normal to its surface were equal to 3.994 and 3.981 Å, respectively. The same parameters for the film grown at T_s = 750°C were equal to 3.993 and 3.983 Å, respectively. It follows from these data that the BSTO films obtained were mainly *a* oriented (the *c* axis was parallel to the substrate plane).

The monocrystalline blocks of a BSTO film grown at T_s = 800°C (we will refer to it as a large-block film)

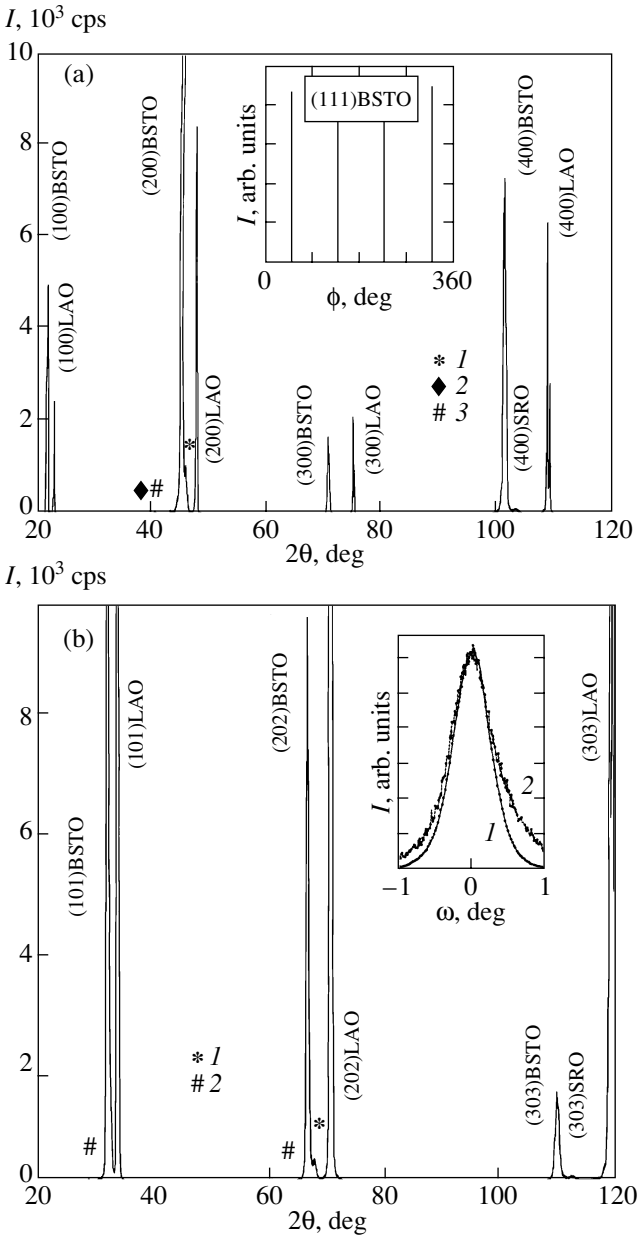

Fig. 1. (a) X-ray ω/2θ diffractogram obtained using CuK_α radiation for the (150 nm)SRO/(700 nm)BSTO/(150 nm)SRO/LAO heterostructure (T_s = 750°C). The diffractogram was obtained under the conditions where the incident and reflected x-ray beams were situated in the plane orthogonal to the (100)LAO plane. (*1*) The (200)SRO reflection and (*2, 3*) CuK_β reflections from the ferroelectric film and substrate, respectively. The inset shows the ϕ x-ray scan for the (111)BSTO reflection from the same heterostructure. (b) The x-ray diffractogram (CuK_α, ω/2θ) for the same heterostructure obtained under the conditions where the incident and reflected x-ray beams were situated in the plane orthogonal to the (101)LAO plane. (*1*) The (202)SRO reflection; (*2*) the CuK_β reflections from the substrate. The inset shows the rocking curves for the (200)BSTO reflection from the (150 nm)SRO/(700 nm)BSTO/(150 nm)SRO/LAO heterostructures grown at different T_s: (*1*) 800 and (*2*) 750°C.

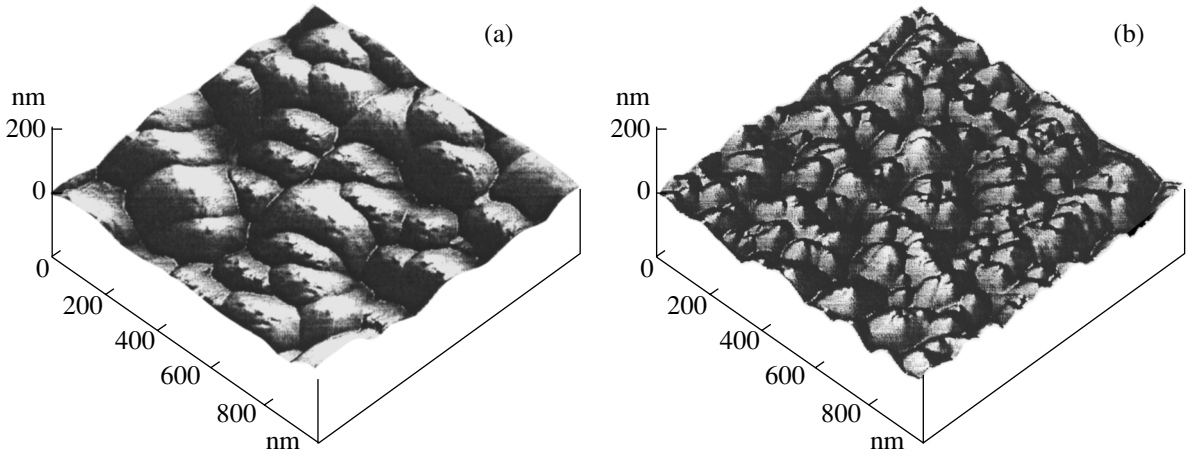

Fig. 2. Images of the free surface of the (700 nm)BSTO films grown at (100)SRO || (100)LAO at different T_s: (a) 800 and (b) 750°C. The images are obtained by atomic force microscopy. The boundaries of the monocrystalline blocks in the ferroelectric film are marked by hollows.

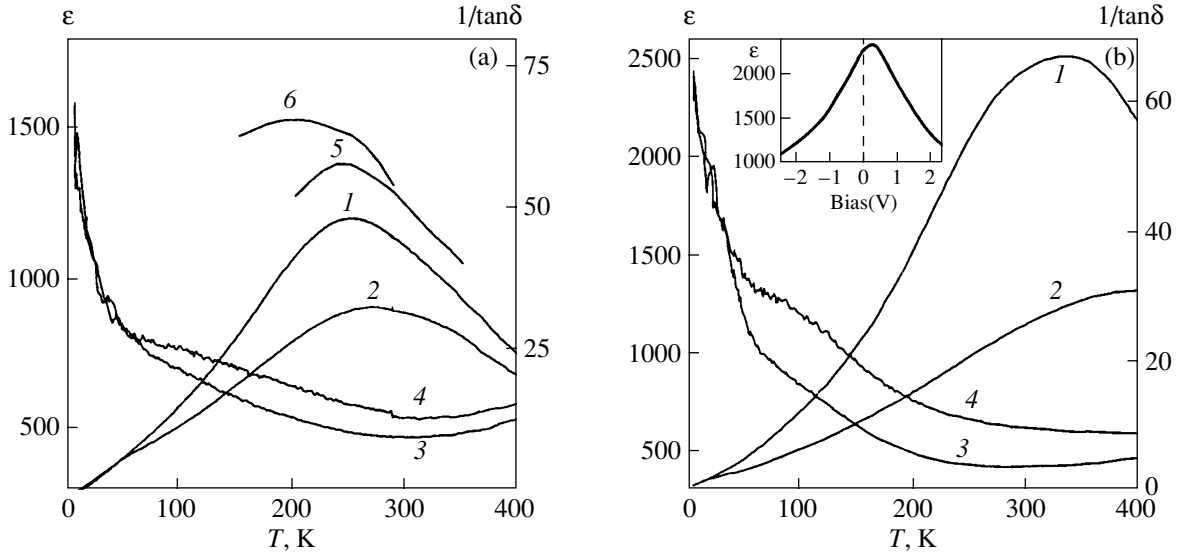

Fig. 3. (a) Temperature dependences of the permittivity ε (curves *1*, *2*, *5*, *6*) and of $1/\tan\delta$ (curves *3*, *4*) for the fine-block BSTO film; curves *1*, *3*, *5*, and *6* are measured at a bias voltage $U_b = 0$; curves *2* and *4*, at 2.5 V; curves *1–4* are measured at a measuring signal amplitude $U_m = 0.05$ V and a frequency $f = 100$ kHz; curve *5*, at $U_m = 0.7$ V and $f = 1$ kHz; and curve *6*, at $U_m = 4.3$ V and $f = 1$ kHz. (b) Temperature dependences of the permittivity ε (curves *1*, *2*) and $1/\tan\delta$ (curves *3*, *4*) for the large-block BSTO film; curves *1* and *3* are measured at a bias voltage $U_b = 0$; curves *2* and *4*, at $U_b = 2.5$ V and $f = 100$ kHz. The inset shows the $\varepsilon(U_b)$ dependence at $T = 300$ K.

had sizes of 150–200 nm in the substrate plane and were decreased in their size by a factor of 3 to 5 at T_s = 750°C (fine-block films) (Fig. 2). The block boundaries possess an excessive free energy, which induces the formation of the characteristic pits at the free surface of a BSTO film. According to the earlier data in [3], the BSTO films grown under analogous conditions had a columnar structure.

Temperature dependencies $\varepsilon(T)$ and $\tan\delta(T)$ (ε is the permittivity) are obtained at the measuring voltage U_m with a frequency of 100 kHz and amplitude of 0.05 V (which is considerably lower than the coercive voltage) and at bias voltages U_b equal to zero and +2.5 V (the polarity at the upper electrode). The temperature dependences of ε were also obtained for measuring voltages of 0.7 and 4.3 V at a frequency of 1 kHz.

The $\varepsilon(T)$ and $\tan\delta(T)$ dependences are represented in Fig. 3. The $\varepsilon(T)$ and $\tan\delta(T)$ curves have broad maxima corresponding to the paraelectric–ferroelectric

phase transition. For all $\varepsilon(T)$ dependences at zero bias voltage, the temperatures of maxima (T_{max}) are below the Curie temperature for the bulk $Ba_{0.8}Sr_{0.2}TiO_3$ solid solution, which approximately equals 340 K [4]. At the same time, T_{max} for the fine-block films is considerably lower than that for the large-block films (260 and 325 K, respectively). The temperatures T_{max} for the fine-block films determined from weak-signal measurements at frequencies of 1 and 100 kHz are approximately the same. However, if U_m increases to a value of 4.3 V (exceeding the coercive voltage), one observes a considerable decrease in T_{max}, down to 200 K. A decrease in ε with decreasing block size is observed in the whole range of temperatures. When the frequency diminishes and the amplitude of the measuring voltage is increased up to values exceeding the amplitude of the coercive voltage, the ε value increases.

Studies of hysteresis loops at different temperatures showed that, when the temperature is varied from values lower than T_{max} to values considerably greater than T_{max}, the loops narrow monotonically, but they still exist even at temperatures 100 K higher than T_{max} (see the inset in Fig. 4). The corresponding temperature dependence of the coercive field E_c is shown in Fig. 4. A considerable (more than two times) narrowing of the hysteresis loop with a decrease in the controlling field frequency from 1 kHz to 120 Hz is observed.

It is found that the $\varepsilon(U_b)$ curves are symmetric at T_{max} and higher temperatures; the maxima of the curves are displaced by +0.3 to +0.5 V with respect to the U_b = 0 value (the inset to Fig. 3b), and the hysteresis effects with increasing and diminishing bias voltage are insignificant. In order to compare the sensitivity of the fine- and large-block films to the bias voltage, we used the curves of Fig. 3 and calculated the values of the $\Delta\varepsilon/\varepsilon(0)$ ratio, where $\Delta\varepsilon$ is the amount of the decrease in the ε value with U_b increasing from 0 to 2.5 V (the bias field is 36 kV/cm) and $\varepsilon(0)$ is the permittivity for U_b = 0. The $\Delta\varepsilon/\varepsilon(0)$ values at T_{max} and at temperatures exceeding T_{max} by 75 K were compared. For the large-block films, this quantity was $\Delta\varepsilon/\varepsilon(0)$ = 0.52 at T_{max} and $\Delta\varepsilon/\varepsilon(0)$ = 0.32 at $T = T_{max} + 75$ K. For the fine-block films, the $\Delta\varepsilon/\varepsilon(0)$ values were 0.26 and 0.17, respectively. Thus, the sensitivity of the large-block films to the bias voltage is much greater than that of the fine-block films both at T_{max} and at higher temperatures. The sensitivity of $\tan\delta$ to the bias field is also considerably greater for the large-block films.

3. DISCUSSION OF RESULTS

The persistence of the ferroelectric properties of the films at temperatures considerably exceeding T_{max} and the broad maxima of the $\varepsilon(T)$ and $\tan\delta(T)$ dependences indicate considerable inhomogeneity of the films. This inhomogeneity can be due to fluctuations of the film chemical composition [5], as well as to the local fields and mechanical stresses. The latter are mainly produced in the vicinity of grain boundaries by dislocations, charged vacancies, and impurity ions.

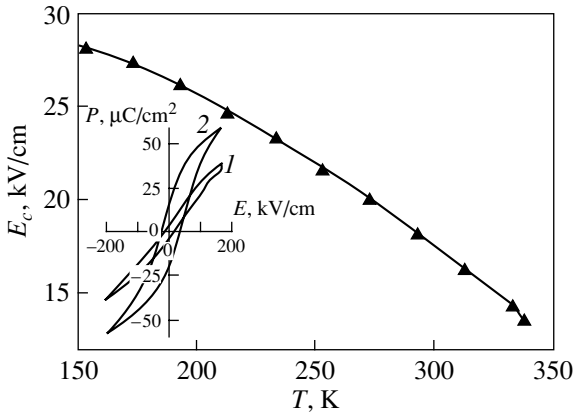

Fig. 4. Temperature dependence of the coercive field for the fine-block BSTO film. The inset shows the dependence of the polarization on the electric field for the fine-block film. The hysteresis loops are measured at temperatures of (*1*) 345 and (*2*) 150 K.

Narrowing of the hysteresis loop with decreasing frequency of the controlling voltage can be explained according to [6] by the concentration of mobile charged oxygen vacancies in the near-electrode regions in the case of a quite slowly varied controlling field. As a result, the field in the near-electrode regions grows, which is favorable to the formation of nuclei of ferroelectric domains upon polarization switching and diminishes the coercive field.

Displacement of the maxima in the $\varepsilon(U_b)$ and $\tan\delta(U_b)$ dependences to more positive potentials of the upper electrode proves the existence of a built-in field in the films. One of the main reasons for the appearance of the built-in electric field in the BSTO layer is the difference in the microstructure of the upper and lower ferroelectric–oxide-electrode interfaces in the SRO/BSTO/SRO heterostructure. The differences in the nucleus formation process of the BSTO film on the SRO layer surface and of the SRO layer on the BSTO film surface lead to different densities of defects in the vicinity of BSTO/SRO boundaries and, therefore, to a difference in the electron parameters of the interfaces [7].

In particular, the built-in field can create a positive charge associated with misfit dislocations at the lower interface of the SRO/BSTO/SRO structure.

Using the data of [1] on the occurrence of nonstoichiometric regions near the 25° interface in an $SrTiO_3$ bicrystal, let us make an order-of-magnitude estimate of the voltage across the film structure that is induced by this charge. According to the data of [1], the distance between the neighboring dislocations in the interface plane is 12 Å and the concentration of the oxygen vacancies in the vicinity of the interface is 6%. In our

case, the distance d between the misfit dislocations, calculated by the formula $d = a_1a_2/(a_1 - a_2)$, where a_1 and a_2 are the lattice constants of the film and the substrate, respectively, is equal to 250 Å. Taking into account that the misfit dislocations form a rectangular network, we find that the dislocation density in our case is approximately 10 times lower than that cited in [1] and, therefore, the vacancy concentration is 10 times lower. Assuming that the vacancy concentration cited in [1] is related to a single atomic plane lying in the interface plane (underestimated value), we obtain that, in our case, the number of doubly charged oxygen vacancies per unit area of the film–substrate interface is 1.7×10^{12} cm^{-2} and the corresponding charge density Q equals 5.5×10^{-7} C cm^{-2}. The voltage U across the film structure can be evaluated from the relation $U = Q/C$, where C is the specific capacity of the structure. As the result, we obtain $U = 0.22$ V, which is of the same order of magnitude as the observed voltage that induces the built-in field.

Consider the reasons for the lowering of T_{max} in the films. The displacement of T_{max} can be caused by mechanical stresses. However, one can make the conclusion from the phase diagram presented in [8] for $BaTiO_3$ films (a chemical composition which is close to $Ba_{0.8}Sr_{0.2}TiO_3$) that the two-dimensional in-plane stresses acting in the film deposited on the substrate must increase the temperature of the paraelectric–ferroelectric phase transition irrespective of the stress sign. This statement contradicts our results. Thus, the mechanical stresses do not play an essential role in this case. This can be explained by the fact that the thermal stretching stresses in the film (the thermal expansion coefficient of the film is greater than that of the substrate) are partially compensated by compression stresses due to the misfit of the crystalline lattice parameters of the film and the substrate (the lattice parameter of the film is greater than that of the substrate). An analogous compensation for stresses is described in [9] for $Ba_{0.85}Sr_{0.15}TiO_3$ having a perfect structure and placed on an MgO substrate.

The decrease in T_{max}, which was also observed earlier in BSTO films [10, 11], can be explained by size effects taking place in thin films and fine-grain bulk ceramics [12, 13]. The size effect is due to a decrease in the polarization near the film surface and near the boundaries of grains and of ferroelectric domains. When the film thickness and the grain sizes are decreased (and, as a consequence, the domain width diminishes [14]), the relative volume of regions with reduced polarization increases. The latter leads to an abrupt fall of T_{max}. For the crystalline block sizes comparable with the ferroelectric correlation length, the ferroelectric effects can be totally suppressed [8, 13]. If, in our case, one takes into account the large dimension of the crystalline blocks in the direction of a normal to the film plane, it will be obvious that the polarization is mainly suppressed in the vicinity of the domain walls oriented along this direction. The polarization is also suppressed near the block boundaries at which electric charges and mechanical stresses, induced by defects and impurities displaced to these boundaries in the course of the film growth process, are concentrated. This is why a decrease in T_{max} is observed to be more noticeable in fine-block films.

The decrease in T_{max} with an increase in the measuring voltage amplitude up to values exceeding the coercive voltage can be related to the accompanying initiation of the polarization switching process, which leads to an increase in the permittivity [15] [this is observed in our case (Fig. 3a)]. As pointed out above, the microvolumes of both paraelectric and ferroelectric phases are present in the films in a quite broad temperature interval. The relative volume of the ferroelectric phase increases with decreasing temperature. As a result, the contribution from the polarization switching to the permittivity grows. This leads to a decrease in T_{max}.

The observed growth of ε with an increase in the crystalline block size is explained by the decreased influence of the size effect considered above. In addition, the growth of the oxygen vacancy concentration in the large-block films (evaporated at higher temperatures) can also serve as the reason for the increase in ε. As a result, the contribution from the polarization caused by oxygen vacancies to ε is also increased [16, 17]. In our case, such a polarization can also be one of the reasons for the above-mentioned low-frequency dispersion of ε (another reason for the low-frequency dispersion can be near-electrode potential barriers [18]). However, we observed no increase in the crystalline cell volume, which should be caused by the growth in the concentration of oxygen vacancies [17] in the large-block films. For example, according to the above data on the crystal lattice parameters in the film plane and along the normal to it, the crystal cell volumes of the large- and fine-block films are equal to 63.296 and 63.386 Å^3, respectively. Using, for an approximate evaluation, the dependences of the cell volume upon the concentration of the oxygen vacancies in $Ba_{0.5}Sr_{0.5}TiO_3$ films [17], we find that the concentration difference does not exceed 7%, with the vacancy concentration being lower in the large-block films. Thus, the growth of the concentration of oxygen vacancies does not serve as the reason for the increase in ε in the large-block films.

The decrease in the sensitivity of ε and $\tan\delta$ to the bias field with a decrease in the crystalline block sizes is explained by the growth of the contribution from the interfaces in the film in the vicinity of which the local electric fields exist. The effect of the bias field on ε becomes weaker against the background of these fields.

Thus, the comparison of the ferroelectric properties of films with different sizes of crystalline blocks showed that the low-angle boundaries in epitaxial films having a columnar block structure considerably affect their properties by lowering the paraelectric–ferroelec-

tric phase transition temperature and also by diminishing the permittivity and its sensitivity to the electric bias field.

ACKNOWLEDGMENTS

This work was supported by the Russian Foundation for Basic Research, project no. 99-02-18022, and by the program "Physics of the Solid-State Nanostructures," project no. 97-2017.

REFERENCES

1. N. D. Browning, H. O. Moltaji, and J. P. Buban, Phys. Rev. B **58** (13), 8289 (1998).
2. S. Y. Hou, I. Kwo, R. K. Wang, *et al.*, Appl. Phys. Lett. **67**, 1387 (1995).
3. Yu. A. Boikov, Z. G. Ivanov, A. N. Kiselev, *et al.*, J. Appl. Phys. **78**, 4591 (1995).
4. V. A. Bokov, Zh. Tekh. Fiz. **27**, 1784 (1957) [Sov. Phys. Tech. Phys. **2**, 1657 (1958)].
5. G. A. Smolenskiĭ and V. A. Isupov, Zh. Tekh. Fiz. **24**, 1376 (1954).
6. B. M. Gol'tsman, V. K. Yarmarkin, and V. V. Lemanov, Fiz. Tverd. Tela (St. Petersburg) **42** (6), 1083 (2000) [Phys. Solid State **42**, 1116 (2000)].
7. Yu. A. Boikov and T. Claesson, J. Appl. Phys. (in press).
8. M. A. Pertsev, A. G. Zembiglotov, and A. K. Tagantsev, Phys. Rev. Lett. **80** (9), 1988 (1998).
9. Z. Suroviak, D. Czekai, and V. P. Dudkevich, Ferroelectrics **192**, 313 (1997).
10. T. Harikava, N. Mikami, T. Mikita, *et al.*, Jpn. J. Appl. Phys. **32**, 4126 (1993).
11. B. M. Gol'tsman, V. V. Lemanov, A. I. Dedyk, *et al.*, Fiz. Tverd. Tela (St. Petersburg) **38** (8), 2493 (1996) [Phys. Solid State **38**, 1368 (1996)].
12. Y. G. Wang, W. L. Zhong, and P. L. Zhang, Phys. Rev. B **51** (8), 5311 (1995).
13. P. Auyub, V. R. Palkar, S. Chatopadhyay, and M. Multani, Phys. Rev. B **51** (9), 6135 (1995).
14. G. Arit, D. Hennings, and G. de Wit, J. Appl. Phys. **58** (4), 1619 (1985).
15. G. F. Smolenskiĭ, V. A. Bokov, V. A. Isupov, N. N. Kraĭnik, R. E. Pasynkov, F. I. Sokolov, and N. K. Yushin, *The Physics of Ferroelectric Phenomena* (Nauka, Leningrad, 1985).
16. Yu. Ya. Tomashpol'skiĭ, *Film Ferroelectrics* (Radio i Svyaz', Moscow, 1984).
17. W. J. Kim, W. Chang, S. B. Quadri, *et al.*, Appl. Phys. Lett. **76** (9), 1185 (2000).
18. M. Sayer, A. Maksingh, A. K. Arara, and A. Lo, Integr. Ferroelectr. **1** (1), 129 (1992).

Translated by A. Sonin

Physics of the Solid State, Vol. 43, No. 5, 2001, pp. 914–915. Translated from Fizika Tverdogo Tela, Vol. 43, No. 5, 2001, pp. 880–881.

MAGNETISM AND FERROELECTRICITY

Electromechanical Nonlinearity of Bi_2TeO_5

A. M. Antonenko, K. V. Domoratsky, A. Yu. Kudzin, and L. Ya. Sadovskaya

Dnepropetrovsk National University, Nauchnyĭ pr. 13, Dnepropetrovsk, 49050 Ukraine

e-mail: elf@ff.dsu.dp.ua

Received October 5, 2000

Abstract—The electromechanical nonlinearity of a bismuth tellurite single crystal (Bi_2TeO_5) is investigated. It is revealed that the noncentral forces of interatomic interaction dominate in this material. The relation between the structural features of Bi_2TeO_5 and its elastic properties is analyzed. © *2001 MAIK "Nauka/Interperiodica".*

Single-crystal Bi_2TeO_5 crystallizes in the orthorhombic crystal system and belongs to the *Abm*2 space group. The unit cell parameters are as follows: a = 11.602 Å, b = 16.461, and c = 5.523 Å. The main structural features of this material are a polar axis which coincides with the [001] crystallographic direction and a quite perfect cleavage plane which corresponds to the (100) crystallographic plane [1].

Analysis of the full matrix of elastic constants for bismuth tellurite showed that the cleavage plane and polar axis virtually do not manifest themselves in the elastic properties of bismuth tellurite within the experimental error [1, 2]. It was of interest to reveal the reason for this inadequate manifestation of the properties of the Bi_2TeO_5 single crystal.

Single crystals of bismuth tellurite for investigations were grown by the Czochralski method [3]. The measurements were carried out by the resonance–antiresonance method.

It is known that the following conditions should be met for certain crystals: (i) all interaction forces between the particles constituting the crystal are central forces, (ii) the particles have a spherical symmetry and are positioned at the symmetry centers of the structure, and (iii) no strain occurs in the initial state of the crystals. If these conditions are fulfilled, we have six additional relationships (Cauchy relationships) between the elastic coefficients: $C_{23} = C_{44}$, $C_{56} = C_{14}$, $C_{64} = C_{25}$, $C_{31} = C_{55}$, $C_{12} = C_{66}$, and $C_{45} = C_{36}$ [4]. For the constants of elastic rigidity of bismuth tellurite, some Cauchy relationships are approximately fulfilled [1, 2]. In order to evaluate the character of the interatomic interaction in this single crystal, the angular dependences of shear moduli $G_1 = \frac{1}{2(S_{23} + S_{33})}$ and $G_2 = \frac{1}{S_{44}}$ were calculated using the elastic constants taken from [1, 2]. The dependences of the G_1 and G_2 moduli for Bi_2TeO_5 with rotation around the crystallographic axes are shown in Fig. 1. For cubic crystals with central forces of interatomic interaction, these dependences should have a similar character. It is seen from Fig. 1 that the dependence for G_1 noticeably differs from the dependence for G_2. This suggests that central interatomic interactions are absent in the Bi_2TeO_5 crystal and, consequently, the non-Coulomb forces are dominant.

For small amplitudes of atomic vibrations, the elastic properties of Bi_2TeO_5 weakly depend on the type of

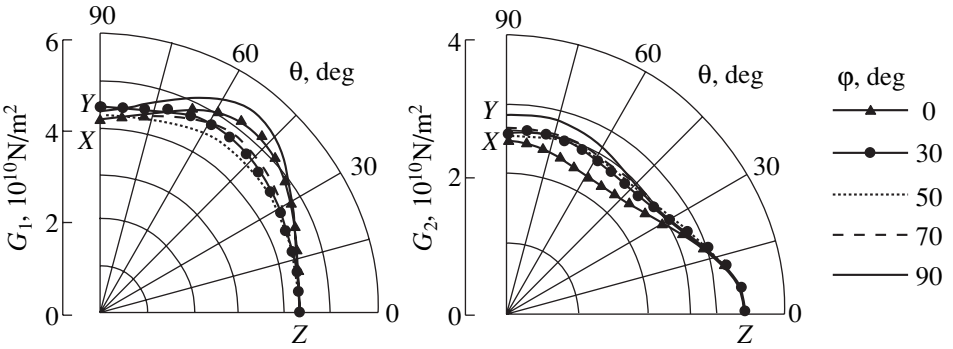

Fig. 1. Angular dependences of the shear moduli for a bismuth tellurite single crystal (φ is the angle between the axes X and Y and θ is the angle between the axes Z and X, Z and Y).

1063-7834/01/4305-0914$21.00 © 2001 MAIK "Nauka/Interperiodica"

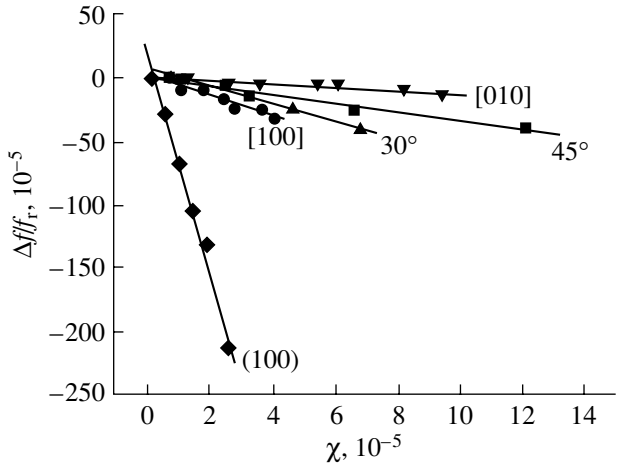

Fig. 2. Dependences of the resonance frequency on the strain induced by the electric field for different samples of Bi_2TeO_5.

interatomic interaction forces in the crystal lattice. This can be due to a small difference in the forms of interaction potentials between the particles in the central- and noncentral-force fields at small vibration amplitudes. With an increase in amplitude, the nonlinear effects begin to play a significant part. The difference between the potentials should have a stronger effect, since the potential is symmetric in the former case and asymmetric in the latter case. For large vibration amplitudes, the repulsive forces should noticeably manifest themselves in the case of non-Coulomb forces. The former forces decrease with distance considerably faster than the Coulomb forces, and even faster than the van der Waals forces [5]. It is possible that the structural features of the Bi_2TeO_5 single crystal will clearly manifest themselves in nonlinear modes.

In order to confirm this supposition, we investigated the electromechanical nonlinearity of bismuth tellurite. The dependences of the resonance f_r and antiresonance f_a frequencies on the strain amplitude (Fig. 2) were measured at room temperature. The samples were prepared in the form of bars, which were cut out along the [100] and [001] axes and along two intermediate directions (at 30° and 45° to the [100] direction) in the auxiliary (010) plane, and rectangular (100) plates. The strain χ_i was calculated as $Q_m d_{ij} E_j$, where Q_m is the mechanical Q factor for the sample, d_{ij} is the piezoelectric modulus of bismuth tellurite [2], and E_j is the electric field applied (which causes sample strain). It is seen from Fig. 2 that the Bi_2TeO_5 single crystal exhibits a noticeable electromechanical nonlinearity at large strains. This effect is especially strong for the (100) plates.

Parameters of the samples investigated

Bar length orientation	f_r, kHz	f_a, kHz	γ_i
[100]	146.075	146.170	–8.7 ± 1.4
30° to [100] in the (010) plane	190.125	190.255	–7.3 ± 0.6
45° between [100] and [010] in the (010) plane	166.630	166.925	–3.6 ± 0.5
[010]	130.390	130.500	–1.6 ± 0.2
(100) plate	748	765	–90 ± 5.0

The data on the electromechanical nonlinearity of bismuth tellurite, which are shown graphically in Fig. 2, are summarized in the table. The quantities $\gamma_i = \frac{1}{f_r}\frac{\partial f_r}{\partial \chi_i}$ characterize the averaged degree of anharmonicity of the crystal lattice toward the i direction.

If the system deviates from the Hooke law and calls for account of the anharmonicity effect, the interaction force F can be expanded into a series to the quadratic term and can be represented as $F = kr(1 + \gamma r)$, where $\gamma \approx \gamma_i$, k is the rigidity, and r is the displacement.

Applying the expression for the anharmonic interaction force to the Bi_2TeO_5 single crystal, we obtain the following relationships:

(1) for the [010] direction, $\gamma = -2$ and $F = kr(1 - 2r)$;

(2) for the [100] direction, $\gamma = -9$ and $F = kr(1 - 9r)$;

(3) for the (100) plane, $\gamma = -90$ and $F = kr(1 - 90r)$.

It is seen from calculations and Fig. 2 that the interatomic interaction force in the (100) plane with respect to the shear strain decreases with distance very drastically. This effect is considerably less pronounced for other planes.

Thus, it is revealed that the noncentral interatomic interaction dominates in the Bi_2TeO_5 single crystal. Because of this, the cleavage plane, which does not manifest itself in the elastic characteristics in the case of linear interatomic interactions, clearly manifests itself even at a relatively small shear deformation of the lattice.

REFERENCES

1. S. Haussuhl, A. Peter, and E. Hartmann, Cryst. Res. Technol. **29** (3), K56 (1994).
2. A. M. Antonenko, K. V. Domoratsky, A. Yu. Kudzin, and L. Ya. Sadovskaya, Condens. Matter Phys. **2** (4), 721 (1999).
3. K. V. Domoratsky, A. Yu. Kudzin, L. Ya. Sadovskaya, and G. Ch. Sokolyanskii, Ferroelectrics **214**, 191 (1998).
4. P. V. Pavlov and A. F. Khokhlov, *Physics of Solid State: Textbook for Institutes of Higher Education* (Vysshaya Shkola, Moscow, 1985).
5. P. P. Pavinskiĭ, *Introduction to the Theory of Solid State: Textbook* (Leningr. Gos. Univ., Leningrad, 1979).

Translated by N. Korovin

Physics of the Solid State, Vol. 43, No. 5, 2001, pp. 916–922. Translated from Fizika Tverdogo Tela, Vol. 43, No. 5, 2001, pp. 882–887.

MAGNETISM AND FERROELECTRICITY

Calculation of Phase Diagrams for Solid Solutions of Ferroelectrics

M. D. Glinchuk*, E. A. Eliseev*, and V. A. Stephanovich**

** Frantsevich Institute of Materials Science Problems, National Academy of Sciences of Ukraine, ul. Krzhizhanovskogo 3, Kiev, 03142 Ukraine*

*** Institute of Mathematics, Opole University, Opole, 45-052 Poland*

e-mail: glin@materials.kiev.ua

Received October 18, 2000

Abstract—The integral equations for calculating ferroelectric and antiferroelectric phase transition temperatures, order parameters, and critical concentrations of solid solution components are derived. The electric dipoles randomly distributed in the system are treated as sources of random fields. The random field distribution function is constructed taking into account the contribution of nonlinear effects and the differences in the dipole orientations for different solid solution components. The dependence of the phase transition temperature on the composition of a binary solid solution in the ferroelectric–antiferroelectric and ferroelectric–paraelectric systems is calculated. Numerical calculations are carried out for the $PbTi_xZr_{1-x}O_3$ and $BaZr_xTi_{1-x}O_3$ solid solutions. The results obtained are in good agreement with the experimental phase diagrams of these systems. Analysis of the results indicates that any solid solution containing ferroelectric (antiferroelectric) and paraelectric components transforms into a relaxor state at sufficiently high concentrations of the paraelectric component.

1. INTRODUCTION

Solid solutions of different-type materials (such as a ferroelectric and an antiferroelectric or a ferroelectric and a paraelectric) with practically useful properties have been investigated extensively in recent years. An example of these materials can be provided by the $PbZr_{1-x}Ti_xO_3$ (PZT) system whose representatives have found wide technical applications [1], including modern branches of electronic engineering [2]. For the most part, the compositions of solid solution materials with important properties fall in the concentration regions near the boundaries between different phases in phase diagrams. In particular, the most interesting regions for PZT lie in the vicinity of the morphotropic curve of the coexistence of two ferroelectric phases with different symmetries and in the vicinity of the boundary between the ferroelectric and antiferroelectric phases [2, 3]. The characteristic features of phase diagrams, as well as the anomalies of the properties, essentially depend on the type of solid solution components (ferroelectric, antiferroelectric, or paraelectric). In this respect, it is of interest to compare the phase diagrams of PZT (a solid solution of antiferroelectric $PbZrO_3$ and ferroelectric $PbTiO_3$) and the $BaZr_xTi_{1-x}O_3$ (BZT) solid solution which consists of ferroelectric $BaTiO_3$ and paraelectric $BaZrO_3$ [4]. The difference in the properties of $BaZrO_3$ and $PbZrO_3$ indicates the special role played by lead ions in phase transitions in materials with a perovskite structure [5]. The phase diagrams of PZT and BZT differ radically (see [6, 7]): several phases with a long-range order are observed in PZT, whereas BZT at $x = 0.27$ exhibits a relaxor behavior. In order to elucidate the mechanisms and driving forces responsible for the phase diagram of solid solutions, it is expedient to perform theoretical calculations. Earlier, we proposed a model which is based on the calculations of electric fields (induced by randomly arranged electric dipoles) and their effect on the order parameter [8]. In the present work, we extended this model by taking into account the contributions of nonlinear and spatial correlation effects and different dipole orientations. As a result, we constructed the concentration dependence of the transition temperature, calculated the order parameters for lattices of different symmetries (i.e., the changes in the solid solution symmetry), and established the existence of the morphotropic region and the formation of the glass state. The more refined model was used to calculate the phase diagrams of the PZT and BZT solid solutions. The theoretical and experimental phase diagrams for these materials are in good agreement.

2. ORDER PARAMETERS

For a solid solution composed of ferroelectric and antiferroelectric materials, we introduce three order parameters. Within the two-sublattice model, there are two order parameters for the antiferroelectric component (ferroelectric L_{2F} and antiferroelectric L_{2A}) which describe the homogeneous and inhomogeneous displacements of ions, respectively. The third order

1063-7834/01/4305-0916$21.00 © 2001 MAIK "Nauka/Interperiodica"

parameter L_{1F} corresponds to the ferroelectric component of the solid solution. By assuming that the electric dipoles capable of aligning along the electric field **E** play the dominant role in the behavior of the system during phase transitions, the order parameters in the Ising model can be represented in the following form [9]:

$$L_{1F} = \tanh((d_1^* E + T_{1F}L_{1F})/T), \quad (1a)$$

$$L_{2F} = \frac{\sinh(2(d_2^* E + T_{2F}L_{2F})/T)}{\cosh(2(d_2^* E + T_{2F}L_{2F})/T) + \cosh(2T_{2A}L_{2A}/T)}, \quad (1b)$$

$$L_{2A} = \frac{\sinh(2T_{2A}L_{2A}/T)}{\cosh(2(d_2^* E + T_{2F}L_{2F})/T) + \cosh(2T_{2A}L_{2A}/T)}. \quad (1c)$$

Here, d_1^* and d_2^* are the effective dipole moments of the first ($x = 1$) and second ($x = 0$) components; T_{1F} is the temperature of the transition to the ferroelectric phase of the first component; and T_{2F} and T_{2A} are the temperatures of transitions to the ferroelectric and antiferroelectric phases of the second solid-solution component, respectively.

In a mixed system, dipoles of both components are arranged in a random way and can be treated as sources of random fields. In this case, the order parameters in formulas (1) should be averaged with a random field distribution function $f(\mathbf{E}, L_{1F}, L_{2F})$. Note that the electric field **E** in the general case is the sum of the external and internal fields. Hereafter, we will assume that the external field is absent. With allowance made for the contribution of the nonlinear and correlation effects to the distribution function [10], the order parameters for a mixed system can be written as

$$L_{1F} = \int \tanh(d_1^* \varphi_1(\mathbf{E}\mathbf{e}_1)/T) f(\mathbf{E}, L_{1F}, L_{2F}) d^3E, \quad (2a)$$

$$L_{2F} = \int \frac{\sinh(2d_2^* \varphi_2(\mathbf{E}\mathbf{e}_2)/T) f(\mathbf{E}, L_{1F}, L_{2F})}{\cosh(2d_2^* \varphi_2(\mathbf{E}\mathbf{e}_2)/T) + \cosh(2T_{2A}L_{2A}/T)} d^3E, \quad (2b)$$

$$L_{2A} = \int \frac{\sinh(2T_{2A}L_{2A}/T) f(\mathbf{E}, L_{1F}, L_{2F})}{\cosh(2d_2^* \varphi_2(\mathbf{E}\mathbf{e}_2)/T) + \cosh(2T_{2A}L_{2A}/T)} d^3E, \quad (2c)$$

$$\varphi_i(E) = E(1 + \alpha_3^{(i)} E^2), \quad \mathbf{e}_i = \frac{\mathbf{d}_i^*}{|\mathbf{d}_i^*|}. \quad (2d)$$

Here, $\varphi_i(E)$ is a nonlinear function of the field which takes the form of expression (2d) for lattices with the center of inversion in the paraelectric phase. In this case, α_3 is the coefficient of the nonlinear term (hereafter, it will be considered maximum among all the expansion terms) and $f(\mathbf{E}, L_{1F}, L_{2F})$ is the random field distribution function. It can easily be shown that, when both components are ferroelectrics, i.e., $L_{2A} = 0$, Eq. (2b) has a form identical to Eq. (2a) (as should be expected) but with other parameters. Therefore, relationships (2a)–(2d) describe the general case. According to these relationships, the dependences of the order parameters on the properties of the solid solution components and their percentage can be expressed through the random field distribution function. It should be emphasized that the L parameters are the fractions ($0 \le L \le 1$) of the coherently aligned dipoles of the solid solution components. The polarization **P** as a true order parameter of the solid solution can be expressed in terms of L_i as follows:

$$\mathbf{P} = \frac{x}{a_1^3} L_{1F} d_1^* + \frac{1-x}{a_2^3} L_{2F} d_2^*, \quad (3)$$

where a_1 and a_2 are the lattice parameters and x and $1 - x$ are the mole fractions of the first (A) and second (B) components of the $A_{1-x}B_x$ solid solution, respectively. Note that, as expected, L_{2A} contributes neither to the polarization of the solid solution nor to the random field distribution function. The orientation of the polarization vector of the solid solution is determined by the vector sum of dipoles according to relationship (3). In order to determine the coefficients of this sum, it is necessary to calculate the order parameters $L_{1,2F}$ from relationships (2), which depend on the form of the $f(\mathbf{E}, L_{1F}, L_{2F})$ function.

3. RANDOM FIELD DISTRIBUTION FUNCTION

In the general case, electric dipoles of both types serve as sources of random fields. Since we are interested in a linear distribution function in which nonlinear and spatial correlation effects are absent, these dipoles can be considered independent. Then, the distribution function for the solid solution is a convolution of the distribution functions for dipoles of two types [11]. In the Gaussian approximation for these functions, the distribution function for the solid solution is described by the following relationship:

$$f(\mathbf{E}) = \frac{1}{(2\pi)^3} \int \exp(i\boldsymbol{\rho}(\mathbf{E} - \mathbf{E}_0) - x\Delta E_1^2 (\mathbf{e}_1\boldsymbol{\rho})^2 - (1-x)\Delta E_2^2 (\mathbf{e}_2\boldsymbol{\rho})^2) d^3\rho, \quad (4)$$

$$\mathbf{E}_0 = x\frac{T_{1F}}{d_1^*} L_{1F}\mathbf{e}_1 + (1-x)\frac{T_{2F}}{d_2^*} L_{2F}\mathbf{e}_2, \quad (5)$$

where $\mathbf{E}_0$ is the mean field and ΔE_1 and ΔE_2 are the half-widths of the distribution functions induced by the d_1^* and d_2^* dipoles, respectively. These half-widths can be written in the form [12]

$$\Delta E_1^2 = \frac{16\pi}{15}\frac{d_1^{*2}}{\varepsilon_1^2 r_{c1}^3 a_1^3}, \quad \Delta E_2^2 = \frac{16\pi}{15}\frac{d_2^{*2}}{\varepsilon_2^2 r_{c2}^3 a_2^3}, \tag{6}$$

where ε_1 and ε_2 are the permittivities and r_{c1} and r_{c2} are the correlation radii of the first and second components of the solid solution, respectively.

From relationships (4)–(6), it follows that the distribution function for the solid solution depends on the concentration of its components, the order parameters L_{1F} and L_{2F}, the transition temperatures T_{1F} and T_{2F}, the dipole moments, and other physical parameters.

4. GENERAL EQUATIONS DESCRIBING THE PHASE DIAGRAM

The phase diagram should describe a variation in the temperatures of transitions to different phases with an increase in the mole fraction of one of the components with due regard for a change in the phase symmetry. The required information can be obtained from the solution of a set of integral equations (2) taking into account relationships (4) and (5). Substitution of expression (4) into the set of Eqs. (2) leads to sixfold integrals which can be simplified using the dependence of all the integrals on the scalar product $\mathbf{E}\mathbf{e}_i$, i.e., only on the parallel $\mathbf{e}_i$ component of the field. This allows us to integrate with respect to the other two components of the $\mathbf{E}$ field and then to perform integration with respect to $d^*\rho$. As a result, we obtain the relationships

$$L_{1F} = \int_{-\infty}^{+\infty} \tanh(d_1^*\varphi_1(E)/T)\exp\left(-\left(\frac{E-E_{01}}{2\Delta_1}\right)^2\right)\frac{dE}{2\sqrt{\pi}\Delta_1},$$

$$L_{2F} = \int_{-\infty}^{+\infty} \frac{\sinh(2d_2^*\varphi_2(E)/T)}{\cosh(2d_2^*\varphi_2(E)/T) + \cosh(3T_{2A}L_{2A}/T)} \times \exp\left(-\left(\frac{E-E_{02}}{2\Delta_2}\right)^2\right)\frac{dE}{2\sqrt{\pi}\Delta_2}, \tag{7}$$

$$L_{2A} = \int_{-\infty}^{+\infty} \frac{\sinh(2T_{2A}L_{2A}/T)}{\cosh(2d_2^*\varphi_2(E)/T) + \cosh(2T_{2A}L_{2A}/T)} \times \exp\left(-\left(\frac{E-E_{02}}{2\Delta_2}\right)^2\right)\frac{dE}{2\sqrt{\pi}\Delta_2},$$

where $E_{0i} = \mathbf{E}_0\mathbf{e}_i$ (i = 1 and 2); i.e., E_{0i} depends on the angle θ between the directions of dipoles of two types, because $\mathbf{e}_1\mathbf{e}_2 = \cos\theta$. The parameters Δ_i also depend on the angle, that is,

$$\Delta_1 = x(\Delta E_1)^2 + (1-x)(\Delta E_2\cos\theta)^2,$$
$$\Delta_2 = x(\Delta E_1\cos\theta)^2 + (1-x)(\Delta E_2)^2. \tag{8}$$

Relationships (7) represent the final form of integral equations that determine the dependence of the order parameters L_{2A}, L_{2F}, and L_{1F} on the mole fraction x. In turn, these order parameters determine the polarization of the system [see formula (3)]. The temperatures T_C and T_A of transitions to the ferroelectric and antiferroelectric phases of the solid solution are derived from relationships (7) in the limiting case when the order parameters tend to zero. Thus, from expressions (7), we can obtain the following set of equations:

$$L_{1F} = \frac{T_{1F}}{T_C}\left(xL_{1F} + (1-x)\frac{\cos\theta}{p\lambda}L_{2F}\right)I_1(T_C), \tag{9a}$$

$$L_{2F} = \frac{T_{2F}}{T_C}(p\lambda x\cos\theta L_{1F} + (1-x)L_{2F})I_2(T_C), \tag{9b}$$

$$L_{2A} = \frac{T_{2A}}{T_A}(1-x)L_{2A}I_2(T_A), \tag{9c}$$

where

$$I_1(T) = \frac{1}{\sqrt{\pi}}\int_0^\infty \frac{(1+3\alpha_i(Q_iu)^2)\exp\left(\left(\frac{u}{2}\right)^2\right)}{\cosh\left[\frac{T_{iF}}{T}Q_iu(1+\alpha_i(Q_iu)^2)\right]}du \tag{10}$$

and

$$p = \frac{d_2^*}{d_1^*}, \quad \lambda_F = \frac{T_{1F}}{T_{2F}},$$
$$\alpha_i = \alpha_3^{(i)}\left(\frac{T_{iF}}{d_i^*}\right)^2, \quad q_i = \frac{d_i^*\Delta E_i}{T_{iF}},$$
$$\lambda_A = \frac{T_{2A}}{T_{2F}}, \quad Q_1^2 = xq_1^2 + (1-x)\left(\frac{q_2\cos\theta}{p\lambda_F}\right)^2, \tag{11}$$
$$Q_2^2 = x(q_1p\lambda_F\cos\theta)^2 + (1-x)q_2^2$$

are the dimensionless variables. As can be seen, the T_A temperature is determined from formula (9c) and the T_C temperature is found from expressions (9a) and (9b). The solution of these equations has the form

$$\tau_C \equiv \frac{T_C}{T_{2F}} = \frac{1}{2}[x\lambda_F I_1(\tau_C) + (1-x)I_2(\tau_C) \pm \sqrt{(x\lambda_F I_1(\tau_C))^2 + ((1-x)I_2(\tau_C))^2 + 2\cos(2\theta)\lambda_F x(1-x)I_1(\tau_C)I_2(\tau_C)}], \quad (12a)$$

$$\tau_A \equiv \frac{T_A}{T_{2A}} = (1-x)I_2(\tau_A). \quad (12b)$$

Expressions (12) are also the integral equations, because I_i [formula (10)] depends on the transition temperature. Their solution gives the dependences of T_A and T_C on the mole fractions and the material parameters of the solid solution components [see expressions (11)].

5. COMPARISON OF THE THEORY WITH EXPERIMENT

5.1. Phase diagram of $PbZr_{1-x}Ti_xO_3$. The components of this solid solution are antiferroelectric $PbZrO_3$ with the transition temperature $T_{2A} = 503$ K ($T_{2F} \approx T_{2A}$ [9]) and ferroelectric $PbTiO_3$ with the temperature $T_{1F} = 763$ K of the transition from the paraelectric to the ferroelectric phase with a tetragonal symmetry. Both components contain electric dipoles which are randomly distributed in the solid solution. With allowance made for the symmetry of the components, it can be assumed that vectors d_1^* and d_2^* are oriented along the crystallographic directions [001] and [111], respectively. From the above data, we have the following parameters: $\lambda_F \approx 1.516$, $\lambda_A = 1$, and $\cos\theta = 1/\sqrt{3}$. The other parameters were obtained by the fitting to the experimental phase diagram of PZT. First of all, we determined the T_A temperature from relationship (12b). The integral I_2 was numerically calculated at $\alpha_2 = 0.3$ and $q_2 = 2.9$. The dependence of T_A on the mole fraction x is depicted by the dashed line in Fig. 1. Note that the T_A temperature decreases with an increase in x and becomes equal to 0 K at $x = x_C = 0.093$ (where x_C is the critical mole fraction at which the antiferroelectric phase disappears). It is seen that the theoretical results are in reasonable agreement with the experimental data shown by open squares in Fig. 1. At the same time, the transition temperature T_C, which was calculated from expression (12a), increases with an increase in x (the solid line in Fig. 1). Our theory holds for small values of x (see the inset in Fig. 1). The fitting of T_C over the entire range of x was performed by varying the values of p, q_1, q_2, α_1, and α_2. The best agreement was achieved at $p = 0.828$, $q_1 = 0.239$, $q_2 = 0.364$, $\alpha_1 = 3.9$, and $\alpha_2 = 4.3$. As can be seen from Fig. 1, the fitting is also satisfactory at $x > 0.6$, i.e., in the titanium-rich region. For intermediate mole fractions in the range $0.1 < x < 0.6$, the accuracy of such a fitting is not as high as in other concentration ranges. In our opinion, this discrepancy is associated with the existence of additional order parameters in the aforementioned range. These order parameters arise upon improper ferroelectric transitions between the high-temperature and low-temperature rhombohedral phases in which the spontaneous rotation of oxygen octahedra induces the phase transition and makes a certain contribution to the spontaneous polarization [6]. The symmetries of different ferroelectric phases, as well as the symmetry of the morphotropic region with the coexistence of both symmetries (the dotted line in Fig. 1), were calculated by formulas (3), (7), and (8) with the same parameters that were used in the calculations of the transition temperatures. It is seen from Fig. 1 that the morphotropic region lies between $x = 0.453$ at $T = 0$ K and $x = 0.463$ at $T = 611$ K. Thus, the theoretical calculations adequately describe the actual phase diagram [13] shown by open squares in Fig. 1. Note that the best agreement was achieved under the assumption that the half-widths Δ_i of the distribution functions for each component are determined by the properties of the other component of the solid solution. This confirms the assumption that sources of random fields of one component disturb the long-range order of the other component.

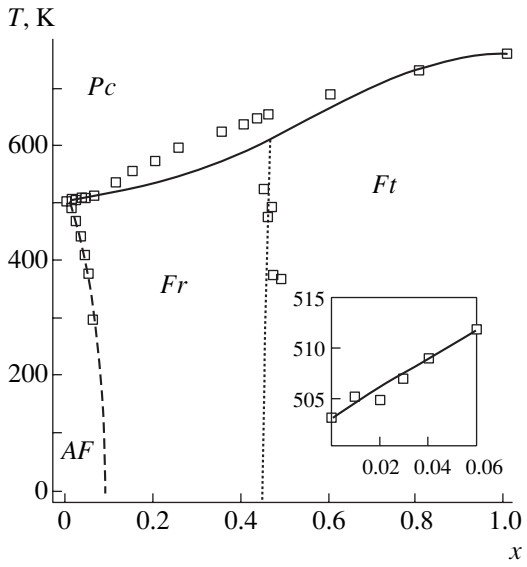

Fig. 1. Phase diagram of $PbZr_{1-x}Ti_xO_3$. Open squares are the experimental data taken from [13]. Calculated transition temperatures are represented by the solid line for the transition from the paraelectric phase *Pc* to the ferroelectric phases *Fr* and *Ft*, the dashed line for the transition from the antiferroelectric phase *AF* to the rhombohedral ferroelectric phase *Fr*, and the dotted line for the transition from the *Fr* phase to the tetragonal ferroelectric phase *Ft*. The inset shows the temperatures of transitions from the *Pc* phase to the *Fr* phase at small *x*.

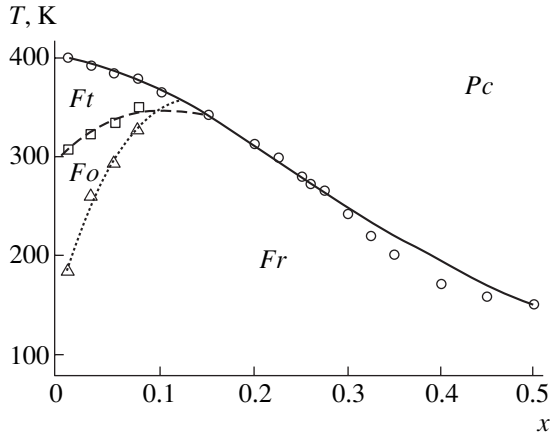

Fig. 2. Phase diagram of $BaZr_xTi_{1-x}O_3$. Open circles, squares, and triangles are the experimental data taken from [7]. The calculated transition temperatures are represented by the dashed line for the transition between the tetragonal *Ft* and orthorhombic *Fo* ferroelectric phases, the dotted line for the transition from the *Fo* phase to the ferroelectric rhombohedral phase *Fr*, and the solid line for the transition from the paraelectric cubic phase *Pc* to the *Ft* and *Fr* phases.

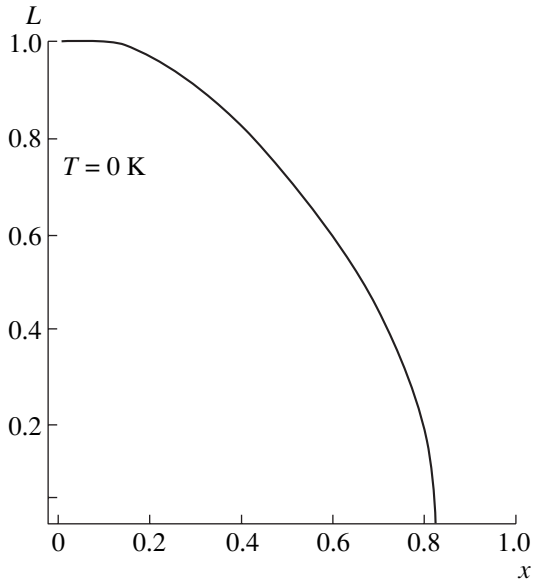

Fig. 3. Dependence of the order parameter on the mole fraction x for the $BaZr_xTi_{1-x}O_3$ system at $T = 0$ K.

5.2. Phase diagram of $BaZr_xTi_{1-x}O_3$. The main component of this solid solution is the $BaTiO_3$ ferroelectric material which can undergo three transitions to the ferroelectric phases with tetragonal, orthorhombic, and rhombohedral symmetries at $T_{2F}^{(1)} = 400$ K, $T_{2F}^{(2)} = 305$ K, and $T_{2F}^{(3)} = 184$ K, respectively. The $BaZrO_3$ phase is paraelectric at all temperatures [4]. In order to fit our theory to the aforementioned experimental findings for BZT, we propose the following model.

It is assumed that zirconium ions in the BZT solid solution can be displaced in such a way that they transform into random electric dipoles for the $BaTiO_3$ component. These dipoles are the main sources of a random field. Since $BaZrO_3$ is treated as a paraelectric phase, the half-width of the distribution function should be larger than the mean field induced by zirconium dipoles. On this basis, we can describe the phase diagram of BZT with the use of relationships (3), (7), and (8) for the following parameters:

$$\begin{aligned} &T_{1F} = 250\ \text{K}, \quad q_1 = 0.6, \quad q_2 = 0, \quad \alpha_1 = 0, \\ &\alpha_2^{(1)} = 0.3, \quad p^{(1)} = 2, \\ &\alpha_2^{(2)} = 2, \quad p^{(2)} = 1.63, \\ &\alpha_2^{(3)} = 8, \quad p^{(3)} = 1.25. \end{aligned} \tag{13}$$

The angles between the dipole directions are chosen from symmetry considerations: $\cos\theta^{(1)} = 1$, $\cos\theta^{(2)} = 1/\sqrt{2}$, and $\cos\theta^{(3)} = 1/\sqrt{3}$. The results of calculations are displayed in Fig. 2. It is seen that the proposed theory adequately describes the experimental phase diagram (see [7] and references therein). Note that the accuracy of the fitting of the dotted and dashed lines to the experimental points at $x > 0.12$ is no more than 10%.

Figure 3 shows the order parameters calculated for the BZT solid solution with the use of the parameters specified by relationships (13) at $T \longrightarrow 0$. It is easy to verify that the order parameters in this limit coincide with each other: $L_1 = L_2$.

As can be seen from this figure, the fraction L of coherently oriented dipoles at $x > 0.3$ is less than 0.9, which corresponds to a mixed ferroelectric glassy state [14]. The critical fraction x_C of zirconium ions at which the formation of the dipole glass occurs ($L = 0$) is equal to approximately 0.82. The behavior inherent in relaxor materials (i.e., the fulfillment of the Vogel–Fulcher law for the dynamic permittivity) was observed at $x \geq 0.25$ in recent works (see [7] and references therein).

The critical value x_C for the transition to the dipole glass phase was predicted by our theory. Unfortunately, the experimental data were obtained only in the concentration range up to $x = 0.5$. Whether or not a state of the dipole glass type exists in a system of $BaTiO_3$ and $BaZrO_3$ solid solutions can be revealed only in the case of complete mutual solubility of the components over the entire concentration range.

6. DISCUSSION

As is known, the differences in the properties of lead and barium compounds are determined by the specific role of lead ions in phase transitions. In a perovskite-type structure ABO_3, all A ions, except lead ions in this position, contribute insignificantly to the lattice polarization. By contrast, lead ions, for example, in $PbTiO_3$,

make the main contribution to the polarization (see, for example, [5] and references therein). In the case of $PbZrO_3$, the antiferroelectric state is characterized by displacements of lead ions. In the framework of the model proposed, the solid solution components introduce electric dipoles with moments $\mathbf{d}_1$ and $\mathbf{d}_2$ into the system. Here, $\mathbf{d}_i$ is the total dipole moment of a unit cell of the corresponding solid-solution component, i.e., the vector sum of the displacements of Pb and Ti ions for $PbTiO_3$ or Ti ions for $BaTiO_3$. Note that all the displacements are considered with respect to an oxygen octahedron. Consequently, the contribution of lead ions can be separated only on the basis of independent microscopic calculations or measurements of the d_1^*/d_2^* ratio, which, in our model, is treated as a fitting parameter. The estimation of this ratio from the known displacements of Ti ions in $PbTiO_3$ and Zr ions in $PbZrO_3$ (see, for example, [5]) gives $p = d_1^*/d_2^* \approx 0.8$, whereas the best fitting is achieved at $p = 0.828$ (see Section 5.1).

Since nothing is known about displacements of Zr ions in $BaZrO_3$, we can calculate the ratios $k_1 = p_1/p_3$ and $k_2 = p_2/p_3$, which are independent of the dipole moment of Zr ions. Then, we compare these values with those obtained from the ratios of polarizations in the corresponding ferroelectric phases (see, for example, [15]): $k_1 = 1.8$ and $k_2 = 1.4$, whereas our model gives $k_1 = 1.6$ and $k_2 = 1.3$ [see relationships (13)]. Moreover, from the p parameters specified by relationships (13), it follows that the displacement of the Zr ion in $BaZrO_3$ is only half as large as the displacement of the Ti ion in the $BaTiO_3$ tetragonal phase. Therefore, the use of our model leads to reasonable ionic displacements in PZT and BZT. Actually, the fitting parameters that depend on the half-width of the distribution function can be estimated from formulas (6) in the case when the correlation radii and the dipole moments are known.

The parameters dependent on the coefficients of nonlinear terms play an important role in describing the features of the phase diagram for BZT, because these parameters determine the location of maxima in the dependence of T_C on x. The fitting parameters $\alpha_2^{(i)}$ are in qualitative agreement with the coefficients of nonlinear terms α for different $BaTiO_3$ phases: $\alpha_2^{(1)} < \alpha_2^{(2)} < \alpha_2^{(3)}$ [see relationships (13)] and $\alpha^{(1)} < \alpha^{(2)} < \alpha^{(3)}$ (see [15]). At the same time, the quantitative evaluation of the $\alpha_2^{(i)}$ parameters is a complex problem whose solution requires independent measurements of these quantities. Nonetheless, the $\alpha_2^{(i)}$ quantities are treated as fitting parameters, whereas other parameters can be estimated from *a priori* considerations. Another interesting feature of the phase diagram for BZT consists in emerging the relaxor properties at $x \geq 0.27$. As far as we know, such a behavior has never been observed for PZT solid solutions. This can be explained by the fact that the spontaneous polarization due to the displacement of lead ions in $PbTiO_3$ is twice as large as the polarization in $BaTiO_3$ [5]. As a result, a random field induced by Zr ions is incapable of destroying the more stable long-range order in $PbTiO_3$. At the same time, this field can destroy the less stable long-range order in $BaTiO_3$ at a sufficiently high concentration of Zr ions.

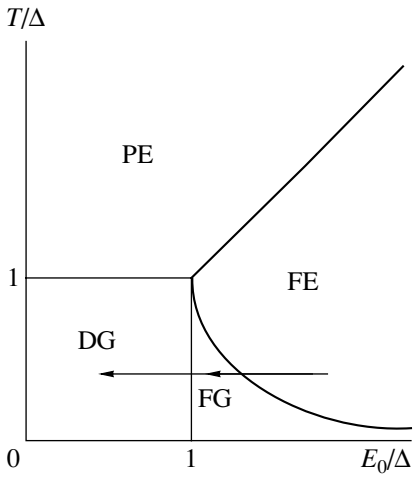

Fig. 4. A schematic phase diagram for a disordered system [16].

In summary, it can be concluded that, in a certain concentration range, the solid solution consisting of a ferroelectric and a paraelectric should transform into the relaxor state. This statement follows from the fact that the contribution of the paraelectric component to the mean field E_0 is sufficiently small, but it completely determines the half-width of the distribution function [$q_2 = 0$, see relationships (13)]. The contribution of the ferroelectric component to E_0 [see formula (5)] decreases because of the decrease in $1 - x$ with an increase in x, provided that subscripts 1 and 2 refer to the paraelectric and ferroelectric phases, respectively, and $T_{2A} = 0$ and $L_{2A} = 0$ in relationships (7). Therefore, an increase in the paraelectric concentration brings about a decrease in the mean field strength and an increase in the half-width of the distribution function Δ [see expressions (8)]. This should lead to a decrease in the ratio E_0/Δ with an increase in x. Since the state of the system under consideration [paraelectric (PE), ferroelectric (FE), dipole glass (DG), and a mixed ferroelectric glass (FG) in which the long-range order coexists with a short-range order of dipole glass] depends strongly on the E_0/Δ ratio (Fig. 4), it can be inferred that, as the mole fraction x increases, the system transforms from the ferroelectric state into the ferroelectric glassy state and then into the dipole glass state at a sufficiently low temperature (see arrows in Fig. 4). It is known that the ferroelectric glassy and dipole glass states are the characteristic features of relaxor materials

[14]. These phases exhibit a nonergodic behavior and follow the Vogel–Fulcher law, which describes the temperature dependence of the dynamic dielectric susceptibility. This can be associated with the formation of random electric fields in the system [17].

From the calculated dependence of the order parameter on the mole fraction x for the $(BaTiO_3)_{1-x}(BaZrO_3)_x$ system, we obtain the mole fraction at which this system transforms into the relaxor state ($x \approx 0.3$, Fig. 3). It is seen from Fig. 3 that the BZT system is in the ferroelectric glass phase in the range $0.3 < x < 0.8$ and could be in the dipole glass phase at $x \geq 0.8$; however, the question as to whether the BZT solid solutions exist at $x > 0.5$ remains open. The assumption that a mixed ferroelectric–paraelectric system transforms into a relaxor state is confirmed by the existence of the dipole glass state and the relaxor properties in the $(BaTiO_3)_{1-x}(SrTiO_3)_x$ system at $x \geq 0.9$ [18]. It is most likely that this transition also occurs in the paraelectric–antiferroelectric system. However, unlike the ferroelectric–paraelectric system in which T_{2F} is the temperature of the transition to the existing ferroelectric phase, T_{2F} in the case under consideration is a characteristic of the hypothetical ferroelectric phase, which follows from the two-sublattice model for antiferroelectrics and is close to (even if slightly less than) the T_{2A} temperature [9].

7. CONCLUSION

Thus, in the present work, the random-field theory was applied to the calculation of the phase diagrams for mixed ferroelectric systems, specifically for the PZT and BZT solid solutions. The theoretical approximation proposed describes, both qualitatively and quantitatively, the experimental phase diagrams, including the relaxor behavior of BZT in the range $x > 0.3$. However, the corresponding experimental value of x is equal to approximately 0.25. This discrepancy can stem from the assumption that the electric dipoles of zirconium ions are the main sources of random fields. Zirconium ions can also be considered dilatation centers or elastic dipoles, which, as is known, destroy the long-range order and lead to the appearance of relaxor properties [14]. Similar calculations and the calculation of the contribution from the tilting of oxygen octahedra to the polarization of PZT are currently being performed by the authors and will be reported in a separate paper.

ACKNOWLEDGMENTS

We are grateful to T. Egami for helpful discussions of the results.

REFERENCES

1. J. C. Burfoot and I. G. W. Taylor, *Polar Dielectrics and Their Applications* (Univ. of California Press, Berkeley, 1979; Mir, Moscow, 1981).
2. H. W. Gundel, Ferroelectrics **184**, 89 (1996).
3. G. H. Haertling, Ferroelectrics **75**, 25 (1987).
4. W. Känzig, Solid State Phys. **4**, 1 (1957); *Ferroelectrics and Antiferroelectrics* (Inostrannaya Literatura, Moscow, 1960).
5. M. E. Lines and A. M. Glass, *Principles and Applications of Ferroelectrics and Related Materials* (Oxford Univ. Press, Oxford, 1977; Mir, Moscow, 1981).
6. M. J. Haun, E. Furman, S. J. Jang, and L. E. Cross, Ferroelectrics **99**, 13 (1989).
7. R. Farhi, M. El. Marssi, A. Simon, and J. Ravez, Eur. Phys. J. B **9**, 599 (1999).
8. V. A. Stephanovich, M. D. Glinchuk, and L. Jastrabic, cond-mat/9907249 (1999).
9. V. G. Vaks, *Introduction to the Microscopic Theory of Ferroelectrics* (Nauka, Moscow, 1973).
10. M. D. Glinchuk, R. Farhi, and V. A. Stephanovich, J. Phys.: Condens. Matter **9**, 10237 (1997).
11. M. D. Glinchuk, V. G. Grachev, M. F. Deĭgen, A. B. Roĭtsin, and L. A. Suslin, *Electrical Effects in Radiospectroscopy* (Nauka, Moscow, 1981).
12. M. D. Glinchuk and V. A. Stephanovich, J. Phys.: Condens. Matter **6**, 1617 (1994).
13. B. Jaffe, W. R. Cook, and H. Jaffe, *Piezoelectric Ceramics* (Academic, New York, 1971; Mir, Moscow, 1974).
14. M. D. Glinchuk and R. Farhi, J. Phys.: Condens. Matter **8**, 6985 (1996).
15. F. Jona and G. Shirane, *Ferroelectric Crystals* (Pergamon, Oxford, 1962; Mir, Moscow, 1965).
16. K. Binder and A. P. Young, Rev. Mod. Phys. **58**, 801 (1986).
17. M. D. Glinchuk and V. A. Stephanovich, J. Appl. Phys. **85**, 1722 (1999).
18. V. V. Lemanov, E. P. Smirnova, P. P. Syrnikov, and E. A. Tarakanov, Phys. Rev. B **54** (5), 3151 (1996).

Translated by O. Borovik-Romanova

Physics of the Solid State, Vol. 43, No. 5, 2001, pp. 923–926. From Fizika Tverdogo Tela, Vol. 43, No. 5, 2001, pp. 888–891.

LOW-DIMENSIONAL SYSTEMS AND SURFACE PHYSICS

Two-Dimensional Wannier–Mott Exciton in a Uniform Electric Field[1]

S. I. Pokutnyi*, M. H. Tyc, W. Salejda**, and J. Misiewicz****

**Illichivsk Educational Research Center, Odessa State University, Illichivsk, Odessa oblast, 68001 Ukraine*

e-mail: univer@ivt.ilyichevsk.odessa.ua

*** Institute of Physics, Wroclaw University of Technology, Wroclaw, 50-370 Poland*

Received July 26, 2000

Abstract—A new treatment of the problem of a two-dimensional Wannier–Mott exciton in a uniform electric field, based on the parabolic coordinates, is presented. The quasi-stationary Hamiltonian is regularized, and the efficient numerical methods are applied. The dependence of the exciton binding energy on the electric field is computed. The results are very close to those obtained by the perturbation theory calculations. © *2001 MAIK "Nauka/Interperiodica".*

The three-dimensional Wannier–Mott exciton (WME) is usually described within the effective-mass approximation [1–11]. The essential effect of an external uniform electric field **E** is that the problem becomes nonstationary. The exciton can be ionized, and its lifetime is finite, which necessitates the use of the time-dependent Schrödinger equation (SE). However, assuming that the exciton lifetime is sufficiently long, one can treat the problem as a quasi-stationary one and employ the time-independent SE

$$\left[-\frac{\hbar^2}{2m_e^*}\nabla_{\mathbf{r}_e}^2-\frac{\hbar^2}{2m_h^*}\nabla_{\mathbf{r}_h}^2-\frac{e^2}{\epsilon|\mathbf{r}_e-\mathbf{r}_h|}+e\mathbf{E}(\mathbf{r}_e-\mathbf{r}_h)\right] \times\Phi(\mathbf{r}_e,\mathbf{r}_h)=(\varepsilon_{\text{exc}}-\varepsilon_g)\Phi(\mathbf{r}_e,\mathbf{r}_h), \quad (1)$$

where ε_g is the energy gap and ε_{exc} is the total exciton energy. It is analogous to the hydrogen atom problem [12].

Equation (1) is not solvable analytically for $E \neq 0$. In the parabolic coordinates, the 3D WME problem transforms to two coupled one-dimensional eigenvalue problems [3, 5–8, 12]. The case when both the electron and the hole motion are restricted to two dimensions (which can be modeled by a very deep and narrow quantum well and is analogous to a two-dimensional atom) can be treated similarly [9]. The 2D problem was solved analytically in [13] for $E = 0$. The case of $E \neq 0$ was investigated numerically in [9]. Both 3D and 2D cases with $E = 0$ were also considered in the momentum space [11].

In this paper, we present a new approach to the 2D WME problem. It is based on a parabolic coordinate system defined in a way different from that in [9]. This approach (1) is a generalization of the standard method presented in [12] for the 3D hydrogen atom, (2) results in the Hamiltonian regularization, and (3) allowed us to perform a numerical analysis of the problem with the help of the efficient modern methods of linear algebra.

In the standard variable-separation procedure, one introduces the center-of-mass coordinate R, the relative coordinate r, and the reduced mass μ. This allows the total envelope function to be written in the form $\Phi(\mathbf{R}, \mathbf{r}) = \exp(i\mathbf{K}\cdot\mathbf{R})\psi(\mathbf{r})$, which gives $\varepsilon_{\text{exc}} = \dfrac{\hbar^2K^2}{2(m_e^*+m_h^*)} + \varepsilon + \varepsilon_g$. The wave function ψ satisfies the dimensionless SE

$$\left[-\nabla^2-\frac{2}{r}+2\mathbf{E}\cdot\mathbf{r}\right]\psi(\mathbf{r}) = \varepsilon\psi(\mathbf{r}). \quad (2)$$

Equation (2) is written in the atomic units of length $a_0 = \dfrac{\epsilon\hbar^2}{\mu e^2}$ (effective Bohr radius), energy $W_0 = \dfrac{\mu e^4}{2\epsilon^2\hbar^2}$ (effective Rydberg), and field $E_0 = \dfrac{e}{\epsilon a_0^2}$.

1. TWO-DIMENSIONAL EXCITON FOR $E = 0$ IN POLAR COORDINATES

In the polar (or cylindrical) coordinate system (r, φ), Eq. (2) for $E = 0$ reads

$$\left[-\frac{1}{r}\frac{\partial}{\partial r}\left(r\frac{\partial}{\partial r}\right)-\frac{1}{r^2}\frac{\partial^2}{\partial\varphi^2}-\frac{2}{r}\right]\psi(r,\varphi) = \varepsilon\psi(r,\varphi).$$

[1] This article was submitted in English.

It is solvable analytically [13]. The normalized eigenfunctions of the bound states are

$$\psi^{c}_{n,m}(r,\varphi) = \frac{\lambda_n^{3/2}}{\sqrt{\pi}}\sqrt{\frac{(n-|m|)!}{(n+|m|)!}} \times e^{-\lambda_n r}[2\lambda_n r]^{|m|}L^{2|m|}_{n-|m|}(2\lambda_n r)e^{im\varphi} \quad (3)$$

for $|m| \le n = 0, 1, 2, \ldots$; $\lambda_n = (n + 1/2)^{-1}$; and c stands for "cylindrical." The eigenenergies are $\varepsilon_{n,m} = \varepsilon_n = -(n + 1/2)^{-2}$. The symbol $L^a_N(x)$ denotes the generalized Laguerre polynomials [14].

2. TWO-DIMENSIONAL EXCITON IN PARABOLIC COORDINATES

This section presents an idea of a new approach to the problem. Let us write the SE (2) in the parabolic coordinate system using Eqs. (A1) and (A3)

$$\left[-\frac{1}{u^2+v^2}\left(\frac{\partial^2}{\partial u^2}+\frac{\partial^2}{\partial v^2}\right)-\frac{4}{u^2+v^2} + (u^2-v^2)E\right]\psi(u,v) = \varepsilon\psi(u,v). \quad (4)$$

We factorize $\psi(u, v) = f(u)g(v)$ and remove the singularity by multiplying Eq. (4) by $u^2 + v^2$. After separating the variables, we get two coupled equations with separation parameter C

$$\left[-\frac{d^2}{du^2}-\varepsilon u^2+Eu^4-2\right]f(u) = \left[-\frac{d^2}{du^2}+V_+(u)\right]f(u) = -Cf(u),$$
$$\left[-\frac{d^2}{dv^2}-\varepsilon v^2-Ev^4-2\right]g(v) = \left[-\frac{d^2}{dv^2}+V_-(v)\right]g(v) = Cg(v). \quad (5)$$

Equations (5) are one-dimensional Schrödinger-like equations. They are eigenvalue problems for the separation parameter C. The binding energy ε is a parameter in the functions $V_\pm$, which we call quasi-potentials (they correspond to potentials in the ordinary SE)

$$V_\pm(\varepsilon; w) = -\varepsilon w^2 \pm Ew^4 - 2, \quad (6)$$

where w denotes the coordinate u or v. The quasi-potentials are shown in Fig. 1.

The numerical procedure of solving Eq. (5) should then consist in finding such a value of $\varepsilon(E)$ for which the eigenvalues C and $-C$ match both equations (5).

Here, we should note that the alternative definition of the parabolic coordinates in Eq. (A4) applied in [9] also leads to variable separation. One then gets a set of two ordinary SEs (with ε being the eigenvalue), but the singularity is not removed and the numerical problem is more difficult.

The value of $f(0)$ is unknown. We cannot impose the convenient boundary condition $f(u = 0) = 0$, because it would imply $\psi(0, 0) = 0$. In order to avoid this difficulty, let us extend the domain of u to negative values (we make use of the properties of the conformal mapping). This involves the condition

$$\psi(u, v) = \psi(-u, -v) \quad (7)$$

(see Appendix). The quasi-potentials in Eq. (6) are even functions. Therefore, from Eq. (7), it follows that $f(u)$ and $g(v)$ have to be either both even or both odd.

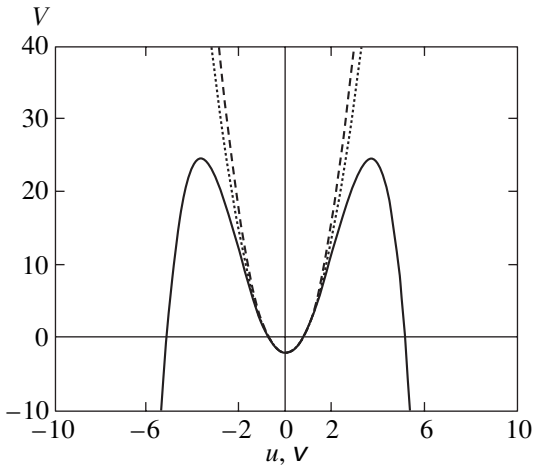

Fig. 1. The quasi-potentials V_+ (dashed line) and V_- (solid line) for $E = 0.15$ and for $E = 0$ (dotted line).

3. ANALYTICAL RESULTS FOR $E = 0$

The case of $E = 0$ is solvable analytically. Equations (5) then read (the plus–minus sign corresponds to the second and the first equation, respectively)

$$\left[-\frac{d^2}{dw^2}+\lambda^2 w^2\right]f_\pm(w) = (2 \pm C)f_\pm(w), \quad (8)$$

where w means u or v; f_- and f_+ denote f and g, respectively; and $\lambda^2 = -\varepsilon$. We note that Eq. (8) is an "inverted" quantum linear oscillator eigenvalue problem with the eigenvalues $2 \pm C = (2n_\pm + 1)\lambda$ for $n_\pm = 0, 1, 2, \ldots$ and the eigenfunctions $f_{n\pm}(x) = \exp(-(1/2)\lambda x^2)H_{n\pm}(\sqrt{\lambda}\,x)$, where $H_N(x)$ denotes Hermite polynomials [14].

It is easy to show that $\lambda_{n_+, n_-} = 2/(n_+ + n_- + 1)$, where n_+ and n_- denote the parabolic quantum numbers. From

Eq. (7), we get $n_+ + n_- = 2n$, where $n = 0, 1, 2, \ldots$ denotes the principal quantum number describing the energy of an eigenstate $\varepsilon_{n_+, n_-} = \varepsilon_n = -\lambda_n^2 = -(n + 1/2)^{-2}$. Normalized wave functions have the form

$$\psi_{n_+, n_-}(u, v) = I_{n_+, n_-}\exp\left[-\frac{1}{2}\lambda_n(u^2 + v^2)\right] \times H_{n_-}(\sqrt{\lambda_n}u)H_{n_+}(\sqrt{\lambda_n}v),$$

where I_{n_+, n_-} is the normalization factor depending only on n: $I_{n_+, n_-} = I_n$. We will change the indices of ψ in order to put n among them. As the secondary quantum number, we choose $j = 1/2(n_+ - n_-) = -n, -n + 1, \ldots, n - 1, n$.

Finally, the normalized eigenfunctions of bound states in parabolic coordinates are

$$\psi^p_{n, j}(u, v) = \frac{\lambda_n^{3/2}}{\sqrt{\pi}}\frac{i^{n+j}\exp[-(1/2)\lambda_n(u^2 + v^2)]}{2^n\sqrt{(n-j)!(n+j)!}} \times H_{n-j}(\sqrt{\lambda_n}u)H_{n+j}(\sqrt{\lambda_n}v), \quad (9)$$

where "*p*" stands for "parabolic."

4. NUMERICAL RESULTS

The solution of Eq. (5) is equivalent to finding a zero of the function

$$h(E; \varepsilon) = C_0^+(E, \varepsilon) + C_0^-(E, \varepsilon)$$

for a given E. Here, $C_0^\pm$ denotes the lowest eigenvalues of the separation constant C obtained from the first and the second equations in (5) for the respective signs.

We computed the eigenvalues $C_0^\pm$ with the help of a precise and efficient grid matrix method [15–17].

The applied methods solve the SE within a finite interval with the boundary conditions assuming the wave function to vanish at its ends. This is equivalent to putting infinite potential barriers there. These boundary conditions cause no essential error for the quasi-potential $V_+(u)$ if the interval considered is sufficiently wide. For the quasi-potential $V_-(v)$, the function $g(v)$ does not vanish for $|v| \longrightarrow \infty$ and the error caused by boundary conditions has to be minimized. We did this by using the modified potential shown in Fig. 2. The interval d was enlarged until it no longer affected the results.

The results of the computation are presented in Fig. 3. We compare the computed correction to the ground state energy $\Delta\varepsilon_0^{\text{comp}}(E)$ with one obtained from the second-order perturbation theory [9]

$$\Delta\varepsilon_0^{\text{pert}}(E) = -\frac{21}{128}E^2 \approx -0.164E^2.$$

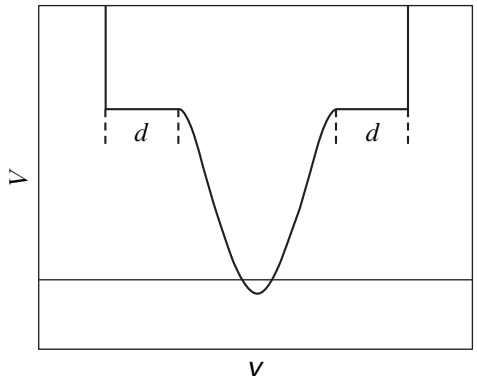

Fig. 2. The modified quasi-potential $V'_-(v)$.

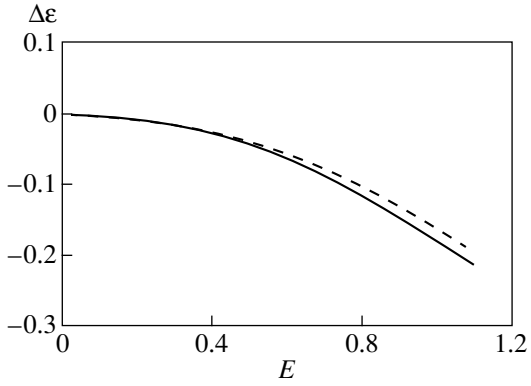

Fig. 3. Numerical results: $\Delta\varepsilon_0^{\text{comp}}$ (solid line) and $\Delta\varepsilon_0^{\text{pert}}$ (dashed line).

The results obtained with these two methods do not differ much ($|\Delta\varepsilon_0^{\text{comp}}(E)|$ is higher than $|\Delta\varepsilon_0^{\text{pert}}(E)|$ by less than 1% for $E < 0.05$ and about 10% for $E \sim 1$). Therefore, the two-dimensional exciton, as a relatively strongly bound system, is weakly polarizable and the perturbation theory gives surprisingly good results. This observation is in agreement with one made in [9]. The situation is different for the 3D case [9, 10].

We also computed the tunneling coefficient T within a WKB-like 1D approximation (tunneling along the x direction). It reaches a relatively high value ($T \sim 0.1$) at $E \sim 0.7$.

5. CONCLUSIONS

The main results presented in this paper are as follows.

(1) The Schrödinger equation describing a two-dimensional Wannier–Mott exciton in a uniform electric field can be transformed to two coupled one-dimensional eigenvalue problems of the anharmonic linear oscillator type.

(2) The applied coordinate transformation results in Hamiltonian regularization, which allows us to use simple and efficient numerical algorithms.

(3) The problem is nonstationary and the applied quasi-stationary approach has an approximate character for strong external fields.

(4) The numerical calculations show that the exciton ground state disappears at $E \simeq 1.1$ (in atomic units).

(5) The computed ground state energy correction does not differ much from the results of the perturbation theory. This means that the 2D exciton is less polarizable than the 3D exciton.

In further investigations, it will be important to solve the time-dependent Schrödinger equation (at least approximately, by using the complex energy $\tilde{\varepsilon} = \varepsilon - i\Gamma$) and to evaluate the exciton lifetime. It also seems interesting to investigate a 2D exciton with a 2D Coulomb potential ($\ln r$).

APPENDIX

THE PARABOLIC COORDINATE SYSTEMS

The parabolic coordinates (u, v) are defined on the x–y plane as [18]

$$x = \frac{1}{2}(u^2 - v^2), \quad y = uv. \tag{A1}$$

We choose $u \geq 0$ and $\operatorname{sgn} v = \operatorname{sgn} y$. Relations (A1) can be written as a two-branch conformal mapping

$$x + iy = re^{i\varphi} = (u + iv)^2; \tag{A2}$$

the connection with the polar coordinates (r, φ) is also simple. The x–y plane is mapped into two equivalent half-planes $u \geq 0$ and $u \leq 0$. Therefore, it is possible to consider only symmetric functions $f(-u, -v) = f(u, v)$, but on the whole u–v plane.

In the parabolic coordinates (A1), we have

$$\nabla^2 = \frac{1}{u^2 + v^2}\left(\frac{\partial^2}{\partial u^2} + \frac{\partial^2}{\partial v^2}\right), \quad dS = (u^2 + v^2)\,du\,dv. \tag{A3}$$

The parabolic coordinates are sometimes defined in a different way [9]

$$x = \frac{1}{2}(u - v), \quad y = \sqrt{uv}; \tag{A4}$$

these relations cannot be written as a conformal mapping.

REFERENCES

1. V. M. Agranovich, *The Theory of Excitons* (Nauka, Moscow, 1968; Pergamon, Oxford, 1970).
2. R. S. Knox, *Theory of Excitons* (Academic, New York, 1963; Mir, Moscow, 1966).
3. E. I. Rashba and M. D. Sturge, *Excitons* (Nauka, Moscow, 1985).
4. G. Bastard, *Wave Mechanics Applied to Semiconductor Heterostructures* (Les Editions de Physique, Les Ulis Cedex, 1988).
5. C. B. Duke and M. E. Alferieff, Phys. Rev. **145**, 583 (1966).
6. J. D. Dow and D. Redfield, Phys. Rev. B **1**, 3358 (1970).
7. D. F. Blossey, Phys. Rev. B **2**, 3976 (1970).
8. D. F. Blossey, Phys. Rev. B **3**, 1382 (1971).
9. F. L. Lederman and J. D. Dow, Phys. Rev. B **13**, 1633 (1976).
10. S. I. Pokutnyi, W. Salejda, J. Misiewicz, and K. Ryczko, Ukr. Phys. J. **43**, 1259 (1998).
11. C. Y. Chao and S. L. Chuang, Phys. Rev. B **43**, 6530 (1991).
12. L. D. Landau and E. M. Lifshitz, *Course of Theoretical Physics*, Vol. 3: *Quantum Mechanics: Non-Relativistic Theory* (OGIZ, Moscow, 1948; Pergamon, New York, 1977).
13. M. Shinada and S. Sugano, J. Phys. Soc. Jpn. **21**, 1936 (1966).
14. *Handbook of Mathematical Functions*, Ed. by M. Abramowitz and I. A. Stegun (Dover, New York, 1979; Nauka, Moscow, 1979).
15. P. Dean, Rev. Mod. Phys. **44**, 127 (1972).
16. J. van der Maelen Uría, S. García-Granda, and A. Menéndez-Velázques, Am. J. Phys. **64**, 327 (1996).
17. B. Lindberg, J. Chem. Phys. **88**, 3805 (1988).
18. E. Madelung, *Die Mathematischen Hilfsmittel des Physikers* (Springer-Verlag, Berlin, 1957; Nauka, Moscow, 1968).

Physics of the Solid State, Vol. 43, No. 5, 2001, pp. 927–931. Translated from Fizika Tverdogo Tela, Vol. 43, No. 5, 2001, pp. 892–895.

LOW-DIMENSIONAL SYSTEMS AND SURFACE PHYSICS

Structural Analysis of Composite Metal–Insulator Materials by Small-Angle X-ray Scattering

I. V. Rozhanskiĭ*, D. A. Zakheim*, T. N. Vasilevskaya, and S. A. Gurevich***

**Ioffe Physicotechnical Institute, Russian Academy of Sciences, Politekhnicheskaya ul. 26, St. Petersburg, 194021 Russia*
e-mail: igor@quantum.ioffe.rssi.ru
***Grebenshchikov Institute of Silicate Chemistry, Russian Academy of Sciences,*
ul. Odoevskogo 24/2, St. Petersburg, 199155 Russia
Received October 5, 2000

Abstract—A small-angle x-ray scattering study of the structure of Cu : SiO_2 composite films obtained by magnetron cosputtering is reported. The experimental spectra are analyzed by direct numerical simulation of scattering from a polydisperse system of spherical particles with a high volume concentration. The calculated scattering spectra were found to fit well to the experiment if a log-normal particle distribution in size is assumed, and the parameters of this distribution were determined. © *2001 MAIK "Nauka/Interperiodica".*

INTRODUCTION

There has recently been an increase in interest in the investigation of composite materials (nanocomposites), i.e., structures containing nanosized metal grains distributed randomly in an insulating matrix [1]. The electrostatic energy of a metal particle of such a size charged by one electron, E_c, should reach hundreds of millielectronvolts, which means that such structures should exhibit macroscopic charge quantization effects at up to room temperatures [2]. This makes nanocomposites promising materials with a device potential for nanoelectronics [3].

The method most widely used in the fabrication of composite materials is magnetron cosputtering from two sources [1]. Metal grains form in these materials as a result of phase separation in a supersaturated solid solution of a metal in an insulator [4]. Because grain formation in a composite material is governed by statistical processes, the grains thus produced are distributed in size. This distribution is an important structural characteristic which should be known for a theoretical analysis of the electrical properties of composite materials [5]. Structural studies of composite materials by transmission electron microscopy (TEM) show the metal grains to be predominantly spherical in shape, as well as permit one to estimate their characteristic size. Nevertheless, there is still no reliable method capable of yielding detailed information on the grain size distribution.

This paper reports on a small-angle x-ray scattering (SAXS) study of the structure of a composite material conducted to learn about the character of the grain distribution in size. SAXS is a diffraction method employed widely to probe the supratomic structure of substances. The most essential merit of SAXS is its capability of analyzing the structure of disordered systems [6]. In the case of systems with a low concentration of spherical scattering centers, the problem of deriving the particle size distribution from a SAXS spectrum can be solved in an explicit form [7]; however, the material under study has a high concentration (28 vol %) of metal grains. Interparticle interference effects play an important part in the scattering from such structures. In this case, the problem of finding the particle size distribution cannot be solved in an explicit form. The scattering data obtained from systems with a high concentration of spherical particles are usually analyzed either within the Percus–Yevick approximation taking into account interparticle interference [8] or by a direct numerical simulation of scattering. Employing numerical simulation for an analysis of scattering from high-concentration systems has, in our opinion, a more universal character, whereas the Percus–Yevick approach introduces a certain error, which increases with increasing concentration [9].

In this work, an analysis of experimental SAXS data through numerical simulation of scattering from a composite material permitted derivation of the grain size distribution with a high accuracy. We also demonstrated the effect of the width of the size distribution and of the concentration of the metallic phase on the SAXS spectral shape.

1. PREPARATION OF Cu : SiO_2 FILMS AND THEIR STRUCTURAL ANALYSIS BY TEM AND X-RAY DIFFRACTOMETRY

We studied composite metal–insulator films prepared by magnetron cosputtering of the metal and insulator on a rotating silicon substrate, with copper used as the metal and amorphous SiO_2 as the insulator. The films were obtained on an SCM-450 magnetron sput-

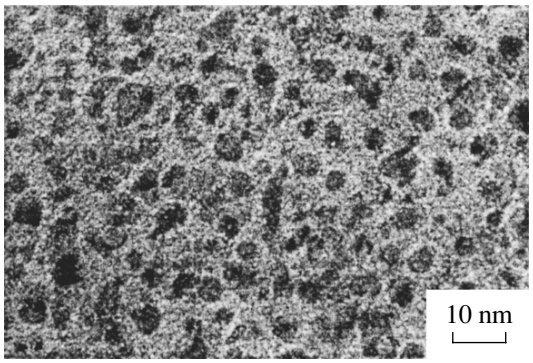

Fig. 1. TEM image of a composite film.

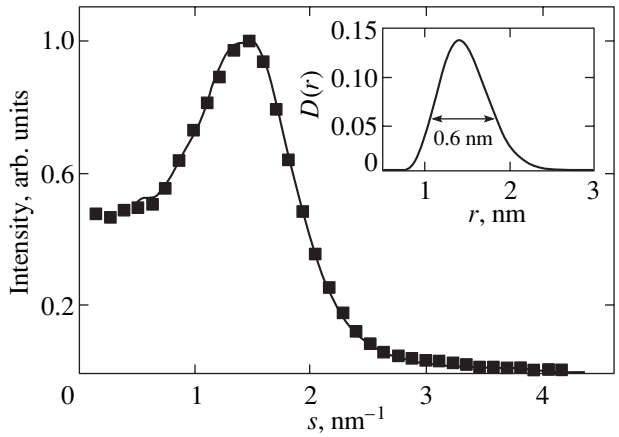

Fig. 2. Experimental SAXS spectrum (symbols) and simulation (solid line). Inset: grain distribution in the radius.

tering setup (Alcatel, France) in an argon environment, with the substrates rotated above the Cu and SiO_2 sources. The sputtering rates were chosen so that less than one monolayer of material would be deposited on the substrate in one transit over the sources. In this way, one obtained 200-nm thick composite Cu : SiO_2 metal–insulator films with a copper concentration of 28 vol %. A detailed description of the technology involved can be found in [10].

Figure 1 presents a TEM photomicrograph of a part of a film. The material prepared is seen to be an amorphous matrix containing randomly spaced metallic clusters of a spherical shape (grains) with an average size of about 3 nm. However, deriving a particle size distribution from such a photograph would be extremely difficult, because the images of individual grains overlap strongly as a result of their high density.

The structure of the Cu : SiO_2 films thus prepared was studied also by x-ray diffractometry. An overall x-ray diffraction spectrum exhibited peaks corresponding to reflections from the ⟨111⟩ (reflection angle $2\theta = 43.3°$) and ⟨200⟩ ($2\theta = 50.5°$) copper lattice planes. The presence of these peaks implies unambiguously that the metal grains in the composite film under study have a crystal structure characteristic of bulk copper.

2. ANALYSIS OF COMPOSITE FILM SAXS SPECTRA

The small-angle x-ray scattering study was made with Cu K_α radiation ($\lambda = 1.54$ Å). The experimental curves were obtained on an x-ray setup with a Kratky collimator. Collimation corrections accounting for the beam height and width were introduced. The SAXS intensity was measured to within ±1%. The x-ray beam measured 0.1×12 mm. The measurement technique is described in detail in [11]. An experimental SAXS spectrum is displayed in Fig. 2 (symbols).

The scattering intensity is given in the general case by the well-known Zernike–Prinz expression [12]

$$I(\mathbf{s}) = NF^2(\mathbf{s})S(\mathbf{s}), \quad (1)$$

where $\mathbf{s}$ is the scattering vector; its magnitude is $s = 4\pi/\lambda \sin\Theta$; 2Θ is the scattering angle; $F(\mathbf{s})$ is the averaged form factor of the scattering particles, which depends only on their shape and size; $S(\mathbf{s})$ is a structural factor depending on the mutual particle location; and N is the number of particles in the system.

For a polydisperse system of particles of the same shape with a size distribution $D(r)$, we have

$$F(\mathbf{s}) = \int f(\mathbf{s}, r)D(r)dr, \quad (2)$$

where the form factor of a sphere of radius r can be written as [6]

$$f(s, r) = \frac{4}{3}\pi r^3 \times 3\frac{\sin sr - sr\cos sr}{(sr)^3}. \quad (3)$$

As can be seen from Eq. (3), the expression for the form factor contains the particle size only in a dimensionless product sr. The structural factor $S(\mathbf{s})$ has the form

$$S(\mathbf{s}) = \frac{1}{N}\sum_{j,k}\exp(is(\mathbf{r}_j - \mathbf{r}_k)), \quad (4)$$

where $\mathbf{r}_j$ is the position vector of the jth particle. Relation (4) can be recast for a macroscopically isotropic system as [13]

$$S(s) = 1 + n\int_{V_0}(g(r) - 1)\frac{\sin sr}{sr}4\pi r^2 dr + nF_0, \quad (5)$$

where V_0 is the volume of the system; $n = N/V_0$ is the density of scattering sites; $g(r)$ is the radial correlation function of mutual particle location [13], which has the meaning of the probability to find the center of a sphere at a distance r from that of the given sphere; and F_0 is the form factor of the scattering system of volume V_0. The contribution of the last term becomes small already

for $s > 2\pi/L$, where L is the dimension of the scattering volume in the direction of the scattering vector.

The composite material under study is a structure with a high concentration of scattering particles; the complex form and the concentration dependence of the $g(r)$ function for such systems does not permit one to solve analytically the inverse problem of deriving the particle size distribution from a SAXS spectrum. The small-angle scattering data for such systems are analyzed by simulating the scattering structure, and the parameters of the distribution are found by fitting the model to the experimental spectrum. Percus and Yevick [8] proposed an analytical approximation to the correlation function $g(r)$ for concentrated systems of spherical particles; however, the error associated with this approximation grows with increasing concentration [9]. An alternative approach valid for any concentration consists in a direct numerical simulation of small-angle scattering, and it is this approach that was used in the present work.

In our model, the composite material was treated as a system of spherical scattering centers (metallic spheres) having a given size distribution. We employed the so-called log-normal distribution, characteristic of a broad class of polydisperse systems, in which clusters form by self-organization [14]

$$D(\ln r) = \frac{1}{\sqrt{2\pi}\beta}\exp\left[-\frac{(\ln r - \ln r_0)^2}{2\beta^2}\right]. \qquad (6)$$

Here, r_0 and β are the parameters of this distribution and the volume concentration c of the spheres is another parameter. Spheres with the size distribution in Eq. (6) were arranged randomly in a given volume $L_x \times L_y \times L_z$ so as to preclude their overlap. The quantities r_0 and β were subsequently used as fitting parameters when comparing the results of the simulation with the experimental curve; however, in actual fact, it suffices to perform fitting by the β parameter in the sr dimensionless coordinates and after that find r_0 by a proper scaling of the spectrum.

Direct calculation of the radial correlation function $g(r)$ involves computational difficulties and requires a large number of averagings, because even small fluctuations in the correlation function $g(r)$ at large r affect the magnitude of the structural factor considerably because of the rapid growth of the r^2 factor in the integrand in Eq. (5). This entails large errors in the determination of the structural factor for small s. A less cumbersome approach lies in a direct calculation of the amplitude and total scattering intensity

$$A = \sum_{j=1}^{N} f_j \exp(i\mathbf{s}\mathbf{r}_j), \qquad I(s) = |A(s)|^2. \qquad (7)$$

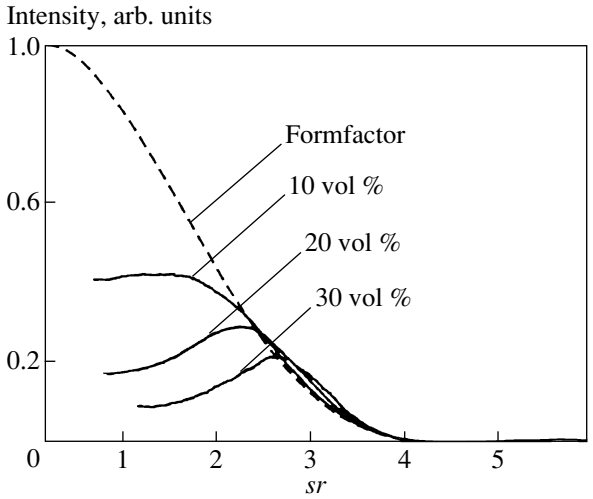

Fig. 3. Calculated SAXS spectra for different metallic-phase concentrations (for a monodisperse system).

The parallelepiped in which the spheres were arranged measured $2500r_0 \times 20r_0 \times 20r_0$, with its long side aligned with the scattering vector. By choosing these dimensions, we succeeded in excluding the effect of scattering from the volume as a whole [the "zeroth peak" corresponding to the last term in Eq. (5)] within the scattering-vector region of interest. The number of the spheres was ~50000 for a volume concentration about 30 vol % and the above dimensions of the parallelepiped. In addition, the scattering spectra obtained were averaged incoherently over 500 random realizations.

3. DISCUSSION OF RESULTS

Before beginning to fit the experimental SAXS spectrum, one has to establish the influence of the parameters of the structure such as the volume concentration c and dispersion β on the shape of this spectrum. This will permit one to estimate the accuracy with which these parameters can be determined by the fitting procedure.

Figure 3 illustrates the influence of the interference effects on the shape of a SAXS spectrum. The dashed line in the figure shows the form factor of a sphere; it should coincide with the SAXS spectrum in the low-concentration limit. One readily sees that as the sphere concentration increases, there appears in the spectrum an interference dip at low angles and a maximum shifting toward increasing s. The position of this maximum corresponds to the average distance between the sphere centers in the system. All the spectra in Fig. 3 were calculated for a monodisperse system.

Figure 4 displays the dependence of the scattering spectrum shape on the standard deviation β. For conve-

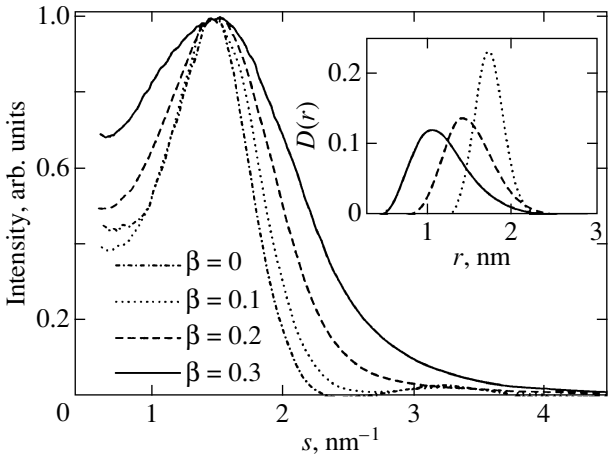

Fig. 4. Calculated SAXS spectra for different β parameters. Inset: corresponding distributions in the radius.

nience of comparison, all spectra are shifted by properly choosing r_0 so that their maxima coincide in position with the maximum in the experimental curve. The size distributions themselves are plotted in the inset.

The experimental SAXS spectrum was fitted using the known volume concentration c = 28 vol %. The fitting procedure was as follows: first, we determined (for a fixed r_0') the value of β providing the best fit of the experimental to the calculated spectrum in dimensionless coordinates sr_0; the maximum of this curve is denoted by $s_{\max} r_0'$. After this, we used the position of the maximum in the experimental curve $s_{\max}^{\exp}$ to find $r_0 = r_0' s_{\max}/s_{\max}^{\exp}$. The results of the fitting are shown in Fig. 2 by a solid line; the parameters of the grain size distribution in the real structure obtained by this fitting are r_0 = 1.4 nm and β = 0.2. The corresponding distribution in the radii is plotted in the inset in Fig. 2. The results of the calculations are seen to coincide with the experimental spectrum with a very good accuracy, which indicates the validity of using the log-normal size distribution in the model.

Note that, as is evident from Fig. 4, the shape of the SAXS spectrum is very sensitive to a variation of the β parameter, thus permitting one to determine its value from the results of the fitting with a high accuracy. The calculated SAXS spectrum was found to deviate noticeably from the experiment when β differed from its optimum value already by $\Delta\beta = 0.025$. The error Δr in the determination of r_0 is governed by that of finding the position of the maximum in the experimental SAXS spectrum, Δs, namely, $\Delta r/r_0 \sim \Delta s/s_{\max}$. In our experiment, the resolution in the scattering vector Δs was 0.1 nm^{-1}, which corresponds to $\Delta r/r \simeq 10\%$.

The average grain radius differs from r_0 because of the asymmetry in the distribution:

$$\bar{r} = \frac{\int_0^\infty r \exp(-(\ln r - \ln r_0)^2/2\beta^2)\,dr}{\int_0^\infty \exp(-(\ln r - \ln r_0)^2/2\beta^2)\,dr} \simeq 1.5 \text{ nm}. \quad (8)$$

This value is in good agreement with the TEM data.

Thus, we have studied spectra of small-angle x-ray scattering in a Cu : SiO_2 composite material prepared by magnetron cosputtering. The Cu volume concentration in the material was 28 vol %; at such concentrations, interference effects play a dominant role in the SAXS spectrum formation. The Cu grain size parameters were derived by direct scattering-intensity simulation. The model calculation was performed under the assumption of the grains having a log-normal size distribution, and we obtained very good agreement of the results of the calculation with the experiment. This permits one to maintain that this form of the size distribution is valid for such materials. The high sensitivity of the SAXS spectral shape to a variation of the distribution parameters permitted us to determine the values of these parameters in the Cu : SiO_2 composite material with a high accuracy: $r_0 = 1.4 \pm 0.1$ nm, $\beta = 0.200 \pm 0.025$. The average grain radius obtained by fitting, $r \simeq 1.5$ nm, is in good agreement with TEM data. Note that no data on the specific size distribution could be obtained earlier by other techniques.

ACKNOWLEDGMENTS

This work was supported by the Russian Foundation for Basic Research (grant no. 98-02-18210) and the Ministry of Science of the RF, "Physics of Solid-State Nanostructures" program (grant nos. 97-2014 and 97-1035).

REFERENCES

1. B. Abeles, P. Sheng, M. D. Coutts, and Y. Arie, Adv. Phys. **24**, 407 (1975).
2. D. V. Averin and K. K. Likharen, *Mesoscopic Phenomena in Solids*, Ed. by B. Al'tschuler, P. Lee, and R. Webb (Elsevier, Amsterdam, 1991), p. 169.
3. S. V. Vyshenski, Pis'ma Zh. Éksp. Teor. Fiz. **61**, 105 (1995) [JETP Lett. **61**, 111 (1995)].
4. I. M. Lifshits and V. V. Slezov, Zh. Éksp. Teor. Fiz. **35**, 479 (1959) [Sov. Phys. JETP **8**, 331 (1959)].
5. D. A. Zakheim, I. V. Rozhanskiĭ, I. P. Smirnova, and S. A. Gurevich, Zh. Éksp. Teor. Fiz. **118**, 637 (2000) [JETP **91**, 553 (2000)].

6. D. I. Svergun and L. A. Feĭtin, *Small-Angle X-ray and Neutron Scattering* (Nauka, Moscow, 1986).
7. J. H. Letscher and P. W. Schmidt, J. Appl. Phys. **37**, 649 (1966).
8. J. K. Percus and G. J. Yevick, Phys. Rev. **110**, 1 (1958).
9. D. Frenkel, R. J. Vos, C. G. de Kruif, and A. Vrij, J. Chem. Phys. **84**, 4625 (1986).
10. S. A. Gurevich, A. I. Ekimov, I. A. Kudryavtsev, *et al.*, Fiz. Tekh. Poluprovodn. (St. Petersburg) **26**, 102 (1992) [Sov. Phys. Semicond. **26**, 57 (1992)].
11. T. N. Vasilevskaya, S. G. Yastrebov, N. S. Andreev, *et al.*, Fiz. Tverd. Tela (St. Petersburg) **41**, 2088 (1999) [Phys. Solid State **41**, 1918 (1999)].
12. F. Zernike and J. A. Prinz, Z. Phys. **41**, 184 (1927).
13. J. M. Ziman, *Models of Disorder: The Theoretical Physics of Homogeneously Disordered Systems* (Cambridge Univ. Press, Cambridge, 1979; Mir, Moscow, 1982).
14. C. G. Granqvist and R. A. Buhrman, J. Appl. Phys. **47**, 2200 (1976).

Translated by G. Skrebtsov

Physics of the Solid State, Vol. 43, No. 5, 2001, pp. 932–934. Translated from Fizika Tverdogo Tela, Vol. 43, No. 5, 2001, pp. 897–899.

LOW-DIMENSIONAL SYSTEMS AND SURFACE PHYSICS

Optical Properties of Magnetic Quasi-2*D* Nanocomposites in the IR Spectral Region

A. N. Drachenko[1], A. N. Yurasov[2], I. V. Bykov[3], E. A. Gan'shina[2], A. B. Granovskiĭ[2], V. V. Ryl'kov[4], D. V. Smirnov[1, 5], J. Leotin[1], and B. Dieny[6]

[1]*LPMC and SNCMP, Complexe Scientifique de Rangueil INSA, 31077 Toulouse Cedex, France*

[2]*Moscow State University, Vorob'evy gory, Moscow, 119899 Russia*

e-mail: yurasov@magn.phys.msu.su

[3] *Vernadsky Institute of Geochemistry and Analytical Chemistry, Russian Academy of Sciences, ul. Kosygina 19, Moscow, 117975 Russia*

[4] *Russian Research Centre Kurchatov Institute, pl. Kurchatova 1, Moscow, 123182 Russia*

[5]*Ioffe Physicotechnical Institute, Russian Academy of Sciences, Politekhnicheskaya ul. 26, St. Petersburg, 194021 Russia*

[6]*CEA/Dep. de Recherche Fondamentale sur la Matiere Condensee, 38054 Grenoble, France*

Received October 10, 2000

Abstract—The optical absorption spectra of magnetic quasi-2*D* Co island films and of hybrid Co/SiO_2 multilayers in which island films are separated by SiO_2 layers were studied. It was found that, when the Co film was masked by a thin SiO_2 layer, the absorption considerably increased and exceeded 0.8. This was observed when the Co fraction was substantially lower than its critical value for the percolation transition. Moreover, the maximal absorption in this case weakly depends on both the effective film thickness and the number of Co layers. Numerical analysis shows that the observed peculiarities of the absorption spectra of the structures based on quasi-2*D* granulated Co films are connected to a great extent with the peculiar features of the interference effects occurring in such systems. © *2001 MAIK "Nauka/Interperiodica".*

The metal–insulator composites (granulated films) are ensembles of chaotically distributed small metallic inclusions of 1 to 10 nm in size and of an insulator filling the space between them. There is some critical fraction of a metal $x = x_c$ (the percolation threshold) above which these materials exhibit metallic properties. Below the threshold, the composite conductivity is determined by tunnel transfer of electrons between separate granules of the metal and is similar to the hopping conductivity of doped semiconductors. From the physical and practical points of view, the most interesting are a number of unique phenomena observed in these materials at metal fractions near the percolation threshold, in particular, anomalous absorption and scattering of radiation and nonlinear optical phenomena [1, 2]. In the case of magnetic nanocomposites, the phenomena of interest are the magnetooptical and magnetorefractive effects, the giant negative magnetoresistance, and the giant anomalous Hall effect [3–5].

At the present time, on the example of quasi-2*D* granulated films based on nonmagnetic metals such as Au [6, 7], it is established that the maximal anomalous absorption in such systems is reached in the vicinity of the percolation transition and does not exceed 0.5, which is in accordance with the results of theoretic calculations [1]. In this work, we report the results of an experimental investigation of the optical absorption spectra of magnetic quasi-2*D* Co island films and hybrid Co/SiO_2 multilayers in which Co island films are separated by SiO_2 layers. It is found that, when the Co film is covered by a thin SiO_2 layer, the absorption grows considerably and exceeds 0.8. This is observed when the Co fraction is substantially lower than its critical value for the percolation transition. Moreover, the maximum absorption in this case weakly depends on both the effective film thickness and the number of Co layers.

The quasi-2*D* structures were prepared by evaporation of a Co island film with an effective thickness of 1.0 to 1.25 nm upon an Si substrate covered with a buffer SiO_2 layer 300 nm thick. The homogeneity of the film was achieved by rotation of the silicon substrate, keeping its temperature at a level of 300 K. The multilayers consisted of alternating Co island films and 3- to 5-nm thick SiO_2 layers. The results of the sample structural studies were reported in [4]. The percolation transition in these systems was observed for an effective Co thickness of ≈2.0 nm [4]. Two types of structures were studied: structures with an external masking SiO_2 layer ≈50 nm thick, preserving the Co films from the effect of the surrounding atmosphere, and structures without this layer.

The absorption A in these structures was determined from measurements of their transmission T and reflection R by the formula $A = 1–T–R$. Measurements were

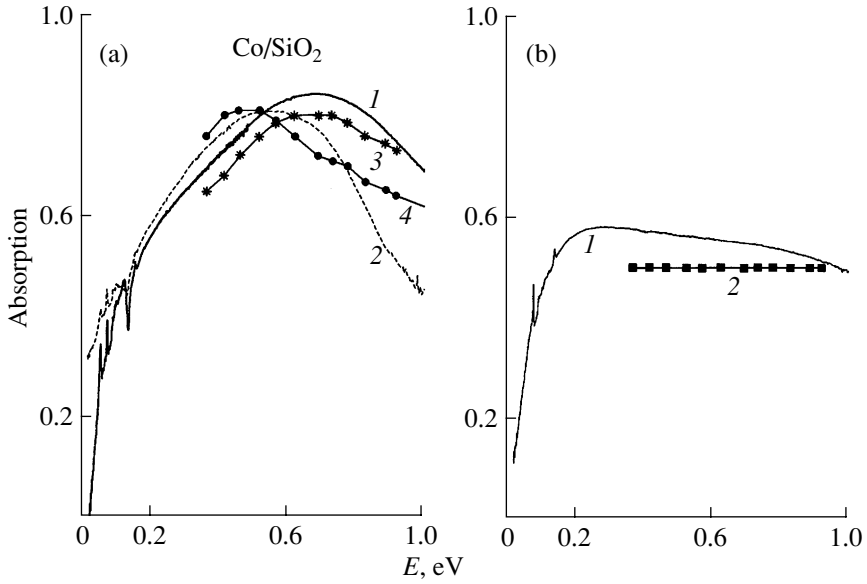

Absorption spectra of a hybrid Co/SiO_2 system. (a) Experimental spectra of the SiO_2 (50 nm)/nanocomposite $Co–SiO_2$/buffer SiO_2 layer (300 nm)/Si system: (*1*) Co (1.3 nm)/SiO_2 bilayer, (*2*) $[Co\ (1.8\ nm)/SiO_2\ (3\ nm)]_{n=8}$ multilayer, (*3*, *4*) theoretical spectra for the SiO_2 (50 nm)/nanocomposite $Co–SiO_2/SiO_2$ buffer layer (300 nm)/Si ($x = 0.4$, $L = 0.8$) system with nanocomposite thickness 5 and 30 nm, respectively. (b) Experimental spectrum of the nanocomposite $Co–SiO_2/SiO_2$ buffer layer (300 nm)/Si system: (*1*) Co (1.8 nm)/SiO_2 bilayer, (*2*) theoretical spectrum of the nanocomposite $Co–SiO_2/SiO_2$ buffer layer (300 nm)/Si system with nanocomposite thickness 5 nm, $x = 0.4$, and $L = 0.8$.

carried out by means of a Bruker IFS 113 Fourier spectrometer in the wavelength range $\lambda = 1.2–70$ μm at 300 K. The results of our studies are presented in the figure.

First, we note that the absorption *A* in the quasi-2*D* structures without a masking SiO_2 layer, with the metal fraction value being in the vicinity of the percolation transition (the effective Co thickness is 1.8 nm), is close to 0.5 and practically does not depend on the quantum energy at frequencies higher than the frequency determined by the inverse electron relaxation time, as was predicted in [1]. A reflection maximum is detected in insulating $Co–SiO_2$ films with Co layers 1.3- to 1.6-nm thick. The energy of this maximum $\hbar\omega \approx 0.67$ eV is considerably lower than the excitation energy of surface plasmons $\hbar\omega_{sp}$ for isolated Co particles (for spherical Co particles in SiO_2, one estimates $\hbar\omega_{sp} \approx 1.3$ eV for the plasma frequency $\hbar\omega_p = 3.7$ eV). We also note that the absorption at the maximum has an anomalous value of 0.84, considerably exceeding the theoretical limit for two-dimensional granulated films. In addition, the shape of the spectrum changes only insignificantly in the midinfrared region with increasing film thickness (from 1.3 to 1.6 nm). It is interesting that for multilayers (the number of Co/SiO_2 bilayers is eight) having a masking covering, the absorption is also 0.8 at a maximum. However, the maximum is observed not at 0.62 eV, as is the case with bilayers, but at 0.5 eV (see figure).

To analyze the observed peculiarities, a numerical calculation of the absorption spectra was carried out. The calculation was made in the framework of the generalized effective-medium model taking into account the form anisotropy of particles [8]. Initially, we calculated the diagonal components of the effective permittivity tensor for a layer of ferromagnetic particles by using the symmetrical Maxwell–Garnett approximation [8]. We considered this layer to be a $Co_x–(SiO_2)_{1-x}$ nanocomposite and varied both the filling factor *x* and the particle form factor *L*. Further on, using the Fresnel formulas, we calculated the absorption of the SiO_2/nanocomposite $Co–SiO_2$/buffer SiO_2 layer/Si system taking into account the reflection at the interfaces and absorption in the substrate. We suppose that the particles (their size is 1 to 2 nm [4]) have, on average, an anisotropic form; however, they are assembled in clusters at intermediate fraction values. In addition, due to their magnetic properties, the new-formed particle clusters (in particular, chains of granules) have an anisotropic form [9]. The results of the calculation are also represented in the figure. As is clear from the figure, the calculations which take into account the fact that elongated objects ("ellipsoids") having a semiminor-to-semimajor axis ratio up to 1 to 5 are formed in the sample satisfactorily describe the spectrum of the samples with an effective Co thickness equal to 1.3 nm. If one considers spherical particles, then the absorption will be lower than 0.8. The main condition for obtaining such a value and the absorption maximum is the interference, which is taken into account in calculations by the Fresnel formulas. One obtains the correct position and the value of the absorption maximum for mul-

tilayers, but the other part of the spectrum differs from the experimental one. This is due to the fact that the multilayer system was calculated in the framework of the effective-medium approximation and the periodicity of layers has not been taken into account; that is, the multilayer system was considered as a granulated alloy. It is also necessary to point out that the description of the quasi-2*D* Co–SiO_2 layer in terms of the effective-medium theory for the three-dimensional case can also lead to additional error, especially in the very vicinity of the percolation threshold [10].

Thus, the numerical analysis shows that the observed peculiarities of the absorption spectra for structures based on the quasi-2*D* granulated Co films are mainly due to the specific features of the interference effects occurring in these systems. The anisotropy of the form of Co clusters, which is due to the ferromagnetic properties of the metal, also plays a noticeable role. We also note that quite a high level of absorption of the Co/SiO_2 bilayers with activated conductivity indicates the principle possibility of their use for creation of highly sensitive bolometric sensors of IR radiation. The absorbing element in such sensors serves at the same time as a temperature indicator.

ACKNOWLEDGMENTS

The authors are grateful to B.A. Aronzon for discussion of the work and for valuable advice.

This work was supported by the Russian Foundation for Basic Research, grant nos. 00-02-17191 and 00-02-17797; by the Russian–French PICS Foundation, grant no. 98-02-22037; and by the Interdisciplinary Research and Development Program "Physics of Solid-State Nanostructures," grant no 97-1081.

REFERENCES

1. A. K. Sarychev, D. J. Bergman, and Y. Yagil, Phys. Rev. B **51** (8), 5366 (1995); V. M. Shalaev and A. K. Sarychev, Phys. Rev. B **57** (20), 13265 (1998).
2. F. Brouers, S. Blacher, and A. K. Sarychev, Phys. Rev. B **58** (23), 15897 (1998).
3. A. B. Granovskiĭ, M. V. Kuz'michev, and J. P. Clerc, Zh. Éksp. Teor. Fiz. **11**, 1762 (1999) [JETP **89**, 955 (1999)].
4. B. Dieny, S. Sankar, M. R. McCarthey, *et al.*, J. Magn. Magn. Mater. **185**, 283 (1998).
5. B. A. Aronzon, D. Yu. Kovalev, A. N. Lagar'kov, *et al.*, Pis'ma Zh. Éksp. Teor. Fiz. **70** (2), 87 (1999) [JETP Lett. **70**, 90 (1999)].
6. Y. Yagil, P. Gadenne, C. Julien, and G. Deutscher, Phys. Rev. B **46** (4), 2503 (1992).
7. S. Berthier, J. Peiro, S. Fagnent, and P. Gadenne, Physica A (Amsterdam) **241** (1–2), 1 (1997).
8. A. Granovsky, M. Kuzmichev, and J. P. Clerc, J. Magn. Soc. Jpn. **23**, 382 (1999).
9. Yu. I. Petrov, *Physics of Small Particles* (Nauka, Moscow, 1982).
10. A. P. Vinogradov, I. G. Busanov, O. P. Posudnevsky, and V. E. Romanenko, J. Phys.: Condens. Matter **6**, 4351 (1994).

Translated by A. Sonin

Physics of the Solid State, Vol. 43, No. 5, 2001, pp. 935–940. Translated from Fizika Tverdogo Tela, Vol. 43, No. 5, 2001, pp. 900–905.

LOW-DIMENSIONAL SYSTEMS AND SURFACE PHYSICS

The Charge State of Conducting Fine-Dispersed Systems in an Insulating Matrix

Yu. V. Medvedev* and A. M. Grishin**

** Donetsk Physicotechnical Institute, National Academy of Sciences of Ukraine, Donetsk, 83114 Ukraine*

*** Department of Condensed Matter Physics, Royal Institute of Technology, S-100 44 Stockholm, Sweden*

Received June 28, 2000; in final form, October 16, 2000

Abstract—The influence of fluctuations in the number of Fermi particles on the charge state of fine-dispersed metallic grains in an insulating matrix is investigated. It is suggested that the system of grains does not form a tunnel medium and that charge transfer between metallic elements of the composite occurs due to thermal excitations of electrons over barriers. As follows from a calculation of the grand partition function, the average charge of the ith grain is a nonlinear function of the potential V_i of the conductor. © *2001 MAIK "Nauka/Interperiodica".*

INTRODUCTION

The unusual electrical properties of fine-dispersed granulated (nanocrystalline) materials are due to the small sizes of grains, the insulating interlayers between them, and charge discreteness [1–6]. In particular, when the characteristic energy of charge fluctuations on metallic grains $E_c = e^2/2C$ (e is the electron charge and C is the typical capacity of grains in contact with each other) exceeds the energy of thermal fluctuations, a phenomenon called Coulomb blockade occurs in charge transfer in a fine-dispersed grain medium [7–10]. This effect, in its simplest form, was observed and explained earlier in the late 1960s [7]. Numerous experiments (see, e.g., [5, 6, 8]) have shown that the voltage–current characteristics (VCC) of these media are nonlinear. In most cases, when the voltage V across a sample is not very large, the experimental dependence $R(T, V)$ can be represented as $R(T, V) = R(T)g(T, V)$, where $g(T, V) \longrightarrow 1$ at $V \longrightarrow 0$ and $R(T)$ is the temperature dependence of the resistance, providing that the Ohm law is valid. Experiments carried out with nanocomposites of various compositions show that $R(T) \sim \exp(T_0/T)^\alpha$, where $T_0 \sim E_c$ has the meaning of activation energy, and the exponent α falls in the range from 1/4 to 1 [1–8]. A similar dependence with the most typical exponent $\alpha = 1/2$ was first obtained in the framework of the theory of activated tunneling [8], by assuming that some "structure relation" exists between the sizes of the grains and the distances between them. However, as has been shown recently [10], the "1/2 law" is not due to any artificial selection rules for the tunnel intergrain junctions but is a simple consequence of a wide spread in the grain sizes, typical of actual nanocomposites. In [3], another approach (based on an analysis of relaxation processes in the system) to the description of current states in granulated media was stated and the peculiarities of conducting tunneling structures containing metallic grains in a barrier layer were considered. It is particularly remarkable that the Coulomb blockade effects are also exhibited by a variety of disordered conductors revealing a diffusion scattering mechanism [11].

The Coulomb blockade effect is clearly observable when investigating single-electron tunneling transport through metallic islands [12, 13] (the island diameter is less than 5 nm): equidistant Coulomb steps occur in the VCC. Each step corresponds to a time-averaged island charge change of unity. A remarkable result of those experiments is the observation of this effect at liquid nitrogen and room temperatures. This is due to extra small diameters of metallic islands, which are attained by their preparation technology using a scanning tunneling microscope and combined electron-beam lithography and ionic-beam deposition.

Another interesting property of such mesoscopic structures is the correlation between the acts of tunneling of individual electrons. The time correlation of tunneling events is most clearly manifested by voltage oscillations with a frequency $f = I/e$ [14], which appear when a junction having a small capacity is connected to a source of a direct current I. In [15], single-electron oscillations were observed in one-dimensional blocks of aluminum–aluminum-oxide–aluminum tunneling junctions (each including from 15 to 53 junctions) with an area of up to 0.006 μm^2 and a capacity of ~0.2 fF.

A theory describing systems with magnetic micrograins was developed in [9]. Spin-dependent electron tunneling combined with the Coulomb blockade was investigated both in Co–Al–O films with various compositions [16] and in a $Co/Al_2O_3/Co$ tunnel junction [17], in which aluminum oxide contained a layer of Co microclusters with dimensions from 2 to 4 nm. The tunneling structure based on a granulated film, which consisted of magnetically hard ferromagnetic nanoparti-

cles of $Co_{80}Pt_{20}$ introduced in a SiO_2 matrix, was investigated in [18].

In the case where the grains are in a superconducting state, the Coulomb energy E_c should be compared with the characteristic energy of the Josephson interaction E_j between the grains [19–22]. For sufficiently small values of the E_j/E_c ratio, the charge fluctuations in grains destroy the long-range phase coherence and, consequently, superconductivity in the granulated systems is suppressed. A phase diagram of the granulated superconductors with allowance made for quantum effects and dissipative currents in the system was thoroughly analyzed in [23].

A theory of all the effects mentioned above is based on the assumption that electrons (Cooper pairs) can overflow from one grain to another by means of activated tunneling, the probability of which is determined by the expression $P \sim \exp(-2\chi s - T_0/T)$, where $\chi = 2\pi h^{-1}(2m\Phi_0)^{1/2}$, m is the free electron mass, Φ_0 is the effective height of a barrier, χ^{-1} is the decay length of the wave function in the insulator, and s is the thickness of the insulating interlayer. In the case where the inequality $\chi_s \ll T_0/T$ is met, the conductivity of the nanocomposites will be associated only with thermal activation of charge carriers and will be due to thermal electron flow over barriers between the microparticles. The effect of the charge fluctuations in such a system of two metallic particles, but forming a usual capacitor rather than a tunneling junction, on the capacity of the system was calculated in [24]. Depending on the relationship between the parameters involved, the differential capacity of the two metallic particles oscillates or exhibits a resonant behavior similar to that of the capacity of a single grain introduced into an insulating layer of a tunnel junction [3]. Therefore, when a nanocomposite is a constituent of an electric circuit, it would be expected that the average charge of the ith grain $\langle Q_i\rangle = e\langle N_i - N_{0i}\rangle$ (N_i is the operator of the Fermi particle number on the ith conductor and N_{0i} is the number of charge carriers on the ith conductor in the absence of a charge on it) will no longer be linearly related to the potentials V_i as occurs in the classic theory of electricity.

The aim of the present work is to calculate the grand partition function Z of a system of charged metallic grains in an insulating matrix with allowance for the fluctuations of an excess number of Fermi particles on the grains. A systematic approach using a microscopic Hamiltonian for the energy of the electrostatic interaction between charges in the system made it possible to perform calculations in a mean-field approximation for micrograins with sizes satisfying the condition $r_{i\,\min}/\lambda_{TF} \gg 1$ (here, $r_{i\,\min}$ is the minimum geometric size of the ith conductor and λ_{TF} is the Thomas–Fermi radius). According to the result obtained for Z, the distribution

$$\langle Q_i\rangle = \beta^{-1}\partial \ln Z/\partial V_i - eN_{0i} = -\partial\Omega/\partial V_i - eN_{0i} \quad (1)$$

(β is the inverse temperature and Ω is the thermodynamic potential of the system) is determined in a nontrivial way by the potentials V_i. In particular, the differential capacity of two neighboring grains becomes dependent on the potential difference between them.

1. GRAND PARTITION FUNCTION OF A SYSTEM OF CHARGED METALLIC GRAINS

We consider a nonideal Fermi gas placed in a thermostat of a grand canonical ensemble with a fixed volume $v = \Sigma v_i$ (here, v_i is the volume of the ith conducting element of the system) and a temperature and chemical potential of the ith conductor $\mu_i = \mu_0 + eV_i$ (μ_0 is the chemical potential of the system at equilibrium). In this case, in order to calculate $\langle Q_i\rangle$ [see Eq. (1)], one should find the thermodynamic potential

$$\Omega(v, T, \mu) = -\beta^{-1}\ln \mathrm{Sp}\{\exp[-\beta(H - \Sigma\mu_i N_i)]\} = -\beta^{-1}\ln Z \quad (2)$$

of a system of conductors in an insulating matrix. Here, $H = \Sigma H_{0i} + H_{\mathrm{int}}$, where H_{0i} are the Hamiltonians of individual elements of the ensemble of conductors, and H_{int} is the operator of the electrostatic interaction energy between the charge densities in the system

$$H_{\mathrm{int}} = 1/2\int d\mathbf{r}d\mathbf{r}'V(\mathbf{r}-\mathbf{r}')\delta\rho(\mathbf{r})\delta(\mathbf{r}'). \quad (3)$$

In Eq. (3), $V(\mathbf{r} - \mathbf{r}')$ is the Coulomb potential and $\delta\rho(\mathbf{r}) = \rho - n$ is the operator of the excess charge density (the density n allowing for the effect of the positively charged background is determined in such a way that $n = N_{0i}/v_i$ when the point $\mathbf{r}$ is in the volume of the ith metallic reservoir). The partition function of a system of charged conductors can be written as the averaged T_τ exponential

$$Z = Z_0\left\langle T_\tau \exp\left[-\int_0^\beta H_{\mathrm{int}}(\tau)d\tau\right]\right\rangle_0. \quad (4)$$

The angle brackets in Eq. (4) denote averaging over the equilibrium ensemble of electron subsystems situated in different grains and not interacting with each other

$$\langle\ldots\rangle = Z_0^{-1}\mathrm{Sp}\{\exp[-\beta\Sigma(H_{0i} - \mu_i N_i)]\ldots\}.$$

The dependence H_{int} on τ in Eq. (4) results from the use of the interaction representation.

The explicit form of the operator H_{int} enables one to represent Eq. (4) for Z in the form of the functional integral [25]

$$Z = A^{-1}\int D\varphi(\mathbf{r}, \tau)$$

$$\times \exp\left\{-\int_0^\beta d\tau \int d\mathbf{r}(\nabla\varphi(\mathbf{r},\tau))^2/8\pi - \beta\Omega_1\{\varphi(\mathbf{r},\tau)\}\right\} \quad (5)$$

$$= A^{-1}\int D\varphi(\mathbf{r},\tau)\exp\{-S\{\varphi(\mathbf{r},\tau)\}\},$$

where

$$A = \int D\varphi(\mathbf{r},\tau)\exp\left\{-\int_0^\beta d\tau\int d\mathbf{r}(\nabla\varphi(\mathbf{r},\tau))^2/8\pi\right\},$$

$$\Omega_1\{\varphi(\mathbf{r},\tau)\} = -\beta^{-1}$$

$$\times \ln\left\{Z_0\left\langle T_\tau \exp\left\{-ie\int_0^\beta d\tau\int d\mathbf{r}\varphi(\mathbf{r},\tau)\delta\rho(\mathbf{r},\tau)\right\}\right\rangle_0\right\}. \quad (6)$$

The representation of the T_τ exponential in Eq. (4) in the form of Eq. (5) is convenient because $\varphi(\mathbf{r}, \tau)$ is defined in Eq. (5) in all space, with $\varphi(\mathbf{r}, \tau)|_{r\to\infty} = 0$.

According to the self-consistent, or mean, field approximation, the main contribution to the integral in Eq. (5) comes from the function $\varphi(\mathbf{r}, \tau)$ corresponding to a minimum of the functional $S\{\varphi(\mathbf{r}, \tau)\}$. In the interior of the ith conductor, this function obeys the equation

$$\nabla^2\varphi_{(\mathrm{in})i}(\mathbf{r},\tau) = -4\pi\delta\Omega_1\{\varphi(\mathbf{r},\tau)\}/\delta\varphi(\mathbf{r},\tau) = -4\pi ie\langle\langle\delta\rho_i(\mathrm{r},\boldsymbol{\tau})\rangle\rangle. \quad (7)$$

In the regions where $\langle\langle\delta\rho_i(\mathbf{r}, \tau)\rangle\rangle = 0$, we have

$$\nabla^2\varphi_{(\mathrm{ex})}(\mathbf{r},\tau) = 0, \text{ with } \varphi_{(\mathrm{ex})}(\mathbf{r},\tau)|_{r\to\infty} = 0. \quad (8)$$

For the average value of a variable in Eq. (7), we have introduced the notation

$$\langle\langle\delta\rho(\mathbf{r},\tau)\rangle\rangle = \frac{\left\langle T_\tau\exp[-ie\int d\tau\int d\mathbf{r}\varphi(\mathbf{r},\tau)\delta\rho(\mathbf{r},\tau)]\delta\rho(\mathbf{r},\tau)\right\rangle_0}{\left\langle T_\tau\exp[-ie\int d\tau\int d\mathbf{r}\varphi(\mathbf{r},\tau)\delta\rho(\mathbf{r},\tau)]\right\rangle_0}. \quad (9)$$

We make a natural assumption that, for a thermodynamically equilibrium state, a solution of Eqs. (7) and (8) should be sought among functions independent of τ. Then, as can easily be seen, Eqs. (7) and (8) are the Poisson and Laplace equations, respectively, for calculation of the electrostatic field of conductors carrying a complex charge, distributed over the metal volumes with a density $\delta\rho_i(\mathbf{r}) = ie\langle\langle\delta\rho_i(\mathbf{r})\rangle\rangle$.

Therefore, the function $\varphi(\mathbf{r})$ can be identified with the electrostatic potential of the field of the system of bodies with complex charges. In particular, it follows that inside the ith grain (far from the surface layer whose thickness is about the Thomas–Fermi radius λ_{TF}, within which the charge of the conductor is concentrated in electrostatics) the sought function $\varphi_{(\mathrm{in})i}(\mathbf{r})$ is equal to a constant. As for the surface layer ($\Delta r \sim \lambda_{\mathrm{TF}}$), here the functions $\varphi_{(\mathrm{in})i}(\mathbf{r})$ change insignificantly; however, in order to calculate these changes, one should make a complicated microscopic consideration with allowance for the real boundary.

It is possible, however, to exclude such small distances and to solve the problem macroscopically. Then, in the zeroth approximation, $\varphi_{(\mathrm{in})i}(\mathbf{r})$ in the overall region occupied by a metal will be equal to the solution of Eq. (7) with the appropriate boundary conditions at the conductor surface. This approximation is possible because, by analogy with electrostatics, in order to calculate $\varphi_{(\mathrm{in})i}(\mathbf{r})$, one can use an expansion of this function into a power series in a small natural parameter $\lambda_{\mathrm{TF}}/r_{i\,\min}$ (here, $r_{i\,\min}$ is the minimal geometric size of the ith grain).

Indeed, considering the quantity $[\varphi_{(\mathrm{in})i}(\mathbf{r}) - \varphi^0_{(\mathrm{in})i}(\mathbf{r})]$ as a perturbation [$\varphi^0_{(\mathrm{in})i}(\mathbf{r})$ is the value of $\varphi_{(\mathrm{in})i}(\mathbf{r})$ corresponding to the electrical neutrality condition deep inside the metallic inclusion] in the definition of $\langle\langle\delta\rho(\mathbf{r}, \tau)\rangle\rangle$ in Eq. (9), one can easily verify that the following equation is valid:

$$\nabla^2\varphi_{(\mathrm{in})i}(\mathbf{r}) = -4\pi ie\int d\mathbf{r}'K(\mathbf{r}-\mathbf{r}')(\varphi_{(\mathrm{in})i}(\mathbf{r}') - \varphi^0_{(\mathrm{in})i}(\mathbf{r}')), \quad (10)$$

where $K(\mathbf{r} - \mathbf{r}')$ is determined by the average $\langle\delta\rho(\mathbf{r})\delta\rho(\mathbf{r}')\rangle_0$. In fact, $K(\mathbf{r} - \mathbf{r}')$ represents the polarization operator of the system of electrons interacting with each other and with the compensating positive background. The results of calculation of $K(\mathbf{r} - \mathbf{r}')$ are well known (see, e.g., [26]). According to these results, as applied to metals, the imaginary part of the kernel $K(\mathbf{r} - \mathbf{r}')$ is equal to zero in the static case (we are interested in the electron–electron interaction only), whereas the character of the $\mathrm{Re}K(\mathbf{r} - \mathbf{r}')$ change enables one to state that, in $\mathbf{r}$ space, this function is essential only at distances $|\mathbf{r} - \mathbf{r}'|$ of the order of λ_{TF}. This fact (along with the weak dependence of the $\varphi_{(\mathrm{in})i}(\mathbf{r})$ function on the coordinate r) enables one to estimate the integral in Eq. (10). It can easily be shown that in the dimensionless variables $r/r_{i\,\min}$ the right-hand part of Eq. (10) is proportional to $(r_{i\,\min})/\lambda_{\mathrm{TF}})^2$.

Consequently, to compensate such large values (the gradients of the function $\varphi_{(\mathrm{in})i}(\mathbf{r})$, as mentioned, cannot be significant because of the smooth behavior of this function), the first correction $\varphi_{(\mathrm{in})i}(\mathbf{r}) - \varphi^0_{(\mathrm{in})i}(\mathbf{r})$ must be $\sim(r_{i\,\min})/\lambda_{\mathrm{TF}})^{-2}$. Based on this result, one can assume that the zeroth approximation to $\varphi_{(\mathrm{in})i}(\mathbf{r})$ is governed by Eq. (7) up to the boundaries of the conductors. The behavior of $\varphi_{(\mathrm{ex})}(\mathbf{r})$ in the insulating matrix will still be described by Eq. (8).

Such an approach is always suggested by the ordinary electrostatics of a system of charged conducting

bodies (see, e.g., [27]). In this approach, along with a volume charge density, a surface charge density $\sigma(\mathbf{r})$ always appears, which determines the boundary conditions for potentials at the surface of conductors. In our case, these conditions completing Eqs. (7) and (8) have the form

$$\begin{aligned}\mathbf{n}_i(\partial\varphi_{(ex)}/\partial\mathbf{r} - \partial\varphi_{(in)i}/\partial\mathbf{r})\big|_{\mathbf{r}=\mathbf{r}_s} &= -4\pi\sigma_i;\\ \varphi_{(ex)}\big|_{\mathbf{r}=\mathbf{r}_s} &= \varphi_{(in)i}\big|_{\mathbf{r}=\mathbf{r}_s}.\end{aligned} \tag{11}$$

In Eq. (11), $\mathbf{n}_i$ is a unit outward normal to the conductor surface and $\mathbf{r}_s$ are points which belong to the surface.

Now, inside any metal inclusion, up to its surface boundary, the electrical neutrality condition $\langle\langle\delta\rho_i(\mathbf{r})\rangle\rangle = 0$ must be satisfied, which determines the zeroth approximation φ_i^0 for $\varphi_{(in)i}$.

Then, we invoke the fact that Eq. (6), which determines the functional Ω_1, can be written as the trace of the operator form

$$\begin{aligned}&\exp(ie\beta\Sigma N_{0i}\varphi_i^0)\\ &\times\Pi\exp\{-\beta\Sigma[H_{0i}(\mathbf{p}) + e(i\varphi_i^0 - V_i)n_{\mathbf{p}i}]\}.\end{aligned} \tag{12}$$

For the metallic grains, the operator $n_{\mathbf{p}i} = \Sigma a^+_{\mathbf{p}\sigma}a_{\mathbf{p}\sigma}$ (where $a^+_{\mathbf{p}\sigma}$ and $a_{\mathbf{p}\sigma}$ are the creation and annihilation operators, respectively, for a particle with a momentum $\mathbf{p}$ and a spin σ) commutes with the Hamiltonians describing the system of free electrons in each grain, and therefore, the trace of the corresponding operator can readily be calculated. As a result we obtain

$$\begin{aligned}\Omega_1 &= \Sigma\Omega_{0i}\\ &- ie\Sigma N_{0i}\varphi_i^0 - 2\beta^{-1}\Sigma\ln[1 + f_{\mathbf{p}}(e^{-\beta e(i\varphi_i^0 - V_i)} - 1)],\end{aligned} \tag{13}$$

where $\Omega_{0i} = -\beta^{-1}\ln Z_i$ is the thermodynamic potential of the noncharged conductor and $f_{\mathbf{p}}$ is the Fermi distribution function.

According to the definition of $\langle\langle\delta\rho_i(\mathbf{r}, \tau)\rangle\rangle$, following from Eq. (7), and Eq. (13) for Ω_1, the requirement $\langle\langle\delta\rho_i(\mathbf{r}, \tau)\rangle\rangle = 0$ is satisfied when

$$e\varphi_i^0 = -ieV_i + 2\pi nT, \quad n = 0, \pm1, \pm2, \pm3, \ldots. \tag{14}$$

On the other hand, the values of the functions $\varphi_i(\mathbf{r})$ at the surface of the conductors can be expressed in terms of the coefficients of the capacity and electrostatic induction C_{ik} and the total "charge" of the kth grain

$$\varphi^0_{(in)i} = \Sigma C^{-1}_{ik}\left(ie\int d\mathbf{r}\langle\langle\delta\rho_k(\mathbf{r})\rangle\rangle\right). \tag{15}$$

Indeed, according to the initial assumptions, the determination of $\varphi_{(ex)}$ is reduced to the standard Dirichlet problem. Therefore, the sought equality (15) results from the boundary conditions for $\varphi_{(in)i}$ and $\varphi_{(ex)}$ in Eq. (11).

Thus, with Eqs. (13) and (14), the functional integration in Eq. (5) makes it possible to represent the grand partition function of the system of charged conductors in the simple form

$$\begin{aligned}Z &= Z_0A^{-1}\exp(e\beta\Sigma N_{0i}V_i)\Sigma\exp[-i\beta/2\Sigma\varphi_i(n)\langle Q_i\rangle]\\ &= Z_0A^{-1}\exp(e\beta\Sigma N_{0i}V_i)\Sigma\exp[-i\beta/2\Sigma C_{ik}\\ &\times(-iV_i + 2\pi nT/e)(-iV_k + 2\pi mT/e)].\end{aligned} \tag{16}$$

The exponent in the upper line of Eq. (16) formally has the form of an expression of the total electrical energy of the system of conductors carrying charges. Therefore, it is not surprising that, when disregarding the fluctuations in the number of electrons on the conductors (with the fixed integer charges $\langle Q_i\rangle = e(N_i - N_{0i})$ when N_i is a number rather than an operator), the calculation in accordance with the scheme presented above results in the expression $i\varphi_i = V_i$ and in the exponent in the form of the classical result for the potential energy of charged conductors. The result (16) is "canonical" with respect to the number of particles, as it is the trace of the operator with a variable number of electrons on the elements of the ensemble of conducting bodies. In this case, some ambiguity appears in the values of the stationary points φ_i of the action and, as a consequence, in the charge [see Eqs. (14), (15)]. This fact is reflected in the additional summation in Eq. (16) over indices n and m.

2. AVERAGE CHARGE OF AN ELEMENT OF THE NANOCOMPOSITE

Relation (16) defines the thermodynamic potential of the ensemble of grains in the mean field approximation and, according to Eq. (1), the average values of the operators Q_i in the same approximation. Compact expressions for $\langle Q_i\rangle$ can be obtained only in some limits in the case of many bodies. In the important particular case $C_{ik} = C_i\delta_{ik}$ (C_i is the capacity of the ith grain), that is, disregarding the long-range Coulomb interaction of the charges on different grains, calculations of Z by formula (16) give the known expressions [3] for $\langle Q_i\rangle$ in the form of nonmonotonic functions of the voltage. If identical metallic grains interact with each other in pairs, we obtain a nontrivial result for the relationship between the average charge of the system and the voltage U presented in [24]. Indeed, for the system of two interacting identical grains, we have $N_{10} = N_{20}$ and the potentials of the grains are $V_1 = U/2$ and $V_2 = -U/2$. Then, using Eq. (16), we find that

$$\begin{aligned}Z &= Z_0\tilde{A}^{-1}\Sigma\exp[-a(ix/2 + \pi n/a)^2]\\ &= Z_0\tilde{A}^{-1}\exp(x^2/4a)\theta_3[-\pi x/2, \exp(-\pi^2/a)].\end{aligned} \tag{17}$$

Here, $\tilde{A}^{-1}$ is the renormalized constant A^{-1} ($\tilde{A}^{-1} = A^{-1}\Sigma\exp[\beta C_0(2\pi mT)^2/2e^2]$, where $C_0 = 2(C_{11} + C_{12})$),

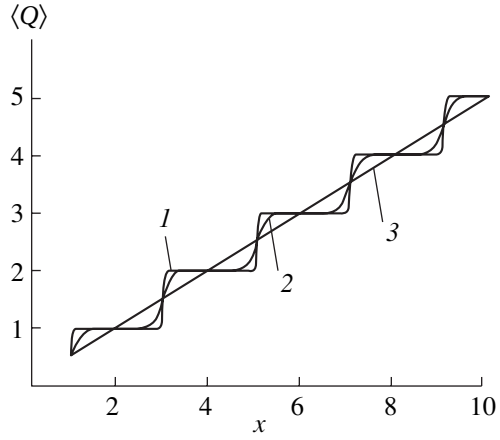

Fig. 1. Dependence of the average charge of a capacitor on the dimensionless variable $x = eU/E_c$ at different values of the parameter a: (*1*) 0.01, (*2*) 0.1, and (*3*) 1.

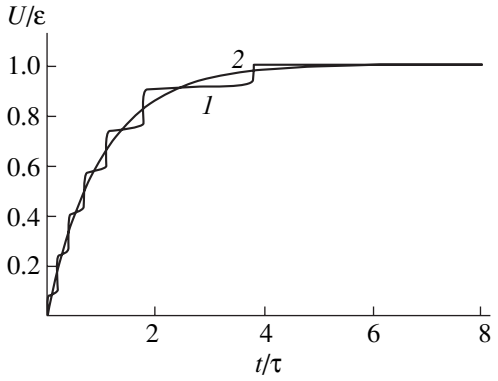

Fig. 2. Dependence of the potential difference of a capacitor (in dimensionless units) on the charging time at different values of the parameter a: (*1*) 0.05 and (*2*) 1.0. The charge changes from zero to 6e.

$x = eU/E_c$, $a = T/E_c$, and $\theta_3(\xi, \zeta)$ is an elliptical θ function.

Substituting Eq. (17) into Eq. (1), we find that the average charge of the capacitor is

$$\langle Q\rangle = CU + ea\partial \ln\{\theta_3[-\pi x/2, \exp(-\pi^2/a)]\}/\partial x. \quad (18)$$

Formula (18) makes allowance for fluctuations of electrons on the grains which form an ordinary capacitor ($Q = CU$ in classical electrostatics). In the limiting cases ($a \ll 1$ and $a \gg 1$), relation (18) leads to the results of [24]. We emphasize that, when the system given is connected to a source of a current, fluctuations of the charge on the capacitor plates can be due to electrons coming from the source or leaving the source.

Figure 1 demonstrates the dependence of the average charge $\langle Q\rangle(x)$ on the dimensionless variable $x = eU/E_c$ at various values of the parameter a. At low temperatures ($a < 1$), the jumps in $\langle Q\rangle$ are consistent with the concepts known about the Coulomb blockade effect in electronics [27]. Due to its discreteness, the charge on the capacitor does not change till the voltage achieves the value which corresponds to the equal probability of detecting the states with k and $k + 1$ electrons. The charge fluctuations between these states smooth the steps on the $\langle Q\rangle(x)$ dependence. When $a \gg 1$, the system becomes nonsensitive to changes in the number of Fermi particles by unity.

A simple numerical calculation shows that the discreteness of charge carriers affects the equilibrium process of the capacitor charging (long characteristic times $\tau = RC$, where R is the ohmic resistance of the circuit), and the potential difference of the capacitor varies in accordance with a complicated nonexponential law (Fig. 2). In Fig. 2, the dimensionless quantity $y = U/\varepsilon$ is plotted on the ordinate axis, where ε is the electromotive force of the source, and the time normalized to τ is plotted on the abscissa axis. The charging current of the capacitor will also exhibit "step" behavior. Therefore, electromagnetic oscillations in resonant circuits containing a capacitor of a small capacity will not go on in time according to a simple periodic law.

In order to elucidate whether the approximation used is valid and adequate to describe the experimental data, we need to estimate the ratio $r_{i\,\min}/\lambda_{TF}$. The Thomas–Fermi radius λ_{TF} is of the order of the interatomic space; therefore, for microparticles of a radius $r \sim 10$ nm, the inequality $r/\lambda_{TF} \gg 1$ is easily satisfied. Next, it is important to have experimental conditions providing a sufficiently large electrostatic energy E_c. The only parameter to control E_c is the geometrical capacity C. When $C \sim 10^{-18}$ F, we have $E_c \sim 10^{-21}$ J. For these values of C, the quantum properties of the system associated with the necessity of allowing for the charge discreteness will be exhibited at temperatures of about 10 K.

In concluding, we emphasize other essential aspects of the calculation made above. First, we assumed that the ensemble of grains in an insulating matrix is not a tunneling medium at a nonzero potential difference between the grains. This is adequate for the case of tunneling junctions with low transparency, and the approximation is valid if the correction to the electron energy due to the tunneling operator is small compared to the electrostatic energy E_c. Second, we disregarded spatial quantization of the electron spectrum, because when the sizes of particles are decreased, the effects of charge discreteness occur before the quantum effects become essential [28].

ACKNOWLEDGMENTS

This work was supported by the Ministry of Education and Science of Ukraine (project no. 2M/71-2000) and the Royal Academy of Sciences of Sweden.

REFERENCES

1. P. Sheng, B. Abeles, M. D. Coutts, and Y. Arie, Adv. Phys. **24**, 408 (1975).
2. P. Sheng, Philos. Mag. B **65**, 357 (1992).
3. I. O. Kulik and R. I. Shekhter, Zh. Éksp. Teor. Fiz. **68**, 623 (1975) [Sov. Phys. JETP **41**, 308 (1975)]; Fiz. Nizk. Temp. **1**, 435 (1975) [Sov. J. Low Temp. Phys. **1**, 215 (1975)]; Fiz. Nizk. Temp. **2**, 21 (1976) [Sov. J. Low Temp. Phys. **2**, 9 (1976)].
4. R. C. Dynes and J. P. Garno, Phys. Rev. Lett. **46**, 137 (1981).
5. B. I. Belevtsev, Yu. F. Komnik, and A. V. Fomin, Fiz. Nizk. Temp. **12**, 821 (1986) [Sov. J. Low Temp. Phys. **12**, 465 (1986)].
6. V. D. Okunev and N. N. Pafomov, Zh. Éksp. Teor. Fiz. **116**, 276 (1999) [JETP **89**, 151 (1999)].
7. H. Z. Zeller and I. Giaver, Phys. Rev. B **181**, 789 (1969).
8. P. Sheng, B. Abeles, and Y. Arie, Phys. Rev. Lett. **31**, 44 (1973).
9. J. S. Helman and B. Abeles, Phys. Rev. Lett. **37**, 1429 (1976).
10. E. Z. Meĭlikhov, Zh. Éksp. Teor. Fiz. **115**, 1484 (1999) [JETP **88**, 819 (1999)].
11. Yu. V. Nazarov, Phys. Rev. Lett. **82**, 1245 (1999).
12. C. Schonenberger, H. van Houten, and H. C. Donkerstoot, Europhys. Lett. **20**, 249 (1992).
13. W. Chen, H. Ahmed, and K. Nakazoto, Phys. Appl. Lett. **66**, 3383 (1995).
14. D. V. Averin and K. K. Likharev, J. Low Temp. Phys. **62**, 345 (1986).
15. P. Delsing, T. Claeson, K. K. Likharev, and L. S. Kuzmin, Phys. Rev. B **42**, 7439 (1990).
16. J. Inoue and S. Maekawa, Phys. Rev. B **53**, R11927 (1996).
17. S. Mitani, S. Takahashi, K. Takanashi, *et al.*, Phys. Rev. Lett. **81**, 2799 (1998).
18. K. Inomata, H. Ogiwara, Y. Saito, *et al.*, Jpn. J. Appl. Phys. **36**, L1380 (1997).
19. B. Abeles, Phys. Rev. B **15**, 2828 (1977).
20. E. Simanek, Solid State Commun. **31**, 419 (1979).
21. K. B. Efetov, Zh. Éksp. Teor. Fiz. **78**, 2017 (1980) [Sov. Phys. JETP **51**, 1015 (1980)]; Zh. Éksp. Teor. Fiz. **87**, 971 (1985) [Sov. Phys. JETP **60**, 554 (1985)].
22. D. M. Wood and D. Stroud, Phys. Rev. B **25**, 1600 (1982).
23. A. D. Zaikin and S. V. Panyukov, Tr. Fiz. Inst. Akad. Nauk SSSR **204**, 86 (1990).
24. Yu. M. Ivanchenko and Yu. V. Medvedev, Fiz. Nizk. Temp. **11**, 537 (1985) [Sov. J. Low Temp. Phys. **11**, 294 (1985)].
25. V. N. Popov, *Functional Integrals in Quantum Field Theory and Statistical Physics* (Atomizdat, Moscow, 1976; Reidel, Dordrecht, 1983).
26. D. Pines, *Elementary Excitations in Solids* (Benjamin, New York, 1963; Mir, Moscow, 1965).
27. J. D. Jackson, *Classical Electrodynamics* (Wiley, New York, 1962; Mir, Moscow, 1965).
28. R. I. Shekhter, Zh. Éksp. Teor. Fiz. **63**, 1410 (1972) [Sov. Phys. JETP **36**, 747 (1973)].

Translated by N. Kovaleva

Physics of the Solid State, Vol. 43, No. 5, 2001, pp. 941–948. Translated from Fizika Tverdogo Tela, Vol. 43, No. 5, 2001, pp. 906–912.

LOW-DIMENSIONAL SYSTEMS AND SURFACE PHYSICS

Specular X-ray Reflection from a Crystal Coated with an Amorphous Film under the Conditions for Strongly Asymmetric Noncoplanar Diffraction

V. A. Bushuev and A. P. Oreshko

Moscow State University, Vorob'evy gory, Moscow, 119899 Russia
e-mail: vab@surfsite.phys.msu.su

Received July 20, 2000

Abstract—The angular dependence of the intensity of specularly reflected x-rays from a crystal coated with an amorphous film under the conditions for glancing noncoplanar diffraction is rigorously analyzed theoretically. The anomalous angular dependence is shown to be very sensitive to the presence of thin amorphous films several nanometers thick. The optimum conditions for recording are realized at glancing angles of 1.5–4 times the critical angle for total external reflection. © *2001 MAIK "Nauka/Interperiodica".*

INTRODUCTION

X-ray diffraction and the phenomenon of total external reflection (TER) are extensively used to analyze the structure of thin surface layers of semiconducting single crystals and crystals covered with amorphous and crystalline films [1] (see also reviews [2–4]). The use of strongly asymmetric geometries of diffraction, in which x-rays are reflected from atomic planes making approximately the Bragg angle with the surface of the crystal, allows one to considerably decrease the penetration depth of the field into the crystal and to probe thinner layers, about 10 nm thick. In these geometries, either the incident or diffracted beam makes a small, glancing angle (comparable to the critical angle for TER) with the crystal surface and the specular reflection of x-rays becomes important in forming the diffraction pattern. The dynamical theory of strongly asymmetric coplanar diffraction was developed in [5–9].

In [10], the amplitudes of the specularly reflected and diffracted waves were calculated for a radically new geometry of noncoplanar diffraction in which the reflecting atomic planes of the crystal are perpendicular to the crystal surface (their tilt with respect to the normal is $\psi = 0$) and the incident, refracted, and diffracted rays do not lie in one plane. In this case, both the incident and diffracted beams can simultaneously make small angles φ_0 and φ_h, respectively, with the crystal surface and undergo strong specular reflection (SR). Experimentally, this geometry of diffraction was realized later [11] for investigating thin crystalline aluminum films 7.5–200 nm thick grown on GaAs substrates by the molecular beam epitaxy method.

In order to analyze diffraction in the glancing geometry, one has to exactly solve the equations of the dynamical theory rather than use the usual two-wave approximation [1–4]. For the case of $\psi = 0$, this theory is based on a solution to a biquadratic dispersion equation and it has been developed for both perfect single crystals [12, 13] and crystals covered with amorphous [14] or crystalline films [15]. It was shown that diffraction reflection curves are highly sensitive to the presence of films and can be used to detect structural imperfections of surface layers as thick as several nanometers and more. The results of numerous experiments in which the predictions of this theory were employed are outlined in [1, 4].

The next important step was made in [16, 17], where the theory of glancing Bragg–Laue x-ray diffraction was constructed for a perfect crystal whose reflecting planes are tilted at a small angle $\psi \neq 0$ to the normal to the crystal surface rather than being perpendicular to this surface. There is considerable current interest in this theory, because in actual practice, it is difficult to achieve strict parallelism of the surface and atomic planes when cutting and grinding a crystal, and a tilt angle ψ even as small as several minutes of an arc leads to noticeable distortions of diffraction curves [1, 4, 16, 17]. Furthermore, crystals with tilt angles of $\psi \sim 3°–4°$ are employed in some semiconductor technologies.

In the case of $\psi \neq 0$, the dispersion relation is a fourth-degree equation and can be solved only numerically. When the glancing angles φ_0 and φ_h exceed the critical angle for TER, the influence of the specularly reflected wave on diffraction becomes much weaker and the problem is simplified. An approximate modified dynamical diffraction theory was developed in [18–20]. This theory allows one to solve the problem analytically for any values of φ_0 and φ_h, except for a narrow range near the critical angle of TER, for both perfect crystals [18, 19] and crystals with an amorphous surface film [18, 20].

1063-7834/01/4305-0941$21.00 © 2001 MAIK "Nauka/Interperiodica"

It should be noted that all the papers mentioned above were primarily concerned with diffraction reflection curves and did not investigate the angular dependence of specular reflection curves. At the same time, as was first indicated in [4], the presence of an amorphous film on the crystal surface can noticeably affect the specularly reflected x-ray intensity as a function of the departure of the angle of incidence from the Bragg diffraction angle.

In this paper, the exact solution to the dispersion fourth-degree equation is found and used to analyze the angular dependences of the specular and diffraction reflections over the entire range of glancing angles and tilt angles of the reflecting planes with respect to the crystal surface. An analysis of specular reflection under the conditions for asymmetric noncoplanar diffraction is of considerable interest because of the high sensitivity of the so-called "specular mark" [4] to thin (about 1–3 nm thick) amorphous surface films. It is shown that the specular-reflection curves are dispersive in character and are similar to yield curves of secondary radiation in the x-ray standing-wave method [4], but the signal is much stronger, which can be a basis for a more rapid method of investigating thin films. The emphasis is on the case of small glancing angles of x-rays and on the situations where the simplified equations of the dynamical theory allow one to make calculations within reasonable accuracy.

1. A PERFECT SINGLE CRYSTAL

First we consider the specular and diffraction reflection of a plane x-ray wave $\mathbf{E}_0\exp(i\mathbf{k}_0\mathbf{r})$ from a perfect single crystal. Radiation is incident from vacuum at an arbitrary glancing angle φ_0 (measured with respect to the crystal surface) such that simultaneous diffraction reflection occurs from atomic planes which make an arbitrary angle ψ with the inward-pointing normal $\mathbf{n}$ (the z axis) to the crystal surface.

In the region $z \le 0$, above the crystal surface, the field consists of three waves:

$$\mathbf{E}(\mathbf{r}) = \mathbf{E}_0\exp(i\mathbf{k}_0\mathbf{r}) + \mathbf{E}_s\exp(i\mathbf{k}_s\mathbf{r}) + \mathbf{E}_h\exp(i\mathbf{k}_h\mathbf{r}), \quad (1)$$

where E_0, E_s, and E_h are the amplitudes of the incident, specularly reflected, and diffracted waves, respectively; $|\mathbf{k}_0| = |\mathbf{k}_s| = |\mathbf{k}_h| = k_0$; $k_0 = 2\pi/\lambda$ is the wave vector in vacuum; λ is the wave length; and $k_{sz} = -k_{0z}$.

In the crystal ($z \ge 0$), the x-ray wave excites two coherent waves, transmitted and diffracted:

$$\mathbf{E}(\mathbf{r}) = \mathbf{D}_0\exp(i\mathbf{q}_0\mathbf{r}) + \mathbf{D}_h\exp(i\mathbf{q}_h\mathbf{r}), \quad (2)$$

where D_0 and D_h are the amplitudes and $\mathbf{q}_0$ and $\mathbf{q}_h = \mathbf{q}_0 + \mathbf{h}$ are the wave vectors of the transmitted and diffracted waves in the crystal, respectively; and $\mathbf{h}$ is a reciprocal lattice vector. The tangential (along the crystal surface) components of the wave vectors of the incident and refracted waves must be equal, and only the normal component is changed; therefore, the wave vector in the medium $\mathbf{q}_0$ is

$$\mathbf{q}_0 = \mathbf{k}_0 + k_0\varepsilon\mathbf{n}, \quad (3)$$

where $\varepsilon \ll 1$ is a quantity to be found; it is small because of the smallness of the x-ray polarizability $\chi \sim 10^{-5}$.

From Maxwell's equations, it follows that the amplitudes D_0 and D_h in Eq. (2) and the quantity ε in Eq. (3) obey a system of dynamical equations [1, 4]:

$$(\varepsilon^2 + 2\gamma_0\varepsilon - \chi_0)D_0 - C\chi_{\bar{h}}D_h = 0, \quad (4a)$$

$$(\varepsilon^2 + 2\gamma_{h0}\varepsilon - \chi_0 - \alpha)D_h - C\chi_h D_0 = 0, \quad (4b)$$

where $\gamma_0 = k_{0z}/k_0$; $\gamma_{h0} = (\mathbf{k}_0 + \mathbf{h})_z/k_0$; χ_g ($g = 0, h, \bar{h}$) are the Fourier transforms of the crystal polarizability $\chi(\mathbf{r})$; $C = 1$ and $C = \cos 2\vartheta$ for the σ and π x-ray polarizations, respectively; ϑ is the angle between the wave vector of the incident wave and the reflecting atomic planes; and $\alpha = 1 - (\mathbf{k}_0 + \mathbf{h})^2/k_0^2 = 2\Delta\vartheta\sin 2\vartheta_B$ is a quantity characterizing the deviation $\Delta\vartheta = \vartheta - \vartheta_B$ of the diffraction angle from the exact Bragg angle ϑ_B, which is defined by the equation $h = 2k_0\sin\vartheta_B$. In terms of the glancing angle φ_0, we can write

$$\gamma_0 = \sin\varphi_0, \quad \gamma_{h0} = \gamma_0 - \psi_B, \quad (5)$$

where $\psi_B = 2\sin\psi\sin\vartheta_B$ is an effective tilt-angle parameter of the reflecting planes ($\psi > 0$, $h_z < 0$). If φ_0, $\psi \ll 1$, then we have $\gamma_0 \approx \varphi_0$ and $\psi_B \approx 2\psi\sin\vartheta_B$.

Let φ_h be the angle (measured from the crystal surface) at which the diffracted wave passes to vacuum; then, the z component is $k_{hz} = -k_0\gamma_h$, where $\gamma_h = \sin\varphi_h$ ($\varphi_h > 0$). Diffraction reflection to the region $z < 0$ (the Bragg geometry) occurs at glancing angles φ_0 such that $\gamma_0 < \psi_B$; i.e., $\gamma_{h0} < 0$ in Eqs. (4) and (5). At given angles φ_0 and ψ the exit angle φ_h is given by [16]

$$\gamma_h = (\gamma_{h0}^2 + \alpha)^{1/2}; \quad (6)$$

therefore, the condition $\alpha > -\gamma_{h0}^2$ determines the allowable values of the deviation $\Delta\vartheta$ from the Bragg angle. The case of the opposite inequality ($\alpha < -\gamma_{h0}^2$), where the diffracted wave decays rapidly in vacuum (see [1–3]), will not be considered in this paper.

The system of equations (4) has a nontrivial solution for the amplitudes D_0 and D_h if the determinant of the system is equal to zero:

$$(\varepsilon^2 + 2\gamma_0\varepsilon - \chi_0)(\varepsilon^2 + 2\gamma_{h0}\varepsilon - \chi_0 - \alpha) - C^2\chi_h\chi_{\bar{h}} = 0. \quad (7)$$

This is a fourth-degree equation in ε; it has four roots ε_j, and, therefore, four transmitted waves and four diffracted waves can propagate in the crystal with amplitudes D_{gj} ($g = 0, h$; $j = 1, 2, 3, 4$). A simple analytical

solution to Eq. (7) can be found only in the case of $\psi = 0$, where the reflecting planes are perpendicular to the crystal surface. Indeed, in this case, we have $\gamma_{h0} = \gamma_0$, and Eq. (7) is reduced to a biquadratic equation. Diffraction of x-rays in this geometry was considered in detail in [12–15]. In the general case, however, the dispersion equation (7) can be solved only numerically. For a thick crystal, only those solutions should be chosen for which $\mathrm{Im}\varepsilon_j > 0$. An analysis shows [16] that only two roots meet this condition in the Bragg geometry, which we will designate by ε_1 and ε_2.

To determine the field amplitudes in Eqs. (1) and (2), we use the conditions of continuity of the tangential components of the electric and magnetic fields at the crystal surface. In the case of glancing angles, the continuity of the magnetic field is equivalent to the continuity of the derivative of the electric field with respect to the coordinate z. Therefore, we have a system of four equations:

$$\begin{aligned} E_0 + E_s &= D_{01} + D_{02}, \\ \gamma_0(E_0 - E_s) &= \Gamma_{01}D_{01} + \Gamma_{02}D_{02}, \\ E_h &= R_1 D_{01} + R_2 D_{02}, \\ -\gamma_h E_h &= \Gamma_{h1}R_1 D_{01} + \Gamma_{h2}R_2 D_{02}, \end{aligned} \tag{8}$$

where

$$\begin{aligned} \gamma_0 &= \sin\varphi_0, \quad \gamma_h = \sin\varphi_h, \\ \Gamma_{0j} &= \gamma_0 + \varepsilon_j, \quad \Gamma_{hj} = \gamma_{h0} + \varepsilon_j \quad (j = 1, 2). \end{aligned} \tag{9}$$

In deriving Eq. (8), we have used the relation $D_{hj} = R_j D_{0j}$ between the amplitudes of the diffracted and transmitted waves in the crystal, which follows from Eq. (4a), where

$$R_j = (\varepsilon_j^2 + 2\gamma_0\varepsilon_j - \chi_0)/C\chi_{\bar{h}}. \tag{10}$$

A solution to system (8) for the coefficients of the field amplitudes for the specular and Bragg reflections, $R_s = E_s/E_0$ and $R_h = E_h/E_0$, respectively, has the form

$$R_s = \frac{\gamma_0 - \gamma_1}{\gamma_0 + \gamma_1}, \quad R_h = \frac{R_1 - \rho R_2}{1 - \rho}(1 + R_s), \tag{11}$$

where we have introduced the notation

$$\gamma_1 = \frac{\Gamma_{01} - \rho\Gamma_{02}}{1 - \rho}, \quad \rho = \frac{R_1(\gamma_h + \Gamma_{h1})}{R_2(\gamma_h + \Gamma_{h2})}. \tag{12}$$

The quantities γ_0, γ_h, and Γ_{gj} are defined in Eq. (9) and R_j is given by Eq. (10). The factor $1 + R_s$ in Eq. (11) for R_h allows for the influence of specular reflection on diffraction. Equations (11) are identical (except for the notation) to the corresponding equations derived in [1, 16], where, however, the emphasis was on the analysis of the diffraction reflection coefficient R_h.

Expressions (11) and (12) are the exact solution to the problem on specular and diffraction reflection of x-rays from a perfect single crystal; they are valid for any glancing angle φ_0 and exit angle φ_h (at $\gamma_0 < \psi_B$) and any allowable deviation $\Delta\vartheta$ from the exact Bragg angle.

Now, we consider some specific limit cases. If the deviation $\Delta\vartheta$ from the Bragg angle corresponding to strong diffraction reflection is large, i.e., $|\alpha| \gg |\chi_h|$, then the partial reflection coefficient R_1 tends to zero. In this case, from Eq. (12), it follows that $\rho \longrightarrow 0$ and $\gamma_1 \longrightarrow \gamma_0 + \varepsilon_1$, where $\varepsilon_1 = \gamma_s - \gamma_0$, as can be seen from Eq. (10) at $R_1 = 0$. For any glancing angles φ_0, we have $\gamma_s = (\gamma_0^2 + \chi_0)^{1/2}$. Therefore, Eq. (11) for the coefficient of specular reflection is reduced to the well-known Fresnel formula $R_s = r_s = (\gamma_0 - \gamma_s)/(\gamma_0 + \gamma_s)$. There is no diffraction reflection in this case, because $R_h \longrightarrow R_1 = 0$.

Now, we analyze the case of the glancing angle φ_0 being much greater than the critical angle for TER $\varphi_c = |\mathrm{Re}\chi_0|^{1/2}$. Taking into account that the polarizability χ_h is small, it can be shown that at $\varphi_0, \varphi_h \gg \varphi_c$, the roots of dispersion relation (7) differ greatly in value, $\varepsilon_1 \ll \varepsilon_2$, where $\varepsilon_2 \approx |\gamma_{h0}| + (\gamma_h^2 + \chi_0)^{1/2} \approx 2|\gamma_{h0}| + (\alpha + \chi_0)/2|\gamma_{h0}|$ and $\mathrm{Re}\varepsilon_1 \sim \chi_{0r}/2\gamma_0 \ll \gamma_0$. Therefore, we have $R_1 \ll R_2$ [see Eq. (10)] and $\gamma_h + \Gamma_{h1} \ll \gamma_h + \Gamma_{h2}$ in Eq. (12); that is, $\rho \ll 1$ and $\gamma_1 \approx \gamma_0 + \varepsilon_1$, where ε_1 can be calculated from Eqs. (4) and (7) by dropping the terms quadratic in ε_1 in them. The same results are obtained solving Eq. (7) numerically. Since $\mathrm{Im}\varepsilon_2 \ll \mathrm{Im}\varepsilon_1$, the field with amplitude D_{02} penetrates anomalously deep into the crystal. In the case at hand, we have $\varepsilon_1 \ll \gamma_0$; therefore, $R_s \ll 1$ and one can ignore the influence of the specular reflection on diffraction. At the same time, the total wave field in the crystal in Eq. (2) dramatically affects the angular dependence of the specular reflection when the diffraction reflection is strong. From Eqs. (11) and (12), the amplitude coefficients of specular and diffraction reflection are found to have a simple form:

$$R_s = -\frac{\varepsilon_1}{2\gamma_0 + \varepsilon_1}, \quad R_h = \frac{2\gamma_0\varepsilon_1 - \chi_0}{C\chi_{\bar{h}}}, \tag{13}$$

where

$$\begin{aligned} \varepsilon_1 &= (1/4\gamma_0)\{\chi_0(1 - b) - \alpha b \\ &\pm [(\chi_0(1 + b) + \alpha b)^2 - 4C^2 b\chi_h\chi_{\bar{h}}]^{1/2}\} \end{aligned} \tag{14}$$

and $b = -\gamma_0/\gamma_{h0}$ is an asymmetry coefficient of Bragg reflection ($b > 0$); the upper or lower sign in Eq. (14) is chosen according to which of them meets the condition $\mathrm{Im}\varepsilon_1 > 0$. Since $\varepsilon_1 \ll \gamma_0$, the angular dependence of the specular reflection coefficient $R_s(\Delta\vartheta)$ is determined fundamentally by the $\varepsilon_1(\Delta\vartheta)$ dependence.

Equation (13) for R_s can also be derived from a simpler line of reasoning. Indeed, at fairly large glancing angles, the specular reflection affects diffraction only slightly and only one strong wave propagates in the crystal. Therefore, instead of Eq. (8), one can write

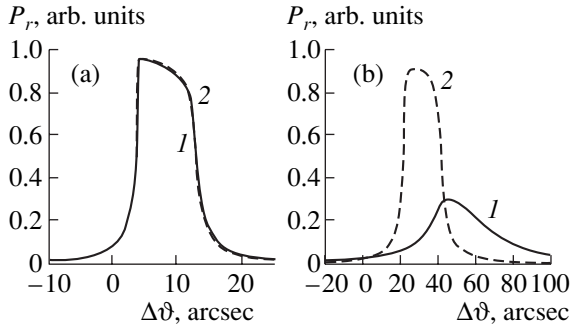

Fig. 1. Diffraction reflection curves from a perfect crystal as a function of the deviation $\Delta\vartheta$ from the Bragg angle at the glancing angle φ_0 equal to (a) 50′ and (b) 13′. The curves are calculated from the exact (curves *1*) and approximate (curves *2*) theories. Si(220) reflection, Cu K_α radiation, and $\psi = 4°$.

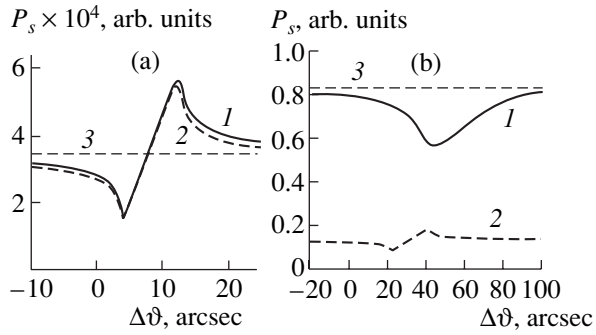

Fig. 2. Angular dependences of the specular reflection curves from a perfect crystal at the glancing angle φ_0 equal to (a) 50′ and (b) 13′. *1*—exact theory; *2*—approximate theory; and *3*—specular reflection without regard for diffraction. Si(220) reflection, Cu K_α radiation, and $\psi = 4°$.

simpler relations $E_0 + E_s = D_{01}$ and $\gamma_0(E_0 - E_s) = (\gamma_0 + \varepsilon_1)D_{01}$, from which Eq. (13) for R_s is immediately obtained.

Figures 1 and 2 show diffraction reflection $P_R = (\gamma_h/\gamma_0)|R_h|^2$ and specular reflection $P_s = |R_s|^2$ curves, respectively. These curves are calculated for the (220) reflection of a single crystal of silicon for Cu K_α radiation in the case of the tilt angle $\psi = 4°$ and different values of the glancing angle φ_0. Solid lines *1* correspond to the exact expressions (11) in which a numerical solution of the general fourth-degree equation (7) is used, while dashed lines *2* are calculated from approximate expressions (13). It is seen from Figs. 1a and 2a that the reflection curves calculated using the exact and approximate theories for the glancing angle $\varphi_0 = 50'$, which is about four times greater than the critical angle for TER $\varphi_c = 13.38'$, almost coincide. Calculations show that the approximate theory can be used for glancing angles $\varphi_0 \geq (2–3)\varphi_c$.

At smaller angles $\varphi_0 \leq (1–2)\varphi_c$, the reflection curves predicted by the exact and approximate theories become significantly different (Figs. 1b, 2b) and the latter theory is inadequate. For example, for a large deviation $\Delta\vartheta$ from the Bragg angle, the specular-reflection curve must asymptotically approach the corresponding Fresnel value calculated without regard for diffraction. This asymptotic behavior takes place only in the exact theory. At the same time, at $|\alpha| \gg |\chi_h|$, it follows from Eq. (14) that $\varepsilon_1 \approx \chi_0/2\gamma_0$. Substitution of this expression into Eq. (13) gives $R_s \approx -\chi_0/4\gamma_0^2$, which is true only for fairly large glancing angles.

The distinctive feature of specular reflection under the condition for diffraction is an anomalous angular dependence $P_s(\Delta\vartheta)$, which is dispersive in character, showing a minimum and a maximum near the diffraction angles $\Delta\vartheta_{1,2} = \Delta\vartheta_0 \mp \Delta\vartheta_B$ (which correspond to the edges of the region of total diffraction reflection), where

$$\Delta\vartheta_0 = -\chi_0(1 + b)/(2b\sin 2\vartheta_B),$$

$$\Delta\vartheta_B = C|\chi_h|/(b^{1/2}\sin 2\vartheta_B).$$

Such an anomalous behavior of specular reflection was first discussed in [4]. It should be noted that much the same behavior is shown by yield curves of secondary radiation $I_{SP} \sim 1 + |R_h|^2 + 2\sigma_i \operatorname{Re} R_h$ with an escape depth small in comparison with the extinction length $L_{ex} = \lambda(\gamma_0|\gamma_{h0}|)^{1/2}/\pi C|\chi_h|$, where $\sigma_i = C|\chi_{hi}|/\chi_{0i}$ and $\chi_{gi} = \operatorname{Im}\chi_g$ [1, 4, 21]. The analogy will be more obvious if one expresses the quantity ε_1 in Eq. (13) in terms of the coefficient of diffraction reflection. In this case, the amplitude of specular reflection becomes

$$R_s \approx -(\chi_0/4\gamma_0^2)(1 + \sigma R_h), \qquad (15)$$

where $\sigma = C\chi_h/\chi_0$. As is the case with the x-ray standing-wave method [1], the second factor in Eq. (15) characterizes the amplitude of the total field at the crystal surface. In contrast to σ_i, however, the quantity σ in Eq. (15) for specular reflection is determined by the ratio of the complex polarizabilities χ_h and χ_0 rather than by the ratio of their imaginary parts.

The minimum and maximum on the specular reflection $P_s(\Delta\vartheta)$ curve in Eq. (15) are due to the fact that, in the case of diffraction reflection, we have $R_h \approx 1$ and the phase of R_h varies almost linearly from π at $\Delta\vartheta = \Delta\vartheta_1$ to zero at $\Delta\vartheta = \Delta\vartheta_2$. In this case, $R_h(\Delta\vartheta_{1,2}) \approx \mp b^{1/2}$. For small glancing angles ($\gamma_0 \ll \psi_B$), the reflection asymmetry coefficient is $b \ll 1$. As the angle φ_0 increases and becomes such that $\gamma_0 \approx \psi_B$, we have $b \gg 1$ and, therefore, the contrast of the specular reflection (P_s) curve increases. At the same time, the width of the maximum on the diffraction reflection curve and the angular range in which the anomaly on the specular reflection curve is observed are decreased.

Under the conditions for specular reflection at large glancing angles, the penetration depth of the field $L_s \gg L_{ex}$ is such that $L_s = \lambda/(2\pi \mathrm{Im}\gamma_s)$ and, therefore, the formation of the refracted wave and of the specular-reflection field in the range where diffraction reflection is strong is determined by the coherent superposition of the transmitted and diffracted waves. By contrast, in the range of small angles, $\varphi_0 \le \varphi_c$, the penetration depth of the field is $L_s \le L_{ex}$ and, therefore, this length is determined fundamentally by total external reflection. The diffraction reflection is formed in a thinner layer and becomes more kinematic, with the result that the maximum on the diffraction reflection curve decreases in height and becomes broader (curve *1* in Fig. 1b). The specular-reflection curve also smoothes noticeably and has a shallow minimum (curve *1* in Fig. 2b). For example, for the parameters that were used in calculating the curves in Figs. 1 and 2, we have $L_s = 1.9$ μm, $L_{ex} = 0.1$ μm, and $b = 0.35$ for $\varphi_0 = 50'$ and $L_s = 0.03$ μm, $L_{ex} = 0.08$ μm, and $b = 0.07$ for $\varphi_0 = 13'$.

2. CRYSTAL COVERED WITH AN AMORPHOUS FILM

Now, let us consider x-ray reflection from a crystal covered with a homogeneous amorphous film with arbitrary thickness d and polarizability χ_1. The fields in vacuum and in the crystal are given by Eqs. (1) and (2), respectively. In the general case, the field in the film consists of four waves:

$$\begin{aligned}\mathbf{E}(\mathbf{r}) &= \mathbf{A}_0\exp(i\mathbf{a}_0\mathbf{r}) + \mathbf{A}_s\exp(i\mathbf{a}_s\mathbf{r})\\ &+ \mathbf{B}_0\exp(i\mathbf{b}_0\mathbf{r}) + \mathbf{B}_s\exp(i\mathbf{b}_s\mathbf{r}),\end{aligned} \tag{16}$$

where A_0 and A_s are the amplitudes of the transmitted and specularly reflected waves in the film, respectively, excited by the incident wave and B_s and B_0 are the amplitudes of the transmitted and specularly reflected waves, respectively, excited in the film by the Bragg wave passing from the crystal to the film. Since the tangential components of the corresponding wave vectors must be equal, we have $a_{0t} = a_{st} = k_0\cos\varphi_0$ and $b_{0t} = b_{st} = k_0\cos\varphi_h$. The relations for the normal components are $a_{0z} = -a_{sz} = k_0 s_0$ and $b_{0z} = -b_{sz} = k_0 s_h$, where

$$s_0 = (\gamma_0^2 + \chi_1)^{1/2}, \quad s_h = (\gamma_h^2 + \chi_1)^{1/2}. \tag{17}$$

The continuity conditions for the electric and magnetic fields at the upper and lower boundaries of the film lead to a system of eight equations for the wave amplitudes in Eqs. (1), (2), and (16). At the vacuum–film boundary, we have

$$\begin{aligned}E_0 + E_s &= A_0 + A_s,\\ \gamma_0(E_0 - E_s) &= s_0(A_0 - A_s),\\ E_h &= B_0 + B_s, \quad -\gamma_h E_h = s_h(B_0 - B_s),\end{aligned} \tag{18a}$$

and at the film–substrate interface, we have

$$\begin{aligned}A_0 f_0 + A_s f_s^{-1} &= \sum_j D_{0j} f_{0j},\\ s_0(A_0 f_0 - A_s f_0^{-1}) &= \sum_j \Gamma_{0j} D_{0j} f_{0j},\\ B_0 f_h + B_s f_h^{-1} &= \sum_j R_j D_{0j} f_{hj},\\ s_h(B_0 f_h - B_s f_h^{-1}) &= \sum_j \Gamma_{hj} R_j D_{0j} f_{hj},\end{aligned} \tag{18b}$$

where $j = 1, 2$; $f_g = \exp(ik_0 s_g d)$ and $f_{gj} = \exp(ik_0\Gamma_{gj} d)$ are coefficients that allow for changes in the phase of the waves and their absorption during propagation of the waves through the film.

A solution to the system of equations (18) for the amplitude coefficients of specular and diffraction reflection can be conveniently written in a compact form:

$$R_s = \frac{r_0 + Q_0 f_0^2}{1 + r_0 Q_0 f_0^2}, \quad R_h = \frac{R_1 - \rho_d R_2}{1 - \rho_d}(1 + R_s)F, \tag{19}$$

where

$$\begin{aligned}Q_0 &= \frac{s_0 - \gamma_1}{s_0 + \gamma_1}, \quad \gamma_1 = \frac{\Gamma_{01} - \rho_d\Gamma_{02}}{1 - \rho_d},\\ \rho_d &= \frac{R_1(s_h + \Gamma_{h1}Q_h)}{R_2(s_h + \Gamma_{h2}Q_h)},\\ Q_h &= \frac{1 - r_h f_h^2}{1 + r_h f_h^2}, \quad r_g = \frac{\gamma_g - s_g}{\gamma_g + s_g} \quad (g = 0, h),\\ F &= \frac{1 - r_h}{1 - r_h f_h^2}\frac{1 + Q_0}{1 + Q_0 f_0^2}\exp[ik_0(s_0 + s_h - \psi_B)d].\end{aligned}$$

Here, $s_g = (\gamma_g^2 + \chi_1)^{1/2}$ and r_0 and r_h are the Fresnel reflection coefficients of the semi-infinite medium with a film with polarizability χ_1 at glancing angles φ_0 and φ_h, respectively.

First, as in the preceding section, we consider some specific cases. At $d = 0$ (no film), we have $f_g, f_{gj} = 1$; $F = 1$; and $\rho_d = \rho$; the general expressions (19) are reduced to Eq. (11) for the perfect crystal. In the case of a thick film ($k_0 \mathrm{Im}\, s_0 d \gg 1$), the factors that allow for absorption tend to zero ($f_0 \longrightarrow 0$, $F \longrightarrow 0$), there is no diffraction ($R_h = 0$), and $R_s = r_0$; that is, specular reflection is determined by the Fresnel reflection coefficient of a medium with polarizability equal to that of the film χ_1.

If $|\alpha| \gg |\chi_h|$ (negligibly weak diffraction), then $\rho_d \ll 1$ (see Section 2), $\gamma_1 = (\gamma_0^2 + \chi_0)^{1/2}$, and we arrive at the familiar Airy formula [22], which describes oscillations

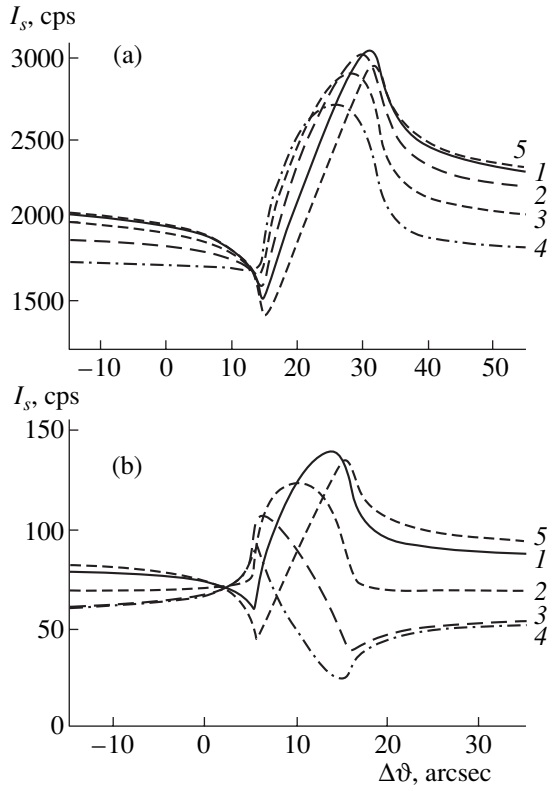

Fig. 3. Effect of the thickness of an amorphous film on the angular anomalies of the specularly reflected intensity. Glancing angle φ_0 is (a) 20′ and (b) 40′. Film thickness d (nm) of (*1*) 1, (*2*) 2, (*3*) 3, (*4*) 4, and (*5*) 0 (perfect crystal). The incident radiation intensity $I_0 = 10^5$ cps, SiO_2 film, (220) reflection, Cu K_α radiation, and $\psi = 4°$.

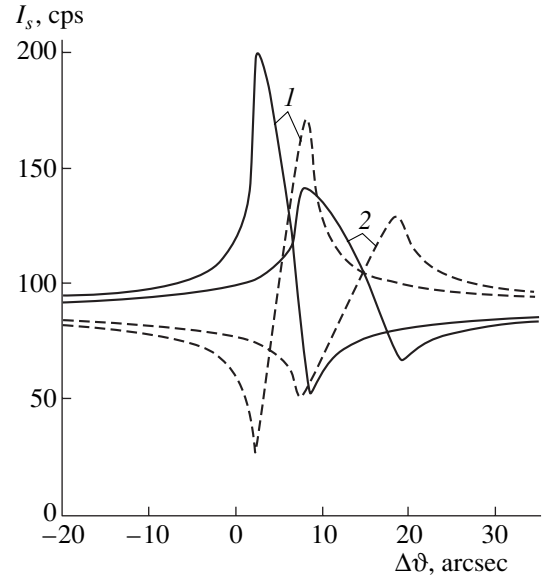

Fig. 4. Effect of the tilt angle ψ of atomic planes on the angular dependence of the specularly reflected intensity from a crystal covered with a film (solid lines) and the perfect crystal (dashed lines) for the thickness of amorphous Si film $d = 3$ nm, glancing angle $\varphi_0 = 40'$, and tilt angle ψ equal to (*1*) 2° and (*2*) 5°. Beam intensity $I_0 = 10^5$ cps, Si(220) reflection, and Cu K_α radiation.

(due to film thickness) in the specular reflection curve for the film–substrate system:

$$R_s = (r_0 + r_1 f_0^2)/(1 + r_0 r_1 f_0^2), \qquad (20)$$

where $r_1 = (s_0 - \gamma_s)/(s_0 + \gamma_s)$ is the Fresnel reflection coefficient characterizing the film–substrate interface and $\gamma_s = (\gamma_0^2 + \chi_0)^{1/2}$. If $\chi_1 = \chi_0$, i.e., the film and substrate have the same optical density for x-rays, then $r_1 = 0$, $r_0 = r_s$, and from Eq. (20) it follows that $R_s = r_s$. In other words, far from the range in which diffraction occurs, the presence of the film on the crystal surface has little or no effect on the specular reflection from such a film–substrate system. At the same time, as will be shown below, if diffraction takes place, then the angular dependence of specular reflection from this system differs markedly from that in the case of the crystal with no film (Fig. 4).

The case of glancing angles $\varphi_{0,h} > \varphi_c$ is of interest; here, the specular reflection curves are highly sensitive to the presence of a very thin amorphous surface layer, even when only several nanometers thick.

Figure 3 shows specularly reflected-intensity curves $I_s = |R_s|^2 I_0$, where I_0 is the intensity of the incident x-ray beam from a single crystal of silicon with an amorphous SiO_2 surface film for different film thickness and various glancing angles (Cu K_α radiation, (220) reflection, $\psi = 4°$). For the SiO_2 film, the critical angle for TER is 12.67′. It is seen from Fig. 3 that the behavior of the specular reflection curves essentially depends on the presence of the film and on its thickness. This dependence is more pronounced for larger glancing angles (cf. the curves in Figs. 3a, 3b). The possibility of using specular reflection in analyzing the structure of the thinnest surface layers was first indicated in review [4] (the "specular mark" method), but a detailed theoretical treatment of this interesting phenomenon was not made in that paper. Specular reflection curves show a general resemblance to photoelectron- and fluorescence-yield curves for thin layers, which suggests that the specularly reflected wave can be considered one of the channels of secondary radiation [4]. Although the specular reflection coefficient is very small at glancing angles $\varphi_0 > \varphi_c$, the specularly reflected intensity can be high enough and considerably (1–3 orders of magnitude, all other things being equal) exceed the counting rate of photoelectrons or fluorescent quanta used in the x-ray standing-wave method.

Let us estimate the ratio of the fluorescence intensity from the film (P_F) to the specularly reflected intensity $P_s = \chi_1^2/16\gamma_0^4$ on the near portion of the tail of the TER curve [$\varphi_0 \sim (2–4)\varphi_c$]. The intensity P_F is determined by the absorbed energy in a film of thickness d; therefore, $P_F \approx (ck_0\chi_{1i}d/\gamma_0\beta)(\Delta\Omega/4\pi)$, where χ_{1i} is the imaginary part of the polarizability of the film, c is the relative concentration of the atoms whose fluorescence radiation is recorded, β is the electron conversion coef-

ficient, and $\Delta\Omega$ is the covered solid angle. Thus, we have

$$P_F/P_s \approx 8c\beta^{-1}(d/\lambda)(\gamma_0^3\chi_{1i}/\chi_1^2)\Delta\Omega.$$

If, for example, $d \approx 1$ nm, $\lambda \approx 0.1$ nm, $\beta \sim 10$–50, $c \approx 0.5$, $\Delta\Omega \approx 2\pi$, and the glancing angle $\varphi_0 \sim 2\varphi_c$, then, for the typical values of polarizability $|\chi_1| \sim 10^{-5}$ and $\chi_{1i} \sim 0.02|\chi_1|$, we obtain $P_F/P_s \sim 3 \times (10^{-3}$–$10^{-2})$; that is, the specularly reflected intensity is one to two orders of magnitude higher than the x-ray fluorescence intensity. This is the reason that the "specular mark" method is expected to have considerable promise.

From general expressions (19), one can derive a simpler approximate expression for the specular reflection coefficient R_s at glancing angles $\varphi_0, \varphi_h > \varphi_c$. Since $\rho_d \ll 1$ in this case, we have $\gamma_1 = \varphi_0 + \varepsilon_1$ and, therefore,

$$R_s \approx (r_0 + R_e)/(1 + r_0R_e), \qquad (21)$$

where

$$R_e = (\chi_1 - 2\varphi_0\varepsilon_1)\exp(2ik_0s_0d)/[2\varphi_0(2\varphi_0 + \varepsilon_1)].$$

Here, $r_0 \approx -\chi_1/4\varphi_0^2$ and $s_0 \approx \varphi_0 + \chi_1/2\varphi_0$.

The sensitivity of the specular-reflection curves to the presence of an amorphous film on the crystal surface is due to the drastic changes in the specular reflection from the film–crystal interface in the range where diffraction reflection is strong. Indeed, outside this range, we have $\varepsilon_1 \approx \chi_0/2\varphi_0$ and R_e in Eq. (21) is proportional to the difference in the polarizabilities $\chi_1 - \chi_0$, whereas in the diffraction range, the polarizability of the crystal χ_0 is replaced by the effective polarizability $2\varphi_0\varepsilon_1(\Delta\vartheta)$ and $\mathrm{Im}(\varepsilon_1) \gg \chi_{0i}/2\varphi_0$. Therefore, $R_e \neq 0$ even if the polarizabilities of the film and substrate are equal, $\chi_1 = \chi_0$. In addition, the effect of the phase factor $\exp(2ik_0s_0d)$, which depends on the film thickness, also increases.

Figure 4 shows the specular reflection curves for a single crystal of silicon covered with a film of amorphous silicon ($\chi_1 = \chi_0$) for two different values of the tilt angle ψ. It is seen that the sensitivity of specular reflection to the presence of the film increases with decreasing angle ψ. Calculations show that specular reflection curves for a perfect crystal and for a crystal with a film differ by 10–30% even in the case of very thin films, about 0.5 nm thick.

The main problem in practical realization of this method is the need for high collimation of the incident radiation with respect to both the glancing angle ($\delta\varphi \sim 1'$) and the diffraction angle ($\delta\vartheta \sim 1''$). The requirements imposed on the x-ray beam divergence in the horizontal plane can be met by employing a highly asymmetric monochromator with asymmetry coefficient $b \sim 1/40$, and those imposed in the vertical plane can be filled using a micro-focus x-ray tube and a narrow slit at the collimator exit (see [1, 18] and references therein).

3. THE MAIN RESULTS AND CONCLUSIONS

In this paper, we developed an exact dynamical theory of specular reflection of x-rays from a crystal covered with an amorphous film in the case where strongly asymmetric noncoplanar Bragg diffraction takes place; that is, the theory is based on the solution of a dispersion (algebraic) equation of the fourth degree. The problems of diffraction and specular reflection are solved in the general case, and the results obtained are valid over the entire range of glancing angles of the incident beam and angles of departure of the diffracted wave. With this theory, it is shown that the angular dependence of the specularly reflected intensity is highly sensitive to the presence of a thin (several nanometers thick) amorphous film on the surface of the crystal and to the film thickness. This problem can be easily generalized to the case of specular reflection from an inhomogeneous film with an arbitrary depth distribution of the electron density by introducing a system of recurrent relations which are a generalization of the well-known Parratt formulas.

The specularly reflected intensity is high enough to make a proximate analysis of the thin surface and transition layers. The sensitivity of this method to the film thickness is about 0.5 nm and increases with the glancing angle; however, this is accompanied by a decrease in the intensity of the reflected signal. The optimum glancing angles lie in the range from 1.5 to 3–4 times the critical angle for total external reflection; at smaller glancing angles, the sensitivity becomes noticeably lower. In actual practice, crystals in which the reflecting atomic planes are tilted at an angle of 1°–5° are preferable. For radiation with a wavelength of 0.15–0.2 nm, the restrictions on the radiation collimation and on the angular resolution of the method are less severe.

In this paper, it is shown that the data on specular reflection under the conditions for Bragg diffraction can be used for nondestructive examination of the structure of very thin surface layers and interfaces.

ACKNOWLEDGMENTS

The authors are grateful to R.M. Imamov for stimulating useful discussions on the problem and on the main findings of this work.

REFERENCES

1. A. M. Afanas'ev, P. A. Aleksandrov, and R. M. Imamov, *X-ray Diffraction Diagnostics of Submicron Layers* (Nauka, Moscow, 1989).
2. A. V. Andreev, Usp. Fiz. Nauk **145** (1), 113 (1985) [Sov. Phys. Usp. **28**, 70 (1985)].
3. M. A. Andreeva, S. F. Borisova, and S. A. Stepanov, Poverkhnost', No. 4, 5 (1985).
4. A. M. Afanas'ev and R. M. Imamov, Kristallografiya **40** (3), 446 (1995) [Crystallogr. Rep. **40**, 406 (1995)].
5. P. Farwig and H. W. Schurmann, Z. Phys. **204** (2), 489 (1967).

6. S. Kishino, J. Phys. Soc. Jpn. **31** (4), 1168 (1971).
7. T. Bedynska, Phys. Status Solidi A **19** (1), 365 (1973).
8. S. F. Rustichelli, Philos. Mag. **31** (1), 1 (1975).
9. J. Hartwig, Phys. Status Solidi A **37** (2), 417 (1976).
10. V. G. Baryshevskiĭ, Pis'ma Zh. Tekh. Fiz. **2** (3), 112 (1976) [Sov. Tech. Phys. Lett. **2**, 43 (1976)].
11. W. C. Marra, P. Eisenberger, and A. Y. Cho, J. Appl. Phys. **50** (11), 6927 (1979).
12. A. M. Afanas'ev and M. K. Melkonyan, Acta Crystallogr., Sect. A: Found. Crystallogr. **A39** (2), 207 (1983).
13. P. A. Aleksandrov, M. K. Melkonyan, and S. A. Stepanov, Kristallografiya **29** (2), 376 (1984) [Sov. Phys. Crystallogr. **29**, 226 (1984)].
14. P. A. Aleksandrov, A. M. Afanasiev, M. K. Melkonyan, and S. A. Stepanov, Phys. Status Solidi A **81** (1), 47 (1984).
15. P. A. Aleksandrov, A. M. Afanas'ev, and S. A. Stepanov, Poverkhnost', No. 8, 9 (1984).
16. P. A. Aleksandrov, A. M. Afanas'ev, and S. A. Stepanov, Kristallografiya **29** (2), 197 (1984) [Sov. Phys. Crystallogr. **29**, 119 (1984)].
17. P. A. Aleksandrov, A. M. Afanasiev, and S. A. Stepanov, Phys. Status Solidi A **86** (1), 143 (1984).
18. A. M. Afanas'ev, S. M. Afanas'ev, A. V. Esayan, and F. R. Khashimov, Poverkhnost', No. 12, 35 (1988).
19. A. M. Afanasev and O. G. Melikyan, Phys. Status Solidi A **122** (2), 459 (1990).
20. A. M. Afanasev and A. V. Esayan, Phys. Status Solidi A **126** (2), 303 (1991).
21. V. A. Bushuev and R. N. Kuz'min, *Secondary Processes in X-ray Optics* (Mosk. Gos. Univ., Moscow, 1990).
22. M. Born and E. Wolf, *Principles of Optics* (Pergamon, Oxford, 1969; Nauka, Moscow, 1973).

Translated by Yu. Epifanov

Physics of the Solid State, Vol. 43, No. 5, 2001, pp. 949–954. Translated from Fizika Tverdogo Tela, Vol. 43, No. 5, 2001, pp. 913–917.

LOW-DIMENSIONAL SYSTEMS AND SURFACE PHYSICS

X-ray Diffractometric Study of the Influence of a Buffer Layer on the Microstructure of Molecular-Beam Epitaxial InN Layers of Different Thicknesses

V. V. Ratnikov, V. V. Mamutin, V. A. Vekshin, and S. V. Ivanov

Ioffe Physicotechnical Institute, Russian Academy of Sciences, Politekhnicheskaya ul. 26, St. Petersburg, 194021 Russia
e-mail: mam@beam.ioffe.rssi.ru

Received September 18, 2000

Abstract—Thin layers of InN are grown by molecular beam epitaxy on (0001) sapphire substrates. The influence of thin (15 nm) InN buffer layers and their temperature treatment on the structural quality of the grown layers is investigated by double-crystal and triple-crystal x-ray diffractometry. It is revealed that the preliminary high-temperature (900°C) annealing of the buffer layer leads to a notable improvement in the quality of the layers grown on this buffer. The densities of vertical screw and vertical edge dislocations decrease (to 1.9×10^8 cm^{-2} and 1.3×10^{11} cm^{-2}, respectively) with an increase in the distance from the interface (by ~1 μm). © *2001 MAIK "Nauka/Interperiodica".*

1. INTRODUCTION

Group III element nitrides have attracted considerable interest due to their unique optical and electronic properties [1]. However, in recent years, researchers have focused particular attention on GaN and its solid solutions AlGaN and InGaN. There are only a few works concerned with the preparation and structural characterization of InN layers grown by organometallic vapor-phase epitaxy [2–4]. The low temperatures and growth rates used in molecular beam epitaxy can play a significant role in the improvement of the structural quality of InN layers. However, all attempts to obtain high-quality molecular-beam epitaxial InN layers have failed because of the low dissociation temperature (~630°C) and the drastic increase in the nitrogen vapor pressure with a rise in temperature in the range of 450–540°C. In our earlier work [5], we described the preparation of qualitative thin molecular-beam epitaxial InN layers and reported the first results of their characterization by different investigation techniques. The purpose of the present work was to investigate thoroughly the structural perfection of molecular-beam epitaxial InN layers as functions of their thickness and the type of buffer layer with the use of double-crystal and triple-crystal x-ray diffractometry.

2. SAMPLE PREPARATION AND EXPERIMENTAL TECHNIQUE

The InN samples 0.4–1.5 μm thick were grown on Al_2O_3(0001) substrates by molecular beam epitaxy with plasma initiation of nitrogen discharge [6]. For this purpose, we used an ASTEX commercial source with electron cyclotron resonance, which provided growth rates of 0.02–0.20 μm/h at nitrogen flow rates of 1–5 cm^3/min (sccm = standard cubic centimeter per minute) and indium cell temperatures in the range 750–780°C.

We studied five InN samples (Table 1): for sample no. 258, the InN layer was grown on a substrate when its temperature decreased to the growth temperature after the high-temperature (1000°C) annealing; for sample no. 254, the base InN layer was grown at a temperature of 470°C on a low-temperature (LT) InN buffer layer, which was preliminarily grown at a temperature of 300°C; and for samples 269, 239, and 280, the buffer layer was subjected to an additional high-temperature (HT) annealing (900°C) prior to the growth of the base InN layer with different thicknesses t_1. The diffracted x-ray intensities were measured on double-crystal and triple-crystal diffractometers using Cu$K_{\alpha 1}$

Table 1. Half-widths ω of the x-ray diffraction reflection curves for InN layers (in seconds of arc)

Sample no.	t_1, μm/buffer	ω_θ 0002	$\omega_{\theta-2\theta}$ 0002	ω_θ 1124	ω_t 1010	ω_{twt}
258	1.50/absent	2140	174	2164	1100	12000
254	0.45/LT	777	80	755	680	8386
269	0.40/HT	698	75	628	638	7555
239	0.65/HT	350	55	566	571	6672
280	1.00/HT	336	43	472	513	5560

1063-7834/01/4305-0949$21.00 © 2001 MAIK "Nauka/Interperiodica"

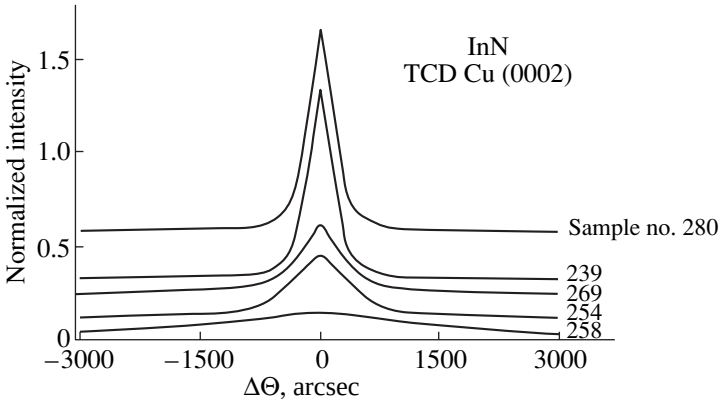

Fig. 1. The θ–TCD curves for the (0002) reflection of InN.

radiation (Bragg geometry) and Mo$K_{\alpha 1}$ radiation (Laue geometry). High-quality Ge(220) crystals were used as a monochromator and an analyzer.

The double-crystal diffraction curves were measured with a wide open detector window for (a) the $(10\bar{1}0)$ symmetrical reflections in the Laue geometry, (b) asymmetrical reflections in the Bragg geometry at a glancing angle of the $(11\bar{2}4)$ incident and $(11\bar{2}\bar{4})$ reflected x-rays (the normal to the surface lies in the scattering plane), and (c) the $(10\bar{1}l)$ symmetrical reflections in the Bragg geometry from planes forming angles with the (0001) surface in the range from 17° to 72° [the "out-of-plane" (oop) curves, the normal to the surface lies outside the scattering plane].

The angular full widths at half-maximum (FWHM) of the diffraction curves for the symmetrical reflections (0002) and (0004) were measured on a triple-crystal diffractometer in the Bragg geometry in two directions: parallel and normal to the diffraction vector [(θ–2θ) and θ scan modes, respectively].

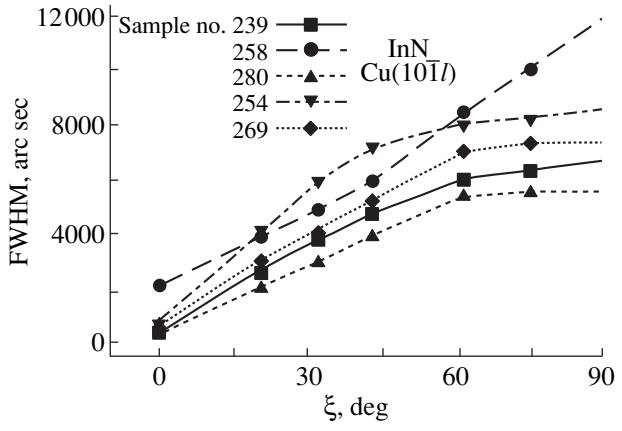

Fig. 2. Dependences of the full width at half-maximum (FWHM) of the diffraction curves for the $(10\bar{1}l)$ reflection of InN on the angle ξ.

3. EXPERIMENTAL RESULTS

The experimental half-widths ω are listed in Table 1. Corrections for the natural half-width, instrumental broadening, and sample bending in analysis of the experimental values of ω were introduced according to the procedure described in [7]. These corrections were insignificant compared to the broadening due to structural defects.

Figure 1 shows variations in the θ–triple-crystal diffraction (TCD) curves for the (0002) reflection as functions of the type of buffer layer used (samples 258, 254, and 269) and the thickness of layers on the high-temperature InN buffer layer (samples 269, 239, and 280).

3.1. Influence of the type of buffer layer on ω. The half-widths of the diffraction curves considerably decrease when going from the layer grown on sapphire without a buffer layer (sample no. 258) to the layer grown on the low-temperature InN buffer layer (sample no. 254) and then to the layer grown on the InN buffer layer subjected to the high-temperature treatment (sample no. 269). For the θ–2θ scan mode, $\omega_{\theta-2\theta}$ is proportional to $\tan\Theta_B$ (where Θ_B is the Bragg angle).

For three samples under consideration, the following condition is met: $\omega_\theta 0002 > \omega_\theta 0004$. In this case, the ratios $\omega_\theta 0002/\omega_\theta 0004$ are approximately identical. At the same time, the ratio between the half-widths of the Bragg curves for the $(11\bar{2}4)$ and $(11\bar{2}\bar{4})$ asymmetrical reflections becomes less than unity when going from sample no. 258 to the layers grown on the InN buffer layer. As follows from these results, the scattering region changes its location with respect to the diffraction vector and the surface of the sample but remains strongly asymmetrical in shape for all three samples ($\omega_\theta \gg \omega_{\theta-2\theta}$). For sample no. 258, we have $\omega_\theta 11\bar{2}4 \approx \omega_\theta 11\bar{2}\bar{4} \approx \omega_\theta 0002$; i.e., the half-width does not depend on Θ_B and the recording geometry, and the scattering region (an ellipse) is extended along the normal to the diffraction vector. For samples with an InN buffer layer,

the following condition is satisfied: $\omega_\theta 11\bar{2}4 < \omega_\theta 11\bar{2}\bar{4}$; i.e., the major axis of the ellipse does not coincide with the normal to the diffraction vector.

The dependences of the half-widths ω_{oop} for a series of the symmetrical Bragg reflections on the ξ angle between the basal plane (0001) and the planes of diffraction are depicted in Fig. 2. As can be seen, all the samples, except for sample no. 258, have a similar dependence $\omega_{oop} = f(\xi)$, which, according to [8], indicates that the disordering in the layer plane and the mosaic spread contribute independently to the measured half-widths ω_{oop}. The approximation of the experimental values of ω_{oop} by relationship (3) taken from [8] results in the half-widths ω_{twt} which are determined only by the degree of layer disordering in the sample plane.

3.2. Influence of the layer thickness on ω for InN samples with a high-temperature buffer. An increase in the layer thickness from 0.4 to 1.0 μm results in a gradual decrease in the half-widths of the diffraction curves for all the reflections. The sole exception is provided by an increase in the half-width of the double-crystal rocking curve for the $(11\bar{2}\bar{4})$ asymmetrical reflection. The ratio $\omega_\theta 11\bar{2}4/\omega_\theta 11\bar{2}\bar{4}$ decreases with an increase in the thickness. This implies that the major axis of the ellipse (the shape of the scattering region) rotates in the reciprocal space from the direction along the normal to the diffraction vector toward the direction parallel to the surface.

4. DISCUSSION

In x-ray diffraction analysis of defect structures with strongly misfit layers (including nitrides), it is usual, with rare exception [9], to measure the broadening of symmetrical and asymmetrical reflections in the Bragg geometry. As a rule, the mosaic model is used for the studied layers with angular rotations of microcrystallites (coherent scattering regions) with respect to each other. This leads to the so-called tilt broadening (ω_{tilt}) of the θ curves, which is identical for all the Bragg reflections in the direction perpendicular to the diffraction vector. At the same time, the broadening associated with the limited size of coherent scattering regions aligned parallel (τ_x) and normal (τ_z) to the sample surface depends on the diffraction angle. This dependence of the contributions to the broadening on the diffraction angle was used in analysis of diffraction curves, for example, in [7, 10]. The disordering (microrotation, the so-called twist) of layers in the sample plane is characterized by the half-width ω_{twt} of the so-called φ scan [4, 10, 11].

The data on ω_{tilt} make it possible to calculate the density of vertical screw dislocations by the formula [12]

$$\rho_{vs} = \omega_{tilt}^2/(4.35b_c^2), \quad (1)$$

where b_c is the Burgers vector of vertical screw dislocations (for InN, its value is equal to 0.5704 nm). The replacement of ω_{tilt} by ω_{twt} gives the density of randomly arranged vertical edge dislocations (b_c is replaced by b_a = 0.3540 nm for the vertical edge dislocation in InN).

Metzger *et al.* [10] noted that x-ray diffraction analysis of the defect structure of GaN on the basis of the half-widths measured only for symmetrical reflections in the Bragg geometry has certain limitations. In our opinion, the use of asymmetrical reflections measured in the Bragg geometry, which was proposed by these authors, is inefficient. This is explained by the fact that, in the general form, the broadening of asymmetrical reflections involves a complex combination (which depends on the projections of the displacement vectors onto the diffraction vector due to the presence of defects) of the contributions from the microrotations and microstrains parallel and normal to the planes of diffraction and also the broadenings associated with limited sizes of coherent scattering regions aligned parallel and normal to the sample. The necessity of simulating the ratio between components in the measured half-widths makes analysis of the defect structure more difficult.

Earlier [13], we demonstrated that the use of x-ray diffraction in the Laue geometry can considerably enhance the potentials of x-ray diffractometric analysis of the crystal perfection of nitride compounds. In this respect, we also measured the symmetrical Laue diffraction from the $(10\bar{1}0)$ planes perpendicular to the sample surface. Unfortunately, because of the low luminosity of the triple-crystal diffractometer, the high normal photoelectric x-ray absorption coefficient for InN, and the small layer thickness, we succeeded only in measuring x-ray diffraction for the $(10\bar{1}0)$ reflection on a double-crystal diffractometer.

An important point in analysis of the dislocation structure is that the experimental half-widths are related by the inequality $\omega_\theta(0002, \text{Bragg geometry}) > \omega_\theta(10\bar{1}0, \text{Laue geometry})$. Analysis of the θ curves in terms of the mosaic spread model of coherent scattering regions showed that, for sample no. 258 and, to a lesser extent, sample nos. 254 and 269, the tilt component which is independent of the recorded reflection makes a dominant contribution to the broadening, whereas the contribution of the size effect is small. If the layer consisted of mutually rotated micrograins with a defect-free lattice, the ω_{tilt} values measured in the Bragg and Laue geometries would be identical. However, we have the inequality $\omega_{tilt}(\text{Bragg}) > \omega_{tilt}(\text{Laue})$. This circumstance indicates the necessity of refining the mosaic model, which was used earlier to analyze the results of x-ray diffractometric measurements for the layers under investigation. Below, we will analyze the broadening of x-ray reflections under the assumption that the broad-

ening of the θ curves is determined by the size effect (due to the limited size of coherent scattering regions) and two misorientation components. The first component ω_{tilt} is associated with the rotation of coherent scattering regions and does not depend on the chosen reflection and the recording geometry. The mosaic spread in nitrides is caused by the considerable lattice mismatch of the layer and the substrate and its attendant island-type three-dimensional growth. The second component ω_φ is determined by the presence of defects (for the most part, the grown-in vertical screw and edge dislocations) in microregions. The contributions to the θ–triple-crystal diffraction curve are summed according to the quadratic law, because the majority of theoretical calculations of x-ray diffraction in crystals with randomly distributed dislocations, as well as our measurements, lead to a Gaussian shape of the broadened diffraction line, that is,

$$(\omega_\theta^{B(L)})^2 = (\omega_{tx(tz)}^{B(L)})^2 + (\omega_{tilt}^{B(L)})^2 + (\omega_\varphi^{B(L)})^2, \qquad (2)$$

where the superscripts B and L refer to the Bragg and Laue geometries, respectively. To put it differently, the broadening of the symmetrical reflection (θ-scan) is associated not only with the size effect along the planes of diffraction ($\omega_{tx(tz)}^{B(L)}$) and the mosaic spread ($\omega_{tilt}^{B(L)}$), but also with the micromisorientations of the planes of diffraction ($\omega_\varphi^{B(L)}$) due to the presence of defects in coherent scattering regions.

The broadening of the θ–2θ curves is determined by two components

$$(\omega_{\theta-2\theta}^{B(L)})^2 = (\omega_{tz(tx)}^{B(L)})^2 + (\omega_\varepsilon^{B(L)})^2, \qquad (3)$$

where $\omega_{tz(tx)}^{B(L)}$ describes the size effect along the normal to the planes of diffraction and $\omega_\varepsilon^{B(L)}$ accounts for the microstrain (proportional to $\tan\Theta_B$) of the planes of diffraction along the normal to them.

The size of coherent scattering regions along the normal to the layer is approximately equal to the layer thickness (Table 2), and the contribution of the size effect to the broadening $\omega_\theta 10\bar{1}0$ of the Laue curves in formula (2) is insignificant. The vertical screw and edge dislocations, which are the dominant type of dislocations in nitrides, do not affect $\omega_\theta 10\bar{1}0$, and the third term in relationship (2) for the Laue geometry is determined only by dislocations of two types: horizontal screw and horizontal edge dislocations with the Burgers vector parallel to the interface (the so-called misfit dislocations). The probability that dislocations of the former type occur is low (see, for example, [10]), and the misfit dislocations localized near the interface can affect the diffraction curve only in the case of thin layers. Therefore, the tilt component in expression (2) for the Laue geometry can be considered predominant. At the same time, all three broadening components contribute to $\omega_\theta 0002$. In this case, the third term is determined only by the presence of vertical screw dislocations (whose displacement vector is parallel to the diffraction vector) in the layers. The occurrence of vertical edge dislocations does not affect $\omega_\theta 0002$, because their Burgers vector is perpendicular to the diffraction vector. Consequently, by subtracting the contribution of the size effect and the tilt contribution (identical for the Bragg and Laue geometries) from $\omega_\theta 0002$, we obtain the broadening component ω_φ^B for the symmetrical Bragg curve, which is determined only by the presence of vertical screw dislocations in the layers. For sample no. 258 (t_1 = 1.5 μm and the influence of a strongly defective region near the interface can be ignored), the calculation by formula (1) gives the density of vertical screw dislocations ρ_{vs}(sample no. 258) = 4.9×10^9 cm^{-2}.

The accuracy in the determination of the dislocation density, which is determined by the accuracy in the measurement of the θ half-widths of the triple-crystal diffraction curves (10%) and the ω_{twt} half-width (20%), is better than 40% for both screw and edge dislocations.

For the samples grown on the low-temperature and high-temperature buffer layers, the dislocation densities ρ_{vs} calculated under the assumption that $\omega_\theta 1010 = \omega_{tilt}$ are equal to 0.51×10^8 and 0.65×10^8 cm^{-2}, respectively. The surprising thing is that ρ_{vs}(sample no. 269) > ρ_{vs}(sample no. 254), because all the half-widths measured for sample no. 254 are larger than those for sample no. 269. This can be explained by the fact that, for thin (<0.5 μm) samples, the defect layer near the interface makes a certain contribution to the broadening of the $\omega_\theta 10\bar{1}0$ half-width measured in the Laue geometry, and hence, we have $\omega_\theta 10\bar{1}0 \neq \omega_{tilt}$. It can be assumed that the growth on the low-temperature buffer layer (less ordered) brings about the formation of a more defective and thicker layer near the interface, which contributes to $\omega_\theta 10\bar{1}0$ (sample no. 254). As a consequence, analysis of the broadenings for sample no. 254 leads to an overestimated contribution of ω_{tilt} and underestimated values of ω_φ and ρ_{vs}. For sample no. 269, this effect manifests itself to a lesser degree. Therefore, the ρ_{vs} densities given in Table 2 for samples no. 254 and 269 have approximate values and should be treated as minimum.

A gradual decrease in the half-widths measured for the samples on the high-temperature buffer layer with an increase in the layer thickness reflects an improvement in their crystal perfection. Analysis of the ratios $\omega_\theta 0002/\omega_\theta 0004$ and $\omega_\theta 11\bar{2}4/\omega_\theta 11\bar{2}\bar{4}$ shows that, as the layer thickness increases, the disposition of the scattering region (ellipse) in the reciprocal space changes from being extended along the normal to the diffraction vector (the tilt effect) to being extended along the surface (owing to the micromisorientations of

the planes of diffraction around vertical screw dislocations). Since the size effect is rather small, only the last term remains in formula (2) and the $\omega_\theta 0002$ half-width measured for samples 239 and 280 is determined primarily by vertical screw dislocations, which are typical of nitrides. Their densities ρ_{vs} calculated using relationship (1) are listed in Table 2.

By assuming the linear dependence $\rho_{vs} = f(t_1)$, we obtain $\rho_{vs} = 2.2 \times 10^8$ cm^{-2} for sample no. 269, which is considerably larger than the ρ_{vs} value calculated for the same sample under the assumption that $\omega_\theta 1010 \approx \omega_{tilt}$. This is indirect evidence in favor of the assumption that, in addition to the tilt component, the $\omega_\theta 10\bar{1}0$ quantity measured for thin samples in the Laue geometry involves the component associated with individual microdefects (misfit dislocations).

For detailed characterization of the structural perfection of epitaxial nitride layers, it is insufficient to measure the symmetrical diffraction in the Bragg symmetry [4, 10, 11, 13]. A three-dimensional growth of nitrides leads to rotations of micrograins with respect to each other in the layer plane. Grown-in (vertical) edge dislocations also bring about microrotations in the layer plane. For this reason, the measurements of crystal lattice disordering in the layer plane are important for the general structural characterization of layers and the quantitative estimation of the density of vertical edge dislocations [from formula (1)].

Two currently available methods are used to measure the disordering in the layer plane. In the glide geometry method, the rocking curve is recorded from the $(10\bar{1}0)$ planes perpendicular to the surface [11, 13]. The limitation of this method resides in the fact that the information derived refers only to an extremely thin surface layer (~10 nm) due to the small angles of incidence (~0.1°). The interpolation of the obtained values of ω_{twt} to the whole sample is open to question.

The so-called ϕ scan method is widely used for measuring ω_{twt} and consists in recording the angular distribution of the diffracted x-ray intensity for an asymmetrical reflection upon azimuthal rotation of the sample around the normal to it (the normal lies in the scattering plane) [10, 11]. Lee *et al.* [4] used this method and obtained very large values of ω_{twt} for InN samples. However, apart from the low sensitivity of this method (because of the large vertical divergence of the x-ray beam), the measured value of ω_{twt} includes the tilt contribution [8]. Srikant *et al.* [8] showed that the correct value of ω_{twt} can be obtained in the Bragg geometry not from the measurement of the ϕ scan curve but from analysis of the dependence of the half-width on the ξ angle between the planes of diffraction and the basal plane (0001) for a series of symmetrical Bragg reflections of the $(10\bar{1}l)$ type. An increase in ξ leads to a decrease in the tilt contribution and an increase in the twist component of the measured half-width. The measurement of the dependence $\omega_{oop} = f(\xi)$ and its approximation by a relationship of type (3) given in [8] allow one to derive (at $\xi = 90°$) the half-width ω_{twt} of the rocking curve recorded from the (1010) plane perpendicular to the basal plane, which is determined only by the twist component of the disordering.

Table 2. Grain sizes along (τ_x) and perpendicular (τ_z) to the surface and the densities of vertical screw (ρ_{vs}) and vertical edge (ρ_{ve}) dislocations

Sample no.	τ_x, μm	τ_z, μm	ρ_{vs}, 10^8 cm^{-2}	ρ_{ve}, 10^{11} cm^{-2}
258	0.08	1.77	48.8	6.21
254	0.17	0.41	≥0.51	3.03
269	0.26	0.49	≥0.65 (2.20)	2.46
239		0.54	2.04	1.92
280		1.15	1.88	1.33

The densities of vertical edge dislocations ρ_{ve} were calculated by formula (1) with the use of the ω_{twt} values obtained in much the same manner as in [8]. The ρ_{ve} densities calculated under the assumption of a random dislocation arrangement are listed in Table 2. It can be seen that the density of vertical edge dislocations decreases when going over to the sample with a high-temperature buffer layer (sample no. 258 ⟶ sample no. 269) and with an increase in the layer thickness (sample no. 269 ⟶ sample no. 280). It is worth noting that the difference in the densities of vertical screw and vertical edge dislocations is rather large (three orders of magnitude). A similar difference was observed earlier by Metzger *et al.* [10] for GaN layers grown by organometallic vapor-phase epitaxy. The data obtained for single-crystal (as a whole) samples no. 239 and 280 characterize the density of randomly distributed vertical edge dislocations, whereas a columnar structure with the low-angle boundaries formed by vertical edge dislocations is characteristic of samples no. 258 and 254 and, to a lesser extent, sample no. 269.

5. CONCLUSION

Thus, in the present work, we investigated the defect structure of thin molecular-beam epitaxial InN layers on sapphire by x-ray diffractometry.

The asymmetry of diffraction scattering in the reciprocal space is characteristic of all the studied samples. The scattering region is extended along the surface of the samples grown on the high-temperature InN buffer layer at $t_1 > 0.5$ μm, which is associated with the geometry of dislocation arrangement (along the *c* axis) and the anisotropy of deformation fields around dislocations.

It was found that the structural quality of layers drastically improves upon growth on the InN buffer

layer subjected to the high-temperature (900°C) treatment.

The defect structure of the layers is characterized by a large number of vertical screw and vertical edge (their number is three orders of magnitude larger) dislocations. The densities of vertical screw and vertical edge dislocations decrease (to 1.9×10^8 cm^{-2} and 1.3×10^{11} cm^{-2}, respectively) with an increase in the distance from the interface (by ~1 μm).

ACKNOWLEDGMENTS

This work was supported by the Russian Foundation for Basic Research, project nos. 99-02-17103, 98-02-18309, and 00-02-16760.

REFERENCES

1. S. Nakamura, Semicond. Sci. Technol. **14** (6), R27 (1999).
2. Q.-X. Guo, T. Yamamura, A. Yoshida, and N. Itoh, J. Appl. Phys. **75** (10), 4927 (1994).
3. W.-K. Chen, Y.-Ch. Pan, H.-Ch. Lin, *et al.*, Jpn. J. Appl. Phys. **36** (12B), L1625 (1997).
4. M.-Ch. Lee, H.-Ch. Lin, Y.-Ch. Pan, *et al.*, Appl. Phys. Lett. **73** (18), 2606 (1998).
5. V. V. Mamutin, V. A. Vekshin, V. Yu. Davydov, *et al.*, Phys. Status Solidi A **176**, 247 (1999).
6. V. V. Mamutin, V. N. Zhmerik, T. V. Shubina, *et al.*, Pis'ma Zh. Tekh. Fiz. **24** (12), 30 (1998) [Tech. Phys. Lett. **24**, 467 (1998)].
7. J. E. Ayers, J. Cryst. Growth **135**, 71 (1994).
8. V. Srikant, J. S. Speck, and D. R. Clarke, J. Appl. Phys. **82** (9), 4286 (1997).
9. R. N. Kyutt and T. S. Argunova, Nuovo Cimento D **19**, 267 (1997).
10. T. Metzger, R. Hopler, E. Born, *et al.*, Philos. Mag. A **77** (4), 1013 (1998).
11. K. Kobayashi, A. A. Yamaguchi, Sh. Kimura, *et al.*, Jpn. J. Appl. Phys. **38** (6A/B), L611 (1999).
12. C. O. Dunn and E. F. Koch, Acta Metall. **5**, 548 (1957).
13. R. N. Kyutt, V. V. Ratnikov, G. N. Mosina, and M. P. Shcheglov, Fiz. Tverd. Tela (St. Petersburg) **41** (1), 30 (1999) [Phys. Solid State **41**, 25 (1999)].

Translated by O. Borovik-Romanova

Physics of the Solid State, Vol. 43, No. 5, 2001, pp. 955–962. Translated from Fizika Tverdogo Tela, Vol. 43, No. 5, 2001, pp. 918–925.

POLYMERS AND LIQUID CRYSTALS

Disjoining Pressure in Free-Standing Smectic-*A* Films and Its Influence on Their Reflectivity

L. V. Mirantsev

Institute of Problems in Machine Science, Russian Academy of Sciences, Vasil'evskiĭ ostrov, Bol'shoĭ pr. 61, St. Petersburg, 199178 Russia
e-mail: miran@microm.ipme.ru

Received August 10, 2000; in final form, October 21, 2000

Abstract—This paper reports the results of calculating the disjoining pressure and average thickness of smectic layers in free-standing liquid-crystal films heated above the temperature of breakdown of the smectic order in the bulk of the mesogens. The effect of the disjoining pressure on the reflectivity of free-standing smectic-*A* films with different numbers of smectic layers has been studied. The results of the calculations agree with the experimental study of the reflectivity of free-standing smectic-*A* films in the optical wavelength range. © *2001 MAIK "Nauka/Interperiodica".*

INTRODUCTION

Smectic liquid crystals (LC) possess a remarkable capability of forming free-standing films, whose area may be of the order of 1 cm^2 [1] and whose thickness varies from a few hundred to two or even one smectic layer [2, 3]. This makes such films ideal subjects for investigating the behavior of two-dimensional physical systems. In addition, they frequently exhibit phenomena not observed in the bulk of an LC [4–15]. For this reason, free-standing smectic films (FSSFs) have been intensively studied both experimentally [2–20] and theoretically [21–30] in the past 15–20 years.

One of the most efficient methods for the experimental study of the FSSFs is the investigation of their optical characteristics, more specifically of the transmission spectra [20] and reflectivity [3, 4, 9–14], in the optical wavelength range. It is the reflectivity measurements [9, 10] made on free-standing smectic-*A* films (FSSAFs) of some LC compounds that revealed in them a new remarkable phenomenon of the abrupt thinning of a film when heated above the temperature at which the smectic order in the bulk phase of the LC breaks down. Due to these jumps, the thickness of an FSSAF may vary sequentially from a few tens to two smectic layers and the temperature at which two-layer films exist may exceed by ~10–20 K that of the smectic-*A*–isotropic (Sm-*A*–I) or Sm-*A*–nematic (Sm-*A*–N) phase transformation in thick samples of the same mesogens. Later high-precision measurements of the optical reflectivity of free-standing films of LC materials exhibiting a similar behavior, for instance, of the partially fluorinated mesogen 2-[4-(1,1-dihydro)-2-(2-perfluorobutoxy)perfluoroethoxy]phenyl-5-octyl pyrimidine [H8F(4,2,1)MOPP], demonstrated considerable compression of the smectic layers in these films [14]. In these studies, the average thickness of the smectic layers in an *N*-layer FSSAF was determined from measurements of its reflectivity *R* by using the relation

$$R = cN^2, \tag{1}$$

where $c = [(n_0^2 - 1)k_0L]^2/4$, n_0 is the ordinary refractive index, k_0 is the wave number of the monochromatic light used in the experiment, and L is the average thickness of the film smectic layer. The quantity n_0 was considered temperature-independent and equal to the ordinary refractive index of the volume smectic-*A* phase of the LC used to prepare the FSSAF. It was found that as an *N*-layer film (N = 10, 9, 8, …, 3) was heated to the highest temperature it could sustain, $T_c(N)$, the average thickness of its layers decreased monotonically down to a minimum value, after which, following a jump down in the number of FSSAF layers by one, it increased, likewise in a jump, to nearly its initial value. When subsequently heated, the FSSAF film, now $(N - 1)$ layers thick, exhibited a similar behavior. The changes in the average thickness of the film smectic layers reached about 1 Å. It should also be pointed out that the minimum average layer thickness in the *N*-layer film, which was reached at $T_c(N)$, decreased with a decreasing layer number N. In other words, the minimum average layer thickness for a nine-layer film was smaller than that of a ten-layer one, for an eight-layer film it was smaller than for a nine-layer one, etc. Reflectivity measurements made on free-standing films of another partially fluorinated LC compound, H10F5MOPP, which were also observed to undergo layer-thinning transitions when heated above the Sm-*A*–I transformation temperature in the volume phase, exhibited a similar behavior of the smectic layers; however, when heated to the maximum temperature $T_c(N)$ they were able to sustain, their reflectivity decreased with increasing temperature nearly two times more slowly than that

of similar films of mesogen H8F(4,2,1)MOPP. These observations are in marked contrast with the data [12] on the reflectivity of FSSAFs of the 54COOBC mesogen, whose molecules have ordinary alkyl tails without fluorine atoms. Although free-standing films of this compound also undergo jumpwise layer-by-layer thinning when heated above the Sm-*A*–I transition temperature in the volume mesogen, increasing the temperature of such a film with a given number of layers N to the maximum possible level $T_c(N)$ does not bring about a noticeable change in its reflectivity. By Eq. (1), a faster decrease in the reflectivity of an N-layer film with increasing temperature corresponds to a larger negative value of the thermal expansion coefficient K_L of its layers. By contrast, if the reflectivity of a film does not change when heated to $T_c(N)$, the temperature at which its thickness decreases in a jump, then the average thickness of the smectic layers of such an FSSAF does not depend altogether on temperature. It follows that the compression of smectic layers in free-standing H10F5MOPP films is lower than that in the H8F(4,2,1)MOPP liquid-crystal FSSAFs, while in free-standing 54COOBC films the layers are not compressed at all. The reason for the layers of free-standing films of different mesogens to behave so differently remains unclear.

It should be pointed out that relation (1), used in the treatment of measurements in all experimental FSSAF reflectivity studies [3, 4, 9–14], is valid only for a homogeneous film with a refractive index which does not depend on the distance to its bounding surfaces [31]. Free-standing smectic films may, however, be considered homogeneous only at temperatures substantially below the Sm-*A*–N or Sm-*A*–I phase-transition temperature in the LC volume. In this case, the Sm-*A* structure is well established throughout the film volume and the orientational and translational molecule orderings in the inner and surface layers of a film differ little from one another. If one assumes that the ordinary, n_0, and extraordinary, n_e, refractive indices in free-standing films, as well as in thick LC samples, depend on the orientational order parameter s [32], then these indices should likewise be practically the same for all film layers. However, as was already mentioned, smectic layers in an FSSAF were observed to be compressed at temperatures substantially in excess of the point at which smectic order breaks down in the mesogen volume. By a microscopic model [24, 25, 27, 29], which reproduces fairly well the behavior of free-standing films heated above the Sm-*A*–N or Sm-*A*–I phase-transition temperatures, both the orientational and translational ordering in the inner layers of a film can be considerably less pronounced than near the free bounding surfaces. This theoretical conclusion was confirmed experimentally [20] in a study of optical transmission spectra of cyanobiphenyl FSSAFs of different thicknesses in the region of the electronic absorption bands of the LC molecules. It was found that orientational ordering of molecules in the surface layer of a film does exceed that in the inner layers. Additionally, one observed a noticeable weakening of the orientational order in an FSSAF under heating. Hence, the refractive indices n_0 and n_e in such films should vary with the distance from the free surface, as well as depend on temperature, which is totally disregarded when using the simple relation (1) in the treatment and interpretation of measurements [3, 4, 9–14] of the FSSAF optical reflectivity. Without taking into account the refractive index profiles in FSSAFs and their temperature behavior, one cannot derive from these data the correct temperature dependence of the thickness of smectic layers and, hence, the extent of their compression. For instance, the experimentally observed [12] absence of a noticeable temperature dependence of the reflectivity of free-standing smectic-*A* 54COOBC LC films heated up to a jumpwise decrease in their thickness by an integral number of layers in no way means the absence of such a compression.

We are showing in this work that the factor responsible for the compression of layers in free-standing smectic-*A* films is the disjoining pressure, which is created in these films when heated above the temperature of the breakdown of the smectic order in a volume LC. The pressures arising in FSSAFs of different thicknesses are calculated in terms of the microscopic model [24, 25, 27, 29]. The temperature dependences of the average thickness of the smectic layers in these films compressed by the disjoining pressure are calculated. These calculations take into account the dependences of the tension (compression) moduli B on the distance from the film bounding surfaces and on temperature, which likewise are determined within the model [24, 25, 27, 29] developed for free-standing smectic-*A* films. A study is made of the effect of disjoining pressure on the reflectivity of FSSAFs with different numbers of smectic layers. The calculation of the reflectivity of free-standing films makes use of a characteristic matrix M [31] constructed for a layered dielectric plate, each layer of which is characterized by a thickness L_i equal to that of the ith smectic film layer compressed by the disjoining pressure and by a "local" refractive index n_i, which is calculated based on the orientational order-parameter profile in the FSSAF found by the microscopic model [24, 25, 27, 29]. The results of the calculations are in agreement with the experimental measurement of the reflectivity of free-standing smectic-*A* films in the optical wavelength range and permit one to explain the difference in the temperature dependences of these quantities between films prepared of partially fluorinated mesogens and LC films formed by molecules with conventional alkyl tails.

1. DISJOINING PRESSURE AND COMPRESSION OF SMECTIC LAYERS IN FREE-STANDING SMECTIC-*A* FILMS

Consider an N-layer, free-standing smectic-*A* film with unit surface area, which is in contact with a reser-

voir of the same mesogen maintained at the same temperature T and external pressure P_{ext}. This reservoir is needed to maintain the film in a stable state [1], because it compensates the losses of its molecules through evaporation. We assume that the thickness of this film decreases by one smectic layer at constant T and P_{ext}. The LC molecules lost by the film as a result of this thinning transfer naturally to the reservoir. Let F_N and F_{N-1} be the free energies of the original, N-layered, and the new, $(N-1)$-layered, FSSAF, respectively; F_{r1} is the free energy of the reservoir before it received the film molecules; and F_{r2}, its free energy after this transfer. Then we can write the change ΔF in the total free energy of the film + reservoir system caused by a decrease in the film thickness by one layer as

$$\Delta F = (F_{N-1} + F_{r2}) - (F_N - F_{r1}). \quad (2)$$

If the temperature T of the film + reservoir system is substantially lower than that of the Sm-*A*–N or Sm-*A*–I phase transition in the LC volume, the reservoir surrounding the FSSAF is in the Sm-*A* phase coinciding with the smectic-*A* film structure and its thinning by one layer is equivalent to a transfer of this layer to the reservoir without any change of its state. Obviously enough, the change in the free energy of the FSSAF + reservoir system is in this case practically zero and the decrease in the film thickness does not require any work to be done.

The situation changes substantially if one considers a decrease in the FSSAF thickness by one smectic layer at a temperature T exceeding the temperature at which the smectic order in the LC volume breaks down. In this case, the reservoir surrounding the film is either in the isotropic or in the nematic phase and the smectic film layer transferring to it will assume one of these less ordered states. Hence, the change in the film + reservoir system energy should be different from zero. For instance, if the Sm-*A* phase in the mesogen forming the FSSAF transfers under heating to an isotropic state, whose free energy is usually taken as the zero level from which the energy will be reckoned, the change ΔF in the total free energy of the film + reservoir system can be written as

$$\Delta F = F_{N-1} - F_N. \quad (3)$$

The quantity ΔF, which can be found by means of the microscopic model [24, 25, 27, 29] for any N-layer FSSAF at any temperature T in the region of its existence, is equal to the work to be done on a film of unit area in order to reduce its thickness by one layer. This work is associated with an additional pressure

$$\Delta P = -\Delta F/L, \quad (4)$$

which is applied to the layers in the FSSAF by its free bounding surfaces. Derjaguin [33] showed that this pressure, which he called disjoining, should act in any bounded thin liquid layer with a structure different from that of the volume phase. If the quantity ΔF in Eq. (4) is positive, then the disjoining pressure precludes FSSAF thinning and the film layers are subjected to tension. By contrast, if $\Delta F < 0$, then the disjoining pressure favors film thinning and its layers are compressed. As we shall show later, it is the latter situation that is realized in an FSSAF when it is heated above the temperature of smectic order breakdown in the LC volume.

Application of disjoining pressure to the smectic layers in free-standing smectic films should result in a change in their thickness. By Hooke's law, the thickness L_i of each ith film layer can be presented as

$$L_i = L_0(1 - \Delta P/B_i), \quad (5)$$

where L_0 is the layer thickness in the absence of disjoining pressure and B_i is the tension (compression) modulus of the ith FSSAF layer. These moduli can be readily found from the following considerations. It is well known that the tension (compression) modulus B of smectic layers in a volume smectic LC is proportional to the squared translational order parameter τ [32]. If we assume that the relations connecting the elastic moduli with the orientational and translational order parameters in free-standing films throughout the temperature range of their existence, including the temperatures above the Sm-*A*–N or Sm-*A*–I phase transition points in a bulk LC, are the same as in the bulk mesophases, then the elastic moduli B_i in Eq. (5) for smectic layers in an FSSAF can also be calculated within the microscopic model of [24, 25, 27, 29]. This model permits determination of the orientational, $s_i(T)$, and translational, $\tau_i(T)$, order parameters for each film layer of an arbitrary thickness and for any temperature T within the range of its existence. Moreover, in the case of very thick films ($N \longrightarrow \infty$), the values of these parameters at the film center obtained by this model coincide completely with the results yielded by the well-known theory of McMillan [34] for the bulk smectic-*A* phase. If one knows the elastic modulus B in the bulk smectic-*A* phase at some temperature T_0 [$B(T_0) \equiv B_0$] lower than the Sm-*A*–I or Sm-*A*–N phase-transition point, then the model of [24, 25, 27, 29] permits one to find the order parameter $\tau(T_0) \equiv \tau_0$ at this temperature, after which one can, using the relation

$$B_i(T) = B_0(\tau_i(T)/\tau_0)^2, \quad (6)$$

determine the elastic moduli B_i for all film layers of a given thickness for any temperature T within the region of the film existence.

2. REFLECTIVITY OF FREE-STANDING SMECTIC-*A* FILMS

In calculating the reflectivity of an N-layered FSSAF, we shall consider the latter as a nonuniform dielectric plate made up of N layers with thicknesses equal to those of the film smectic layers L_i and "local"

refractive indices n_i. By [31], propagation of a normally incident monochromatic light through such a plate can be fully described by a characteristic 2×2 matrix M, whose elements are determined by the relations

$$M_{11} = M_{22} = 1, \tag{7}$$

$$M_{12} = -ik_0 \sum_{i=1}^{N} L_i, \tag{8}$$

$$M_{21} = -ik_0 \sum_{i=1}^{N} n_i^2 L_i. \tag{9}$$

For the reflectivity R of such a layered dielectric plate, we have [31]

$$R = |r|^2, \tag{10}$$

where

$$r = [(M_{11} + M_{12}) - (M_{21} + M_{22})]/[(M_{11} + M_{12}) + (M_{21} + M_{22})]. \tag{11}$$

If the condition

$$k_0 \sum_{i=1}^{N} (n_i^2 + 1) L_i \ll 1,$$

which is valid for visible radiation and not too thick FSSAFs ($N \le 10$), is met, one comes readily to the relation

$$R \approx (k_0^2/4) \left[\sum_{i=1}^{N} (n_i^2 - 1) L_i \right]^2. \tag{12}$$

One can easily verify that if the film is assumed spatially homogeneous ($n_1 = n_2 = \ldots = n_i = \ldots = n_N = n_0$), as is done in [3, 4, 9–14], Eq. (12) transforms to Eq. (1).

The local refractive indices n_i for FSSAF layers can be found from considerations similar to those used by us earlier for determination of the elastic tension (compression) moduli B_i of the film layers. It is known that the dependences of the ordinary, n_0, and extraordinary, n_e, refractive indices for a bulk LC phase on the orientational order parameter s can be cast as follows [32, 35]

$$n_0^2 = 1 + A(\bar{\beta} - (1/3)\Delta\beta s), \tag{13}$$

$$n_e^2 = 1 + A(\bar{\beta} + (2/3)\Delta\beta s), \tag{14}$$

where A is a constant characteristic of a given mesogen, $\bar{\beta}$ is the mean polarizability of the LC molecules, and $\Delta\beta$ is the anisotropy of their polarizability. If one knows these refractive indices for the bulk smectic-A phase at the above-mentioned temperature T_0 [$n_0(T_0) \equiv n_0^{(0)}$, $n_e(T_0) \equiv n_e^{(0)}$], which is lower than the Sm-A–I or Sm-A–N phase-transition point, the model of [24, 25, 27, 29] makes it possible to find the orientational order parameter $s(T_0) \equiv s_0$ at this temperature and, by combining Eqs. (13) and (14), to determine the quantities $A\bar{\beta}$ and $A\Delta\beta$ entering them. If one also assumes the local refractive indices n_i and the local orientational-order parameters s_i in free-standing films to be connected by the same relations as in the bulk of the mesophases, then the local refractive indices for the FSSAF layers can be calculated by means of Eqs. (13) and (14) by substituting in them the obtained values of $A\bar{\beta}$ and $A\Delta\beta$ and the local orientational-order parameters s_i calculated by the microscopic model of [24, 25, 27, 29]. For normal incidence of light on the film, the final expression for the local refractive indices n_i takes the form

$$n_i^2 = [(n_e^{(0)})^2 + 2(n_0^{(0)})^2]/3 - [(n_e^{(0)})^2 - (n_0^{(0)})^2](s_i/s_0). \tag{15}$$

Equations (12) and (15), as well as the relations (4)–(6) derived earlier, solve completely the problem of finding the reflectivity R of an N-layered FSSAF for any temperature T within the region of its existence.

3. RESULTS OF THE NUMERICAL CALCULATIONS AND THEIR DISCUSSION

We carried out numerical calculations of the disjoining pressure ΔP, average smectic-layer thickness $L = (1/N)\sum_{i=1}^{N} L_i$, and reflectivity R for FSSAFs consisting of N = 10, 9, 8, 7, and 6 layers. These films were assumed to be made of an LC undergoing a strong first-order transition from the isotropic to the smectic-A phase. In the model of McMillan for a bulk smectic-A phase [34], as well as in the model of [24, 25, 27, 29] developed for free-standing smectic-A films, the model parameter $\alpha = 2\exp[-(\pi r_0/L)^2] \ge 0.98$ corresponds to this case. Here, r_0 is a characteristic radius of interaction for the model pairwise intermolecular potential used in the theory of McMillan. We used $\alpha = 1.05$ in the calculations. This choice was motivated by the fact that the reflectivity measurement [12, 14] was done on free-standing films of mesogens undergoing a first-order Sm-A–I phase transition. By the model of McMillan [34], for $\alpha = 1.05$, the temperature of the Sm-A–I phase transition in the bulk of the LC is $T_{AI} = 0.2249(V_0/k_B)$, where V_0 is the intermolecular interaction constant and k_B is the Boltzmann constant. The intermolecular interaction constant V_0 was chosen such that the absolute temperature T_{AI} of the Sm-A–I phase transition in the bulk of the LC coincided with the experimentally found temperature (344 K [14]) of this transition in the partially fluorinated LC [H8F(4,2,1)MOPP]. The orienting action of the film free surface on LC molecules was assumed to be strong enough. The ratio of the interaction constant W, which in the model of [24, 25, 27, 29] determines the effective external field simulating this

action, to the intermolecular interaction constant V_0 was taken to be 1.8. By this model, for such a strong orienting action of the free surface on the LC molecules, heating an FSSAF to the high-temperature limit of its existence brings about not its rupture but rather a jumpwise thinning by an integral number of layers. It is this effect that was observed to occur experimentally [12, 14] in free-standing LC films of H10F5MOPP, H8F(4,2,1)MOPP, and 54COOBC. The smectic-layer thickness L_0 in the absence of disjoining pressure was assumed equal to $L_0 = 30$ Å, and the concentration ρ_0 of the molecules in the LC was taken to be $\rho_0 = 1.5 \times 10^{21}$ cm^{-3}, a figure typical of most mesogens. The elastic tension (compression) modulus of smectic layers, B_0, was considered determined at a temperature slightly lower than the Sm-*A*–I transition point T_{AI} in the bulk of the LC and taken equal to $B_0 = 5.5 \times 10^8$ dyn/cm^2, a figure nearly an order of magnitude larger than the values ($B_0 \sim 10^7$–10^8 dyn/cm^2) typical of conventional LCs consisting of molecules with alkyl tails. The reason for this choice consists in that it is the partially fluorinated mesogens [13, 18], whose FSSAFs demonstrate jumpwise layer-by-layer thinning under heating, that are characterized by tension (compression) moduli of smectic layers larger than the same moduli for the conventional LCs. For the sake of simplicity, the refractive indices $n_0^{(0)}$ and $n_e^{(0)}$ were also considered determined at a temperature slightly below T_{AI}. The first of them was assumed to be $n_0^{(0)} = 1.48$, the figure used in the experiments [3, 4, 9–14]. As for the second refractive index, $n_e^{(0)}$, we used three values in the calculations, $n_e^{(0)} = 1.6$, 1.65, and 1.7. The reasons for this choice will be discussed later.

First, we calculated by the model of [24, 25, 27, 29] the disjoining pressure ΔP for FSSAFs of different thicknesses and for different temperatures, up to the limiting temperatures of their existence, $T_e(N)$. Figure 1 presents the dependence of ΔP on the reduced temperature $T^* = k_B T/V_0$, which corresponds to the heating of a free-standing film, initially ten smectic layers thick, above the temperature T_{AI} of the breakdown of smectic order in the LC bulk. In this process, the film undergoes a sequence of layer-by-layer thinnings ($10 \longrightarrow 9 \longrightarrow 8 \longrightarrow 7 \longrightarrow \ldots$); these thinnings, identified by breaks in the temperature dependence, divide it into sections describing the behavior of disjoining pressure in a ten-, nine-, eight-, and seven-layer FSSAF. Within each of these sections, this pressure is positive and grows monotonically with increasing temperature, to reach its largest value at the highest temperature at which a film with given number of layers can exist. Hence, in all the FSSAFs, the smectic layers are acted upon by a compressive force, which increases with their heating. The maximum value of ΔP for a nine-layer film is larger than that for a ten-layer one, for an eight-layer film it is larger than for a nine-layer one, etc. One also sees that the absolute value of the disjoining pressure in free-standing LC films may be quite large. For instance, in a seven-layer FSSAF, the maximum ΔP exceeds the atmospheric pressure nearly fivefold.

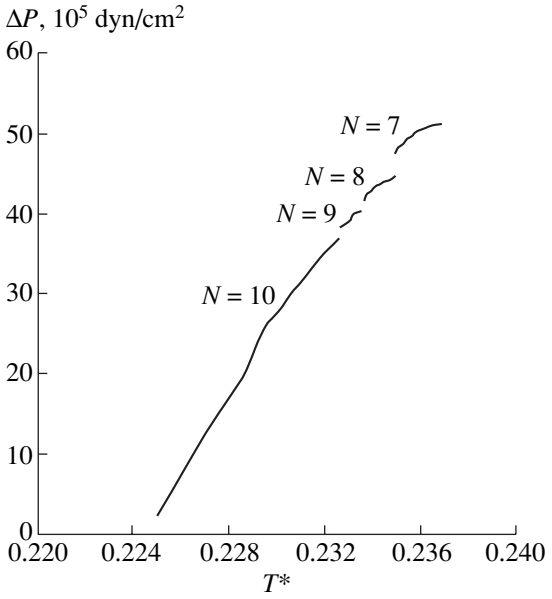

Fig. 1. Temperature dependence of the disjoining pressure ΔP in an FSSAF which initially contained ten smectic layers. The figures ($N = 10, \ldots, 7$) above individual sections of the plot refer to the number of layers in the film.

Next, using relations (5) and (6), from the above temperature dependence of disjoining pressure in the initially ten-layer FSSAF, we derived the temperature dependences of the thicknesses of the layers of this film acted upon by this pressure. The results obtained in this way are shown in Fig. 2, which displays the temperature dependence of the average thickness L of the film smectic layers. As in Fig. 1, this relation consists of separate sections for a ten-, nine-, eight-, and seven-layer FSSAF, separated by breaks at the temperatures corresponding to the layer-by-layer thinning of the film. Within each of such sections, L falls off monotonically with increasing temperature to reach its smallest value at the highest possible temperature of existence of a film with a given number of layers. However, as the number of layers decreases in a jump by one, the average film thickness also increases in a jump. This theoretical result, which is in excellent agreement with the experiments [14] made on H8F(4,2,1)MOPP liquid-crystal FSSAFs, allows the following fairly simple qualitative explanation. As was already mentioned, the model of [24, 25, 27, 29] predicts a monotonic growth of disjoining pressure in an N-layered, free-standing film heated to the highest temperature $T_c(N)$ it can sustain (Fig. 1). In addition, the model predicts a decrease in the local parameters of the orientational, $s_i(T)$, and translational, $\tau_i(T)$, order for FSSAF layers under such

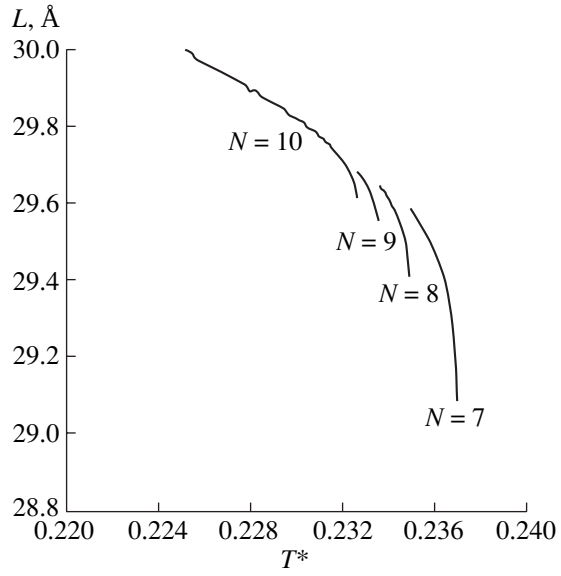

Fig. 2. Dependence of the average thickness L of smectic layers in an FSSAF on reduced temperature T^*. The film consisted initially of ten layers. Notation as in Fig. 1.

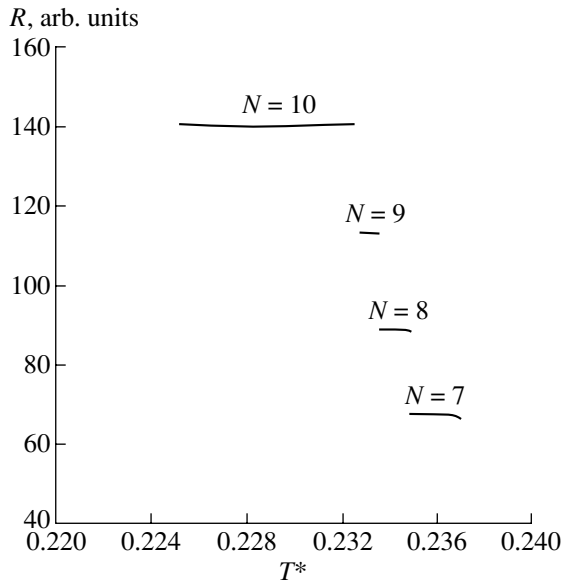

Fig. 3. Temperature dependence of the reflectivity R of a free-standing smectic-A film, which consisted initially of ten smectic layers. $n_e^{(0)} = 1.6$. Notation as in Figs. 1 and 2.

heating and, hence, a decrease in their tension (compression) moduli B_i. Thus, by Eq. (5), the thickness L_i of smectic layers in an N-layer film should decrease with increasing temperature because of the action of the disjoining pressure. When reaching the limiting temperature $T_c(N)$, an N-layer FSSAF loses one smectic layer, which brings about, by this model [24, 25, 27, 29], a jumpwise increase in the disjoining pressure, as well as in the order parameters, $s_i(T)$ and $\tau_i(T)$. However, the jump in the disjoining pressure is fairly small (Fig. 1), while the abrupt growth of the order parameters and, hence, of the B_i elastic moduli is substantial. As a result, by Eq. (5), the thicknesses L_i of the smectic layers of an $(N-1)$-layer film should increase in a jump compared with those for an N-layered FSSAF. It should also be pointed out that the lowest average layer thicknesses in an N-layer film reached at $T_c(N)$ were shown by us to decrease with decreasing layer number N (Fig. 2) because of the growth of the maximum disjoining pressure (Fig. 1). This result, as well as the order of magnitude (~1 Å) of the theoretically calculated absolute value of the decrease in the average layer thickness of free-standing films heated above the Sm-A–I transition point in a bulk LC, also agrees well with the experiment [14].

Relations (12) and (15) were used to calculate the temperature dependence of the reflectivity R of an FSSAF, originally ten smectic layers thick, which was heated above T_{AI} (Fig. 3). We used for this purpose the temperature dependences of the film layer thicknesses L_i calculated earlier. As was already mentioned, the magnitude of the ordinary refractive index $n_0^{(0)}$ of the volume smectic-A phase used in the calculations was taken equal to 1.48. As for the extraordinary refractive index of the volume smectic-A phase, the temperature dependence plotted in Fig. 3 was calculated assuming it to be $n_e^{(0)} = 1.6$. Our choice was based on the following considerations. As a rule, the birefringence $\Delta n = n_e - n_0$ of LCs consisting of molecules with conventional alkyl tails is ~0.2 [35]. However, Δn decreases substantially when the fluorine atoms are substituted for hydrogen in the alkyl tails [14]. Because in the experiment in [14] one measured the reflectivity of FSSAFs made of partially fluorinated LC H8F(4,2,1)MOPP and because we are comparing our calculations with the results obtained in that work, the value of Δn was assumed to be one-half that of the conventional LCs. Similarly to the above temperature dependences of ΔP and L (Figs. 1, 2), the temperature dependence of the film reflectivity displayed in Fig. 3 consists of sections (steps) separated by breaks which correspond to layer-by-layer FSSAF thinning. Each step describes the temperature dependence of the reflectivity of a film with a given number of layers. One readily sees that all these steps have a small negative slope, which is in full agreement with the experimental results [14].

Finally, we studied the dependence of the reflectivity of an FSSAF with a given number of layers on the extraordinary refractive index $n_e^{(0)}$ of the volume LC phase. Figure 4 shows the temperature dependences of the reflectivity R of a six-layer film calculated for $n_e^{(0)} = 1.6$, 1.65, and 1.7. One readily sees that the reflectivities calculated for the first two values of $n_e^{(0)}$ decrease monotonically with increasing temperature;

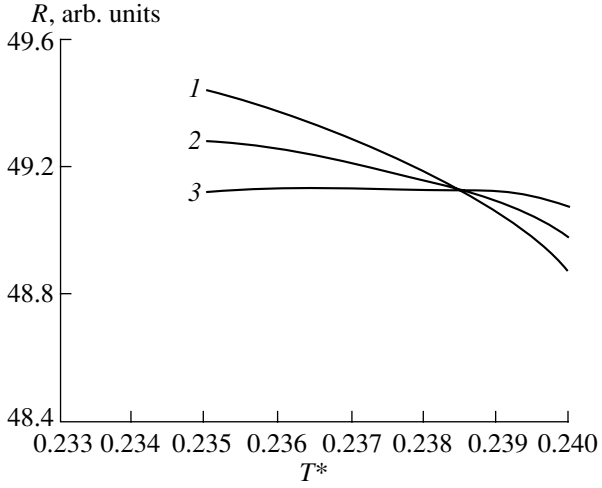

Fig. 4. Temperature dependences of the reflectivity R of a six-layer FSSAF calculated for different extraordinary refractive indices $n_e^{(0)}$ in the volume Sm-*A* phase: (*1*) 1.6, (*2*) 1.65, and (*3*) 1.7.

also, for $n_e^{(0)} = 1.6$, the reflectivity R falls off about two times faster than it does for $n_e^{(0)} = 1.65$ with increasing T^*, while for $n_e^{(0)} = 1.7$ the film reflectivity practically does not change under heating. These observations can be explained as follows. As can be seen from Eqs. (12) and (15), the temperature dependence of the FSSAF reflectivity R is determined, for a given number N of its layers, by two competing processes. One of them is the decrease in the smectic layer thickness L_i caused by the increase in the disjoining pressure ΔP and the decrease in the elastic moduli B_i with increasing temperature. The other competing process is the increase in the local refractive indices n_i, which is initiated, by Eq. (15), by the decrease in the local orientational-order parameters s_i of the film subjected to heating. Relation (15) also suggests that the larger the difference between the $n_e^{(0)}$ and $n_0^{(0)}$ indices, the steeper the growth of the local refractive indices n_i, and vice versa. Hence, in the case of weak birefringence Δn, the second of the competing processes contributes less than the first one and the film reflectivity decreases with increasing temperature. For larger Δn, this decrease slows down. Finally, for a large enough birefringence of the volume Sm-*A* phase, the growth of the local refractive indices n_i can completely compensate the decrease in the smectic layer thickness L_i of the film, as a result of which the reflectivity of the latter will not change under heating. This theoretical conclusion accounts completely for the difference in the behavior of FSSAFs prepared from the partially fluorinated LCs H10F5MOPP and H8F(4,2,1)MOPP and the 54COOBC LC consisting of molecules with conventional alkyl tails, which was pointed out in the Introduction. As was already mentioned, the birefringence of the first two mesogens should be smaller than that of the third one. Therefore, heating of their free-standing films brings about a decrease in the reflectivity of the latter for a fixed number of smectic layers. The birefringence Δn of the 54COOBC LC is ~0.2, as a result of which heating its FSSAF does not affect their reflectivity noticeably.

ACKNOWLEDGMENTS

This work was supported by the Russian Foundation for Basic Research project no. 98-03-32448.

REFERENCES

1. P. Pieranski, L. Beliard, J. P. Tournellec, *et al.*, Physica A (Amsterdam) **194** (1–4), 364 (1993).
2. C. Rosenblatt, R. Pindak, N. A. Clark, and R. B. Meyer, Phys. Rev. Lett. **42**, 1220 (1979).
3. M. Veum, C. C. Huang, C. F. Chou, and V. Surendranath, Phys. Rev. E **56** (2), 2298 (1997).
4. C. Rosenblatt and N. M. Amer, Appl. Phys. Lett. **36** (6), 432 (1980).
5. S. Heinekamp, R. A. Pelcovits, E. Fontes, *et al.*, Phys. Rev. Lett. **52** (12), 1017 (1984).
6. D. J. Bishop, W. O. Sprenger, R. Pindak, and M. E. Neubert, Phys. Rev. Lett. **49** (25), 1861 (1982).
7. C. Bahr and D. Fliegner, Phys. Rev. A **46**, 7657 (1992).
8. I. Kraus, P. Pieranski, E. Demikhov, *et al.*, Phys. Rev. E **48** (3), 1916 (1993).
9. T. Stoebe, P. Mach, and C. C. Huang, Phys. Rev. Lett. **73** (10), 1384 (1994).
10. E. I. Demikhov, V. K. Dolganov, and K. P. Meletov, Phys. Rev. E **52** (2), R1285 (1995).
11. V. K. Dolganov, E. I. Demikhov, R. Fouret, and C. Gors, Phys. Lett. A **220**, 242 (1996).
12. A. J. Jin, M. Veum, T. Stoebe, *et al.*, Phys. Rev. E **53**, 3639 (1996).
13. P. Johnson, P. Mach, E. D. Wedell, *et al.*, Phys. Rev. E **55** (4), 4386 (1997).
14. P. Mach, P. Johnson, E. D. Wedell, *et al.*, Europhys. Lett. **40** (4), 399 (1997).
15. E. A. L. Mol, G. C. L. Wong, J. M. Petit, *et al.*, Physica B (Amsterdam) **248**, 191 (1998).
16. R. Geer, C. C. Huang, R. Pindak, and J. W. Goodby, Phys. Rev. Lett. **63** (5), 540 (1989).
17. P. Mach, S. Grantz, D. A. Debe, *et al.*, J. Phys. II **5** (2), 217 (1995).
18. J. D. Shindler, E. A. L. Mol, A. Shalaginov, and W. H. de Jeu, Phys. Rev. E **54** (1), 536 (1996).
19. E. A. L. Mol, G. C. L. Wong, J. M. Petit, *et al.*, Phys. Rev. Lett. **79**, 3439 (1997).
20. V. K. Dolganov, V. M. Zhilin, and K. P. Meletov, Zh. Éksp. Teor. Fiz. **115** (5), 1833 (1999) [JETP **88**, 1005 (1999)].
21. R. Holyst, Phys. Rev. A **44** (6), 3692 (1991).
22. A. Poniewerski and R. Holyst, Phys. Rev. B **47** (15), 9840 (1993).
23. A. N. Shalaginov and V. P. Romanov, Phys. Rev. E **48** (2), 1073 (1993).

24. L. V. Mirantsev, Phys. Lett. A **205**, 412 (1995).
25. L. V. Mirantsev, Liq. Cryst. **20** (4), 417 (1996).
26. Y. Martínez-Ratón, A. M. Somoza, L. Mederos, and D. E. Sullivan, Phys. Rev. E **55** (2), 2030 (1997).
27. L. V. Mirantsev, Phys. Rev. E **55** (4), 4816 (1997).
28. L. V. Mirantsev, Fiz. Tverd. Tela (St. Petersburg) **41** (10), 1882 (1999) [Phys. Solid State **41**, 1729 (1999)].
29. L. V. Mirantsev, Liq. Cryst. **27** (4), 491 (2000).
30. L. V. Mirantsev, Phys. Rev. E **62** (1), 647 (2000).
31. M. Born and E. Wolf, *Principles of Optics* (Pergamon, Oxford, 1969; Nauka, Moscow 1973).
32. S. Chandrasekhar, *Liquid Crystals* (Cambridge Univ. Press, Cambridge, 1977; Mir, Moscow, 1980).
33. B. V. Derjaguin and N. V. Churaev, *Fluid Interfacial Phenomena*, Ed. by C. A. Croxton (Wiley, New York, 1986), p. 663.
34. W. L. McMillan, Phys. Rev. A **4** (3), 1238 (1971).
35. L. M. Blinov, *Electro-Optical and Magneto-Optical Properties of Liquid Crystals* (Nauka, Moscow, 1978; Wiley, New York, 1983).

Translated by G. Skrebtsov

Physics of the Solid State, Vol. 43, No. 5, 2001, pp. 963–966. Translated from Fizika Tverdogo Tela, Vol. 43, No. 5, 2001, pp. 926–929.

FULLERENES AND ATOMIC CLUSTERS

On the Energy Stability of Carbon Nanoclusters

S. V. Kozyrev, D. V. Leshchev, and I. V. Shakleina

Institute of Highly Efficient Calculations and Databases, St. Petersburg, 198005 Russia
e-mail: kozyrev@fn.csa.ru, Leschev@Softhome.net

Received July 10, 2000; in final form, October 5, 2000

Abstract—A method for evaluating the energy stability of carbon nanoclusters is proposed. The stabilities of the nanoclusters with different structures, such as diamond and graphite, tubulenes and graphite, are compared. Two series of stable clusters with new structures, namely, alm-ene and alm-ine, are derived. A comparison is performed for small graphite clusters containing boron atoms that play a significant role in the reaction of fullerene formation. *© 2001 MAIK "Nauka/Interperiodica".*

1. INTRODUCTION

Investigation into the formation, growth, and transformation of carbon nanoclusters is a fundamental problem of nanomaterials science [1]. A detailed theoretical treatment of the microscopic properties of nanoclusters, as a rule, is performed by quantum-chemical methods. However, none of the currently available quantum-chemical methods, as applied to cluster systems, can be considered efficient by virtue of their specificity (a wide variety of structures and sizes, unusual valence, the presence of strongly delocalized electrons, and a substantial contribution of the surface energy). As a consequence, there is a need to compare the results obtained by different computational methods. This leads to considerable problems, especially when comparing the energy stabilities of carbon nanoclusters.

A distinguishing feature of clusters as a state of matter is the nonmonotonic dependence of their properties on the number of particles (molecules, atoms, and ions) in a cluster. Unlike molecules, a cluster possesses an "individuality." This means that, beginning with a certain number of atoms N, the cluster involves "an infinitely large" number of different stable structures. This also implies that experimental studies deal with the averaged quantities, and the mesoscopic effects can take place.

An infinite variety of clusters consisting of N atoms can be partitioned into series of sets. In terms of quantum-chemical calculations, each set contains clusters that converge to the same arrangement of atoms in the course of geometric optimization. It is clear that this partition should depend on the calculation procedure and the method and parameters of optimization. Hereafter, an individual carbon nanocluster will be taken to mean one of the representatives of a set that corresponds to a particular valley of the potential energy surface, for example, a cluster whose geometry corresponds to a minimum of this valley.

In this respect, it is necessary to discuss separately the problem of describing (constructing) an individual carbon nanocluster. Formally, in some cases, any two clusters should be considered to be different (even though these clusters differ little in their atomic positions), because their properties differ substantially. However, except for the case when all atomic positions are known, a cluster can be defined using the structural diagram that is usually constructed according to special rules. Such a unified approach allows one to avoid confusion when comparing different clusters.

For example, the structure of an individual carbon nanocluster can be described with the use of (i) the main unit A (an analog of the unit cell), (ii) the method of constructing (a set of symmetry operations T_i) the whole cluster from the main units, and (iii) a set of defects D_i. Therefore, each cluster can be treated as a result of sequential applications of the above operations to the main unit, i.e., $\Sigma D_i(\Sigma T_i(A))$. The unit cell is constructed using the mean bond lengths and bond angles, except for special cases. Formally, the unit cell involves not only the atomic positions but also the multiplicities of bonds between atoms.

2. DETERMINATION OF THE ENERGY STABILITY OF CARBON NANOCLUSTERS

The energy stability of carbon nanoclusters can be determined by the method proposed in the present work. This method makes it possible to compare the stabilities of the clusters with different numbers of atoms under vacuum and in a condensed phase. This approach is based on the assignment of a specific energy parameter [the energy of a conventional atom (ECA) or the energy of a conventional bond (ECB)] to each cluster.

The algorithm for determining the energy of a conventional atom in a carbon cluster consisting of N atoms is as follows.

(1) A cluster is constructed in such a way that all dangling bonds are saturated with stabilizing elements (hydrogen or pseudocarbon atoms). This is required to

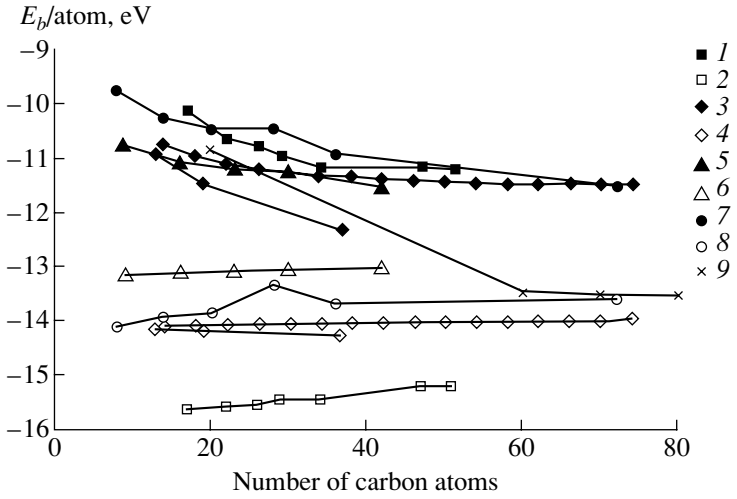

Fig. 1. Energy of a conventional atom in carbon clusters: (*1*, *2*) diamond (this series is obtained using a carbon skeleton of an adamantane molecule), (*3*, *4*) graphene (clusters contain an integral number of rings), (*5*, *6*) alm-ene (clusters are formed by the main units of a bicyclooctatriene carbon skeleton), (*7*, *8*) alm-ine (clusters are formed by the main units of a tetraethynylmethane carbon skeleton), and (*9*) fullerene series (the dashed line indicates "globular" graphene clusters) [2]. Calculations are performed (*1*, *3*, *5*, *7*, and *9*) with inclusion of dangling bonds and (*2*, *4*, *6*, and *8*) without regard for these bonds.

exclude the strong dependence of the optimized geometry of the cluster, its electronic properties, and the energy on the computational method.

(2) The geometry of the cluster is optimized by quantum-chemical methods, and the cluster energy is calculated.

(3) The cluster energy is divided by the total number of bonds in the cluster (the resulting quantity will correspond to the energy of a conventional bond) and then should be multiplied by the valence (the number of bonds for a given atom), which is characteristic of the carbon atom in the cluster (the valence can have a fractional value). As a result, we obtain the energy of a conventional atom.

A comparison of the conventional-atom energies of the clusters allows us to determine their relative energy stability. The larger the absolute value of the conventional-atom energy of the clusters, the higher their relative energy stability. When analyzing the energies of the clusters with a similar structure, we can separate the contributions of the carbon–carbon and carbon–hydrogen bonds. As a rule, the energy of the C–H bond is 20–25% less than that of the C–C bond. A comparison of the energies for cluster series should be performed with this correction under the assumption that the stabilization occurs through bonding carbon atoms. However, inclusion of this correction is meaningless for individual carbon clusters, because their individuality will be lost during averaging.

In order to calculate the upper limit of the ranges where the energies of clusters with different degrees of surface stabilization can fall, the energy of the C–H bonds (ECB $\cdot N_H$) should be subtracted from the total energy and the conventional-atom energy should be recalculated. When comparing the cluster series, it is expedient to compare the aforementioned ranges of possible conventional-atom energies.

The algorithm proposed was used to calculate carbon nanoclusters with the following structures: diamond, graphite, nanotube, alm-ene, alm-ine, and fullerene. All the calculations were performed using the HyperChem 4.5 program for SGI on an OCTANE workstation. The molecular geometry was optimized with the PM3 method. The PM3 method is currently considered the best semiempirical method used for these purposes. For large-sized systems, we applied the PM3/MM2 scheme, which, according to preliminary calculations, led to the same qualitative results as the PM3 method.

3. STABILITY OF CARBON NANOCLUSTERS WITH DIAMOND AND GRAPHITE STRUCTURES

We carried out a comparative evaluation of the stabilities of diamond and graphite nanoclusters. Our calculations demonstrate that diamond clusters are more stable than the graphene fragments (Fig. 1). However, the correction for the difference between the energies of the carbon–carbon and carbon–hydrogen bonds leads to a change in the relative stability of clusters. This means that the stability of a carbon nanocluster is completely determined by the interaction on its surface.

It is worth noting that even clusters with the characteristic properties of a bulk material are still sufficiently small with respect to the dominant role of the surface for their stabilization. For example, the difference between HOMO and LUMO was estimated at 5.6 eV (this value is characteristic of the diamond band structure) when the number of atoms in a cluster was of the

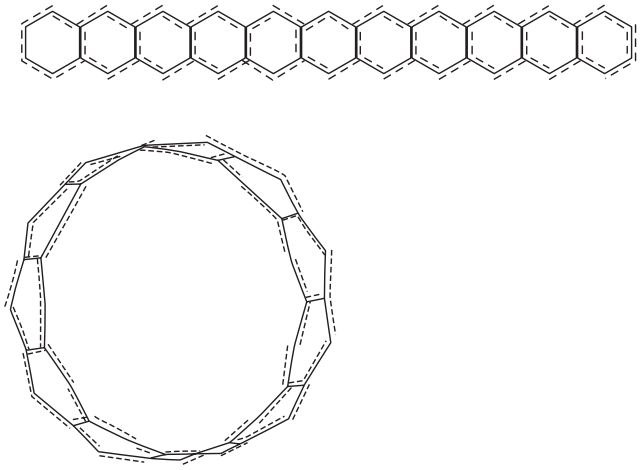

Fig. 2. A graphene ribbon and a nanotube ring.

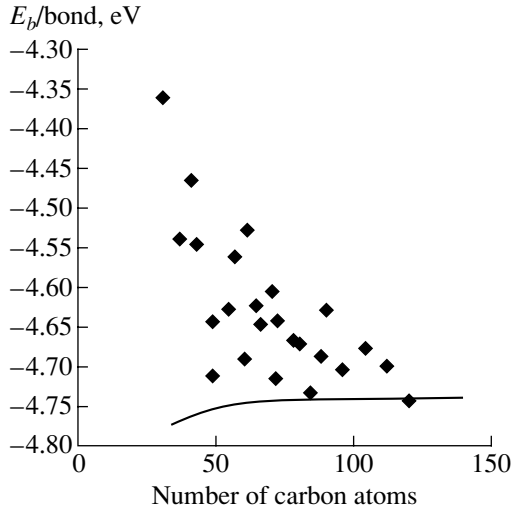

Fig. 3. Dependence of the energy E_b per C–C bond on the number of carbon atoms for a graphite fragment (solid line) and tubulenes.

order of 10^2: 200 atoms (the MM2/MINDO3 scheme) and 60 atoms (the PM3/MINDO3 scheme), depending on the basic parameters used in the calculation.

4. STABILITY OF NANOTUBES

The stability of nanotubes was also estimated using the proposed algorithm. It is generally believed that the energy of the nanotube formation does not depend on the symmetry type and can be determined only by the radius R of the cylinder.

We calculated the energies of the linear chains of graphene (up to four rows) and the rings of nanotubes (Fig. 2). Figure 3 shows the binding energies E_b per C–C bond as a function of the number of carbon atoms for a graphene ribbon and a nanotube ring. As can be seen from these data, the sufficiently large nanotubes (containing more than 100 atoms) have the same energy as the graphene fragments.

According to the theory of chemical bonding, each carbon atom in a graphite structure forms three identical σ bonds with the neighboring carbon atoms in the plane and the free p_z orbital (not involved in the σ bonding) is perpendicular to this plane. The overlap of the p_z orbitals brings about the formation of the π bonds and further stabilization due to conjugation (aromaticity). The graphene bending into a tube is accompanied by a decrease in the overlap of p_z orbitals, a weakening of the π bonds, and the stabilization due to a partial saturation of the dangling bonds [2].

The calculations performed demonstrate that, at sufficiently large radii (larger than 5 Å and seven benzene rings), the energy loss due to the overlap of p_z orbitals is compensated and the nanotube becomes almost identical in energy to the graphene fragment (for nanotubes of small radii, the repulsion of their opposite walls is significant). Therefore, it can be concluded that whether a nanotube or a graphene cluster is formed is determined only by the kinetic parameters of the process (the presence of a catalyst, material for cluster growth, etc.). A similar situation occurs in the diamond synthesis when the kinetic parameters completely determine the efficiency of the synthesis procedure.

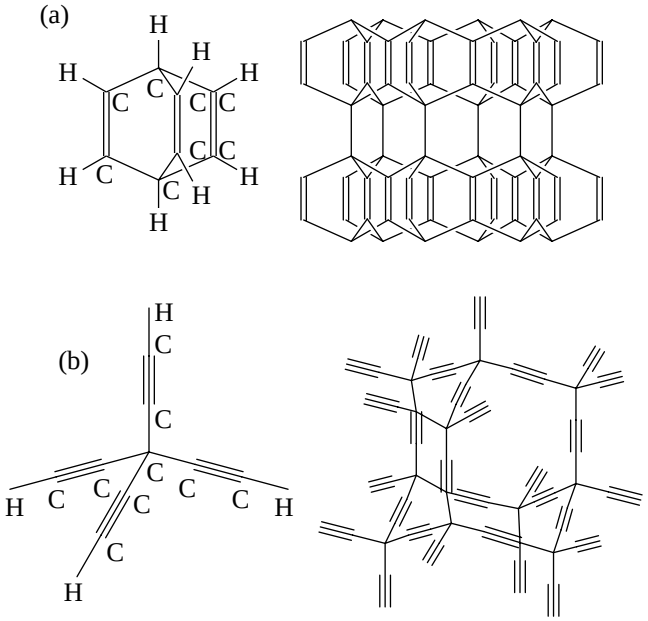

Fig. 4. Structures of nanoclusters: (a) bicyclooctatriene (hydrogen atoms are shown) and carbon nanocluster structures of the alm-ene and (b) tetraethynylmethane (hydrogen atoms are shown) and carbon nanocluster structures of the alm-ine.

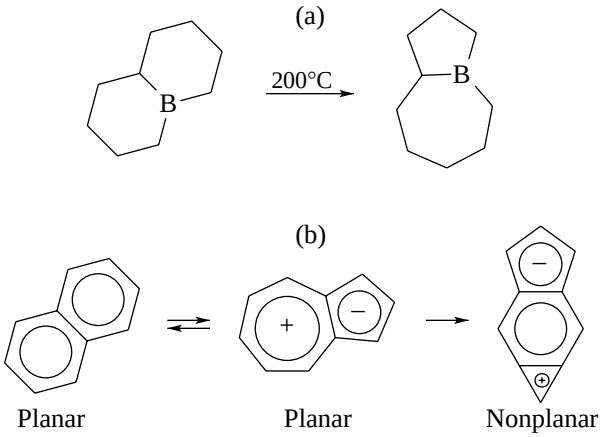

Fig. 5. Reactions of (a) transformation of the 6–6 structure into the 5–7 structure and (b) bending of a planar cluster.

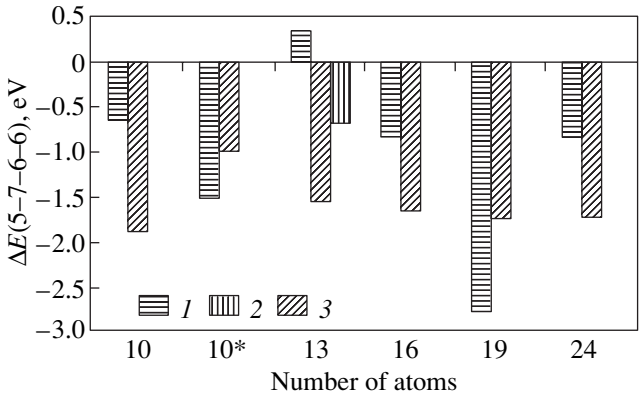

Fig. 6. Dependence of the energy ΔE (5–7–6–6) on the number of atoms in a cluster: (*1*) boron atom at the cluster boundary, (*2*) boron atom at the center of the cluster, and (*3*) pure carbon clusters. 10* designates a negatively charged cluster.

5. STABLE CARBON NANOCLUSTERS WITH A NEW STRUCTURE

It should be noted that, although diamond is the hardest material, the binding energy in the graphite plane is higher than that in diamond. We attempted to construct the three-dimensional carbon phases with a combination of the diamond and graphite properties. The phase with single and double bonds was termed alm-ene (the main unit is a bicyclooctatriene molecule), and the phase with single and triple bonds was referred to as alm-ine (the main unit is a tetraethynylmethane molecule) (Fig. 4).

It follows from the results obtained (Fig. 1) that the clusters of these structures correspond in energy to the range of conventional-atom energies of diamond and graphite clusters and, as a consequence, can occur in nature. If crystalline phases of these structures were synthesized, these materials should be very light and hard.

Theoretically, an infinitely wide variety of clusters containing double and single bonds and benzene rings occurs in nature. In general, their structure can be conceived as a result of spatially inhomogeneous diamond–graphite transformation into an intermediate state (upon transition from the diamond to the graphite structure, the rings of diamond cyclohexane skeleton transform into the graphite benzene rings). This phase is thermodynamically unstable for the transformation into diamond or graphite and can exist only in the form of carbon nanoclusters due to surface interactions.

6. FORMATION OF HEAVY FULLERENES AND A BORON ATOM

The above algorithm was applied for evaluating the stability of small graphene clusters with inclusions of boron atoms. From the standpoint of organic chemistry, the behavior of boron has a characteristic feature, namely, the displacement reaction of carbon–carbon bonds similar to those shown in Fig. 5 (the formation of the so-called 5–7 defect). It is quite possible that the 5–7 defect is responsible for the bending of planar graphene fragments into a fullerene. We carried out a series of calculations for the formation of a 5–7 defect in small graphite clusters. The calculation was performed according to the general scheme; however, the energy was not converted per atom for simplicity. As can be seen from Fig. 6, the presence of boron leads to a substantial decrease in the difference between the cluster energies of the 6–6 and 5–7 structures, which should encourage a more frequent formation of the 5–7 defects. The energies of negatively charged clusters were calculated according to the same procedure. It was found that the presence of a charge in a system consisting of two rings (naphthalene) also favors a decrease in the difference between the cluster energies.

It is our opinion that these results should be taken into account in analysis of the formation of fullerenes by the arc discharge method, because, according to [3], the presence of boron atoms in an electric arc promotes the formation of heavy fullerenes.

ACKNOWLEDGMENTS

This work was supported by the “Fullerenes and Atomic Clusters” Program of the Russian Federation, project no. 3-7-98.

REFERENCES

1. Yu. E. Lozovik and A. M. Popov, Usp. Fiz. Nauk **167** (7), 751 (1997) [Phys. Usp. **40**, 717 (1997)].
2. V. V. Rotkin and R. A. Suris, Fiz. Tverd. Tela (St. Petersburg) **41** (5), 809 (1999) [Phys. Solid State **41**, 729 (1999)].
3. L. V. Golubev, V. I. Karataev, S. I. Shevchenko, and A. Ya. Vul’, in *Abstracts of International Workshop on Fullerenes and Atomic Clusters, IWFAC-97, St. Petersburg, 1997*, p. 76.

Translated by O. Borovik-Romanova

Physics of the Solid State, Vol. 43, No. 5, 2001, pp. 967–972. Translated from Fizika Tverdogo Tela, Vol. 43, No. 5, 2001, pp. 930–935.

FULLERENES AND ATOMIC CLUSTERS

Formation of Closed Carbon Particles from Fullerene Nuclei

V. I. Berezkin

Research Center for Environmental Safety, Russian Academy of Sciences, Korpusnaya ul. 18, St. Petersburg, 197110 Russia
e-mail: VIB@VF4493.spb.edu

Received May 26, 2000; in final form, September 21, 2000

Abstract—The model proposed earlier for the formation of closed carbon particles from fullerene nuclei is discussed. Experimental data in support of this model are analyzed. The possible mechanisms of particle formation are treated within the microscopic concepts. Theoretical relationships for describing the rate and the time of particle growth are derived, and a number of quantitative estimates are made. The conclusion is drawn that the particle growth is similar in a number of traits to crystal growth from the gaseous phase. Consideration is also given to the specific features of the particle growth. © *2001 MAIK "Nauka/Interperiodica".*

1. INTRODUCTION

In my previous work [1], a new model was proposed for the structure of closed carbon particles, their nucleation, and growth. Consideration was given to soot particles in the form of nanoparticles composed of several layers—the so-called onionlike carbon form. In my opinion, all these particles differ in size, i.e., in the number of layers, the shape, and the number and the type of defects.

Essentially, the model is as follows: defect-containing fullerenes serve as particle nuclei, and the particles themselves are multilayer formations with a hole at the center whose size and configuration correspond to the size and configuration of the initial fullerene nucleus. Concentric layers which grow around the central core as a result of a gas–solid phase transition and are separated by a distance of ~3.4 Å consist of distorted and defective carbon networks.

The function of defects of fullerene nuclei and neighboring carbon layers can be fulfilled by vacancies and their aggregates, adjacent pentagons C_5, seven-membered rings C_7, stacking faults characteristic of graphites (such as the rotation of layer regions around the normal), incomplete shells, heteroatoms (H, O, N, S, etc.), stressed bonds (which can arise from the curvature of the growing surface), and others.

In the present work, an attempt was made to obtain some estimates for this model.

Leaving aside nanotubes, we will distinguish, for definiteness, the following forms of disperse solid carbon: single-layer fullerenes, soot consisting of closed multilayer particles of different sizes and shape and their aggregates, and carbon (including fullerene) black which involves single (planar or bent) carbon network fragments or their small-sized stacks.

2. JUSTIFICATION OF THE MODEL

It is known that, according to the classical theory, growth on perfect crystal surfaces involves the formation of a two-dimensional nucleus under statistical fluctuations of adsorbed atoms [2]. In this case, the nucleation requires very high activation energies ($\sim 3.6 \times 10^3\ kT$, where k is the Boltzmann constant and T is the temperature), so that the growth rates at real temperatures should be close to zero [3]. In actual fact, even at very low supersaturations, the growth rates are sufficiently high at the expense of nucleation on the structural defects. Atoms or molecules adsorbed on the surface are bound to it owing to an additional energy of the defect, and the fluctuation formation of two-dimensional nuclei is not necessary. Similarly, perfect fullerenes cannot serve as nuclei of soot particles by virtue of their stability, i.e., a low reactivity as compared to defective fullerenes, and, hence, they can be obtained in a free state. In particular, Lozovik and Popov [4] simulated a defect-free fullerene C_{60} as the first surface of a multilayer nanoparticle and reached the conclusion that single carbon atoms and C_6 microclusters cannot be adsorbed on the fullerene surface even at temperatures above 182 and 30 K, respectively.

On this basis, the assumption on the role of structural defects as sources of soot particle growth is wholly justified. The electron microscope images obtained by Iijima [5, 6] confirm the fact that multilayer globular particles contain a large number of structural defects both in central spheroids with a diameter of 8–10 Å and in adjacent concentric shells. Other experimental data that can be considered indirect evidence in favor of the model proposed are also available.

Gerhardt *et al.* [7] noted that, upon combustion of hydrocarbons, the number of soot particles is larger in the flame regions in which the number of fullerenes formed is greater.

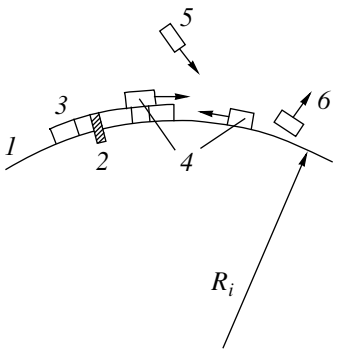

A schematic representation of carbon particle growth: (*1*) surface of a soot globule of radius R_i, (*2*) layer defect, (*3*) surface nucleus, (*4*) adsorbed particles, (*5*) carbon vapor particle, (*6*) evaporated particle. Particles *4–6* correspond to carbon atoms or carbon molecules (clusters).

According to Goeres and Sedlmayr [8], the introduction of hydrogen into helium suppresses fullerene formation upon electric arc evaporation of graphite. As a consequence, the presence of excess H_2 in flames leads to cessation of the growth of soot particles [9].

It is known that soot particles are formed after the completion of a preliminary process, which is confirmed by the existence of the induction time t_{ind}, i.e., the time from the onset of the soot formation to the appearance of the first particles. Upon combustion of hydrocarbons, the induction time is estimated at $t_{ind} \sim 10^{-4}$–10^{-3} s [9], which coincides with the time of fullerene formation [7, 10].

Ugarte [11] observed the formation of spherical particles upon heating samples with an electron beam to temperatures of 800–2400°C. Amorphous carbon collected in an arc-discharge apparatus in the form of both soot and carbon black which contained fragments with sizes of the order of several angstroms was studied. The particles arose from the structural transformation of the material as a result of growing defective concentric layers around the central spherical core 6–10 Å in diameter. The multilayer nanotubes transformed into globules in which the number of layers was larger than that in the initial particles. The longer the time of heating and the higher its temperature, the larger the size of globules and the closer their shape to spherical. After the completion of the process, the sample transformed into soot which almost completely consisted of spherical particles. Particles with diameters up to several microns were observed upon prolonged annealing.

3. NUCLEATION AND GROWTH OF PARTICLES

A theoretical description of soot particle nucleation presents considerable difficulties. This is explained by the fact that a universally accepted microscopic model for the formation of fullerenes is currently unavailable (some existing variants can be found, for example, in [12]). We can only argue that, since carbon atoms cannot be joined at once in amounts necessary for fullerene formation, this process has a complex nature and involves a number of sequential elementary acts, each proceeding very rapidly.

There also exist certain difficulties associated with the following circumstances. Many macroscopic concepts are inapplicable to the early stages of the condensation of any vapor. In particular, the notion of surface tension cannot be used in the case when we consider the formation of nuclei containing several tens of atoms, because the latter cannot be separated into surface and bulk atoms in order to determine the corresponding free energies. It is also impossible to use the concepts of liquid and solid states. For this reason, despite numerous attempts to overcome these and other difficulties, a rigorous statistical solution to the problem of vapor condensation is absent.

Let us assume that a fullerene nucleus has already been formed and a carbon globule with a current radius R_i grows. Here, $1 \le i \le N$ is the ordinal number of a carbon layer and N is the number of layers. The centers of the layer growth (surface nuclei) are formed at the surface points with structural defects which capture carbon particles (in our case, atoms or molecules) of mass M. These nuclei grow and coalesce to form a continuous layer. The material for the growth comes either directly from the surrounding medium (the supersaturated carbon vapor at pressure P) or in the form of adsorbed particles which migrate over the surface until they are attached to the growth center or evaporate back into the surrounding medium (see figure).

According to [3], the surface diffusion coefficient is given by

$$D_s = a^2 \nu_1 \exp(-U_s/kT) \quad (1)$$

and the mean lifetime of a particle τ_s in the adsorbed state can be defined as

$$1/\tau_s = \nu_2 \exp(-W_s/kT). \quad (2)$$

By assuming that the frequency factors $\nu_1 \sim \nu_2 \sim \nu$ and taking into consideration that the mean displacement of a molecule in the adsorbed state is represented as $\lambda_s^2 = D_s\tau_s$, we obtain

$$\lambda_s \sim a \exp[(W_s - U_s)/2kT], \quad (3)$$

where W_s is the evaporation energy and U_s is the activation energy for the transition between two equilibrium positions separated by a distance a on the surface. When the binding energy between carbon layers is taken equal to 42 kJ/mol [13] (which corresponds to 0.435 eV per atom) with allowance made for the fact that, in the general case, we have $W_s/U_s > 3$, the value of λ_s can be as great as $\sim 10^4 a$. Therefore, the surface diffusion can make the main contribution.

The diffusion flux along the surface toward the formed step with height h, which corresponds to the interlayer distance, can be written as

$$J_s = -D_s \mathrm{grad} n_s, \quad (4)$$

where n_s is the number density of adsorbed particles, which determines the surface supersaturation $\sigma_s = n_s/n_{s0} - 1$. The equilibrium number density of adsorbed particles is given by

$$n_{s0} = n_0 \exp(-W_s/kT), \quad (5)$$

where n_0 is the surface atom density. We assume that the number $n_{sv}/\tau_s = P(2\pi MkT)^{-1/2}$ of particles comes from a vapor onto a unit area in a unit of time and that the number n_s/τ_s of particles evaporates back. From the condition for the conservation of adsorbed particles, it follows that

$$\mathrm{div} J_s = (n_{sv} - n_s)/\tau_s$$

and the diffusion equation has the form

$$\lambda_s^2 \nabla^2 n_s - (n_s - n_{sv}) = 0. \quad (6)$$

If the number of defects in a soot particle is equal to Ξ, the mean surface density of defects is defined by

$$\langle \xi \rangle = \Xi/S_\Sigma, \quad (7)$$

where $S_\Sigma = \sum_i S_i$ is the total surface area of layers, which for a spherical particle is represented as

$$S_\Sigma = 4\pi \sum_{i=1}^{N} [R_i + (i-1)h]^2$$

$$= 2\pi N \{R_1^2 + [R_1 + (N-1)h]^2\}.$$

Let us assume that the value of $\langle \xi \rangle$ is sufficiently large, so that spherical surface regions between defects can be approximated by planes. By using relationship (4) and the boundary conditions $\sigma_s = 0$ near the step (high-rate capture of adsorbed particles) and $\sigma_s = \sigma$ far from the step [3] with due regard for expressions (1), (2), and (5), we obtain the following solution of Eq. (6) for the rate of step motion $v = -J_s/n_0$:

$$v = 2a\sigma v \exp\left(-\frac{3W_s + U_s}{2kT}\right), \quad (8)$$

where $\sigma = (P - P_0)/P_0$ is the relative supersaturation and P_0 is the saturation carbon vapor pressure at a given temperature. Factor 2 accounts for fluxes on both sides of the step.

The mean time t_i of the layer growth when the area of the growth island reaches a value of $\sim 1/\langle \xi \rangle$ is $t_i \sim 1/\langle \xi \rangle^{1/2} v$, and the time of forming the whole globule is defined by the relationship

$$t_\Sigma = N/\langle \xi \rangle^{1/2} v. \quad (9)$$

The mean rate of particle growth in the direction normal to the surface is as follows:

$$V_N = R_N/t_\Sigma. \quad (10)$$

4. FEATURES OF PARTICLE GROWTH FROM CARBON VAPOR

The supersaturation of a medium plays an important role in growth from the gaseous phase, because it determines the driving force of the phase transition:

$$\mu_v - \mu_s = \Delta\mu = kT \ln\sigma,$$

where μ_v is the chemical potential of a vapor and μ_s is the chemical potential of a solid phase. The pressure P_0 of equilibrium carbon vapor in the temperature range 2402–3199 K falls in the range 1.33×10^{-3}–13.3 Pa [13]. Upon thermal decomposition of hydrocarbons, efficient soot formation usually occurs at temperatures below 3000 K and pressures close or comparable to atmospheric [9, 14, 15]. Therefore, the degree of supersaturation of a gaseous medium, as a rule, is very high. In our opinion, it is quite reasonable to assume that, upon laser or arc graphite evaporation, the pressure of nonequilibrium carbon vapor in local regions of high-rate formation of soot particles also considerably exceeds the saturation carbon vapor pressure.

It is common knowledge that carbon atoms have a clear-cut tendency to aggregation, and the amount of atomic carbon upon thermal decomposition of carbon compounds is negligibly small. For example, the laser evaporation of graphite results in the formation of clusters C_n with $n \geq 2$ [16]. According to Modak *et al.* [17], the ignition of an electric arc across graphite electrodes in toluene or benzene is accompanied by the formation of clusters with $n \geq 4$ in the solution. Upon combustion of acetylene and benzene, ions $C_nH_3^+$ with $3 \leq n \leq 19$ were observed by Gerhardt *et al.* [7] in flame regions with the highest temperatures.

The smallest-sized carbon clusters C_{2-19}^+ are very stable, and their dissociation energy lies in the range ~5–7 eV [18]. This is many times larger than the mean thermal motion energy that is typical of soot formation temperatures. Atomic carbon vapor can exist at elevated temperatures. Particularly, reasoning from the distribution of ^{12}C and ^{13}C isotopes in fullerenes, Ebbesen *et al.* [19] drew the inference that atoms are completely mixed in an electric arc in which the temperatures can be as high as ~10000°C [20].

As follows from the calculations performed by Yi and Bernholc [21], a cluster with $n = 2$ can easily (without an energy barrier) be incorporated into the structure of a fullerene layer, which leads only to an increase in the size of a closed shell. The reactions with C_3 results not in incorporation but in surface chemosorption. The distance between a single adsorbed atom and the surface turns out to be half as large as d_{002} of graphite. To

put it differently, there are grounds to believe that the soot formation has a cluster nature and soot particles can efficiently grow at $n > 2$.

Clusters C_6 play an important role in the formation of closed carbon particles. Taylor *et al.* [22] demonstrated that fullerenes can be efficiently synthesized by pyrolysis of naphthalene $C_{10}H_8$ when C_{60} is built up of clusters C_{10}, i.e., double hexagons C_6. The cluster nature of the soot formation can be corroborated by the following facts. The addition of aromatic or polyaromatic hydrocarbons to methane in amounts of ~1 vol % brings about an increase in the number of formed soot particles and the soot yield (the ratio between the weights of soot and carbon in an initial material) by several times. The soot yield is maximum (~95%) upon burning of polyaromatic hydrocarbons [15] and minimum (no more than 4% [23]) upon combustion of methane. In other words, compared to simple hydrocarbons, the use of aromatic compounds as an initial material can lead to the formation of a substantially larger number of fullerene nuclei. Soot particles also readily grow from clusters of hexagons C_6 and their aggregates. When atomic carbon is formed upon decomposition of an initial material, it can be assumed that the process as a whole involves the stage of the formation of hexagons C_6 [24], including multiple hexagons. On the other hand, it is difficult to justify limitations on the growth from the C_n clusters, where $2 < n < 6$. It seems likely that the growth from C_6 or clusters with the closest sizes is most efficient. Growth directly from atomic vapor is improbable.

5. EXPERIMENTAL DATA AND DISCUSSION

Upon soot formation, the supersaturation of a medium determines the flow of matter and, as in usual (for example, epitaxial) growth, the number of defects Ξ. This is consistent with the data obtained by Guo *et al.* [25]. Upon laser evaporation of graphite, a decrease in the temperature of the furnace with an initial sample (which is equivalent to an increase in σ) was attended by an increase in the defectiveness of the resulting multilayer nanotubes.

According to formula (10), the growth rate of soot particles depends on the degree of defectiveness, because $\langle\xi\rangle$ determines the density of surface nuclei. Actually, as follows from [9], the growth rate of pyrocarbon layers on the formed soot particles changes at the initial stage. For acetylene soot obtained upon spontaneous (explosive) decomposition of C_2H_2 at temperatures up to 3000 K, the growth rate increases by several times. By contrast, for channel soot produced upon burning of hydrocarbons in a laminar flow at $T = 1550$–1700 K, the growth rate decreases several times. The growth rate in different experiments reaches a steady-state value after the deposition of carbon in amounts equivalent to 0.1–1.5 monolayers. This can be explained as follows. The defectiveness of layers is increased in the channel soot and decreased in the acetylene soot. Therefore, the growth rate at the initial stage reaches a rate that corresponds to defectiveness under the given experimental conditions, i.e., to specific supersaturation.

As regards supersaturation, it is known that the crystal growth rate at large σ is directly proportional to σ for any growth mechanism [26]. A similar dependence is observed for soot particles over a wide range of pressures, specifically in the range from 0.1 Torr to 21 atm for methane. The temperature dependences of the growth rate on the Arrhenius coordinates are straight lines with a negative slope [9, 14]. To put it another way, the character of the dependences on σ, T, and $\langle\xi\rangle$ in relationships (8) and (10) is in agreement with experimental data and, as a consequence, it can be assumed that these formulas, as a whole, correctly describe the main regularities of the particle growth process. Now, we estimate the particle growth time from formula (9). Let $N = 100$, which corresponds to a diameter of ~700 Å. This diameter is typical of acetylene soot particles with mean sizes. Let defectiveness (7) be such that there is one imperfect ring for each 10–100 carbon rings. By assuming that a particle is built up of C_6 clusters at $T \sim 3000$ K and $\sigma \sim 10^4$, we obtain $t_\Sigma \sim 1$–3 μs, which is close to the formation times of acetylene soot particles [9, 14, 15].

The total time $\mathcal{T}$ of soot particle formation can be conveniently separated into the nonstationarity time t_n, the time t_f of fullerene nucleus formation, and the particle growth time t_Σ, that is,

$$\mathcal{T} = t_n + t_f + t_\Sigma = t_{\text{ind}} + t_\Sigma.$$

The time t_n is the time it takes for the size distribution of clusters (that corresponds to the given conditions) to be attained in a medium after "switching on" the supersaturation, so that t_n, in its meaning, can be considered the induction time of fullerene formation. For a gaseous phase, the time t_n can be represented in the form [26]

$$t_n \sim n_c^{4/3}/w_+ = n_c^{4/3}(2\pi M_c kT)^{1/2}/Pa_c^2, \qquad (11)$$

where n_c is the number of atoms in a cluster of mass M_c and w_+ is the frequency of the attachment of atoms to this cluster. For carbon clusters with $n_c = 6$–18, the nonstationarity times are approximately identical. For example, under the conditions of the experiments carried out by Gerhardt *et al.* [7] (temperatures up to 2000 K and a pressure of 27 mbar), $t_n \sim 10^{-5}$ s. As was noted above, the total time measured for the fullerene formation by these authors (or t_{ind} in our designations) is no longer than 1 ms [7]. In other words, with allowance made for the estimate obtained from formula (11), we have $t_{\text{ind}} \approx t_f$. The induction time is virtually independent of the concentration and is determined by the temperature and the type of the initial material. Upon combustion at 1500°C, t_{ind} is equal to 1.9 ms for acetylene and 0.9 ms for toluene and is less than 0.22 ms for green oil (a mixture of polycyclic hydrocarbons). On the other hand,

the times $\mathcal{T}$ are of the same order of magnitude. For example, at $t_{ind} \approx 1$ ms, we have $\mathcal{T} \approx 4$ ms. For acetylene soot, at $t_{ind} \approx 2$ μs, $\mathcal{T} \approx 5$–7 μs [9, 14]. Consequently, t_f and t_Σ are also of the same order of magnitude and soot particles grow very rapidly. It is known that the normal growth rates V_N for combustion processes are of the order of several μ*m*/*s*. Similar rates are also characteristic of epitaxial films which grow at comparable (i.e., very high) supersaturations. These films are formed in the amorphous or polycrystalline state due to the high rate of their growth [26].

6. ON THE GROWTH MECHANISMS

The island (or Volmer–Weber) mechanism is realized upon growth of soot particles, because the bonds between atoms of a deposited material are stronger than the bonds between these atoms and the surface on which they are adsorbed. In this case, the following condition should be met [26]:

$$\Delta\alpha = 2\alpha - \alpha_s = (\varepsilon_1 - \varepsilon_s)/a^2 > 0, \quad (12)$$

where α is the free surface energy, α_s is the free adhesion energy, ε_1 is the binding energy between the nearest atoms, and ε_s is the binding energy between the adsorbed atoms and the substrate. In the case of carbon, relationship (12) is fulfilled with a large margin. For the island mechanism, the relation between crystal and substrate orientations is weakly pronounced and the surface diffusion is facilitated. Therefore, not only single atoms but aggregates can migrate. For this reason, the fact that estimates with the use of formulas (3) and (8)–(10) were obtained for C_6 clusters rather than for carbon atoms, to a first approximation, seems to be reasonable.

Normal rather than layer-by-layer (tangential) growth is observed upon crystal growth under the conditions of large supersaturations. Consequently, there are grounds to believe that, upon growth of closed carbon particles, shells are not formed sequentially (one after another), but several carbon layers grow simultaneously; in this case, each layer has a large number of growth centers due to the high degree of defectiveness. The annealing favors the same orientation and a decrease in the number of defects. Just as amorphous or crystalline epitaxial films crystallize upon annealing, so turbostratum carbon structures (as is well known) graphitize. For example, pyrocarbon transforms into pyrographite at temperatures of ~3000 K. At these temperatures, soot globules are polygonized [27, 28]; i.e., the layers become ordered, and plane surfaces in the form of crystal facetings are formed in the initially spherical particles. As a result, the graphitized soot, like graphite, is chemically inert [29]. Faceted particles can also arise upon their growth at high temperatures [5]. At $T > 3000$ K, the sublimation of carbon brings about the destruction of globules [30].

The shape of a faceted particle can be analytically described as an envelope of a set of planes in terms of the Wulf theorem [2, 26]. In our case, it can be represented as

$$(\mathbf{rn}) = \int_0^{t_\Sigma} V(\mathbf{n}, t)dt, \quad (13)$$

where **n** is the normal to the particle surface at the point specified by the radius vector **r**. When the normal growth rate *V* is independent of time and a soot particle has a spherical shape, it is easy to see that relationship (13) is equivalent to formula (10) and that we have a sphere instead of a set of planes.

Morphological stability is observed upon soot formation, and dendritic forms are not formed despite the large supersaturation. The particles retain their configuration, which is originally determined by the shape of the fullerene nucleus. If the nucleus is formed under isotropic conditions, the shape of a soot particle is close to spherical. By contrast, particles with a lower symmetry are observed in the case of preferential directions of the physical fields and flows of matter, including, most probably, a rather short-term (during nucleus formation) anisotropy. Moreover, the nucleus shape can depend on the defect type.

7. CONCLUSION

All the foregoing allows us to make the following inferences. The model proposed in [1] was confirmed experimentally and theoretically. The growth of a closed carbon particle can be treated as the formation of pyrolytic carbon layers on a single-layer nanosubstrate due to the vapor–solid phase transition. To put it differently, the formation of soot particles can be reduced to a process similar to the crystal growth from the gaseous phase with a number of specific features. In both cases, the growth in a specified direction and at a sufficiently high rate is realized only when the structure involves broken chains with strong bonds. These bonds are observed in the presence of defects.

A microscopic theory of soot formation is absent. Apart from the problems discussed above, theoretical interpretation of this process involves serious problems when analyzing processes at the interface, because atomic carbon is unlikely to make a considerable contribution and the growth from clusters is theoretically poorly understood. Moreover, an important role can be played by the attendant nonstationary effects, which were virtually omitted in our discussion.

Most likely, the soot formation is a unique process which proceeds according to the same scenario irrespective of conditions. Rapid phenomena (combustion, explosion, and electric arc) and the processes occurring on a time scale of the order of tens of minutes (annealing of carbon black and production of thermal soot by hydrocarbon pyrolysis) lead to the same result—the formation of closed particles with concentric layers and a fullerene-like core at the center.

ACKNOWLEDGMENTS

This work was supported by the Russian Foundation for Basic Research, project no. 98-03-32684.

REFERENCES

1. V. I. Berezkin, Fiz. Tverd. Tela (St. Petersburg) **42** (3), 567 (2000) [Phys. Solid State **42**, 580 (2000)].
2. R. Laudise and R. Parker, *The Growth of Single Crystals* (Prentice-Hall, Englewood Cliffs, 1970; Mir, Moscow, 1974).
3. W. Burton, N. Cabrera, and F. Frank, in *Elementary Processes of Crystal Growth* (Inostrannaya Literatura, Moscow, 1959), p. 11.
4. Yu. E. Lozovik and A. M. Popov, Teplofiz. Vys. Temp. **33** (4), 539 (1995).
5. S. Iijima, J. Cryst. Growth **50** (3), 675 (1980).
6. S. Iijima, J. Phys. Chem. **91** (13), 3466 (1987).
7. Ph. Gerhardt, S. Löffler, and K. H. Homann, Chem. Phys. Lett. **137** (4), 306 (1987).
8. A. Goeres and E. Sedlmayr, Fullerene Sci. Technol. **1**, 563 (1993).
9. P. A. Tesner, *Carbon Formation from Hydrocarbons of the Gas Phase* (Khimiya, Moscow, 1972).
10. H. Kroto, Science **242**, 1139 (1988).
11. D. Ugarte, Nature **359**, 707 (1992).
12. Yu. E. Lozovik and A. M. Popov, Usp. Fiz. Nauk **167** (7), 751 (1997) [Phys. Usp. **40**, 717 (1997)].
13. S. V. Shulepov, *Physics of Carbon-Based Materials* (Metallurgiya, Chelyabinsk, 1990).
14. *Processing of Natural Gases*, Ed. by P. A. Tesner (Gostoptekhizdat, Moscow, 1961).
15. V. P. Zuev and V. V. Mikhaĭlov, *Carbon Black Production* (Khimiya, Moscow, 1970).
16. E. A. Rohlfing, D. M. Cox, and A. Kaldor, J. Chem. Phys. **81** (7), 3322 (1984).
17. D. K. Modak, S. Mukherjee, B. K. Chaudhuri, *et al.*, Indian J. Phys., A **67** (4), 307 (1993).
18. M. B. Sowa-Resat, P. A. Hintz, and S. L. Anderson, J. Phys. Chem. **99** (27), 10736 (1995).
19. T. W. Ebbesen, J. Tabuchi, and K. Tanigaki, Chem. Phys. Lett. **191** (3/4), 336 (1992).
20. L. P. F. Chilante, A. Thess, J. M. Alford, *et al.*, J. Phys. Chem. **97** (34), 8696 (1993).
21. J.-Y. Yi and J. Bernholc, Phys. Rev. B **48** (8), 5724 (1993).
22. R. Taylor, G. J. Langley, H. W. Kroto, and D. R. M. Walton, Nature **366**, 728 (1993).
23. V. B. Fenelonov, *Porous Carbon* (Inst. Kataliza Sib. Otd. Ross. Akad. Nauk, Novosibirsk, 1995).
24. J. Lahaye, Carbon **30** (3), 309 (1992).
25. T. Guo, P. Nikolaev, A. G. Rinzler, *et al.*, J. Phys. Chem. **99** (27), 10694 (1995).
26. A. A. Chernov, in *Modern Crystallography*, Vol. 3: *Crystal Growth*, Ed. by B. K. Vaĭnshteĭn (Nauka, Moscow, 1980; Springer-Verlag, Berlin, 1984).
27. P. L. Walker, Carbon **10** (4), 369 (1972).
28. R. D. Heydenreich, W. M. Hess, and L. L. Ban, J. Appl. Crystallogr. **1** (1), 1 (1968).
29. A. S. Fialkov, *Carbon–Graphite Materials* (Énergiya, Moscow, 1979).
30. *Production and Properties of Carbon Black*, Ed. by V. F. Surovikin (Zap.-Sib. Knizhnoe Izd., Omsk, 1972).

Translated by O. Borovik-Romanova

Physics of the Solid State, Vol. 43, No. 5, 2001, pp. 973–981. Translated from Fizika Tverdogo Tela, Vol. 43, No. 5, 2001, pp. 936–943.

FULLERENES AND ATOMIC CLUSTERS

Possible Scheme of Synthesis–Assembling of Fullerenes

F. N. Tomilin[1, 2], P. V. Avramov[2], S. A. Varganov[2], A. A. Kuzubov[2, 3], and S. G. Ovchinnikov[2, 3]

[1] *Institute of Chemistry and Chemical Technology, Siberian Division, Russian Academy of Sciences, Krasnoyarsk, 660049 Russia*

e-mail: felix@iph.krasn.ru

[2] *Kirenskiĭ Institute of Physics, Siberian Division, Russian Academy of Sciences, Akademgorodok, Krasnoyarsk, 660036 Russia*

[3] *Krasnoyarsk State Technical University, Krasnoyarsk, 660074 Russia*

Received June 6, 2000; in final form, October 5, 2000

Abstract—A new scheme of fullerene formation is proposed on the basis of the similarity between the experimentally detected carbon structures. According to experimental data, the microclusters of C_2 and C_{10} are synthesized first and then either an intermediate nucleus cluster or an obtainable lower fullerene is assembled from them. A high-symmetry fullerene can be assembled with a high probability from a nucleus cluster with a "good" symmetry. The atomic and electronic structures of molecules such as C_{36}, C_{60}, C_{70}, and C_{76} are analyzed. For C_{36}, the NMR spectra are calculated and compared with the experimental data. © *2001 MAIK "Nauka/Interperiodica".*

INTRODUCTION

The very fact of the existence of fullerenes with a definite symmetry is astonishing, although the reasons behind the formation of precisely such fullerenes among the variety of carbon structures are unknown. For example, only one isomer for C_{60} (Fig. 1) and for C_{70} with the highest symmetry [1, 2] and, hence, with a minimal entropy has been detected in a macroscopic amount, although a much larger number of isomers can exist theoretically for each molecule. It is not completely clear why only some fullerenes with a definite symmetry are formed under identical conditions. In all probability, a comparison of the peculiarities in the structure of the existing molecules with the theoretically constructed fullerenes would clarify the mechanism of formation of carbon-based nanostructures.

1. A REVIEW OF SOME MODELS

The first assumption explaining the formation of fullerenes was that fragments of monolayers ejected from the surface of evaporating graphite are coiled into a spherical molecule [1, 3]. However, subsequent experiments with carbon isotopes proved that the growth of fullerenes begins from monatomic vapor. According to the experimental data [4, 5], the condensation of carbon atoms follows the following scheme: after the complete mixing of atoms in a plasma, clusters grow in the form of linear chains. After the chain length becomes ten or more atoms, the chains are closed to form stable ring-shaped structures.

At present, several models of the synthesis of fullerene molecules exist [6–11]. These models are mainly constructed using the methods of molecular-dynamic simulation. We will consider models of two types: the droplet model [7–9] and the model of polycyclic structures [10].

In the droplet model, the following mechanism of fullerene formation from the supersaturated carbon vapor is proposed. At the initial stage of the process (condensation), nanosize nuclei are formed. With decreasing temperature, the nuclei are grouped into clusters whose size increases and the structure becomes more and more complex, leading to the formation of fullerenes. Thus, according to the droplet model, the formation of carbon molecules passes through the following three stages: the formation of a nuclei in the form of small linear clusters and their branching; the formation of cycles and of a two-dimensional surface; and the growth of the surface and its closure into fullerene structures.

The droplet model explains the growth of "droplets" (fullerenes) as the result of collisions. The structural rearrangement occurs during the annealing between collisions. However, this model has a number of obvious drawbacks. In particular, it fails to explain the formation of high-symmetry molecules and the absence of structural isomers. For example, apart from the I_h symmetry (Fig. 1), C_{60} can theoretically exist in the form of a molecule with symmetry D_{2d}, C_2, C_{2v}, D_5, etc. Along with the experimentally obtained molecules, the theory erroneously predicts the highly probable formation of undetected fullerenes such as C_{58}.

In the model of polycyclic structures [10], for $N > 20$ (N is the number of carbon atoms), clusters are formed whose structure is interpreted as two coupled rings in the form of a propeller. For $N > 30$, clusters appear in the form of three coupled rings resembling a

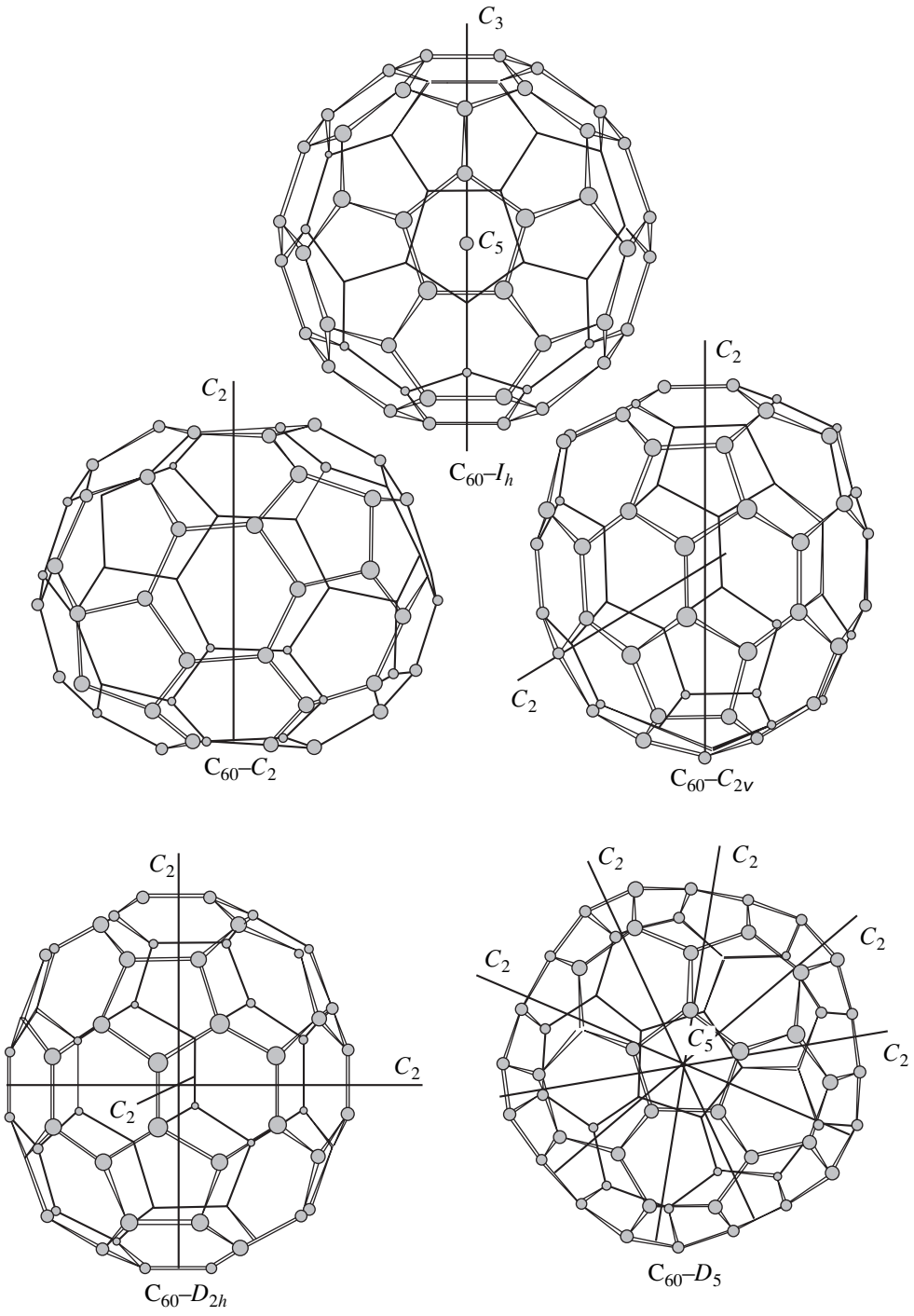

Fig. 1. Some isomers of fullerene C_{60}.

flower bud, and so on. The relative concentration of such polycyclic structures increases with the cluster size, significantly exceeding the concentration of simple rings for $N > 30$. It is assumed that the growth of coarse clusters occurs predominantly through the coagulation of ring structures. Aleksandrov *et al.* [10] analyzed the coiling into a fullerene of the structures consisting of three rings connected to form a bud or a three-blade propeller. The formation occurs through the connection of the nearest atoms at the base of the structure and resembles the closing of a bud. The fullerene formed in this way has an ellipsoidal shape and contains adjacent pentagons (it can also have heptagonal cycles). Subsequently, the pentagons grow apart over a

Table 1. Heat of formation for isomers of fullerene C_{78} calculated using the Hartree–Fock semiempirical method PM3

Fullerene	Heat of formation, K/mol	Experimentally detected fullerenes [13]
C_{78}–C_{2v}	6100	+
C_{78}–C'_{2v}	6075	+
C_{78}–D_3	6115	+
C_{78}–D_{3h}	6110	–
C_{78}–D'_{3h}	6185	–

sphere (as in the droplet model), which leads to a decrease in the angular stress in the structure (Stone–Wales isomerization [12]).

The model of polycyclic structures cannot explain the absence of intermediate fullerenes such as C_{62}, C_{64}, C_{66}, etc., as well as the isomers of C_{60} and C_{70}. In view of its reversibility, the Stone–Wales isomerization generally presumes the existence of several structural isomers for a fullerene, e.g., for C_{60}. However, it can be seen, for example, for higher fullerenes (Table 1) that not all isomers are formed in spite of all the premises including the small difference in energy. The model also predicts a high probability for the existence of

Table 2. Maximum and minimum atomic spacings in fullerene molecules*

Fullerene		Bond length, Å		Fullerene		Bond length, Å	
		min	max			min	max
1	C_{20}–I_h	1.45	1.52	25	C_{54}–C_{2v}	1.38	1.49
2	C_{24}–D_{6h}	1.38	1.52	26	C_{56}–D_2	1.36	1.49
3	C_{26}–D_{3h}	1.38	1.50	27	C_{58}–C_s	1.35	1.49
4	C_{28}–T_d	1.39	1.54	28	C_{60}–I_h	1.38	1.46**
5	C_{30}–C_{2v}	1.36	1.53	29	C_{60}–C_2	1.37	1.48
6	C_{30}–D_{5h}	1.39	1.50	30	C_{60}–C_{2v}	1.45	1.49
7	C_{32}–D_2	1.39	1.52	31	C_{60}–D_{2h}	1.35	1.50
8	C_{32}–D_3	1.39	1.51	32	C_{60}–D_{5d}	1.38	1.49
9	C_{34}–C_1	1.39	1.52	33	C_{62}–C_2	1.37	1.48
10	C_{36}–D_{2d}	1.38	1.50	34	C_{64}–D_2	1.39	1.48
11	C_{36}–D_{3h}	1.37	1.49	35	C_{66}–C_2	1.38	1.48
12	C_{36}–D_{6h}	1.41	1.50	36	C_{68}–C_2	1.39	1.48
13	C_{38}–C_2	1.36	1.53	37	C_{70}–D_{5d}	1.38	1.46***
14	C_{40}–D_2	1.37	1.51	38	C_{76}–D_2	1.37	1.47
15	C_{40}–D_{2h}	1.35	1.53	39	C_{76}–T_d	1.37	1.48
16	C_{40}–D_{5d}	1.40	1.51	40	C_{78}–C_{2v}	1.36	1.47
17	C_{40}–T_d	1.39	1.49	41	C_{78}–C'_{2v}	1.36	1.48
18	C_{42}–D_3	1.37	1.50	42	C_{78}–D_3	1.37	1.47
19	C_{44}–D_2	1.37	1.50	43	C_{78}–D_{3h}	1.35	1.48
20	C_{46}–C_2	1.37	1.50	44	C_{78}–D'_{3h}	1.36	1.46
21	C_{48}–C_2	1.38	1.50	45	C_{80}–I_h	1.39	1.47
22	C_{50}–C_2	1.40	1.49	46	C_{84}–D_2	1.36	1.47
23	C_{50}–D_{5h}	1.38	1.48	47	C_{84}–D_2 (helical)	1.36	1.46
24	C_{52}–C_2	1.37	1.49	48	C_{84}–D_{2d}	1.36	1.47
				49	C_{84}–T_d	1.36	1.46

* The average of the minimum values is 1.38 Å; the average of the maximum values is 1.49 Å.

** Experiment: min 1.37 ± 0.01; max $1.47 \pm \binom{0.01}{0.03}$ [2].

*** Experiment: min 1.39 ± 0.01; max 1.44 ± 0.01 [2].

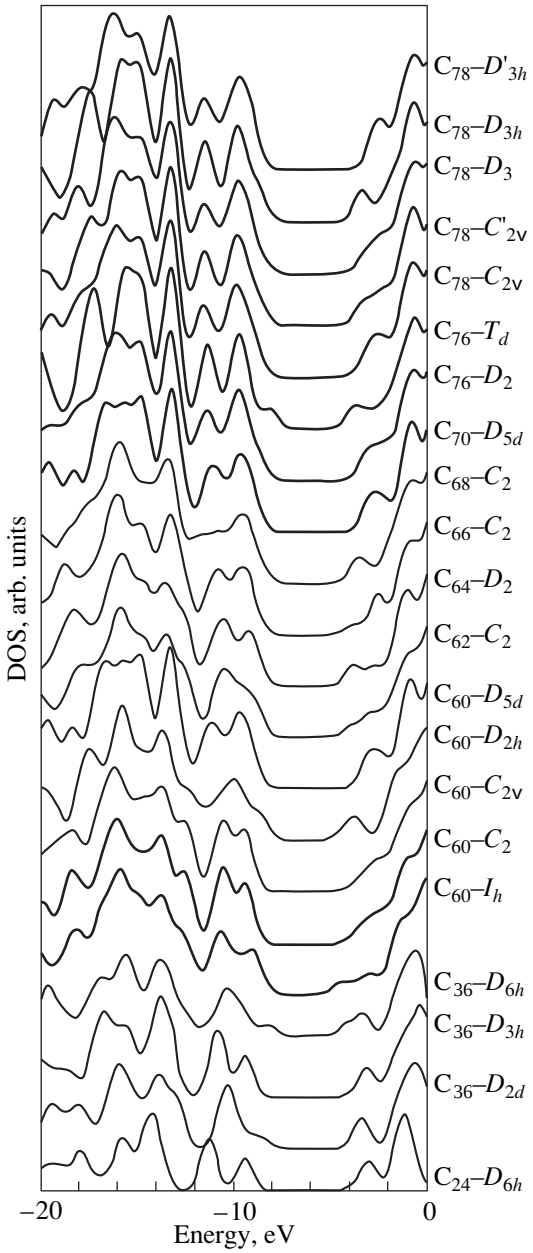

Fig. 2. Total electron densities of states for some fullerene molecules (bold curves correspond to experimentally detected structures).

molecules which have not been detected experimentally.

The electronic structure has been disregarded in the current models of fullerene formation. Simulations of the synthesis conditions have been carried out using the methods of molecular dynamics on the basis of model potentials which do not reflect the complex electronic structure at plasma temperatures (3000 to 5000 K).

The present work is devoted to an analysis of the electronic structure and the energy parameters of the possible fullerenes in the ground state in order to determine the potential difference between the experimentally detected and undetected molecules. The problem was solved using the quantum-chemical approach.

2. QUANTUM-CHEMICAL ANALYSIS

In order to calculate the equilibrium atomic and electronic structures, we applied the Hartree–Fock semiempirical quantum-chemical method PM3 using the program GAMESS [14]. The choice of the quantum-chemical approach was dictated by the fact that the application of semiempirical quantum-chemical methods reduces the computer time as compared to the *ab initio* methods. At the same time, the results obtained by using *ab initio* and semiempirical quantum-chemical methods are in good agreement. Semiempirical methods correctly describe the electronic structure, as well as the equilibrium geometry of the C_{60} and C_{70} molecules (Table 2 also presents, for comparison, the experimental results obtained in [2]). It was proved in [15] that the semiempirical MNDO and PM3 methods reproduce the results obtained by *ab initio* calculations (3–21G) and provide a satisfactory description for the experimental photoelectronic-microscopy data [16]. The semiempirical methods successfully describe carbon-based systems such as fullerenes. Thus, the choice of the semiempirical methods for such systems is quite justified.

In order to determine the behavior of carbon clusters in the atomic and electronic structures, we consider here the maximum number of theoretically possible and experimentally obtained carbon clusters and their isomers. In all, 49 fullerenes were constructed, from C_{20} to C_{84} [13, 17–21]. First of all, we considered the experimentally observed fullerenes C_{60}–I_h, C_{70}–D_{5d}, C_{78}–C_{2v}, C_{78}–C'_{2v}, and C_{78}–D_3 [1, 2, 13] and their isomers, as well as intermediate fullerenes such as C_{40}, C_{42}, …, C_{62}, C_{64}, …. The choice of the isomers was determined by the computer time and by their reasonable number (for example, about five hundred different isomers with trigonal, tetragonal, pentagonal, hexagonal, and heptagonal cycles can be constructed for C_{36} [20]).

Table 2 gives the bond lengths in fullerene molecules. In view of a considerable spread in the values of bond lengths, only the minimum and maximum nuclear spacings were taken for the analysis. It follows from Table 2 that the minimum lengths of the bonds for all the molecules presented here lie in the same interval with an average minimum bond length of 1.38 Å. The same is true of the maximum bond lengths for which the average value is 1.49 Å. Proceeding from the fact that the nuclear spacings for various types of bonds lie in definite intervals, we can assume that the atomic structures of these fullerenes are identical.

The total densities of states were constructed as the energy spectrum of a cluster in which the energy of each molecular orbital was presented as a line, and the

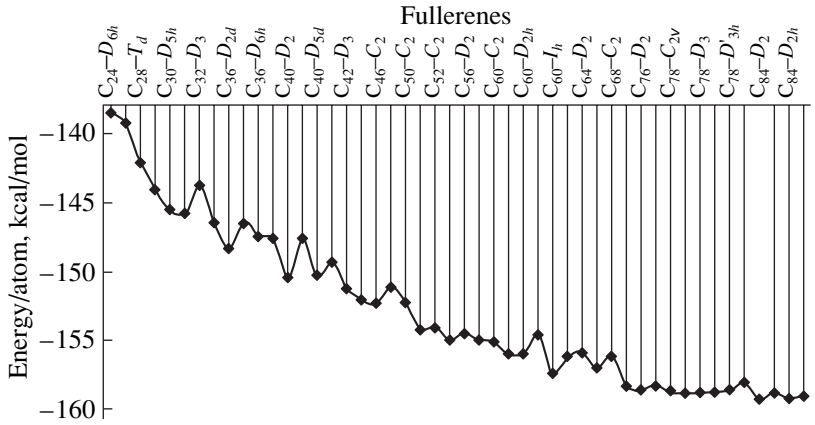

Fig. 3. Dependence of the total energy per atom on the molecular weight of fullerenes.

intensities of all lines were assumed to be equal to unity. Further, each line was replaced by the Gaussian distribution with a half-width of 0.4 eV, and the intensities of all the distributions for each energy value were summed. The electron density distribution in Fig. 2 shows the absence of any basic difference in the structures of the top of the valence bands, primarily in the gap width and the shape of peaks both for known fullerenes and for undetected molecules.

An analysis of the dependence of the total energy per atom on the molecular weight of fullerenes (Fig. 3) indicates a general tendency towards an increase in the fullerene stability upon an increase in their molecular weight. It can be seen from this dependence that the choice according to the total energy per atom in the process of the formation of molecules does not play any significant role. For example, the energies of formation of the experimentally detected fullerenes C_{60} and C_{36} differ approximately by a factor of two, but no intermediate fullerenes (C_{38}, C_{40}, C_{42}, C_{44}, etc.) were detected in macroscopic amounts in spite of the fact that their energies of formation lie in the interval between those for C_{60} and C_{36}.

The right-hand side of the graph in Fig. 3 shows that the difference in the total energy for higher fullerenes is small. This can apparently be explained by the fact that the isomeric effect does not play any significant role here as, for example, in the case of lower fullerenes since pentagons in different isomers are in isolated states. Thus, judging from the energy criterion, all isomers of higher fullerenes must exist since the energy difference between them is small (see Table 1).

A comparison of the electron densities, the bond lengths, and the binding energies of the theoretically predicted molecules shows that, from the viewpoint of the electronic and atomic structures, all fullerenes can rightfully exist. The entropy does not noticeably affect the formation of fullerenes either since isomers with the highest symmetry (I_h for C_{60}) are predominantly formed. Consequently, it can be concluded that the possibility of the formation of a certain isomer of a fullerene cannot be determined proceeding from the atomic and electronic structures and energy stability.

Thus, while constructing the model of the fullerene synthesis on the basis of the analysis of the atomic and electronic structures of calculated carbon clusters, we must exclude such factors as the energy advantage of a certain fullerene or an isomer, the peculiarities of the electronic structure, and the binding energy for the obtained fullerene. Proceeding from the above-mentioned factors, it is impossible to construct a model correctly describing the obtaining of only certain fullerenes and, hence, it is impossible to select the existing molecules by comparing their energies. Consequently, we must determine other conditions affecting the process of fullerene formation.

3. MODEL OF SYNTHESIS–ASSEMBLING OF FULLERENES

After the quantum-chemical analysis was completed, we endeavored to find some other differences morphologically between the obtained and undetected molecules on the basis of the above conclusions. For this purpose, we considered the mutual arrangement of pentagons and hexagons, as well as the fullerene synthesis conditions.

The experiments show (see above, as well as [4, 5]) that first the C_2 (“twos”) and similar structures, as well as the ring structures with a size starting from ten atoms, are synthesized in the plasma from a monatomic vapor, the presence of C_{10} (“tens”) being regarded as preferable [10]. On the basis of these experimental data, molecules were disassembled into their components with the subsequent recognition of similar fragments among detected molecules and with revealing the differences between the experimentally observed and the possible fullerenes.

While disassembling the experimentally detected fullerene molecules (C_{60} with I_h, C_{70} with D_{5h}, C_{78} with

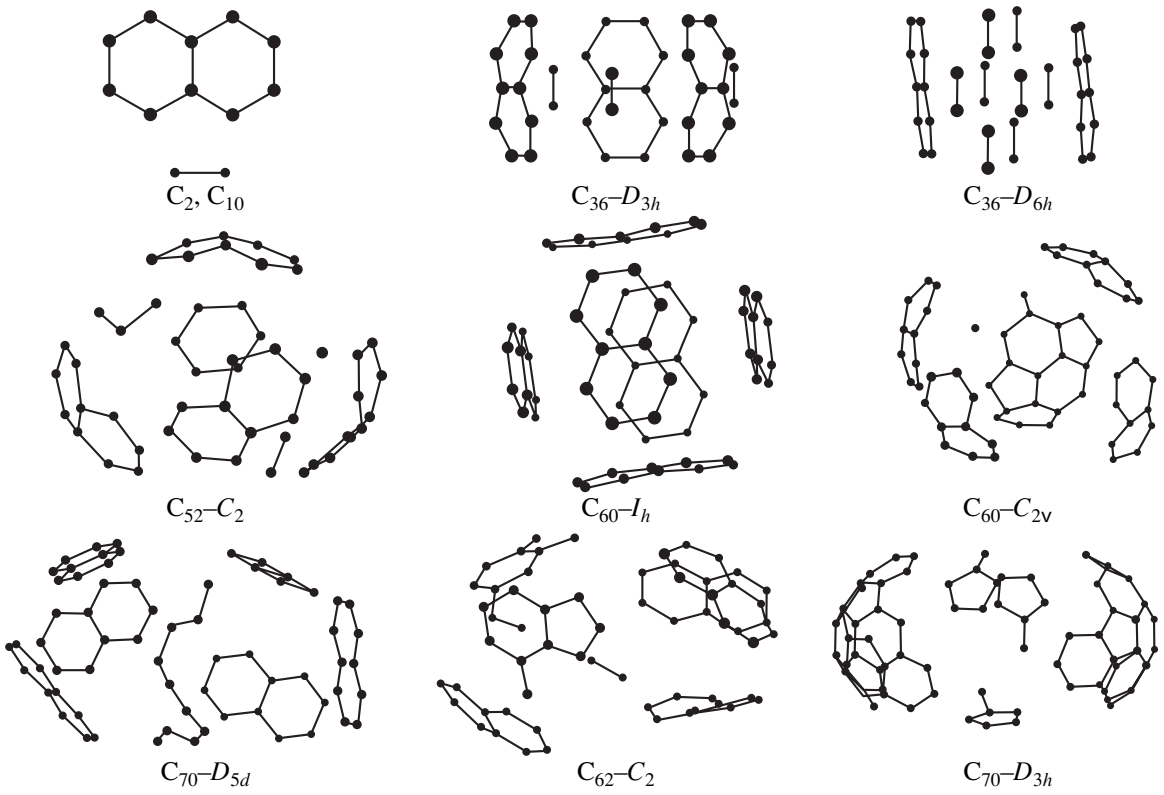

Fig. 4. Various fullerene molecules disassembled visually into components, in which the common fragments C_2 and C_{10} are singled out.

C_{2v}, C_{78} with C'_{2v}, C_{78} with D_3, etc.) into components, we paid attention to the fact that all the existing fullerenes have similar fragments C_2 and C_{10} or only the fragment C_{10} (in the form of a doubled hexagon), as in the case of C_{60} (Fig. 4). The remaining (undetected) fullerenes contain additional fragments in the form of hexagons, solitary carbon atoms, etc., which are not encountered in the experimental data. Consequently, while analyzing the model of fullerene synthesis, we must presume that at a certain stage, fullerenes are probably synthesized via the C_{10} and C_2 structures, which are combined into the "initial" carbon cluster, viz., a nucleus cluster.

Let us now consider a possible process of formation of molecules such as C_{60} and C_{70}. At the first stage, carbon structures are synthesized in the form of linear chains from a monatomic plasma flow [4, 5]. At the second state, the linear structures are closed when the chain length comprises ten or more atoms. Judging from the experimental data, the formation of twos and tens is preferential [10]. Then these structures successively collide and coalesce to form carbon nucleus clusters. At this stage, the C_2 microclusters are also absorbed in the case of C_{70}.

Figure 5 shows a possible course of the formation of carbon clusters. The end product of the synthesis is determined by the symmetry of the nucleus cluster. The figure illustrates a possible course of the synthesis for C_{60} and C_{70} molecules (in the case of C_{70}, five more C_2 fragments are added). For fullerene molecules with the number of atoms greater than 70, the number of fragments in nucleus clusters can exceed three and the dimension of the fragments themselves may be larger.

As the number of nucleus clusters increases, they start colliding, which leads to assembling large clusters followed by crystallization into fullerene molecules. At this stage, we must pay attention to the symmetry of the nucleus clusters obtained, which determines the number of effective collisions leading to the growth of the carbon skeleton. In the case of C_{60}, the nucleus cluster has the principal symmetry axis C_3 (see Fig. 5 (*4*)). In the given case, this is apparently the optimal symmetry since three ways of bonding with a similar cluster are possible (each time, through an angle of $2\pi/3$) (see Fig. 5 (*5*)). It is perhaps for this reason that the probability of the formation of a fullerene on the basis of a nucleus cluster with a low symmetry (C_1) is low, because the cluster structure contains surface regions inaccessible for effective collisions which may lead to the formation of a closed system such as a fullerene.

It should be emphasized that the scheme of assembling presented here is not the only possible scheme;

the formation of the initial clusters with another symmetry and, hence, with a different probability of assembling into a fullerene is also possible.

Piskoti *et al.* [21] recently synthesized the lower fullerene C_{36} in a macroscopic amount. At the same time, they investigated the obtained fullerene by using ^{13}C NMR spectroscopy and compared the results with the theoretical NMR spectra for various hypothetical isomers of C_{36}. We used the synthesis–assembling model constructed by us to analyze the lower fullerene C_{36} and to find its isomer which can be formed in accordance with the results of the NMR experiments. It follows from spatial considerations (see Fig. 4) that in all probability the formation of C_{36} with D_{3h} is easier and preferred.

Piskoti *et al.* [21] stated that the NMR spectrum corresponds to the D_{6h} symmetry. However, the experimental spectrum obtained with such a resolution can be interpreted in a different way. To this end, we theoretically calculated the ^{13}C NMR spectra for three isomers of C_{36}: with D_{6h}, D_{2d}, and D_{3h} (the first two correspond to the fullerenes reported in [21]) by using the GIAO method with the 6–31(d) basis. The experimental spectrum was compared with our theoretical NMR spectra. It can be seen from Fig. 6 that the theoretically calculated spectrum of the molecule with symmetry D_{6h} may correspond to the experimental spectrum. It should be noted that the peak in the experimental spectrum with a chemical shift ~137.5 ppm has a relatively larger half-width than the peak with ~149 ppm, although the areas under these peaks are approximately equal (see Fig. 6b). For this reason, two lines in the peak with the larger amplitude (with a chemical shift of 149 ppm) are closely spaced and give an amplitude twice as large as that in the peak with 137.5 ppm. Similarly, the latter peak may also contain two lines, but their separation is larger than in the peak with 149 ppm; consequently, the 137.5 ppm peak has a larger half-width but a smaller amplitude. The broadening of the peak with the 137.5 ppm shift cannot be explained by the existence of only one isomer with D_{6h} (see Figs. 6c, 6d) as in [21]. The situation is possible when the system contains other isomers, e.g., with D_{3h} (see Fig. 6e), which can explain the experimentally observed broadening of the 137.5 ppm peak. In our opinion, the isomer with the D_{3h} symmetry is advantageous from the spatial considerations (see Fig. 4), although it is less advantageous from the energy point of view (see Fig. 3).

Thus, the synthesis–assembling model of carbon structures presented above can explain the existence of structures C_{36}, C_{60}, C_{70}, … and the absence of many lower fullerenes; the intermediate structures between C_{60} and C_{70} (such as C_{62}, C_{64}, C_{66}, …); and the structural isomers of the C_{60} and C_{70} molecules, as well as the absence of a large number of isomers for the molecules of higher fullerenes since they cannot be assembled from the intermediate clusters C_{10} and C_2. Consequently, the assembling of fullerenes is determined by the symmetry of the nucleus cluster obtained and by the symmetry-dependent probability of the effective collision between the fragments of clusters in the plasma. These factors determine the molecular weight of fullerenes, as well as the number of molecules with a definite symmetry being synthesized.

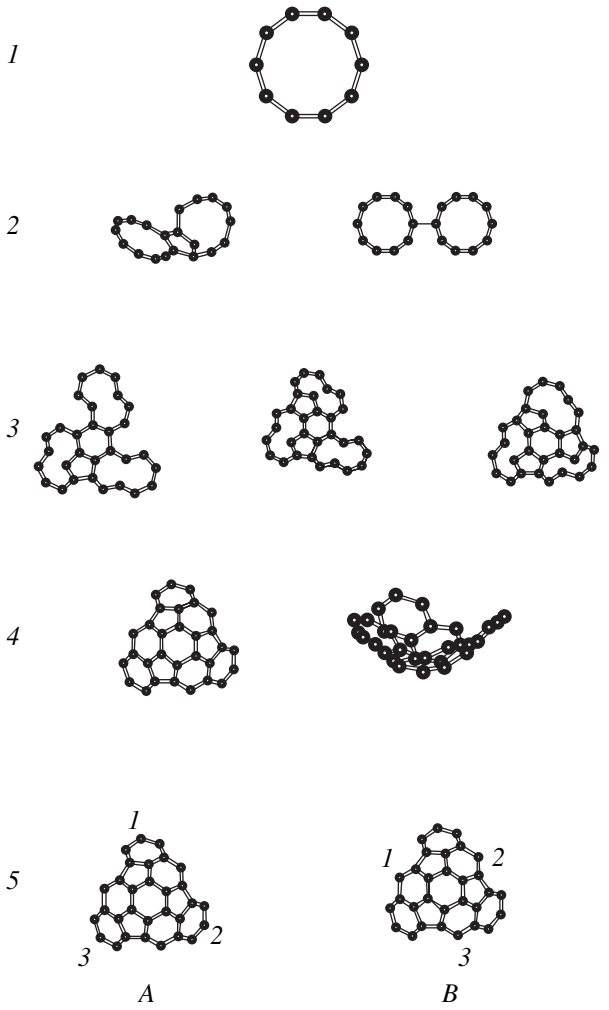

Fig. 5. Hypothetical scheme of synthesis–assembling of fullerene molecules: (*1*) formation of carbon chains from a monatomic vapor; (*2*, *3*) the result of collision of ring structures leading to the formation of one of the possible nucleus clusters; (*4*, *5*) three possible ways of collision between nucleus clusters *A* and *B* (1*A*–1*B*, 2*A*–2*B*, 3*A*–3*B*), (1*A*–2*B*, 2*A*–3*B*, 3*A*–1*B*), (1*A*–3*B*, 2*A*–1*B*, 3*A*–2*B*).

4. CONCLUSIONS

Our results can be summarized as follows.

(1) In order to develop the model of the formation of carbon clusters, we theoretically constructed 49 fullerenes. First of all, the experimentally detected

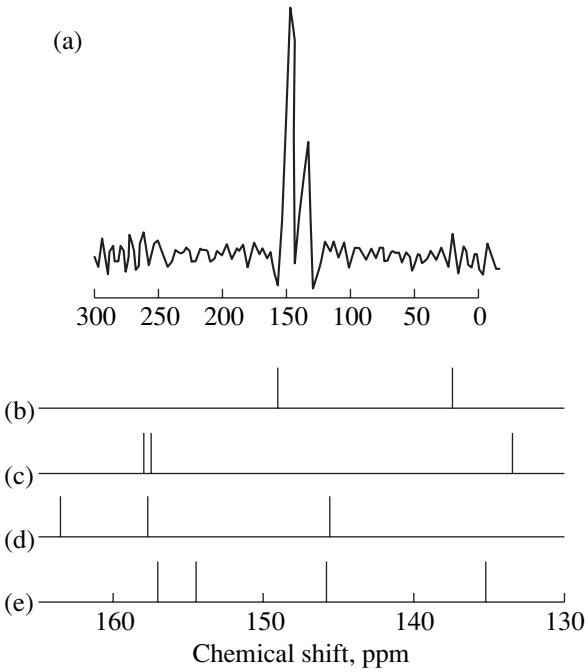

Fig. 6. The ^{13}C NMR spectrum for the lower fullerene C_{36}: (a) experimental spectrum from [21]; (b) experimental spectrum; (c) calculated spectrum for C_{36} with D_{6h} from [21], (d) our calculation of the spectrum for C_{36} with D_{6h}, and (e) our calculation of the spectrum for C_{36} with D_{3h}.

molecules C_{60}–I_h, C_{70}–D_{5d}, C_{78}–C_{2v}, C_{78}–C'_{2v}, and C_{78}–D_3 and their isomers were constructed. Since the symmetry of C_{36} is unknown as yet, we constructed three isomers with D_{6h}, D_{2d}, and D_{3h}. We also considered intermediate fullerenes such as C_{40}, C_{42}, …, C_{62}, C_{64}, ….

(2) The existence of any fullerene with five- and six-atom cycles in the structure is not forbidden from the viewpoint of the atomic and the electronic structure.

(3) The synthesis–assembling model was verified for the recently discovered lower fullerene C_{36}. On the basis of our model and from a comparison with the experimental NMR spectra, it can be predicted that the formation of fullerene C_{36} with D_{3h} is most probable.

(4) We proposed a possible scheme of the formation of fullerene molecules on the basis of "twos" and "tens," which was developed from the similarity of the experimentally detected molecules (their components) and, accordingly, from the difference between the experimentally obtained fullerenes and hypothetical carbon clusters. In this model, the effect of the electronic structure and the energy parameters as factors in the process of high-temperature synthesis can be regarded as insignificant. The Stone–Wales isomerization should apparently also be disregarded.

The impossibility of a correct quantum-chemical simulation under the conditions of the high-temperature synthesis of fullerenes necessitates the construction of formal phenomenological models based on the experimental data concerning the behavior of carbon atoms in the plasma and on the indirect evidence based on the morphological similarity between the experimentally detected carbon clusters.

The probability of effective collisions resulting in the formation of a fullerene with a high symmetry is higher for nucleus clusters with a high symmetry. Consequently, the form of the nucleus cluster determines the symmetry of the future fullerene, its molecular weight, and the number of molecules being synthesized.

ACKNOWLEDGMENTS

This research was carried out at the Collective Center "Quantum-Chemical of Nanoclusters" of the Krasnoyarsk Science and Education Center of High Technologies, which was created with support from the Federal Program "State Support of the Integration of Higher Education and Fundamental Science" (grant no. 69). This study was supported by the State Programs on HTSC (project no. 99019) and "Fullerenes and Atomic Clusters" (project no. 97018), as well as by the NATO Scientific Affairs Division, project PST.CLG 974818.

REFERENCES

1. H. W. Kroto, J. K. Heath, S. C. O'Brien, *et al.*, Nature **318**, 162 (1985).
2. A. V. Eletskiĭ and B. M. Smirnov, Usp. Fiz. Nauk **165**, 977 (1995) [Phys. Usp. **38**, 935 (1995)].
3. D. H. Robertson, D. W. Brenner, and C. T. White, J. Phys. Chem. **96**, 6133 (1992).
4. G. Meijer and D. S. Bethune, J. Chem. Phys. **93**, 7800 (1990).
5. J. M. Hawkins, A. Meyer, S. Loren, and R. Nunlist, J. Am. Chem. Soc. **113**, 9394 (1991).
6. Yu. E. Lozovik and A. M. Popov, Usp. Fiz. Nauk **167**, 751 (1997) [Phys. Usp. **40**, 717 (1997)].
7. S. Maruyama and Y. Yamaguchi, Chem. Phys. Lett. **286**, 336 (1998).
8. S. Maruyama and Y. Yamaguchi, Therm. Sci. Eng. **3**, 105 (1995).
9. T. Yu. Astakhov, G. A. Vinogradov, and Sh. A. Shaginyan, Zh. Fiz. Khim. **2**, 310 (1997).
10. A. L. Aleksandrov, V. M. Bedanov, Yu. N. Morokov, and V. A. Shveĭgert, Zh. Strukt. Khim. **37**, 664 (1996).
11. V. I. Berezkin, Fiz. Tverd. Tela (St. Petersburg) **42**, 567 (2000) [Phys. Solid State **42**, 580 (2000)].
12. A. J. Stone and D. J. Wales, Chem. Phys. Lett. **128**, 501 (1986).
13. X.-Q. Wang, C. Z. Wang, B. L. Zhang, and K. M. Ho, Chem. Phys. Lett. **200**, 35 (1992).
14. M. W. Shmidt, K. K. Baldridge, J. A. Boatz, *et al.*, J. Comput. Chem. **14**, 1347 (1993).

15. S. A. Varganov, P. V. Avramov, and S. G. Ovchinnikov, Fiz. Tverd. Tela (St. Petersburg) **42**, 378 (2000) [Phys. Solid State **42**, 388 (2000)].
16. A. L. Shakhmin, S. V. Murashov, N. V. Baranov, and M. A. Khodorovskiĭ, Fiz. Tverd. Tela (St. Petersburg) **40**, 168 (1998) [Phys. Solid State **40**, 150 (1998)].
17. G. B. Adams, M. O'Keeffe, and R. S. Ruoff, J. Phys. Chem. **98**, 9465 (1994).
18. B. L. Zhang, C. Z. Wang, and K. M. Ho, Phys. Rev. B **47**, 1643 (1993).
19. B. L. Zhang, C. Z. Wang, K. M. Ho, *et al.*, J. Chem. Phys. **97**, 5007 (1992).
20. Z. Slanina, X. Zhao, and E. Osawa, Chem. Phys. **219**, 193 (1997).
21. C. Piskoti, J. Yargen, and A. Zettl, Nature **393**, 771 (1998).

Translated by N. Wadhwa

Physics of the Solid State, Vol. 43, No. 5, 2001, pp. 982–988. Translated from Fizika Tverdogo Tela, Vol. 43, No. 5, 2001, pp. 944–950.

FULLERENES AND ATOMIC CLUSTERS

Optical Spectra of High-Symmetry Isomers $C_{60}(CH_3–r_6–H)_n$ at $n = 3, 6$

S. S. Moliver* and Yu. F. Biryulin**

** Ul'yanovsk State University, ul. L'va Tolstogo 42, Ul'yanovsk, 432700 Russia*
e-mail: moliver@sv.uven.ru
*** Ioffe Physicotechnical Institute, Russian Academy of Sciences, Politekhnicheskaya ul. 26, St. Petersburg, 194021 Russia*
e-mail: biryulin@nano.ioffe.rssi.ru

Received October 19, 2000

Abstract—Earlier, we found the energies of formation and the electron band structures of the fullerene molecule C_{60} and its methylated and hydrogenated chemical derivatives with saturated r_6 bonds of the type $C_{60}(CH_3–r_6–H)_n$ with n from 1 to 6. Based on the self-consistent molecular-orbital method, we found the energies of singlet and triplet excitations for each molecule by the ΔSCF technique. We compared the electron structure of the fullerene molecule with experimental data and other theoretical calculations and showed that the semiempirical quantum-chemical technique used in our work satisfactorily explains the experimental photoluminescence spectra of fullerene-containing star-shaped polystyrenes. Partial or complete removal of the dipole inhibition for the transitions in isomers that are formed upon chemical saturation of double bonds makes it possible to follow changes in the electron structure of the $p\pi$ shell of the fullerene molecule by spectroscopic techniques. Specific optical spectra of the first excited singlet states (spectra of absorption, luminescence, and excitation of luminescence) as well as phosphorescence of the first spin–triplet state are described. © *2001 MAIK "Nauka/Interperiodica".*

INTRODUCTION

Let us consider a chemical modification of a fullerene molecule in which a partial saturation of the covalent bond r_6 that separates two hexagonal faces of the fullerene molecule occurs. The corresponding derivatives with n saturated bonds will be designated $C_{60}(R_1–r_6–R_2)_n$. Such a modification occurs, e.g., upon the methylation of fullerene, when the radical is the CH_3 group, or upon hydrogenation, when the radical is a hydrogen atom. The chemical synthesis of fullerene-containing star-shaped polystyrenes [1] leads to a mixed saturation of the type $C_{60}(CH_3–r_6–H)_n$, where the methyl group represents a polymer chain attached to a fullerene.

The tight-binding model [2] and quantum-chemical calculations [3] show that the change of the electron structure of the $p\pi$ shell upon such chemical modification can be described through the effect of the nearest monomeric unit, e.g., the methyl group. These theoretical conclusions are confirmed by the photoluminescence spectra of films and solutions of fullerene-containing star-shaped polystyrenes with a variable number n of covalently attached polymer rays [2, 4].

Earlier, we found the energies of formation and the electron structures of the fullerene molecule C_{60} and its methylated and hydrogenated derivatives with saturated bonds r_6 of the type $C_{60}(CH_3–r_6–H)_n$ with n from 1 to 6 [3]. The calculations were performed using a quantum-chemical program with a semiempirical parametrization (INDO) in the RHF (restricted Hartri–Fock–Roothan) approximation, since all the above molecules have a closed electron shell (the standard quantum-chemical terminology is used [5]). It was found in particular that the highly symmetric isomers of fullerene, whose saturated bonds are located uniformly over the fullerene surface, have a greater heat of formation than the low-symmetrical ones and, therefore, must be formed in a greater concentration. Based on the self-consistent molecular-orbitals (MOs) method, the energies of singlet excitations were found by the ΔSCF technique for each molecule. These calculations make it possible to represent the shape of the optical spectra of a real mixture of isomers that is formed as a result of the reaction of chemical synthesis and predict how the type of location of saturated bonds affects the polarization dependences.

The aim of this work was as follows:

(1) to complement the spectrum of singlet states [3] with triplet states for both the C_{60} molecule and its isomers with saturated bonds;

(2) to compare the obtained electron structure of the fullerene molecule with experimental data and other theoretical calculations; and

(3) to clarify to what extent the semiempirical quantum-chemical method used in this work is adequate for the explanation of experimental spectra of photoluminescence of fullerene-containing star polystyrenes [2].

1. EXCITED STATES OF THE FULLERENE MOLECULE C_{60}

In the figure below, we give, along with the results of calculations of lower singlet excitations [3], new data on the lower triplet excitations of the fullerene molecule and its most symmetrical isomers with three and six saturated bonds. The ΔSCF calculation method is described in the Appendix; the dimensionality of the expansion was from 591 to 597 determinants, depending on the irreducible representation of the term sought. The excitations of all types with energies that are greater than those shown in the figure form an almost continuous spectrum that begins from the upper levels shown in each band.

The experimental data on the photoluminescence of polymers with covalently bound fullerene [2] can successfully be interpreted with the help of the right-hand half of the figure if the calculated spectrum of the fullerene molecule shown in the left-hand side of the figure is correctly compared with the experiment.

On the whole, the spectrum of excitations agrees with the present-day concepts of the C_{60} molecule (the references below are given not only and not necessarily to the pioneering works, but rather to recent and comprehensive or review papers).

(1) There is a low-located singlet state S_1 ($^1T_{2g}$ = 2.220 eV [3] in the figure); corresponding transitions are shown by dashed arrows. The marking S_1 shows the level 0–0 from which the electron-vibrational lines that are observed in the optical spectra are measured. In experiments, the dipole-forbidden transitions between S_1 and the ground state S_0 can be detected in many ways, e.g.,

(a) in the optical absorption and luminescence of solutions [6–9], e.g., upon freezing to helium temperatures [10]; $S_1 \approx 1.88$ eV was obtained from the mirror-symmetry rule of the luminescence spectra (the lower marking in the figure);

(b) in the spectra of photoexcited luminescence (fluorescence) from cryocrystal matrices of Ne and Ar [11] and in the spectra of two-photon ionization in the gaseous phase [12]; $S_1 \approx 1.94$ eV was obtained by extrapolation of the line spectra based on quantum-chemical calculations of the oscillator strengths upon electron-vibrational transitions (the upper marking in the figure);

(c) in the spectra of energy losses of protons H^+ and H_2^+ ions [13], there are maxima at 2.26 and 1.9 eV, which fall into the range of optical absorption related to the dipole-forbidden singlet transitions.

(2) The dipole-allowed optical electron transition $S_0 \longrightarrow S_n$ (for the symmetry group I_h, this the $^1A_g \longrightarrow {}^1T_{1u}$ transition) is separated from the dipole-forbidden transitions. In the figure, the allowed transition is shown by a solid arrow from the ground state into the state $^1T_{1u}$ = 2.764 eV (which was calculated in our previous paper [3]). In the experiment, this transition is related to a narrow line in the spectrum of optical absorption whose position is only slightly affected by the surroundings of the molecule, irrespective of whether these are the molecules of the solvent or crystal. For a solution of C_{60} in toluene, this is the line at 3.05 eV (407 nm) [14] marked in the figure by S_n. In the spectrum of optical absorption, this line is separated from the absorption band caused by electron-vibrational transitions by a wide dip, which can be related to the absence of singlet solutions in the range of 2.220–2.714 eV in the figure.

In the spectrum of energy losses of protons H^+ [13], the dipole-allowed transition is associated with the maximum 2.98 eV. That fact that it is not so sharp as in optics (although the authors of [13] note that it is the sharpest of all scattering peaks) can be explained by the insufficient selectivity of the method in symmetry; it is seen from the figure that, according to our calculation, there are singlet states $^1T_{1g}$, ^1G_g, $^1T_{2u}$, and ^1G_u close in energy near $^1T_{1u}$.

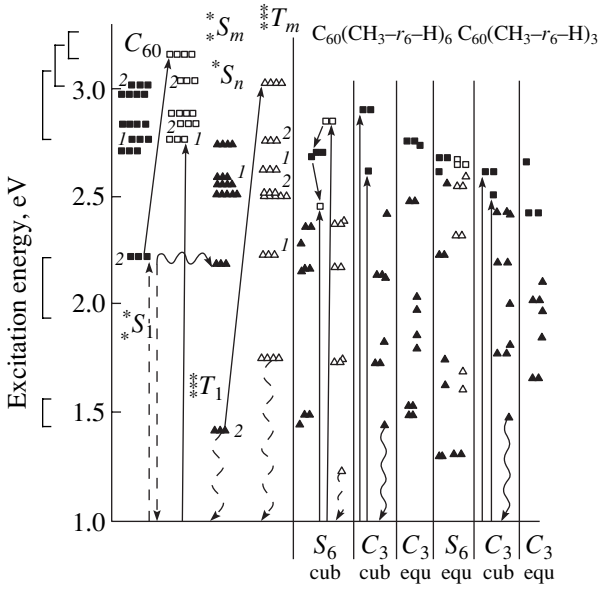

Results of calculations, using the ΔSCF method, of excited states of the fullerene molecule C_{60} and its derivatives of the type $C_{60}(CH_3–r_6–H)_n$. Designations of the excited states: squares stand for singlet states; triangles, triplet states; solid symbols, even states; and open symbols, odd states. The degeneration (1–5 for the fullerene and 1–2 for its derivatives) is indicated by the number of symbols given at a specified level. The numerals *1* and *2* near the orbital triplets of the molecule distinguish the T_{1p} and T_{2p} representations ($p = g, u$ stands for the parity). The spectra of the fullerene derivatives are ordered with respect to the energy of formation [3]; to the left in each line with a given n, the spectrum of the basic isomer is shown. The spectra of isomers are marked by their symmetry group and by the type of the location of saturated bonds [3]. The asterisks correspond to experimental data. The solid arrows show dipole-allowed transitions; dashed arrows, dipole-forbidden transitions; and wavy arrows, spin-forbidden transitions.

(3) The triplet excitations of the C_{60} molecule manifest themselves in the kinetics of the luminescence of the singlet excited state S_1 and, possibly, in the spectra of energy losses of H_2^+ ions [13], when spin transfer from electrons of the fullerene to the electron of the scattered ion is possible. An analysis of the kinetics of luminescence was performed for the model with a single triplet state T_1 below S_1 and led to the magnitude of the singlet–triplet energy gap $S_1 - T_1 = 35 \pm 2$ kJ/mol = 0.36 ± 0.02 eV [6] (in the figure, two of the three markings T_1—the upper and the lower—were obtained by subtracting this experimental value from S_1). According to our calculation, there are four singlet states into which the singlet excitation S_1 can "overflow" as a result of internal conversion rather than one; two of them are the low-lying states ${}^3T_{2g} = 1.414$ eV and ${}^3G_u = 1.750$ eV and it is these states to which the low-energy wing of the luminescence band could be related.

The luminescence of the triplet state (phosphorescence) was observed only at helium temperatures [10]. To provide this luminescence, spin–orbit interaction, which removes the transition inhibition, should be increased; this can be made by adding substances with heavy atoms to the solution (in the above-cited work, ethyl iodide C_2H_5I was used). In the figure, the middle marking $T_1 = 12531$ cm$^{-1} \approx 1.55$ eV represents the experimental position of the phosphorescence maximum [10].

Note that the term ${}^3T_{2g}$ is the most low lying excitation of the molecule C_{60} according to all electron-structure calculations, whereas the data concerning the low-lying singlet states exhibit substantial scatter, which will be considered below. Two triplet states, ${}^3T_{1u}$ and ${}^3T_{1g}$, according to calculations, are close in energy to the first singlet excitation; their existence can explain the extremely efficient internal conversion of the molecule C_{60} after the optical excitation $S_0 \longrightarrow S_1$ [14]. In the figure, this hypothetical transition with small energy transfer, caused by spin–orbit interaction, is shown by a wavy horizontal line; after this transition, the energy can drop rapidly through the triplet levels.

(4) Optical absorption on triplet transitions $T_1 \longrightarrow T_m$ in the band with a maximum at 740 nm (1.68 eV) is observed upon the application of the excitation $S_0 \longrightarrow S_1$ [15, 16]. These experiments made it possible to relate the lifetime of the triplet state T_1 at various temperatures to the density of vibrational modes of the molecule both in the gaseous and condensed phases [17]. If we assume that the maximum is associated with a dipole-allowed transition, this transition should be ${}^3T_{2g} \longrightarrow {}^3G_u$, ${}^3H_u$. According to our calculation, the low-lying states ${}^3G_u = 1.750$ eV and ${}^3H_u = 2.510$ eV do not fit the role of the final state T_m in energy in the experimental spectrum. The IR radiation corresponding to these transitions is possibly not detected at room temperature in solutions; or the matrix elements of these dipole transitions are small. The next excitation of the dipole related to the ground triplet excitation, ${}^3G_u(2) = 3.026$ eV (the highest of the triplet excitations in the figure), can already be compared in energy with the experimentally observed state T_m; this is shown in the figure by a solid arrow.

Turning to the scattering spectrum of H_2^+ ions [13], we find that, most likely, the T_m state is located in the band with a maximum at 3.2 eV: it is only for this band that we obtain $T_1 \approx 3.2 - 1.68 = 1.52$ eV ($\approx$820 nm), which lies in the above-indicated ranges of fluorescence and phosphorescence. Of course, this is a very rough estimate of the position of the ground triplet state, since the scattering spectra in [13] are given on a coarse scale; however, the method itself is a substantial supplement to optical experiments, being selective in spin and nonselective in the dipole moment of excitations.

(5) The optical excitation of even singlet states $S_1 \longrightarrow S_m$ occurs in the absorption band with a maximum at 910 nm (1.36 eV; reckoned from S_1 in the figure) [15]; the solid arrow corresponds to the dipole-allowed transition ${}^1T_{2g} \longrightarrow {}^1G_u(2)$ between the corresponding calculated states.

Thus, the above quantum-chemical calculation satisfactorily describes the whole body of experimental data concerning the excited states of the molecule C_{60}; the deviation of experimental markings from the calculated values is $\pm(0.1–0.3)$ eV (it is shown in the figure by brackets drawn to the left from the energy axis). The error is due to the need for restricting the ΔSCF method in the dimensionality as well as for ignoring the electron correlations in the energy and wave function of the ground state in the Hartree–Fock approximation [18].

The only large discrepancy with some theoretical methods concerns the position of the even singlet states ${}^1T_{1g}$ and ${}^1G_g$ with respect to the first singlet excitation $S_1 = {}^1T_{2g}$; the gap between them was found to be $S_2 - S_1 \approx 0.5$ eV. The basic contribution to all even states comes from the transitions between the HOMO and LUMO states $h_u \longrightarrow t_{1u}$: already in terms of such a 15-dimensional ΔSCF problem the gap proves to be about 0.2 eV. This means that the discrepancy between the results of semiempirical calculations of the $S_2 - S_1$ gap is most likely to be due to the contribution of interelectron integrals of a certain type [5], which, although only insignificantly affecting the electron structure of the ground state, prove to be substantial in the ΔSCF approximation. The INDO (intermediate neglect of differential overlap) parametrization used in this work takes into account a greater number of types of two-center interelectron integrals and, therefore, is more preferable than the CNDO/S parametrization (complete neglect of the differential overlap), which was used when the small value of $S_2 - S_1 \approx 50$ cm^{-1} was obtained in [11]. In view of the low accuracy of quantum-chem-

ical methods, we cannot rely on the fact that the levels of different symmetry proved to be close in energy; this small value has also not been confirmed by calculations based on other parametrizations [19]. Nevertheless, the model with three closely lying excited singlet states is assumed to be correct [19, 20] since it quantitatively explains the large number of electron-vibrational lines in the optical spectra of fullerene molecules in cryocrystalline matrices [11, 12].

On the one hand, the quantitative simulation of spectra in [11] is based on a quantum-chemical estimation of oscillator strengths for various singlet excitations, and the good agreement with experiment indicates the validity of the calculation technique used. On the other hand, the role of empirical factors upon simulation is too large: the calculation is based on a large number of close vibrational frequencies that are known from experiment, which does not always permit one to strictly identify the type of vibration; the spectrum shapes were obtained after an adjustment of the "weights of radiating states" ${}^1T_{2g}$, ${}^1T_{1g}$, and ${}^1G_g$, which also admits other possibilities, e.g., the splitting of the electron term ${}^1T_{2g}$ due to either the field of the cryocrystal matrix (it is not by chance that the weights proved to be different for the Ne and Ar matrices) or to the dynamic Jahn–Teller effect. Thus, the problem of the first excited singlet state of the full-symmetry C_{60} molecule cannot be considered solved and the width of the $S_2 - S_1$ gap should be found by a nonempirical method, i.e., using *ab initio* calculations.

2. EXCITED STATES OF DERIVATIVES OF C_{60} WITH SATURATED BONDS

Now, we turn to the right-hand half of the figure. Note the following features of the excitation spectra of the fullerene derivatives with saturated bonds. From the chemical point of view, the changes in the spectra as compared to the initial molecule are insignificant and can be explained in terms of the tight-binding approximation for the basic $p\pi$ orbitals (radially directed hybrid atomic C 2*p* orbitals). From the point of view of spectroscopy, the changes are more significant and are due to the reduced molecule symmetry: these are, first, partial (S_6) or complete (C_3) removal of the dipole forbiddenness for singlet transitions and, second, the appearance of optical polarization.

2.1. Isomers of $C_{60}(CH_3–r_6–H)_3$. Among the isomers with $n = 3$, the greatest heat of formation is characteristic of the isomer with a C_3 symmetry and a "cube"-type arrangement of saturated bonds (the bonds are located on three neighboring faces of the cube into which the fullerene molecule is inscribed [3]). As can be seen from the spectrum of this isomer in the figure, instead of the singlet states $S_{1, 2, \ldots, n}$ of the fullerene separated by a gap, it has the first singlet excitations ${}^1A$ (σ-polarized transition from the ground state) and ${}^1E$ (π-polarized transition). The spectrum of the optical absorption of the isomer is expected to have significant differences from that of the fullerene, since the transitions into both states are allowed and both are located in the range of the dip in the absorption spectrum; in addition, the two features corresponding to them at the absorption edge of the isomer should have a characteristic ratio of the intensities of the σ and π components equal to 1 : 2. A similar feature should be observed in the excitation spectrum of luminescence of the state ${}^1A$, which is connected by a dipole-allowed transition with ${}^1E$.

In comparison with the luminescent first singlet state of the fullerene $S_1 = {}^1T_{2g}$, the first singlet states of the isomer are shifted upward by 0.3 eV; qualitatively, this agrees with measurements [2].

Because of the low symmetry, the internal conversion in the isomers with $n = 3$ is forbidden only in spin; therefore, the phosphorescence of this isomer (no attempts to detect it experimentally have been made so far) can turn out to be more intense and less prolonged than that of the fullerene; the transition energy, according to calculations, remains almost unchanged (see figure).

2.2. Isomers of $C_{60}(CH_3–r_6–H)_6$. The two isomers with $n = 6$ with the greatest and closest heats of formation have an arrangement of saturated bonds of the "cube" type; apparently, they should be synthesized in almost equal concentrations. The excitation spectrum of the isomer with the C_3 symmetry is similar to that of the above-described isomer with $n = 3$, except that its first singlet excitations are located higher and the splitting of the σ- and π-polarized components is greater by a factor of about 3 (0.3 eV). Thus, the changes in the shape of the luminescence bands and the shift of the energy maximum with changing n (experimentally observed in [2]) are qualitatively reproducible.

Apart from the shape of the band, the excitation spectra (see figure) make it possible to judge the comparative intensity of luminescence in isomer series. Indeed, we see that the luminescence intensity increases in parallel with the shift of the maximum with increasing n (the number of polystyrene chains attached to fullerene [2]). As the reference samples, we used films of C_{60} on silicon obtained by vacuum sublimation and solutions of fullerene in toluene (1 mg per 1 ml). In comparison with these reference samples, the intensity of luminescence of fullerene-containing polystyrenes (FPS) increases severalfold and is maximum for $n = 6$. Taking into account that the concentration of fullerene in FPS samples is a few percent or even a few fractions of a molar percent, we should conclude that the quantum efficiency of the luminescence of the fullerene entering into an FPS increases by more than an order of magnitude. This indicates that the saturation of double bonds of the fullerene molecule C_{60} upon the attachment of polystyrene chains, which leads to the removal of the dipole forbiddance of optical transitions, plays an important role in the mechanism of luminescence. A quantitative comparison requires additional

experiments on the separation of luminescence and absorption bands into isolated components.

For the isomer with the S_6 symmetry, the splitting of σ- and π-polarized components of dipole-allowed singlet transitions is even greater (0.4 eV), but in this case there appears an important feature, namely, an almost unpolarized singlet dipole-forbidden excitation ($^1A_g \approx {}^1E_g$) located between the dipole-allowed excitations. The optical spectra of the luminescence excitation from the ^1A_u state of this isomer should differ in both the shape and intensity from all other spectra shown in the figure, since the decrease in the energy upon transition from the excited state ^1E_u occurs predominantly through the ^1E_g and ^1A_g states rather than directly into the first singlet state $S_1 = {}^1A_u$.

Finally, the energy of phosphorescence of this isomer (see figure) is the lowest of all the others; it is lower by approximately 0.2 eV than that for the fullerene and two other isomers that were considered.

CONCLUSIONS

The above investigation permits us to make the following conclusions.

The partial or complete removal of the dipole forbiddance of the transitions in isomers that are formed upon chemical saturation of n double bonds makes it possible to use spectroscopic methods to follow changes in the electron structure of the $p\pi$ shell of the fullerene molecule.

At $n = 3$ and 6, the greatest heats of formation are characteristic of the isomers of high symmetry with saturated bonds located at the faces of the cube that circumscribes the fullerene molecule.

In comparison with the luminescent first singlet state of fullerene, the center of gravity of the split (into the σ and π components) first singlet state of the isomer with $n = 3$ is shifted upward, into the region of small optical absorption of fullerene; for the two isomers with $n = 6$, this state is located even higher and the splitting into polarized components is greater than for $n = 3$. This qualitatively explains the change in the shape of the luminescence band and the shift in the energy of its maximum with increasing n that was observed in experiment [2].

The isomers with $n = 3$ and 6 and symmetry C_3 should have almost mirror optical-absorption and luminescence spectra with two features at the absorption edge (σ and π components) with a characteristic ratio of intensities of 1 : 2. A similar feature should be observed in their luminescence excitation spectra of the lower (σ-polarized) state, which is connected by a dipole-allowed transition with the upper state. For the isomer with $n = 6$ and symmetry S_6, both the mirror symmetry of the absorption and luminescence spectra and the correlation between the luminescence spectrum and the spectrum of excitation of σ luminescence are broken, since there is an almost unpolarized singlet dipole-forbidden state located between the components of the dipole-allowed excitation.

The internal conversion into the spin-triplet state in the isomers with saturated bonds is forbidden only in spin; therefore, their phosphorescence can prove to be more intense and less prolonged than that of fullerene; the energy of the transition decreases markedly (by about 0.2 eV, according to calculations) only for isomers with symmetry S_6.

APPENDIX

The ΔSCF Method for Electron Excitation of the Ground State with a Closed Shell

Consider a multielectron system with a closed shell. The molecular orbital (MO) method yields for it a single-determinant ground state Φ_0. A quantum-chemical calculation using the restricted Hartree–Fock method (RHF) gives self-consistent MOs of two types: occupied orbitals of type a with two electrons of opposite spins $\sigma = \alpha, \beta$ (the determinant Φ_0 is formed precisely of these orbitals) and unoccupied (virtual) orbitals of type v. We will mark the spatial parts of MOs that are degenerate in energy by primes. Thus, $i = a, v$ means one of the occupied or unoccupied electron shells belonging to the irreducible representation Γ_i of the space group of the multielectron system, and i' will correspond to one of the MOs of this shell (the number i' of MOs is equal to the dimensionality of the representation Γ_i).

The single-electron excitations, according to the Brillouin theorem, should be constructed by replacing one of the MOs entering into Φ_0 (i.e., $a'\sigma'$), by one of the virtual MOs ($v''\sigma''$). For brevity, we will designate such a construction $a'\sigma' \longrightarrow v''\sigma''$ and the corresponding determinant $\Phi^{v''\sigma''}_{a'\sigma'}$. The Brillouin theorem on the orthogonality [5]

$$\langle \Phi^{v''\sigma''}_{a'\sigma'} | \Phi_0 \rangle = 0 \qquad \text{(A1)}$$

provides the possibility of expanding the wave function of an excited state in determinants (A1). If the ground state has only closed (completed) shells, then the orbital energies of the shells found on the basis of self-consistent MOs,

$$\varepsilon_i = \langle i'|h|i'\rangle + \sum_{a_1} \sum_{a_1'' \in a_1} [\langle i'a_1''|g|i'a_1''\rangle - \langle i'a_1''|g|a_1''i'\rangle], \qquad \text{(A2)}$$
$$i = a, v,$$

make it possible to estimate the energies of excitation as $\Delta E \approx \varepsilon_v - \varepsilon_a$ (Koopman's theorem [5]). Here, h denotes the single-electron part of the Hamiltonian (the kinetic energy of electrons and their potential energy in the field of the cores) and g is the two-electron energy (Coulomb repulsion of electrons).

Let us calculate the energy of an excited term Γ. Then, we should choose excitations $a \longrightarrow v$ such that for them the condition

$$\Gamma_a \times \Gamma_v = \Gamma + \ldots \tag{A3}$$

be fulfilled.

The wave functions of the spin–singlet ($^1\Gamma$) and spin–triplet ($^3\Gamma$) terms are constructed in the form

$$\Phi_\Gamma^{(S, M_s)} = \sum_{a, v: \Gamma_a \times \Gamma_v = \Gamma + \ldots} C_{av}^{(S)} \sum_{a' \in a, v'' \in v} \Phi_{a'}^{v''} \Gamma_{a'v''},$$

$$\Phi_{a'}^{v''} = \begin{cases} \dfrac{1}{\sqrt{2}}(\Phi_{a'\alpha}^{v''\alpha} \pm \Phi_{a'\beta}^{v''\beta}), & S = 0, 1;\ M_s = 0 \\ \Phi_{a'\beta}^{v''\alpha}, \Phi_{a'\alpha}^{v''\beta}, & S = 1, \quad M_s = \pm 1. \end{cases} \tag{A4}$$

The symmetrizing (projection) coefficients $\Gamma_{a'v'}$ are given by group relationships, and the expansion coefficients $C_{av}^{(S)}$ should be found by solving the variational problem (they should minimize the quantum-mechanical average of the Hamiltonian of the system for the wave functions (A4)). According to the Slater rules [5], the average is written through the matrix elements

$$H_{a_1'v_1'', a_2'v_2''}^{(S)} = \langle \Phi_{a_1'}^{v_1''} | H | \Phi_{a_2'}^{v_2''} \rangle = \delta_{a_1'a_2'} \delta_{v_1''v_2''} (\varepsilon_{v_1} - \varepsilon_{a_1}) - \langle v_1'' a_2' | g | v_2'' a_1' \rangle + \Delta \langle v_1'' a_2' | g | a_1' v_2'' \rangle, \tag{A5}$$

where $\Delta = 2$ at $S = 0$ (singlet excitation) and $\Delta = 0$ at $S = 1$ (triplet excitation). The variational problem for Eq. (A4) reduces to the eigenproblem of the form

$$\sum_{a_2', v_2''} H_{a_1'v_1'', a_2'v_2''}^{(S)} C_{a_2', v_2''}^{(S)} = \Delta E^{(S)} C_{a_1'v_1''}^{(S)}. \tag{A6}$$

When numerically solving Eq. (A6), there is no need to consider the projection coefficients $\Gamma_{a'v''}$. It suffices to choose those pairs of shells for single-electron excitations that satisfy condition (A3); then, the projection coefficients will factor the coefficients $C_{a'v''}$ in Eq. (A6) and the vector columns constructed of these coefficients will prove to be the partners of all irreducible representations, including Γ, that are formed by direct products (A3) that enter into the expansion.

In order to achieve good accuracy of calculations, it is necessary to perform expansion in as large a number of excited determinants as possible; therefore, the calculations using the ΔSCF method usually begin with the introduction into Eq. (A4) of, primarily, those excitations $a \longrightarrow v$ that have the smallest difference in the orbital energies (A2); then, the convergence of the excitation energies calculated from Eq. (A6) is investigated with increasing dimensionality of the expansion. In this step, the most important advantage of high-symmetry systems manifests itself; many excitations can be eliminated from the expansion from symmetry considerations (A3). Apart from an increase in the accuracy, another aim is achieved in this case: to the calculated excitation energies, an irreducible representation is ascribed, which is necessary to analyze experimental spectra.

The eigenvectors (A6) can be used for group-theoretical analysis of MOs of complex systems. Thus, with only the results of a quantum-chemical calculation of the I_h–C_{60} molecule at hand, it is quite difficult to determine to which of the irreducible representations (T_{1p} or T_{2p}) the triply degenerate shell belongs (the parity $p = g$ and it can easily be determined from the MO LCAO coefficients of atoms connected by inversion). Let, for example, there be need of classifying two completed shells of the same parity $a = t_{iu}, t_{ju}$. We choose any fourfold-degenerate unoccupied shell of arbitrary parity, e.g., $v = g_g$, and numerically solve the problem (A6) at

$$(a \longrightarrow v) = t_{iu} \longrightarrow g_g, \quad t_{ju} \longrightarrow g_g \tag{A7}$$

with 24 determinants in the expansion. For the icosahedron group I, we have

$$T_1 \times G = T_2 + H + G, \quad T_2 \times G = T_1 + H + G,$$

i.e., the excitation $t_{iu} \longrightarrow g_g$ does not contribute to the term T_{iu}. At $i \neq j$, the eigenvectors C_{av}, whose eigennumbers ΔE are triply degenerate, belong to either T_{1u} or T_{2u} and have an easily detectable feature: 12 of its 24 components are zero on that half of excitations (A7) that does not contribute to the corresponding term. The above example shows that the group-theoretical analysis with the help of eigenvectors of the ΔSCF problem can significantly simplify the investigation of the spatial symmetry of MOs.

ACKNOWLEDGMENTS

This work was performed within the framework of the Russian Interbranch Scientific and Technical Program "Fullerenes and Atomic Clusters," project no. 98076 ("Polymer-2"); the work was also supported in part by the Russian Foundation for Basic Research, project no. 98-02-03327.

REFERENCES

1. A. N. Aleshin, Yu. F. Biryulin, N. B. Mironkov, *et al.*, Fullerene Sci. Technol. **6** (3), 545 (1998).
2. Yu. F. Biryulin, V. S. Vikhnin, and V. N. Zgonnik, Fiz. Tverd. Tela (St. Petersburg) **42** (1), 188 (2000) [Phys. Solid State **42**, 197 (2000)].
3. S. S. Moliver and Yu. F. Biryulin, Fiz. Tverd. Tela (St. Petersburg) **42** (10), 1899 (2000) [Phys. Solid State **42**, 1952 (2000)].
4. Yu. F. Biryulin, V. S. Lebedev, S. N. Mikov, *et al.*, Fiz. Tverd. Tela (St. Petersburg) **42** (10), 1904 (2000) [Phys. Solid State **42**, 1958 (2000)].
5. R. McWeeny, *Methods of Molecular Quantum Mechanics* (Academic, London, 1989).
6. F. A. Salazar, A. Fedorov, and M. N. Berberan-Santos, Chem. Phys. Lett. **271**, 361 (1997).

7. J. S. Ahn, K. Suzuki, Y. Iwasa, and T. Mitani, J. Lumin. **72–74**, 464 (1997).
8. J. S. Ahn, K. Suzuki, Y. Iwasa, *et al.*, J. Lumin. **76–77**, 201 (1998).
9. S.-K. Lin, L.-L. Shiu, K.-M. Chien, *et al.*, J. Phys. Chem. **99** (1), 105 (1995).
10. D. J. van den Heuvel, G. J. B. van den Berg, E. J. J. Groenen, *et al.*, J. Phys. Chem. **99** (30), 11644 (1995).
11. A. Sassara, G. Zerza, and M. Chergui, J. Chem. Phys. **107** (21), 8731 (1997).
12. K. Hansen, R. Müller, P. Brockhaus, *et al.*, Z. Phys. D **42**, 153 (1997).
13. C. M. Lock, A. G. Brenton, and D. Mathur, Chem. Phys. Lett. **273**, 1 (1997).
14. V. P. Belousov, I. M. Belousova, V. P. Budtov, *et al.*, Opt. Zh. **64** (12), 3 (1997) [J. Opt. Technol. **64**, 1081 (1997)].
15. G. Sauvé, N. M. Dimitrijević, and P. V. Kamat, J. Phys. Chem. **99** (4), 1199 (1995).
16. A. F. Benedetto and R. B. Weisman, Chem. Phys. Lett. **310**, 25 (1999).
17. H. T. Etheridge III, R. D. Averitt, N. J. Halas, and R. B. Weisman, J. Phys. Chem. **99** (29), 11306 (1995).
18. S. S. Moliver, Fiz. Tverd. Tela (St. Petersburg) **42** (4), 655 (2000) [Phys. Solid State **42**, 673 (2000)].
19. M. Diehl, J. Degen, and H.-H. Schmidtke, J. Phys. Chem. **99** (25), 10092 (1995).
20. A. Sassara, G. Zerza, V. Ciulin, *et al.*, J. Lumin. **83–84**, 29 (1999).

Translated by S. Gorin

Physics of the Solid State, Vol. 43, No. 5, 2001, pp. 989–992. Translated from Fizika Tverdogo Tela, Vol. 43, No. 5, 2001, pp. 951–954.

FULLERENES AND ATOMIC CLUSTERS

Modeling of the Molecular and Electronic Structures of Multiple-Decker Sandwich Macromolecules with η^5–π Bonds on the Basis of Biscyclopentadienyl Derivatives $C_{60}H_{10}$ of a C_{60} Fullerene

E. G. Gal'pern, I. V. Stankevich, and A. L. Chistyakov

Nesmeyanov Institute of Organoelement Compounds, Russian Academy of Sciences, ul. Vavilova 28, Moscow, 117813 Russia
e-mail: stan@ineos.ac.ru

Received October 24, 2000

Abstract—The molecular and electronic structures of the $(CpFe)_2C_{60}H_{10}$ complex of the D_{5d} symmetry, where Cp is the $\dot{C}_5H_5$ cyclopentadienyl radical, are simulated using the *ab initio* Hartree–Fock–Roothaan method in the 3-21*G* basis set. In this complex, hydrogen atoms are attached to carbon atoms of the C_{60} fullerene which occupy α-positions with respect to two oppositely lying five-membered rings. Each FeCp semisandwich moiety is linked to atoms of one of these five-membered rings by the η^5–π-type bond. It is found that the energy of the η^5–π Fe–$C_{60}H_{10}$ bonds in the $(CpFe)_2C_{60}H_{10}$ complex is comparable to that of the η^5–π Fe–Cp bond in the $FeCp_2$ ferrocene molecule. The optimum geometry calculated for the $(CpFe)_2C_{60}H_{10}$ complex is used for modeling of the structure of the quasi-linear macromolecule $[–FeC_{60}H_{10}–]_n$, $n \gg 1$ (**I**). The band structure of the energy spectrum of macromolecule **I** is calculated in the valence approximation of the extended Hückel method within the crystalline-orbital approach. The band gap in the spectrum of macromolecule **I** is ~2.27 eV. The band structure of the spectrum of this macromolecule is compared with the spectra of the hypothetical molecules $[–FeCp–]_n$ and $[–FeC_{20}–]_n$. © *2001 MAIK "Nauka/Interperiodica".*

1. INTRODUCTION

Organometallic polymers have long attracted the attention of physicists and chemists as substances which can be used for fabrication of new current-conducting and magnetic materials.

In principle, organometallic polymers can be of different types. In coordination polymers, for example, metalloporphyrins, metal atoms are directly bonded to each other due to the interaction between the *d* orbitals. Organometallic polymers of other types contain bridge ligands joining the metal atoms. Aromatic cyclic molecules and radicals (for example, the $\dot{C}_5H_5$ cyclopentadienyl radical, the C_6H_6 benzene molecule, chalcogenides, and halides [1]) can serve as bridges. Multiple-decker sandwich compounds $M_n(Cp)_{n+1}$ or $M_n(C_6H_6)_{n+1}$, where Cp = $\dot{C}_5H_5$ and *M* are transition metal atoms, can be considered oligomer precursors of organometallic macromolecules of this type. In these macromolecules, metal atoms are arranged between cyclic ligands (the C_6H_6 benzene molecules or the $\dot{C}_5H_5$ radicals) and are linked to each of them through the η^6–π- or η^5–π-type bond, respectively; i.e., they are bonded to all carbon atoms of these ligands.

The triple-decker complex ($Ni_2Cp_3^+$) was originally synthesized by Werner and Salzer [2, 3]. X-ray diffraction analysis [4] revealed that this complex consists of three parallel cyclopentadienyl rings separated by Ni atoms [3]. However, further attempts to increase the number of fragments in these complexes and to obtain the macromolecules with the η^5–π-type bonds between the repetitive units failed. This can be explained by the decrease in strength of the *M*–Cp bonds in the *M*–Cp*M* fragments with an increase in the number of monomer units in these complexes. At the same time, it was demonstrated that the use of electron-deficient boron-containing heterocycles (for example, the $C_3B_2H_5$ five-membered heterocycle) as bridge ligands made it possible to synthesize the $M_n(C_3B_2H_5)_{n+1}$ oligomers with a sandwich structure and even the $[–NiC_3B_2H_5–]_n$ organometallic polymers. The electrical conductivity of these polymers at room temperature was equal to the conductivity of germanium ($\kappa = 10^{-2}$ s cm^{-1} [1]).

An efficient method for synthesis of the multiple-decker sandwich systems in a gas phase has been developed in recent years. This method is based on the laser-induced evaporation of the substance. In particular, Kaya and coworkers [5], as well as other researchers (see, for example, [6, 7]), succeeded in synthesizing new multiple-decker oligomer and polymer sandwich transition-metal complexes $M_n(C_6H_6)_{n+1}$ (*M* = Co, Ti, etc.) with the η^6–π-type bonds, in which benzene molecules alternate with metal atoms.

Revealing the superconducting properties of alkali metal fullerides stimulated the search for superstruc-

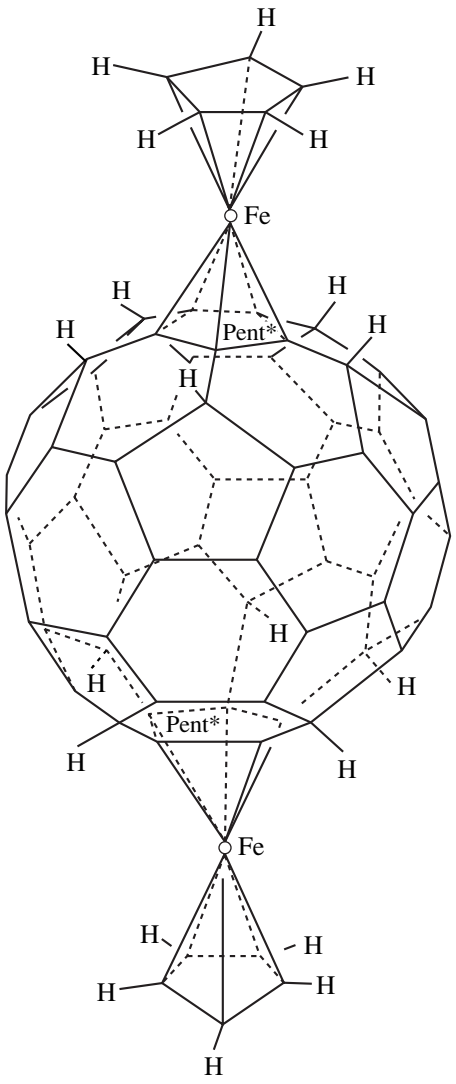

Fig. 1. Complex $2\eta^5$–π-$(FeCp)_2C_{60}H_{10}$ (**Ia**).

tures which could be synthesized from fullerene complexes (or their derivatives) with metals. For example, the complexes $M_n(C_{60})_m$ (where M = Sc, Ti, or V) were prepared by the aforementioned laser method in the gas phase. It was demonstrated by chemical methods that some of these complexes have a multiple-decker sandwich structure in which metal atoms are coordinated in the η^6 mode with atoms of the carbon cage and alternate with C_{60} fullerenes [8–11].

Naturally, the question arises about the possible existence of fullerene complexes of this type but with an η^5–π-type bonding. If these complexes have a quasi-linear structure, they can be considered analogues of the M_nCp_{n+1} structures. In this case, it should be expected that the energy of the η^5–π M–C_{60} bond in these complexes should depend only slightly on the number of monomers due to the remoteness of the five-membered rings of the C_{60} fullerene whose atoms are bonded to metal atoms.

It was shown earlier in our publications [12, 13] that the existence of the stable η^5–π complexes of the polyhedral carbon cluster C_{60} is highly improbable. The reason is that the C_{60} conjugated system is rather strongly delocalized, and the polarization of the atoms of the five-membered face is weak (see also references in [12]). However, when the pure carbon cluster is replaced by its cyclopentadienyl derivatives $C_{60}R_5$, i.e., the systems in which the functional R groups are attached to carbon atoms located in the α-positions with respect to the same five-membered face, the conjugated system is disrupted. This leads to an increase in the probability of the formation of sufficiently stable complexes of the η^5 type. For example, it was proved that the energy of the η^5-type Fe–$C_{60}H_5$ bond in the η^5–π-$CpFeC_{60}H_5$ complex is comparable to the energy of the Fe–Cp bond in the ferrocene molecule [12]. Moreover, the theoretical predictions were confirmed by the synthesis of the semisandwich $MC_{60}Ph_5$ complexes, where M = Li, In, or Tl [14].

Biscyclopentadienyl derivatives of the C_{60} fullerene, namely, the $C_{60}R_{10}$ systems in which the cyclopentadienyl rings separated by R groups are arranged on the opposite faces of this polyhedral biradical, can be considered bulk bridges which join metal atoms into the quasi-linear polymers $[–MR_5C_{60}R_5–]_n$ (**I**).

It was of interest to investigate the current-conducting properties of these polymers and related structures, namely, the hypothetical quasi-linear macromolecules $[–M–Cp–]_n$ (**II**) and $[–M–C_{20}–]_n$ (**III**).

In the present work, this problem was solved for M = Fe as an example. The C_{20} cluster is chosen as a fullerene whose conjugated system had the minimum length. For this reason, the degree of delocalization of molecular orbitals, which are suitable for bonding with the M atom, should be considerably less than that for C_{60}. The synthesis of the C_{20} fullerene in the gas phase was described in detail in [15].

2. CALCULATION PROCEDURE

The monomer systems were calculated by the *ab initio* Hartree–Fock (HF) method in the 3-21*G* basis set using the GAMESS software package [16]. The geometric parameters thus obtained were used for modeling the structure of the repetitive units of macromolecules **I**–**III**. The band structures of the energy spectra of these systems were calculated in the valence approximation of the extended Hückel method [17] within the crystalline-orbital formalism. The calculations were performed with the LATTIC program [18]. The parameters used in the extended Hückel method were taken from [19], in which the triple-decker sandwich structures were investigated. The computations were carried out on a DEC 3000 AXP 400X workstation.

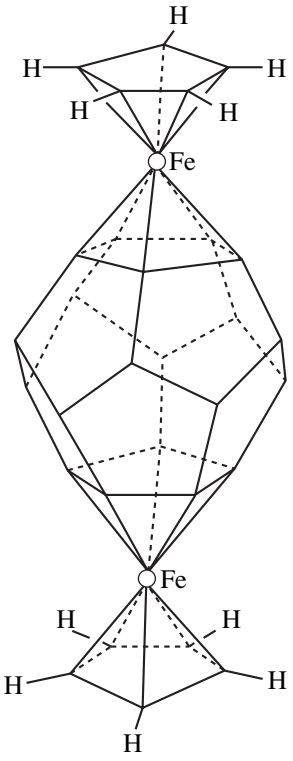

Fig. 2. Complex $2\eta^5$–π-$(FeCp)_2C_{20}$ (**IIIa**).

3. RESULTS AND DISCUSSION

The geometry of the repetitive units of macromolecules **I**–**III** was determined as follows.

(a) The structure of the $(FeCp)_2C_{60}H_{10}$ complex (**Ia**) is shown in Fig. 1. The Fe–$H_5C_{60}H_5$ fragment of this complex can be considered a repetitive unit of macromolecule **I**. It was assumed that complex **Ia** has the D_{5d} symmetry. The local energy minimum was found as a result of the HF/3-21*G* optimization of the energy of this complex by the geometric parameters. The structure which corresponds to this minimum is shown in Fig. 1. Complex **Ia** is a rather stable molecule. The energy of the CpFe–$H_5C_{60}H_5$ bond is comparable to the energy of the Fe–Cp bond in the ferrocene molecule (~78 kcal mol^{-1}, see also [12]). Note that the distance from the Fe atom to the nearest carbon atoms of the fullerene and cyclopentadienyl fragments is approximately the same (differs by 0.02 Å). For this reason, the distance between the Fe atoms, which is equal to 10.1 Å, was taken as the magnitude of the translational vector for macromolecule **I**. The atomic coordinates determined for the $FeC_{60}H_{10}$ fragment of complex **Ia** were used as the atomic coordinates of the repetitive unit of macromolecule **I**.

(b) When constructing the structure of the repetitive unit –FeCp– of macromolecule **II**, we used the results of the *ab initio* calculation of the ferrocene molecule $Fe(Cp)_2$ with the D_{5d} symmetry in the same 3-21*G* basis set. The length of the translational vector for macromolecule **II** was taken to be equal to the distance between the five-membered rings in the ferrocene molecule (~3.33 Å). The atomic coordinates determined for the FeCp fragment of the ferrocene molecule were used as the atomic coordinates of the repetitive unit of macromolecule **II**.

(c) The structure of the $2\eta^5$–π-$CpFeC_{20}FeCp$ complex (**IIIa**) is shown in Fig. 2. The FeC_{20} fragment of this complex can be considered a repetitive unit of macromolecule **III**. It was assumed that complex **IIIa** has the D_{5d} symmetry. The local energy minimum was

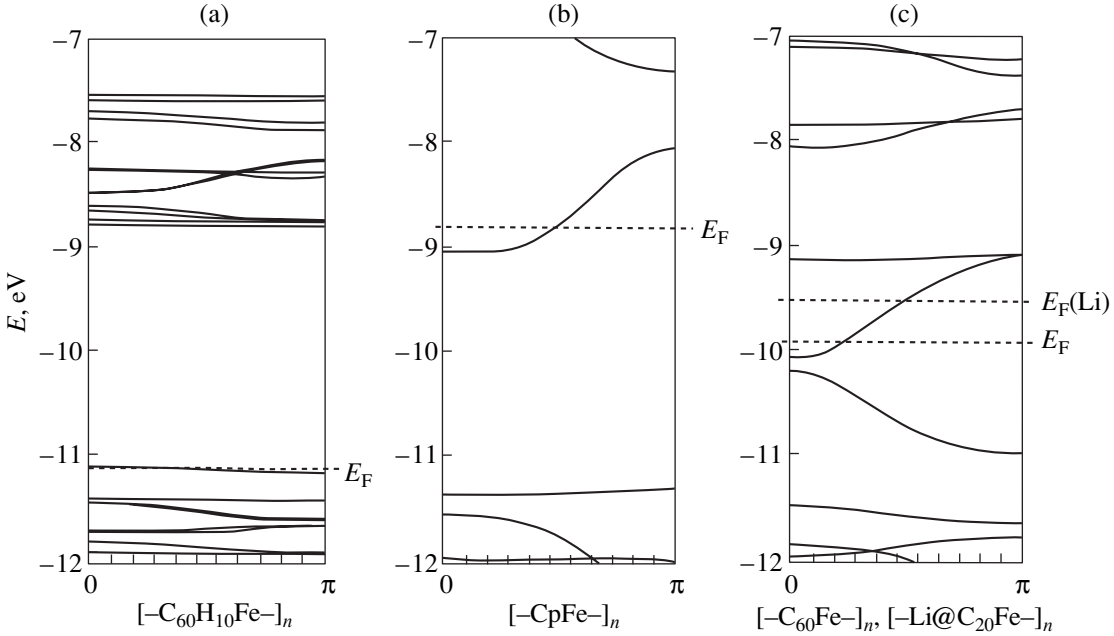

Fig. 3. Schematic diagram of the single-electron energy levels of macromolecules **I**–**III**: (a) $[–C_{60}H_{10}Fe–]_n$ (**I**), (b) $[–CpFe–]_n$ (**II**), and (c) $[–FeCp_{20}–]_n$ (**III**) and $[–Li@C_{20}Fe–]_n$ (**III'**).

found as a result of the HF/3-21*G* optimization of the energy of this complex by the geometric parameters. The structure which corresponds to this minimum is shown in Fig. 2. Complex **IIIa** is a rather stable molecule. The energy of the $CpFe–C_{20}$ bond is equal to ~76 kcal mol^{-1}. The length of the translational vector for macromolecule **III** was taken to be equal to the distance between the iron atoms (7.27 Å). Atomic coordinates of the FeC_{20} fragment of complex **IIIa** were used as those for the repetitive unit of macromolecule **III**.

The variance curves for the single-electron spectrum of macromolecule **I** are shown in Fig. 3a. It is seen that this spectrum has a semiconductor character with a band gap of ~2.27 eV. This character of the spectrum can be associated with the disturbance of the conjugated system in the macromolecule due to attachment of the H atoms to C_{60} fullerenes.

The spectrum of macromolecule **II** is displayed in Fig. 3b. The elementary fragment of **II** contains an odd number of electrons. Therefore, this spectrum has a metallic character with a rather narrow top of the valence band. Its width is as small as ~0.3 eV.

The spectrum of macromolecule **III** is shown in Fig. 3c. This spectrum has a metallic character. The top of the valence band is also narrow (~0.2 eV). This character of the spectrum indicates that molecule **III** can be considered a quasi-linear conjugated system with a nearly uniform distribution of conduction electrons.

The spectrum of the $[–Li@C_{20}Fe–]_n$ ($n \gg 1$) fragment of macromolecule **III'** is also shown in Fig. 3c. It was assumed that one Li atom is located at the center of each fullerene. It turned out that the variance curves for the doped **III'** and undoped **III** systems in the vicinity of the Fermi level are virtually identical. The Fermi level shifts upward by ~0.45 eV, and the band gap increases.

In conclusion, we note that macromolecule **I** is of most interest among three hypothetical macromolecules under consideration. For this molecule, the energy of the η^5–π M–$C_{60}H_{10}$ bonds is comparable to the energy of the η^5–π Fe–Cp bond in the ferrocene molecule. Moreover, this energy should depend weakly on the number of repetitive units, because the metal atoms are widely spaced in the molecule. The macromolecules built up of the $MC_{60}R_{10}$ particles do not necessarily have a quasi-linear structure. Two-dimensional or three-dimensional systems can be formed depending on the mutual arrangement of the cyclopentadienyl fragments of the $C_{60}R_{10}$ biradical.

ACKNOWLEDGMENTS

This work was supported by the Russian Foundation for Basic Research (project nos. 98-03-33016 and 99-02-17578), the Scientific and Technical Program "Fullerenes and Atomic Clusters," and the Ministry of Science (project no. 9.4.06).

REFERENCES

1. W. Siebert, Usp. Khim. **60** (7), 1553 (1991).
2. H. Werner and A. Salzer, Synth. React. Inorg. Met.-Org. Chem. **2**, 239 (1972).
3. A. Salzer and H. Werner, Angew. Chem. **84**, 949 (1972).
4. E. Dubler, M. Textor, H. R. Oswald, and A. Salzer, Angew. Chem. **86**, 125 (1974).
5. K. Hoshino, T. Kurikawa, H. Takeda, *et al.*, J. Phys. Chem. **99**, 3053 (1995).
6. T. Kurikawa, M. Hirano, H. Takeda, *et al.*, J. Phys. Chem. **99**, 16248 (1995).
7. T. Yasuike, A. Nakajima, S. Yabushita, and K. Kaya, J. Phys. Chem. **101**, 5360 (1997).
8. T. Yasuike and S. Yabushita, J. Phys. Chem. A **103**, 4533 (1999).
9. S. Nagao, Y. Negishi, A. Kato, *et al.*, J. Phys. Chem. A **103**, 8909 (1999).
10. A. Nakajima and K. Kaya, J. Phys. Chem. A **104**, 176 (2000).
11. M. Hirano, K. Juda, A. Nakajima, and K. Kaya, J. Phys. Chem. A **101**, 4893 (1997).
12. A. L. Chistyakov and I. V. Stankevich, Izv. Akad. Nauk, Ser. Khim., No. 9, 1649 (1999).
13. A. L. Chistyakov, I. V. Stankevich, and N. P. Gambaryan, Izv. Akad. Nauk, Ser. Khim., No. 5, 855 (1995) [Russ. Chem. Bull. **44**, 828 (1995)].
14. M. Sawamura, H. Iikura, and E. Nakamura, J. Am. Chem. Soc. **118**, 12850 (1996).
15. H. Prinzbach, A. Weiler, P. Landenberger, *et al.*, Nature **407**, 60 (2000).
16. W. Schmidt, K. K. Baldridge, J. A. Boatz, *et al.*, J. Comput. Chem. **14**, 1347 (1993).
17. R. Hoffmann, J. Chem. Phys. **39**, 1397 (1963).
18. D. A. Bochvar, E. G. Gal'pern, and I. V. Stankevich, Zh. Strukt. Khim. **29** (1), 26 (1988).
19. J. W. Lauher, M. Elian, R. H. Summerville, and R. Hoffmann, J. Am. Chem. Soc. **98**, 3219 (1976).

Translated by N. Korovin